APPLICATIONS OF QUANTITATIVE METHODS AND CHAOS THEORY IN ICHNOLOGY FOR ANALYSIS OF INVERTEBRATE BEHAVIOR AND EVOLUTION

by

James Richard Woodson Lehane

A dissertation submitted to the faculty of
The University of Utah
in partial fulfillment of the requirements for the degree of

Doctor of Philosophy

in

Geology

Department of Geology and Geophysics

The University of Utah

August 2014

The University of Utah Graduate School

STATEMENT OF DISSERTATION APPROVAL

The dissertation of **James Richard Woodson Lehane**

has been approved by the following supervisory committee members:

Allan A. Ekdale	, Chair	**May 5th, 2014** Date Approved
Randall B. Irmis	, Member	**June 6th, 2014** Date Approved
Marjorie A. Chan	, Member	**May 5th, 2014** Date Approved
Elena A. Cherkaev	, Member	**June 12th, 2014** Date Approved
Leif Tapanila	, Member	**June 6th, 2014** Date Approved

and by **John M. Bartley**, Chair/Dean of

the Department/College/School of **Geology and Geophysics**

and by David B. Kieda, Dean of The Graduate School.

ABSTRACT

Trace fossils are the result of animal behaviors, such as burrowing and feeding, recorded in the rock record. Previous research has been mainly on the systematic description of trace fossils and their paleoenvironmental implications, not how animal behaviors have evolved. This study analyzes behavioral evolution using the quantification of a group of trace fossils, termed graphoglyptids. Graphoglyptids are deep marine trace fossils, typically found preserved as casts on the bottom of turbidite beds. The analytical techniques performed on the graphoglyptids include calculating fractal dimension, branching angles, and tortuosity, among other analyses, for each individual trace fossil and were performed on over 400 trace fossils, ranging from the Cambrian to the modern.

These techniques were used to determine various behavioral activities of the trace makers, including feeding and behavioral evolution. Graphoglyptids have been previously identified as representing mining, grazing, farming, and/or trapping. By comparing graphoglyptids to known mining burrows and grazing trails, using fractal analysis, it was possible to rule out mining and grazing behaviors for graphoglyptids. To determine between farming and trapping, a review of all known trapping burrows was required. The hypothesis that graphoglyptids were trappers was based entirely on the hypothesized feeding behaviors of the worm *Paraonis*. Close examination of *Paraonis* burrows indicated that the burrows are not traps. This means that, since *Paraonis* does

not trap prey, graphoglyptids should not be considered traps either. Therefore, graphoglyptids likely represent farming behavior.

This study also shows that previous interpretations of graphoglyptid behavioral evolution was far too simple. The results of the morphological analyses indicate that major changes to the behavioral evolution occurred during the Late Cretaceous and the Early Eocene. Previous hypotheses about Late Cretaceous evolutionary influences were validated. However there were additional influences like the Paleocene-Eocene Thermal Maximum that were not overly emphasized before. Finally, of the many theories about the driving force of evolution, chaos theory has often been overlooked. Chaos theory is a powerful tool, such that, by knowing the similarities between chaos theory and evolutionary theory, it may be possible to map out how environmental changes could shift the evolution of a species.

This dissertation is dedicated to my lovely daughter, who has taught me the valuable lesson that no hardship is too tough, that you can't press on through it.

"For our own species, evolution occurs mostly through our behavior. We innovate new behavior to adapt."
—Michael Crichton, *The Lost World* (1995)

TABLE OF CONTENTS

LIST OF TABLES

ACKNOWLEDGEMENTS

This project, which has been five years in the making, has been helped and influenced by a lot of people and I would be remiss to not include or acknowledge at least a few of those people. I would like to thank my advisor, Tony Ekdale, for excellence in guidance and becoming an ichnological father figure to me. I thank the rest of my dissertation committee as well, Marjorie Chan, Leif Tapanila, Randy Irmis, and Elena Cherkaev, for providing guidance and insight into aspects of my research that I had not considered before and opening my eyes to new possibilities. I am especially indebted to Tommy Good, Andreas Wetzel, and Paula Dentzien-Dias for field work in Spain; Alfred Uchman, Jolanta Gruza, Quintin Sahratian, Elizabeth Gierlowski-Kordesch, and Mark Goodwin for museum, paleontological, and sample assistance; William Miller, Murray Gingras, Waldemar Obcowski, Andrew Milner, and Louis Buatois for geological and paleontological field and sample information; Dirk Knaust and Roy Plotnick for manuscript suggestions; Ron Bruhn, Lucas van Vliet, Kees van der Voort Maarschalk, Andreas Baucon, Jordi de Gibert, and Glen Mackie for mathematical and computer programming assistance; Małgorzata Bednarz and Serjoscha Evers for help in translations.

Life in graduate school would not be complete without sharing the trials with other students, officemates, and friends. Those friends who have impacted this research in both big and small ways include Sherie Harding, Matthew Heumann, Jared Gooley,

Ian Semple, Steve Pinta, Brendon Horton, Patrick Dooling, Luke Pettinga, Deanna Brandau, Morgan Rosenberg, Andrew McCauley, Tyler Szwarc, Joshua Lively, Carrie Levitt, Heather Judd, Mark Gorenc, Brenton Chetnik, Ryan Purcell, David Wheatley, Leah Toms, Julia Mulhern, Simon DeRuyscher, Nathan McClenathan, and Brett Nolan.

While I have been here I have had the privilege to teach several labs under the guidance of John Bowman and Paul Jewell, without whom I would have been lost. Other funding was made possible by the ExxonMobil Geoscience Grant for Students, the William Lee Stokes Graduate Fellowship from the Department of Geology & Geophysics, and the Graduate Research Fellowship from the University of Utah. I also wish to acknowledge all of the societies and journals who have allowed me to reprint their material within this dissertation. Their individual acknowledgements are listed within the text.

I would not be where I am today without the continued support through all of my schooling from my family, especially my mom, my dad, and my sisters. And last, but certainly not least, I could not have done this without the relentless support of my wife, Veronica, and the understanding from my daughter, Annabelle, who usually let daddy work when he needed to.

CHAPTER 1

INTRODUCTION AND BACKGROUND

1.1 Overview

1.1.1 Introduction

Ichnology (the study of trace fossils) is an important field in geology and paleontology for many reasons, but mainly because trace fossils are autochthonous (found in place) indicators of paleoecological conditions. The autochthonous nature of trace fossils removes some of the doubt that is present when working with other paleoecological indicators (like invertebrate body fossils) that can become easily reworked, erasing important information in the process. Trace fossils provide an ecological usefulness that is not available from body fossils, because one animal will leave behind one skeleton (at most), but it could leave behind a countless number of footprints or a seemingly endless line of burrow trails, making them the most abundant type of fossils in the fossil record.

Trace fossils result from animal behaviors, such as crawling, walking, burrowing, and feeding, which have been recorded in the rock record. For most of the nearly two centuries of ichnological research, focus has been mainly on the systematic description of trace fossils and their paleoenvironmental implications. Much less emphasis has been focused on how animal behaviors have evolved through time.

1.1.2 Purpose and approach

The focus of this dissertation is to study the trace fossil record of invertebrate feeding patterns in the deep-sea through geologic time by employing quantitative descriptive methods. Behavioral evolution is an important topic, since animal behavior is one of the principal driving forces of evolution. Anatomical evolution proceeds in concert with behavioral evolution to drive the ways that species act and interact. The vast majority of studies in evolutionary paleontology deal strictly with morphologic changes expressed in body fossils. However, in exploring the long evolutionary history of life on Earth, the evolutionary trends of behavioral aspects should not be ignored. Without attempting to understand how behaviors evolve, we can only hope to understand one half of the equation. While some types of animal behavior are unpreservable, there are many aspects that in fact do have a potential for preservation as trace fossils. As discussed at length by many authors (e.g., see Seilacher, 1967, 2007; Ekdale et al., 1984a; Ekdale, 1985; Bromley, 1996; McIlroy, 2004; Buatois and Mangano, 2011), these preservable aspects include diverse modes of feeding, dwelling, and locomotion.

Ichnologists often describe trace fossils using vague descriptors like "narrow," "dumbbell-like," and "free meanders" (Häntzschel, 1975), but rarely, if ever, do they provide quantitative descriptions of the trace fossils. The problem with qualitative descriptions is that their precise meaning is hard to pin-point exactly. Different authors could assume different meanings for the same terms. Testing a qualitative hypothesis provides a weak test. For example, if something is either "meandering" or "not meandering," there is no middle ground with types, sizes, and/or degrees of meandering (Turchin, 1998). Quantitative descriptors offer a more precise basis for analyzing the

trace fossil. They are less ambiguous and subjective to what they are illustrating. A five centimeter wavelength on a meander is a five centimeter wavelength; there is no confusion. Qualitative hypotheses also allow for more definitive tests. Instead of a "yes" or "no" answer, there is "yes," "no," and "how much." If the previously mentioned trace fossil is meandering, there are specific questions that can be answered, like "how much is it meandering" and "are the sizes of the meanders consistent" (Turchin, 1998).

One of the problems with Euclidean quantitative analyses is that there are a limited number of measurements that can be made. Beyond length, width, and thickness, ichnologists are often hard pressed to come up with other linear measurements that can be made. Lengths and widths also do not work well when dealing with trace fossils that could represent different ontogenetic stages of the trace maker's life or imperfect preservation of the trace fossil. When dealing with traces of varying ontogenetic stages, it is often best to use non-Euclidean (nonlinear) measurement techniques that will provide similar results for a wide range of trace fossils that contain a similar structure but vary in scale. In many cases, they produce consistent numbers that can be used as comparison tools among many different trace fossils. This approach also is useful for trace fossils that are incompletely preserved. Typically if you only have a fraction of a trace fossil, it is difficult to ascertain all the information you need from it, but with scale-invariant measurement techniques you can obtain similar results from a whole trace fossil as you would from a partial one. As long as the fossil is preserved as a complete, substantial piece, nonlinear techniques are useful.

Computer simulations of idealized feeding patterns have been attempted by several workers (Raup and Seilacher, 1969; Papentin, 1973; Hammer, 1998; Plotnick,

2003; Plotnick and Koy, 2005), but computer analyses of actual trace fossils from the real world have not been accomplished to any appreciable extent. The analytical approach of this project includes morphometrics (quantitative characterization of morphologic attributes) of actual graphoglyptid (discussed below) trace fossils in two-dimensional space using a variety of mathematical techniques, including fractal analysis (Mandelbrot, 1983; Feder, 1988; Slice, 1993), which has been applied only rarely in the field of ichnology (Jeong and Ekdale, 1996, 1997; de Gibert et al., 1999; Puche and Su, 2001; Le Comber et al., 2002; Romanach and Le Comber, 2004; Katrak et al., 2008; Baucon, 2010). Measurements of topology, tortuosity, occupied space percentage, branching angles, and burrow area shape also are employed. Use of such objective mathematical techniques allows a quantifiable interpretation of the trace fossils and provides a view of them with both size-dependent and size-independent parameters.

1.2 Graphoglyptids

To study the evolution of behavior meaningfully, it is useful to limit the scope of the trace fossils that are being analyzed. The most promising trace fossils for analyses are those that are limited in sedimentologic extent and distributed over a long time period. The purpose of this project is to study the behavioral evolution of highly patterned deep-marine invertebrate feeding patterns, commonly referred to in the literature as "graphoglyptids" and/or "agrichnia" (Fuchs, 1895; Seilacher, 1977; Ekdale, 1980; Miller, 1991b; Uchman, 1995, 2003; Wetzel, 2000), using new quantitative methods (Fig. 1.1).

The use graphoglyptid trace fossils enables the comparison of traces made in a very stable, consistent environment, since graphoglyptids are almost invariably preserved

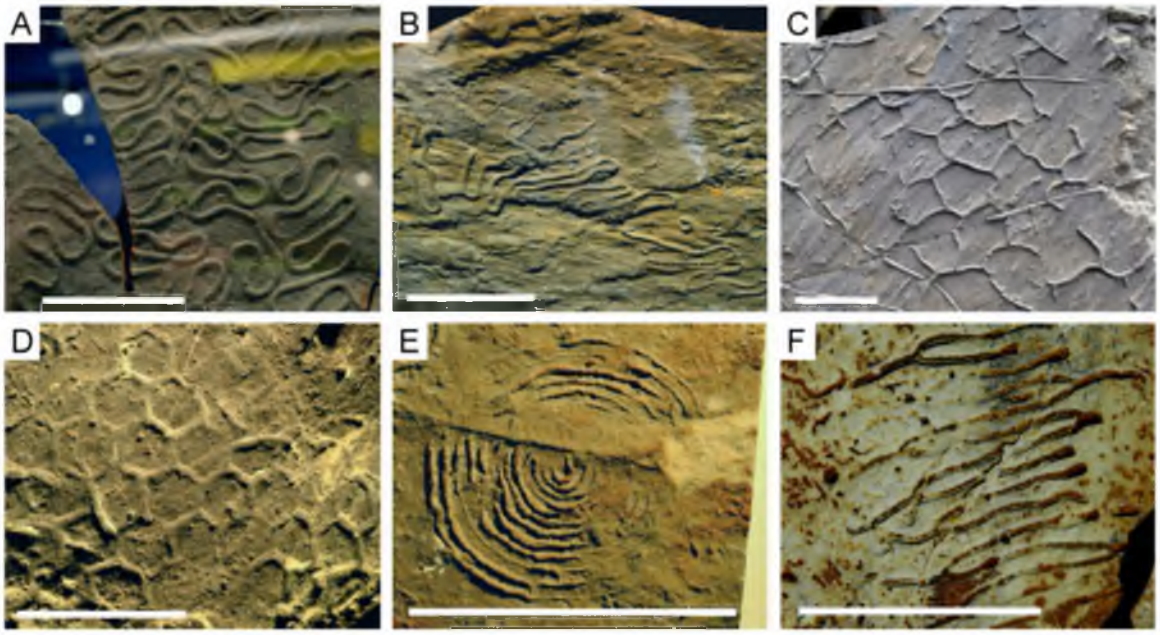

Figure 1.1. Images of some common graphoglyptids. A) *Cosmorhaphe* from the Paleocene to Lower Eocene Variegated Shales of Poland. Sample number UJTF-2684. B) *Helminthorhaphe* from the Oligocene Krosno Beds of Poland. Sample number UJTF-1362. C) *Megagrapton* from the Early Eocene Guipuzcoan Flysch of Zumaia, Spain. Field photograph of sample labeled Z_Megagrapton1. D) *Paleodictyon* from the Jurassic Longobucco Sequence of Calabria, Italy. Sample number UUIC-721 E) *Spirorhaphe* from the Late Cretaceous of Kilwa, Tanzania. Sample number UUIC-1904. F) *Urohelminthoida* from the Messinian Azagador Limestone from the Vera Basin, Spain. Field photograph by A.A. Ekdale of a sample labeled VBUrohelm1. Scale bars are 5cm. UJTF = Institute of Geological Science, Jagiellonian University, Kraków, Poland, Trace Fossil. UUIC = University of Utah Ichnology Collection, Salt Lake City, Utah.

from the deep-sea on the base of turbidite beds, through time and across geographic boundaries. The deep sea is the largest and most stable single habitat on Earth. This fact suggests that animals and animal behaviors in the deep sea likely evolved very slowly through time (Seilacher, 1974). This dissertation provides insights about the rate of behavioral evolution, what factors influenced the evolution of behavior, and what feeding methods are represented by different burrow patterns.

1.2.1 Graphoglyptid history

The study of animal behavior in the fossil record goes back at least as far as 1836, when Edward Hitchcock first started looking at vertebrate footprints preserved in Triassic strata of the Connecticut River Valley (Hitchcock, 1858). He recognized that the fossil trackways directly reflect the locomotory behavior of extinct beasts. The vertebrate traces were easier to identify, because ancient footprints preserved in rocks look very much like modern footprints in modern sand and mud. Invertebrate traces, however, were a little more difficult to discern. A century or two ago, many invertebrate traces were thought to be the products of algal growths (fucoids) or plants. Alfred Nathorst (1873) demonstrated that many of these types of fossils actually were organism traces that had counterparts in modern sedimentary environments.

In 1895, Theodor Fuchs described a group of trace fossils that he found on the soles of turbidite beds. Fuchs used the term "Graphoglypten" to describe these problematical fossils that he noted as being raised reliefs on the underside of turbidite beds and often ornamental in design (Fig. 1.1). Fuchs (1895) noticed that although these graphoglyptid traces were diverse, they had enough in common to be considered a natural group of trace fossils. Fuchs initially suggested that these were casted surface tracks, but he subsequently concluded that they cannot be, because the original trace mold was never found, they never crossed one another, and there was no gradual coming and going of the tracks – they just appeared and disappeared.

Fuchs' studies, along with those of other scientists, frequently lumped together graphoglyptids with flute casts and other basal turbidite features as "hieroglyphs" (e.g., Sujkowski, 1957; Dzulynski et al., 1959). A theory of formation that was presented by

Sujkowski (1957) for hieroglyphs was that they "are the infillings of impressions which were on the surface of the shale layer at the time of deposition."

When working with turbidite deposits, Seilacher (1962) determined that there are two main types of trace fossils: predepositional and postdepositional. The predepositional trace fossils are those that are produced on the sea floor before a turbidite comes in and either destroys or preserves the upper layers of the sea-floor deposits. The post-depositional trace fossils are those produced in the turbidite deposits immediately or soon after the turbidite is deposited. Following a turbidite event, the postdepositional organisms produce the majority of traces until the food supply is exhausted and the bioceonosis returns to the normal quiescence of deep-sea life (Miller, 1991b).

A few years later, Seilacher (1974) re-coined the term "graphoglyptid" for trace fossils that are "generally found on the soles of sandy flysch turbidites, as smooth and cylindrical casts" (Seilacher, 1977). He stated that they are open mud burrows that have been partially uncovered then casted by the overlying turbidite. With this terminology, he separated the hieroglyphs into two groups, the predepositional biogenic graphoglyptids and the nonbiogenic flute and cast structures produced by the turbidite.

It was initially unclear whether graphoglyptids really represented open burrow systems, as had been hypothesized, or whether they were fecal-filled burrows where the fecal matter was stripped out during preservation. Ekdale (1980) put this issue to rest when modern graphoglyptids were discovered on the deep-sea floor in box cores. These observations showed conclusively that the graphoglyptids found on the soles of ancient turbidite beds were present in modern sediment as open tunnels.

1.2.2 Graphoglyptid preservation

Modern graphoglyptid burrows are found mostly in the deep-sea. One exception of a trace that is sometimes grouped with graphoglyptids (Minter et al., 2006) is the burrow of the intertidal polychaete worm, *Paraonis,* which is discussed in Chapter 3. In the rock record, graphoglyptids are found on the base of turbidites, as was first described by Fuchs (1895). There are many hypotheses regarding how graphoglyptids originally were formed and how they eventually ended up as hyporeliefs on the soles of turbidite beds (Fig. 1.2).

The current consensus is that the burrows started out as open tunnels, as seen in modern examples (Fig. 1.3A). A turbidity current, also known as a density-driven gravity current, produced a mass of moving sediment intermixed with water that traveled along the sea-bottom. As the turbidity current moved down slope, it stripped away the surface veneer of sediment along its course. The sediment is removed from the seafloor by the suction power of the current front, pulling the sediment upwards into the water column, as opposed to scrapping it off of the surface as is typically assumed (Shanmugam, 1996). The open graphoglyptid burrows produce a weakened zone of sediment that allow the turbidite to remove the sediment from the top half, leaving the bottom half of the burrow intact. The sediment is incorporated within the turbidite and also kicked up into the water column. Closer to the more proximal limits of the turbidite, the amount of material that is stripped away is more significant, while further out from the proximal area, near the end lobes of the depositional fan, the amount of material removed is only a few millimeters off of the top of the bed (Fig. 1.3B).

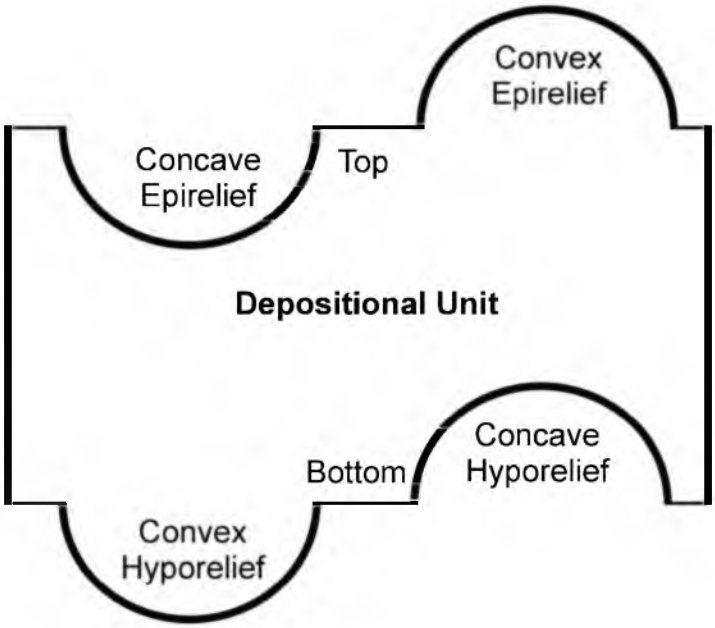

Figure 1.2. Diagram illustrating the terminology for characterizing trace fossils depending on whether they are found on the top or bottom of the bed and whether they are either raised above or excavated into the bed.

The largest particles in the turbidity current typically are sand-sized grains that settle in the bottom part of the open burrow, creating a cast of it (Fig. 1.3C). The cast that is preserved is a two-dimensional representation of a three-dimensional fossil. Most of the trace fossils that are analyzed in this dissertation are assumed to have been formed primarily in two-dimensional space (i.e., *Paleodictyon, Spirorhaphe, Cosmorhaphe,* etc.), but certain trace fossils were not analyzed, since they are assumed to be the remnants of a mostly three-dimensional trace fossil with only a cross-section preserved in two-dimensional space (i.e., *Lorenzinia, Glockerichnus,* etc.).

Rock units that preserve extensive turbidite sequences are often known in European literature as "flysch." Even though this is primarily an archaic term, flysch is still in use in much of the current scientific literature.

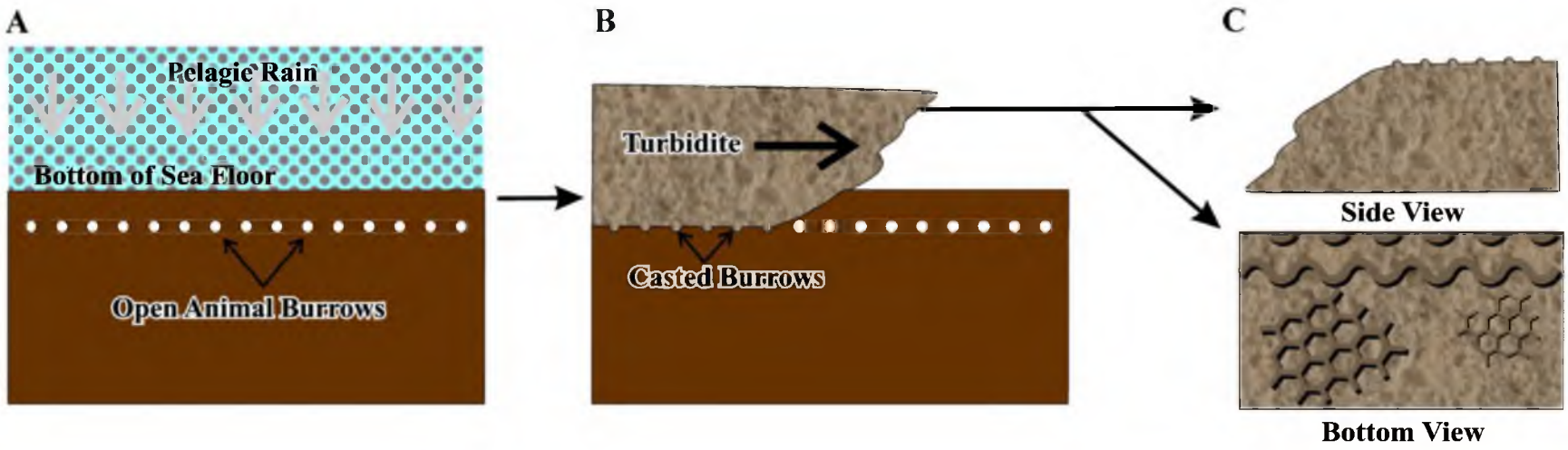

Figure 1.3. Diagram illustrating the preservation of graphoglyptid trace fossils. A) The open burrows of graphoglyptids are formed in the deep sea. B) A turbidite comes in and removes the upper layers of sediment overlying the burrows. C) Sandstone portion of the turbidite slab on which the graphoglyptids are preserved on the bottom. Rock unit shown in profile and bottom views highlighting the raised relief of the casted burrows.

1.3 Sampling

In order to investigate the broad scope of graphoglyptid trace fossil occurrences, a wide temporal and regional spectrum of sites needs to be examined. Examples for this project were chosen for their high abundance and diversity of graphoglyptid trace fossils in museum collections or at easily accessible field sites. Museum material is very useful, since a wide variety of trace fossils that have been collected previously can be photographed in a short period of time. In addition, pertinent field sites were visited, because not all trace fossil specimens are easily collectable. Some of the best preserved trace fossils occur in rocks that are too large to be collected and therefore must be left in the field. The four field sites that were studied in this project include the following (listed in geochronologic order): Point Saint George Turbidites, Franciscan Complex (Middle Jurassic to Middle Cretaceous), Northern California; Guipuzcoan Flysch, Higuer-Getaria Formation (Ypresian, Lower Eocene), Zumaia, Spain; Azagador limestone (Messinian, Miocene), Vera Basin, Almería, Southeastern Spain; and intertidal deposits (Recent), Willapa Bay, Washington. Museum collections that were photographed include: University of Utah Ichnology Collection, Salt Lake City, UT; Institute of Geological Sciences, Jagiellonian University, Krakow, Poland; and the University Of California Museum Of Paleontology, Berkeley, CA.

Most of the field samples were photographed *in situ* due to the constraints on sample collection and transport, both nationally and internationally, and large number of samples that were needed for the research. Samples for this dissertation were obtained in two ways. The first was taking photographs and samples from museum collections and in the field. Museum collections were photographed along with all pertinent information

including age, locality, and formation. A more complete analysis was supplemented by photographs from the literature representing graphoglyptids across the globe and geologic time. Uchman (2004) previously provided a comprehensive list of available graphoglyptid literature available. These were sorted and analyzed by ichnogenus, time period, and rock unit. The result was that the quantitative analyses were performed on more than 400 graphoglyptid specimens across the geologic time scale for this dissertation.

1.3.1 Field Sampling Localities

1.3.1.1 Point Saint George Turbidites, Franciscan Complex (Middle Jurassic to Middle Cretaceous), Northern California. This unit contains a rich graphoglyptid fauna not commonly seen in North America. Most of the turbidites represented on the west coast of the U.S. are slightly to heavily metamorphosed, so the presence of any trace fossils is not common and the presence of graphoglyptids in particular is rare. Graphoglyptids are preserved in the trench-slope basin or possibly the trench-floor setting (Miller, 1993). They include such distinctive graphoglyptid ichnotaxa as *Belorhaphe*, *Megagrapton*, and *Squamodictyon*. The turbidites here are considered to be inner- to mid-submarine fan deposits (Aalto, 1989). Due to the proximal location of the depocenter, this turbidite occurrence provides a different paleoenvironmental setting than most of the other turbidite examples to be studied for this project, where the deposition was more distal and sedimentation rate was lower.

1.3.1.2 Guipúzcoan Flysch, Higuer-Getaria Formation (Ypresian, Lower Eocene), Zumaia, Spain. Well-exposed sections of this graphoglyptid-rich turbidite

sequence are well-known for their high abundance and diversity of deep-marine trace fossils (Seilacher, 1977; Wetzel, 2000). *Paleodictyon*, *Spirorhaphe*, *Cosmorhaphe* and *Helicolithus* are especially abundant and widespread here. Samples and photographs were collected from Itzurun beach, near Zumaia, and up-section, approximately midway between Zumaia and Getaria (Fig. 1.4). Previous work has shown that this is a deep-water, siliclastic and calcareous turbidite interbedded with interturbidites and pelagic limestones. The facies that are represented by the turbidites are the basin-plain, outer fan, and deposition lobe of the middle fan (Leszczyński, 1991a), deposited on the order of one every few to several thousand years (Gawenda et al., 1999).

The geological map used in this study (Fig. 1.4) is a combination of several geologic maps of the region, including those from Rosell et al. (1985), Pujalte et al. (2000), Bernaola et al. (2009), and Cummings and Hodgson (2011b). These authors focused on different scales of the region and used different terminology for the rock units, hence the reason for an amalgamated map. The trace fossil-bearing units are in the Lower Eocene Higuer-Getaria Formation (also known as the "Eocene Flysch" [Bernaola et al., 2009] and the Jaizkibel Sequence [Rosell et al., 1985; Cummings and Hodgson, 2011b]), the Lower Eocene Hondarribia Formation (also known as the "Eocene Flysch" [Bernaola et al., 2009]; and the Sarikola Sequence in Zumaia [Rosell et al., 1985; Cummings and Hodgson, 2011b]), and the Upper Cretaceous Zumaia-Algorri Formation (also known as the San Telmo Red Carbonate Sequence [Rosell et al., 1985; Cummings and Hodgson, 2011b]).

1.3.1.3. Azagador Limestone (Messinian, Miocene), Vera Basin, Almería, Southeastern Spain. The Vera Basin of Almería in Southeastern Spain is unique among

Figure 1.4. Geologic map of Zumaia, Spain, and surrounding region, showing sampling localities (A–C). The map is modified from Rosell et al. (1985, fig. 2), Pujalte et al. (2000, figs. 10 and 12), Bernaola et al. (2009, fig. 1), and Cummings and Hodgson (2011, fig. 1).

graphoglyptid localities, because it contains some of the youngest fossilized graphoglyptids in the world (Ekdale and de Gibert, 2014), with few to no other localities known that are geologically younger, except for the modern graphoglyptids (Ekdale, 1980). Another reason that this is a valuable graphoglyptid locality is that the environment of deposition is a relatively shallow (maybe only a few hundred meters deep), short-lived basin. The formations in which the graphoglyptids are found are hemipelagic marl deposits interbedded with turbidites that contain a diverse graphoglyptid ichnofauna (Braga et al., 2001).

1.3.1.4 Intertidal deposits (Recent), Willapa Bay, Washington. Ancient graphoglyptids have been related to modern burrows of the polychaete annelid, *Paraonis*, by some researchers (Röder, 1971; Seilacher, 1977; Minter et al., 2006). This small intertidal worm creates an open burrow system in a neatly spiraling pattern that rarely, if ever, intersects itself (Fig. 1.5). The geometric pattern and the open nature of the burrow system have made it a popular model for interpreting virtually all graphoglyptid feeding systems, especially the enigmatic double-spiraling graphoglyptid, *Spirorhaphe*. To evaluate the validity of this common claim, modern *Paraonis* burrows were analyzed. These are known to be accessible in intertidal flats of northern coastal regions, including the shores of Washington (Gingras et al., 1999), the Gulf of St. Lawrence (Brunel et al., 1998), and the North Sea (Röder, 1971). The closest locality to observe modern *Paraonis* in its burrow is in Willapa Bay, Washington (Fig. 1.6). This bay is a mesotidal estuary with a tidal range of 2 to 3 meters, and it is protected from the Pacific Ocean by the North Beach Peninsula. The sediments there are dominated by siliciclastic sand. Because *Paraonis* mainly occupies the middle to lower intertidal zone, Willapa Bay was visited

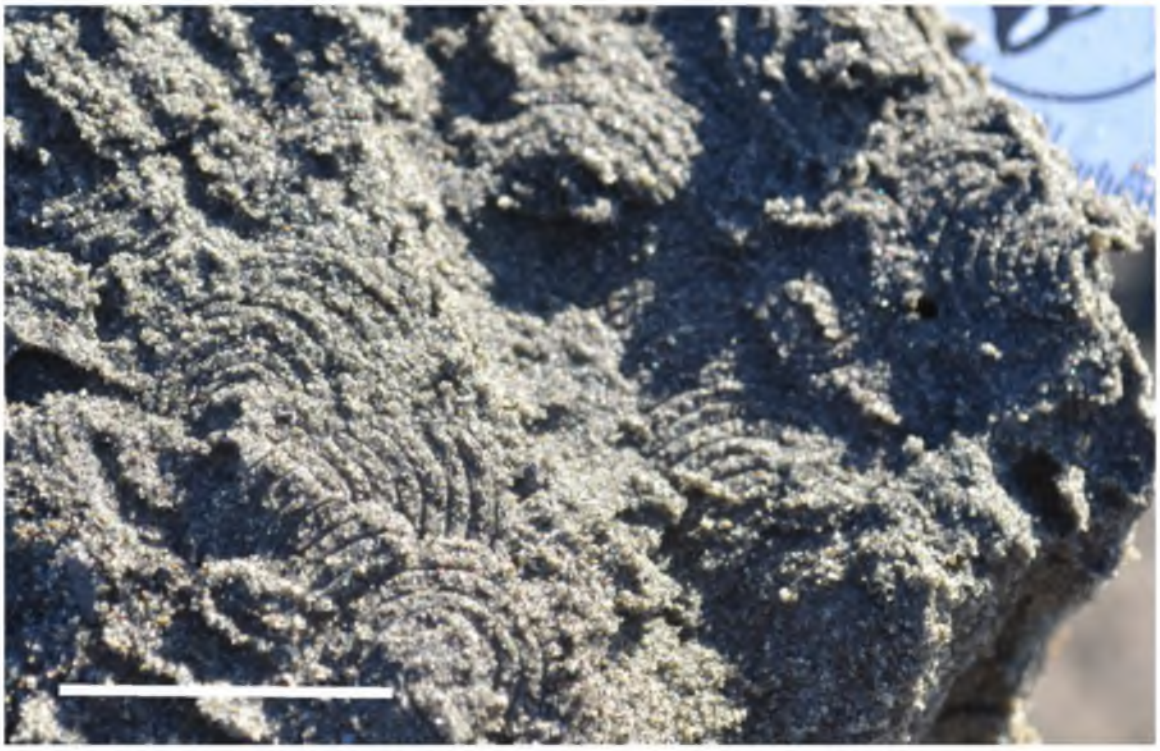

Figure 1.5. Horizontal view of *Paraonis fulgens* burrows at Goose Point, Willapa Bay, Pacific County, Washington State. Scale bar is 3 cm.

during a spring tide when the tidal range was at its greatest (~3 meters).

1.3.2 Museum Sampling Localities

1.3.2.1 The University of Utah Ichnology Collection, Salt Lake City, UT. The University of Utah Ichnology Collection (UUIC) in the Department of Geology and Geophysics houses more than 3,000 curated trace fossil specimens from all over the world and from multiple types of sedimentary deposits. The collection includes graphoglyptid specimens from North America, South America, Europe, and Africa, ranging in age from Jurassic to Miocene.

1.3.2.2 The Institute of Geological Sciences, Jagiellonian University, Krakow, Poland. The Institute of Geological Sciences houses the extensive collection of

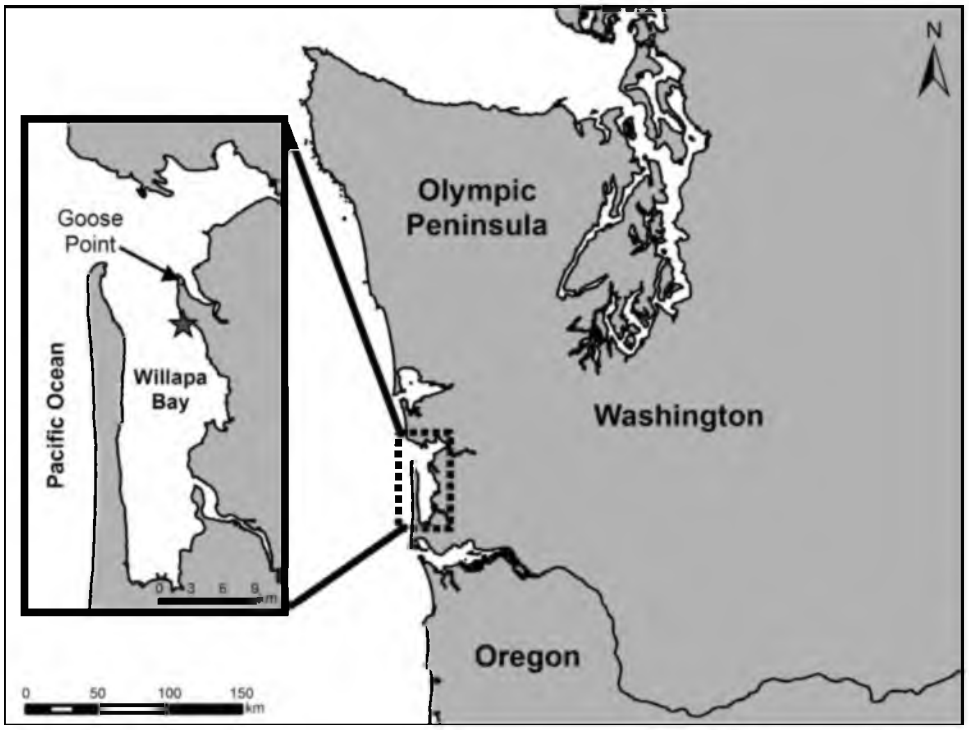

Figure 1.6. Location of modern *Paraonis* burrows at Goose Point, Willapa Bay, Pacific County, Washington State. Sampling locations indicated by the star.

graphoglyptids amassed by M. Książkiewicz (1970) and other subsequent workers (e.g., Uchman, 1998). Samples come from many sites in Europe and range from Early Cretaceous to Oligocene.

1.3.2.3 The University of California Museum of Paleontology, Berkeley, CA. The University of California Museum of Paleontology houses the graphoglyptid specimens that were collected from the Point Saint George turbidites of Northern California. Samples are Early Cretaceous in age.

1.3.3 Scientific Questions and Hypotheses

1.3.3.1 Question 1. Deep-marine, preturbidite trace fossils, termed "graphoglyptids," are generally assumed to be geometrically complex and very regular in

shape. This observation suggests that it may be possible to quantify such shapes with a variety of methods ranging from fractal analysis to geometric morphometrics. The question arises: Is it possible to quantify the fundamental shape attributes of graphoglyptids, and when the trace fossils are characterized quantitatively will they fit into ethologically meaningful categories of ichnogenera (Uchman, 2003)? In other words, can quantifiable geometric attributes of graphoglyptid burrows contribute to their systematic classification and to our interpretation of their paleoethologic significance?

1.3.3.2 Working Hypothesis 1. Graphoglyptid geometry tends to be sufficiently regular that similar trace fossils (i.e., ichnogenera) can be classified using quantification methods not normally used in the field of ichnology. Some types of burrow shapes are likely to produce a range of values, whereas other shapes will likely produce values diagnostic of that graphoglyptid ichnotaxon.

1.3.3.3 Question 2. The geometric regularity of the graphoglyptids presumably represents a distinct regularity in the feeding pattern of the organisms that created the traces. It has been hypothesized that the types of feeding behavior represented by graphoglyptids may be grazing (pascichnia), mining the sediment (fodinichnia), cultivating microbes inside their burrows (agrichnia), and/or trapping organisms passing through the sediment (irretichnia). It is reasonable to assume that some of these feeding patterns will yield a characteristic fractal dimension as well as other characteristic variables. The question arises: Is it possible that by analyzing the shapes of graphoglyptids, the feeding strategy can be discerned on the basis of quantitative measures?

1.3.3.4 Working Hypothesis 2. Some feeding patterns, like deposit feeding (grazing and mining), serve to optimize the amount of sediment that they utilize. Farming and trapping behaviors would be expected to have a more structured pattern, similar to a farmer's field and a spider web, respectively. These two groups of strategies (deposit feeding versus farming and trapping) would be expected to produce noticeably different morphometric results. Also, due to the wide variety of shapes and patterns of graphoglyptids, it is possible that there is a wide variety of feeding strategies that are represented by each specific graphoglyptid ichnogenus.

1.3.3.5 Question 3. In previous literature dealing with graphoglyptids, they often are described as perfectly formed nets, spirals, meanders, etc. (Seilacher, 1967, 1977; Ekdale et al., 1984a; Crimes and Crossley, 1991; Levin, 1994; Minter et al., 2006). The question arises: How closely do the actual trace fossils resemble the idealized perfect geometric forms that they represent?

1.3.3.6 Working Hypothesis 3. Graphoglyptids usually are regular in form, but on close inspection they are not geometrically perfect. Analyzing the graphoglyptid tunnel shapes allows us to illustrate this. It is expected that the patterns would be close to perfect, and any irregularities may be tied to specific environmental reasons (e.g., current direction, paleoslope, food concentration, etc.).

1.3.3.7 Question 4. Evolution typically is studied in the fossil record by looking at the changing anatomy of individual animals through geologic time. This is not possible for some kinds of animals, because they either do not leave behind a fossil record or have such a scant fossil record that it is not possible to study them from an evolutionary perspective. Trace fossils represent behavior, so by analyzing similar trace fossils, it

might be possible to determine the evolution of their behavior, by similar methods as paleontologists who study anatomical evolution. This has been accomplished for certain behavioral traits of modern organisms (Wenzel, 1992; Paterson et al., 1995; McLennan and Mattern, 2001; Price and Lanyon, 2002; Lopardo et al., 2004), but rarely has it been done for trace fossils. The question arises: Is it possible to study changes in behavior through time by just studying the trace fossils that have been left behind?

1.3.3.8 Working Hypothesis 4. It would be impossible to study the evolution of behavior by just looking at randomly selected trace fossils, but graphoglyptids are found in such a constrained environment with specific characterizations (deep marine; open burrow system; extremely shallow burrows) that it might be possible that the organisms producing the burrows are closely related and therefore that the behaviors they are illustrating can be linked in an evolutionary way.

1.4 Significance of research

1.4.1 Ichnologic significance

The study of ichnology rarely delves into the quantitative realm, and when it does, it usually deals only with the percentage of disturbed sediment and the size of the trace fossils (e.g., Droser and Bottjer, 1986; Uchman, 2003). This dissertation expands the possibilities for studying trace fossils with scale-invariant (non-Euclidean) measures, such as fractal dimension and tortuosity, combined with more familiar Euclidean geometric parameters, such as branching angles of burrow tunnels. The methodology employed in this project enables ichnologists to study different varieties of trace fossils in a more objective manner than what is typically done.

1.4.2 Paleoecologic significance

The functional purpose of graphoglyptids has long been debated (passive feeding, setting traps for other organisms, farming microbes, etc.), and the use of these quantitative methods helps to identify the feeding purposes of the trace makers. Different feeding methods are grouped on the basis of their quantitative attributes. By analyzing a variety of known feeding habit traces it is possible to interpret the feeding methods of graphoglyptids as well as provide tools for ichnologists to use for analyzing different trace fossils beyond graphoglyptids.

1.4.3 Behavioral evolution significance

The fields of paleontology and behavioral biology seldom intersect. When they do, it typically involves trace fossils, since they are the tangible result of animal behavior, but behavioral evolution is rarely studied in the paleontologic record due to limited information. Some behavioral biologists have performed cladistic analyses on limited datasets of behavioral traits, and several workers have shown that with only behavioral characteristics it is possible to determine animal lineages (Wenzel, 1992; Paterson et al., 1995; McLennan and Mattern, 2001; Price and Lanyon, 2002; Lopardo et al., 2004). Studying the evolution of behavior in an ichnologic sense has been attempted only very rarely (Ekdale and Lamond, 2003), and in such analyses there generally are not the same level of mathematical standards that are now obligatory with modern cladistic and behavioral biology analyses. Even though this study is not cladistical in nature, it manages to bridge the gap between the two related fields of ichnology and behavioral biology.

1.4.4 Paleoclimate significance

The deep sea is the largest, most stable habitat on Earth. Any changes to behavior in the deep sea should take a very long time unless something significant were to occur to alter the environment drastically. By studying the rate at which the graphoglyptid trace fossils changed it is possible to show paleoclimactic events which had a very large impact on the behaviors of organisms, and also to see if there were any large scale events, which possibly did not have any influence on the deep sea.

1.5 Summary of following chapters

1.5.1 Chapter 2 – Fractal analysis of graphoglyptid trace fossils

The second chapter of this dissertation focuses on the feeding patterns represented by graphoglyptids, which have been interpreted as fodinichnial (mining), pascichnial (grazing), and/or agrichnial (farming). For this chapter, several species of graphoglyptid trace fossils were analyzed using fractal analysis to determine the fractal dimension of each of the traces. The fractal dimension combines shape complexity and space usage into one number. Fractal dimensions of graphoglyptid burrows were compared with those of known fodinichnial burrows, such as *Zoophycos,* and pascichnial trails, such as *Scolicia*, all from a similar time period and a consistent rock unit from Zumaia, Spain.

The results from the study indicate that the deposit-feeding burrows (fodinichnia and pascichnia) illustrate a high fractal dimension. Graphoglyptids illustrate a consistently lower fractal dimension than the deposit-feeding burrows, thus providing evidence against the suggestion that they represent fodinichnial or pascichnial behaviors, supporting the hypothesis that graphoglyptids represent the agrichnial feeding habit.

1.5.2 Chapter 3 – Pitfalls, traps, and webs in ichnology: Traces and trace fossils of an understudied behavioral

The third chapter reviews what types of behavior are contained within the group of agrichnial trace fossils. Previously, the term agrichnia has been applied to graphoglyptids and has been used to denote both trapping and farming behaviors, but the two behaviors display distinctly different feeding strategies. The trapping of prey is a specialized type of feeding behavior that is identified in the trace fossil record only rarely. Trapping traces that have been reported in the literature include spider webs, ant-lion burrows, scorpion pits, cerianthid tube anemone burrows, echiuran worm burrows, *Paraonis* worm burrows, and deep-sea graphoglyptids burrows. This chapter reviews all known trapping traces in both modern environments and fossilized occurrences.

There is uncertainty, however, if all examples described as trapping traces truly represent traps. *Paraonis* burrows, for example, have been represented as trapping traces, but there is a question if they actually represent this kind of behavioral strategy. Previous references and new field work indicate that *Paraonis* likely employs a selective deposit feeding strategy. The interpretation that at least some graphoglyptids (e.g., *Spirorhaphe*) represent trapping was based on the trapping model for *Paraonis*, but since *Paraonis* does not trap prey, the question arises whether any graphoglyptids should be considered as representing trapping behavior. The new behavioral category 'irretichnia' is proposed here to encompass trapping trace fossils, due to its unique behavioral significance and to separate trapping from farming.

1.5.3 Chapter 4 – Analytical tools for quantifying the morphology of invertebrate trace fossils

The fourth chapter expands upon some of the analytical techniques that were introduced in the second chapter. The analytical techniques are meant to quantify the shape of trace fossils, enabling scientists to compare trace fossils described by different people with greater precision and accuracy. This chapter describes several methods for quantifying invertebrate trace fossils, including morphology dependent methods (motility index, mesh size, topology, tortuosity, branching angle, and the number of cell sides) and morphology independent methods (fractal analysis, burrow area shape, and occupied space percentage). These tools were performed on selected graphoglyptid trace fossils, demonstrating how these methods allow for objective comparisons between different trace fossils.

1.5.4 Chapter 5 – Behavioral evolution reflected in the geologic record of graphoglyptid trace fossils

The fifth chapter addresses the evolution of graphoglyptid behaviors through time. The analytical techniques developed in the previous chapter were used on over 400 graphoglyptid traces that ranged in age from the Cambrian to the modern. Previous analyses of the behavioral evolution of graphoglyptids indicated that they were slowly diversifying, becoming optimized, and getting smaller over time until the Late Cretaceous, when a sudden increase in diversification occurred. This interval of rapid diversification of graphoglyptid ichnotaxa was likely attributed to the evolution of the angiosperms on land. Although some previous studies indicate that graphoglyptids were

getting smaller through time, results reported in this dissertation suggest that the feeding patterns they represent were not following any clearly established evolutionary trends. The behavioral evolution of the graphoglyptid trace makers was influenced many times during the past including the rapid diversification that started in the Late Cretaceous and continued through the Early Eocene, followed by a crash in diversity during the Oligocene. The initial diversity explosion was likely due to either the angiosperm evolution or an increase in foraminiferal/calcareous ooze and the Eocene diversification was likely continued because of the Paleocene-Eocene Thermal Maximum (PETM), which raised deep-sea water temperatures 4 to 5°C. The subsequent crash in the Oligocene was likely due to the Eocene-Oligocene Boundary Crisis which was a result of the growing ice sheets reducing sea level and increasing sediment deposition in the ocean due to erosion. Overall, graphoglyptids did not show the stability that is often attributed to them due to the stability and predictability of the deep-sea environment, but may in fact be sensitive indicators or deep-sea environmental change.

1.5.5 Chapter 6 – Evolution in chaos: Chaos theory as a guiding principle for patterns of anatomical and behavioral evolution

The sixth chapter explores possible ways that chaos theory influences evolution. Previous applications of chaos theory in evolutionary studies have not taken the spotlight as the driving force of biological evolution. Chaos theory is based on nonlinear algebra, where the solution to one set of equations becomes the variable in the next iteration of the function, thus producing a feedback loop. There are six main principles to chaos theory, which can be related directly to biological evolutionary theory. Both theories embody

solutions to the problems that: 1, cannot repeat themselves; 2, are bounded within a specific region of space; 3, are heavily dependent on initial conditions; 4, are not random; 5, are unpredictable; and 6, are based on a series of feedback loops.

Nonlinear systems can be depicted using a phase map, which illustrates all possible solutions of a problem depending on each initial value. In evolutionary theory, the phase map represents morphospace, which is the conceptual framework for mapping clusters of organisms based on specific attributes. The clustering of organisms is due to convergences, where many different genetic lines converge on similar solutions to various problems. The clustering in a phase map is concentrated around a point or region of space known as an 'attractor'. External stimuli push the solution from the attractors to new attractors. Evolutionary external stimuli include changes in environmental factors, such as shifts in climate, or the introduction of new species. By using chaos theory as a template to study biological evolution, it may be possible to map out how human induced environmental changes could shift the evolution of species in the near future.

CHAPTER 2

FRACTAL ANALYSIS OF GRAPHOGLYPTID TRACE FOSSILS[1]

2.1 Abstract

Graphoglyptids are a group of deep-sea trace fossils that exhibit ornate burrow geometries. Feeding patterns represented by these burrows have been interpreted as fodinichnial (mining), pascichnial (grazing), and/or agrichnial (farming). In this study, several different graphoglyptid trace fossils were analyzed quantitatively using fractal analysis to determine which of these three feeding modes is most appropriate as an interpretation. Graphoglyptid burrows lend themselves to fractal geometric analysis, because they commonly exhibit the essential fractal characteristics of scale invariance and self similarity. Fractal analysis is presented as a tool for analyzing geometric configurations by combining shape complexity and space usage into one number, the fractal dimension. Fractal dimensions of such graphoglyptid burrows as *Paleodictyon* and *Spirorhaphe* were compared with those of known fodinichnial burrows, such as *Zoophycos,* and pascichnial trails, such as *Scolicia*, all from Zumaia, Spain. Results indicate that the deposit-feeding burrows (fodinichnia and pascichnia) illustrate a high

[1]Reprinted from Fractal analysis of graphoglyptid trace fossils, by James R. Lehane and A. A. Ekdale, PALAIOS, vol. 28, p. 23–32 with permission from SEPM (Society for Sedimentary Geology).

fractal dimension, as would be expected for a deposit feeding–optimal foraging strategy. Graphoglyptids illustrate a consistently lower fractal dimension than the deposit-feeding burrows, thus providing evidence against the suggestion that they represent fodinichnial or pascichnial behaviors. This observation supports the hypothesis that graphoglyptids represent agrichnial activity rather than mining or grazing activities.

2.2 Introduction

Graphoglyptid trace fossils are geometrically complex, predepositional, open burrow systems commonly preserved in convex hyporelief on the soles of deep-sea turbidite beds (Fig. 2.1). The function of graphoglyptid burrows has been attributed to several different feeding strategies, including fodinichnial (mining), pascichnial (grazing), and/or agrichnial (farming) behavior patterns (e.g., Seilacher, 1974, 1977; Ekdale, 1980; Bromley, 1990; Rona et al., 2009).

Fodinichnia (Seilacher, 1953), or sediment-mining traces, record the activity of an organism making repeated, closely spaced probes in the sediment to maximize the extraction of food resources. Pascichnia (Seilacher, 1953), or grazing traces, reflect the activity of a burrower feeding on organic material as the burrower moves through the sediment. Agrichnia (Ekdale et al., 1984a), or farming traces, are permanent (or semipermanent) dwelling burrows used for cultivating food.

Seilacher (1974) suggested that graphoglyptids may be deep-sea feeding traces that developed geometrically complex patterns for efficiency of acquiring food, a strategy now sometimes referred to as optimal foraging. Optimal foraging strategy (OFS) refers to the maximization of the nutritional benefit from food versus the energetic cost of seeking

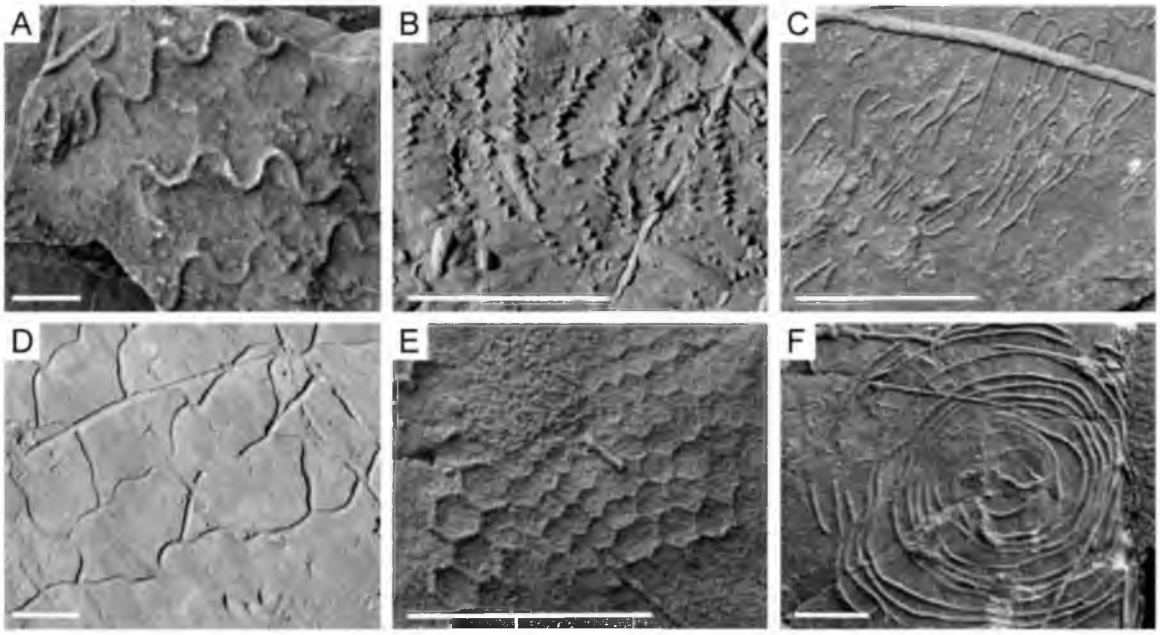

Figure 2.1. Images of some common graphoglyptids, all of which were photographed in the field in the Eocene Guipúzcoan Flysch of Zumaia, Spain. A) *Cosmorhaphe*. B) *Helicolithus*. C) *Helminthorhaphe*. D) *Megagrapton*. E) *Paleodictyon*. F) *Spirorhaphe*. Scale bars 4 cm.

and exploiting a food resource (Charnov, 1976; Schneider, 1984; Plotnick and Koy, 2005). There are various applications of OFS, ranging from predator-prey relations to deposit feeding. A deposit-feeding optimal foraging strategy (DF-OFS) would apply where an organism ingests as much food-rich sediment as the organism can with as little effort as possible, in the process maximizing the coverage of the food-rich deposit (Levinton and Kelaher, 2004). The shapes of graphoglyptid burrow systems were thought to have become more geometrically complex throughout geologic time in a trend of increasing optimization during feeding (Seilacher, 1967, 1974, 1977, 1986). Alternatively, some workers have suggested that the graphoglyptid OFS was optimized early on but merely increased in geometric complexity for other poorly understood reasons (Crimes and Fedonkin, 1994; Uchman, 2003). Both of these suggestions seem to indicate that a DF-OFS was being employed by the trace-maker.

The agrichnial (farming) strategy is a behavior that seems to fit the geometric structure of graphoglyptids better than a DF-OFS strategy (Seilacher 1977, 2007; Rona et al., 2009). Support for the agrichnial hypothesis includes the possibility that graphoglyptids possess a mucus-lined wall, as might be suggested by the sharp outlines of the burrows when they are found as fossils. Geochemical tests of the burrow margin would be necessary to detect the presence of mucus. Rona et al. (2009) did such tests on modern *Paleodictyon* and found no evidence of mucus.

The highly patterned graphoglyptid burrows likely represent a K-selected population strategy for survival in a stable, but resource-limited, environment where the burrowers have the time to build elaborate structures (Ekdale, 1985). The numerous openings of *Paleodictyon* to the sediment surface have been postulated as aeration holes, so that oxygenated water can be supplied throughout the burrow system. The main support for an agrichnial strategy is that most marine animals cannot break down the cellulose-based organic material that is found in the deep-sea environment (Seilacher, 1977, 2007; Cummings and Hodgson, 2011b). For these animals to take advantage of the available organic matter, bacteria must be involved to breakdown the cellulose. The burrowers move back and forth through their burrow tunnels and consume the bacteria that they scrape off of the burrow walls.

One of the questions arising from these hypotheses is whether or not all graphoglyptids are ethologically related, that is, if the unbranched burrows, branching burrows, and anastomosing burrow networks all represent the same activity. Some graphoglyptids may display one type of activity, whereas another group may display an entirely different activity. All graphoglyptids exhibit the same preservation mode (Fuchs,

1895), but this does not necessarily mean that all of the burrow patterns are functionally related or that the producing organisms are taxonomically related. There could be multiple evolutionary pathways to explain behaviors converging on a similar model of tunnel formation, but with completely different purposes.

Each suggested graphoglyptid behavior (fodinichnia, pascichnia, and agrichnia) likely presents different quantifiable patterns in the rock record. The extent that the graphoglyptids exploit the sediment in which they are located could be an indication of the burrow's behavioral significance. Spiral shapes, meandering shapes, and networks are geometrically different, but if they cover the sediment in essentially the same way, the burrowers may be creating them for the same purpose (i.e., grazing or farming). The most promising way to compare the different types of burrow forms is to quantify their geometric configuration. Quantification offers an objective view of the behavior patterns that the shapes might represent. To study the geometric configuration of trace fossils requires a method that can give similar results for complete and incomplete trace fossils, as well as a method that will yield the same results at different scales (i.e., scale invariant).

Fractal analysis is a useful method for expressing both the shape characteristics of the burrow and the extent of the sediment that is covered. The study described here tests the hypothesis that fractal analysis also can be meaningful in interpreting the type of behavior represented by the burrow geometry. Fractal analysis has been used in many animal behavior studies, including vertebrate foraging paths (Crist et al., 1992; With, 1994a, 1994b; Etzenhouser et al., 1998; With et al., 1999; Mårell et al., 2002), vertebrate burrows (Le Comber et al., 2002; Romañach and Le Comber, 2004), invertebrate burrows

(Puche and Su, 2001; Katrak et al., 2008), simulated foraging paths (Plotnick,2003), and trace fossils (Jeong and Ekdale, 1996, 1997; de Gibert et al., 1999; Baucon, 2010). This paper is the first time that fractal analysis is used as a basis for describing different trace fossils in an attempt to interpret their behavioral significance.

2.3 Methods and materials

Fractal geometry is a concept first described by Mandelbrot (1983) as a way to characterize complexity and quantify morphologies. The fractal approach can measure how completely a shape fills the space it occupies (Plotnick and Prestegaard, 1995; Wagle et al., 2005). A fractal is a shape that occupies a space where the precise dimension of that shape exceeds the topological dimension (Mandelbrot, 1983). A common view of fractals relates to their property of scale invariance, that is, when they look the same no matter the scale at which they are viewed (Fig. 2.2A). These are considered to be perfect fractals. A slightly looser, more pragmatic interpretation is that different scales of a fractal resemble the whole in some way (Feder, 1988). This definition applies to fractals that are not perfectly scale invariant but are considered to have a statistical scale invariance, i.e., a natural fractal (Slice, 1993; Plotnick and Prestegaard, 1995). This means that when the image is examined at different magnifications, all of the magnifications are not exactly the same; they just have a strong geometrical resemblance to one another (Fig. 2.2B).

Fractals are illustrated by their fractal dimension (D), which is the space occupied as represented by a real number (allowing for a fractional dimension) rather than an integer. In Euclidian geometry, a straight line is one dimension, a plane is two

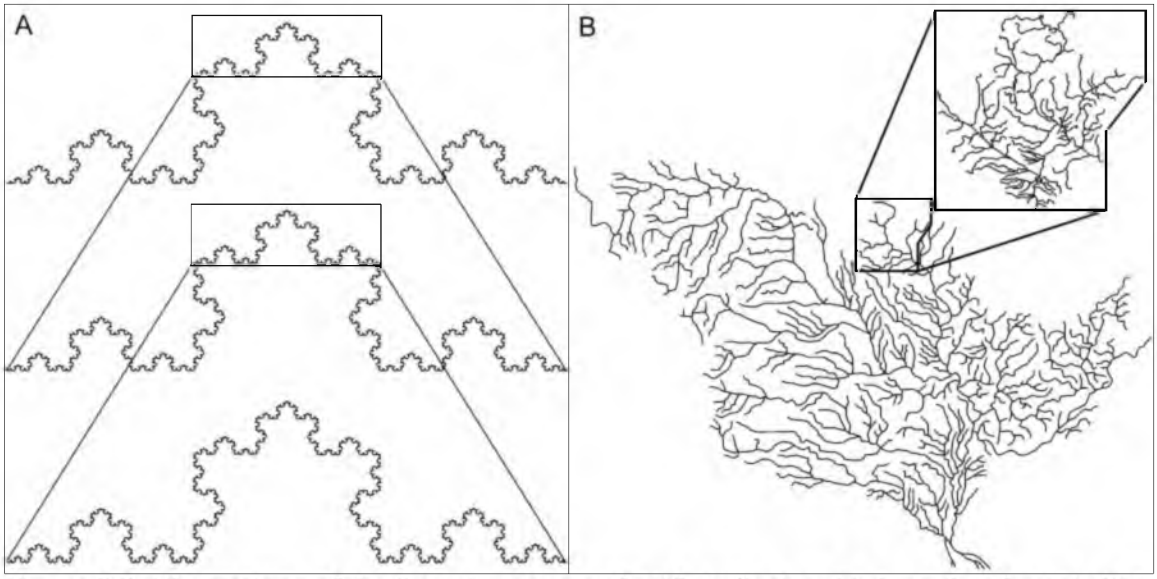

Figure 2.2. Illustrations of the fractal property of self similarity. A) A perfect fractal. The artificially created Koch curve (von Koch, 1904, 1993), where magnification of a tiny portion of the line results in exactly the same image as the previous view. B. A natural fractal. The naturally occurring Mississippi River drainage basin with a portion of the river drainage expanded to show its similarity to the whole. A scale bar is irrelevant in this figure because of the scale invariant nature of fractal images.

dimensions, and a volume is three dimensions (Strogatz, 1994). When a shape takes up only a part of the space, the shape cannot be considered as occupying an integer dimension. A nonstraight line (e.g., a meandering trail) would occupy more than one dimension but less than two. An object radiating in the third dimension but not filling the third dimension (e.g., a subhorizontal branching burrow) would occupy a fractal dimension somewhere between two and three dimensions. The fractal dimension can be useful in understanding real shapes in nature, because the fractal dimension identifies the actual dimension that a particular shape occupies.

Several methods have been used for calculating the fractal dimension. The fractal dimension for shapes in a two-dimensional space is best calculated using the Box Counting Method (D_{Box}) or the Information Dimension Method (D_{Info}). D_{Box}

superimposes the shape on a grid (i.e., a set of boxes of specific size) and counts how many of the boxes are occupied by the shape in question (also see Baucon, 2010). The box size is then decreased by a set amount, and the boxes are counted again; this process is repeated over and over. The result yields a straight line in a log plot of box size versus number of occupied boxes, where the slope of the line is related to the fractal dimension (Fig. 2.3). D_{Info} takes into account how much of the shape is located in each box, giving greater weight to the boxes with more of the shape inside the box. The application that was used to calculate the fractal dimension in this study was BENOIT Version 1.31 created by TruSoft Int'l, Inc., 1999 (Fig. 2.3; also see Appendix A).

2.3.1 Fractal properties of trace fossils

There are two properties that a trace fossil should possess in order to be analyzed as a fractal. One property is scale invariance, where the image produces a similar fractal dimension no matter what scale at which the image is being observed. The other property is self similarity, where the image yields similar results when looking at different portions of it.

2.3.1.1 Scale invariance. The problem with using fractal dimensions in ichnological studies is that very different ichnotaxa may illustrate a similar fractal dimension, while similar ichnotaxa may illustrate varying fractal dimensions. This even could apply to a single specimen, where different parts of the trace fossil may produce different fractal dimensions. Graphoglyptid burrows are so geometrically regular in comparison with many other types of trace fossils that this concern is expected to be minimal.

Figure 2.3. The fractal dimension program BENOIT, highlighting the location of the fractal dimension (1.475 in this instance) and the standard deviation (0.051 in this instance). The x-axis of the graph is the box size of each analysis, and the y-axis is the resulting number of boxes occupied. The fractal dimension is calculated from the slope of the graph. Also visible in this figure are the input parameters Side-length of largest box, Coefficient of box size decrease, Number of box sizes, and Increment of grid rotation (0–90). The removed analyses are highlighted (see Appendix A for description).

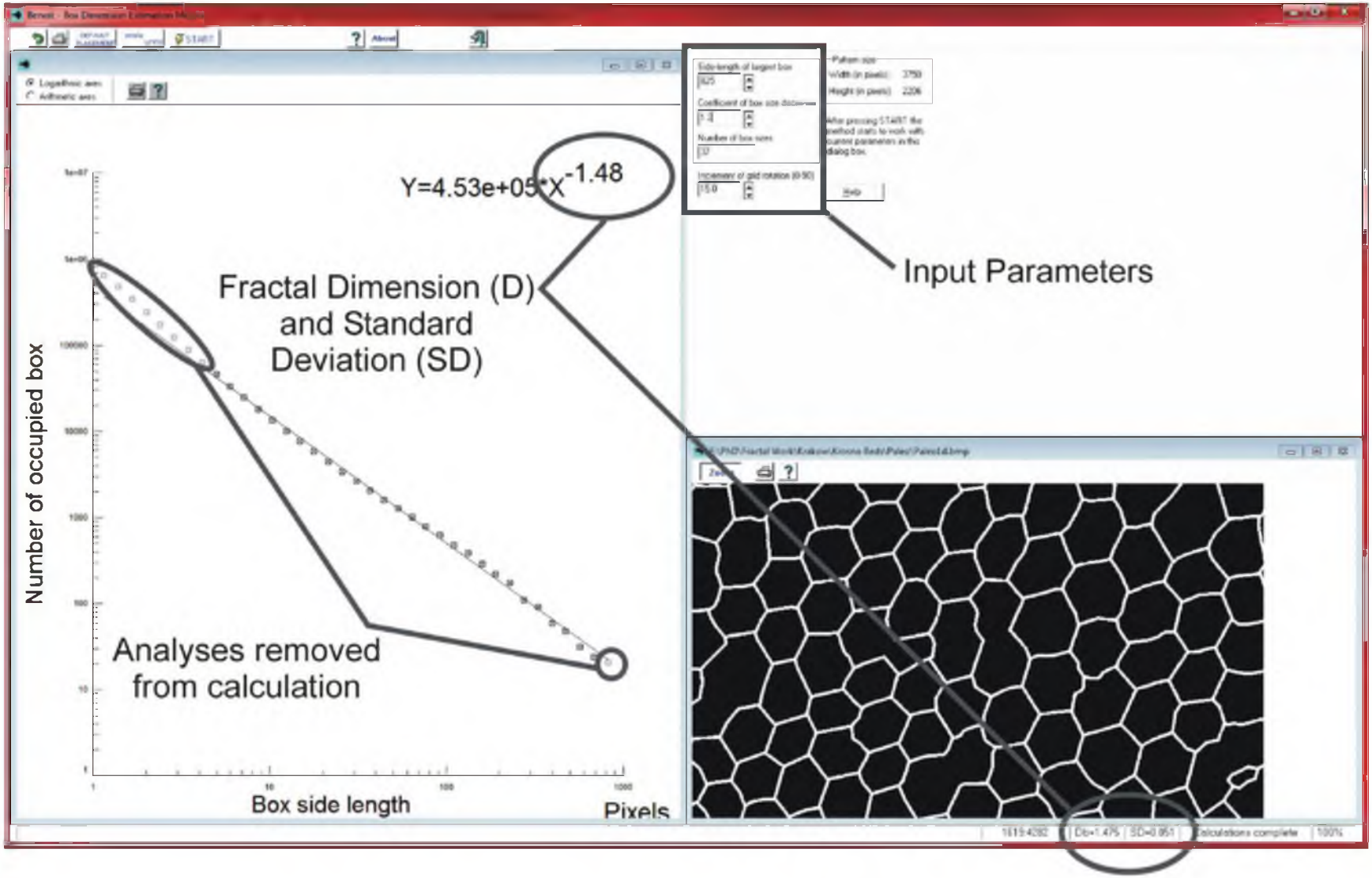
Y=4.53e+05*X-1.48
Fractal Dimension (D) and Standard Deviation (SD)
Input Parameters
Number of occupied box
Box side length
Pixels
Analyses removed from calculation

To determine if a single image could produce varying fractal dimensions, a trace of a large (~25 cm wide) specimen of *Paleodictyon majus* (Meneghini *in* Peruzzi, 1880) from the Oligocene flysch of Poland was analyzed (Figs. 2.4–2.7). It should be kept in mind that all possible fractal dimensions (D) for forms that partially cover a plane are between 1.0 and 2.0. A dimension of 1.0 means the trace is a thin, straight line, and a dimension of 2.0 means that the trace completely covers the entire surface that is being analyzed.

To test for scale invariance, the *Paleodictyon majus* specimen was analyzed at full scale, and then it was cropped down and rescaled in order to produce the same quality image for each scaled image (a–h in Fig. 2.5). This analysis was conducted using both D_{Box} and D_{Info}, yielding results that ranged narrowly (D_{Box} from 1.450 to 1.553). In the graph (Fig. 2.5B), there is a reduction in the fractal dimension starting around 150 cm^2, but the total reduction is only ~0.09. Although this is a significant decrease on a narrow scale, when viewed in relation to the entire scale (1.0 – 2.0), this finding demonstrates a very good control (the average D_{Box} is 1.500 ± 0.058). Once the overall area of the *Paleodictyon* was reduced below ~25 cm^2, the results were appreciably different than the previous results, probably because at this point the form of the burrow stopped being a network and started to represent a branching form.

2.3.1.2 Self similarity. The *Paleodictyon majus* specimen then was analyzed for self similarity by taking the same size section (section "h" in Fig. 2.5) and finding the fractal dimension for various parts across the whole image (Fig. 2.6). The average fractal dimension (D_{Box}) of these boxes is 1.441 ± 0.023. Overall, the variation is far less in the self-similarity case than in the scale-invariance case. The D_{Box} range was 0.046 for the

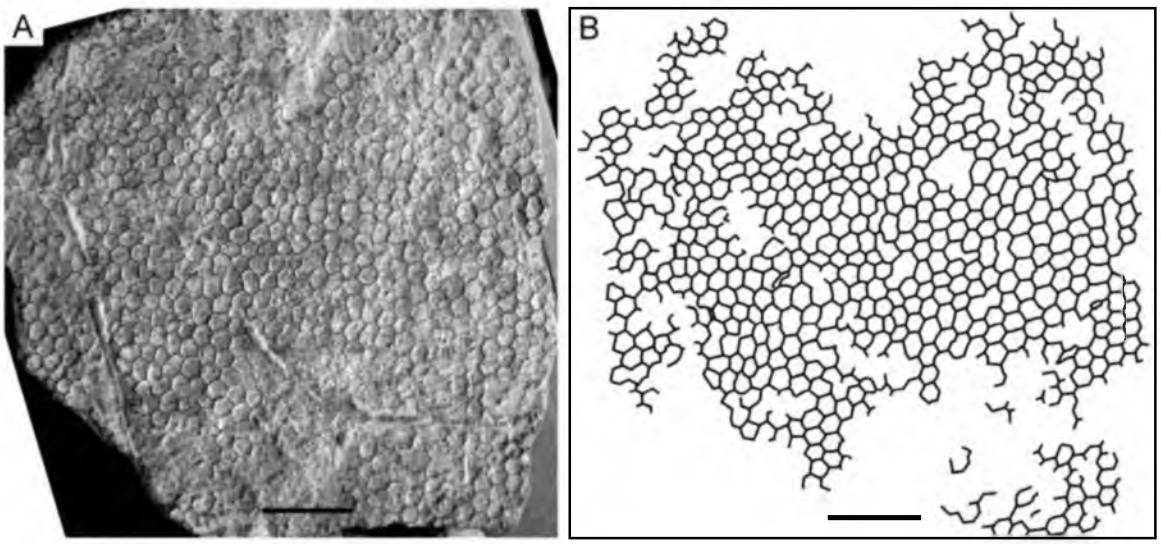

Figure 2.4. Tracing of a *Paleodictyon majus* from the Oligocene Krosno Beds of Poland (un-numbered specimen in the Institute of Geological Science, Jagiellonian University, Kraków, Poland). A) Photo of *Paleodictyon majus*. B) Tracing of the *Paleodictyon majus* specimen. Scale bar 4 cm.

self-similarity test versus a range of 0.089 for the scale invariance test.

2.3.1.3 Eroding traces. There is an apparent relationship between the amount of preserved material in the sections in Figure 2.6 and the fractal dimension. More complete sections of the burrow (a, c, and d) have a higher fractal dimension than those where large portions are missing due to erosion (b, e, and f). This raises the question of whether an accurate (if slightly lower) representation of the fractal dimension is possible in situations where a trace fossil is incompletely preserved. To answer this question, the same *Paleodictyon majus* specimen was divided into 100 equal-sized sections (Fig. 2.7). A random number generator was used to remove (i.e., erode) parts of the trace until there was nothing left. This process was repeated ten times in order to demonstrate consistency of the results. The graph on the right side of Figure 2.7 shows what happens to the fractal dimension as the trace is eroded over ten iterations. The limits of the scale invariance and

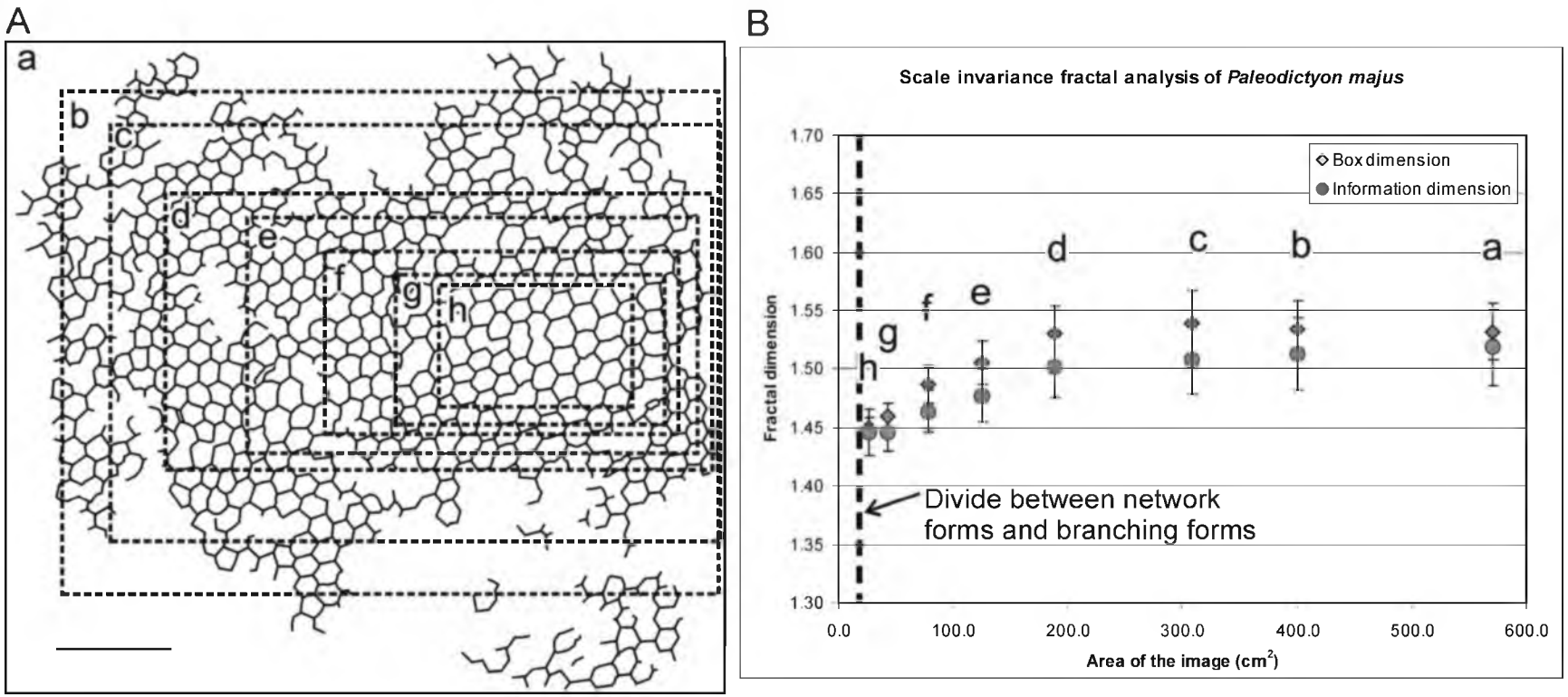

Figure 2.5. Fractal analysis of multiple scales of a *Paleodictyon majus* from the Krosno Beds of Poland. A) The fractal dimension (D) was calculated individually for each box after being scaled and reproduced using the same parameters listed in the text. B) Comparison of the Box Counting Method (D_{Box}) and the Information Dimension Method (D_{Info}) to the area of the actual specimen in cm2. Error bars are the standard error that is calculated from the standard deviation calculated by BENOIT during the determination of the fractal dimension. Scale bar 4 cm, and error bars represent the standard error.

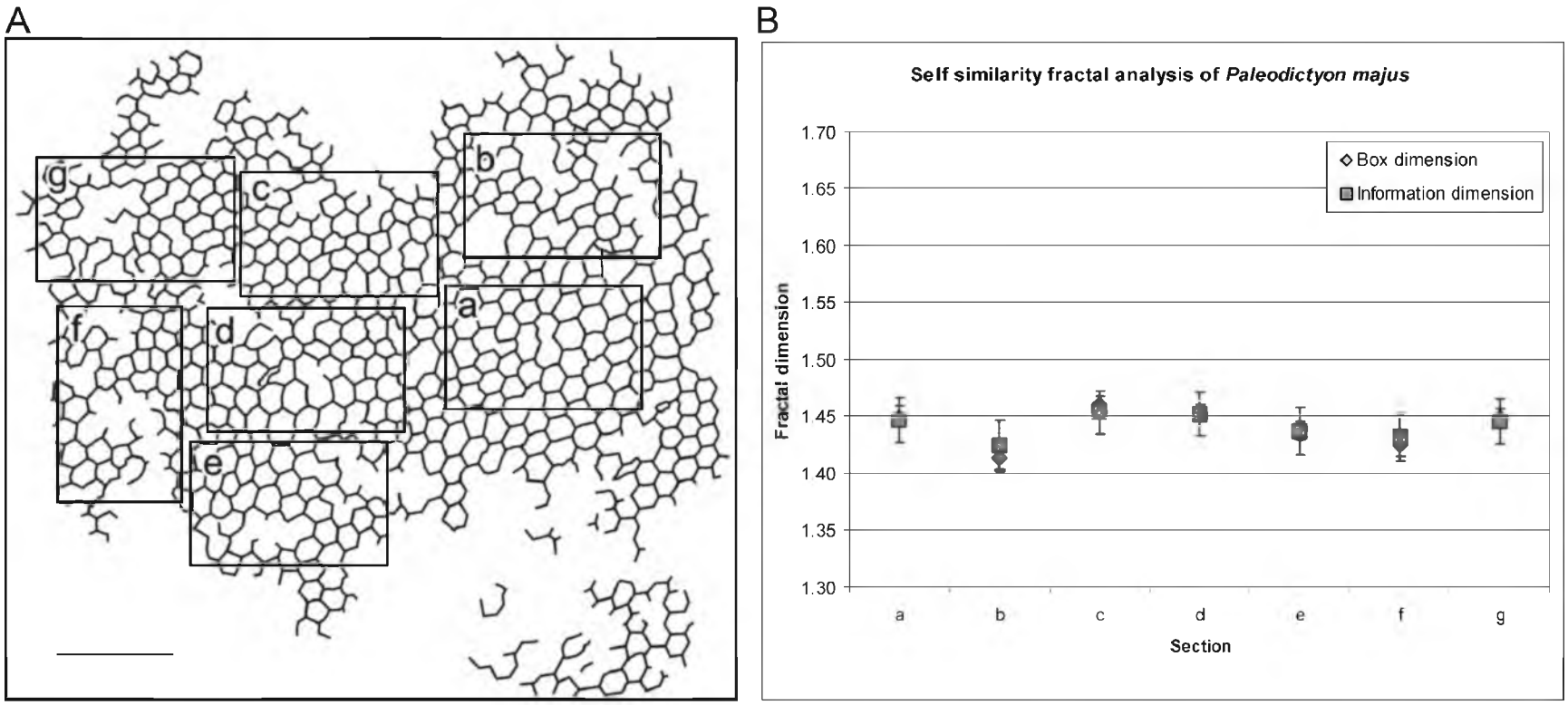

Figure 2.6. Fractal analysis of multiple regions in a *Paleodictyon majus* from the Krosno Beds of Poland. A) The fractal dimension (D) was calculated for seven same-size sections (a–g). Section "a" corresponds with Section "h" on Figure 5. B) Comparison of the D_{Box} and the D_{info} for each of the sections in A. Scale bar 4 cm, and error bars represent the standard error.

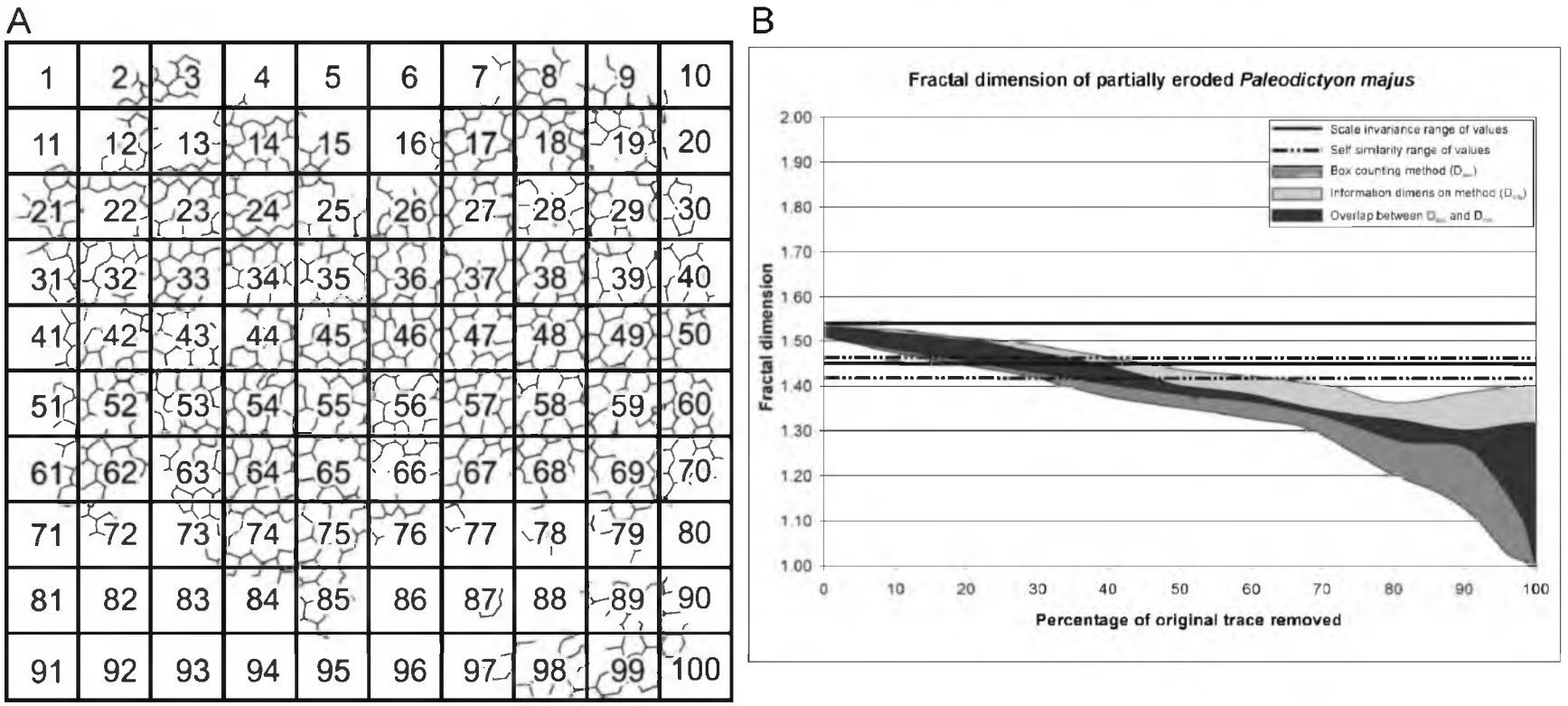

Figure 2.7. Fractal analysis of *Paleodictyon majus* from the Krosno Beds of Poland as if the specimen were partially eroded. A) A random number generator was used to pick different portions of the *Paleodictyon* to be "eroded" and the resulting values were plotted after each 10% was removed. B) The plot of the eroded *Paleodictyon* calculated for ten iterations. The lines indicate the range of values of fractal dimensions reported in Figures 2.5 and 2.6.

self similarity analyses also are represented on this figure. The graph indicates that when the amount of the trace fossil that is eroded exceeds 40–50%, the values of D_{Box} and D_{Info} begin to diverge, and they decrease below the values obtained in the previous two analyses. This erosion analysis demonstrates that even if as much as half of the original trace fossil has been removed by erosion, an accurate estimate of its fractal dimension is possible to obtain.

One of the results that these three fractal analyses show is that the graphoglyptid burrow tunnels usually are thin enough that the percentage of area covered in each box does not give an appreciable difference in fractal dimension between D_{Box} and D_{Info}. For this reason, only D_{Box} was used in the subsequent fractal analyses.

2.3.2 Fractals of feeding behavior

One possible implication of using the fractal dimension is in the determination of a DF-OFS (deposit-feeding optimal foraging strategy) by graphoglyptids. With increased optimization, the burrowing pattern could become more geometrically complex and/or the burrowing organism could ingest more of the food-rich sediment. Either of these explanations would lead to a higher fractal dimension – most likely closer to D = 2.0 than to 1.0. It also is understood that several factors may affect how optimal or complex a forager's pathway could be, which could affect the fractal dimension of the resulting trace (Levinton and Kelaher, 2004).

To test the hypothesis that optimization of DF-OFS leads to a higher fractal dimension, artificial burrow simulations of Papentin (1973) were analyzed. Papentin (1973) developed a computer program where a society of approximately 100 virtual

"worms" (nicknamed "*Rectangulus rectus*") were allowed to "evolve" following a set of parameters derived from an analysis of burrows of the modern polychaete worm *Paraonis*. Using the images that Papentin (1973) published of a few selected steps, the fractal dimension was calculated for each step and then plotted (Fig. 2.8; Papentin, 1973, fig. 4). Over the course of 140 generations for a population of approximately 100 "worms," the fractal dimension increased each subsequent time from D_{Box} = 1.659 to 1.752. This analysis shows that the optimization of the feeding patterns occurred very quickly at first and then proceeded much more slowly after the sixth generation.

2.3.3 Comparing trace fossils

The *Rectangulus* experiment of Papentin (1973) represents the development of one type of systematic feeding pattern in the sediment, as was discussed for the DF-OFS. The most instructive way to determine what ethologic strategies might have been used by graphoglyptid producers would be to compare real graphoglyptid specimens with other types of trace fossils in a similar time period and environment.

For this study, a number of graphoglyptid examples from the Guipuzcoan Flysch of the Higuer-Getaria Formation (Lower Eocene), Zumaia, Spain were examined (Fig. 2.9). Well-exposed sections of graphoglyptid-rich turbidite sequences in this region are celebrated for their high abundance and diversity of deep-marine trace fossils (Seilacher, 1977; Wetzel, 2000). The turbidite facies represented include basin plain, outer fan, and depositional lobes of the middle fan (Leszczynski, 1991a), where each turbidite layer was deposited once every few thousand years (Gawenda et al., 1999). The stratigraphic sequence contains an uninterrupted succession from the Upper Cretaceous through the

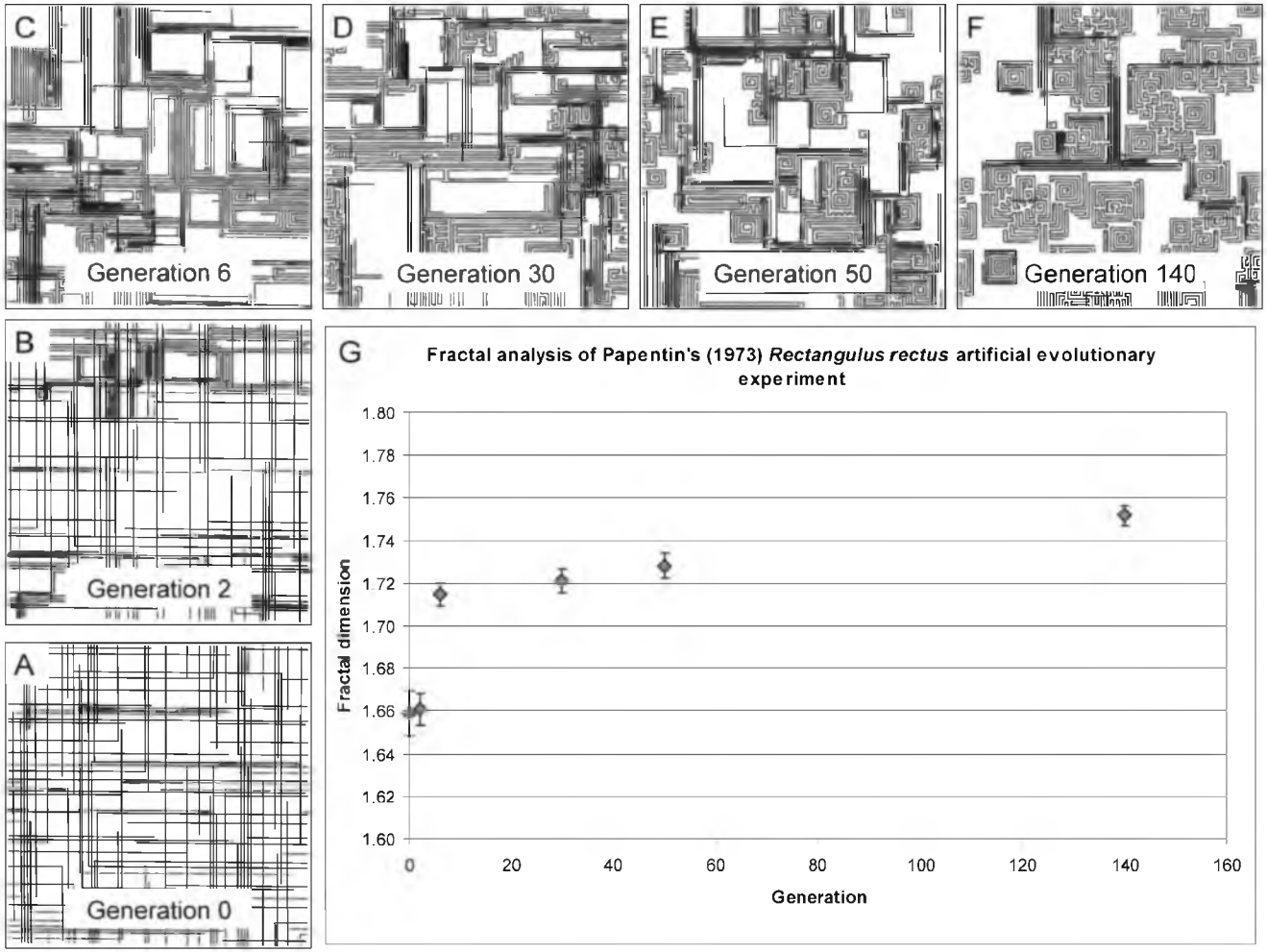

Figure 2.8. Papentin's (1973, fig. 4) computer-generated evolutionary experiment. A) Generation 0. B) Generation 2. C) Generation 6. D) Generation 30. E) Generation 50. F) Generation 140. G) The plot shows a comparison of generation versus fractal dimension (D) for the D_{Box}. Error bars represent the standard error.

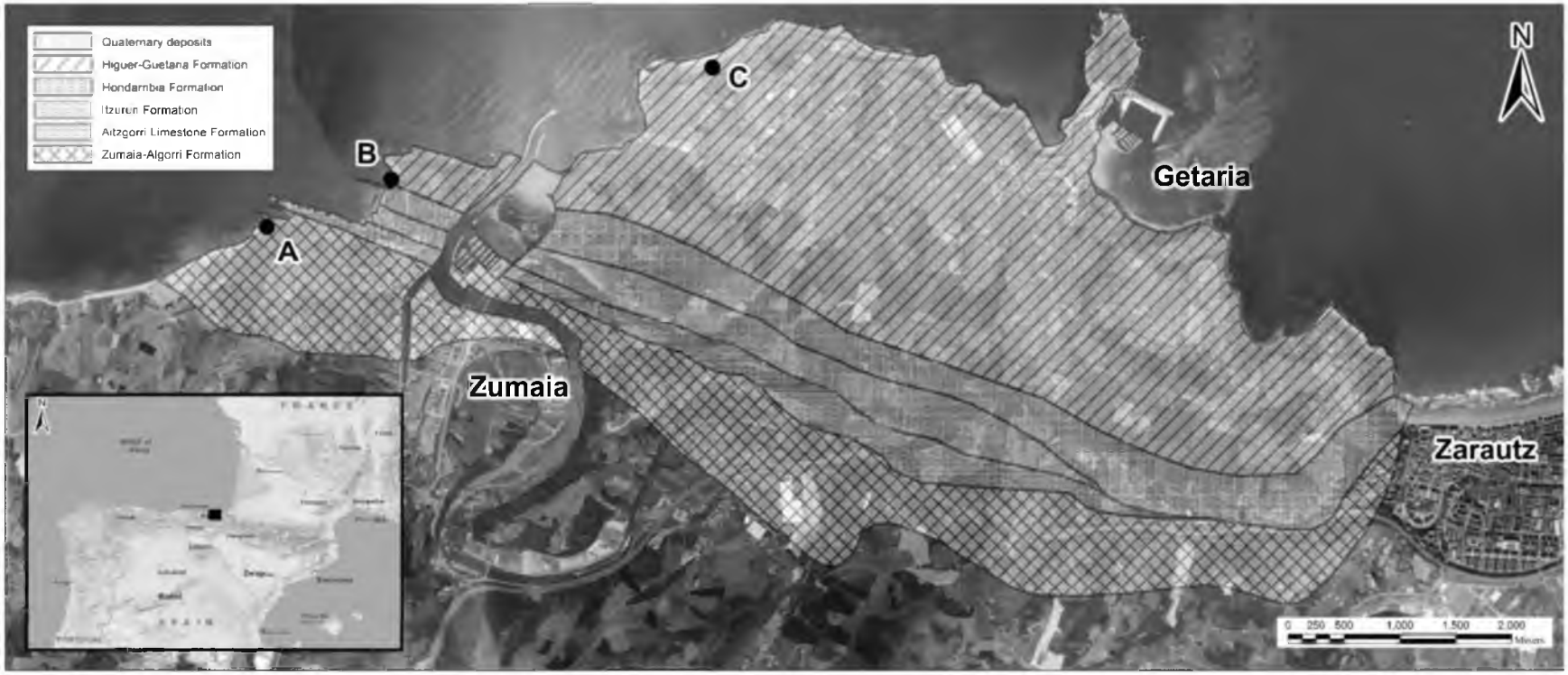

Figure 2.9. Geologic map of Zumaia, Spain, and surrounding region, showing sampling localities (A–C). The map is modified from Rosell et al. (1985, fig. 2), Pujalte et al. (2000, figs. 10 and 12), Bernaola et al. (2009, fig. 1), and Cummings and Hodgson (2011, fig. 1).

lower Eocene. Trace fossils were photographed in the field for analysis, since the rock slabs were too large to be collected.

The graphoglyptid specimens that were analyzed occur at a single locality along the coast between Zumaia and Getaria (Point C on Fig. 2.9). The representative graphoglyptids include *Cosmorhaphe, Helicolithus, Helminthorhaphe, Megagrapton, Spirorhaphe,* and *Paleodictyon* (Fig. 2.1). All of these graphoglyptids are understood to represent burrowing activity in a 2-dimensional space. Examples of *Lorenzinia* and similar radiating traces were not analyzed, since they likely represent only a portion of a 3-dimensional trace. The graphoglyptids were compared to known deposit feeding traces, including both pascichnia (*Scolicia*) and fodinichnia (*Zoophycos),* which were selected from within the same sequence of rocks. *Zoophycos* samples are Late Cretaceous in age (Point A on Fig. 2.9), and *Scolicia* samples are Early Eocene in age (Points B and C on Fig. 2.9).

2.4 Results

The fractal dimensions were determined for all of the analyzed trace fossils (Fig. 2.10; Table 2.1). Results show that the fractal dimension of sediment deposit-feeders is significantly higher than that of any of the graphoglyptids. The D_{Box} of the sediment deposit-feeders ranged from 1.767 to 1.850, whereas the D_{Box} of the graphoglyptids ranged from 1.277 to 1.626. In the case of "*Rectangulus*" and *Scolicia*, the reason for the higher D_{Box} is because there are multiple pathways that overlap each other. This likely resulted from the same organism (or multiple organisms) retreading the same ground. In the case of *Zoophycos,* the reason for the higher D_{Box} is because this is an example of a

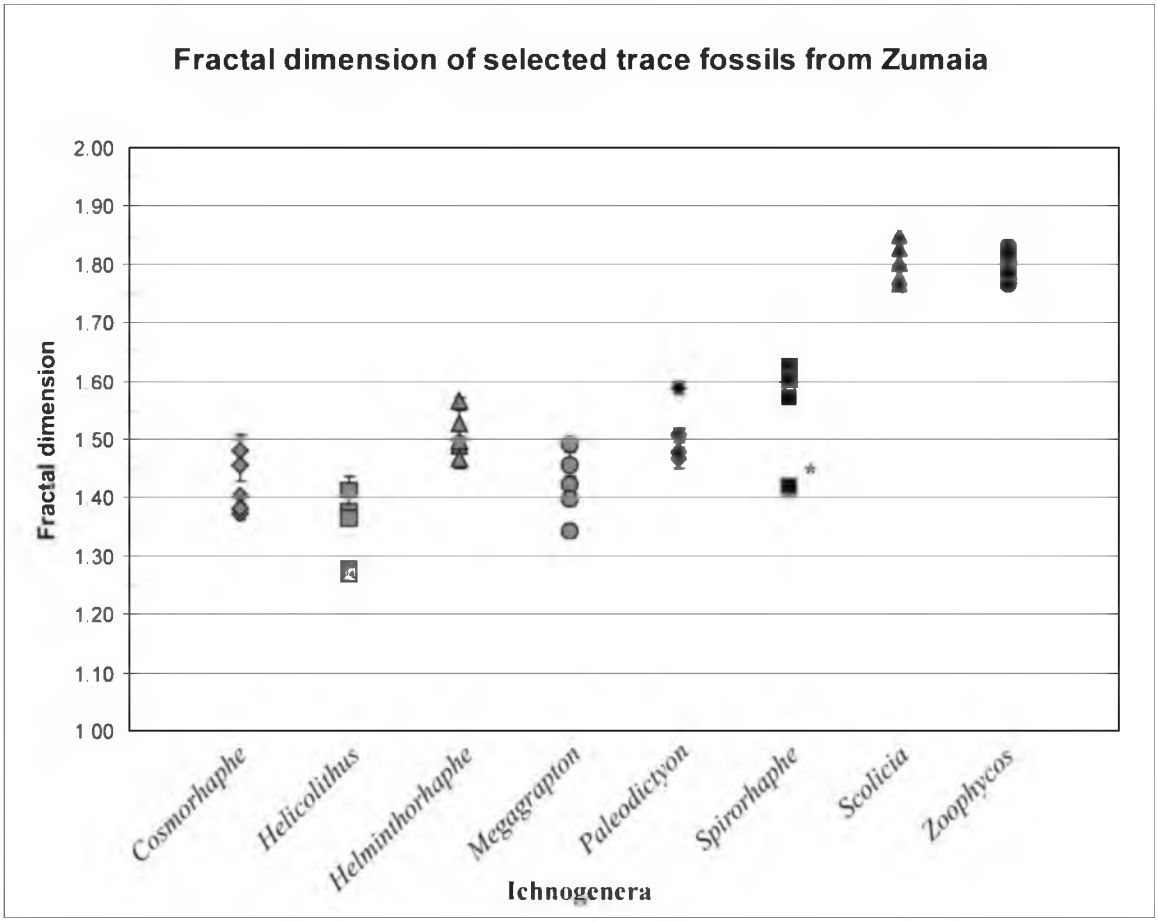

Figure 2.10. Fractal dimension of selected trace fossils from Zumaia, Spain. The fractal dimension (D_{Box}) scale extends for the entire range possible for planar trace fossils (1.0 – 2.0). Ichnogenera include graphoglyptids (*Cosmorhaphe*, *Helicolithus*, *Helminthorhaphe*, *Megagrapton*, *Paleodictyon*, and *Spirorhaphe*) and nongraphoglyptids (*Scolicia* and *Zoophycos*). Individual sample values are listed in Table 2.1. Error bars represent the standard error. The asterisk indicates a sample that was significantly eroded.

single organism being extremely efficient and producing very tightly packed feeding tunnels.

2.5 Discussion

The use of fractal dimensions to analyze various trace fossils supports the theory that graphoglyptids represent agrichnia instead of a deposit feeding strategy (pascichnia

Table 2.1. Fractal analysis results of Zumaian trace fossils

Trace	Sample	D_{Box}	Trace	Sample	D_{Box}	Trace	Sample	D_{Box}
Cosmorhaphe	1	1.405 ± 0.003	*Megagrapton*	5	1.491 ± 0.005	*Spirorhaphe*	4	1.626 ± 0.006
Cosmorhaphe	2	1.482 ± 0.026	*Paleodictyon*	1	1.468 ± 0.017	*Spirorhaphe*	5	1.604 ± 0.005
Cosmorhaphe	3	1.373 ± 0.011	*Paleodictyon*	2	1.588 ± 0.011	*Scolicia*	1	1.850 ± 0.002
Cosmorhaphe	5	1.456 ± 0.028	*Paleodictyon*	3	1.507 ± 0.013	*Scolicia*	2	1.848 ± 0.002
Cosmorhaphe	6	1.382 ± 0.009	*Paleodictyon*	4	1.507 ± 0.011	*Scolicia*	3	1.802 ± 0.003
Helicolithus	1	1.377 ± 0.010	*Paleodictyon*	5	1.478 ± 0.008	*Scolicia*	4	1.777 ± 0.007
Helicolithus	2	1.277 ± 0.008	*Megagrapton*	1	1.423 ± 0.010	*Scolicia*	5	1.827 ± 0.006
Helicolithus	3	1.268 ± 0.012	*Megagrapton*	2	1.457 ± 0.020	*Scolicia*	6	1.767 ± 0.003
Helicolithus	4	1.365 ± 0.002	*Megagrapton*	3	1.344 ± 0.011	*Zoophycos*	1	1.811 ± 0.002
Helicolithus	5	1.413 ± 0.023	*Megagrapton*	4	1.399 ± 0.011	*Zoophycos*	2	1.830 ± 0.001
Helminthorhaphe	1	1.489 ± 0.002	*Megagrapton*	5	1.491 ± 0.005	*Zoophycos*	3	1.804 ± 0.004
Helminthorhaphe	2	1.498 ± 0.005	*Paleodictyon*	1	1.468 ± 0.017	*Zoophycos*	4	1.807 ± 0.002
Helminthorhaphe	3	1.528 ± 0.022	*Paleodictyon*	2	1.588 ± 0.011	*Zoophycos*	5	1.776 ± 0.002
Helminthorhaphe	4	1.468 ± 0.018	*Paleodictyon*	3	1.507 ± 0.013	*Zoophycos*	6	1.797 ± 0.001
Helminthorhaphe	5	1.566 ± 0.005	*Paleodictyon*	4	1.507 ± 0.011	*Zoophycos*	7	1.774 ± 0.001
Megagrapton	1	1.423 ± 0.010	*Paleodictyon*	5	1.478 ± 0.008	*Zoophycos*	8	1.766 ± 0.002
Megagrapton	2	1.457 ± 0.020	*Spirorhaphe*	1	1.573 ± 0.004	*Zoophycos*	9	1.821 ± 0.001
Megagrapton	3	1.344 ± 0.011	*Spirorhaphe*	2	1.571 ± 0.006	*Zoophycos*	10	1.787 ± 0.002
Megagrapton	4	1.399 ± 0.011	*Spirorhaphe*	3	1.419 ± 0.009			

The fractal dimension of selected trace fossils from Zumaia, Spain, that are illustrated in Figure 2.10. Ichnogenera include graphoglyptids (*Cosmorhaphe*, *Helicolithus*, *Helminthorhaphe*, *Megagrapton*, *Paleodictyon*, and *Spirorhaphe*) and non-graphoglyptids (*Scolicia* and *Zoophycos*). Variance in the fractal dimensions is represented by the standard error.

and fodinichnia). The producers of graphoglyptids were not deposit feeders, based on comparisons of the fractal dimensions of the graphoglyptid burrows with those of known deposit-feeding (pascichnial and fodinichnial) traces. In this study, a systematic deposit-feeding strategy creates a higher fractal dimension (in this study, greater than 1.75; see Table 2.1). The higher fractal dimension is possibly a result of the organism feeding from as much of the sediment as possible. The fractal dimensions of both *Scolicia* and *Zoophycos* are more representative of complete coverage of the sediment area (D_{Box} = 1.767 to 1.850) than what is seen for any of the graphoglyptids (D_{Box} = 1.277 to 1.626). This finding suggests that the tightly spaced geometric attributes of deposit-feeding burrows, which yield a high fractal dimension, is a result of a feeding pattern that maximizes the coverage of a food-rich path of the sediment. The fractal dimension of the graphoglyptid burrows is too low compared with that of the deposit-feeding burrows in the same geologic age and setting, although repeated tests would be needed to confirm these results.

Jeong and Ekdale (1996, 1997) suggested that the fractal dimensions of some Paleozoic deposit-feeding burrows reflected the efficiency of systematic feeding within the sediment. De Gibert et al. (1999) used fractal analysis to analyze the geometry of the trace fossil *Sinusichnus*. The fractal dimension of *Sinusichnus* was determined to range from 1.22–1.58, corresponding with the fractal dimension range of graphoglyptids in this study. The low to medium fractal dimension results were used to support the hypothesis that *Sinusichnus* represented an agrichnia trace. Baucon (2010) calculated the fractal dimensions of various types of trace fossils, including some graphoglyptids, from specimens illustrated in the literature. According to his results (Baucon, 2010, fig. 14),

the highest fractal dimensions are seen in fodinichnia (*Zoophycos*) and pascichnia (*Helminthoida*), whereas the fractal dimensions of graphoglyptids (*Paleodictyon*, *Spirorhaphe*, *Cosmorhaphe*) are lower. Baucon's (2010) calculations conform well to those obtained in the current study, and they corroborate the observation that graphoglyptids typically display a noticeably lower fractal dimension than what might be expected for a fodinichnial or pascichnial feeding strategy.

Examination of the fractal dimensions of the different graphoglyptid ichnogenera analyzed for this study show that most of the fractal dimensions overlap significantly. This is strong support of the hypothesis that the different ichnogenera were using the same behavior, since similar fractal dimensions indicate that they covered the surface to the same extent, even though they are composed of significantly different shapes. These interpretations lead to the conclusion that graphoglyptid burrows likely represent an agrichnial strategy. The overlap of fractal dimensions also lends credence to the hypothesis that graphoglyptids comprise a single ethologic group of trace fossils and not an amalgamation of similarly preserved trace fossils.

Results of the analyses in this study (Fig. 2.10; Table 2.1) indicate that the fractal dimensions of the different graphoglyptid ichnogenera are well constrained. The only obvious anomaly is that of a low fractal dimension for one specimen of *Spirorhaphe*, which probably was due to poor preservation of that particular specimen. The graphoglyptid fractal dimensions ranged from 1.277 to about 1.626, with each particular ichnogenus having a fractal dimension range of 0.097 to 0.147.

2.6 Conclusion

The inferred behavioral significance of graphoglyptid burrows has been a debatable issue among ichnologists. A quantifiable means for comparing various kinds of trace fossils can be achieved by using a fractal geometric approach for analyzing trace fossils that represent different feeding behaviors. The results of the fractal analyses in this study show that pascichnial and fodinichnial behavior patterns display a high fractal dimension, whereas the graphoglyptid traces display a much lower fractal dimension. This observation indicates that graphoglyptid feeding patterns do not represent the maximum coverage of sediment, as would be expected for a deposit feeding strategy. The best-supported hypothesis for the graphoglyptid feeding patterns, therefore, is that they represent an agrichnial (farming) behavior.

This study demonstrates that fractal analysis offers a useful methodology for ichnological interpretation. Fractal analysis can be used successfully in determining feeding behavior, and it also may be a helpful approach for determining ichnotaxobases of similar trace fossils. When examining the fractal characteristics of individual ichnogenera, each ichnogenus apparently has a narrow fractal dimensional range, although more analyses of graphoglyptids from different time periods and formations would help support this. Fractal analysis also is able to provide information on incomplete specimens. As long as the amount of missing information due to erosion is minimal, fractal analysis can be a powerful ichnological tool in the paleontologist's tool belt.

CHAPTER 3[1]

PITFALLS, TRAPS, AND WEBS IN ICHNOLOGY: TRACES AND TRACE FOSSILS OF AN UNDERSTUDIED BEHAVIORAL STRATEGY

3.1 Abstract

The trapping of prey, where predators use external resources to help capture prey, is a specialized type of feeding behavior that is identified in the trace fossil record only rarely. Trapping traces that have been reported in the literature include spider webs, ant-lion burrows, scorpion pits, cerianthid tube anemone burrows, echiuran worm burrows, polychaete worm (*Paraonis*) burrows, and deep-sea graphoglyptids burrows. There is uncertainty, however, if all of these examples actually represent traps. *Paraonis* burrows, for example, have been represented as trapping traces, but there is a question if they actually represent this kind of behavioral strategy. Previous references and new field work indicate that *Paraonis* likely employs a selective deposit feeding strategy. In the fossil record, most of the known trapping traces are represented by spider webs, which are preserved in amber, and graphoglyptid burrows. Trace fossils that could represent trapping strategies may exhibit some basic morphological attributes, including (1) a

[1]Reprinted from Palaeogeography, Palaeoclimatology, Palaeoecology, v. 375, James R. Lehane and A.A. Ekdale, Pitfalls, traps, and webs in ichnology: Traces and trace fossils of an understudied behavioral strategy, pp. 59-69, 2013, with permission from Elsevier.

conical depression composed of loose sediment; (2) an open pit; (3) a physical snare composed of a sticky substance; and/or (4) adequate spacing between the burrows, pits, or snare material without much overlapping. The interpretation that at least some graphoglyptids (e.g., *Spirorhaphe*) represent trapping was based on a trapping model for *Paraonis*, but since *Paraonis* does not trap prey, the question arises whether graphoglyptids should be considered trapping at all. The variety of graphoglyptid morphologies supports the idea that graphoglyptids were not all doing the same thing. Previously, the ethological category of agrichnia has been applied to graphoglyptids and has been used to denote both trapping and farming behaviors, although the two behaviors display distinctly different feeding strategies. Some graphoglyptids may represent farming traces, while others may represent trapping traces, but it is unlikely that an individual burrow represented both behaviors. The new behavioral category 'irretichnia' is proposed here to encompass trapping trace fossils, due to its unique behavioral significance and also to separate trapping from farming.

3.2 Introduction

The trapping of prey is a highly specialized feeding behavior in the animal kingdom. Trapping involves the employment of external resources to help a predator capture prey. Traps can include sticky materials, pits to fall into, or any other activity where the predator does not search for and subdue the prey, but rather waits and ensnares the prey. Trapping does not include animals that use burrows or other structures as ambush points to attack prey. In this study, prey is considered as an animal (multicellular heterotroph) that is captured and consumed by a predator.

Among the most widely recognized examples of true trapping behavior by invertebrates are spiders that capture prey in intricately constructed webs. Another type of trap, exemplified by modern ant-lion burrows, has even made its way into the movies (as featured as the sandy 'sarlaac' pit in the film, *Return of the Jedi*). Even though some examples of predator traps, such as spider webs, are common in the modern environment, confirmed cases of predator traps in the fossil record are exceedingly rare. The purpose of this paper is to illustrate all of the cited examples of trapping in the animal kingdom, both modern and ancient, assess their identification in the modern and ichnological record, and analyze some known trace fossils that could represent trapping behavior. The designation of a new behavioral category "irretichnia" is introduced here to represent trapping traces in the trace fossil literature.

3.3 Modern trapping traces and their fossil equivalents

3.3.1 Ant-lion burrows

Ant-lion larvae (Insecta, Myrmeleontidae) build traps by creating conical, pit-like burrows in loose sand. When a hapless ant stumbles into the burrow, the ant-lion proceeds to kick-up sand, preventing the ant from climbing out (Turner, 1915; Heinrich and Heinrich, 1984). The hapless ant then is eaten by the ant-lion. Several different species of ant-lions produce a range of pit morphologies (Fig. 3.1A), some with V-shape walls and others with nearly vertical walls (Griffiths, 1980, 1986).

Ant-lion burrows have not yet been identified in the fossil record. Ant-lions are known from the body fossil record since the Early Permian (Rasnitsyn and Quicke, 2002), but their feeding on ants probably has been a more recent adaptation, since ants

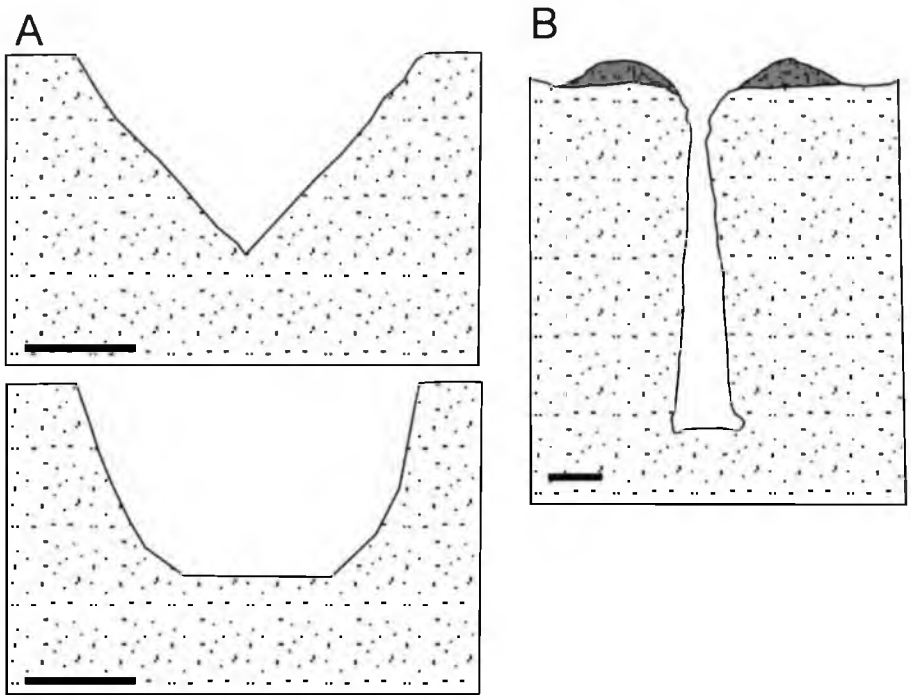

Figure 3.1. A, Cross-sectional view of ant-lion burrows (based on discussion by Griffiths, 1980). Scale bar is ~1 cm. B, Cross-sectional view of scorpion pits and burrows (modified from Harington, 1977). Scale bar is ~3 cm.

are known only from the Albian (Heads et al., 2005). This of course does not preclude the possibility that ancient ant-lions may have fed on other kinds of insects in the same manner as they feed on ants today. An ant-lion burrow likely produces a V-shaped trace fossil that cuts across the layers of the sediment and is filled with unstratified sediment. There is one example of a burrow that has these characteristics from the Devonian (Morrissey et al., 2012), far earlier than the known occurrences of ant-lion body fossils.

3.3.2 Scorpion burrows and pits

Scorpions (Chelicerata, Scorpionidae) create multiple types of burrows ranging from large, low-angle, branching burrows to vertical-walled pits, several of which are constructed to act as traps (Williams, 1966; Shorthouse and Marples, 1980; Harington,

1977; Hembree et al., 2012). The longer scorpion burrows with gently sloping entrances usually serve as shelter from predators, but the openings also may serve as traps for passing prey (Hembree et al., 2012). The scorpion sits just inside the burrow openings to wait for the prey. The scorpion then attacks as the prey enters the burrow while trying to escape the high daytime surface temperatures (Shorthouse and Marples, 1980).

Vertical scorpion burrows, which are constructed to be pitfall traps, are made by *Cheloctonus jonesii* (Pocock, 1892). Unlike the low-angle scorpion burrows, *C. jonesii* digs the pit and then returns later to retrieve the prey that has fallen in (Harington, 1977). The walls of the pitfall trap range from vertical to inwardly inclined, with the base of the trap being larger in diameter than the opening (Fig. 3.1B). Scorpion burrows are produced in a firmer substrate than the ant-lion burrows, including soils and firmer sands that can be compacted to stabilize the burrows.

Terrestrial scorpion body fossils are known since the Early Mississippian (Kjellesvig-Waering, 1986). Most species of scorpions today create a burrow where the cross-section of the entrance has a flat bottom and crescent-shaped upper half, mirroring the cross-section of a scorpion body. This type of burrow is unique to scorpions, whereas most other burrowing animals create circular or oval burrow openings (Polis et al., 1986). Scorpion burrows are extremely rare in the fossil record, only being recorded in the Pleistocene of Sonora, Mexico (Phelps, 2002), but there probably are many that are unrecognized in the ichnofossil record (Hembree et al., 2012). Identification of many scorpion burrows in the fossil record should be straightforward if the observer knows what to look for, since they have a unique geometry (Phelps, 2002).

3.3.3 Spider webs

Spiders (Chelicerata, Araneidae) produce sticky strands of 'silk' that many species, most commonly orb-weaver spiders, weave into a web for trapping prey (Kaston, 1964). The strength, structure, and shape of the webs are often taxon-specific, leading some researchers to infer that lineages of spider taxa might be determined using spider web morphology (Eberhard, 1990). Spiders have been producing silk since at least the Middle Devonian (Selden et al., 2008), and the silk produced in modern spiders is as strong as bulletproof clothing (Vollrath and Knight, 2001), thus rendering silk an effective material to be used in construction of a trap. In spite of the long history of spiders and the extreme strength of spider silk, spider webs are extremely rare in the fossil record. The problem is that even though spider silk is very strong, it also is very biodegradable and rarely preserved, except in amber, which is where all of the known fossil spider webs are found.

Of the few findings of spider silk in the fossil record, the oldest is the occurrence of silk still attached to a spider from the Middle Devonian (Selden et al., 2008). The first reports of spider webs, or at least silk strands, occur in the Early Cretaceous (Zschokke, 2003; Jarzembowski et al., 2008; Brasier et al., 2009), followed by fossil silk found in the Middle Cretaceous, Eocene, and Miocene (Zschokke, 2004). Most of these examples are single threads, not full webs. There are a few reports of branching threads (Penney, 2008; Brasier et al., 2009) that might be construed as a partial trapping structure, and there are even fewer reports of fossilized spider webs with evidence of the web being used as a trap (Poinar and Poinar, 1999: figs. 70 and 71; Poinar and Buckley, 2012).

3.3.4 Cerianthid tube anemone burrows

Cerianthid tube anemones (Cnidaria, Anthozoa, Cerianthidae) are stationary predators that live in short vertical burrows in intertidal sand flats, as seen in Cholla Bay, Sonora, Mexico (Fig. 3.2A). The burrowing anemone completely covers itself and waits for an unsuspecting victim to crawl across its camouflaged oral disk of poison-laden tentacles, where the victim is killed and ingested by the predator (Fig. 3.2B).

Burrows of sea anemones have been identified in the trace fossil literature, often referred to the ichnogenera *Conostichus* and *Bergaueria* (Fig. 3.3). Even though at least some *Conostichus* and *Bergaueria* could be regarded as predatory trapping traces, these trace fossils are commonly referred to as anemone dwelling traces (domichnia) (Alpert, 1973; MacEachern and Pemberton, 1992; Mata et al., 2012). In fact, infaunal anemones have been identified as possible predators as early as the Cambrian, based on trilobite fragments found in the central portion of the trace fossil *Dolopichnus gulosus* (Alpert and Moore, 1975). The paleoethologic interpretation of *D. gulosus* is that the predatory anemone used its burrow as a trap to catch, subdue, and ingest trilobite prey.

3.3.5 Echiuran worm burrows

Even though the majority of marine organisms are denser than salt water (1,075 kg/m^3 versus 1,026 kg/m^3 for salt water), the ability of a marine predator to set up an effective pitfall trap for prey could be a problem due to some degree of buoyancy preventing the prey from sinking quickly (Alexander, 1990). One of the potential answers to counter prey buoyancy is a form of feeding done by the echiuran worm, *Urechis caupo* (Fisher and MacGinitie, 1928). This worm feeds by producing a mucus net across the top

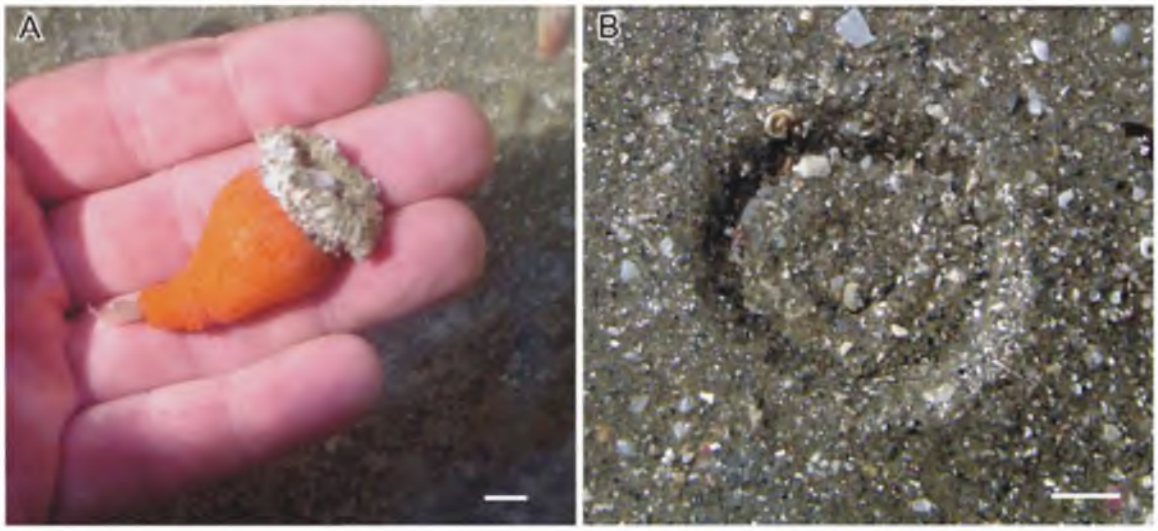

Figure 3.2. Burrowing sea anemone at Cholla Bay, Sonora, Mexico. A, Sea anemone removed from the sediment. B, Sea anemone in its burrow and covered with sediment. Scale bar is 1 cm.

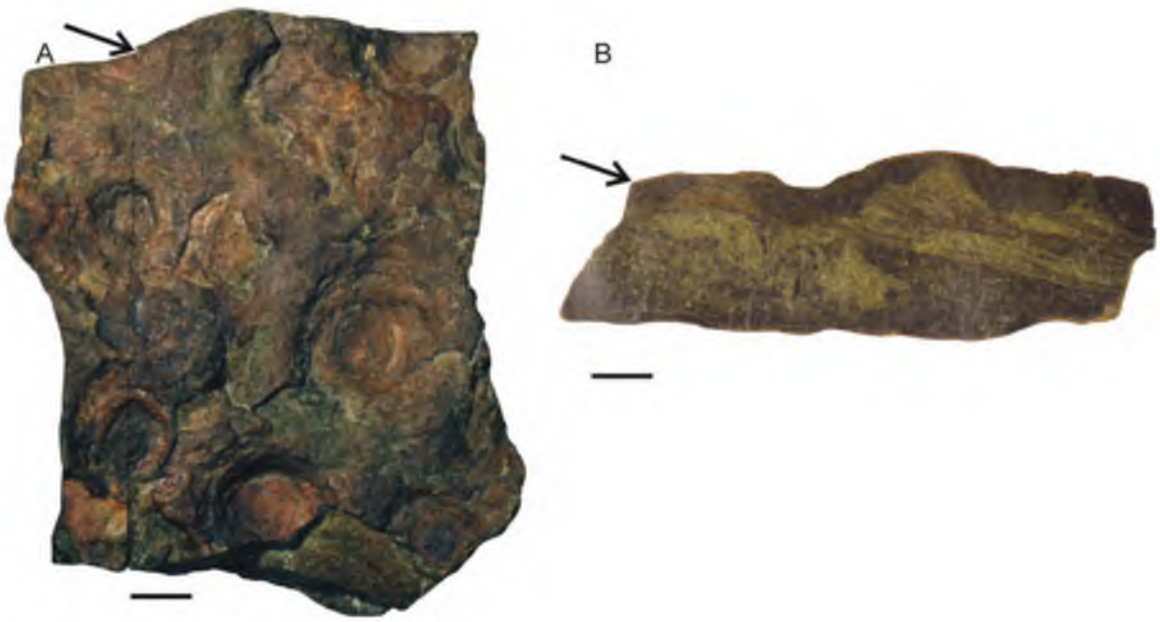

Figure 3.3. *Bergaueria* isp. from Lower Cambrian Brigham Quartzite of Two Mile Canyon, Idaho (Specimen UUIC-1428 in University of Utah Ichnology Collection). A, Top view. B, Side view of the polished right hand portion of the cut surface. The arrows indicate the same location along the cut surface of the sample. Scale bar is 2 cm.

of one end of its U-shaped burrow, functioning in a similar way to a spider web (Ricketts and Calvin, 1968). The worm generates a suction current through the burrow by the use of rhythmic contractions, which causes water to be drawn across the net trapping plankton and other food particles (MacGinitie and MacGinitie, 1968). *U. caupo* then proceeds to eat the mucus net containing the trapped food all at once. The feeding methods of *U. caupo* are sometimes considered to be a type of filter feeding, even though an external net is employed. The mucus net combines some of the pertinent features of a scorpion pit and ant-lion burrow with a spider web into one structure, because the prey animal gets stuck in the net rather than falling passively into a pit.

Burrows of echiuran worms have been identified in the trace fossil literature. *Diplocraterion parallelum* var. *quadrum* (Ekdale and Lewis, 1991) is a U-shaped burrow with a spreite from the Late Quaternary of New Zealand that very closely resembles modern echiuran burrows in the same area (Ekdale and Lewis, 1991). This trace fossil almost certainly is a fossil example of an echiuran trapping burrow. There is a possibility that some of the other U-shaped burrows in the trace fossil record (e.g., *Diplocraterion* and *Arenicolites*) also may have been created as trapping burrows by echiurans, or other similar organisms.

3.3.6 *Paraonis* burrows

Paraonis fulgens (Levinsen, 1882) is an infaunal polychaete annelid worm that lives in sandy, intertidal zones along the coasts of North America and Europe today (Papentin, 1973; Risk and Tunnicliffe, 1978; Gaston et al., 1992). Previous reports in the literature have stated that *Paraonis* creates an open burrow system to facilitate a

specialized diet of benthic diatoms by using the burrows as a trap for diatoms. The *Paraonis* trapping model suggests that when the worm burrows through the sediment, it selects the diatoms by pushing the non-organic sediment grains aside, and at the same time it solidifies its burrow walls with mucus (Risk and Tunnicliffe, 1978). At a later point in time, live diatoms migrate through the sediment and become trapped in the mucus-lined burrows, allowing the worm to return through its burrow and feed on the trapped diatoms (Röder, 1971; Seilacher, 1977; Risk and Tunnicliffe, 1978). Röder's (1971) initial trapping model for *Paraonis* was based on the the geometrically consistent pattern of the burrows, the few burrow intersections, and the fact that the the majority of the *Paraonis* gut contents were benthic diatoms (along with smaller amounts of foraminifer, small crabs, soft-bodied metazoans, and green algae).

Paraonis worms are found primarily in sandy substrates (96-99% sand) in littoral to sublittoral intertidal environments and are restricted to temperate latitudes (Gaston et al., 1992). The burrows of *Paraonis* can be found within oxic to anoxic sediments (Röder, 1971). In the oxic and dysoxic sediments, *Paraonis* worms create open burrow systems that are constructed as horizontal to semi-horizontal spirals, which emanate from the center and spiral outward (Fig. 3.4; Fig. 3.5A). The burrow path then continues in a horizontal plane spiraling outwards (*Spirorhaphe*-type) and will sometimes turn back upon itself following the initial curve of the spiral (*Helminthoida*-type). Within the sediment, the burrow system will often consist of multiple spiral tunnels tiered on top of each other. These spirals can be sufficiently dense as to completely bioturbated the sediment (~100 burrows/1,000 cm^3). In the deeper, anoxic sediment, *Paraonis* creates semi-vertical branching burrows (Röder, 1971).

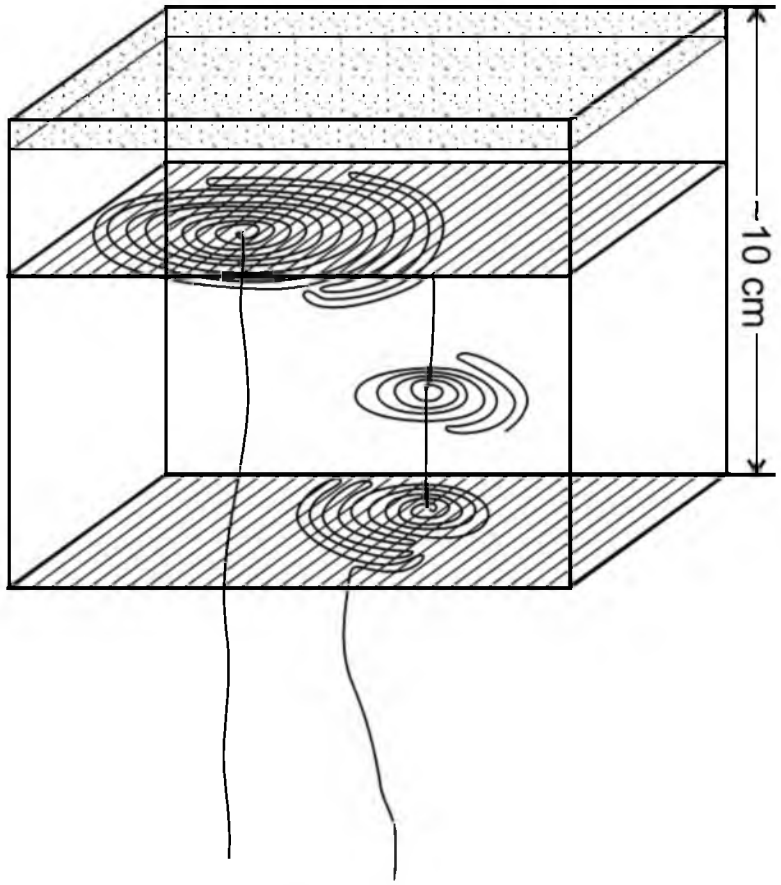

Figure 3.4. View of tiered structure of burrows of *Paraonis fulgens* (Levinsen, 1882), a polychaete annelid (modified from Röder, 1971: fig. 11). The 10 cm depth illustrated here indicates where the spiral burrows are located within the oxic and dysoxic sediments. Below 10 cm is the anoxic sediment. The speckled pattern at the top of the box represents the topmost centimeter, the only level where living diatoms are found.

Some questions arise regarding the *Paraonis* trapping model. Röder (1971) stated that the spirals were built quickly and were short-lived (>76% of the burrows were destroyed within five days), although the *Paraonis* worms were reported to have traveled along the burrows multiple times within those five days. There were no diatoms discovered within the mucus lining of the burrows, and no vertical migration of living diatoms was witnessed, although there was an assumption that the light needed for the investigation stalled any migration (Röder, 1971). There also is evidence that the *Paraonis* worm possibly was not feeding on a specialized diet of diatoms after all. The

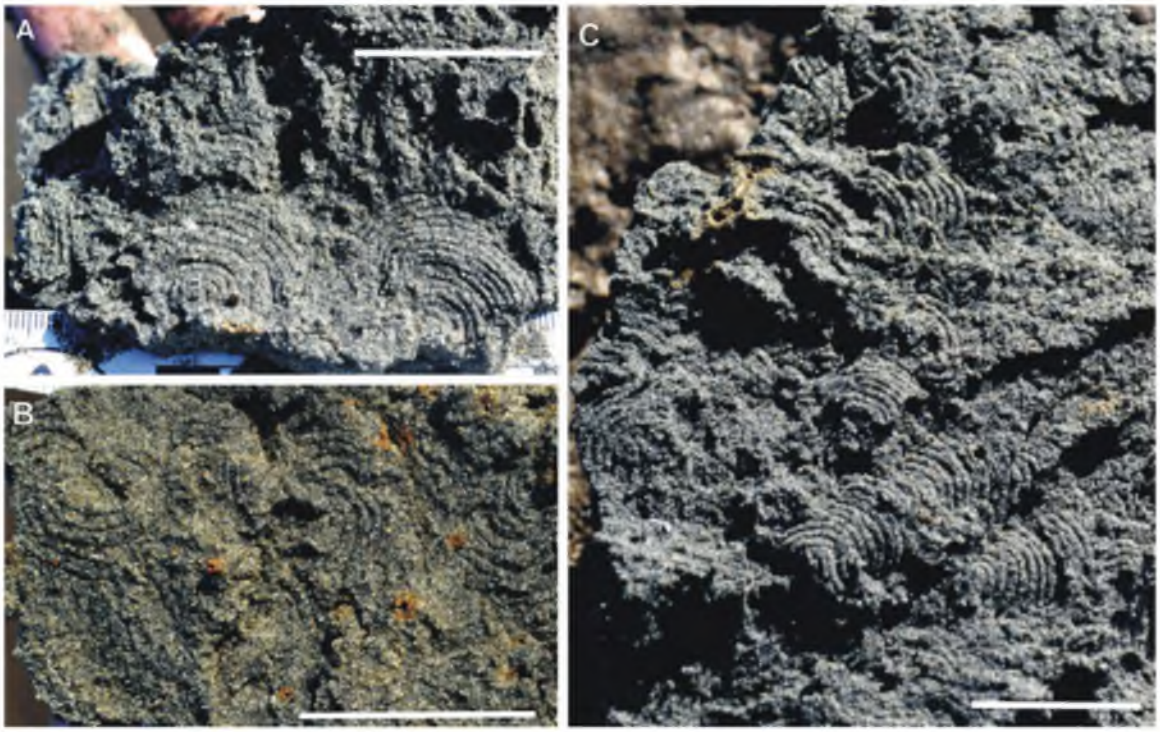

Figure 3.5. *Paraonis fulgens* burrows at Goose Point, Willapa Bay, Pacific County, Washington State. All of the photos were taken at SL3. A, Pair of typical *Spirorhaphe*-type *Paraonis* burrows. B, Sediment cross section showing *Paraonis* burrows and cross-cutting vertical worm burrows with oxidized burrow margins. C, Subhorizontal cross-section of the sediment illustrating multiple burrows covering different depths of the sediment from one to six centimeters in depth. Scale bars are 3 cm.

food discovered in the guts of some *Paraonis* worms was more representative of a deposit feeding organism containing mostly empty diatom frustules, dinoflagellates, and detritus (Gaston et al., 1992). To explain the reason that the worms analyzed by Röder (1971) had such a high concentration of diatoms in them, there was a suggestion that the gut contents of the worm simple reflected the sediment composition and not necessarily the "feeding method" of the worm.

Paraonis burrows are found in several localities in modern environments, including the North Sea (Röder, 1971), Gulf of Saint Lawrence (Brunel et al., 1998), Bay of Fundy (Risk and Tunnicliffe, 1978), Gulf of Mexico (Gaston et al., 1992), and Willapa

Bay in Washington State, USA (Gingras et al., 1999). Contrary to suggestions from previous workers (Risk and Tunnicliffe, 1978), there appear to be few factors that favor preservation of an open burrow system in a dynamic intertidal environment, so there is not an expectation that these burrows would be prevalent in the fossil record. There is one report of a *Paraonis*-like burrow in the fossil record from Permian tidal flat deposits in New Mexico (Minter et al., 2006). The spacing of the spiraling tunnels in the Permian fossil are much closer than has been observed in modern examples, but the general morphology is similar.

In order to determine which of the feeding habits was more likely (trapping or deposit feeding) another investigation of the burrows was needed. Therefore, for this study, burrows of *Paraonis* were observed at Willapa Bay in Washington State (Fig. 3.6).

3.3.6.1 Study area. Willapa Bay is a mesotidal (2-3 m tidal range) estuary that is separated from the Pacific Ocean by the North Beach Peninsula, a 27 km-long spit in the state of Washington. *Paraonis* burrows were observed at Goose Point along the eastern shore of the bay and were restricted mostly to the middle to lower intertidal deposits along Goose Point (Figs. 3.6-3.8). There were no upper intertidal deposits in this area owing to the edge of the tidal flat ending in a sea wall along the coast. The middle intertidal zone was composed of compacted sand with the upper 1 cm composed of oxygenated sand and the middle 2-10 cm composed of dysoxic sand. The *Paraonis* burrows did not exhibit any oxidized burrow margins but cross-cutting vertical worm burrows did show some evidence of oxidization (Fig. 3.5B). The lower intertidal zone was composed of loose sand and was similar to the middle intertidal zone in that the upper 1 cm was oxygenated and the middle 2-10 cm was dysoxic (Fig. 3.9). In both

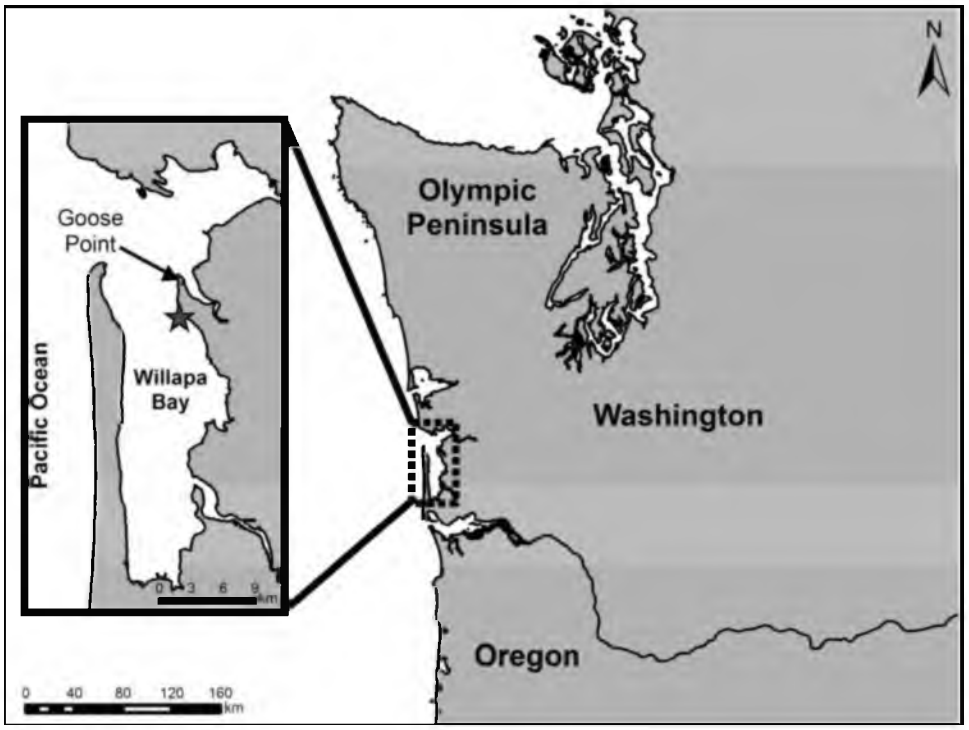

Figure 3.6. Location of modern *Paraonis* burrows at Goose Point, Willapa Bay, Pacific County, Washington State. The star indicates the sampling locations (SL) featured in Figure 3.7.

zones, the sand was composed of ~90% fine sand with negligible clay content, and the composition is mainly quartz in both locations.

Burrows were located by digging in rippled sand, free of eelgrass (*Zostera marina*), and with a lower concentration of open burrows on the surface (which were produced by decapod crustaceans and other polychaete worms) in the lower and middle intertidal zones. The burrows could be found by inserting a shovel into the sediment and pulling out clumps of sand. The sand clumps were broken by hand along sedimentary layering, horizontal to the surface. The *Paraonis* burrows were sufficiently distinct from other burrows to be identified easily (Gingras et al., 1999). Some *Paraonis* burrows were not perfectly horizontal, but instead they appeared to be following subhorizontal laminae

Figure 3.7. Field map of sampling locations (SL) for *Paraonis* burrows at Goose Point, Willapa Bay, Pacific County, Washington State. Stars indicate sites where *Paraonis* burrows were identified. The dotted line identifies the approximate divide between different tidal zones.

within the rippled sand. Burrows also could be identified as a line of small holes along the broken edge of the sand clump (Fig. 3.9).

3.3.6.2 Observations. Paraonis burrows were found from within the top centimeter of the sediment to 10 cm below the surface. In the lower intertidal zone, the burrows frequently were found isolated and very friable, meaning the burrows fell apart easily if the sediment was disturbed. The friability of the sediment made identification of the deeper individual burrows more difficult, so most of the identified burrows occurred within the top 4 cm (Table 3.1). One to two burrows were found within each clump at

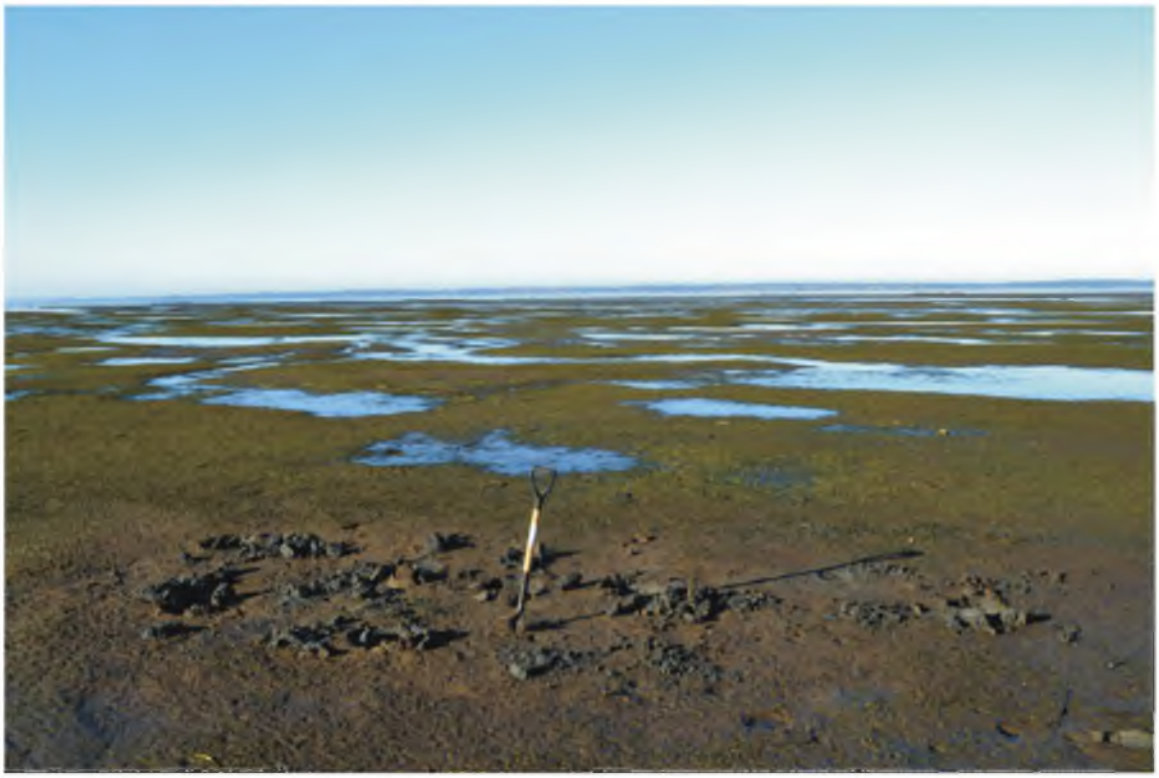

Figure 3.8. Photo of the intertidal flats at Goose Point, Willapa Bay, Pacific County, Washington State. Photo was taken at low tide at site SL3, facing west towards the current shoreline. Shovel for scale.

various depths. In the middle intertidal zone, the burrows were identified in one location free of eelgrass in harder packed sand where the cohesion of the sand grains prevented slight disturbances from destroying the burrows. Burrows in the middle intertidal zone were spaced closer together than the lower intertidal zone. The burrows were so abundant that they seemed to pervade the sediment, with burrows stacked within centimeters on top of each other. Due to the shear abundance of *Paraonis* burrows in the middle intertidal zone, they were not counted at different levels within the sediment, but every cross section for the 17 different holes analyzed had approximately 5-10 *Paraonis* burrows per 100 cm^2 on each horizontal surface.

Figure 3.9. Sediment cross-section containing *Paraonis fulgens* burrows at Goose Point, Willapa Bay, Pacific County, Washington. The cross-section is from the lower intertidal zone taken at SL2. Arrow highlights the burrows as seen in cross-section. Dashed line indicates the transition from oxic to dysoxic sediment. Scale bar is 1 cm.

Throughout the intertidal zone, the burrows were found most often as portions of circular burrow networks extending outward into meandering arcs. Both types of *Paraonis* burrows (*Spirorhaphe*-type and *Helminthoida*-type) were identified in the field. Close inspection of the burrow walls with a hand-lens did not identify any supporting mucus or other material. Even though there was no mucus was visible microscopically, there is a possibility that small amounts of mucus may be lining the walls. Individual

Table 3.1. Number of *Paraonis* burrows identified within the lower intertidal zone at Goose Point, Willapa Bay, Pacific County, Washington State at ~40 studied locations.

Depth below surface (cm)	Number of *Paraonis* burrows
0-1	2
1-2	8
2-3	9
3-4	5
4-5	1
5-6	0
6-7	0
7-8	0
8-9	0
9-10	1
Unsure	2

burrows were ~0.5 mm wide with ~2 mm spacing between each whorl. Burrow networks ranged in width from 1 cm to several centimeters. *Paraonis* worms were found in the sediment, although there were no worms found within the *Paraonis* burrows or observed in the process of making any of the burrows.

3.3.6.3 Discussion – Testing the Paraonis *trapping model.* The ethologic model of *Paraonis* burrows as diatom traps is questionable. Diatoms have been shown to burrow in the sediment, although they typically only burrow down a few millimeters, up to a maximum depth of 1.4 cm. Diatoms also tend to live in sediment with higher silt and clay content because of the water that is retained (Hay et al., 1993; Aleem, 1950). The deepest *Paraonis* burrow (10 cm) is over seven times deeper than the depth of the deepest burrowing diatom. This indicates that although the shallowest burrows of *Paraonis* could be diatom traps, any burrow deeper than 1.4 cm would not function as such. If *Paraonis* burrows functioned as traps, then the *Paraonis* worms must be using them to trap some type of prey other than diatoms.

Another problem with the trap model is that the burrows would need to withstand some disturbance while the *Paraonis* worm re-enters the burrow in order to feed. Previous observations indicate that most of the burrows are destroyed within five days (Röder, 1971). Personal field observations indicate that there is not enough mucus, if any, to support the burrows as open tunnels, so that the burrows in looser sediment collapse with minimal disturbance. The sediment is readily disturbed by the shifting tides, which move the sand within the tidal flat twice a day. Even though it has been hypothesized that *Paraonis* revisited the burrows to feed on the diatoms which got stuck in the mucus-lined walls, there has been no observed proof of any diatoms trapped in mucus (Röder, 1971).

The morphology of the burrows also is inconsistent with a trapping model. For the worm burrows to act as a trap, the individual nets would need to be semi-isolated. Stacking the nets on top of each other could render the central nets useless, since passing organisms would get stuck on the outer nets. The *Paraonis* burrows at Willapa Bay are stacked upon each other in layers and packed so tightly together in some spots as to completely permeate the sediment (Fig. 3.3B).

All of this evidence indicates that the *Paraonis* worm was not trapping its prey, as has been suggested, but was likely a selective deposit feeding worm. The open burrow system was produced as a side effect of the worm moving through the grains selecting out the individual food items that it wanted, while pushing the inorganic sediment aside. The mucus on the body of the worm helped it slide through the sediment causing the burrows to remain open temporarily, even though the worm would likely not need to travel back through the open burrows.

3.4 Possible ancient traps

The few trace fossils representing undoubted examples of traps identified in the fossil record include reports of fossilized spider webs in amber (Penney, 2008; Brasier et al., 2009), a Devonian funnel-shaped pit that has been cited as a possible analogue to a modern ant-lion burrow (Morrissey et al., 2012), and Pleistocene scorpion burrows (Phelps, 2002). There is a possibility that many other trace fossils described in the literature, whose overall morphology resembles that of modern trapping pits and burrows, may have been misinterpreted. There are several common biogenic sedimentary structures, including some in the marine realm, which could be reinterpreted as trapping structures.

For a trace fossil to be interpreted as a trap, the trace fossil would likely possess several key features, including one or more of the following: (1) a conical depression composed of loose sediment; (2) an open pit; (3) a physical snare composed of a sticky substance; and/or (4) adequate spacing between the burrows, pits, or snare material without any overlapping. Snare material would not be preserved in most cases, except via preservation in amber, but there is a possibility that some structures could indicate the former presence of snare material, like the mucus used to compose the tube walls of many annelid worms (Ekdale et al., 1984a). Spacing is needed in a spider web to provide the largest net possible while using the least amount of material. Spacing is needed in burrows and pits to provide a 'landmine' approach to the field where close spacing would work counter to this by preventing more prey from entering the 'minefield'. While the previously mentioned criteria apply to terrestrial traps, they also may be extended to the

marine realm. Several existing marine ichnotaxa fit the criterion of a conical depression filled with loose sediment.

3.4.1 Simple pits and burrows

The simplest type of trapping trace is a pit of the kind created by ant-lion larvae and certain scorpions. These can be formed in loose sand with a conical shape (ant-lion like) or in a firmer substrate with vertical walls (scorpion like). Even though such pits commonly are found in a terrestrial environment there is a possibility that pits in the marine environment also could represent trapping traces.

Conical marine trace fossils, which would mimic the ant-lion method of trapping, include the following (Table 3.2): *Monocraterion*, a 'funnel-shaped' trace fossil (Goodwin and Anderson, 1974); *Conichnus* (Fig. 3.10), a conical ichnofossil that contains cone-in-cone chevron laminations that do not widen upwards (Myannil, 1966; Weissbrod and Barthel, 1998; Buck and Goldring, 2003); *Conostichus*, a cone-in-cone structure with interbedded sandy and muddy layers that contained concentrated sand around the outer walls of the funnel (Chamberlain, 1971; Pfefferkorn, 1971); *Cornulatichnus,* a sub-vertical conical burrow with massive infilling that is interpreted as a subaqueous open burrow (Carroll and Trewin, 1995); and *Altichnus*, a funnel-shaped tube that is always oriented perpendicular to the surface (Gaillard and Racheboeuf, 2006). Other possible trapping structures include un-named escape traces (Fugichnia), 'funnel-shaped' structures (Weissbrod and Barthel, 1998; Magyar et al., 2006; Jamer et al., 2011), and 'cone-in-cone' collapse structures (Buck and Goldring, 2003), where the inward collapse of the sediment was the result of depression in the underlying sediment.

Table 3.2. List of possible trapping traces and structural features previously mentioned in the trace fossil literature.

Trace fossil or Structure	Description
Altichnus	a funnel-shaped tube that is always oriented perpendicular to the surface
Bergaueria	Conical trace fossil
Cone-in-cone structures	inward collapse of the sediment was the result of depression in the underlying sediment
Conichnus	conical ichnofossil that contains cone-in-cone chevron laminations that do not widen upwards
Conostichus	cone-in-cone structure with interbedded sandy and muddy layers that contained concentrated sand around the outer walls of the funnel
Cornulatichnus	sub-vertical conical burrow with massive infilling that is interpreted as a subaqueous open burrow
Diplocraterion parallelum var. *quadrum*	U-shaped burrow with a spreite
Dolopichnus gulosus	Conical trace fossil with trilobite fragments
Fugichnia structures	Funnel-shaped structures interpreted as the result of a buried organism trying to escape
Funnel-shaped structures	Funnel-shaped trace fossils with unknown behavioral significance
Monocraterion	'funnel-shaped' trace fossil

3.4.2 Graphoglyptid burrows

Graphoglyptids trace fossils have been interpreted as representing traps and/or farming burrows (agrichnia) by several workers (e.g., Röder, 1971; Seilacher, 1977; Miller, 1991b; Uchman, 2003; Minter et al., 2006). Graphoglyptid burrows are geometrically complex, predepositional, open burrow systems, commonly preserved in positive hyporelief on the soles of deep-sea turbidite beds (Fig. 3.11). The taxonomic affinities of the producers of graphoglyptids are unknown, but they most likely represent the work of some type of worm or arthropod (Garlick and Miller, 1993). The geometric shapes of graphoglyptids range from meanders (*Cosmorhaphe*) to spirals (*Spirorhaphe*) to intricate networks (*Paleodictyon*). The width of individual graphoglyptid burrow tunnels ranges

Figure 3.10. *Conichnus conicus* (Myannil, 1966) from Middle Ordovician Yiyhvits Horizon of Estonia (Specimen UUIC-1148 in University of Utah Ichnology Collection). Scale bar is 1 cm.

from approximately 0.1 cm to greater than 5 cm (Uchman, 2003).

Modern graphoglyptids are found within the top few centimeters of deep-sea sediment (Ekdale, 1980), which is characterized by three zones: the Mixed Layer, the Transition Layer, and the Historical Layer (Berger et al., 1979; Ekdale et al., 1984b). Graphoglyptid burrows are formed within the uppermost couple of centimeters of the Mixed Layer, which extends down from the sediment-water interface to depths of 3 to 10 cm. This uppermost zone of the deep-sea sediment typically is completely homogenized by very active burrowers, so in a continuously accreting pelagic substrate, graphoglyptid burrows are not preserved (Ekdale et al., 1984b).

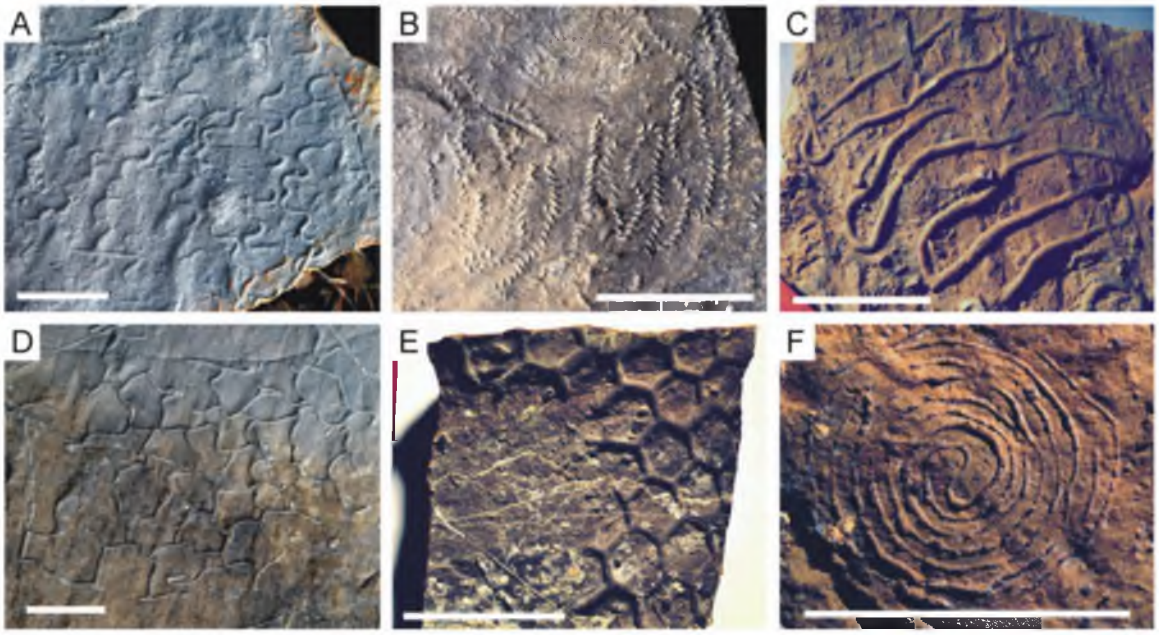

Figure 3.11. Photos of selected graphoglyptids. A. *Cosmorhaphe* from the Lower Eocene Guipúzcoan Flysch of Zumaia, Spain. B. *Helicolithus* from the Lower Eocene Guipúzcoan Flysch of Zumaia, Spain. C. *Helminthorhaphe* from the Upper Cretaceous of Tanzania (Specimen UUIC-1911 in University of Utah Ichnology Collection) D. *Megagrapton* from the Lower Eocene Guipúzcoan Flysch of Zumaia, Spain. E. *Paleodictyon* from the Jurassic of Calabria, Italy (Specimen UUIC-1164 in University of Utah Ichnology Collection). F. *Spirorhaphe* from the Upper Cretaceous of Tanzania (Specimen UUIC-1902 in University of Utah Ichnology Collection). Scale bars are 4 cm.

Unlike the other examples of possible trapping, graphoglyptid burrows have been recognized primarily from the fossil record, with modern examples only being discovered within the last 35 years (Ekdale, 1980). Graphoglyptid trace fossils are known since the Cambrian, but the producers of graphoglyptid burrows have not yet been identified in fossil or recent occurrences of the burrows (Ekdale, 1980; Rona et al., 2009).

The graphoglyptid trapping model is based on the interpretations of Röder (1971) for *Paraonis* burrows. The model was extended by Röder (1971) and Seilacher (1977) to interpret graphoglyptids, who cited the following similarities between *Paraonis* and graphoglyptids: (1) they are both open burrow systems; (2) the sharp outlines of fossil graphoglyptids indicated that the walls were likely reinforced by a "stronger than usual

mucus film"; (3) branching has been observed in both graphoglyptids and *Paraonis* burrows, which would be counterintuitive for a deposit feeding strategy; (4) careful distance is maintained between the burrows in both groups; and (5) the is no backfill in either group of burrows, which would indicate deposit feeding and would prevent turning around and retreading through the burrows. Since that time, the trapping model has been expanded to include all graphoglyptids, no matter the shapes (e.g., Miller, 1986, 1991b; de Gibert et al., 1999; Uchman, 2003).

3.4.2.1 Questioning the graphoglyptid trap model. For the trapping model to explain the behavior represented by graphoglyptid burrows, the graphoglyptid trace producers must be feeding on organisms that migrate through the sediment. The prey organisms must be small enough to get trapped in an open graphoglyptid burrow (<0.1 cm). Unlike the trapping model for *Paraonis* that is based on diatoms, photosynthetic protists like diatoms are immediately ruled out as potential graphoglyptid prey, since the deep-sea graphoglyptids occur far below the photic zone. Some of the potential prey organisms that could be caught in a trap are the ones that are mixing the sediment in the Mixed Layer. These organisms are the meiofauna (between 60 and 300 μm), which includes foraminifera, nematodes, harpacticoid copepods, polychaetes, ostracods, and crustacean nauplii (Wolff, 1977).

Paraonis burrows have been regarded by some ichnologists as an analogue for at least some graphoglyptids, both modern and ancient. The conclusion that *Paraonis* burrows probably are not traps makes the theory questionable whether any of the deep-sea graphoglyptids could represent trapping behavior. The similarities between the two types of burrow systems pointed out by Seilacher (1977) are correct, and if those

structures indicate selective deposit feeding by *Paraonis*, it could possibly indicate selective deposit feeding by some graphoglyptids. The many different shapes made by graphoglyptids alone (e.g., spirals, meanders, mesh network, etc.) should indicate that they likely are not all doing the same thing. To state that all graphoglyptids should be traps and/or gardening is misleading to the interpretation of their behavioral significance, so a clear distinction between trapping traces and gardening traces needs to be made.

3.5 Discussion

Trapping is a unique predatory behavior that is significantly different from most other forms of predation, since trapping requires the predator to patiently wait for its prey to get ensnared rather than to actively hunt down the prey. Trapping in many instances can be considered a more complex predatory behavior, because trapping requires the predator to construct a device to trap its prey as opposed to the relatively simple actions of running down its prey or sitting and waiting for the prey to pass by and then stomping on it. In modern settings, ecosystems dominated by trapping predators can change the balance and types of prey that are available, in comparison with ecosystems dominated by search-and-subdue predators (Rogers et al., 2012).

In the trace fossil literature, preserved evidence of trapping behavior usually has been included in the ethological category of agrichnia, which represents permanent (or semi-permanent) burrows used for cultivating and/or capturing food (Ekdale et al., 1984a). Agrichnial trace fossils have since become synonymous with graphoglyptids (Miller, 1991b). Farming (cultivating) food stuffs and trapping (capturing) prey are distinctly different habits, and trace fossils representing these two disparate behaviors

therefore should not be lumped into a single ethological category. In marine environments, farming burrows are constructed in such a way as to circulate water through the burrows, promoting bacterial and/or fungal growth on the burrow walls within the sediment, providing food sources for the burrowers (Seilacher, 1977). In contrast, traces constructed for the purpose of trapping are intended to ensnare mobile prey as they travel either through the sediment or pass by an open trap/burrow.

The behavioral activities of farming and trapping are fundamentally different, and there is need for a new ethological term to reflect the trapping of live prey, which may be included as a subset of praedichnia (i.e., predation traces). The behavioral category of agrichnia does not adequately encompass the trapping behavior, so use of the term agrichnia should be restricted to farming traces, as suggested for such ichnogenera as *Paleodictyon* (Seilacher, 1977, Lehane and Ekdale, 2013) and *Spongeliomorpha iberica* (de Gibert and Ekdale, 2010).

The new ethological term 'irretichnia' (from the Latin *irretio*, meaning 'to ensnare') is proposed here to encompass modern and ancient traces constructed for the purpose of trapping of live prey. Modern and fossil examples of animal traces that represent trapping behaviors include spider webs, ant-lion burrows, scorpion pits, cerianthid tube anemone burrows, echiuran worm burrows, and possibly some deep-sea graphoglyptid burrows. The new category 'irretichnia' will clarify paleoethological discussions when agrichnia is mentioned by distinguishing clearly between traces that represent farming and trapping behaviors. There are very few reports of genuine trapping traces in the literature, but by highlighting this type of behavior, there is anticipation that trapping behavior will be recognized more widely in the fossil record.

3.6 Conclusion

Trapping is a specialized form of predatory feeding behavior that is rarely recognized in the fossil record. The reasons for this include poor preservation (as with spider webs) or unrecognized evidence (as with ant-lion burrows and scorpion traps). There are enough examples of modern trapping behavior for us to conclude that fossil evidence of traps should be much more prevalent than is currently recognized.

Trapping behavior has been identified in the modern and ancient environments, including spider webs, ant-lion burrows, scorpion pits, cerianthid tube anemone burrows, echiuran worm burrows, and possibly some graphoglyptid burrows. Identification of the burrows of the polychaete worm *Paraonis* as representing trapping is likely incorrect based on field analysis, and we conclude that *Paraonis* should be regarded as a selective deposit feeder rather than a trapper. The insinuation that graphoglyptids also are traps based on the feeding models of *Paraonis* as trapping behavior should also be questioned. Whether that indicates that most graphoglyptids are traps or not is uncertain, but graphoglyptids should not be regarded as traps based solely on the initial misinterpretations of *Paraonis* behavior.

Trace fossil traps are grouped together in the new ethologic category, irretichnia, in order to distinguish them from farming burrows (agrichnia) and also to emphasize the importance of this type of predatory behavior. This new ethologic category draws attention to other possible trapping traces and also solidifies the argument that agrichnial trace fossils should represent only farming behavior and not represent an amalgamation of various types of feeding behaviors.

CHAPTER 4

ANALYTICAL TOOLS FOR QUANTIFYING THE MORPHOLOGY OF INVERTEBRATE TRACE FOSSILS[1]

4.1 Abstract

The analysis of trace fossils usually is performed qualitatively, which makes comparing trace fossils from different units less objective than quantitative approaches. Quantifying the shape of trace fossils enables scientists to compare trace fossils described by different people with greater precision and accuracy. This paper describes several methods for quantifying invertebrate trace fossils, including morphology dependent methods (motility index, mesh size, topology, tortuosity, branching angle, and the number of cell sides) and morphology independent methods (fractal analysis, burrow area shape, and occupied space percentage (OSP)). These tools were performed on a select group of graphoglyptid trace fossils, highlighting the benefits and flaws of each analytical approach. Combined together, these methods allow for more objective comparisons between different trace fossils.

---

[1]Reprinted from Journal of Paleontology, v. 88, James R. Lehane and A.A. Ekdale, Analytical tools for quantifying the morphology of invertebrate trace fossils, pp. 747-759, 2014, with permission from The Paleontological Society.

4.2 Introduction

Analyses of trace fossil shapes typically are subjective due in part because trace fossils are grouped on the basis of their overall morphological appearance, although there have been recent attempts at making ichnogeneric determination more consistent (Knaust, 2012). Most trace fossils have been described largely in qualitative terms, although there have been some significant attempts to characterize ichnological data in quantitative terms, including analyses of ichnofabrics (Droser and Bottjer, 1986, 1987; Magwood and Ekdale, 1994), bioturbation (Miller and Smail, 1997), vertebrate trackways (e.g., Thulborn, 1990; Bates et al., 2008), deep-sea cores (Ekdale et al., 1984b), spatial patterns (Pemberton and Frey, 1984), feeding patterns (Lehane and Ekdale, 2013), and ichnotaxonomy (Uchman, 1995, 2003; Orr, 1999).

To avoid misinterpretations based on variations in size and shape, there is a need for analytical methods that are not constrained by the size of the burrows. The purpose of this paper is to describe a few helpful methods that may be employed to quantify various aspects of trace fossils. The paper also will expand the ichnologist's toolbox with a few more analytical techniques while being able to describe ichnogenera and ichnospecies based on the shape alone, irrespective of size.

4.3 Methodology: Starting out

4.3.1 Preparing the trace fossils for analysis

In order to highlight the utility of the following analytical approaches, graphoglyptid trace fossils provide a useful template. Graphoglyptids are predepositional, geometrically complex, open burrow systems commonly preserved in convex hyporelief

on the soles of deep-sea turbidite beds (Fig. 4.1). Ichnogenera of graphoglyptids range from forms that are constructed mostly in two dimensions, such as *Cosmorhaphe, Paleodictyon, Helminthorhaphe,* and *Spirorhaphe*, to those constructed mostly in three dimensions, of which they are only partially preserved in two dimensions, such as *Lorenzinia* and *Glockerichnus* (e.g., Fuchs, 1895; Seilacher, 1977; Uchman, 1995, 2003; Uchman and Wetzel, 2012).

To illustrate the quantification methods described in this paper, selected trace fossils were photographed or copied from published sources, and they were traced using the graphics program CorelDRAW (vers. 9.439) (Fig. 4.2). Other similar graphics programs, such as Adobe Illustrator, also could be used. Tracing the trace fossil consisted of drawing a line along the midline of the burrow portion of the trace fossil. The line width was then selected based on the average width of the exposed trace fossil to cover up as much of the trace fossil as possible. This gives the most accurate representation of the original trace fossil, since most graphoglyptids were likely burrowed with a consistent width throughout (Monaco, 2008). Variations in burrow width are assumed to represent erosion, imperfect preservation, or some other undetermined variable. The line drawing then may be resized or exported into a variety of different formats for the various analyses. It is best if the line drawing of the trace fossil is rotated, so that the drawing fills a rectangle with a minimum amount of extra space.

4.3.2 Basic analyses

One of the first aspects to be measured is burrow width (*W*), which usually is not affected by alteration due to diagenesis or erosion. However, the width could be affected

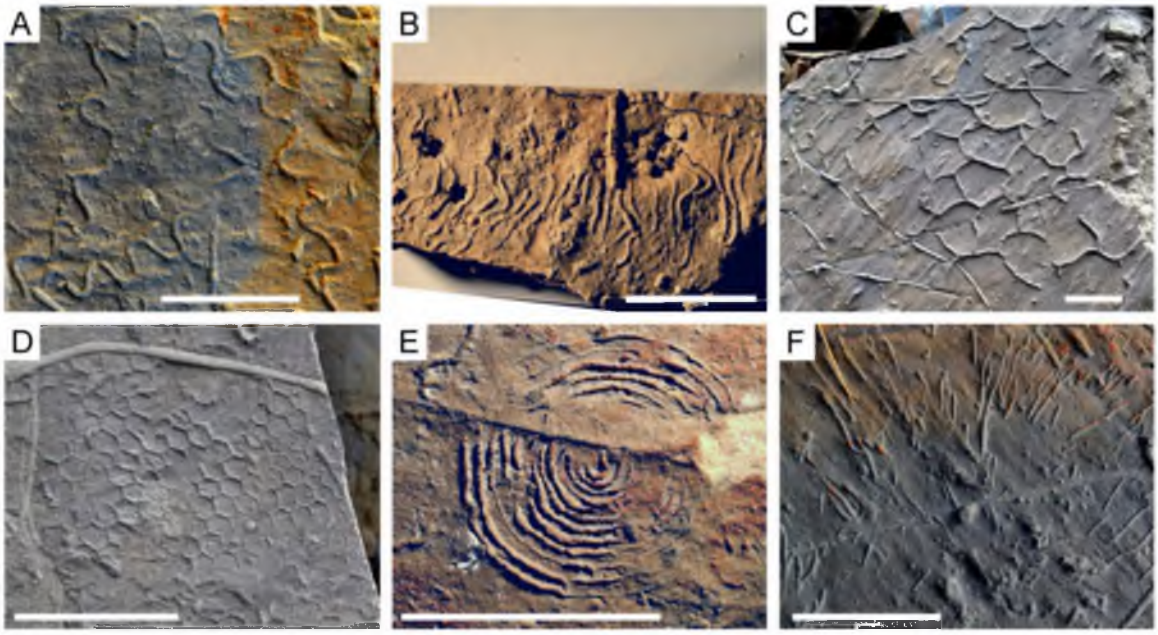

Figure 4.1. Selected graphoglyptid trace fossils: A, Cosmorhaphe, Lower Eocene Guipúzcoan Flysch, Zumaia, Spain (Specimen Z_Cos3 in Tables 4.1 and 4.2); B, Helminthorhaphe, Upper Cretaceous, Tanzania (Specimen UUIC-1912 in University of Utah Ichnology Collection in Tables 4.1 and 4.2); C, Megagrapton, Lower Eocene Guipúzcoan Flysch, Zumaia, Spain (Specimen Z_Mega1 in Table 3); D, Paleodictyon, Lower Eocene Guipúzcoan Flysch, Zumaia, Spain (Specimen Z_Paleo5 in Table 4.3); E, Spirorhaphe, Upper Cretaceous, Tanzania (Specimen UUIC-1904 in University of Utah Ichnology Collection in Tables 4.1 and 4.2); F, Urohelminthoida, Lower Eocene Guipúzcoan Flysch, Zumaia, Spain (Specimen Z_Urohelm2 in Tables 4.1 and 4.2). Scale bars are 4 cm.

by prediagenetic processes such as current action and slumping (Monaco, 2008). Alternatively, burrow length is not often as meaningful, since preservation plays a strong role in how long an individual burrow appears. Certain lengths are useful, however, and are measured in this study, such as the motility index (MI) which has been defined as a unitless number where the amplitude (a) is divided by the wavelength (λ) of a series of meanders (Janssen et al., 2008). The MI applies to trace fossils that exhibit sinuosity, like *Cosmorhaphe* or *Urohelminthoida* (Fig. 4.1). The amplitude is the distance between the midline and the crest of the burrow meander. For this study the MI is calculated by using the average of all available first order amplitudes and wavelengths. The amplitude and

Figure 4.2. Tracings of the graphoglyptid trace fossils used in the analyses. A1, *Cosmorhaphe*, sample Z_Cos1; A2, *Cosmorhaphe*, sample Z_Cos2; A3, *Cosmorhaphe*, sample Z_Cos3; A4, *Cosmorhaphe*, sample Z_Cos4; A5, *Cosmorhaphe*, sample Z_Cos5; B1, *Helminthorhaphe*, sample Z_Helmin1; B2, *Helminthorhaphe*, sample Z_Helmin2; B3, *Helminthorhaphe*, sample Z_Helmin3; B4, *Helminthorhaphe*, sample Z_Helmin4; B5, *Helminthorhaphe* sample Z_Helmin5; C1, *Megagrapton*, sample Z_Mega1; C2, *Megagrapton*, sample Z_Mega2; C3, *Megagrapton*, sample Z_Mega3; C4, *Megagrapton*, sample Z_Mega4; C5, *Megagrapton*, sample Z_Mega5; D1, *Megagrapton*, sample Z_Mega6; D2, *Megagrapton*, sample Z_Mega7; D3, *Paleodictyon*, sample Z_Paleo1; D4, *Paleodictyon*, sample Z_Paleo2; D5, *Paleodictyon*, sample Z_Paleo3; E1, *Paleodictyon*, sample Z_Paleo4; E2, *Paleodictyon*, sample Z_Paleo5; E3, *Spirorhaphe*, sample Z_Spiror1; E4, *Spirorhaphe*, sample Z_Spiror2; E5, *Spirorhaphe*, sample Z_Spiror3; F1, *Spirorhaphe*, sample Z_Spiror4; F2, *Spirorhaphe*, sample Z_Spiror5; F3, *Urohelminthoida*, sample Z_Urohelm1; F4, *Urohelminthoida*, sample Z_Urohelm2; F5, *Helminthorhaphe*, sample UUIC-1911; G1, *Helminthorhaphe*, sample UUIC-1912; G2, *Helminthorhaphe*, sample UUIC-1913; G3, *Paleodictyon*, sample UUIC-1916; G4, *Paleodictyon* sample UUIC-1917; G5, *Spirorhaphe*, sample UUIC-1902; H1, *Spirorhaphe*, sample UUIC-1903; H2, *Spirorhaphe*, sample UUIC-1904; H3, *Spirorhaphe*, sample UUIC-1905; H4, *Spirorhaphe*, sample UUIC-1907; H5, *Spirorhaphe*, sample UUIC-1908. Traces A1 through F4 are all from the Lower Eocene Guipuzcoan Flysch of Zumaia, Spain, which were photographed in the field. Traces F5 through H5 are from the Upper Cretaceous of Tanzania, which are stored in the University of Utah Ichnology Collection (UUIC). Scale bars = 4 cm except for D4, G3, and G4, which are 1 cm.

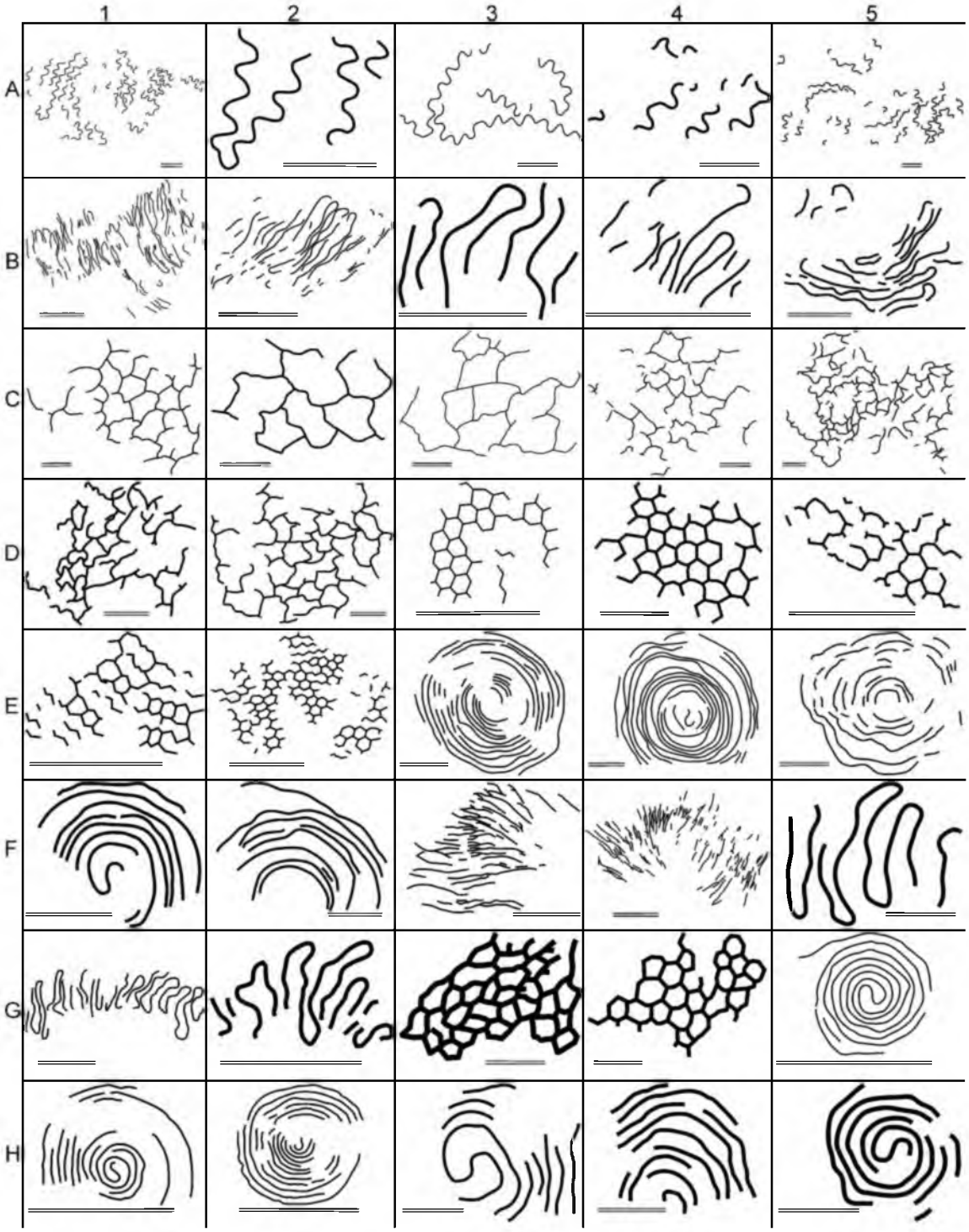
1
2
3
4
5
A
B
C
D
E
F
G
H

wavelength values are calculated as averages separately, since the a and λ values can differ between meanders, and there is a possibility that the number of calculable amplitudes would not equal the number of calculable wavelengths. The MI for this study is defined as:

$$MI = a/\lambda \qquad \text{(Eq. 4.1)}$$

where MI = the motility index; a = the average amplitude, or the distance from the midline to the top of one meander, of all calculable amplitudes; and λ = the average wavelength, or the distance between adjacent curves, of all calculable wavelengths.

Higher MI values indicate longer meanders with closer spacing. Trace fossils like *Helminthorhaphe* (Fig. 4.1B) would have a much higher MI than *Cosmorhaphe* (Fig. 4.1A), since the meanders of *Cosmorhaphe* are much more regular. The MI alone is able to give a mental image of the general shape of the meandering trace.

The MI only applies to sinuous 'meandering forms' so a separate calculation is required for spiral 'meandering forms' such as *Spirorhaphe*. For spiral forms, a measure called Spiral Spacing (*SS*) is calculated by dividing the average burrow spacing by the width (*W*). Higher SS values indicate larger spacing between each subsequent rotation of the burrows.

Another standard measure is the ratio of the cell size (C_{Size}) to the W in the network forms (Fig. 4.3) as provided by Uchman (1995, 2003), who assigned the multiple morphotypes of *Paleodiction* to different ichnospecies based on the ratio of burrow diameter versus cell size. A 'cell' is defined as each unit of the network in network forms. A problem with Uchman's (1995, 2003) approach is that the method does

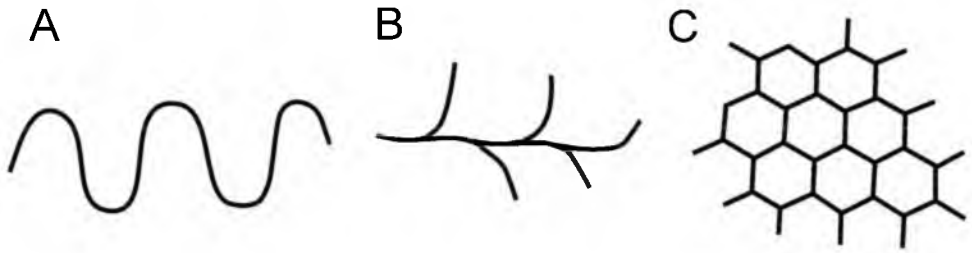

Figure 4.3. Topological classifications of graphoglyptids: A, meandering form; B, branching form; C, network form.

not take into account organisms of different size that can create the same pattern at different scales. For this study the mesh size (MS) was calculated by dividing C_{Size} by the W. The C_{Size} was the average of the cell sizes measured from the burrow midlines, across the smallest diameter of each cell. The MS is defined as such:

$$MS = C_{Size}/W \qquad \text{(Eq. 4.2)}$$

where MS = mesh size; C_{Size} = the average size of the network cells; and W = the burrow width.

Even though this may not be a definitive ichnotaxamomic variable, the MS still could provide some important morphological information.

4.4 Morphology dependent methods

There are two main groups of analyses presented in this study: Analyses that are dependent on the morphology of the trace fossil, more specifically the topology, and analyses that are independent of the morphology. The morphology dependent methods include topology, tortuosity, burrow angle, and number of cell sides.

4.4.1 Topology

Topology is the basic geometric configuration that remains invariant under bending and stretching. Topology of a burrow system is a reflection of the fundamental ground plan of the burrows. Gong and Huang (1997) divided trace fossil analyses among three different topological classifications: lines, trees, and networks. A line is composed of a shape with two non-parting points, while trees and networks have three or more end-points.

The three main topological classifications that are used in this study are grouped according to meandering forms (lines), branching forms (trees), and network forms (meshes) (Fig. 4.3). Meandering forms are continuous lines that have no naturally occurring breaks in them, barring erosion or imperfect preservation. Branching forms are similar to meandering forms, except that a given line splits into two or more lines repeatedly. The branches do not reconnect to the main trunk or any of the other branches. Network forms are like the branching forms, except the branches reconnect to the main trunk or any of the other branches. Several of the analyses discussed below vary based on which of the three forms are represented, and will be discussed accordingly.

4.4.2 Tortuosity

Tortuosity (τ) is a measure of how much a trail or tunnel winds back and forth. Tortuosity is a unitless number that is a useful means for determining how direct a pathway or burrow trail is. The directness of the burrow may reflect the efficiency of a grazing pattern that is exploiting a uniformly distributed food resource.

The τ of a straight burrow or trail is 1.0, whereas τ of a winding burrow or trail could be much higher (1.0001 and beyond). The higher the value of τ, the longer the travel distance between point A and point B. Another way to look at this is that tortuosity is the ratio between the shortest distance between point A and point B and the actual length of the path that it takes to get there. Measuring the τ of a trace fossil is not a new method and has been done in previous ichnological and animal movement studies (e.g., Orr, 1999; Benhamou, 2004; Koy and Plotnick, 2010; Platt et al., 2010), although the methodology used in this study has not been attempted for trace fossils before now. To determine the tortuosity of a line, the following formula is used:

$$\tau = L_{Actual} / L_{Euclidean} \qquad \text{(Eq. 4.3)}$$

where τ = tortuosity of a line; L_{Actual} = the distance traveled along the line; and $L_{Euclidean}$ = the straight line distance between the two endpoints.

A trace fossil represents the actual path of the organism, the L_{Actual}. The organism making the burrow would not have made a wide, curved burrow if the organism were small and able to travel straight through the burrow to avoid the curves. Therefore, it is likely that the organism filled all or most of the cross section of the burrow at the time of formation. When calculating tortuosity, a wide burrow could allow for a smaller organism to follow a straighter line than would be possible for an organism that filled the entire width of the burrow. For example, if a person were driving a car on a wide, winding highway with no lane restrictions, the car would be able to travel in a straighter line than the highway, because although the road is winding, the car has more room to straighten out its path (Fig. 4.4). For that reason, a line following the midline of the burrow is recommended to calculate the tortuosity, since it would be able to produce a

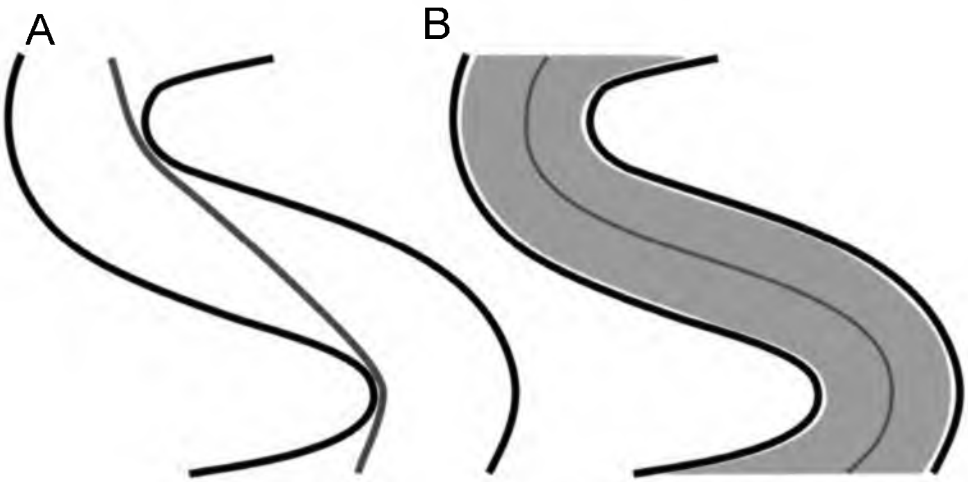

Figure 4.4. Schematic illustrating differences between tortuosity measures: A, tortuosity ($\tau = 1.09$) for a thin line within a large burrow; B, tortuosity ($\tau = 1.28$) for a thick line within a large burrow. The center line of the burrow was used to calculate the tortuosity.

more accurate tortuosity value.

For meandering forms, determining the tortuosity is a straightforward process. A couple of issues arise with trace fossils though, and graphoglyptids in particular, when measuring tortuosity. The first problem is when portions of the trace fossil are missing due to erosion or non-preservation. A second problem is related to the sinuous nature of many graphoglyptids, since the completeness of the trace fossil can have a significant impact on the measurement of the tortuosity (Fig. 4.5). *Spirorhaphe*, for example, is a trace that spirals inward and then outward, so the tortuosity peaks with every rotation around the circle then bottoms out at the furthest extent from the starting point. This means that the tortuosity is heavily dependent on the length of the trace fossil present making it impossible to compare the tortuosity of a 10 cm length of *Spirorhaphe* to a 50 cm length of *Spirorhaphe*.

Three methods can help to correct for these problems. The first approach is to fill in the blanks using an estimation of what is missing based on what is present. This

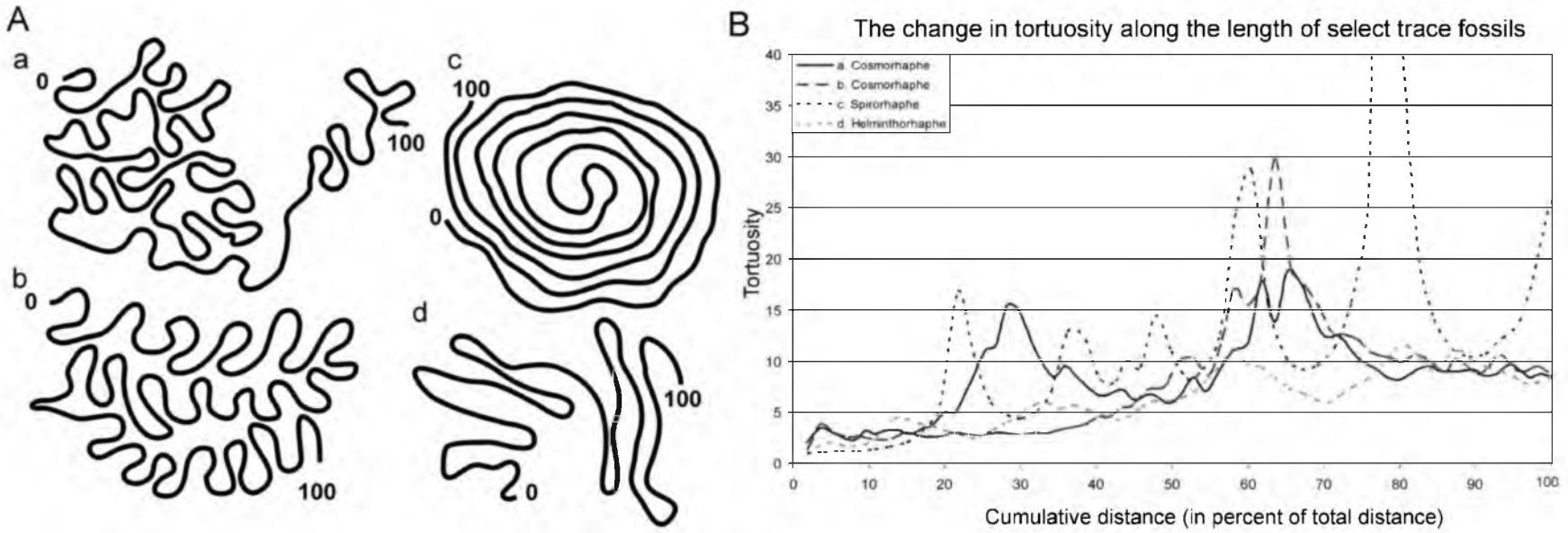

Figure 4.5. Tortuosity (τ) of select trace fossils: A, tracings of selected trace fossils. 0 and 100 represent percentages illustrated in the graph; specimens: A.a, *Cosmorhaphe* from the Eocene Beloveža Formation of Poland (Specimen UJ TF 77 at the Institute of Geological Science, Jagiellonian University, Kraków, Poland [Książkiewicz, 1977: plate 19.6]), A.b, *Cosmorhaphe* from the Tertiary of Italy (pictured in Bromley, 1996), A.c, *Spirorhaphe* from the Upper Paleocene to Lower Eocene Ciężkowice Sandstone of Poland (Specimen UJ TF 1519 at the Institute of Geological Science, Jagiellonian University, Kraków, Poland [Książkiewicz, 1977: plate 18.1]), A.d, *Helminthorhaphe* from the Upper Paleocene to Lower Eocene Ciężkowice Sandstone of Poland (Specimen 42.a at the Institute of Geological Science, Jagiellonian University, Kraków, Poland); B, The cumulative tortuosity as the tortuosity is measured from 0 to 100 percent of the total length of the line.

method bears the risk of becoming too subjective, and there is no way to extend beyond the end of the trace fossil, so that all analyzed trace fossils are the same length. The second method is to take short sections of the line and average them together to get a generalized tortuosity. The third method takes ever increasing size measurements (e.g., 5 cm, 10 cm, 15 cm, etc.), averages all results of the same size, and places the results in a chart as separate tortuosities. This last method is able to provide comparable results between different trace fossils, since the tortuosity measured at one size would not necessarily equal a measurement of a longer size, even in the same fossil.

In examples described for this study, calculations of the τ start with a L_{Actual} of 5 cm and increase at 5 cm intervals up through 30 cm. The 5 to 30 cm limit was set based on the size and lengths available of the majority of the trace fossils. For larger or more complete specimens a longer L_{Actual} might be beneficial. If a trace fossil was broken up into many pieces, calculations were done only on the most complete piece that could be guaranteed to be from the same trace fossil. This was done to exclude the possibility of averaging together multiple pieces from different trace fossils. A full description of the methods employed in this study is available in Appendix B.

Branching forms were treated similarly to meandering forms, except that they have extra sections due to the branches. The τ was calculated along the main trunk of the trace fossil. Additional calculations were made for the individual branches as if they were isolated pieces. The measurements for the branches then were averaged into a measurement for the main trunk.

Network (mesh) forms are significantly different than meandering and branching forms, since they offer a large number of possible pathways along which an organism can

travel. Previous calculations of Network Tortuosity (NT) have been performed for a variety of systems, including crack networks in clay soils (Chertkov and Ravina, 1999) and cubic sodium chloride compacts (Wu et al., 2006), but such calculations have not been determined previously for trace fossils. Calculation of the NT applies the same basic methods as the meandering and branching forms. In a network, the tortuosity is calculated for a straight line path from one edge of the image to the other and then recalculated for every possible path between the two sides using the 'grey-weighted distance transform' (Rutovitz, 1968; Piper and Granum, 1987; Verbeek and Verwer, 1990).

Calculation of the NT is performed with a binary image where the traces are in black and the background is white, but the script can be edited to work with a white trace on a black background. A script is provided (Appendix B) to calculate the NT and was created using Matlab, Version 7.12.0 (R2011a). The Matlab script converts the binary colors of the image into different elevations. The grey-weighted distance transform creates height to each of the pixels, so that pathways can be determined with the low grey-value pixels producing faster pathways (Piper and Granum, 1987). The resulting NT is indicative of both how tortuous each individual segment is and also how many pathways are available. Where a straight line has a tortuosity of 1.0, the tortuosity of a grid of straight lines would be slightly higher due to the multiple pathways that are available (Fig. 4.6).

The NT was determined by adjusting each of the traces to contain lines at a standard of 2.0 point (pt). Calculation of NT uses a standard line thickness of 2.0 pt as the thinnest line possible, because for thinner lines the program would act as if the lines were

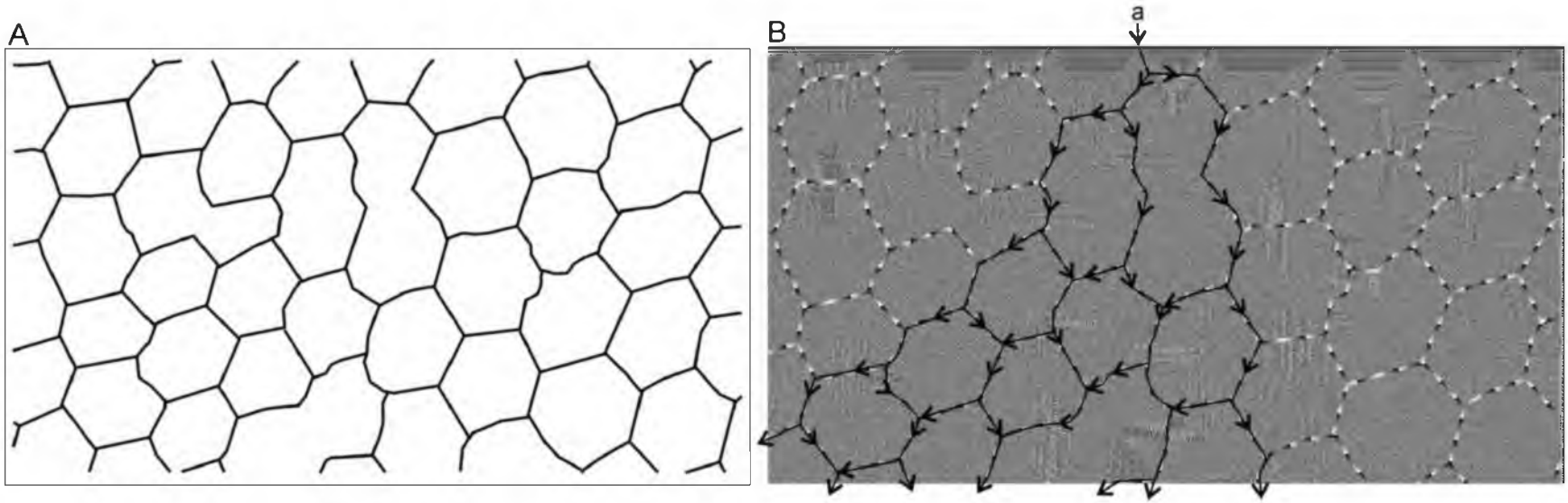

Figure 4.6. Wave front propagation illustrating network tortuosity (NT): A, trace of a portion of *Paleodictyon majus*, from the Oligocene Krosno Beds of Poland (un-numbered specimen in the Institute of Geological Science, Jagiellonian University, Kraków, Poland); B, resulting waves of the Matlab analyses. The black lines illustrate possible pathways from location "a" through the burrows proceeding downwards.

not there. For line thicknesses greater than 2.0 pt, the program pathways cut corners through the burrows and become shorter than would be possible for the burrowing organism (Fig. 4.4).

The NT in this experiment is calculated using DIPimage Tools (www.diplib.org), which is available online for use in Matlab (Appendix B). The Matlab script calculates the NT in two groups. In the first group, the starting point occurs at every pixel on the top of the image and the program runs to the bottom of each image (Fig. 4.6). In the second group, the pathways are determined from the left side of the image and the program runs to the right side of the image. The Matlab script produces a wave front as the program runs through the image, such as what would be seen in a puddle if a pebble were to be dropped in it. The differences in the heights of the pixels, due to the shade of the pixels, represent the two sets of materials that the waves travel through. The background color (white in these experiments) represents the sediment, and is designed to produce longer travel times for the wave front than the burrow color (black). In Figure 4.6 this can be seen as many small waves seen close together. Each wave is pictured as starting with black and fading into white. The traces (black in Fig. 4.6) represent the favorable path for the waves. It takes fewer waves to travel the length of the image along the traces, producing a faster travel speed. The waves are propagated along the burrows until the waves reach the other side. The amount of waves needed to cross the image along the faster pathways in correlation with the width of the image itself was used to calculate the tortuosity of each segment. These values then were averaged for all possible pathways to give the NT in each direction. The script produces an image with the original image

input, the wave front propagation image, and the average NT's for the vertical direction, horizontal direction, and both averaged together.

Calculations were based on the size of the image measured in pixels. The first run of the image was adjusted to be 150 pixels away from each edge. The next NT run was shrunk by 150 pixels, for a total of 300 pixels from each edge. The runs were repeated in this way until the remaining image was nonexistent. The NT values for each run were then taken and plotted versus area, which in this experiment were pixels^2. The plots of these graphs often produced a 'U' or a ' ⌐ ' shape with a flattened middle (Fig. 4.7). The reason for the right portion being higher was because for larger areas, less of the image was contacting the outer edge, forcing the NT to be higher to cross the empty space. As the outside empty space was eliminated, the NT leveled out, producing the true NT. For smaller area values, the NT starts to act like a branching or a meandering form and the NT values are less consistent, sometimes going up, as in the 'U', and sometimes going down, as in the ' ⌐ ' shape. For this reason the true NT value for the trace fossil was the average of the flat-line mid-values.

4.4.3 Branching angle

The angle of the branches in both branching forms and network forms can indicate the type of movement, anatomical body plan, and behavioral aspects of the organism(s) creating the burrows. Branches with one predominantly low angle indicate movement primarily in one direction, while branches where all of the angles are approximately equal, such as three 120° angles, indicate that movements of the

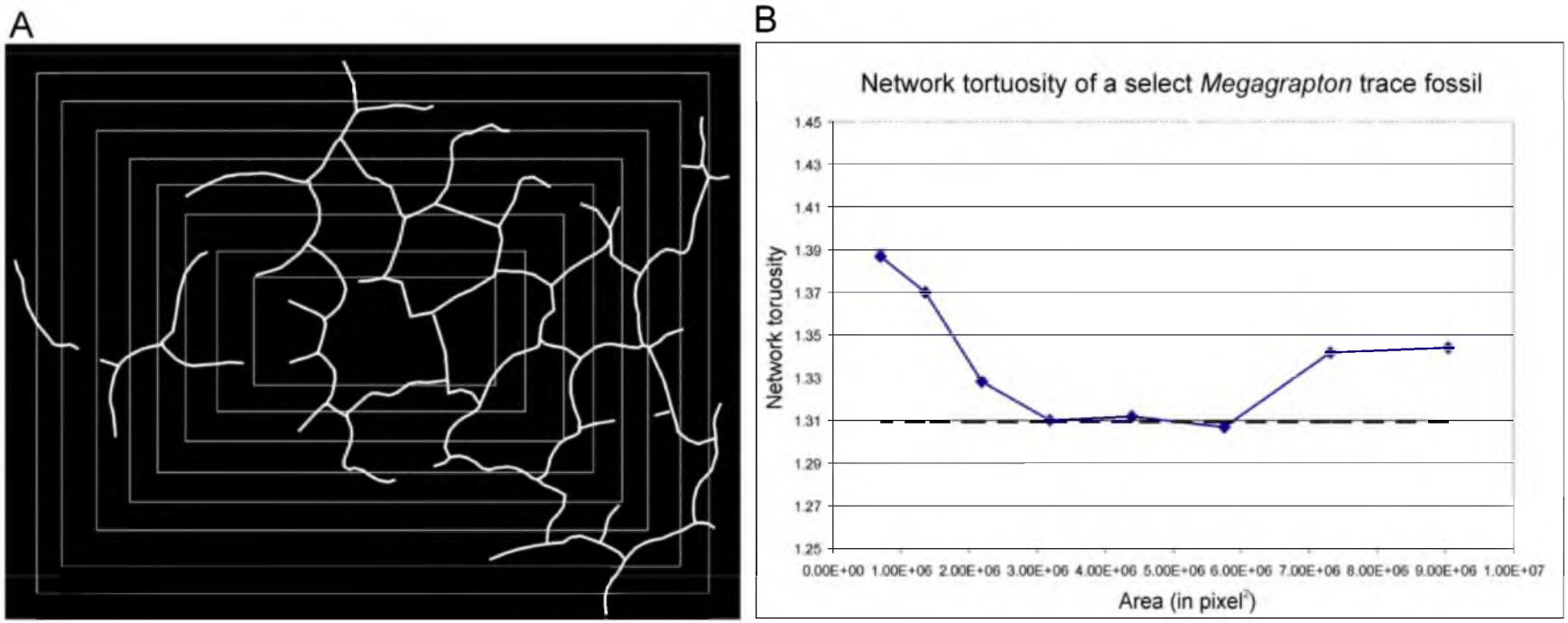

Figure 4.7. Network Tortuosity (NT) calculation of a *Megagrapton* specimen sample Z_Mega1: A, trace of the trace fossil with the different size boxes outlined for each NT calculation; B, graph of the NT values for each size box with the NT of the sample highlighted by the horizontal dashed line.

organism(s) were equal in all directions. By measuring the branching angle it is possible to infer the primary movements of the organism(s) creating the trace fossils.

Calculating the branching angle is a straightforward process that can be done by hand with a protractor, but using a computer program is faster and more precise. Programs that can calculate branching angles include ArcGIS, CorelDRAW, and Adobe Illustrator. Within ArcGIS, the COGO (coordinate geometry) toolbar provides a method for calculating angles by clicking along the angle to be measured in three locations. The COGO toolbar does not save the angle information within the file, so ArcGIS was not used for calculating the branching angle. Alternatively, CorelDRAW was ideal for this study, since it calculated the branching angle and then placed that information directly on the drawing (Fig. 4.8).

There is no branching angle to be calculated for meandering forms, so branching forms are the first to be measured. For branching forms, the branching angle is the smallest angle measured off the main trunk. The smallest angles then were averaged for each trace fossil (Fig. 4.8A). There is an assumption that the organism is moving predominantly in one main direction in branching forms. This would explain why one angle was significantly smaller than the other two at each branching point.

In network forms, it is assumed that the organism(s) is moving back and forth throughout the burrow many times from different directions. This is why the angles of the branches are closer to being equal. At most of the branching points in a network form there are three main angles and three tunnels intersecting. If the three angles were to be averaged together, they would always equal 120°, since all three angles add up to 360°. For this reason, averaging the angles would not be meaningful, so the smallest angle of

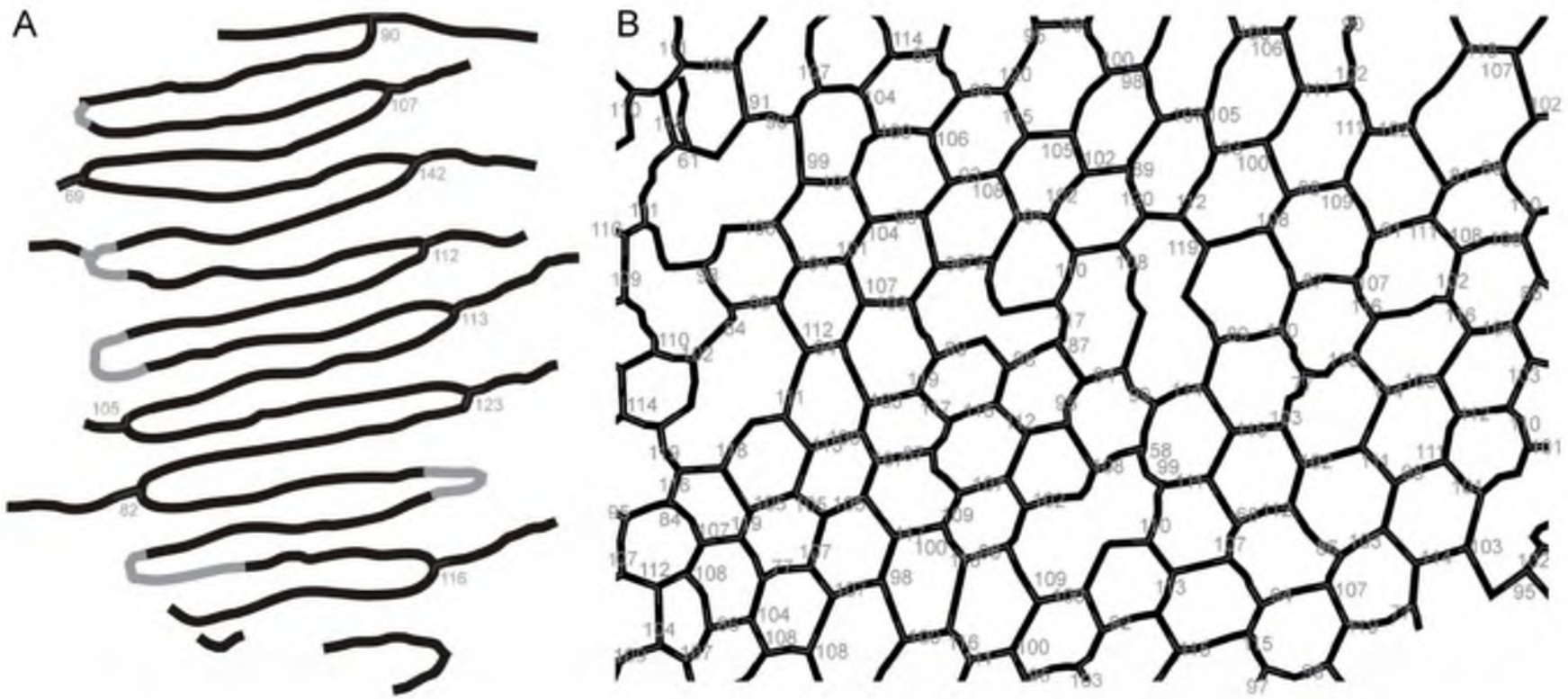

Figure 4.8. Branching angle calculations: A, branching angle of the branching form graphoglyptid, *Urohelminthoida*, from the Miocene Azagador Limestone, Vera Basin, Spain; B, branching angle of a network form graphoglyptid, *Paleodictyon majus*, from the Oligocene Krosno Beds of Poland (un-numbered specimen in the Institute of Geological Science, Jagiellonian University, Kraków, Poland).

each of the branches was the only one measured (Fig. 4.8B). These angles were averaged to get the branching angle for each network form.

4.4.4 Number of cell sides (S)

The amount of sides that each cell (S) contains is indicative of the behavior needed to create that cell. If all of the cells have the same number of sides, that indicates a much more rigid behavior than if there were a wide variety of the number of sides on the cells. For this study three calculations were performed. The first is the weighted average of the number of cell sides ($S_{Average}$), which is where the number of sides of each separate cell was counted between branching points. Due to preservation problems, sometimes the branching points were difficult to determine in poorly preserved specimens. If the branching points were able to be reasonably identified in a cell then those cells were counted towards the $N_{Average}$. The total of the number of polygons is then added up for each number of polygons.

$$S_{Average} = \sum (N_i * P_N) \qquad \text{(Eq. 4.4)}$$

where $S_{Average}$ = the weighted average of the cell sides; N = the number of individual cell with a specific number of sides; i = the specific number of sides ($i \geq 3$); and P_N is the percentage of each number of sides (totaling 100% for all of the sides).

For example, if a shape has 120 cells, 114 of them have 6 sides, and 3 of them have 5 sides, and 3 of them have 4 sides:

$S_{Average} = 6*0.95 + 5*0.025 + 4*0.025 = 5.925$

The second measurement is the calculation of the variance of the number of cell sides ($S_{Variance}$). The $S_{Variance}$ illustrates the rigidity (or lack of rigidity) of the behavioral

system, the smaller the variance, the more rigid the behavior that is used to create the network.

The third measurement is the mode of the cell sides (S_{Mode}). The S_{Mode} identifies the largest number of cells with a particular number of sides. The $S_{Average}$ can be influenced by a wide variety of cell sides so the S_{Mode}, in conjunction with $S_{Average}$, and the $S_{Variance}$ provide more complete depiction of the cell shapes.

4.5 Morphology independent methods

Analytical methods that are independent of morphology are referred to as nonlinear. Linear characteristics of a trace fossil include its size and shape. Nonlinear characteristics are those that are independent of size and shape. When only a portion of a trace fossil is preserved, nonlinear methods will result in the same, or very similar, results as if the whole trace fossil were present. Nonlinear methods are also useful since they can be applied uniformly to each trace fossil no matter which topology they represent. Several different methods are easy to employ and can give you interpretable numbers for each of the trace fossils that are being analyzed. The morphology independent methods discussed in this paper include fractal analysis, burrow area shape, and occupied space percentage calculations.

4.5.1 Fractal analysis

Fractal geometry is a concept that has been recognized since the late nineteenth century (e.g., Cantor, 1883, 1993; von Koch 1904, 1993; Menger 1926, 1993). Mandelbrot (1983) described and expanded upon the fractal concept as a method to

characterize geometric complexity and quantify irregular morphologies. Fractal analysis may be used to determine how completely an object fills a given space by combining the occupied space of the object with the shape of the object into one number (Plotnick and Prestegaard, 1995; Wagle et al., 2005). Shapes occupy a fractal dimension, which is a precise dimension for a shape that exceeds its topological dimension. For instance, the topological dimension of a line, no matter what the shape is, is one. A non-straight line would have a greater fractal dimension, since the line fills more of the two-dimensional space than a straight line would. A fractal dimension is very useful in understanding shapes in nature, because natural objects are not perfect Euclidean shapes. Most objects are difficult, if not impossible, to describe with precision in the Euclidean sense. Fractal analysis has seen limited use in ichnology (de Gibert et al., 1999; Puche and Su, 2001; Le Comber et al., 2002; Romanach and Le Comber, 2004; Katrak et al., 2008; Baucon, 2010; Lehane and Ekdale, 2013).

Fractals possess the feature of scale invariance, where the image looks the same and therefore will produce a similar fractal dimension no matter the scale. Fractals also exhibit self similarity, where the image gives similar fractal dimension results no matter what portion of the image is being examined. Previous research demonstrated the validity of fractals in ichnology by determining the self-similarity and scale invariance of various trace fossils (Lehane and Ekdale, 2013). That study also showed that as long as the trace fossil was not eroded by more than 50-60%, the trace fossil could provide a useful fractal dimension.

There are multiple ways to calculate a fractal dimension and a variety of applications that can be used. BENOIT, version 1.31, created by TruSoft Int'l, Inc., 1999,

was used for this study (Appendix C). The most useful methods for calculating fractal dimensions depend on the basic shape. The most commonly employed methods for calculating fractal dimensions are the Ruler Dimension Method (D_{Ruler}), the Box Counting Method (D_{Box}), and the Information Dimension Method (D_{Info}).

When analyzing a continuous line, the Ruler Dimension Method is the ideal method. The Ruler Dimension is calculated by measuring the line with a ruler of set length. This is plotted on a log plot of ruler length vs. line length. The ruler is then shrunk down by discreet amounts with each line length plotted on the graph. The measurements will form a straight line if the shape is a fractal, and the slope of the line is used to calculate the fractal dimension. This might seem the ideal method for calculating the fractal dimension of trace fossils produced during grazing or deposit feeding. This is not often the case, however, because the Ruler Dimension Method is limited to lines that are complete and unbranching, both of which may be difficult to find in ichnology. If the trace is eroded, the analyst can introduce bias by filling in the blanks of the missing sections. The ideal case would be a method that could be used for branching and continuous lines without the need to fill in missing details and calculate how a trace fossil covers a surface or fills a space. These limitations indicate that the Ruler Dimension may not be very suitable for use in ichnology, since the Ruler Dimension would treat each trace fossil as if it were an isolated line.

The Box Counting Method and the Information Dimension Method calculate the fractal dimension of a planar surface. The Box Counting Method is similar to the Ruler Dimension Method, except that a grid is placed on the surface of the image and the numbers of occupied boxes are counted. The size of the boxes is shrunk repetitively by a

consistent amount, and the number of occupied boxes is counted and re-counted again. This information is plotted on a log plot of box size vs. number of occupied boxes. The series of measurements will form a straight line if the trace fossil is a fractal, and the slope of the line will be used to calculate the fractal dimension.

The Information Dimension Method is similar to the Box Counting Method, except that instead of the binary approach of the Box Counting Method (i.e., occupied or not occupied), the amount of the image located in each box is taken into account. This gives greater weight to boxes with more of the image in them and less weight to boxes containing only a portion of the image. The Information Dimension Method is a useful tool for analyzing images with very thick lines or images with varying thicknesses. In the case of trace fossils where most of the lines are thin and consistent, such as for graphoglyptids, results from the Information Dimension Method did not differ appreciably from those obtained from the Box Counting Method (Lehane and Ekdale, 2013). For this study the Box Counting Method was used to calculate the fractal dimension.

4.5.2 Burrow area shape (BAS)

When analyzing the shape of the trace fossil, the overall shape is as important as the shape of the individual portions. Calculation of the overall shape is referred to as the Burrow Area Shape (BAS) (Romanach and Le Comber, 2004). The BAS is not a direct calculation of any particular aspect of the trace fossil, but rather BAS is a calculation of the overall geometry of the space being utilized. The BAS is useful in ichnology because it helps to define how an organism is moving through the sediment. Even if the burrows

and trails are winding back and forth, a BAS closer to 0 indicates the organism was moving predominantly in one direction. A BAS closer to 1 indicates the organism was not moving predominately in any one direction but preferred to remain within a set distance from the center of the burrow. The formula for the BAS is:

$$BAS = (4*\pi*A)/(P^2) \qquad \text{(Eq. 4.5)}$$

where BAS = the burrow area shape; A = the area that the shape occupies; and P = the perimeter of the occupied shape used to calculate A.

The result of the BAS is a unitless number that ranges from 0 to 1, with 0 representing an area of a straight line and 1 representing the area of a circle. The more equidimensional a trace fossil is (i.e., length and width approximately equal), the closer to 1 the result will be. This analysis is independent of burrow width and length.

One problem that may arise is that the BAS is strongly dependent on completeness of the trace fossils. Partial trace fossils can provide some useful information though, since they can give an outline to where the trace fossil used to cover the surface before the trace fossil was destroyed. To provide an unbiased result, the BAS is calculated by creating a buffer around the outsides of the burrows. The buffer distance is set to the average distance between each burrow (Fig. 4.9). In the case of meanders and branching forms, this is the average distance between known adjacent burrows or in the case of network forms, the average width of the cells (C_{Size}). The buffer around the traces creates enough space to include individual elements that may have been isolated by erosion and also not give more space around the trace fossil than normally would be expected for any particular shape. Details of how the BAS was calculated in these analyses are provided in Appendix D.

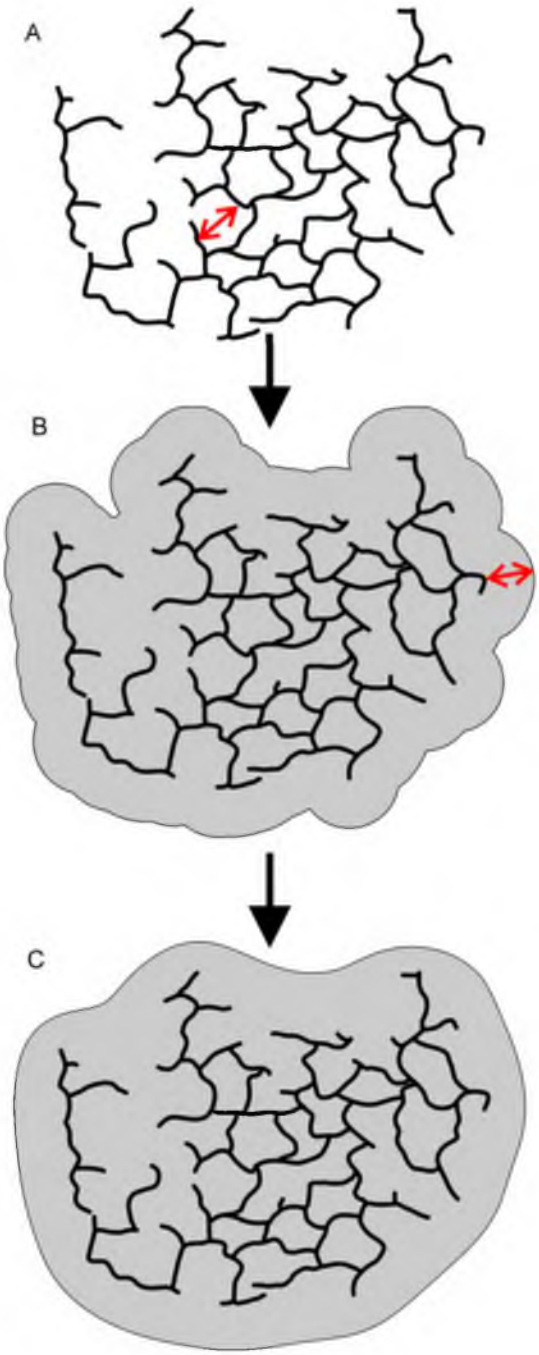

Figure 4.9. Methods for creating a smooth buffer for a *Megagrapton* specimen (Z_Mega7): A, initial trace of the *Megagrapton* trace fossil. The arrow indicates the average size of the cell; B, a buffer is created around the initial trace with the same size as the average cell size; C, the buffer is smoothed out with a smoothing tolerance of four times the buffer distance.

4.5.3 Occupied space percentage (OSP)

The amount of space that the trace fossil occupies compared to the amount of total space is known as the Occupied Space Percentage (OSP). The OSP provides the amount of sediment that the organism is utilizing. Sediment-ingesting organisms or deposit feeders tend to utilize more of the sediment as they feed (Lehane and Ekdale, 2013), so the OSP values of their burrows should be higher than those organisms that do not feed on the sediment. Due to the large spaces between the burrows of graphoglyptids, the OSP values are much lower than for deposit feeders. This supports the assumption that graphoglyptids were not deposit feeders (Lehane and Ekdale, 2013). While it may seem that the OSP is similar to the degree of bioturbation (Droser and Bottjer, 1986, 1987), the OSP is the measure of the space occupied by a singular burrow system. This is different than the degree of bioturbation, which is affected by the amount of burrows within a volume of sediment.

One of the problems with the OSP is that it might be possible that the fractal dimension (D) would have a direct correlation with the OSP, since D is partially based on the amount of space occupied by the analyzed shape. By comparing the D with the OSP, it is possible to see that the patterns are different (Fig. 4.10). Figure 4.10 shows that the OSP remains consistent for different scales even more than the Fractal Dimension does. This indicates that the shape of the burrow must play a significant role in the calculation of the D and that the OSP alone can be used as a unique quantification term for the shape of a burrow. As with the fractal dimension the OSP exhibits scale-invariance, self-similarity, and reliance on available material.

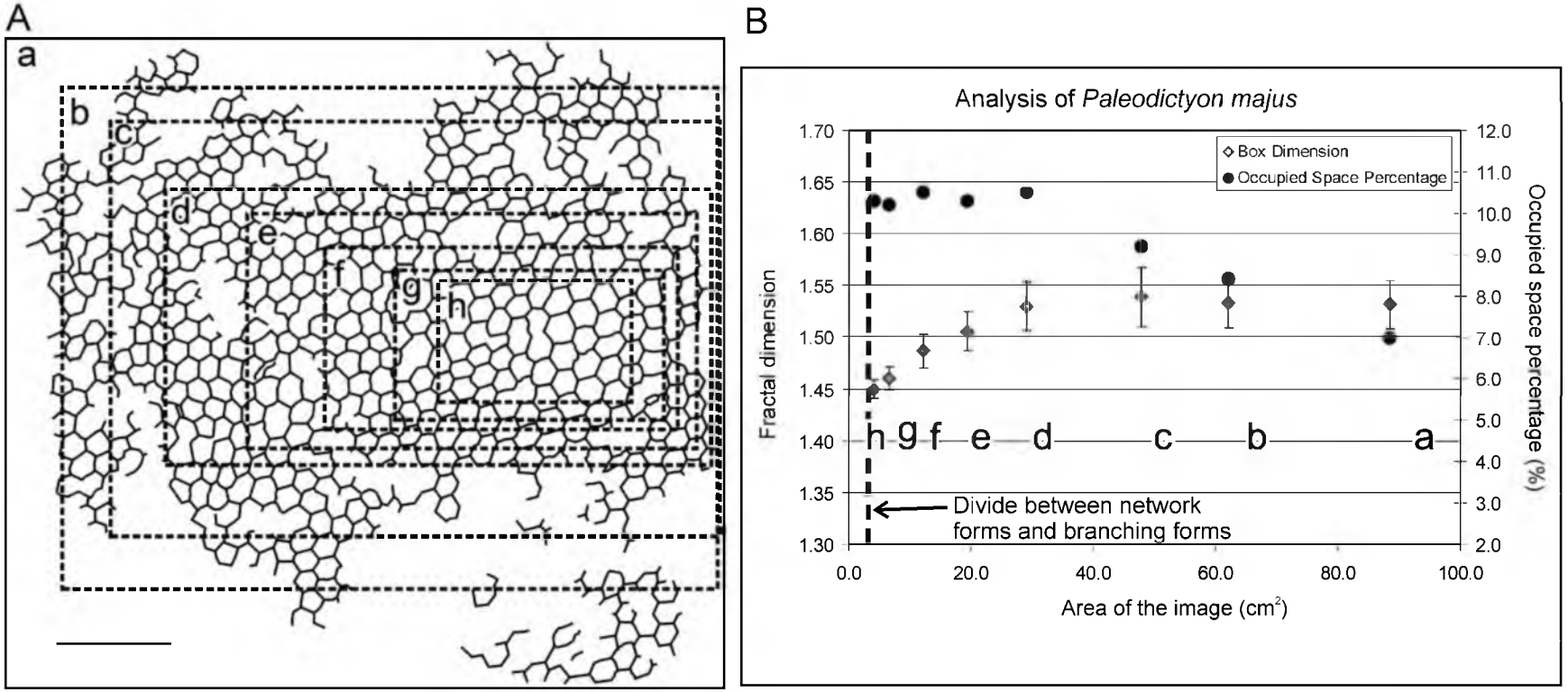

Figure 4.10. Fractal dimension using the Box Counting Method (D_{Box}) versus occupied space percentage (OSP) of a *Paleodictyon majus* from the Krosno Beds of Poland: A, the D_{Box} and the OSP were calculated individually for each box after being scaled and reproduced; B, comparison of the D_{Box} and the OSP to the area of the actual specimen in cm^2. Error bars are the standard error determined from the standard deviation calculated by BENOIT. Scale bar is 4 cm.

Another problem with the OSP is that this number can be greatly influenced by the amount of material present in the samples. The greater the amount of the object that is missing, the lower the OSP will be. In order to counteract the diminishing value of the OSP by extra empty space around the outside of the shape, the buffer that was created for the BAS calculations was used for the OSP calculations as well. The buffer makes it possible to get a much more representative number for the OSP than would be available otherwise. The OSP was calculated for this experiment using the Image Process Tools available in Matlab (Appendix D). The script calculates the number of black pixels versus the number of white pixels and yields a percentage of each. A full detailed description of the methodology is given in Appendix D.

4.6 Materials

Specimens of graphoglyptid trace fossils from four locations were chosen for analysis to highlight the preceding methods.

4.6.1 Zumaia, Spain

Graphoglyptid trace fossils from the Guipúzcoan Flysch of the Higuer-Getaria Formation (lower Eocene) from Zumaia, Spain, were studied. The turbidite sequences containing the graphoglyptids are well-exposed and celebrated for their high abundance and diversity of deep marine trace fossils (Seilacher, 1977; Wetzel, 2000). The depositional environment for these turbidite sequences includes the basin plain, outer fan, and depositional lobes of the middle fan (Leszczyński, 1991b). The graphoglyptids were photographed in the field due to the large size of the rock slabs. Graphoglyptid examples

include *Cosmorhaphe*, *Helminthorhaphe*, *Megagrapton*, *Paleodictyon*, *Spirorhaphe*, and *Urohelminthoida* (Fig. 4.2A1 – 4.2F4).

4.6.2 Kilwa, Tanzania

Several well preserved specimens from an unnamed formation (Campanian) from the District of Kilwa between Dar es Salaam and Lindi, Tanzania, were studied. The Tanzanian trace fossil specimens are housed in the University of Utah's Ichnology Collection (UUIC). The turbidite sequences in Tanzania were exposed due to new road construction from 1985 to 1987. The depositional environment of the region was determined to be an epeiric continental shelf, which was considered to be too shallow for graphoglyptids (Ernst and Zander, 1993). Ernst and Zander (1993), therefore had suggested that the region had 'steep zones' due to faulting, which would provide secluded deep water depressions capable of accommodating the graphoglyptid organisms. Graphoglyptid examples include *Helminthorhaphe*, *Paleodictyon*, and *Spirorhaphe* (Fig. 4.2F5 – 4.2H5).

4.6.3 Carpathian Mountains, Poland

Several of the figured specimens were from different formations in the Carpathian Mountains of Poland. The Polish specimens are currently housed at the Institute of Geological Science, Jagiellonian University in Kraków, Poland. The represented trace fossils are *Cosmorhaphe* (Fig. 4.5Aa) from the Eocene Beloveža Formation of Lętownia Górna, Poland, *Spirorhaphe* (Fig. 4.5Ac) and *Helminthorhaphe* (Fig. 4.5Ad) from the Lower Eocene Ciężkowice Sandstone of Grodek, Poland, and *Paleodictyon* (Figs. 4.6,

4.8B, 4.10) from the Oligocene Krosno beds of Poland. The Beloveža Formation is a turbidite deposit representing the basin plain up through the fan lobes of a prograding fan (Wetzel and Uchman, 2001). The Ciężkowice Sandstones are deep water interbedded conglomerates, pebbly sandstones, and sandy mudstones deposited by mudflows and channel-fill and lobe deposits (Klecker et al., 2001). The Krosno beds are deep-water turbidite deposits that are composed of interbedded marlstones, thin-bedded sandstones, black calcareous shales, and non-calcareous shales (Bąk et al., 2001).

4.6.4 Vera Basin, Spain

One figured specimen, *Urohelminthoida* (Fig. 4.8A), was from the Miocene Azagador Limestone from the Vera Basin of Spain. The Azagador Limestone is a shallow water deposit (several hundred meters deep), containing turbidites interbedded with hemipelagic marls (Braga et al., 2001).

4.7 Discussion

The quantitative methods described here have both effectiveness and drawbacks in analyzing trace fossil shapes (Tables 4.1–4.3). The morphology dependent methods, including tortuosity (τ), branching angle, and the number of cell sides (S), each quantify only a small portion of the overall number of trace fossils and cannot be used to compare different topologies. The morphology independent methods, including fractal dimension, BAS, and OSP, provide means for comparing all of the traces to each other. Some of the analyses, like the BAS, are heavily dependent on the completeness of preservation of the specimen, so the overall BAS values are more reminiscent of what remains of the trace

Table 4.1. List of meandering and branching trace fossils and their values for various analytical methods for samples from Zumaia, Spain (Z) and Tanzania (T). Formations (Form.) mentioned (e.g., 3a, 4a, etc.) are described in Ernst and Zander (1993). The Topology (Top.) lists whether the trace fossil is a meandering form (*M*) or a branching form (*B*). An en-dash (–) indicates that the analysis does not apply to the specific trace analyzed; variance in the values is represented by the standard error; τ = tortuosity.

Ichnogenera	Sample ID	Form.	Burrow Width (mm)	Top.	τ for 10 cm
Cosmorhaphe	Z_Cos1	Z-R2	2.5	M	1.603 ± 0.043
Cosmorhaphe	Z_Cos2	Z-R2	1.1	M	1.482 ± 0.019
Cosmorhaphe	Z_Cos3	Z-R2	1.2	M	1.602 ± 0.105
Cosmorhaphe	Z_Cos4	Z-R2	1.9	M	1.583 ± 0.034
Cosmorhaphe	Z_Cos5	Z-R2	2.3	M	1.523 ± 0.059
Helmithorhaphe	Z_Helmin1	Z-R2	0.9	M	2.79 ± 0.908
Helmithorhaphe	Z_Helmin2	Z-R2	0.7	M	1.192 ± 0.092
Helmithorhaphe	Z_Helmin3	Z-R2	1.2	M	1.197 ± 0.081
Helmithorhaphe	Z_Helmin4	Z-R2	0.6	M	3.759 ± 2.705
Helmithorhaphe	Z_Helmin5	Z-R2	1.3	M	2.847 ± 1.171
Helmithorhaphe	UUIC-1911	T-3	2.4	M	1.626 ± 0.267
Helmithorhaphe	UUIC-1912	T-4A	1.2	M	2.264 ± 0.48
Helmithorhaphe	UUIC-1913	T-1A?	1.5	M	4.712 ± 1.012
Spirorhape	Z_Spiror1	Z-R2	1.3	M	1.052 ± 0.008
Spirorhape	Z_Spiror2	Z-R2	1.5	M	1.071 ± 0.017
Spirorhape	Z_Spiror3	Z-R2	1.3	M	1.100 ± 0.024
Spirorhape	Z_Spiror4	Z-R2	1.4	M	1.298 ± 0.103
Spirorhape	Z_Spiror5	Z-R2	1.8	M	1.045 ± 0.007
Spirorhape	UUIC-1902	T-4A	0.5	M	2.58 ± 0.483
Spirorhape	UUIC-1903	T-?	0.5	M	2.559 ± 0.889
Spirorhape	UUIC-1904	T-3A	0.5	M	1.199 ± 0.025
Spirorhape	UUIC-1905	T-?	2.0	M	1.069 ± 0.023
Spirorhape	UUIC-1907	T-?	2.3	M	1.107 ± 0.053
Spirorhape	UUIC-1908	T-4B	2.3	M	1.317 ± 0.113
Urohelminthoida	Z_Urohelm1	Z-R2	0.9	B	2.929 ± 0.650
Urohelminthoida	Z_Urohelm2	Z-R2	1	B	2.554 ± 0.403

τ for 20 cm	τ for 30 cm	τ for 40 cm	τ for 50 cm	τ for 60 cm
1.843 ± 0.139	2.961 ± 0.912	–	–	–
1.651 ± 0.168	3.396 ± 0.247	–	–	–
2.005 ± 0.239	2.217 ± 0.292	1.994 ± 0.282	–	–
1.632 ± 0.05	–	–	–	–
1.699 ± 0.207	–	–	–	–
2.03 ± 0.627	–	–	–	–
13.807 ± 12.461	–	–	–	–
–	–	–	–	–
–	–	–	–	–
–	–	–	–	–
2.640 ± 0.672	5.233 ± 1.122	4.389 ± 0.637	4.994 ± 0.151	–
5.586 ± 1.377	6.587 ± 1.437	5.226 ± 1.172	–	–
20.847 ± 14.351	7.315 ± 2.931	–	–	–
1.157 ± 0.085	–	–	–	–
1.194 ± 0.032	1.568 ± 0.166	3.368 ± 0.982	5.492 ± 1.595	9.223 ± 3.558
1.167 ± 0.064	1.200 ± 0.047	–	–	–
1.981 ± 0.638	1.186 ± 0.026	–	–	–
1.983 ± 0.113	1.326 ± 0.107	–	–	–
7.67 ± 1.867	6.436 ± 1.059	11.806 ± 2.213	25.117 ± 11.406	11.899 ± 1.557
–	–	–	–	–
3.264 ± 1.648	–	–	–	–
1.257 ± 0.099	2.406 ± 0.651	2.747 ± 0.673	3.666 ± 0.76	–
1.174 ± 0.049	1.146 ± 0.015	–	–	–
2.654 ± 0.886	4.035 ± 0.675	–	–	–
–	–	–	–	–
3.627 ± 0.763	4.961 ± 1.206	–	–	–

Table 4.2. List of meandering and branching trace fossils and their values for various analytical methods for samples from Zumaia, Spain (Z) and Tanzania (T) continued. Formations (Form.) mentioned (e.g., 3a, 4a, etc.) are described in Ernst and Zander (1993). An en-dash (–) indicates that the analysis does not apply to the specific trace analyzed; variance in the values is represented by the standard error. Abbreviations: Ind = indeterminate analyses; a = amplitude; λ = wavelength; MI = motility index; SS = spiral spacing; D_{Box} = fractal dimension using the Box Counting Method; OSP = occupied space percentage; BAS = burrow area shape.

Ichnogenera	Sample ID	Form.	a (cm)	λ (cm)	MI
Cosmorhaphe	Z_Cos1	Z-R2	0.348	1.360	0.256
Cosmorhaphe	Z_Cos2	Z-R2	0.373	1.423	0.262
Cosmorhaphe	Z_Cos3	Z-R2	0.392	1.580	0.248
Cosmorhaphe	Z_Cos4	Z-R2	0.467	1.716	0.272
Cosmorhaphe	Z_Cos5	Z-R2	0.336	1.629	0.206
Helmithorhaphe	Z_Helmin1	Z-R2	3.133	0.425	7.365
Helmithorhaphe	Z_Helmin2	Z-R2	2.502	0.589	4.249
Helmithorhaphe	Z_Helmin3	Z-R2	Ind	1.709	Ind
Helmithorhaphe	Z_Helmin4	Z-R2	Ind	0.521	Ind
Helmithorhaphe	Z_Helmin5	Z-R2	2.946	0.926	3.181
Helmithorhaphe	UUIC-1911	T-3	3.488	2.453	1.422
Helmithorhaphe	UUIC-1912	T-4A	1.064	0.753	1.413
Helmithorhaphe	UUIC-1913	T-IA?	0.991	1.156	0.857
Spirorhape	Z_Spiror1	Z-R2	-	-	-
Spirorhape	Z_Spiror2	Z-R2	-	-	-
Spirorhape	Z_Spiror3	Z-R2	-	-	-
Spirorhape	Z_Spiror4	Z-R2	-	-	-
Spirorhape	Z_Spiror5	Z-R2	-	-	-
Spirorhape	UUIC-1902	T-4A	-	-	-
Spirorhape	UUIC-1903	T-?	-	-	-
Spirorhape	UUIC-1904	T-3A	-	-	-
Spirorhape	UUIC-1905	T-?	-	-	-
Spirorhape	UUIC-1907	T-?	-	-	-
Spirorhape	UUIC-1908	T-4B	-	-	-
Urohelminthoida	Z_Urohelm1	Z-R2	0.565	0.617	0.917
Urohelminthoida	Z_Urohelm2	Z-R2	0.613	0.415	1.478

SS (cm)	Branching Angle (deg)	D_{Box}	BAS	OSP
-	–	1.405 ± 0.003	0.334	8.3%
-	–	1.482 ± 0.026	0.864	5.7%
-	–	1.373 ± 0.011	0.514	5.1%
-	–	1.456 ± 0.028	0.802	5.5%
-	–	1.382 ± 0.009	0.355	9.2%
-	–	1.497 ± 0.002	0.269	14.1%
-	–	1.498 ± 0.005	0.782	10.3%
-	–	1.528 ± 0.022	0.966	5.9%
-	–	1.468 ± 0.018	0.813	9.6%
-	–	1.566 ± 0.005	0.731	15.8%
-	–	1.590 ± 0.019	0.982	9.3%
-	–	1.570 ± 0.002	0.662	12.4%
-	–	1.621 ± 0.010	0.928	10.6%
3.235	–	1.573 ± 0.004	0.966	19.2%
3.880	–	1.633 ± 0.003	0.614	21.8%
5.353	–	1.481 ± 0.008	0.764	11.3%
3.576	–	1.627 ± 0.006	0.670	21.1%
3.581	–	1.604 ± 0.005	0.420	19.8%
4.428	–	1.575 ± 0.007	0.820	17.1%
3.791	–	1.539 ± 0.008	0.171	17.9%
3.891	–	1.611 ± 0.004	0.397	22.2%
5.767	–	1.646 ± 0.013	0.648	21.1%
3.225	–	1.642 ± 0.010	0.868	21.4%
2.583	–	1.705 ± 0.006	0.913	27.9%
-	44.8 ± 2.12	1.574 ± 0.003	0.694	16.2%
-	43.1 ± 2.15	1.526 ± 0.002	0.193	17.7%

Table 4.3. List of network trace fossils and their values for the various analytical methods for samples from Zumaia, Spain (Z) and Tanzania (T). Formations (Form.) mentioned (e.g., 3a, 4a, etc.) are described in Ernst and Zander (1993). Variance in the values is represented by the standard error. Abbreviations: C_{Size} = average cell size; MS = mesh size; NT = network tortuosity; $S_{Average}$ = weighted average of the cell sides; $S_{Variance}$ = variance of the number of cell sides; S_{Mode} = mode of the cell sides; D_{Box} = fractal dimension using the Box Counting Method; OSP = occupied space percentage; BAS = burrow area shape.

Ichnogenera	Sample ID	Form.	Burrow Width (mm)	C_{Size} (cm)	MS (cm)
Megagrapton	Z_Mega1	Z-R2	1.7	2.722	16.010
Megagrapton	Z_Mega2	Z-R2	1.5	2.988	19.918
Megagrapton	Z_Mega3	Z-R2	1	3.191	31.911
Megagrapton	Z_Mega4	Z-R2	1.2	2.405	20.039
Megagrapton	Z_Mega5	Z-R2	2	1.828	9.141
Megagrapton	Z_Mega6	Z-R2	2	1.327	6.634
Megagrapton	Z_Mega7	Z-R2	2	2.218	11.092
Paleodictyon	Z_Paleo1	Z-R2	0.5	0.635	12.706
Paleodictyon	Z_Paleo2	Z-R2	0.4	0.315	7.885
Paleodictyon	Z_Paleo3	Z-R2	0.8	0.677	8.464
Paleodictyon	Z_Paleo4	Z-R2	0.6	0.511	8.513
Paleodictyon	Z_Paleo5	Z-R2	0.8	0.541	6.763
Paleodictyon	UUIC-1916	T-2A	0.9	0.286	3.226
Paleodictyon	UUIC-1917	T-3A	1.0	0.288	2.881

NT	Branching Angle (deg)	$S_{average}$	$S_{Variance}$	S_{mode}	D_{box}	BAS	OSP
1.314 ± 0.004	85.2 ± 3.04	6.00	0.51	6	.423 ± 0.01	0.842	5.9%
1.334 ± 0.009	85.7 ± 5.11	5.25	0.00	5	.457 ± 0.02	0.955	4.9%
1.355 ± 0.002	77.9 ± 3.19	5.50	0.25	5	.344 ± 0.01	0.953	3.1%
1.877 ± 0.028	79.9 ± 2.1	5.00	0.70	4	.399 ± 0.01	0.965	5.0%
1.818 ± 0.016	80.6 ± 2.07	5.13	1.00	5	.491 ± 0.00	0.628	10.8%
1.434 ± 0.014	78.0 ± 2.88	5.13	0.55	5	.562 ± 0.00	0.788	13.3%
1.418 ± 0.017	80.4 ± 2.42	5.19	0.38	5	.511 ± 0.00	0.920	9.6%
1.412 ± 0.009	110.6 ± 0.97	6.00	0.43	6	.468 ± 0.01	0.943	6.3%
1.205 ± 0.003	105.4 ± 1.42	6.00	0.00	6	.588 ± 0.01	0.937	12.7%
1.434 ± 0.023	105.3 ± 2.53	6.00	0.00	6	.507 ± 0.01	0.833	9.7%
1.284 ± 0.005	99.8 ± 2.54	6.00	0.00	6	.507 ± 0.01	0.828	10.5%
1.291 ± 0.015	104.5 ± 1.04	6.00	0.00	6	.478 ± 0.00	0.674	13.4%
1.228 ± 0.003	80.0 ± 2.8	5.60	0.25	6	.750 ± 0.00	0.852	31.0%
1.223 ± 0.003	101.5 ± 2.3	5.86	0.13	6	.669 ± 0.00	0.850	19.7%

fossil and less of what was originally created by the organism. Fractal analysis and OSP show promise for providing valuable quantitative values, even for poorly preserved specimens. Some analyses, like the line thickness, topology, τ , and S, already have been used by ichnologists as a method for identifying different trace fossils. The methods described in this paper, however, provide a new technique for calculating τ and S, which result in a reproducible average that can be compared across different ichnogenera and localities.

The use of these methods creates a table of numbers for each trace fossil (Tables 4.1–4.3). These numbers can be used to compare similar trace fossils from different formations or time periods in a similar way to the application of cladistics in anatomical evolutionary studies. The cladistics approach uses numerical characters for different parts of the anatomy and then compares them between groups of taxa. Closely related taxa possess the most numerical characters in common. Trace fossils that are closely related or similar would be grouped together based on a large number of analyses that give similar results. These methods also could be used to help quantify changes in trace fossil morphology through time.

Various measurement techniques are available to scientists today, but the use of most of them in the field of ichnology has been limited. The methods presented here (tortuosity, branching angle, number of polygon sides, fractal dimension, burrow area shape, and occupied space percentage) provide effective means to quantify burrows and trails that otherwise are known only in a qualitative sense. Both morphology dependent and independent techniques will help scientists to better understand the behavior represented by the trace fossils that are being studied.

CHAPTER 5

BEHAVIORAL EVOLUTION OF BENTHIC ORGANISMS REFLECTED IN THE GEOLOGIC RECORD OF GRAPHOGLYPTID TRACE FOSSILS

5.1 Abstract

Analyses of the behavioral evolution of graphoglyptid trace fossils by previous workers indicated that they were slowly diversifying, becoming optimized, and getting smaller over time until the Late Cretaceous, when a sudden increase in diversification occurred. This interval of rapid diversification of graphoglyptid ichnotaxa was attributed, at least in part, to the evolution of the angiosperms on land. The current study quantifies the morphology of over 400 different graphoglyptid trace fossils, ranging in age from Cambrian to the present, in order to evaluate the behavioral evolutionary interpretations made previously. Results from this study indicate that although some general evolutionary patterns can be discerned, they are not as simple as previously reported. Different topological categories of trace fossils represent organisms' responses to evolutionary pressures in unique ways. While meandering traces were becoming smaller over time, as predicted by previous workers, network traces were becoming smaller only until the Late Cretaceous, when they started to get larger again.

The times of significant evolutionary changes in behavior were not consistent among various types of graphoglyptids, with some morphological features of the trace fossils being affected in the Late Cretaceous and others during the beginning of the Eocene. It is possible that deep marine global influences were related to the evolution of angiosperms and/or the increase in foraminiferal oozes, as previously predicted for the Late Cretaceous and the Paleocene-Eocene Thermal Maximum (PETM) during the Paleocene-Eocene boundary. Even though it has been previously assumed that graphoglyptids showed slow or no behavioral evolutionary trends throughout most of geologic time, the current study indicates that this is not the case. The graphoglyptid trace makers apparently were more sensitive to variable conditions on the deep ocean bottom than was previously thought.

5.2 Introduction

The study of the behavior of ancient organisms is elusive, because trace fossils are the only tangible record of animal behavior. Trace fossils provide a geologic record with a potential of showing changes in animal behavior, that is, behavioral evolution, throughout geologic time (Seilacher, 1974). Previous workers have catalogued the record of behavioral evolution through time simply by counting the numbers of ichnogenera and ichnospecies as they occur throughout the fossil record and adding up those numbers in each time period (Seilacher, 1974; Uchman, 2003). One of the problems with this approach is that ichnospecies identifications can be subjective, leaving later workers to reclassify previously identified species (e.g., Uchman, 1995; McKeever and Haubold, 1996; Wetzel and Bromley, 1996). Misidentifications will cause problems in constructing

trace fossil evolutionary lineages, because they raise the possibility of changing the number of ichnospecies and possibly even ichnogenera within any given time period. To avoid such problems in interpreting how trace fossils have changed through time, it is necessary for the trace fossils to be measured quantitatively and viewed in groups based on morphologic characteristics. This approach minimizes the subjectivity in ichnotaxonomy while still analyzing meaningful aspects of the forms of the traces.

A major problem with deciphering behavioral evolution from trace fossils is that the same animal can make many different types of trace fossils, and many different types of animals can make the same trace fossil. To reduce the amount of uncertainty, trace fossils produced in a restrictive environment with a similar mode of preservation should be used. For that reason, graphoglyptid trace fossils were used in this study.

Graphoglyptids are predepositional, geometrically complex, predominantly horizontal, open burrow systems commonly preserved in convex hyporelief on the soles of turbidite beds. Graphoglyptids are instructive trace fossils to study behavioral evolution, because they are typically found in deep-sea deposits, where they formed as open tunnels within a few centimeters of the sediment surface, and typically are preserved as casts on the soles of turbidite beds. The intricate geometric patterns exhibited by the majority of graphoglyptid ichnogenera display a similar degree and type of complexity to warrant the assumption that they probably were made by closely related species (Miller, 2003).

5.3 Basis of analyses

This study analyzed graphoglyptids and some other trace fossils preserved in the same method (i.e., *Gordia* and *Helminthopsis*). By restricting the study to graphoglyptid trace fossils, the number of possible variables is limited, since graphoglyptids generally were created in similar environments with similar conditions and were preserved under similar circumstances. The analyses in this study focused only on those forms preserved as convex hyporelief on the sole of turbidite beds, except in rare instances where other preservation modes were found, for instance in modern graphoglyptids (Ekdale, 1980).

The analyses were limited to graphoglyptids that were formed predominantly in a horizontal plane. Graphoglyptids that are initially formed three-dimensionally (e.g., *Lorenzina*, *Desmograpton*, and *Helicolithus*) lose significant behavioral information in the preservation process, so it is only by looking at multiple examples that it is possible to piece together the complete forms in three dimensions (Uchman, 1998). For that reason, predominantly horizontal graphoglyptids, (e.g., *Cosmorhaphe* and *Paleodictyon*) were the only forms studied.

The graphoglyptids were grouped into four different categories based on their topology: meandering forms, spiraling forms, branching forms, and network forms (Fig. 5.1; also see Lehane and Ekdale, 2014). Due to the inconsistencies with identification of trace fossils, for purposes of this study the trace fossil identifications were simplified to the ichnogeneric level.

Each trace fossil was analyzed and compared to all of the other trace fossils within one of the four topological groups. This reduced the amount of subjectivity introduced by naming the trace fossils. For instance, some examples of *Cosmorhaphe* and

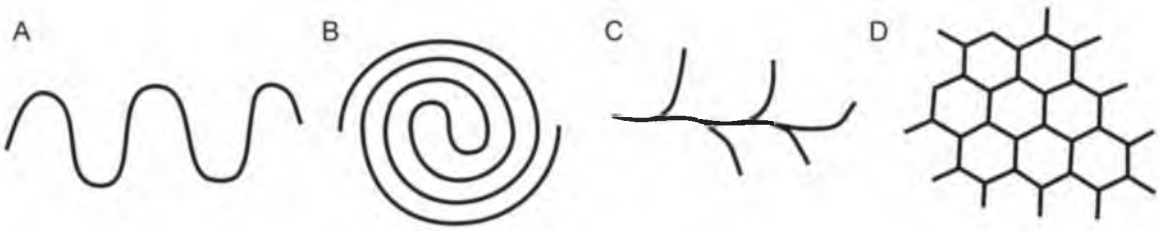

Figure 5.1. Topological classification of graphoglyptid trace fossils. A. Meandering forms. B. Spiraling forms. C. Branching forms. D. Network forms.

Helminthorhaphe could be interchangeable depending on the identifiers preferences for the amplitude-to-wavelength ratio of the meanders for each ichnospecies (e.g., D'Alessandro, 1982; Tavola 43 fig. 6; and Yeh, 1987, fig. 2A).

5.4 Ichnotaxonomy and topology groups

The definitions and descriptions of the following trace fossils are given as they are used in this research. In general, when a morphological description is referred to as regular, it means that the structure is modular (as illustrated in Crimes, 1977), with different parts of the burrow looking identical to each other. A morphological description that is referred to as complex means that it contains highly intricate patterns. Another way of stating complexity is that the more complex a pattern is, the more variables it takes to describe it (Ekdale and Lamond, 2003).

5.4.1 Meandering forms

Meandering forms (Fig. 5.1A) are continuous nonbranching tunnels that have no natural breaks in them (barring effects of erosion or imperfect preservation) and an overall sinuous morphology. These are grouped together, because although they may appear to vary significantly in shape, many forms are just variations on the common

theme. By altering the wave-length and wave-height of the meanders, it is possible to convert a trace fossil from *Cosmorhaphe* to *Helminthorhaphe*. The identification of many trace fossils reflect this ambiguity, where one scientist may call a given trace fossil one ichnospecies, another will call it something else, both being equally valid within the rules of nomenclature. The graphoglyptid trace fossils that are included in this category include *Belocosmorhaphe*, *Belorhaphe*, *Cosmorhaphe*, *Helminthopsis*, *Helminthorhaphe*, *Oscillorhaphe*, *Paleomeandron*, and *Spirocosmorhaphe*.

Belocosmorhaphe Uchman 1998

Description: Tunnel with first- and second-order meanders with short, lateral, knobby appendages (Uchman, 1998).

Remarks: *Belocosmorhaphe* is similar to *Cosmorhaphe*, a more common graphoglyptid, except that the *Belocosmorhaphe* meanders are much less regular and "sine-wave like." *Belocosmorhaphe* was listed as a "branched winding structure" by Uchman (1998); however, the knobby appendages do not constitute branches within these analyses.

Belorhaphe Fuchs 1895

Description: Tunnel with fine, angular, zigzag second order meanders, which are thicker around points of curvature, and wide first order meanders. Short, lateral protrusions extend from the curved points (Uchman, 1998).

Remarks: *Belorhaphe* also is similar to *Cosmorhaphe*, except that the second order meanders are much sharper at the apex. The short lateral protrusions cause this ichnogenus to be placed in the branched winding structure by Uchman (1998); however, they are not large enough to necessitate placing this ichnogenus with the branching forms for these analyses.

Cosmorhaphe Fuchs 1895

Description: Regularly meandering, unbranched tunnel with at least two orders of meanders (Uchman, 1998).

Remarks: A short segment of *Cosmorhaphe* often resembles the "sine-wave" with perfectly symmetrical meanders. Although the diagnosis emphasizes two orders of meanders, often only the smaller, second order meanders are found.

Helminthopsis Heer 1877

Description: Simple, unbranched, elongate, cylindrical tunnel with curves, windings, or irregular open meanders (Wetzel and Bromley, 1996).

Remarks: *Helminthopsis* is the simplest trace fossil form analyzed, because it exhibits no complex structural elements. *Helminthopsis* is not strictly a graphoglyptid, since the various ichnospecies include forms that are preserved in convex hyporelief and those that are not. Although the diagnosis is purely morphological and not preservational, Wetzel and Bromley (1996) reevaluated the ichnogenus and eliminated incorrectly identified

specimens. The possibility exists that graphoglyptid forms and nongraphoglyptid forms could be identified as *Helminthopsis*. Therefore, these analyses focus only on specimens that are preserved in convex hyporelief.

Helminthorhaphe Seilacher 1977

Description: Nonbranching trace fossil of small tunnel diameter with only one order of smooth, systematic meanders of very high amplitude, usually preserved as hypichnial semireliefs (Uchman, 1998).

Remarks: Ichnotaxonomic problems with the ichnogenera *Helminthorhaphe*, *Helminthoida*, and *Nereites* have plagued ichnologists in a spectrum of situations where similar trace fossils had been given any one of the three designations. Uchman (1995) attempted to solve this problem by dividing *Helminthoida*, which often was used as a catch-all term, into the hypichnial, loosely packed *Helminthorhaphe* and the back filled, densely packed *Nereites*. With this division, the ichnogenus name *Helminthoida* was eliminated altogether. This is the classification of these ichnogenera that was followed for these analyses.

Oscillorhaphe Seilacher 1977

Description: Tunnels arranged in high amplitude meanders, whose sharp turning points are marked by a distinct cross bar (Uchman, 1998)

Remarks: *Oscillorhaphe* is listed as a branching form by Uchman (1998); however, the reason for this is the same as for *Belocosmorhaphe* and *Belorhaphe*, which has an enlarged section near the turning points. As with the other forms, these enlarged sections are not large enough to necessitate placing this ichnogenus within the branching forms. The enlarged sections in *Oscillorhaphe*, *Belorhaphe* and others were interpreted by Seilacher (2007) to represent the vertical branching points for aeration tunnels to the seafloor.

Paleomeandron Peruzzi 1880

Description: Meandering tunnel, with small, more or less regular, rectilinear, second-order meanders (Uchman, 1998).

Remarks: *Paleomeandron* apparently includes two distinctive types of trace fossils in the ichnogenus. Most of the ichnospecies are shallow meanders with rectangular turns; however, there is one ichnospecies, *Paleomeandron robustum*, which appears more like a larger form of *Cosmorhaphe* than a larger *Paleomeandron* in most diagnoses, and it even was questioned whether it should be included with *Paleomeandron* by the scientist who initially assigned the name (Książkiewicz, 1977). Within the ichnogenus are included forms that have branches; however, since all but one of the forms that were analyzed for this study did not have branches, *Paleomeandron* has been included in the meandering form group, with the one exception being referred to as *Protopaleodictyon* instead.

Spirocosmorhaphe Seilacher 1989

Description: Unbranched tunnels, whose secondary meanders appear interrupted with ends in juxtaposition; interruptions appear in regular positions and correspond to loops in a plane outside the eroded surface (Seilacher, 1989).

Remarks: This is a semicontinuous meandering trace resembling *Cosmorhaphe* with mushroom-shaped tops to the meanders. Many of the meanders may stop and continue directly adjacent to the previous meander. This is likely the result of the burrow looping around and out of the preserved two-dimensional plane. Even though this means that much of the burrow is not preserved, there is enough information preserved in the two-dimensional space to provide meaningful analytical results.

5.4.2 Spiraling forms

Spiraling forms (Fig. 5.1B) are continuous nonbranching tunnels that have no natural breaks in them (barring effects of erosion or imperfect preservation) and an overall spiraling morphology. Only one graphoglyptid ichnogenus fits into this category, *Spirorhaphe*.

Spirorhaphe Fuchs 1895

Description: Doubly spiraling tunnels consisting of an inward spiral, a central loop and an outward spiral, guided between the turns of the inward spiral (Uchman, 1998).

Remarks: This description applies to *Spirorhaphe involuta* (de Stefani, 1895) specifically. There are other species of *Spirorhaphe* that are questionable as to whether or not they should be considered deep-sea graphoglyptids, so they were not included in these analyses. *Spirorhaphe* is first reported in the Ordovician, where it is known from only one instance (Pickerill, 1980). The next youngest occurrence is a tentative identification in the Triassic, and the first certain occurrence is in the Cretaceous (Uchman, 2003). This large gap in the geologic range of *Spirorhaphe* has led some workers to question the identification of the Ordovician specimen (Uchman, 1998).

5.4.3 Branching forms

Branching forms (Fig. 5.1C) are similar to the meandering forms, except that a given burrow splits into two or more burrows repeatedly. These branches do not reconnect to the main trunk or any other branch. The graphoglyptids that are included in this category are *Protopaleodictyon*, *Ubinia*, and *Urohelminthoida*.

Protopaleodictyon Książkiewicz 1958

Description: Tunnels with wide first-order meanders and more or less regular second-order meanders with one or two appendages usually branching from the apex of the second-order meanders (Uchman, 1998).

Remarks: *Protopaleodictyon* resembles *Cosmorhaphe* with the addition of short branches extending from the apex of the meanders. Poorly preserved *Megagrapton* specimens sometimes have been misdiagnosed as *Protopaleodictyon* (Książkiewicz, 1977; Uchman,

1998). For these analyses, if the structure forms a network, then it is not identified as *Protopaleodictyon*.

Ubinia Grossgeim 1961

Description: Straight or slightly winding tunnel with an axial string from which arcuate or straight simple branches extend (Wetzel and Uchman, 1997).

Remarks: This is an uncommon graphoglyptid that contains a central trunk with several branches curving off from it. It maintains enough of a central trunk to be considered for analysis.

Urohelminthoida Sacco 1888

Description: A tunnel with deep meanders and short lateral appendages protruding outwardly from the curved bends of the meanders (Uchman, 1998).

Remarks: *Urohelminthoida* resembles *Helminthorhaphe* but differs in possessing short branches off the apexes of the meanders.

5.4.4 Network forms

Network forms (Fig. 5.1D) are similar to branching forms, except the branches reconnect to each other or reconnect back to the main trunk. To be assigned to this group of network forms, there must be at least one complete cell (an individual unit within a

mesh or network). The graphoglyptids that are included in this category are *Gordia*, *Megagrapton*, *Paleodictyon*, and *Squamodictyon*.

Gordia Emmons 1844

Description: Slender, smooth, loosely meandering tunnels with frequent crossovers (Książkiewicz, 1977).

Remarks: This ichnogenus is represented by a series of crisscrossing burrows without forming an interconnected network, but they are considered with the network forms due to the overall pattern that is formed. *Gordia* often is preserved as a convex hypichnial trace, placing it in the same category as graphoglyptids, although it lacks the typical geometrical regularity of a graphoglyptid. Only samples that display a graphoglyptid-type preservation mode were used in this study.

Megagrapton Książkiewicz 1968

Description: Slender meandering tunnels, which connect to form a network of irregularly sized and shaped cells (Uchman, 1998).

Remarks: *Megagrapton* often resembles an intermediate between *Protopaleodictyon* and *Gordia.* The main difference from *Protopaleodictyon,* is that in *Megagrapton* the extending branches have the same morphology as the meandering section, and they interconnect to form a network. The principal difference between *Gordia* and

Megagrapton is that the tunnel junctures in *Megagrapton* usually form a "T" intersection, while the junctures in *Gordia* often resemble a burrow crossover, forming an "X".

Paleodictyon Meneghini in Peruzzi 1880

Description: Three-dimensional trace fossil network consisting of a horizontal net composed of regular to irregular hexagonal meshes and short, vertical outlets (Uchman, 1998).

Remarks: In this study, the diagnosis of *Paleodictyon* is reserved for specimens that show at least one complete cell, with straight segments and angular burrow intersections.

Squamodictyon Vialov and Golev 1960

Description: Network of tunnels without consistent straight tunnel segments or angular bends. The individual cells are formed like rounded scales (Seilacher, 1977).

Remarks: Although sometimes diagnosed as a subichnogenus of *Paleodictyon* (Seilacher, 1977), *Squamodictyon* is also frequently listed as its own ichnogenus (Crimes and Crossley, 1991). It is listed here as such due to the formational differences between the hexagonal network of *Paleodictyon* and the rounded scale form of *Squamodictyon*.

5.4.5 Graphoglyptid ichnogenera not included in this study

The term graphoglyptid is partially a preservational term for trace fossils that are preserved as two-dimensional casts. This means that many graphoglyptids are only

partially preserved in semirelief. The analyses used in this study were designed for trace fossils in two-dimensional space. Depending on the degree of preservation, some graphoglyptids were not ideal for these analyses. There are 27 total graphoglyptid ichnogenera, not including *Gordia* or *Helminthopsis* (Uchman, 2003), 14 of which are included in the analyses for this research (Table 5.1).

There are a few reasons as to why some graphoglyptids were not used for this study. For example, horizontal spiraling graphoglyptids, like a spring lying on its side, could be useful if they preserve a long enough continuous pathway, as in the case of *Spirocosmorhaphe*. However, *Helicolithus* and *Teptichnus* are tightly spiraling graphoglyptids, like a corkscrew, that often are preserved as short, parallel, angled burrow segments. Without a continuous meander to follow, the analyses would be largely conjectural. Other trace fossils that are likely the result of larger three-dimensional networks include *Desmograpton* and *Acanthorhaphe,* where the burrows that are preserved are often incomplete and noncontinuous.

Another group of graphoglyptids that are not studied here are radial graphoglyptids, which are those with multiple tunnels that radiate out from a central location. These clearly are partially preserved three-dimensional structures. Without a continuous pathway to map, they have been left out of the analysis. Such radial graphoglyptids include *Arabesca, Glockerichnus, Lorenzinia, Capodistria, Chondrorhaphe, Fascisichnium, Dendrorhaphe,* and *Yacutatia*.

Table 5.1 List of graphoglyptids

Analyzed	Topology Group	Not Analyzed	Reason
Belocosmorhaphe	M	*Acanthorhaphe*	3D
Belorhaphe	M	*Arabesca*	R
Cosmorhaphe	M	*Capodistria*	R
*Helminthopsis**	M	*Chondrorhaphe*	R
Helminthorhaphe	M	*Dendrorhaphe*	R
*Gordia**	N	*Desmograpton*	3D
Megagrapton	N	*Estrellichnus*	R
Oscillorhaphe	M	*Fascisichnium*	R
Paleodictyon	N	*Glockerichnus*	R
Paleomeandron	M	*Helicolithus*	3D
Protopaleodictyon	B	*Lorenzinia*	R
Spirocosmorhaphe	M	*Treptichnus*	3D
Spirorhaphe	S	*Yacutatia*	R
Squamodictyon	N		
Ubinia	B		
Urohelminthoida	B		

Graphoglyptids are catalogued on whether they were used or not used for these analyses. * indicates ichnogenera which are not exclusively preserved as convex hyporelief on the base of turbidites; however, the analyses were restricted to those that are preserved as such. M = Meandering forms, S = Spiraling forms, B = Branching forms, N = Network Forms, 3D = Mostly three-dimensional graphoglyptids, R = Radiating graphoglyptids.

5.5 Materials

For these analyses, graphoglyptid images were taken from three different sources: field photographs, museum specimens, and images from the published literature. The field photographs were taken in the Guipúzcoan Flysch, Higuer-Getaria Formation (Ypresian, Lower Eocene), Zumaia, Spain, which is known as one of the best locations in the world to find graphoglyptids, as well as the Vera Basin, Almería, southeastern Spain, and the Point Saint George Turbidites, Franciscan Complex (Middle Jurassic to Middle Cretaceous), northern California. The museum specimens that were photographed are housed in the University of Utah Ichnology Collection, Salt Lake City, UT, the Institute of Geological Sciences, Jagiellonian University, Krakow, Poland, and the University of

California Museum of Paleontology, Berkeley, CA. The remaining samples were collected from previously published images in the literature. The source of many of the references collected for the literature search was the list of reference citations in Uchman (2003), which is one of the most comprehensive collection of turbidite trace fossil papers known. A list of known turbidite deposits is included in Figure 5.2 and Appendix F, which highlights how many turbidite deposits are known to contain graphoglyptids and how many of those were used in these analyses.

The total number of specimens analyzed includes 414 individual graphoglyptid specimens that ranged from Lower Cambrian to modern examples (Figs. 5.2 and 5.3; Appendix E) and from sites throughout the world (Appendix G). This total includes 140 meandering forms, 27 spiraling forms, 65 branching forms, and 182 network forms.

5.6 Methodology

To describe the evolutionary trends of the graphoglyptids through time, the morphology of the trace fossils must be studied analytically and objectively. Graphoglyptid trace fossils are regarded as planar structures, and therefore they allow for two-dimensional analyses of the morphology. A complete chart of the analytical results is provided in Appendix H. Some techniques were described in detail in Lehane and Ekdale (2013; 2014) with changes or extensions of those analyses described in detail in Appendix I.

Each of the trace fossils was photographed and traced following the midline of the burrow. The line width was set to the average thickness of the burrow, giving a best

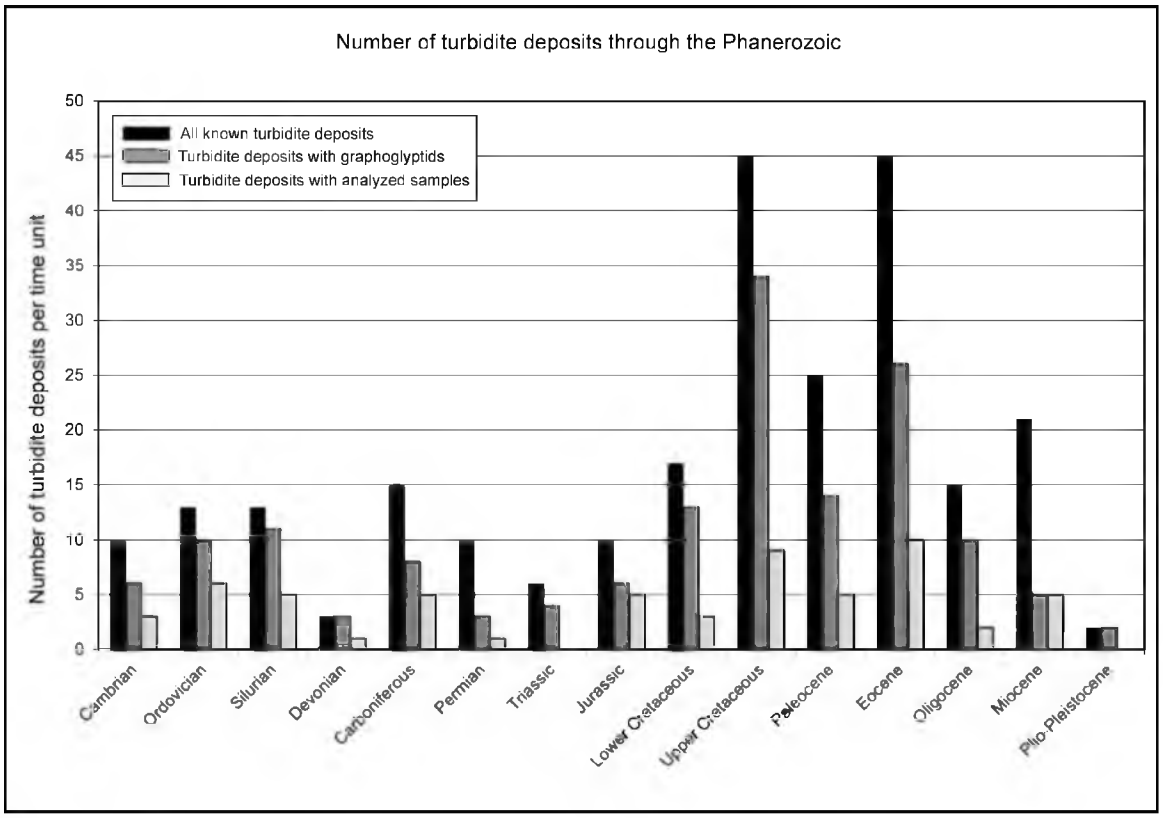

Figure 5.2. Number of known turbidite (flysch) deposits for each time period of the Phanerozoic. The black bars tabulate the total number of known turbidite deposits. The dark gray bars tabulate the number of turbidite deposits with graphoglyptids as listed by Uchman (2004). The light gray bars tabulate the number of turbidite deposits with graphoglyptids specimens used for these analyses. Individual turbidite deposits are listed in Appendix F. If a deposit is known to cross unit boundaries, it was counted for both units.

approximation of the diameter of the original burrow (Appendix E). The identification of the trace fossil was based in part on its topology (Fig. 5.1), and different analyses were performed for each form. The basic measurements that were taken for the trace fossils included the following: motility index (MI), which is equal to the amplitude (a) of a meander divided by the wavelength (λ) of meandering forms; spiral spacing (SS), which is the average burrow spacing of spiraling form divided by the burrow width (W); and mesh size (MS), which is the average cell size of a network form divided by W.

Figure 5.3. Geologic ranges of the graphoglyptid taxa analyzed. M = Meandering forms, S = Spiraling forms, B = Branching forms, N = Network forms.

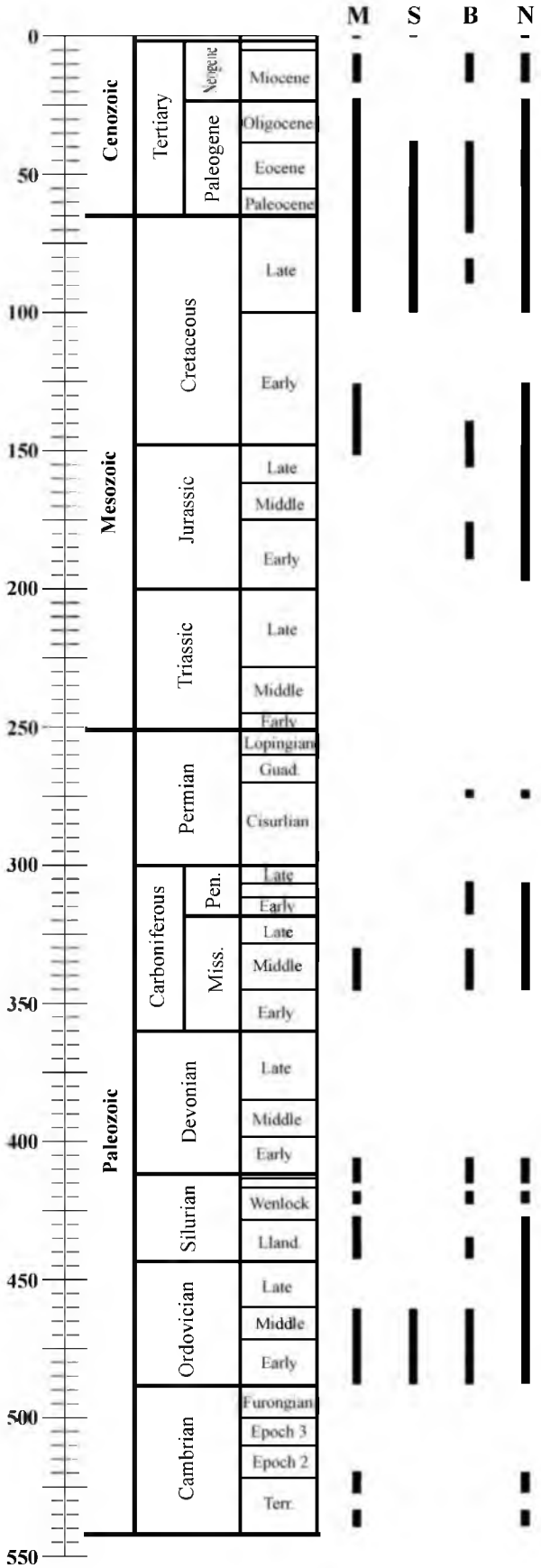
M
S
B
N
0
50
100
150
200
250
300
350
400
450
500
550
Cenozoic
Mesozoic
Paleozoic
Tertiary
Neogene
Paleogene
Miocene
Oligocene
Eocene
Paleocene
Cretaceous
Late
Early
Jurassic
Late
Middle
Early
Triassic
Late
Middle
Early
Permian
Lopingian
Guad.
Cisurlian
Carboniferous
Pen.
Late
Early
Miss.
Late
Middle
Early
Devonian
Late
Middle
Early
Silurian
Wenlock
Lland.
Ordovician
Late
Middle
Early
Cambrian
Furongian
Epoch 3
Epoch 2
Terr.

For the meandering, spiraling, and branching forms, the tortuosity (τ) was calculated by dividing the average length of the line by the straight line distance between the end points of the trace (Fig. 5.4A). These measures were compared using similar sized sections in each trace fossil (5 cm, 10 cm, 15 cm, etc.). For example, in Figure 5.4A the two different length tortuosities were calculated by:

$$\tau_{\text{Short segments}} = \text{average}\left[\overline{ab}/L_1 + \overline{bc}/L_2\right] \qquad \text{(Eq. 5.1)}$$

$$\tau_{\text{Long segment}} = \overline{ac}/L_3$$

Equal length segments from different trace fossils then may be compared to one another.

The τ of the network forms was determined in a similar way, except all of the available pathways were measured and averaged together both horizontally and vertically (Fig. 5.4B). In Figure 5.4B, this is calculated by determining the τ of line segments $\overline{de}$ and $\overline{fg}$, along with all other possibilities ($\overline{dg}$, $\overline{fe}$, etc.), and averaging the resulting τ values together. The network tortuosity (NT) was calculated for decreasing size regions across the trace fossil, until the τ did not vary for each analyzed region. Decreasing the measured region of the trace fossil eliminated portions of the outer edge of the trace fossils which were incompletely preserved. The NT was calculated using Matlab from an updated script (Appendix J), which was employed in previous analyses (Lehane and Ekdale, 2014).

The average branching angles were measured for both the branching and the network forms. In order to maintain consistency between different trace fossils, the branching angle that was used was the smallest possible angle. Within the network forms, the number of sides of each cell, an individual unit within a network, also was counted.

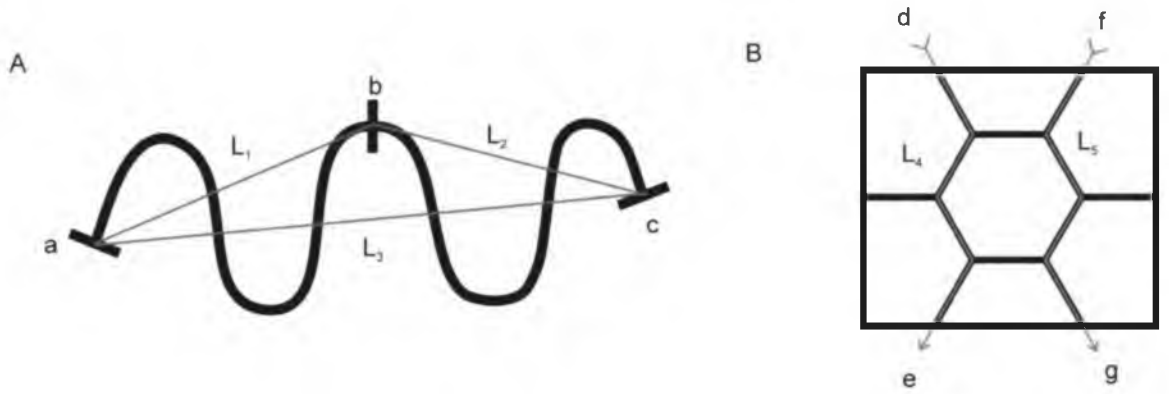

Figure 5.4. Tortuosity measurements. A. Tortuosity measurements for meandering forms. a and c are end points, b is the midpoint. L_1, L_2, and L_3 represent the lengths of each respective line. B. Tortuosity measurement for network forms. d, e, f, and g are the endpoints of the measuring lines. L_4 and L_5 represent the lengths of each respective line.

Some analyses that were performed were morphology independent. The principal morphology independent analysis involved calculating the fractal dimension of each trace. Fractal analysis combines the amount of space the trace fossil covers with the intricacy of the design into one number, the fractal dimension, which ranges between 1.0 and 2.0 for planar trace fossils (Lehane and Ekdale, 2013).

The next analysis involved calculation of the occupied space percentage (OSP), which is the amount of the surface that is covered by the trace fossil. The final analysis involved calculation of the burrow area shape (BAS), which is the overall shape of the trace fossil, where a perfect circle has a value of 1.0 and a straight line has a value of 0.0. The BAS was used to determine network forms that were not fit for the NT study. For any trace fossil with a BAS of less than 0.45, either the NT was not measured, or else the trace fossil image was cropped to exclude disconnected pieces of the trace. BAS values between 0.45 and 0.50 were evaluated to determine if they should be cropped, excluded, or analyzed in full. All values of the BAS of 0.50 or greater were analyzed in full.

5.7 Results

The analytical results for each graphoglyptid form are reported here in separate sections. Not all of the analyses are discussed in detail; however, all of the results are listed in Appendix H. Within the figures, the median value of the results for each time period are plotted with the error bars represented by the 95% confidence interval, except for the spiraling forms figures. The 95 % confidence interval provides a better determination of where the majority of the samples would lie, while removing the outliers. For the spiraling form figures, all of the samples were plotted due to the low number of samples. Plotting the 95% confidence interval would have eliminated the Ordovician specimen, which is the only sample in the analyses that is found prior to the Late Cretaceous.

5.7.1 Meandering forms

The study set of the meandering forms consisted of 140 specimens, ranging from the Cambrian to the modern, including the ichnogenera *Belocosmorhaphe*, *Belorhaphe*, *Cosmorhaphe*, *Helminthopsis*, *Helminthorhaphe*, *Oscillorhaphe*, *Paleomeandron*, and *Spirocosmorhaphe* (Fig. 5.3). The measures of burrow width (W), fractal dimension (D_{Box}), tortuosity (τ), and motility index (MI) were plotted against the age of the specimens in order to determine any noticeable trends (Figs. 5.5 and 5.6). The complete results of the analyses are shown in Appendix H. Within the meandering forms, there is a large gap in data from the Devonian to the Early Cretaceous. Part of the cause of this gap is due to using the 95% confidence interval, which does not allow for the plotting of time

Figure 5.5. Results of meandering form analyses. A. Measure of the burrow width (W) in mm over time, plotted in millions of years before present. The trend line is represented by the 2nd-order polynomial best fit line. B. Measure of the fractal dimension calculated by the Box Method (D_{Box}) over time, plotted in millions of years before present. The boundary between the Early Cretaceous and the Late Cretaceous is highlighted. The arrow is represented by the linear best fit line for all data points to the right of the boundary line. The error bars for both plots represent the 95% confidence interval of the data set per time period and the ages represent the median age of the estimated age range of the specimen. If the time period did not have more than one data point it was not included in the chart.

A

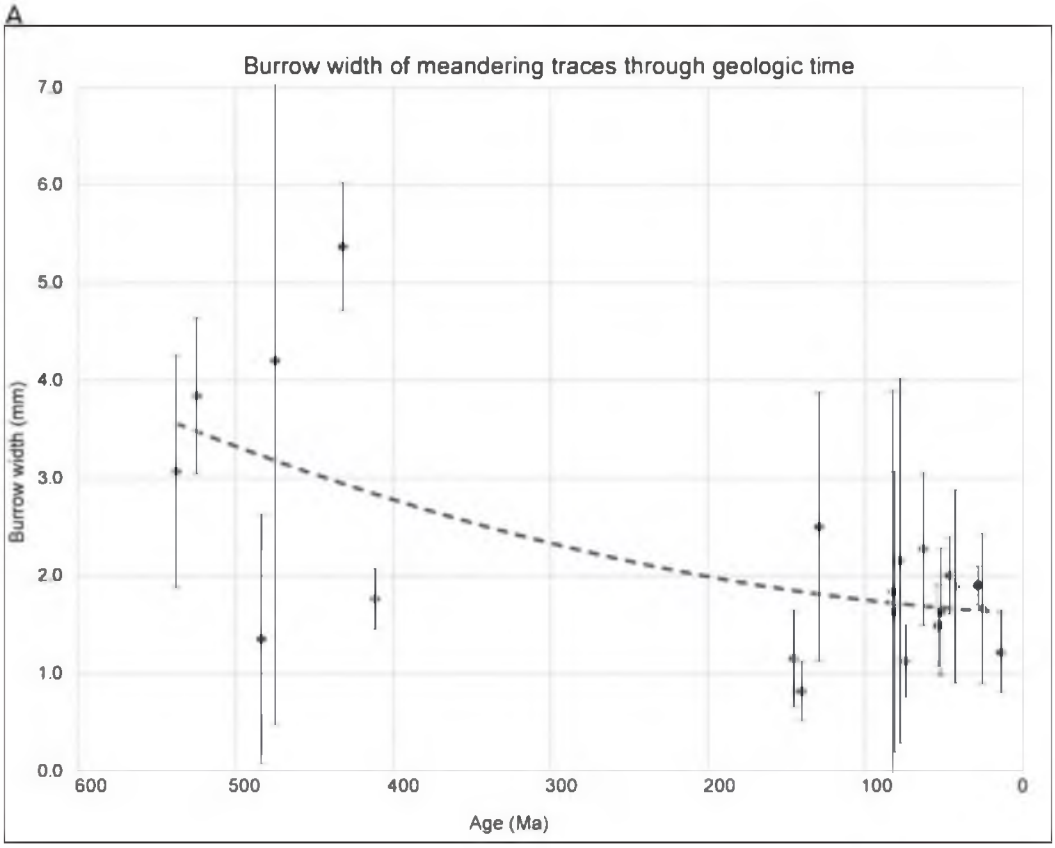
Burrow width of meandering traces through geologic time
Burrow width (mm)
7.0
6.0
5.0
4.0
3.0
2.0
1.0
0.0
600
500
400
300
200
100
0
Age (Ma)

B

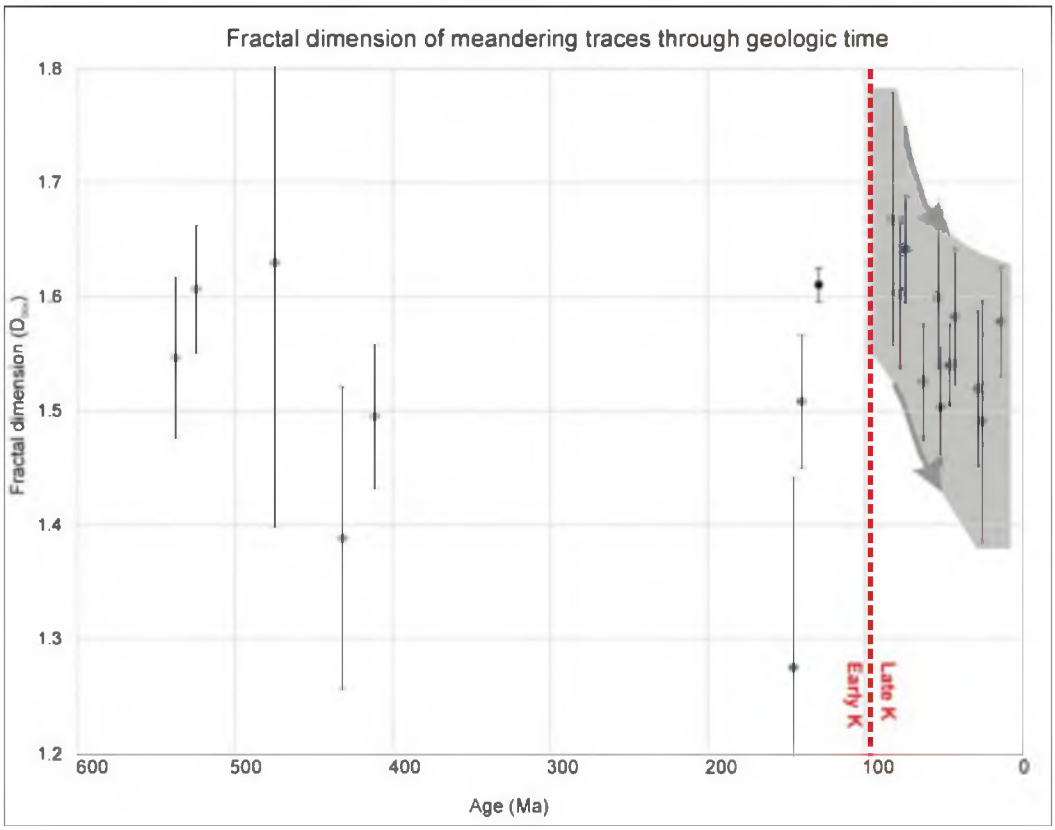
Fractal dimension of meandering traces through geologic time
Fractal dimension (D_{ind})
1.8
1.7
1.6
1.5
1.4
1.3
1.2
600
500
400
300
200
100
0
Age (Ma)
Late K
Early K

Figure 5.6. Results of meandering and branching form analyses. A. Measure of the tortuosity (τ) of meandering forms over time, plotted in millions of years before present. The 5 cm (circles) and 30 cm (triangles) τ are plotted on the graph. The 2nd-order polynomial best fit trend lines are plotted for the 5 cm, 10 cm, 15 cm, 20 cm, 25 cm, and 30 cm τ. The Cambrian-Ordovician, Early Cretaceous-Late Cretaceous, and Eocene-Oligocene boundaries are also highlighted. B. Measure of the motility index (MI) of meandering forms (triangles) and branching forms (circles) over time, plotted in millions of years before present. The Cambrian-Ordovician, Early Cretaceous-Late Cretaceous, Eocene-Oligocene, and Oligocene-Miocene boundaries are also highlighted. General trends of the data are highlighted with the arrows and the gray background. The error bars for both plots represent the 95% confidence interval of the data set per time period and the ages represent the median age of the estimated age range of the specimen. If the time period did not have more than one data point it was not included in the chart.

A

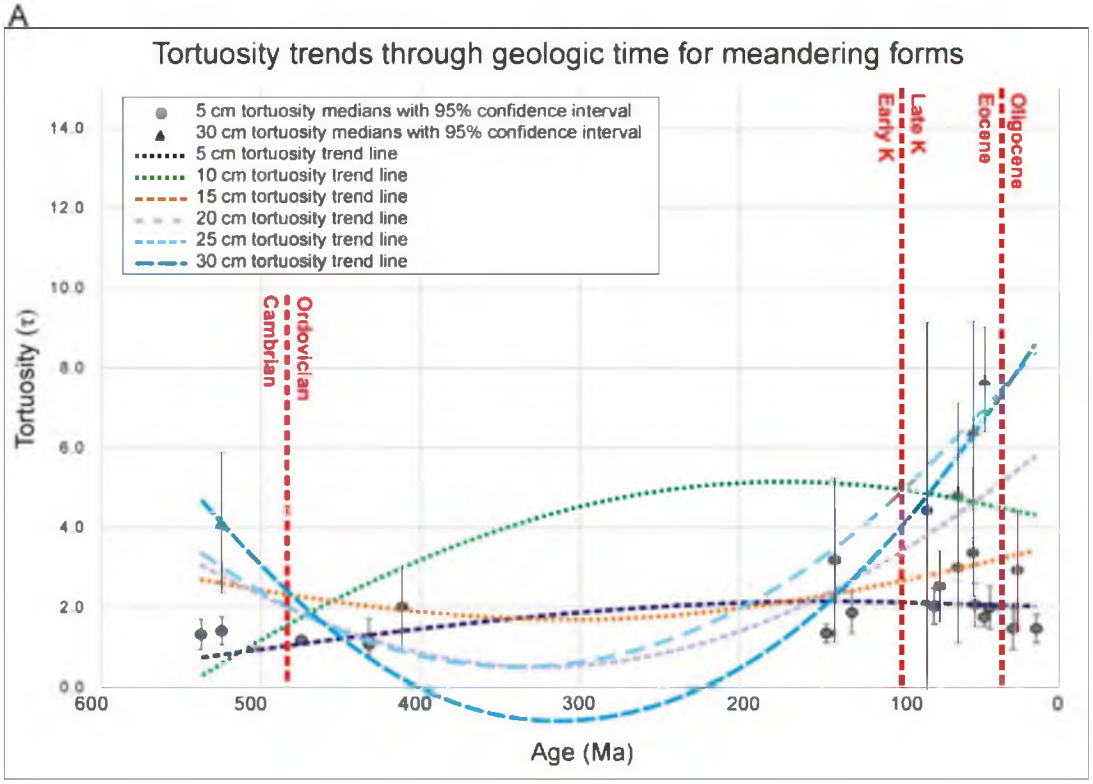
Tortuosity trends through geologic time for meandering forms
5 cm tortuosity medians with 95% confidence interval
30 cm tortuosity medians with 95% confidence interval
5 cm tortuosity trend line
10 cm tortuosity trend line
15 cm tortuosity trend line
20 cm tortuosity trend line
25 cm tortuosity trend line
30 cm tortuosity trend line
Late K
Early K
Oligocene
Eocene
Ordovician
Cambrian
Tortuosity (τ)
14.0
12.0
10.0
8.0
6.0
4.0
2.0
0.0
600
500
400
300
200
100
0
Age (Ma)

B

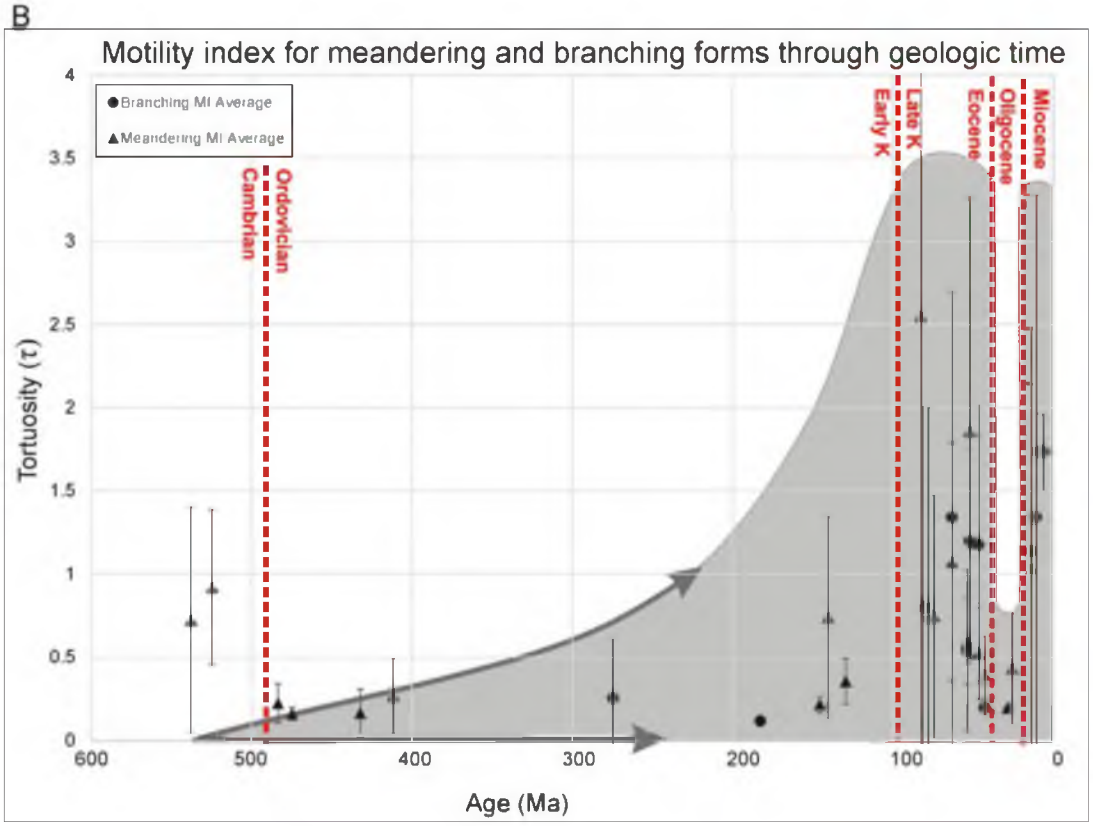
Motility index for meandering and branching forms through geologic time
Branching MI Average
Meandering MI Average
Late K
Early K
Oligocene
Eocene
Miocene
Ordovician
Cambrian
Tortuosity (τ)
4
3.5
3
2.5
2
1.5
1
0.5
0
600
500
400
300
200
100
0
Age (Ma)

periods with only one specimen or a group of specimens where the specific analysis can be applied to only one of them (e.g., in the Jurassic and the Carboniferous).

The plot of the burrow width (W) over geologic time (Fig. 5.5A) shows two groupings of meandering traces, Cambrian to Devonian, and Early Cretaceous to modern. The two groups show distinctly different patterns, with the W of the Paleozoic specimens having a very large range of about 8 mm (95% confidence interval of ~0.2 to ~7.8 mm), while the Mesozoic and Cenozoic group has a range of only about 4 mm (95% confidence interval of ~0.1 to 4.0 mm). The Paleozoic samples show a lack of similarity between the trace fossils within and across the different time periods, while the later samples show a much tighter fit between and within each time period. A 2^{nd}-order polynomial line is shown as the best fit line through all of the time periods. The best fit line shows that between these two time period groups, the average W had decreased by almost half.

The plot of fractal dimension (D_{Box}) over geologic time (Fig. 5.5B) also illustrates the two main groupings of meandering traces. The graph shows that up until the Late Cretaceous (the red line on Fig. 5.5B), the D_{Box} was quite variable. After the Late Cretaceous, the D_{Box} values hit close to their peak and steadily declined.

Tortuosity (τ) trends through geologic time (Fig. 5.6A) are a little more complex than the previous analyses. The graph shows the median values and 95% confidence intervals for the 5 cm and 30 cm tortuosity calculations. The 2^{nd}-order polynomial trend lines are shown for the 5 cm, 10 cm, 15 cm, 20 cm, 25 cm, and 30 cm tortuosity calculations. The Cambrian-Ordovician, Early Cretaceous-Late Cretaceous, and the Eocene-Oligocene boundaries are also highlighted. To avoid cluttering up the graph, only

the 5 cm and 30 cm median points are shown; however, a list of all the source values can be found in Appendix H. Even though there is a large gap in time between the two groups of trace fossils, there is a trend that can be seen going from the 5 cm tortuosity up to the 30 cm tortuosity. Through time, the 5 cm tortuosity has remained basically the same, as shown by the nearly horizontal trend line. The 10 cm tortuosity shows a convex trend line, which displays an increase in the τ, peaking in the Eocene. Starting with the 15 cm τ and continuing through the 30 cm τ, the τ of the meandering traces peaks in the Eocene with a sudden drop off in the Oligocene. This means that the longer the traces are, the more tortuous they tend to be, and the τ range of the Mesozoic/Cenozoic group is far larger than the τ range of the Paleozoic group.

The motility index (MI) for both the meandering and the branching forms is plotted over geologic time (Fig. 5.6B). The Cambrian-Ordovician, Early Cretaceous-Late Cretaceous, Eocene-Oligocene, and Oligocene-Miocene boundaries also are highlighted on the graph. Even though many of the same analyses can be applied among the different topological forms, the trends that they display are often different. However, in this instance the meandering and branching forms align nicely, so they have been plotted on the same graph. Several trends for the MI can be seen on the graph. The first is that there is a significant drop in MI from the Cambrian through the rest of the Paleozoic. The low MI also matches up with the tortuosity for the Cambrian or the rest of the Paleozoic. The low MI values then start to rise, peaking in the Late Cretaceous. The MI remains fairly high until the Oligocene, where the MI value drops off steeply to almost Paleozoic values, and then it increases again in the Miocene. The gray background and arrows are included to help illustrate these changes in values.

5.7.2 Spiraling forms

The study set of the spiraling forms consisted of 27 specimens, ranging from the Ordovician to the modern, all represented by the ichnogenus *Spirorhaphe* (Fig. 5.3). Although this is a long time range, aside from one specimen in the Ordovician and two in the modern, the remaining 24 specimens all occur during a 36 ma time span from the Late Cretaceous to the Eocene. The measures of fractal dimension (D_{Box}), spiral spacing (SS), and tortuosity (τ), were plotted with regard to geologic time (Fig. 5.7). The complete results from the analyses can be found in Appendix H. Unlike the other forms, due to the small sample size, the graphed samples represent the actual samples analyzed and not the 95% confidence interval of the samples. Calculating the 95% confidence interval would have eliminated the only sample prior to the Cretaceous, i.e., the Ordovician *Spirorhaphe*.

Considering all of the analyses from the Late Cretaceous to the modern, the total number of samples is insufficient for any noticeable trends of any of the measurements to be discerned. When the Ordovician *Spirorhaphe* is included, it clearly is separated morphologically from the other samples. The W places it right in the middle of the range of the other specimens, but the SS and the D_{Box} measurements place the Ordovician specimen towards the outer edge of the range of the remaining 27 specimens. By comparing the SS directly to the D_{Box}, the Ordovician outlier is obvious (Fig. 5.7A), and it clearly lies outside the grouping made by the remaining 26 fossils. Within the clustering of the other *Spirorhaphe* samples, the modern samples tend toward the bottom of the graph (highlighted in orange), although not outside of the other samples. The

Figure 5.7. Results of spiraling form analyses. A. Measure of the fractal dimension calculated by the Box Method (D_{Box}) versus the spiral spacing (SS) for all spiraling form samples analyzed. Time periods are labeled with the Ordovician sample (square) and the modern samples (orange) highlighted. B. Measure of the tortuosity (τ) of meandering forms over time, plotted in millions of years before present. The 10 cm (triangles) and 20 cm (circles) τ are plotted on the graph. The error bars represent the standard error for both graphs and the ages represent the median age of the estimated age range of the specimen.

A

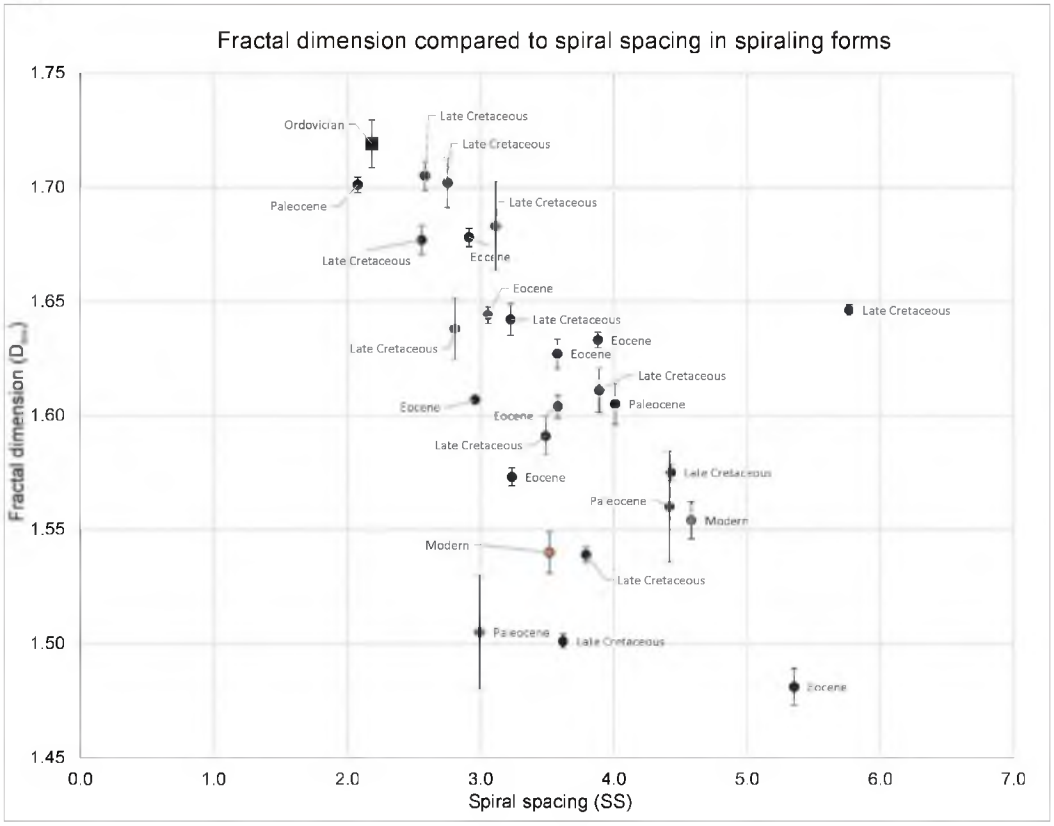
Fractal dimension compared to spiral spacing in spiraling forms
Fractal dimension (D_{fm})
Spiral spacing (SS)
1.75
1.70
1.65
1.60
1.55
1.50
1.45
0.0
1.0
2.0
3.0
4.0
5.0
6.0
7.0
Ordovician
Late Cretaceous
Late Cretaceous
Paleocene
Late Cretaceous
Late Cretaceous
Eocene
Late Cretaceous
Late Cretaceous
Eocene
Late Cretaceous
Late Cretaceous
Eocene
Eocene
Late Cretaceous
Paleocene
Eocene
Late Cretaceous
Eocene
Late Cretaceous
Paleocene
Modern
Modern
Late Cretaceous
Paleocene
Late Cretaceous
Eocene

B

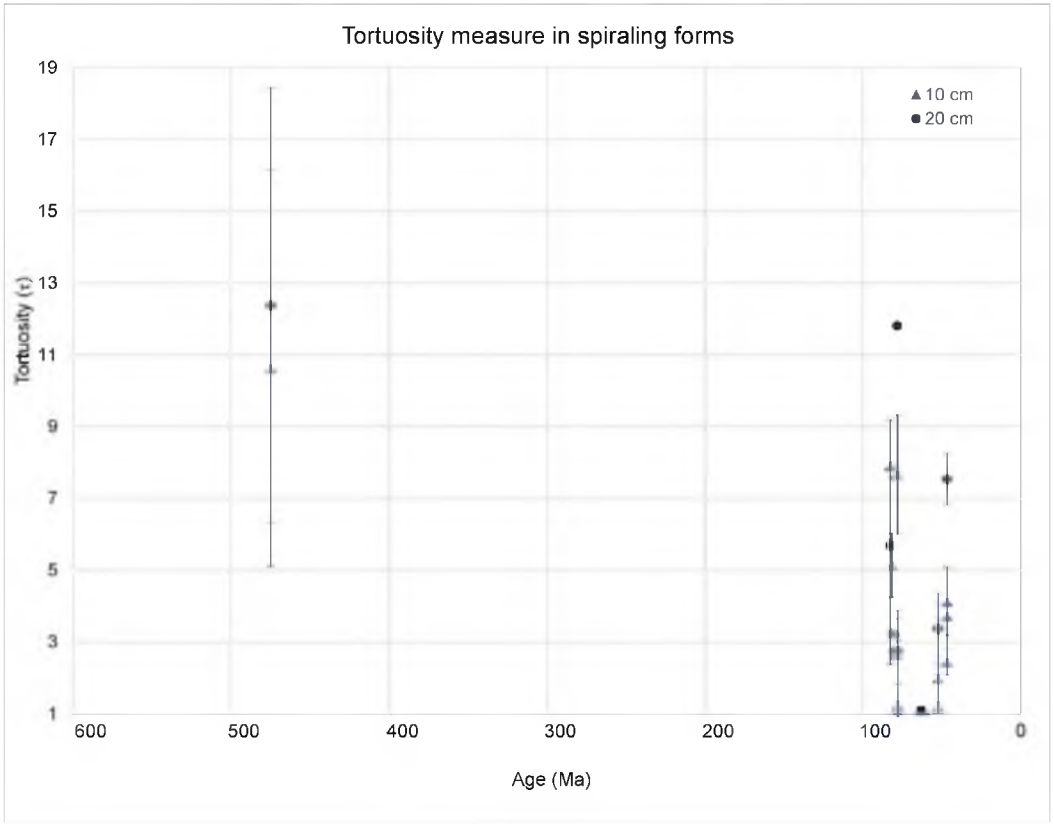
Tortuosity measure in spiraling forms
Tortuosity (τ)
Age (Ma)
10 cm
20 cm
19
17
15
13
11
9
7
5
3
1
600
500
400
300
200
100
0

remaining specimens from the Late Cretaceous to the Eocene are jumbled together with no discernable pattern.

By studying the τ of the samples, it can be seen that the Ordovician *Spirorhaphe* is more tortuous at the 10 cm and 20 cm lengths (Fig. 5.7B); however, it is not significantly so, with the error bars heavily overlapping between the two time periods. It is hard to gauge the importance of the τ for spiraling forms, since the values can have a wide range of values due to the spiraling nature of the trace fossil (Lehane and Ekdale, 2014). Even with short segments, a small, tightly spiraling trace will have a wider range of values than a larger spiral. So for the spiraling traces it is more than likely that the size of the error bars, rather than the value of the τ, will represent a significant morphological feature. In this case, the Ordovician specimen has an error range of almost twice the next closest value. This could indicate that the Ordovician specimen is significantly different from the remaining *Spirorhaphe* specimens studied.

5.7.3 Branching forms

The study set of branching forms consists of 65 specimens, ranging from Ordovician to Miocene in age, including the ichnogenera *Protopaleodictyon*, *Ubinia,* and *Urohelminthoida* (Fig. 5.3). The measures of motility index (MI), fractal dimension (D_{Box}), burrow width (W), and branching angle (BA) were plotted against the age of the specimens to determine any noticeable trends (Figs. 5.6B, 5.8, and 5.9A). The branching form can be considered a cross between the meandering forms and the network forms, so the individual measurements that are the same as the other two forms were compared directly with them (i.e., the motility index with the meandering forms and the branching

Figure 5.8. Results of branching form analyses. A. Measure of the fractal dimension calculated by the Box Method (D_{Box}) over time, plotted in millions of years before present. B. Measure of the burrow width (W) in mm over time, plotted in millions of years before present. The error bars for both plots represent the 95% confidence interval of the data set per time period and the ages represent the median age of the estimated age range of the specimen. If the time period did not have more than one data point it was not included in the chart.

A

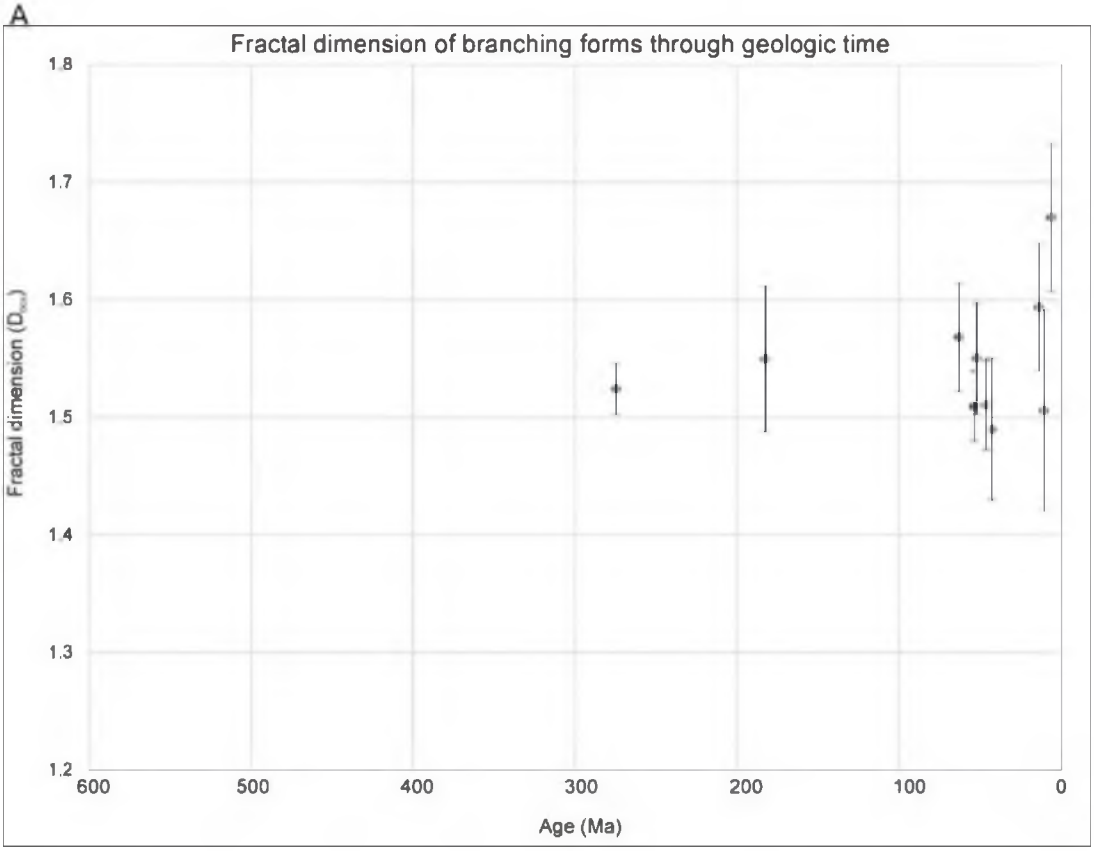
Fractal dimension of branching forms through geologic time
Fractal dimension (D_{box})
1.8
1.7
1.6
1.5
1.4
1.3
1.2
600
500
400
300
200
100
0
Age (Ma)

B

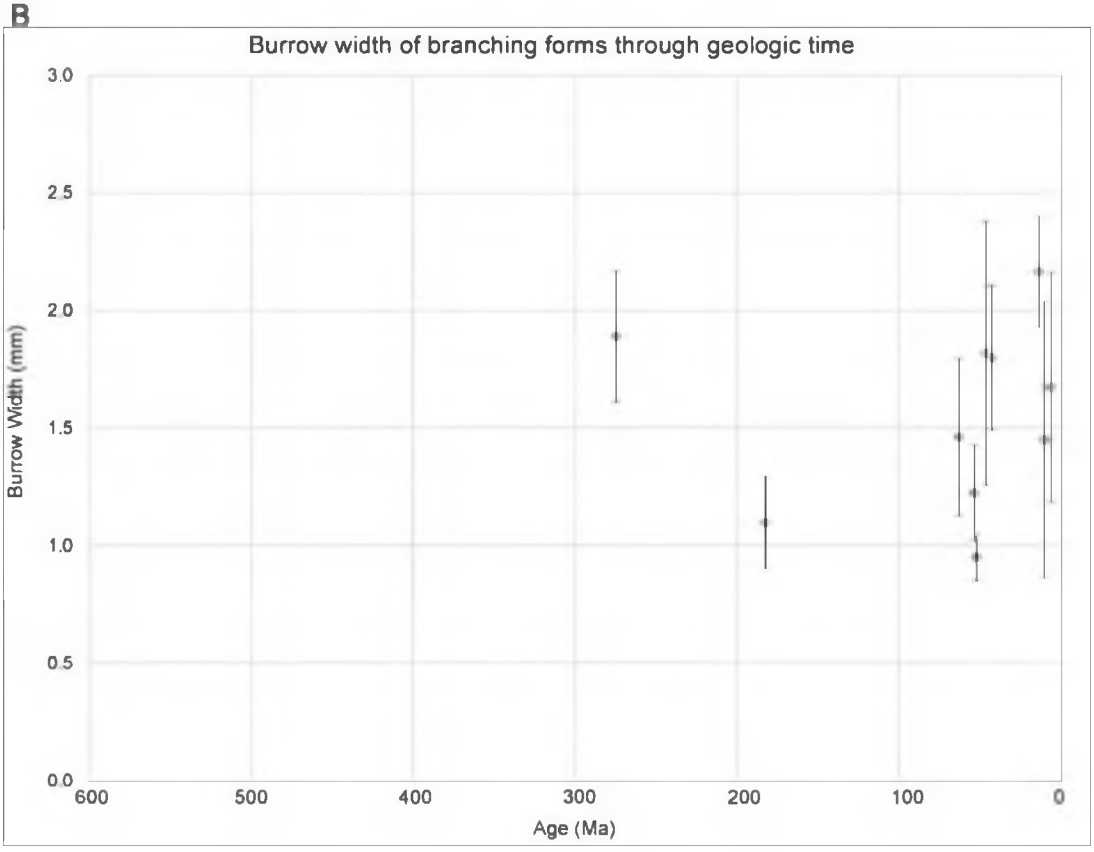
Burrow width of branching forms through geologic time
Burrow Width (mm)
3.0
2.5
2.0
1.5
1.0
0.5
0.0
600
500
400
300
200
100
0
Age (Ma)

Figure 5.9. Results of branching angle analyses in branching and network forms. A. Measure of branching angles (BA) in degrees for branching forms. B. Measure of branching angles (BA) in degrees for network forms. The trend line is represented by the 2nd order polynomial best fit line. The error bars for both plots represent the 95% confidence interval of the data set per time period and the ages represent the median age of the estimated age range of the specimen. If the time period did not have more than one data point it was not included in the chart.

A

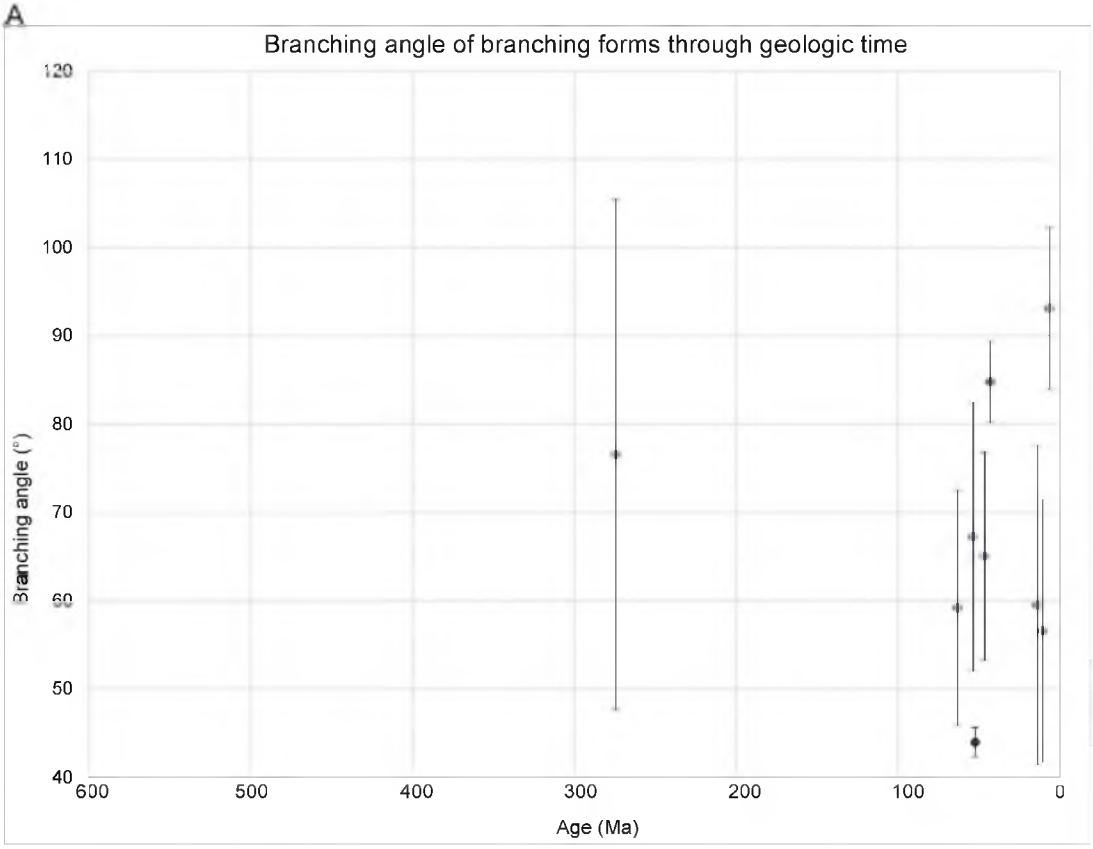
Branching angle of branching forms through geologic time
Branching angle (°)
120
110
100
90
80
70
60
50
40
600
500
400
300
200
100
0
Age (Ma)

B

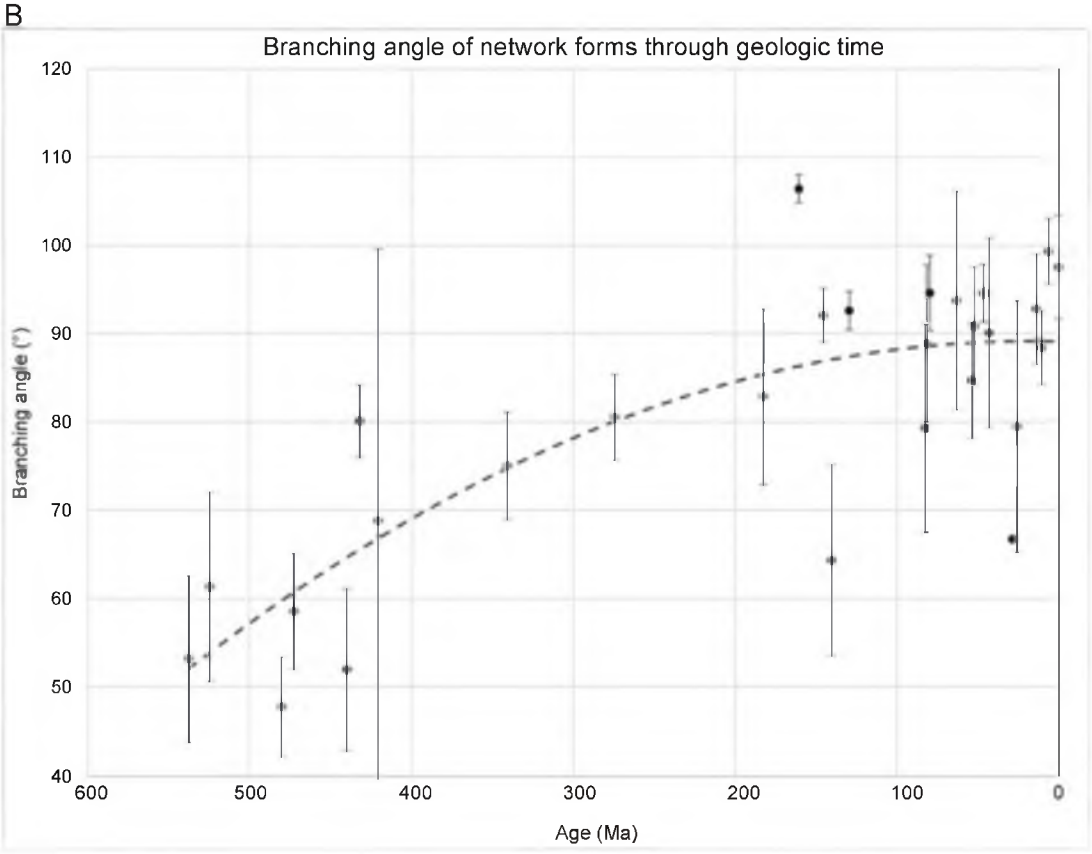
Branching angle of network forms through geologic time
Branching angle (°)
120
110
100
90
80
70
60
50
40
600
500
400
300
200
100
0
Age (Ma)

angle with the network forms). The complete results of the analyses are shown in Appendix H.

The motility index follows the same pattern as seen in the meandering forms (Fig. 5.6B), with values starting low in the Paleozoic and increasing dramatically during the Late Cretaceous. The range of the branching forms is much more restricted, however, so it is not possible to confirm if the branching forms follow the same pattern during the Oligocene, since we do not have any branching Oligocene specimens. However, the branching specimens do help confirm the repressed MI values during the later Paleozoic seen within the meandering forms.

The D_{Box}, W, and BA all show a very similar pattern across the analyzed samples (Figs. 5.8 and 5.9A). For each of the analyses, the Paleozoic samples fall within the range of the Mesozoic/Cenozoic samples without any discernable trend visible across the time interval analyzed. With more samples it might be possible to discern more of pattern, but without more data there cannot be any meaningful speculation. One interesting pattern is that the branching angles in the branching forms do not follow the same trend as the angles in the network forms (Fig. 5.9).

5.7.4 Network forms

The study set of network forms consists of 182 specimens, ranging in age from the Fortunian (Early Cambrian) to the modern, including the ichnogenera *Gordia*, *Megagrapton*, *Paleodictyon*, and *Squamodictyon* (Fig. 5.3). The measures of branching angle (BA), network tortuosity (NT), burrow width (W), mesh size (MS), and fractal dimension (D_{Box}) were plotted against the age of the specimens in order to determine any

noticeable trends (Figs. 5.9B, 5.10, and 5.11). The remaining results of the analyses are shown in the tables in Appendix H.

The plot of branching angle over geologic time (Fig. 5.9) shows one of the strongest trends of any of the analyses performed. The trend line is represented by the 2nd-order polynomial best fit line. Possible branching angles can range from ~5°, as a minimum measurable angle, up to 120°, as the maximum angle possible. A measure of 120° would represent a perfect juncture of three burrows, like a "Y" junction where every angle is equal. While the branching forms had average branching angles ranging from 40° to ~100° for their occurrence period, the network forms showed a distinct trend through time. As the network forms occur from the Cambrian through the Early Cretaceous, the average BA slowly increases from ~55° up to an average of 90°. As with the other forms, the range of values for each time slice decreases closer to the Cenozoic samples. Towards the Cenozoic, the maximum BA levels off at ~90°, even though a perfect hexagonal mesh would have an average branching angle of 120°.

The network tortuosity plot over geologic time (Fig. 5.10A) indicates that there was a slow decline in NT values up until the Late Cretaceous. The Paleozoic data again lack the uniformity of the Late Cretaceous and Cenozoic data; however, there is a slight decreasing trend for the Paleozoic data. During the Late Cretaceous and Cenozoic, the decrease steepens, and the values become less scattered. The arrows are the linear best fit trend lines for each group of data. An idealized network tortuosity for a perfect hexagonal mesh would lie around NT = 1.2.

The burrow width follows a similar pattern to the network tortuosity (Fig. 5.10B); however the shift point is different. The Paleozoic and Mesozoic data decrease steadily

Figure 5.10. Results of network form analyses. A. Measure of network tortuosity (NT) over time, plotted in millions of years before present. The Early Cretaceous-Late Cretaceous boundary is highlighted. The arrow on the left is represented by the linear best fit line for all data points to the left of the boundary line. The arrow on the right is represented by the linear best fit line for all data points to the right of the boundary line B. Measure of burrow width (W) in mm over time, plotted in millions of years before present. The Early Cretaceous-Late Cretaceous boundary is highlighted. The arrow is represented by the linear best fit line for all data points to the left of the boundary line. The error bars for both plots represent the 95% confidence interval of the data set per time period and the ages represent the median age of the estimated age range of the specimen.

A

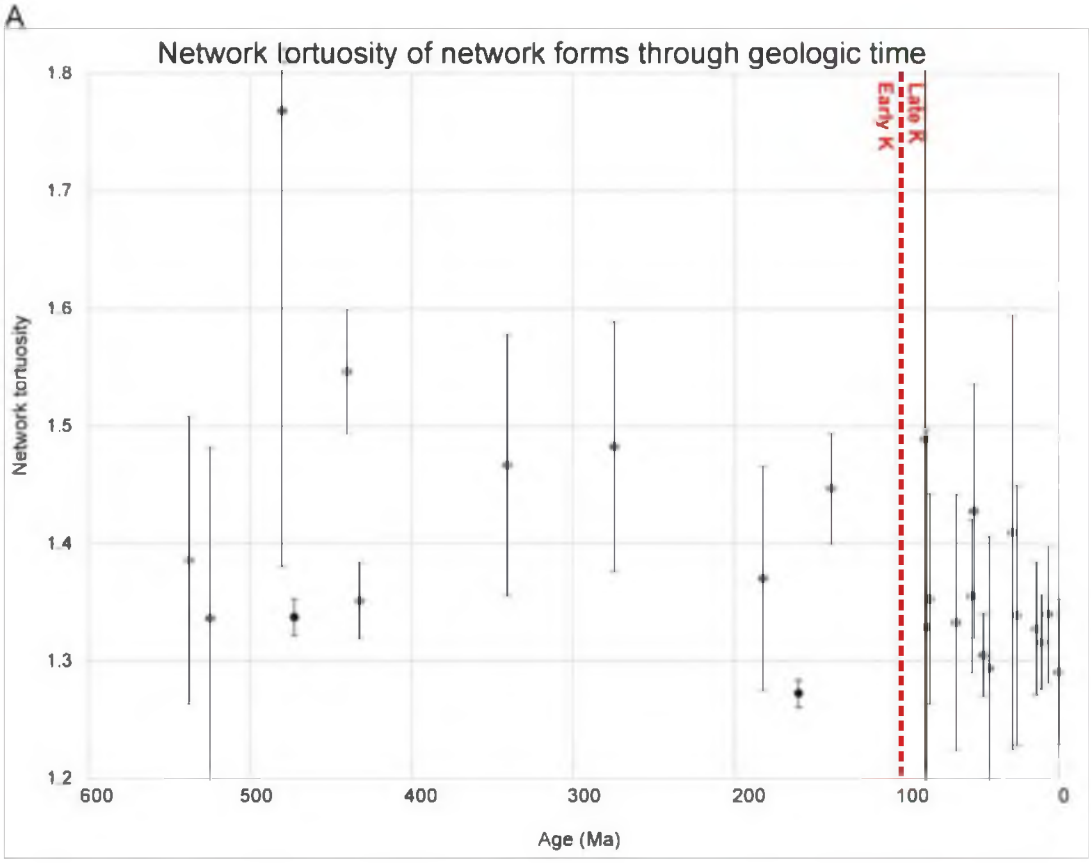
Network tortuosity of network forms through geologic time
Network tortuosity
1.8
1.7
1.6
1.5
1.4
1.3
1.2
600
500
400
300
200
100
0
Age (Ma)
Early K
Late K

B

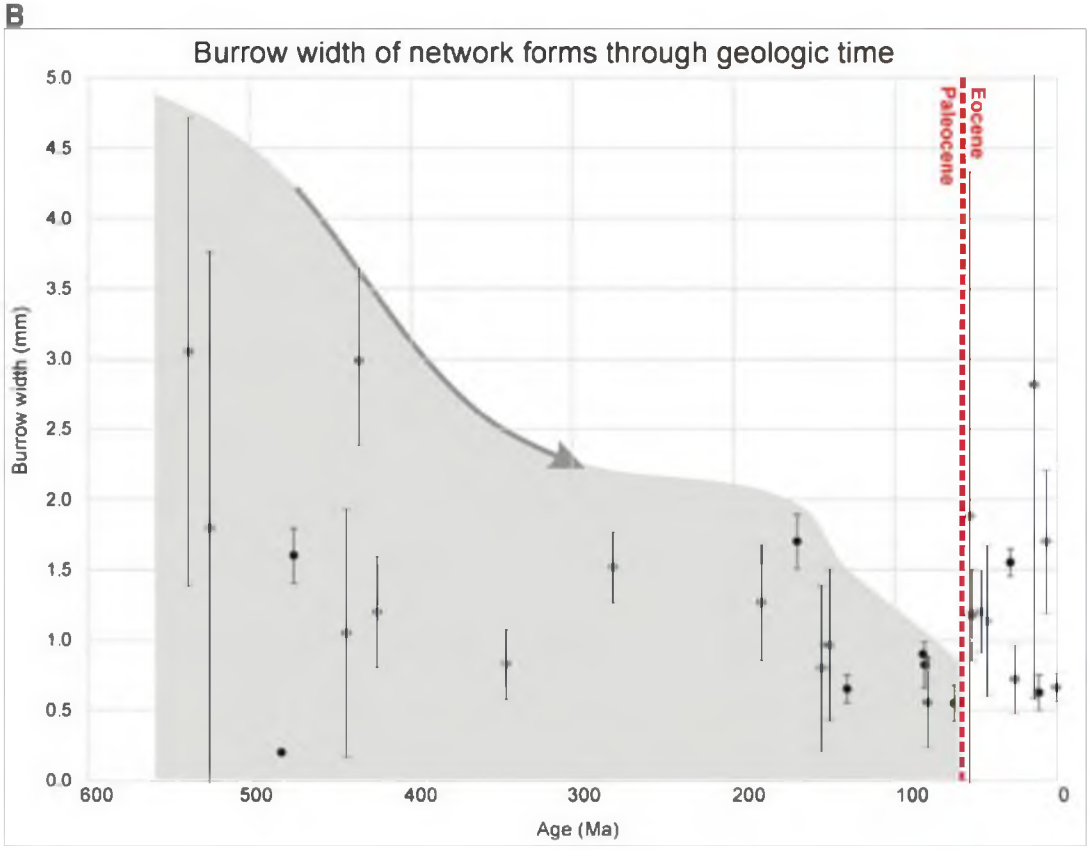
Burrow width of network forms through geologic time
Burrow width (mm)
5.0
4.5
4.0
3.5
3.0
2.5
2.0
1.5
1.0
0.5
0.0
600
500
400
300
200
100
0
Age (Ma)
Paleocene
Eocene

Figure 5.11. More results of network form analyses. A. Measure of mesh size (MS) over time, plotted in millions of years before present. The Jurassic-Cretaceous, Cretaceous-Paleocene, and Eocene-Oligocene boundaries are highlighted. Measure of the fractal dimension calculated by the Box Method (D_{Box}) over time, plotted in millions of years before present. The Cretaceous-Paleocene boundary is highlighted. The error bars for both plots represent the 95% confidence interval of the data set per time period and the ages represent the median age of the estimated age range of the specimen.

A

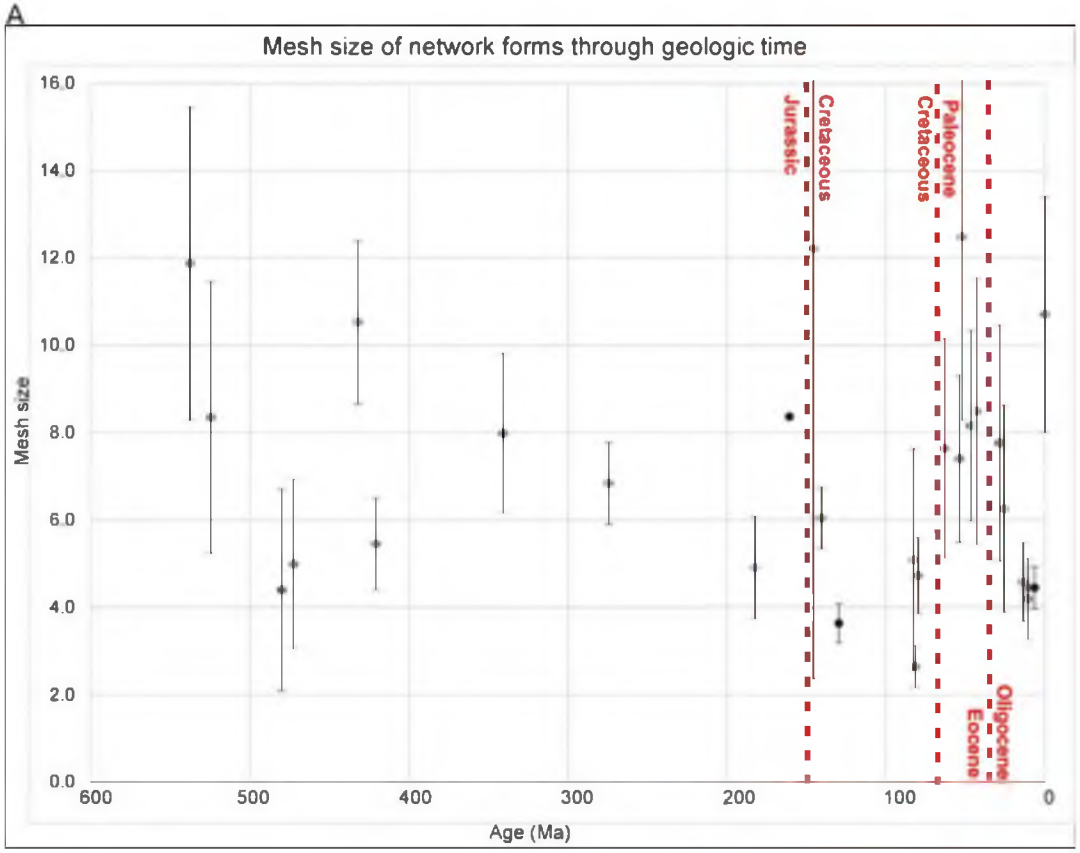
Mesh size of network forms through geologic time
Mesh size
16.0
14.0
12.0
10.0
8.0
6.0
4.0
2.0
0.0
600
500
400
300
200
100
0
Age (Ma)
Jurassic
Cretaceous
Cretaceous
Paleocene
Eocene
Oligocene

B

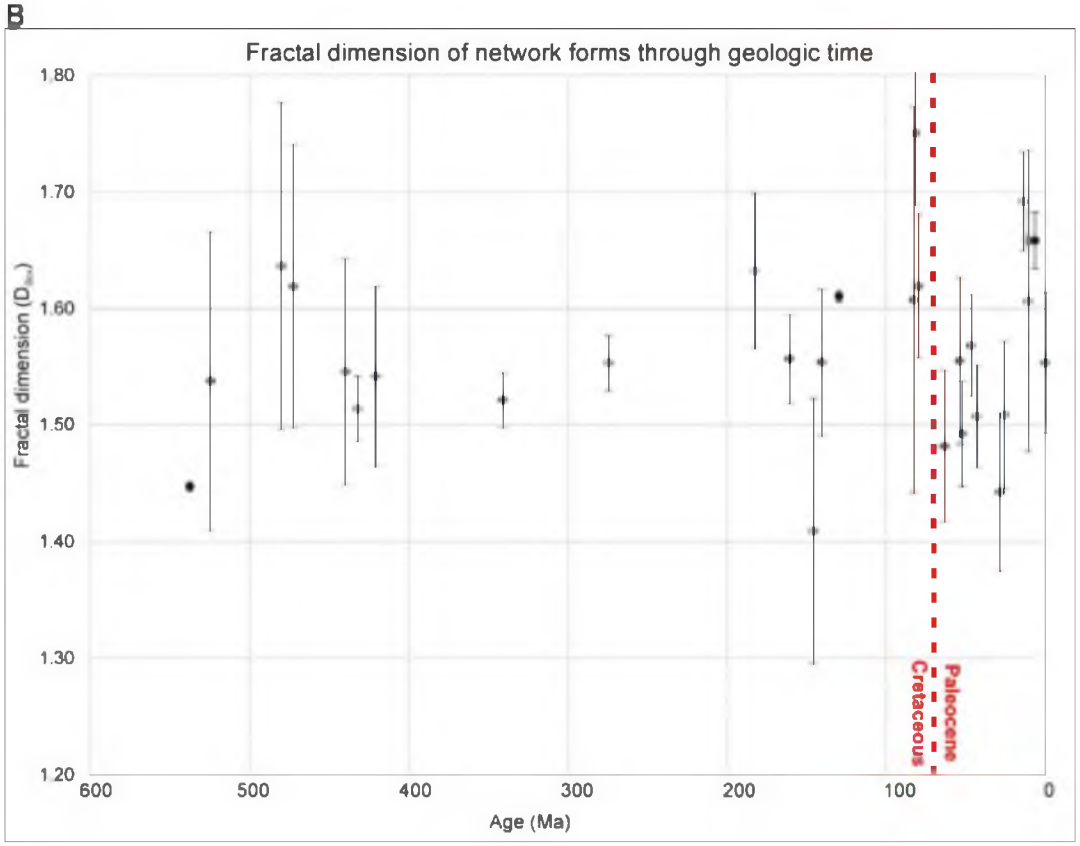
Fractal dimension of network forms through geologic time
Fractal dimension (D_{ss})
1.80
1.70
1.60
1.50
1.40
1.30
1.20
600
500
400
300
200
100
0
Age (Ma)
Cretaceous
Paleocene

until the Paleocene-Eocene boundary. Then at the start of the Eocene, the values shift to a larger burrow width and both increase in size and stop following any sort of trend. The arrow represents the linear trend line for the Paleozoic and Mesozoic data. Burrow width has a wide range in values in the early Paleozoic that persists until most of the data range is reduced and remains fairly well constrained in the Silurian. This narrow range of values continues up until the Eocene, when the range of values increases fourfold.

The plot of mesh size over time (Fig. 5.11A) appears to have no obvious trends up through the Jurassic. Within the Cretaceous, the MS numbers level out, but there is no real indication that anything different is occurring during the Cretaceous than before it. Right at the Cretaceous-Paleocene boundary, however, there is a sharp shift in values. The average MS jumps up from ~5 to ~8. After the jump, the average MS stabilizes through the Paleocene and Eocene, and then it starts to decrease again until the modern.

The final graph shows fractal dimension through geologic time (Fig. 5.11B). This is similar to the mesh size plot, since it does not show any strong trends through time. From the Cambrian to the end of the Mesozoic, the fractal dimension remains mostly stable, based on the 95% confidence interval. However, right before the end Cretaceous the fractal dimension values jumped up to an average of almost D = 1.7. This jump is unusual, since the majority of D_{Box} measurements across all graphoglyptids rarely went over D = 1.7 (Lehane and Ekdale, 2013). Following the Cretaceous-Paleocene boundary, the D_{Box} values took a sharp decline, averaging only 1.5. From there they averaged out or climbed just a little.

It should be noted that the analyses of the occupied space percentage (OSP), the MS, and the D_{Box} for the network forms, when plotted with each other in three

dimensions, create a banana-shaped grouping (Fig. 5.12). Although the full significance of this grouping is not entirely clear, it does show that the three analyses are all related to one another, but maybe not directly. This observation may explain some of the similarities between the plots of fractal dimension and the mesh size over time. Results reported by Lehane and Ekdale (2014) indicate that OSP and D_{Box} may be related, but they do not demonstrate a simple one-to-one correlation, indicating that both analyses can be used without the results being interchangeable.

5.8 Discussion

5.8.1 Previous studies

The deep-sea has been a discussion point of evolutionary theory for many years. It has been suggested that the relative stability of environmental conditions in the deep-sea allowed benthic communities to flourish and evolution to be practically nonexistent (Sanders, 1968, 1969; Seilacher, 1974). Seilacher (1974; 1977) expanded this hypothesis into behavioral evolution using trace fossils by invoking ichnospecies as a proxy for faunal diversity. Seilacher's analyses showed that the number of ichnotaxa of flysch trace fossils expanded slowly over time, until the Cretaceous when they exploded in diversity (Fig. 5.13). The slow evolution in the Paleozoic and Mesozoic was attributed to the time-stability hypothesis of Sanders (1968, 1969). However, it was noted graphoglyptids were evolving into smaller forms, presumably optimizing their intake of the food resources in the sea floor. (This is seemingly contrary to "Cope's Rule," which states that body size trends toward larger forms with time.) Seilacher (1974; 1977) suggested that this evolutionary trend occurred until the Late Cretaceous, when the evolution of angiosperms

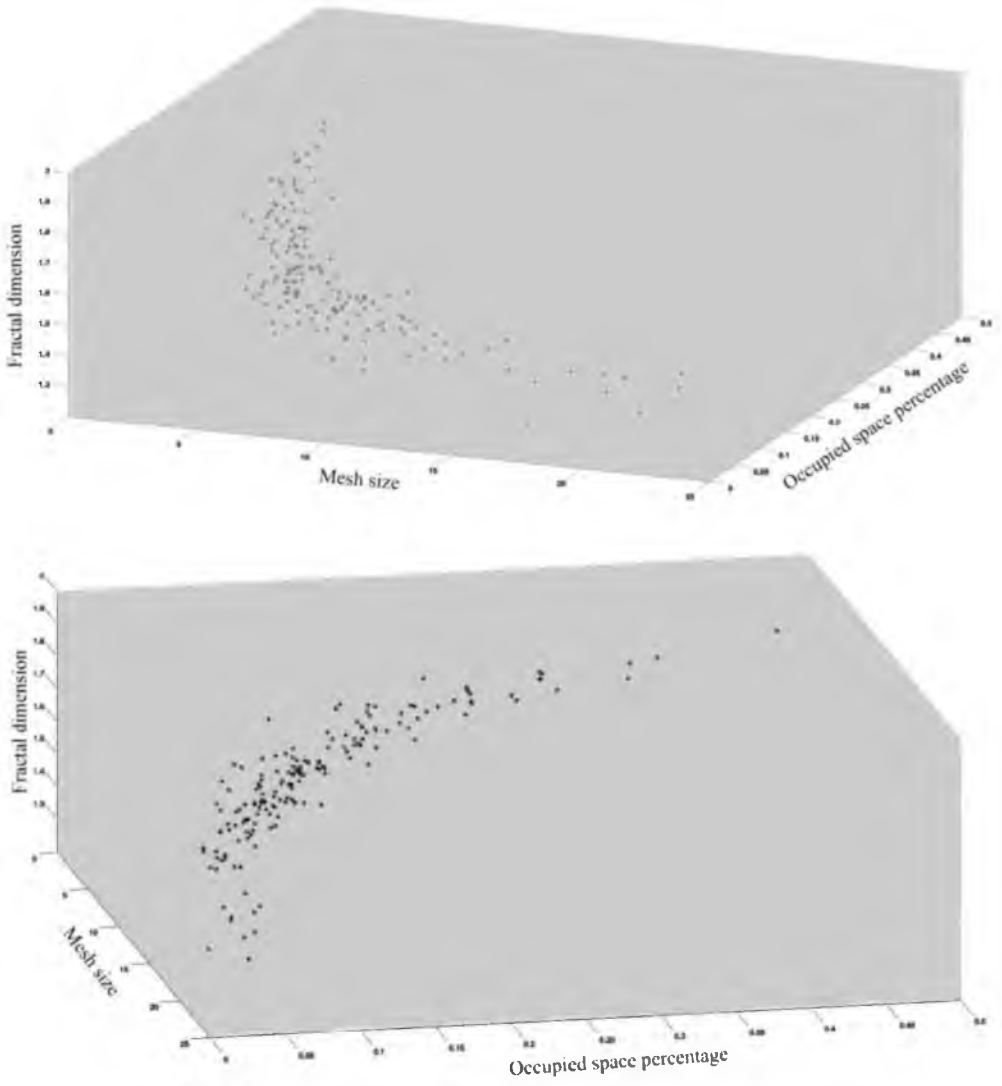

Figure 5.12. Two views of the three-dimensional plot of mesh size (MS) vs. occupied space percentage (OSP) vs. fractal dimension (D_{Box}). The two views are provided to help illustrate the three dimensions.

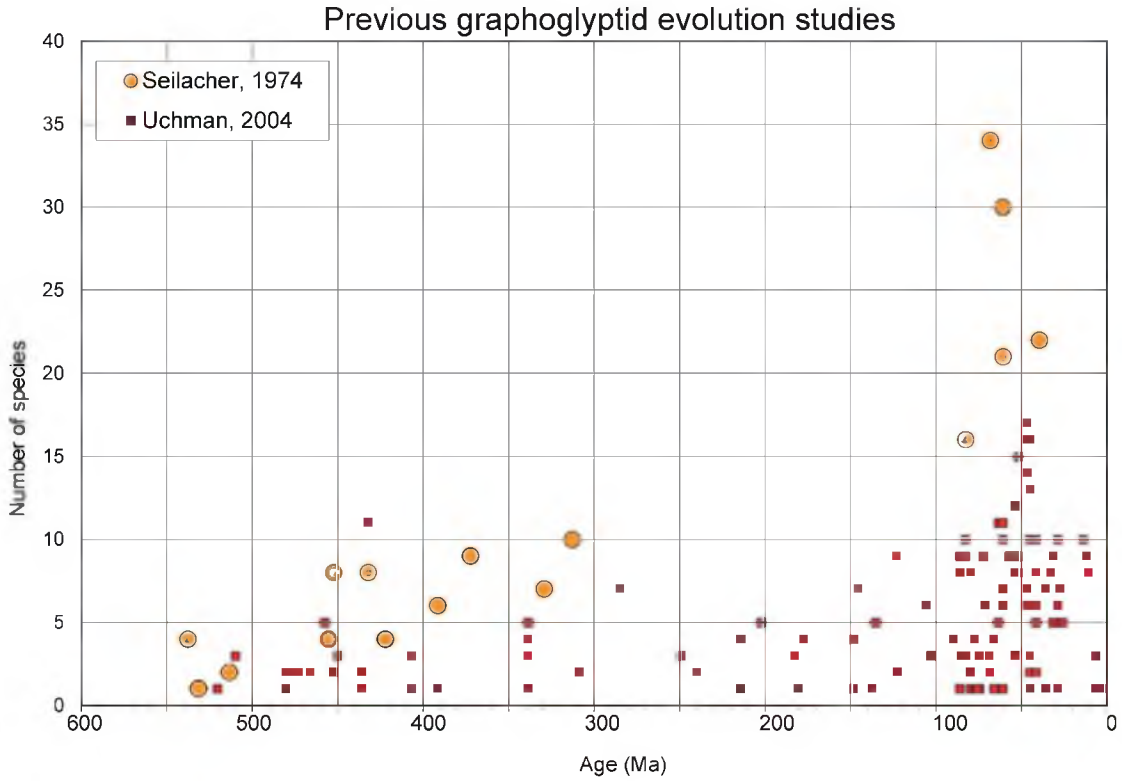

Figure 5.13. Early attempts by Seilacher (1974) and Uchman (2003) to illustrate the evolution of deep-sea trace fossils, as interpreted by the number of ichnospecies throughout the Phanerozoic. The Seilacher data include all flysch trace fossils, while the Uchman data include only the graphoglyptids.

provided abundant food material for the deep-sea endobenthos or increased amounts of foraminiferal oozes caused a rapid behavioral diversification.

Crimes and Fedonkin (1994) agreed that ichnogeneric diversity accelerated in the Cretaceous; however, they refuted the claims that there was any type of behavioral optimization taking place. By highlighting a few select trace fossil forms from various time periods, Crimes and Fedonkin (1994) had hoped to show that the increase in available knowledge in the literature had proved the gradual evolutionary optimization hypothesis untenable. Although they presented an interesting hypothesis, there was a dearth of data; they presented only one or two trace fossil morphologies per time period.

As can be seen by the range of morphologies presented in the present study (Figs. 5.5-5.11), one or two examples per time period is not nearly enough information to be able to draw any definitive conclusions from.

Uchman (2003; 2004) followed these earlier works by compiling the largest flysch trace fossil data set to date, analyzing over a hundred articles and localities in order to identify any significant trends with ichnospecies diversification over time (Figs. 5.2 and 5.13 and Appendix F). By considering trace fossil speciation rates, Uchman supported Seilacher's hypothesis that diversity slowly increased throughout the Paleozoic and Mesozoic, however, not as continuously as had been previously thought. Uchman surmised that the diversity of the graphoglyptids and other flysch trace fossils waxed and waned throughout the Paleozoic and Mesozoic due to various factors, including glaciation, deep-ocean warming, and tectonic episodes. He also noted the expansion of trace fossil diversity in the Late Cretaceous, especially during the Turonian Stage (Uchman, 2003; 2004). The initial diversification was again attributed to the appearance of angiosperms and/or increased foraminiferal oozes. According to Uchman, this expansion continued until the Eocene optimum due to the advent of oligotrophic conditions. Following the Eocene maximum was a significant Oligocene decrease due to the Eocene/Oligocene boundary crisis, an interval of time with significantly decreased ocean bottom water temperatures. According to Uchman, improved conditions during the Miocene did not increase graphoglyptid diversity, so the graphoglyptid diversity remained constant. The niche optimization and miniaturization that was predicted for the graphoglyptids by Seilacher (1977) was questioned by Uchman (2003; 2004).

Uchman's (2003; 2004) analyses focused on *Paleodictyon* and *Squamodictyon* as one continuous group, in a similar manner as they are being examined here, without breaking them down into individual ichnospecies. The results produced evolutionary patterns that were discerned for different time ranges (Paleozoic, Paleogene, and Mesozoic/Miocene), resulting in different evolutionary trends for each time range. These trends were attributed to the evolution of the trace maker.

Another behavioral evolutionary study involving a computer simulation of feeding traces was accomplished by Papentin (1973), who modeled the possible behavioral evolution of sediment intake optimization by a deposit-feeding organism over many generations (Fig. 5.14). That study produced a network-like pattern similar to *Gordia* with abundant crossings. Previous evaluations of Papentin's results show that over the course of evolution, the fractal dimension increased rapidly and then leveled out (Lehane and Ekdale, 2013). The network tortuosity displays a similar pattern when added onto the graph, where it increases rapidly at first and then settles out to a value of around NT = 1.4. This NT value is higher than most of the post Early Cretaceous-Late Cretaceous boundary trace fossil values (Fig 5.10A). Evaluation of Papentin's experiments with the current analytical techniques shows that the behavioral evolution of graphoglyptids likely would have occurred at a rapid pace at first and then proceeded to settle out. This indicates that the initial rapid pace of graphoglyptid evolution would have occurred over far too short a time interval to be adequately displayed by the analyses presented here, so any noticeable evolutionary changes would have resulted in leveled out values that appear to shift dramatically over time.

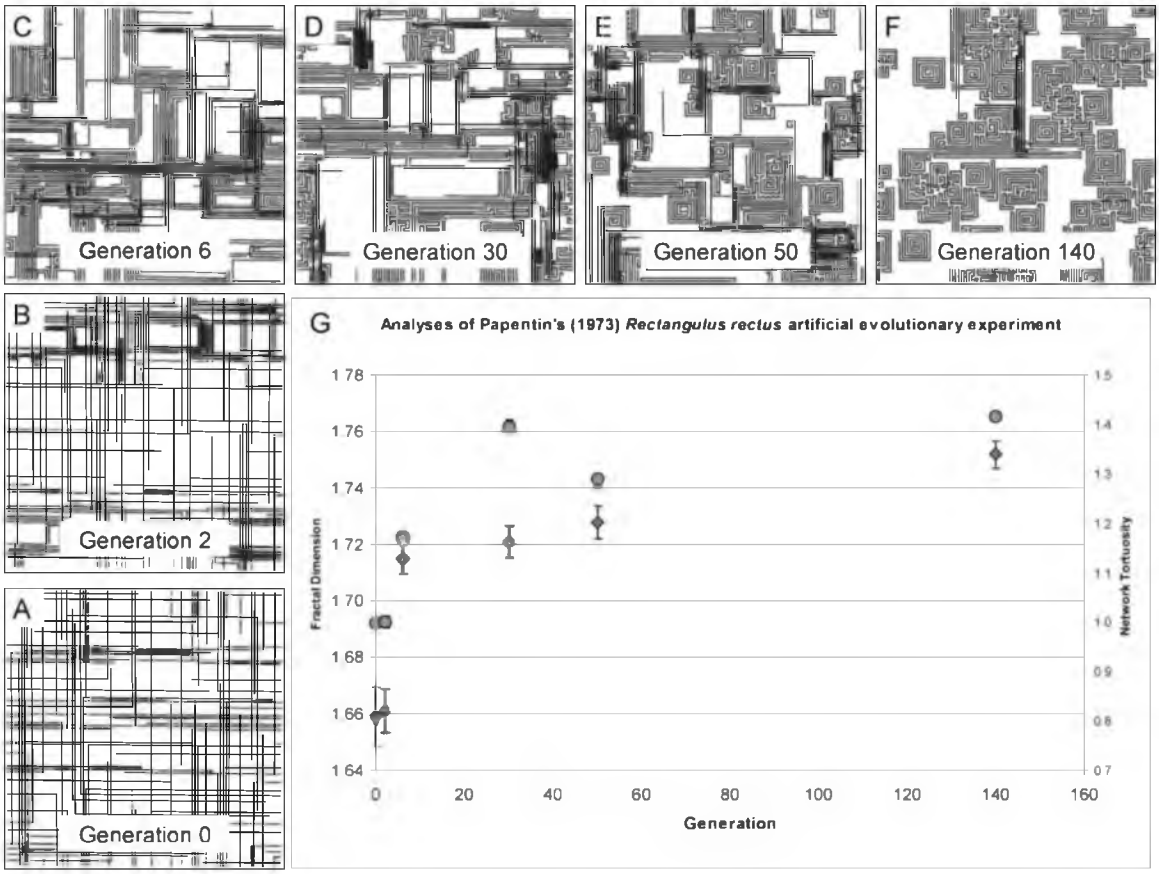

Figure 5.14. Papentin's (1973, fig. 4) computer-generated models of the evolution of burrow forms. A) Generation 0. B) Generation 2. C) Generation 6. D) Generation 30. E) Generation 50. F) Generation 140. G) The plot shows a comparison of generation versus fractal dimension (D_{Box}) and the network tortuosity (NT). Error bars represent the standard error. Figure updated and modified from Lehane and Ekdale (2013).

5.8.2 Implications from the current study

5.8.2.1 Basis of the study. In order to get a better picture of how graphoglyptids have changed through time, a closer look at the trace fossils was necessary. Just cataloguing the number of ichnogenera per time period was not sufficiently in-depth to fully document how the burrowing behavior has changed through time. Ichnogenera can easily be misidentified or misdiagnosed based on subtle differences that may or may not be due to the preservation of the specimen. This can easily lead to changes in the

numbers of ichnogenera as future researchers add or take away from the data following employment of more up to date research techniques. The goal of this study was to remove the bias in the identification of the ichnogenera and to study the trace fossils based on their topological forms: meandering, spiraling, branching, and network forms. Each of these types of forms were unique enough that they required a distinctive skill set to create. Therefore, if any behavioral evolutionary trends truly exist, they most likely would occur within a topological form, rather than across different forms.

The best way to determine any changes in behavior over time is to have a robust dataset that is evenly distributed across time. This, however, is not possible in most geological and paleontological studies. Within this dataset, the Paleozoic to mid-Mesozoic sample sets are often widely spaced and sparsely populated. This makes identification of any trends within the Paleozoic difficult, if not impossible. The dearth of data may be due to the limited number of turbidite deposits found in these time periods (Fig. 5.2), or it could reflect the actual paucity of the graphoglyptid trace fossils during this period. The Late Cretaceous to the Miocene dataset, however, is extremely robust, and patterns found within there should represent actual patterns found in the fossil record. The Miocene samples are the latest known graphoglyptid trace fossils found. Only modern examples are known after that.

Graphoglyptids are a result of behavior, so there is the possibility that there could be a wide variance of behaviors or organism morphologies to produce similar traces such as the size of a particular species producing the burrows. This variance would result in a range of values that would be created within any particular time period. To visualize that

range of data, the graphs were plotted with the median data value and a 95% confidence interval to represent the vast majority of the specimens analyzed, removing any outliers.

5.8.2.2 Diversification of graphoglyptids. Of the several hypotheses proposed for the behavioral evolution of graphoglyptid trace fossils, diversification is the most widely accepted. Originally, diversification was identified by the number of ichnogenera per time period in Seilacher's approach. However, it can also be expanded to include diversification of morphologies within a topological form. Using Seilacher's (1974) and Uchmans's (2004) previous diversity estimates (Fig. 5.13), it is easy to note a distinct lack of graphoglyptid deposits from the Carboniferous to the beginning of the Late Cretaceous. Seilacher reported no data for this time interval, while Uchman did include data from this interval, but it is depressed from the surrounding values. A similar occurrence has been observed in this study. If it is assumed that this depression of ichnodiversity is a real phenomenon, then that must be taken into account when describing the behavioral evolution of the graphoglyptid trace makers. This observation would mean that diversification was not a simple increase over time function, which increased exponentially during the Late Cretaceous through the Eocene. The diversity dropped dramatically during the second half of the Paleozoic for an unknown reason, perhaps due to global glaciations and the formation of Pangea (Uchman, 2003). The lack of data, however, makes the exact time of the diversity change difficult to pinpoint, making interpretations of causal relationships impossible. What is noticeable is that the large range of morphology values (the 95% confidence interval) seen in the early Paleozoic (Figs. 5.5, 5.9B, 5.10, and 5.11) gets significantly shorter in the specimens found in the late Paleozoic and Mesozoic, up until the Late Cretaceous (Figs. 5.6, 5.8,

5.9B, 5.10, and 5.11). Environmental pressures (e.g., changes in temperature, acidity, or chemical composition of the water and/or sediment), being placed on the graphoglyptid trace makers during this time also could account for the restricted diversity of forms.

Starting in the Late Cretaceous and proceeding through the Miocene, there is a shift not only in the abundance of graphoglyptids, but also in their morphological forms. Diversity appears to begin increasing exponentially at this point, as can be seen in the increased range of the motility index in both meandering and branching forms (Fig. 5.6B), tortuosity in meandering forms (Fig. 5.6A), shear abundance of spiraling forms (Fig. 5.7), and range of mesh size in network forms (Fig. 5.11). This observation supports the hypothesis that the graphoglyptids were diversifying over time; however, it was not a linear increase from the Cambrian to later times.

5.8.2.3 Miniaturization of graphoglyptids. Miniaturization of burrow sizes through time can be detected by looking at the burrow widths of meandering and network forms (Figs. 5.5A and 5.10B). The meandering and network forms are the most robust of the four topological data sets, and within those two groups the burrow width was decreasing through the Paleozoic and Mesozoic. For the meandering forms, this decreasing trend continued through the Cenozoic as well and can be seen within the fractal dimension trend, which is a number heavily influenced by the burrow width (Fig. 5.5B). For the network forms, there is a strong shift at the Paleocene-Eocene boundary, where the average burrow width shifts from a steadily decreasing trend and jumps to a larger and more ranged burrow width. Another indication of the size of the burrows in network forms is the mesh size. Average mesh size should be decreasing if the network forms are miniaturizing over time (Fig. 5.11A). During the Paleozoic, it is difficult to tell

if in fact they are decreasing in size due to the lack of data, but it is clear that during the Cretaceous there is a stabilization of values at the low end of their range followed by a sharp jump in values and range at the Cretaceous-Paleocene boundary. In essence, even though network forms may be decreasing in size over the majority of the Paleozoic and Mesozoic, there is a clear increase in size during the Cenozoic.

5.8.2.4 Optimization and perfection of graphoglyptids. The final major trend previously mentioned identified in the literature is optimization. The problem with citing optimization as a trend is that there are no generally agreed upon qualifiers for what "optimization" is, which makes it difficult to assert that a trace fossil is optimized for a particular environment. In general, optimization in deposit feeding is taken to mean that the animal will get the most food out of the sediment with as little effort as possible; however, that is not easily translated to farming and/or trapping traces. Is it even possible to identify what is an optimized farming or trapping trace? Theoretically, behavioral evolution should occur at a rapid rate, so if we could identify what optimization is supposed to be, any of the evidence for optimization would be preserved in the rock record only as jumps in morphologies (as seen in Fig. 5.14). For these reasons, perhaps optimization is not the ideal word to use in evolutionary language.

There are, however, visible trends seen in the graphoglyptids to suggest that they are "perfecting" the forms that they are creating, specifically within the network traces. Unlike the meandering and branching traces, it is easier to identify an idealized morphology within the network traces. Using *Paleodictyon* as an example, these idealized forms would be created as a perfect hexagonal mesh, where the hexagons would have consistent angles of 120°, with little to no variances (i.e., mistakes). Looking at the

branching angle in network forms (Fig. 5.9B) a clear trend is visible, starting in the Cambrian and continuing to the Late Cretaceous, at which point in time the values level out. This trend demonstrates that the mesh patterns became more consistent, not only across different samples but within a single specimen as well. Even though the branching angles never reach an idealized 120°, perhaps the networks were perfected for their environment with 90° average branching angles.

While the network forms were becoming more consistent in morphology, the meandering and branching forms were becoming more complex. This is evident in the increase in tortuosity and motility index, which indicates an increased numbers of meanders (i.e., compactness of the traces) (Fig. 5.6). Increasing complexity implies increasing the amount of food intake by increasing their coverage of the sediment. Whatever trends the graphoglyptids may have shown through time, it is still difficult to state that they were optimizing their feeding strategies due to the vagueness of the basic concept of optimization.

5.8.2.5 Spiraling forms. The spiraling forms were separated from the other topological forms because of the fundamentally different way in which they are formed. While the meandering forms move progressively outward and forward, the spiraling forms, *Spirorhaphe* in particular, move inward. This type of movement creates patterns that are difficult to explain behaviorally, let alone evolutionarily. For an organism to accomplish spiraling inward and then outward again, all the while not crossing over itself, without being able to visualize what it is doing, is truly an impressive accomplishment.

To understand the evolution of this type of inward and outward spiraling behavior, we would need specimens that span evenly over the whole occurrence timescale (Ordovician to modern). Unfortunately, we only have one specimen from the Paleozoic (Ordovician), two modern specimens, and the remaining 24 specimens all occur within a time span of 36 ma from the Late Cretaceous to the Eocene (Fig. 5.7). The one specimen that is available from the Ordovician does provide a little insight into the evolution of this behavioral strategy. This single specimen shows attributes that place it apart from the other trace fossils, suggesting that there was clearly an evolutionary change in spiraling behavior from the Ordovician to the Late Cretaceous. Besides behavioral evolution, another possible explanation of the large time gap between the Ordovician and Cretaceous is that the trace maker of the Ordovician *Spirorhaphe* was not the same kind of animal as that which made any of the more recent examples. This possibility would explain why there are no traces between the two sets of data and why the Ordovician sample falls outside the morphological range of the more recent specimens.

5.8.2.6 Environmental factors. Whatever trends may be occurring prior to the Late Cretaceous, it is evident that there were changes in the global marine environment in the Late Cretaceous continuing into the Eocene (highlighted by the red lines in Figs. 5.5, 5.6, and 5.10). Previous studies for a large scale change in graphoglyptid diversity pointed to the Late Cretaceous alone as the time at which that diversification started (Seilacher, 1977). By analyzing morphologic changes in graphoglyptids through time, as opposed to simply tabulating the number of ichnospecies, it appears that there were separate shifts in morphology seen in both the Late Cretaceous and the Eocene. Some of

the changes took place within the Late Cretaceous, and these changes could be the result of either the evolution of the angiosperms or the increased flux of foraminiferal ooze to the deep-sea floor, as was previously hypothesized. There is no way to determine definitively within this study between the two hypotheses, or even if the cause could be something else entirely. Several other morphological characteristics of the traces seemed to be immune to these environmental influences and evolved later, during the Paleocene-Eocene boundary. This possibly was due to the increased ocean bottom temperatures associated with the Paleocene-Eocene Thermal Maximum (PETM). Following the ichnodiversity maximum in the Eocene, there was a crash in diversity, which is most apparent when considering the motility index of the meandering and branching forms (Fig. 5.6B). This decrease in values has been noted by Uchman (2003; 2004) and attributed to the Eocene-Oligocene boundary crisis, which was associated with a drop in oceanic water temperatures.

A possible explanation for the explosion of graphoglyptid morphologic diversity during the Early Eocene, producing the most abundant graphoglyptid occurrences in history (Uchman, 2003) was the Paleocene-Eocene Thermal Maximum (PETM), which was an event of abrupt, high magnitude, global warming. This was the case even in the deep-sea, where an increase of bottom water temperature of 4 to 5°C (Higgins and Schrag, 2006) occurred along with water column stratification (Bralower, 2002). Other deep-marine trace fossils (e.g., *Ophiomorpha*) also show an abrupt change at the P-E boundary (Cummings and Hodgson, 2011a). Although the PETM was identified as the cause of a 50% extinction of benthic foraminifera taxa (Alegret et al., 2009), perhaps it also spawned increased growth and evolution of other benthic organisms, and therefore

their trace fossils, as well. The stratification of the oceans during the PETM is regarded as producing a starvation scenario in the open oceans by locking up food sources on the shallow shelves (Bralower, 2002). It may be possible that during the Paleozoic, graphoglyptid diversity declined due to a decrease in the relative abundance of food sources in the sediment. Once those food sources were restricted, graphoglyptids needed to diversify in order to obtain the same amount of nourishment from a steadily decreasing source of food. That, along with the warmer ocean temperatures, reinforced the diversification of feeding behaviors.

The sharp decrease in graphoglyptid diversity at the start of the Oligocene is attributed by Uchman (2003) to the Eocene-Oligocene Boundary Crisis. It was noted that the direct cause of the decrease was related to a sudden drop in deep-sea temperatures during this time. Other studies, however, suggest that even though this was the first major continental-scale ice accumulation of the Cenozoic, there was no drop in deep-sea temperatures (Lear et al., 2000). The growth of the Antarctic ice sheets at this time caused a global drop in sea level, increasing limestone erosion worldwide, which increased the deposition of inorganic carbon in the oceans and lowered the carbonate compensation depth (CCD). This increase in the flux of inorganic carbon to the deep-sea floor could have caused the severe reduction in graphoglyptid morphologies during this time. It is also possible that the change in ocean chemistry may have caused the majority of graphoglyptid trace makers to migrate into pelagic (nonturbiditic) sediment in deeper water, where the traces were not generally preserved in the rock record. As the deep-sea environment started to equalize from the influx, graphoglyptid diversity responded with an increase in diversity as seen during the Miocene. Chemical conditions have been

known to affect the migration patterns of benthic marine invertebrate larvae before, where the larvae search for specific chemical cues in determining their resting places (Pawlik, 1992). It is possible that a similar event was occurring where the graphoglyptid trace makers were not suited to the changing chemical conditions and therefore migrated into deeper water.

5.8.2.7 Uniquely evolving topological forms. One more interesting observation of note is that even though several of the topological forms share similar morphological aspects, it appears that the different topological forms evolved separately. Changes in morphology in one form were not directly related to changes in another. For example, the branching angles in both the branching forms and the network forms follow a distinctly different evolutionary pattern. The same is the case for the tortuosity of the meandering and branching burrows, as compared to the network tortuosity of the network forms. This indicates that while the meandering burrows were becoming more complex, the network burrows were becoming less complex and more regular. This is an indication that possibly different species of animals were producing the same burrow topologies and that the evolutionary driving forces behind the behavioral evolution resulted in unique responses by each species.

5.9 Conclusion

Behavioral evolution is a topic that is not often studied due to the difficulties in finding tangible evidence of fossil behavior that is easy to interpret. Trace fossils provide the principal method for studying behaviors of ancient creatures, and by studying the trace fossil record through geological time it is possible to determine how at least some

types of behaviors have evolved. Graphoglyptids are a group of trace fossils that are ideal for studying behavioral evolution because of their typical occurrence in deep-marine settings along with their characteristic mode of formation as open burrow systems, often preserved on the base of turbidite beds. Graphoglyptid trace fossil evolution has been studied by a few ichnologists over the past 40 years, principally by using the number of ichnospecies as a proxy for diversification of specific behavior. Problems arise with this approach when considering how many fossils may be misidentified and/or renamed, thus changing the numbers of ichnospecies, or individuals within an ichnospecies, documented at any given point in geologic time.

In order to deal with the problem of subjectivity in ichnotaxonomy, for this study graphoglyptid trace fossils were analyzed within different topological form categories: meandering, spiraling, branching, and network forms. Each specimen, over 400 in total, was analyzed by several quantitative analytical techniques, including fractal analysis, branching angle, burrow width, network tortuosity, tortuosity, motility index, and mesh size. Previous analyses concluded that graphoglyptids were evolving for purposes of optimization of feeding patterns, while getting smaller through time until the Late Cretaceous, when a sudden increase in diversification occurred. This interval of rapid diversification of graphoglyptid ichnotaxa was attributed by previous workers to either the evolution of the angiosperms on land or the sudden increase in foraminiferal ooze in the deep sea.

Results of this analytical study suggest that understanding the behavioral evolution of the graphoglyptid trace makers is more complicated than simply documenting trends in ichnotaxonimic diversity through time. The different topological

forms evolved separately from each other, and while some were following previously proposed evolutionary patterns, others were not. In general, the pattern of graphoglyptid behavioral evolution can be broken into three different time intervals: (a) Paleozoic and Mesozoic prior to the Late Cretaceous, (b) Late Cretaceous to the end of the Eocene, and (c) post Eocene. During the interval prior to the Late Cretaceous, graphoglyptids were miniaturizing and decreasing in diversity. Starting in the Late Cretaceous, the graphoglyptid diversity was exploding, while meandering forms continued to miniaturize and network forms enlarged. During this interval, meandering forms also were increasing in complexity while network forms were becoming more regular.

These evolutionary changes in deep-sea feeding behavior can be attributed to oceanic changes during the Late Cretaceous, possibly including angiosperm evolution or an increase in foraminiferal ooze, and increased ocean bottom water temperatures during the Paleocene-Eocene Thermal Maximum (PETM). After the Eocene, graphoglyptid diversity dropped, likely due to the Eocene-Oligocene boundary event, which involved an influx of inorganic carbon to the deep-sea floor due to increased erosion of the ocean shelves.

Previously, it has been assumed that graphoglyptids showed slow and/or no behavioral evolutionary trends throughout most of geologic time due to the stability and predictability of the dark, cold, quiet deep-sea environment. Close examination of the morphology of the graphoglyptids, however, indicates just the opposite. Apparently the deep ocean bottom was not as stable an environment as was originally thought, and the perhaps graphoglyptid trace makers were more sensitive to changing environmental conditions on and in the deep-sea floor than was previously imagined.

CHAPTER 6

EVOLUTION IN CHAOS: THEORETICAL APPROACH OF CHAOS THEORY AS A GUIDING PRINCIPLE FOR UNDERSTANDING PATTERNS IN BIOLOGICAL EVOLUTION

6.1 Abstract

Nonlinear dynamics is the area of mathematics where the solution to one set of equations becomes the variable in the next iteration of the function, thus producing a feedback loop. Chaos theory is a subset of nonlinear theory where slight perturbations of the initial starting values lead to unpredictable results. Chaos theory has been used to explain heartbeat rhythms, economic trends, business patterns, geological systems, and even evolutionary pathways. However, before now it has not taken the spotlight as the driving force of biological evolution. Chaos theory has six main components, which can be related directly to biological evolutionary theory. Both theories state that the solutions to the problems: 1, cannot repeat themselves; 2, are bounded within a specific region of space; 3, are sensitive to initial conditions; 4, are not random; 5, are unpredictable; and 6, are based on a series of feedback loops. These attributes apply to both anatomical evolution, as reflected in the body fossil record, and behavioral evolution, as represented in the trace fossil record. One method for describing nonlinear systems involves the use

of a phase map, which illustrates all possible solutions of a problem depending on the initial value. In biological evolutionary theory, the phase map usually is called morphospace, which is the conceptual framework for mapping clusters of organisms based on specific attributes. Organisms have a tendency to group into clusters in accordance with the theory of convergences, where intermediaries are unstable. In a nonlinear phase map, these clusters would be concentrated around a point or area termed an 'attractor'. The solutions to the equations settle in an area influenced by the attractors until an external stimulus kicks them out. In evolution, this external stimulus is most likely a major change in some environmental factor, such as an abrupt shift in the climate. By using chaos theory as a template to study biological evolution, it may be possible to map out how changes in climate have shifted species within the framework of multidimensional morphospace.

6.2 Introduction

Chaos theory is the study of nonlinear dynamical systems where slight perturbations of the starting values can lead to unpredictable results. Chaos sometimes is misinterpreted as random, but chaos follows a set of rules that are not even close to truly random. Chaos theory has been employed to explain a wide variety of phenomena, including heartbeat rhythms (Goldberger et al., 1990), international relations (Grossman and Mayer-Kress, 1989), economic trends (Kelsey, 1988), business patterns (Levy, 1994), geological systems (Middleton, 1991; Turcotte, 1991, 1997) and evolutionary theory (Kauffman, 1991, 1995; Calsina and Perelló, 1995; Lloyd, 1995; Baake and Gabriel, 2000; Huisman and Weissing, 2001;Morris, 2003; and López-Ruiz and Fournier-

Prunaret, 2009). Even though chaos theory has been cited in evolutionary theory papers, it has rarely taken the spotlight as the driving force of evolution. This paper illustrates how anatomical and behavioral convergences, within the theoretical framework of morphospace, represent the physical manifestations of chaos theory.

6.3 Chaos theory

Chaos theory originated with Lorenz (1963), who introduced a series of equations in an attempt to describe turbulent air patterns in the atmosphere. The solutions to these equations never repeated or fell into a consistent rhythm, but they always remained within a bounded region of phase space. This discovery by Lorenz started a field of mathematics where solutions were unpredictable over long periods of time and were calculated using iterative methods. Iterative calculations used the results from one set of equations as the variables in the next.

The main factors of a chaotic system are that it (1) does not repeat itself, (2) has the possibility to be 'bounded' within the orbits around 'attractors', (3) is sensitive to initial conditions, so that slight changes could cause large variances in the results, (4) is not random, (5) is not predictable for any time 't', except for extremely short term predictions, and (6) is based on a system of feedbacks where the results of one equation are the variables used in the next iteration (Strogatz, 1994).

In nonlinear dynamics, and specifically in chaos, each successive solution is heavily influenced by the previous values, producing a feedback loop (Brent, 1978; Mishel, 1990). For example, refer to the following equations:

$$x' = x + 2xy \qquad \text{(Eq. 6.1)}$$

$$y' = 3 - 3xy$$

If $(x_o,y_o) = (1,1)$, then $(x',y') = (3,0) = (x_1,y_1)$ and the results from the first iteration (3,0) are placed back into the equation. This is continued until (x_t, y_t), where 't' is equal to some future time (e.g., 60 iterations in the future). It is not possible to solve for t without going through all of the previous steps for any particular starting point. The complexity of a problem increases with each simultaneous equation, where each equation used is directly related to the number of dimensions in which a solution exists. For example, the solution to equation set 1 is represented in two-dimensional space, because there are two equations; three equations are represented in three-dimensional space; four equations are represented in four-dimensional space; and so on.

The solution to a nonlinear problem is dependent on the number of iterations that have been completed; therefore time plays a significant role. One complication with nonlinear equations is that even though there is a feedback loop, the results are not predictable into the future due to imperfections in initial values (Strogatz, 1994). A difference in initial values, even infinitely finite differences, could cause extremely large variances in the values at some point in the future. No measurement is perfect, so there always will be some difference between the measured and actual starting values (Strogatz, 1994). These variances will increase exponentially as *t* increases (Ruelle, 1979).

Phase portraits often are used to visualize the solutions to nonlinear problems (Fig. 6.1), as they illustrate all possible trajectories and attractors to any particular set of equations. The smaller arrows in Figure 6.1 indicate the direction that the equation will

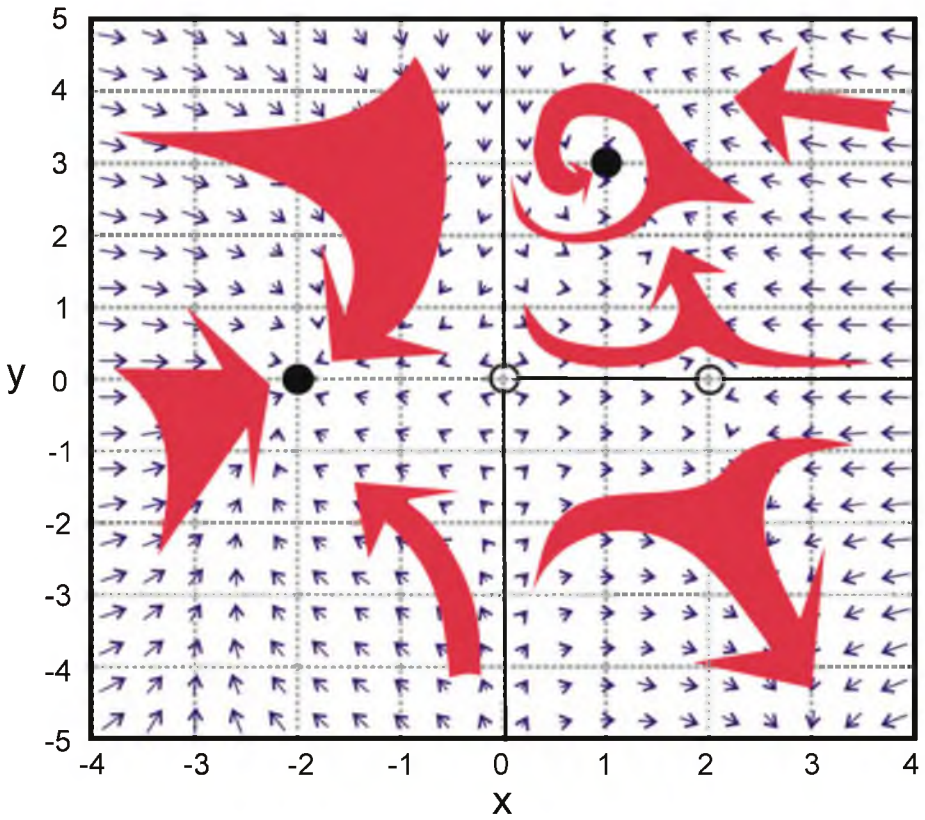

Figure 6.1. Example of a phase diagram in two-dimensional space based on the equations $\dot{x} = x(4-y-x^2)$ and $\dot{y} = y(x-1)$. Solid circles illustrate stable fixed points. Open circles illustrate unstable fixed points. The smaller arrows illustrate flow directions that depend on initial xy values. The larger arrows show the generalized flow of values for each region. The mathematical concept of a phase diagram as seen here is extremely similar to the biological concept of morphospace (Fig. 6.2), both visually and conceptually.

move for each starting xy value. The larger arrows depict the overall movement of the equation for each region of the graph. The different types of attractors in three-dimensional space include point attractors, limit cycles, limit tori, and strange attractors (Goodings, 1991). The point attractor is a single point, the limit cycle is a fixed orbit, and the limit torus is a donut shaped orbit, where the solution produces an orbit resembling a spring wrapped around the donut. The strange attractor is an undefined region of space around which the solutions orbit. The strange attractor was termed as such, because the attractor is not a specific solution like the previously known attractors (Ruelle and

Takens, 1971). The concept of a strange attractor is similar to the model of an atom, where the area of the nucleus acts like the strange attractor, and the electron cloud represents the possible orbits where the solution to any particular problem could exist. In an open system, such as those encountered frequently in biology and geology, future states almost always converge on a series of strange attractors (Middleton, 1991).

Chaos theory is often used to explain nonlinear changes within a given system. External shocks have the ability to knock a stable system out of its orbit and onto a new trajectory (Mishel, 1990). This means that solutions that reside in one portion of the phase space can get knocked into another portion of phase space. The stability of the phase space is determined by the size of the shock and the size of the attractor (Kauffman, 1991). A larger phase space needs a larger shock in order to knock the system out, otherwise the system will settle back down to the attractor in which it was aligned previously (Mishel, 1990).

6.4 Chaos theory in evolution

Chaos theory has not been applied widely in the study of biological evolution (Kauffman, 1991, 1995; Calsina and Perelló, 1995; Lloyd, 1995; Baake and Gabriel, 2000; Huisman and Weissing, 2001; Morris, 2003;; and López-Ruiz and Fournier-Prunaret, 2009). Previous hypotheses have suggested that biological evolution takes place somewhere in the realm between ordered and chaotic systems. This realm is thought to support the maximum complexity that a behavioral network could achieve due to the concept of self-organization (Kauffman, 1991, 1995). Contrary to these ideas, self-organization should be thought of as a principal component of chaos theory, where

complex systems drive towards stability (Pool, 1989). Self-organized islands are like regions of stability within in a chaotic system (Fichter et al., 2010), which are intricately linked with the fluctuations caused by the external environment (Mishel, 1990). In general, evolution is a genetically based system driven by environmental changes (Valentine, 1973), whereas chaos is considered to represent 'deterministic randomness' (Fichter et al., 2010). The intrinsic (biologic, in the case of evolution) factors drive the system towards self-organization and stability around attractors, while the randomness is supplied by the extrinsic factors (environmental changes), which knock the system out of equilibrium and send it off in a new direction until it settles down again (Valentine, 1973; Pool, 1989).

Evolutionary theory shares many similarities with chaos theory. Evolutionary pathways have a very restrictive nature, since natural selection limits what possibilities are available for future selection. Once a developmental pathway has evolved, it is almost impossible to change that pathway in future species, so in essence, that pathway becomes 'burdened' (Riedl, 1977) or contains 'historical constraints' (Gould, 1989). For example, all vertebrates are descended from animals with a backbone, and almost all descendants of the original tetrapods still have four limbs. The burden restricts the specific body-plans that may be capable of evolving, precluding the ability for a species to backtrack and appear identical to a distant ancestor. The burden, however, in no way limits the number of specific body plans that can evolve; it limits only the general types that can evolve.

Another common attribute of chaos and evolutionary theory is that once extinct, a species will not reappear within an evolutionary lineage. In biological evolution, the descendants of one species will not be identical to the species from which they are

descended. There is no repetition. In chaos theory as well, the solution is never repeated. If the solution were to be repeated, even after as many as 10^{100} iterations, then the system would be cyclic. A truly chaotic system is not cyclic, but a cyclic system with a very long period could be misinterpreted as chaotic (Kelsey, 1988).

A third commonality of evolutionary theory with chaos theory is that the evolutionary theory of convergence provides a physical representation of chaotic attractors. An evolutionary convergence occurs where multiple different lineages arrive at a similar solution independently. Some examples of evolutionary convergences include the senses (e.g., seeing and hearing) as well as body plans (e.g., limbless snakes and caecilian amphibians). There are only so many solutions to any given problem, hence convergences are inevitable, but they are never perfect, whether they are anatomical convergences or behavioral convergences. Convergences, however, do not indicate cessation of evolution. It is possible that an organism can converge on a solution and continue to evolve, while still remaining in the same morphological space. The strange attractor hypothesis allows for some degree of morphological flexibility. The strange attractor draws a solution towards it, but still allows it to orbit. Each point around the strange attractor represents a different morphology. All of the points within the orbit of the strange attractor represent all possible morphologies of the species. For example, this can be seen in the different visual abilities within humans alone, where human beings range from completely blind at birth to some having 20:10 eyesight with every variation in between. Theoretically, the concept of convergences suggests that it might be possible for evolution to be predictable (Stern and Orogozo, 2009), at least for hypothetical

organisms (Russell and Séguin, 1982), but predictability is elusive in real world situations.

Deniers to the concept of organic evolution, such as many creationists, often call for "intermediaries" or "missing links" to prove that evolution has occurred. The evolution deniers seemingly want every little parcel of morphospace to be covered with examples in the fossil record. Evolutionary convergences are analogous to the chaotic attractors (Morris, 2003). These attractors are 'islands' surrounded by fields of unstable options, where the intermediaries never are likely to be occupied. It is not that these intermediaries have not been found in the fossil record; it is that they do not and cannot exist. The morphological possibilities do not encompass the entire morphospace, but instead they make small leaps and jumps from island to island within the morphospace, such as described by the concept of punctuated equilibrium (Eldredge and Gould, 1972). Natural selection drives evolution until the species can persist in stable environmental conditions. An external disturbance will kick the animals out of their attractor onto a new path. Such external disturbances can take the form of changes in the environment or changes in the interactions between species. Evolution then proceeds quickly until a new stable anatomy is discovered.

6.5 Morphospace

In nonlinear dynamics, different equations lead to different phase portraits (Fig. 6.1) with differing numbers of attractors, from zero on up. Phase portraits resemble a concept in evolutionary theory called phenotypic space or morphospace (Raup, 1966; Alberch, 1989). In morphospace, two (or more) measurements are plotted against one

another to create a multidimensional map of all possible variations. The available taxa are plotted within those diagrams, and instead of covering the entire diagram, groups of taxa often will cluster around specific regions to produce a graphic representation of evolutionary convergences (Fig. 6.2). Convergences occur, because islands (like attractors) exist where the intervening regions are unstable, meaning that all possible phenotypes would not be found in nature (Alberch, 1989).

The extrinsic events (drivers of natural selection) that lead to anatomical evolution have only so much influence on the anatomy of the individual species. Intrinsic factors (genetic mutation and genetic stability) play the primary role in determining what an organism will look like and how it will behave. It is these intrinsic factors which determine the size and stability of a morphological island in morphospace. Gaps in morphospace represent unstable taxa, which will more often than not survive beyond a few days, and definitely will not survive to reproduce. The sizes of the bubbles in the morphospace are directly related to the genetic stability of the organism. Organisms with more stable morphotypes will have larger bubbles, while unstable morphotypes will have smaller bubbles (Fig. 6.2).

The trajectory of human evolution exemplifies the instability of the intermediate regions in morphospace. In newborn babies, it has been shown that the majority of genetic mutations that cause a physical manifestation are not to the benefit of the individual. Most genetic mutations are either detrimental to the mutated individual or benign. Detrimental genetic mutations in humans are a leading cause of infant mortality in the United States (Southard et al., 2012). The rare cases where the mutated individuals are found on the edge of a stable morphospace region, or perhaps even in the intermediate

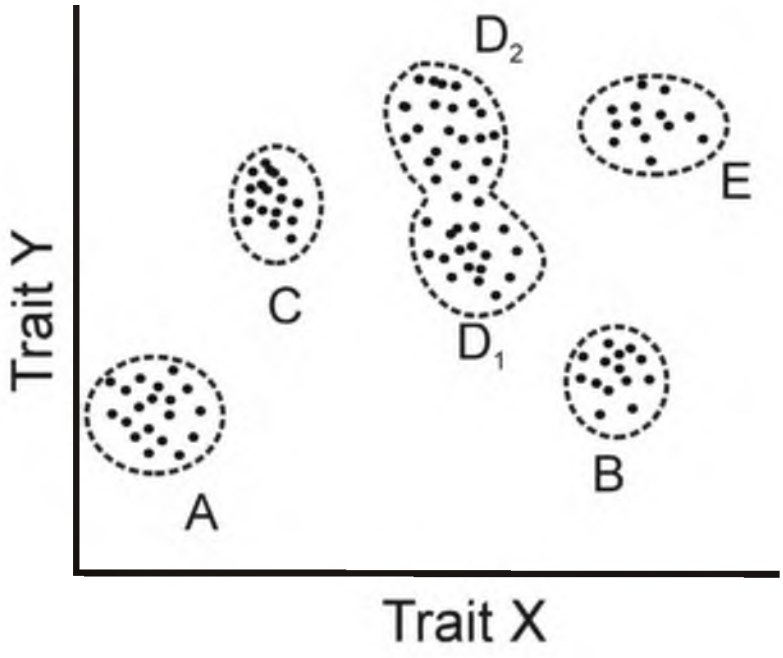

Figure 6.2. A hypothetical morphospace, as defined by the measurements X and Y. Available phenotypes are represented as dots. Different species are denoted by dashed outlines encircling sets of phenotypes. (Modified from Alberch, 1989).

region, are termed structural abnormalities. They include such abnormalities as extra body parts (limbs, eyes, etc.) or deformed body parts (cleft palates, macrocephaly, etc.). Such anatomical intermediaries are usually unstable, often resulting in an early death.

To fully understand the concept of morphospace, it is necessary to understand that even though there are convergences, different traits of an organism can converge on different solutions, creating a multidimensional morphospace where different aspects of morphology may be convergent within different species. This can be illustrated using the beloved toy *Mr. Potato Head*, which can be constructed from an almost unlimited variety and combination of anatomical components, but all have the same standard body plan. The multidimensional morphospace concept can be seen in animal anatomy where squids converge on the camera-type eye that humans also possess. Squids and humans, however,

have very different mouth structures; squids have a beak and humans have teeth. The beak of the squid, on the other hand, closely resembles that of the parrot. The squid therefore represents the multidimensional aspect by converging on features of both humans and parrots.

The pull of the attractors in morphospace can be attributed to the Ornstein-Uhlenbeck (OU) process (Hansen, 1997). The evolution of a trait that follows the OU process evolves toward a stationary peak or optimum at a certain rate. The optimum is the function of all of the demands being placed on the trait, factoring in all of the trade-offs and conflicts to obtain an optimal solution. The attraction parameter of the OU process is the same thing as the strange attractor in chaos theory. The pull of the attractor causes traits to be pulled back should they stray too far from it. This "rubber band" effect keeps species within their morphological bubbles (Slater, 2013). Most evolutionary changes within the OU process are attributed to changes in the position of the optimum (Hansen, 1997).

6.6 Behavioral evolution

Unlike anatomical evolution, behavioral evolution has not been studied extensively via theoretical approaches. Behaviors evolve in much the same way that anatomies evolve (e.g., Harvey and Nee, 1997; Ekdale and Lamond, 2003; Koy and Plotnick, 2010), but the tangible evidence for behavioral evolution is much more fleeting. Preservation of behaviors in the rock record is limited to animal interactions with the sediment, i.e., trace fossils. Behavior patterns result from both, innate (inherited) and learned (acquired) components working together, and they may be influenced by other

factors, such as environmental conditions, diet, circadian rhythms, and external stimuli (Jensen, 1961; Lorenz, 1965).

Learned and innate behaviors both can be passed from one generation to the next (Breder and Halpern, 1946; Jensen, 1961). Learned behaviors are taught by a parent or other member of the species. They form the basis for human society, where most of what we know and how we act is based on learning from other people in our lives. Innate behaviors are present in us from birth and are passed on to subsequent generations via genes. Although genetics are known mostly for passing on physical traits, instinctual behaviors also are known to be genetically linked, including various human behaviors (Plomin, 1994), bird singing behavior (Kroodsma and Canady, 1985), mammalian digging behavior (Dudek et al., 1983), salamander foraging behavior (Ransom, 2012), and movement patterns of fruit flies (Kendler and Greenspan, 2006). Virtually all animals possess some form of instinctual behavior.

The way that behaviors evolve has been studied in modern (extant) organisms by doing cladistic analysis on several different animal species and by comparing the results to morphologic and molecular cladistic analyses (Lauder, 1986; Paterson et al., 1995; McLennan and Mattern, 2001; Ryan, 2005), by using behavioral patterns in concert with morphologic and molecular data (Blackledge et al., 2009), and by using behaviors to model changes in morphology (Legendre et al., 1994). Unfortunately, fossil species do not lend themselves to behavioral studies the same way that living species do. The principal method of studying the behaviors of prehistoric organisms is to examine trace fossils, which record such behaviors as walking (via footprints), crawling (via trails), burrowing (via tunnels), feeding (via bite traces and other structures), as well as a number

of other behaviors. Even though chaos has been mentioned in ichnology (Pemberton et al., 2008), it was defined simply as the complete bioturbation of the sediment. On the other hand, chaos theory (as defined in this paper) has not been employed previously to study the evolution of behavioral patterns.

Behavioral evolution, like anatomical evolution, is based on intrinsic factors (genetic mutation and genetic stability) being acted upon by extrinsic factors (natural selection). The preservation and guidance of these behaviors, however, is partially limited by the environment. Animals have a plasticity of behavior, meaning that they sometimes act one way in one type of environment and another way in a different environment (Bromley and Frey, 1974). For example, the same taxa of decapod crustaceans will produce different types of burrow walls in muddy substrates (e.g., the trace fossil *Thalassinoides*) than they will in sandy substrates (e.g., the trace fossil *Ophiomorpha*). With these ideas in mind, some salient questions about behavioral evolution arise. Are behaviors dictated by the same genetic constraints as anatomy? Is it possible to map behaviors on a diagram in the same way that morphologic features can be mapped onto morphospace? Behaviors that are mapped onto a morphospace would indicate different groupings of behaviors while highlighting intermediate impossibilities (Fig. 6.3). The behavioral morphospace concept presented here illustrates different forms of locomotion, from walking to burrowing. When plotted on a graph comparing trace width (e.g., burrow thickness or footprint width) with the traces' fractal dimension, there are several large gaps where no traces occur. The fractal dimension is the measure of how much the space is filled up by any particular trace combined with the intricacy of the patterns made by the trace maker (Lehane and Ekdale, 2013).

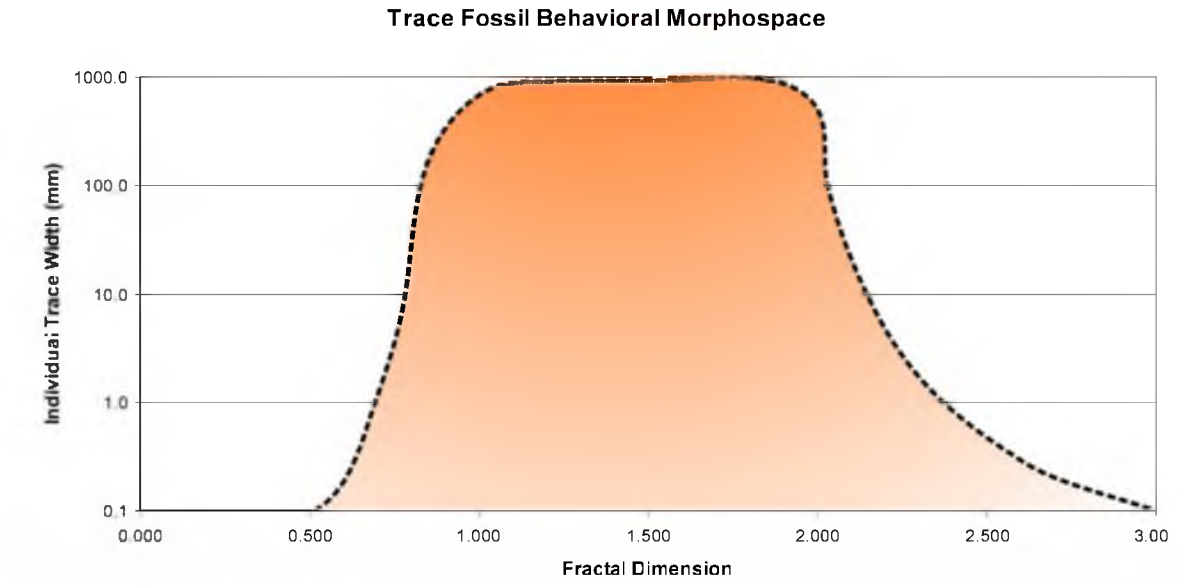

Figure 6.3. Graphic comparison of the fractal dimension versus the individual trace width for a select set of trace fossils illustrating the behavior-space. Dashed line indicates estimated limits to the diagram.

Gaps in the behavioral morphospace are the spaces around the stable behavior island. This view is limited by many things, including the anatomy of the animal making the trace, but it also is limited by the environment and substrate in which the traces are produced. Traces that occupy less space, such as spider trackways in firm sediment (where D is <1.0), would have a much lower fractal dimension than mole burrows in soft sediment (where D is >2.0), which take up much more space and radiate into three dimensions. Sediment that is less cohesive, such as dune sand, will preserve different types of traces than a muddy substrate that is more cohesive (Davis et al., 2007).

Gaps in behavioral morphospace also may be illustrated by animal locomotion. Although animals walk, run, crawl, hop, and fly, there are no animals whose principal method of locomotion is rolling. A gap in behavioral morphospace would occur where the trace of a roller would have a higher fractal dimension than that of a runner, or a

walker, but it would be similar to that of a crawler, because in both cases the whole body would be in contact with the sediment surface. The impressions left by a roller would be different from those left by a crawler, because a crawler would push sediment away from its body, whereas a roller would consistently compress the sediment on which it was rolling. A roller also would be less likely to produce a winding trace than a crawler due to a decreased level of flexibility, producing a lower fractal dimension.

6.7 Discussion

Chaos theory can help us understand much of what happens in our constantly changing world, including such disparate subjects as stock market trends (Chen, 1996) and shifts in the magnetic fields of the Earth (Goodings, 1991). It also can be extended to biological evolutionary theory. Chaos theory is a branch of nonlinear dynamics, which extends itself to studies of evolutionary theory, specifically with regard to food webs and biological interactions (e.g., Lotka, 1925; Volterra, 1926; Ackland and Gallagher, 2004; Reichenbach et al., 2006). Even though nonlinear dynamics is based on a series of equations that cannot be solved for any specific time, this method lends itself to the creation of a phase space/morphospace showing the trajectories of different solutions to any given problem based on different starting values.

Evolutionary and chaos theories have common threads that are highlighted by analyzing the six components of chaos theory and comparing them to elements of evolutionary theory. The first component of chaos theory is that it does not repeat itself, which is a principal factor in evolution, since no species can reappear once they have gone extinct (i.e., replaced by new species). The evolution of traits of species are based

on the traits of their ancestors with slight changes occurring between each subsequent generation. The ability to go backwards (i.e., to re-trace the path of the exact same evolutionary steps in reverse) is impossible due to the burden that is placed on the genetic code of the previous generations.

The second component of chaos theory is that it is possible for chaotic solutions to be bounded within the orbits around attractors, specifically strange attractors. Evolutionary theory embodies concepts identical to these attractors in the sense of morphospace. Some anatomical traits are not stable, thus leaving gaps in the morphospace. These gaps are passed on to their offspring and then are continued along the line of their descendants. Such gaps in the morphospace also influence the behaviors that are inherited by these organisms, creating gaps in their behavior morphospace as well.

The third component is that chaos theory is sensitive to initial conditions, so much so that even a slight change in starting value could lead to major differences in the results. In evolution, the ancestral species places a burden on the descendent species, which provides for the appearance of certain attributes and prevents other attributes from appearing. This burden builds up in each step along the lineages from the first ancestors to all subsequent life forms. Should those first ancestors have been different, their progeny would have turned out differently.

The fourth component is that chaos is not random. Genetic mutation may occur randomly, but the natural selection forces that act on species and populations are far from random. In fact, such forces are selective, resulting in the survival of the best fit organisms.

The fifth component is that chaos is not predictable, except for extremely short periods of time. In evolution, we may try to predict possible evolutionary trends (Russell and Seguin, 1982; Bostrom, 2009; Stern and Orgogozo, 2009), but the farther we speculate into the future, the less our predictions are based on facts and the more they are based on hypothetical situations.

The sixth component of chaos theory is that it is based solely on a system of feedbacks, the iterative functions. In evolution, the next species to evolve is based on the previous species. It can be summed up in the equation:

Species A * (Genetic Mutation) * (Natural Selection) = Species A' (Eq. 6.2)

where natural selection involves a whole wide range of other species (e.g., Species X, Species Y, and Species Z) as well as environmental factors (e.g., meteorite strikes, volcanic eruptions, deforestation) (see Table 6.1 and Appendix L).

If we are able to know all of the attractors in the evolutionary morphospace, then we might be able to determine the course of evolution, at least for the near future. However, due to the uncertainties inherent in chaos theory and evolution, the distant future remains unknown. Some scientists feel that if the clock were to be rewound, and if evolution were to start over again from a previous step, the animal landscape that we would see today would be completely different (Gould, 1989; Beatty, 2006). In contrast, some other scientists think it would appear almost the same (Travisano et al., 1995; Losos et al., 1998; Morris, 2003). Regardless of the theory, the variables for evolution remain the same (natural selection, genetic mutation, environmental interactions, adaptation, etc.). The larger question then would be if the attractors are the same in a different evolutionary experiment. Looking at our current biological diversity, we see many of the

Table 6.1. Evolutionary factors that directly affect the evolution of a given species.

Internal	Interspecies	Extra-Species	Environmental
Mutation	Sexual Selection	Competition (food or space)	Climate
	Population Density	Predation	Landscape Changes
	Food Competition		Food Availability
			Temperature

same features that have evolved separately in many different lineage (i.e., eyes, bipedalism, flight, etc.). Therefore, it is possible to assume that, since so many unrelated organisms evolved very similar morphological features, biological morphospace is in a fixed state, determined by the internal characteristics of the organism (DNA replication, chemical processes, and synaptic functions). In essence, since the attractors would not change in a rerunning of the evolutionary clock, the only things that could possibly change would be the external stimuli. Should the evolution clock be rewound, it would be the external stimuli (e.g., environmental changes, organism interactions) that would be primarily in charge of directing the course of evolution. Thus, evolution would proceed by the external stimuli moving the organisms through the genetically based morphospace.

6.8 Implications

A way to test if there is indeed a correlation between evolutionary theory and chaos theory would be to compare the size of morphological stability islands to the rate of evolution between different adjacent morphologies. The larger the morphological space, the longer it would take for an offshoot species to develop due to the strong attraction of the strange attractor. Smaller morphological spaces would have less of a hold on the individuals within the species and therefore evolution could proceed at a

faster rate. The size of the morphological stability islands is dependent on the disparity of each individual species. The more disparity in a species, the larger the island.

The fossil record offers a bountiful selection of possible test subjects for this type of analysis. By cataloguing specific morphologies and seeing how they have varied through time, even on a small scale, it may be possible to witness the shifts in morphological variation needed to test this theory. Numerous studies have attempted to quantify minute morphological variations of taxa across well dated sedimentary strata, particularly among invertebrates and conodonts, providing the tools needed to calculate the degree of disparity and the rate of evolution (e.g., Balter et al., 2008; Webster, 2007). The fragmentary nature of the paleontological record might cause some limitations by making placement of a given individual within a given species difficult; however, the robust nature of many fossil invertebrate and conodont studies renders many of these concerns moot.

6.9 Conclusion

By analyzing the results of evolutionary change, it is possible to get a map of behavior and anatomical morphospace. Nonlinear dynamics, chaos theory in particular, provides a similar map called phase space based on the results of iterative equations. This link suggests that evolution could be guided by the principles of chaos theory. Knowing this, it is possible to better understand the factors acting on evolution and help future research in evolutionary theory to understand links between evolution and other chaotically controlled disciplines.

Turning back the clock on evolution is an interesting idea, but it is impossible to know with any certainty whether life would have turned out radically different or remotely similar. However, if the game were to be played again from the start, the environmental stimuli would be the primary force making the rules.

APPENDIX A

BENOIT PARAMETERS

A major challenge with analytical computer programs is that they are heavily reliant on the input parameters. Small changes in the parameters can change the results drastically. This is the reason why most scientists develop a set of parameters that are useful for their own analysis and keep them consistent throughout the entire experiment. These are the parameters that were employed for the experiment reported in this paper:

A.1 Image processing

Due to the constraints of the BENOIT program, the analyzed images need to be in two-tone (black background with a white image to be analyzed) bitmap files (BMP). The resolution of the images needed to be at least 500 dots per square inch (dpi). Anything smaller, and the pixilation of each image was too high and greatly affected the outcome. Anything higher than 500 dpi did not seem to produce a better result, so 500 dpi was chosen.

Even though the fractal dimension is supposed to be scale invariant, to reduce the amount of potential variability, all images were created with an approximate longest side length of 19 cm (± 0.5 cm). The length of the other side was variable depending on the image being analyzed.

A.2 Fractal analysis

The size of the boxes in the D_{Box} and the D_{Info} are based on the size of the pixels in the image. This means that no matter what the dpi of the image is, the image will always be pixelated at the smallest analyses in the program. For this reason any points with a box side length less than five pixels should be omitted from the fractal dimension

calculation. The largest box side length also should be omitted from calculation, since the fractal dimension calculation often breaks down towards the outer limits of the analysis (see the grayed-out analyses in Fig. 2.3).

The other parameters of the program include "Side-length of largest box," "Coefficient of box size decrease," and "Increment of grid rotation (0–90)." The "Coefficient of box size decrease" indicates the amount that each box is shrunk down per image analysis. This coefficient was set at 1.2 to give a large number of analyses per image. This was used to calculate the "Side-length of largest box" with 5 pixels set at the smallest box size. The largest box size was determined to be 825, which is large enough for all the images analyzed, as well as to give a large number of analyses in the process. The final parameter is the "Increment of grid rotation (0–90)," which allows the user to set an angle and rotate the boxes, thus recording the minimum fractal dimension as the boxes are rotated 90°. The rotation of the boxes produces an accurate D_{Box} and D_{Info}, since the orientation of the image does not affect the result. This was set at the standard value of 15.0°. This measures the fractal dimension calculated for each box side length at 15.0° increments. The smallest value was plotted on the graph. This prevents the problem where some images would produce different fractal dimensions depending on the angle at which they were analyzed. These parameters resulted in 28 individual analyses of each image, from which the fractal dimension was calculated.

APPENDIX B

TORTUOSITY CALCULATIONS

B.1 Step-by-step tortuosity calculation methodology

Calculations of tortuosity (τ) for meandering and branching forms in this study were done by uploading the images into ArcGIS, Version 10.0, via a DXF AutoCAD file. The DXF was converted to a shapefile within ArcGIS by running the *Unsplit Line* tool, which merged all of the individual elements together. This converted the DXF into a shapefile while correcting the issue where the DXF will often segment the line along vertices. The coordinate system was set to Behrmann (world), because that setting offers the least distortion and allows the user to measure the lines with precision. Without a coordinate system set, ArcGIS will not allow the user to measure anything. The specific scales of the lines do not matter in the calculation of τ, since τ is unitless as long as L_{Actual} and $L_{Euclidean}$ are measured in the same scale.

The current version of ArcGIS (10.0) does not have a tool which can subdivide a line into specific length segments so a work around must be done. The *Dice* tool can subdivide a line based on the number of vertices that are in the line. To create approximately equal line lengths, the amount of vertices needed to be increased so that they were approximately equal distance from each other. The *Densify* tool was used to increase the number of vertices based on the distance between each vertex. The distance was set to $9x10^{-3}$ m (9e-3 m) in the *Densify* tool and run. The line then was split with the *Dice* tool into approximately equal size pieces by setting the 'Vertex Limit' to the approximate number of vertices in a 5 cm long section. The Vertex Limit is dependent on the scale of the figure, so the number of vertices in a 5 cm long section needs to be determined for each analysis. The *Split* tool was used to determine the number of vertices in a set length of line, since the *Split* tool can divide a line into exact length pieces. The

problem with the *Split* tool is that it can only divide one piece of one section at a time making it a useful tool, if there is not a long line or a lot of lines to be subdivided. The *Dice* tool provides a shapefile with the lines subdivided that are approximately the length chosen. The dice tool will subdivide lines equally within a segment, so for example if there is a 5.1 cm long line being subdivided by 5 cm increments, the line will be subdivided into two 2.55 cm long pieces, not one 5 cm long piece and one 0.1 cm long piece. This is important to keep in mind when measuring the tortuosity of individual pieces. The $L_{Euclidean}$ is then measured for each diced piece and then associated with the L_{Actual} for each segment. It is then a simple matter of calculating the tortuosity of all the segments.

B.2 Network tortuosity calculations

The network tortuosity (NT) calculations were done using DIPimage Tools (www.diplib.org) within the Image Process Tools for Matlab, Version 7.12.0 (R2011a). The Matlab script in this study was modified from a script originally used and mentioned, but not printed, in Wu et al. (2006) and was only available in Wu's PhD Dissertation (2008).

To calculate the NT, the images should be produced as either two-tone black and white or grayscale. The script will convert the grayscale to two-tone black and white for you. The file format may be jpeg (.jpg), bitmap (.bmp), or tiff (.tif) but the dots per square inch (dpi) are extremely important for the size of the area being calculated. For these set of parameters, 500 dpi was kept standard. When creating the image, the thickness of the burrows should be set to 2.0 pt. This allows for the proper calculation of

the tortuosity without the artificial lowering of the number by an excessively thick burrow, which would allow the thin calculation line to travel in a straighter path.

The principal variable that can be altered is the area to be tested. Initially the settings are listed as "a = a(150:3000,150:2000)," meaning that the image being tested is from 150 pixels to 3000 pixels in the x-direction and 150 pixels to 2000 pixels in the y-direction for this particular image. The second number of each dimension (3000 and 2000 in this instance) is particular to the size of the image you are using and should be 150 pixels less than the greatest extent. The 150 pixel buffer reduces the problem of lines not going to the edge of the image. These numbers can be changed to isolate different portions of the image. For each run of the image the image size should be reduced by 150 pixels in all directions until there is no more image to analyze.

The program is set up for a black trace on a white background but by reordering the variables as noted in the script the image can be flip-flopped. The output image can also be altered via the periodicity, which has no influence on the tortuosity calculation itself. The periodicity has been initially set to 18 but can be changed to the user's visual preference. The resulting script produces a pop-up image with the original image, the resulting tortuosity image showing all of the wave fronts, and the image results with the horizontal, vertical, and average tortuosities listed.

B.2.1 Matlab network tortuosity (NT) script

```
%This algorithm calculates the network tortuosity in images. It is
based on
%the script used in 'The determination of relative path length as a
measure
%for tortuosity in compacts using image analysis', Eur.J.Pharm.Sci.
2006,
%28 (5): 433-440. For more information on DIPimage see www.diplib.org
```

```
clc;                    %Clears workspace
clear all;              %Delete all variables
close all;              %Close all figure windows except those created by
imtool
imtool close all;       %Close all figure windows created by imtool
workspace;              %Make sure the workspace panel is showing
fontSize = 14;

%Pull in original image in MATLAB in 8-bit grayscale, reverse image (or
see
%line 19), 500 DPI, file format = jpg, bmp, or tif
grayImage = imread('C:\document.bmp');
a = dip_image(grayImage);
%Select a square image set away from the edge to remove any edge-effect
a = a(750:3001,750:1899);
%Switch to "255-subsample(a,1)" for an image with white background and
%black traces.
a = 255-subsample(a,1);

% Make network slightly thicker for the wave to propagate through
a = dilation(a,3,'elliptic');
a = subsample(a,2);

% Fill in the scaling (Matrix vs. Trace speed), then thresholding.
% The best value for scaling is found to be 30.
scaling = 30;
b = (scaling-1) * threshold(a,'isodata',Inf)+ 1;

% Fill in the filter size for opening and closing
fsize = 4;
b = maxf(minf(b,fsize,'elliptic'),fsize,'elliptic');

% Search for the fastest vertical path through the traces
% Output image d = time, e = distance
% Seedimage = c
c = yy(b)-min(yy(b));
c = (c>1);
[d1,e1] = gdt(c,max(b)-b+1,3);
Vert_Trace = mean(e1(2:end-2,end-2))/size(e1,2);
Vert_Trace2 = round(Vert_Trace*10000)/10000;

% Search for the fastest horizontal path through the traces
% Output image d = time, e = distance
% Seedimage = c
c = xx(b)-min(xx(b));
c = (c>1);
[d2,e2] = gdt(c,max(b)-b+1,3);
Hor_Trace = mean(e2(end-2,2:end-2))/size(e2,1);
Hor_Trace2 = round(Hor_Trace*10000)/10000;

%Creates image with a periodicity of the wave fronts set to 18.
Vert = stretch(mod(d1,18));
Hor = stretch(mod(d2,18));

%Creates an output image with the tortuosity listed
```

```
Avrg_Tortuosity = round(((Vert_Trace2+Hor_Trace2)/2)*1000)/1000;
subplot(1, 3, 1);
imshow (grayImage);
title('Original Image', 'FontSize', fontSize);
subplot(1, 3, 2);
imshow (dip_array(Vert,'uint8'));
title('Tortuosity Analyzed', 'FontSize', fontSize);
message = sprintf('Image Results:\nVertical Tortuosity = %g\nHorizontal
Toruosity = %g\nAverage Tortuosity = %g', Vert_Trace2, Hor_Trace2,
Avrg_Tortuosity);

subplot(1, 3, 3);
axis([0 20 0 20]);
text (0,10,message);
axis off;
```

APPENDIX C

FRACTAL DIMENSION CALCULATIONS

C.1 BENOIT analysis parameters

To calculate the fractal dimension of an image, the BENOIT program requires analyzed images to be in two-tone (black background with a white image to be analyzed) bitmap files (BMP). The resolution of the mages needed to be at least 500 dots per square inch (dpi). All images were creates with the longest side length of 19 cm (± 0.5 cm). The length of the other side was variable depending on the image being analyzed.

Analyses of the fractal dimension are limited to five pixels or larger without inclusion of the largest analysis. The other parameters of the program include:

Side-length of largest box = 825

Coefficient of box size decrease = 1.2

Increment of grid rotation (0-90) = 15.0^{o}

These parameters resulted in 28 individual analyses of each image, from which the fractal dimension was calculated. For a more comprehensive review of the fractal dimension calculation procedures please refer to Lehane and Ekdale (2013).

APPENDIX D

OCCUPIED SPACE PERCENTAGE AND BURROW SHAPE CALCULATIONS

D.1 Step-by-step burrow shape methodology

The calculation of the burrow area shape (BAS) and the occupied space percentage (OSP) required the creation of a representative buffer, which was done as a series of steps (Fig. 4.9). The procedure started with exporting the initial shape as a DXF file from CorelDRAW into ArcGIS. The DXF was brought into ArcGIS with the Coordinate System set to Behrmann (world). The DXF file converts the initial trace of the burrows into a line with minimal thickness, so the original thickness of the line needed to be restored. To do this, the DXF was converted to a shapefile by running the *Unsplit Line* tool, which merged all of the individual elements of the line. The *Buffer* tool was then run with the radius of the actual trace fossil to recreate the traces as they were in CorelDRAW to get an 'actual trace representation'.

The *Buffer* tool was then run again on the actual trace representation with the distance set to the average distance between the burrows. The setting, 'Dissolve Type', in the *Buffer* tool was set to 'All' in order to merge all of the buffers together. This created a single (or possible multiple depending on the spacing of the burrows) outline of all of the traces with equal spacing. Following the creation of the buffer, doughnuts and islands were eliminated, leaving the largest one (or two) buffers as one (or two) solid piece(s). The *Smooth Polygon* tool then was used to smooth out the edges of the buffer. The distance of the *Smooth Polygon* tool was set to four times the buffer distance. This process created a Final Buffer that was representative of the overall shape and but does not conform to each and every nook and cranny, which would artificially decrease the BAS value. The calculation of the BAS was accomplished by measuring the perimeter and area of the Final Buffer using the *Measure* Tool in ArcGIS.

D.2 Occupied space percentage calculations

To calculate the OSP, the Final Buffer from the BAS calculations was set to black with the actual trace representation placed on top and set to white. These layers then were exported as an EMF file. The EMF file was brought into CorelDRAW and exported as a grayscale PNG file with the transparent background turned on. The dpi does not have much of an impact in the calculations for higher dpi values, so 500 dpi was kept standard. The reason ArcGIS was not used to export the PNG file directly was that the background did come through as transparent so an alternative method needed to be determined. The PNG file was then ready to be run through the Matlab script.

Calculation of the OSP was done using the Image Process Tools, Version 2.4.1, which was found within Matlab, Version 7.12.0 (R2011a). There are no variables within the OSP script that need to be altered. The Matlab script converts the image from grayscale to black and white, then counts the individual pixels and calculates the percentage of black and white. The final image the script creates is a figure with the picture analyzed next to the results of the analysis. The results include the total number of pixels in the image, the percentage of black pixels, and the percentage of white pixels. The Matlab script was modified from a script originally created by Brett Shoelson of The Mathworks and is available online at:

http://www.mathworks.com/matlabcentral/newsreader/view_thread/279293

D.2.1 Matlab occupied space percentage (OSP) script

```
clc;                    %Clears workspace
clear all;              %Delete all variables
close all;              %Close all figure windows except those created by
imtool
imtool close all;       %Close all figure windows created by imtool
workspace;              %Make sure the workspace panel is showing
```

```
fontSize = 15;

%Pull in original image in MATLAB in 8-bit greyscale, 500 DPI, png with
%transparent background
OriginalImage = 'File_Location.png';

%Set different files to read with and without background color so that
it
%is not counted in the final analysis
grayImage1 = imread(OriginalImage, 'BackgroundColor',1);
grayImage2 = imread(OriginalImage);
grayImage3 = imread(OriginalImage, 'BackgroundColor',0.8);


%Convert original images to binary image. It sets the value between the
%range of black and white from 2-tone original image
binaryImage1 = grayImage1 > 100;
binaryImage2 = grayImage2 > 100;
[rows columns numberOfColorBands] = size(binaryImage2);
subplot(1, 2, 1);
imshow(grayImage3);
title('Trace Fossil Analyzed', 'FontSize', fontSize);

%Calculates the number of White and Black Pixels
numberOfWhitePixels1 = sum(sum(binaryImage1));
numberOfBlackPixels2 = sum(sum(binaryImage2 == 0));
numberOfWhitePixels2 = sum(sum(binaryImage2));

%Determines the number of extra pixels that are within the transparent
%background
numberOfExtraPixels = numberOfWhitePixels1 - numberOfWhitePixels2;
totalNumberOfPixels = (rows * columns) - numberOfExtraPixels;
numberOfBlackPixels = numberOfBlackPixels2 - numberOfExtraPixels;
numberOfWhitePixels = numberOfWhitePixels2;

%Calculates percentages of pixels
percentBlackPixels = 100.0 * numberOfBlackPixels / totalNumberOfPixels;
percentWhitePixels = 100.0 * numberOfWhitePixels / totalNumberOfPixels;
message = sprintf('Image Results\nTotal number of pixels = %d\nBlack
pixels = %d = %.1f%%\nWhite pixels = %d = %.1f%%', totalNumberOfPixels,
numberOfBlackPixels, percentBlackPixels, numberOfWhitePixels,
percentWhitePixels);

subplot(1, 2, 2);
axis([0 100 0 100]);
text (20,50,message);
axis off;
```

APPENDIX E

SAMPLE IMAGES AND TRACES

Figure E.1. Modern traces and Miocene trace fossils.
Modern traces.

A. *Cosmorhaphe*. Sample INMD 98BX. Nannofossil ooze, Atlantic Ocean (Modern). Figured in part in Ekdale, 1980, Fig. 1C and photopgraphed in part by A.A. Ekdale. Scale = 2 cm. (Originally identified as *Cosmorhaphe sinuosa*). From Ekdale, 1980. Reprinted with permission from AAAS and A.A. Ekdale.
B. *Paleodictyon*. Sample INMD 128BX-1. Pteropod Ooze, Atlantic Ocean (Modern). Figured in Ekdale, 1980, Fig. 1D. Scale = 2 cm. (Originally identified as *Paleodictyon minimum*). From Ekdale, 1980. Reprinted with permission from AAAS and A.A. Ekdale.
C. *Paleodictyon*. Sample INMD 128BX-2. Pteropod ooze, Atlantic Ocean (Modern). Figured in Ekdale, 1980, Fig. 1D. Scale = 2 cm. (Originally identified as *Paleodictyon minimum*). From Ekdale, 1980. Reprinted with permission from AAAS and A.A. Ekdale.
D. *Spirorhaphe*. Sample INMD 94BX. Nannofossil ooze, Atlantic Ocean (Modern). Figured in Ekdale, 1980, Fig. 1A. Scale = 2 cm. (Originally identified as *Spirorhaphe involuta*). From Ekdale, 1980. Reprinted with permission from AAAS and A.A. Ekdale.
E. *Spirorhaphe*. Sample INMD 123 BX. Nannofossil ooze, Atlantic Ocean (Modern). Figured in Ekdale, 1980, Fig. 1B. Scale = 2 cm. (Originally identified as *Spirorhaphe involut*a). From Ekdale, 1980. Reprinted with permission from AAAS and A.A. Ekdale.
F. *Paleodictyon*. Sample VOTD-3957. Valley of the Paleodictyon, Atlantic Ocean (Modern). Featured in *Volcanoes of the Deep Sea* (2003) at time 0:39:57. Scale = 5 cm. Image from *Volcanoes of the Deep Sea* (2003), produced by The Stephen Low Company in association with Rutgers University and courtesy of A. Seilacher and P. Rona.
G. *Paleodictyon*. Sample VOTD-4001. Valley of the Paleodictyon, Atlantic Ocean (Modern). Featured in *Volcanoes of the Deep Sea* (2003) at time 0:40:01. Scale = 5 cm. Image from *Volcanoes of the Deep Sea* (2003), produced by The Stephen Low Company in association with Rutgers University and courtesy of A. Seilacher and P. Rona.
H. *Paleodictyon*. Sample VOTD-4003. Valley of the Paleodictyon, Atlantic Ocean (Modern). Featured in *Volcanoes of the Deep Sea* (2003) at time 0:40:03. Scale = 5 cm. Image from *Volcanoes of the Deep Sea* (2003), produced by The Stephen Low Company in association with Rutgers University and courtesy of A. Seilacher and P. Rona.
I. *Paleodictyon*. Sample VOTD-4006. Valley of the Paleodictyon, Atlantic Ocean (Modern). Featured in *Volcanoes of the Deep Sea* (2003) at time 0:40:06. Scale = 5 cm. Image from *Volcanoes of the Deep Sea* (2003), produced by The Stephen Low Company in association with Rutgers University and courtesy of A. Seilacher and P. Rona.

Figure E.1 continued.
Modern traces.

J. *Paleodictyon*. Sample VOTD-4009. Valley of the Paleodictyon, Atlantic Ocean (Modern). Featured in *Volcanoes of the Deep Sea* (2003) at time 0:40:09. Scale = 5 cm. Image from *Volcanoes of the Deep Sea* (2003), produced by The Stephen Low Company in association with Rutgers University and courtesy of A. Seilacher and P. Rona.

K. *Paleodictyon*. Sample VOTD-4012. Valley of the Paleodictyon, Atlantic Ocean (Modern). Featured in *Volcanoes of the Deep Sea* (2003) at time 0:40:12. Scale = 5 cm. Image from *Volcanoes of the Deep Sea* (2003), produced by The Stephen Low Company in association with Rutgers University and courtesy of A. Seilacher and P. Rona.

Miocene trace fossils.

L. *Helminthorhaphe*. Sample VBHelmin1. Azagador Limestone, Vera Basin, Spain (Messinian). Photo courtesy of A.A. Ekdale. Scale = 5cm.

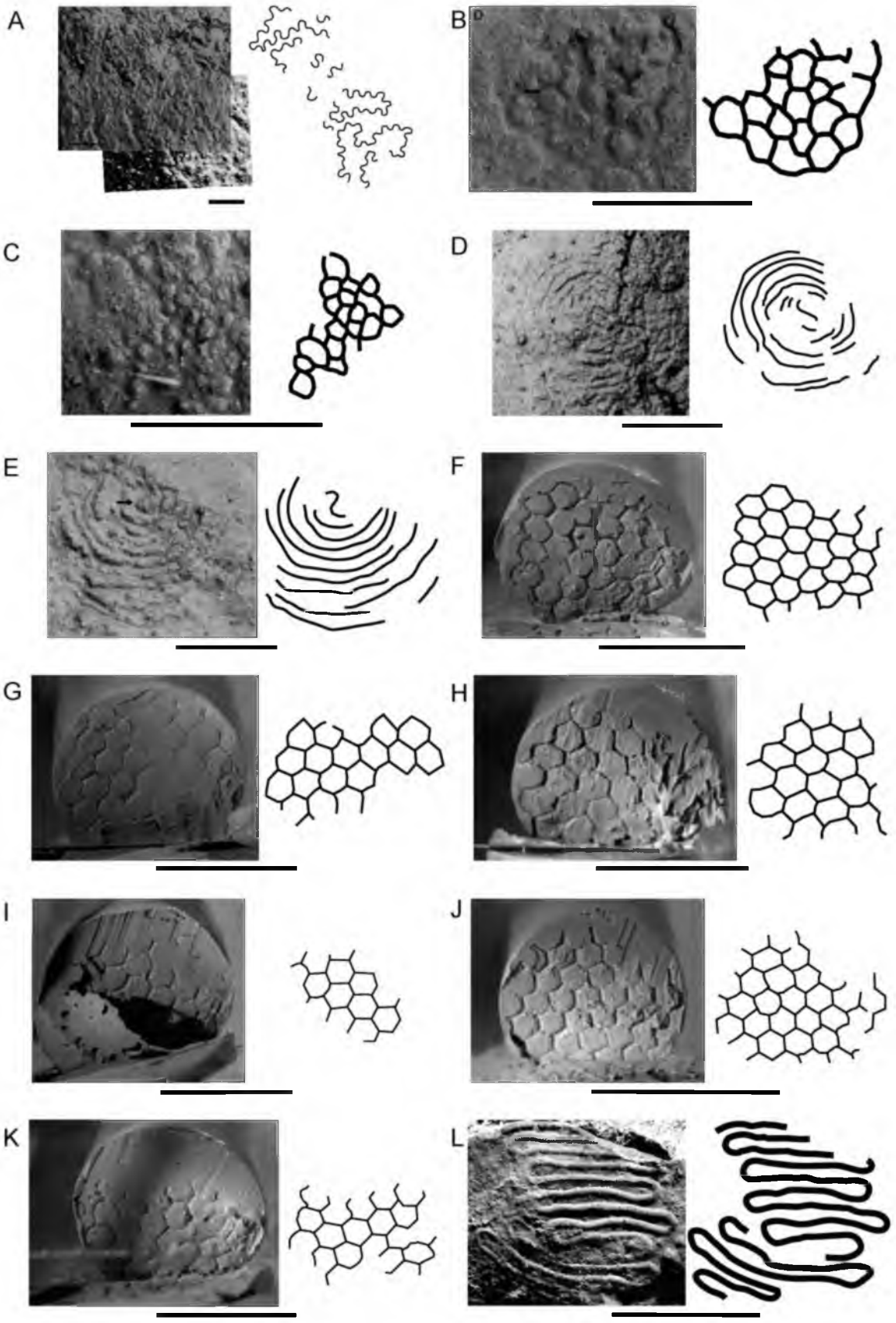
A
B
C
D
E
F
G
H
I
J
K
L

Figure E.2. Miocene trace fossils.
Miocene trace fossils.

A. *Paleodictyon*. Sample VBPaleo1. Azagador Limestone, Vera Basin, Spain (Messinian). Photo courtesy of A.A. Ekdale. Scale = 5cm.
B. *Paleodictyon*. Sample VBPaleo2. Azagador Limestone, Vera Basin, Spain (Messinian). Photo courtesy of A.A. Ekdale. Scale = 5cm.
C. *Paleodictyon*. Sample VBPaleo3. Azagador Limestone, Vera Basin, Spain (Messinian). Photo courtesy of A.A. Ekdale. Scale = 5cm.
D. *Paleodictyon*. Sample VBPaleo4. Azagador Limestone, Vera Basin, Spain (Messinian). Photo courtesy of A.A. Ekdale. Scale = 5cm.
E. *Paleodictyon*. Sample VBPaleo4b. Azagador Limestone, Vera Basin, Spain (Messinian). Photo courtesy of A.A. Ekdale. Scale = 2cm.
F. *Paleodictyon*. Sample VBPaleo5. Azagador Limestone, Vera Basin, Spain (Messinian). Photo courtesy of A.A. Ekdale. Scale = 2cm.
G. *Paleodictyon*. Sample VBPaleo6. Azagador Limestone, Vera Basin, Spain (Messinian). Photo courtesy of A.A. Ekdale. Scale = 5cm.
H. *Paleodictyon*. Sample VBPaleo6b. Azagador Limestone, Vera Basin, Spain (Messinian). Photo courtesy of A.A. Ekdale. Scale = 2cm.
I. *Paleodictyon*. Sample VBPaleo7. Azagador Limestone, Vera Basin, Spain (Messinian). Photo courtesy of A.A. Ekdale. Scale = 5cm.
J. *Urohelminthoida*. Sample VBUrohelm1. Azagador Limestone, Vera Basin, Spain (Messinian). Photo courtesy of A.A. Ekdale. Scale = 5cm.
K. *Urohelminthoida*. Sample VBUrohelm2. Azagador Limestone, Vera Basin, Spain (Messinian). Photo courtesy of A.A. Ekdale. Scale = 5cm.
L. *Urohelminthoida*. Sample VBUrohelm2b. Azagador Limestone, Vera Basin, Spain (Messinian). Photo courtesy of A.A. Ekdale. Scale = 2cm.

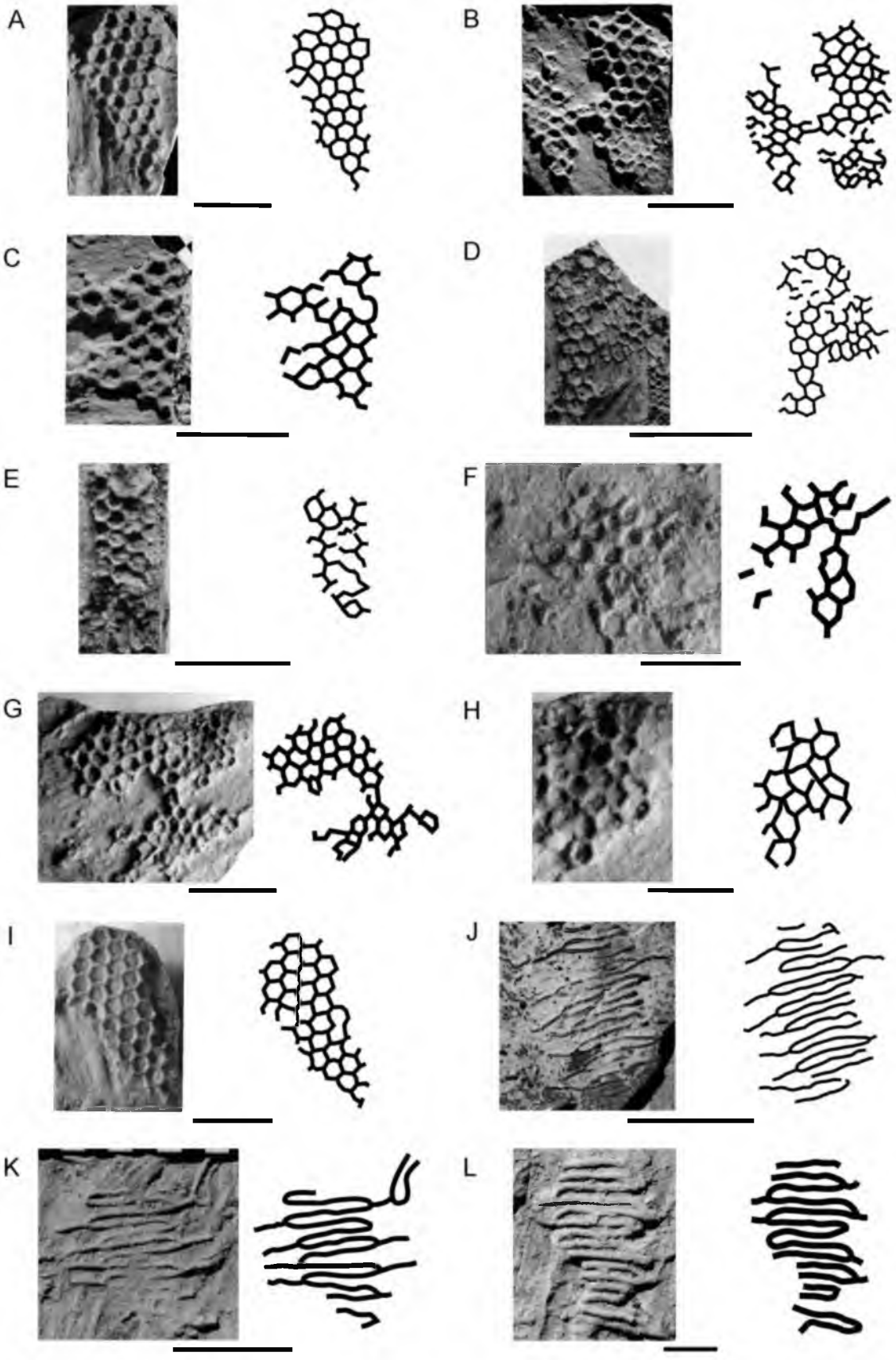
A
B
C
D
E
F
G
H
I
J
K
L

Figure E.3. Miocene trace fossils.

Miocene trace fossils.

A. *Urohelminthoida.* Sample VBUrohelm3. Azagador Limestone, Vera Basin, Spain (Messinian). Photo courtesy of A.A. Ekdale. Scale = 5cm.
B. *Cosmorhaphe*. Sample Uchman and Demircan 1999 Fig 5A. Locality B, Cingoz Formation, Turkey (Langhian - L. Serrvalian). Figured in Uchman and Demircan, 1999, Fig 5A. Scale = 5 cm. (Originally identified as *Cosmorhaphe sinuosa*). Reprinted from Uchman, A., and H. Demircan, 1999, Trace fossils of Miocene deep-sea fan fringe deposits from the Cingöz Formation, Southern Turkey, Annales Societatis Geologorum Poloniae, v. 69, pp. 125-135, with permission from the Polish Geological Society.
C. *Cosmorhaphe*. Sample Uchman and Demircan 1999 Fig 5C. Locality B, Cingoz Formation, Turkey (Langhian - L. Serrvalian). Figured in Uchman and Demircan, 1999, Fig 5C. Scale = 5 cm. (Originally identified as *?Cosmorhaphe* isp.). Reprinted from Uchman, A., and H. Demircan, 1999, Trace fossils of Miocene deep-sea fan fringe deposits from the Cingöz Formation, Southern Turkey, Annales Societatis Geologorum Poloniae, v. 69, pp. 125-135, with permission from the Polish Geological Society.
D. *Helminthorhaphe.* Sample Uchman and Demircan 1999 Fig 7F. Locality B, Cingoz Formation, Turkey (Langhian - L. Serrvalian). Figured in Uchman and Demircan, 1999, Fig 7F. Scale = 5 cm. (Originally identified as *Helminthorhaphe flexuosa*). Reprinted from Uchman, A., and H. Demircan, 1999, Trace fossils of Miocene deep-sea fan fringe deposits from the Cingöz Formation, Southern Turkey, Annales Societatis Geologorum Poloniae, v. 69, pp. 125-135, with permission from the Polish Geological Society.
E. *Helminthorhaphe.* Sample Uchman and Demircan 1999 Fig 7G. Locality B, Cingoz Formation, Turkey (Langhian - L. Serrvalian). Figured in Uchman and Demircan, 1999, Fig 7G. Scale = 5 cm. (Originally identified as *Helminthorhaphe flexuosa*). Reprinted from Uchman, A., and H. Demircan, 1999, Trace fossils of Miocene deep-sea fan fringe deposits from the Cingöz Formation, Southern Turkey, Annales Societatis Geologorum Poloniae, v. 69, pp. 125-135, with permission from the Polish Geological Society.
F. *Urohelminthoida.* Sample Uchman and Demircan 1999 Fig 5B. Locality B, Cingoz Formation, Turkey (Langhian - L. Serrvalian). Figured in Uchman and Demircan, 1999, Fig 5B. Scale = 5 cm. (Originally identified as *Urohelminthoida dertonensis*). Reprinted from Uchman, A., and H. Demircan, 1999, Trace fossils of Miocene deep-sea fan fringe deposits from the Cingöz Formation, Southern Turkey, Annales Societatis Geologorum Poloniae, v. 69, pp. 125-135, with permission from the Polish Geological Society.
G. *Helminthorhaphe.* Sample CS 12. Gorgoglione Formation, Castelmezzano, Italy (Middle - Upper Miocene). Figured in D'Alessandro, 1982 Tavola 43 Fig. 6. Scale = 5 cm. (Originally identified as *Cosmorhaphe tremens*). Reprinted from D'Alessandro, A, 1982, Processi tafonomici e distribuzione delle tracce fossili nel flysch di Gorgolione (Appennino Meridionale), Rivista Italiana di Paleontologia e stratigrafia, v. 87, no. 3, pp.511-560 with permission.

Figure E.3 continued.
Miocene trace fossils.

H. *Paleodictyon.* Sample CM 22. Gorgoglione Formation, Castelmezzano, Italy (Middle - Upper Miocene). Figured in D'Alessandro, 1980 Tavola 38 Fig. 3. Scale = 5 cm. (Originally identified as *Paleodictyon strozzii*). Reprinted from D'Alessandro, A, 1980, Prime osservazioni sulla ichnofaua Miocenica della 'formazione di Gorgoglione' (Castelmezzano, Potenza), Rivista Italiana di Paleontologia e stratigrafia, v. 86, no. 2, pp.357-398, with permission.

I. *Paleodictyon.* Sample FG 1. Gorgoglione Formation, Castelmezzano, Italy (Middle - Upper Miocene). Figured in D'Alessandro, 1982 Tavola 41 Fig. 6. Scale = 5 cm. (Originally identified as *Paleodictyon minimum*). Reprinted from D'Alessandro, A, 1982, Processi tafonomici e distribuzione delle tracce fossili nel flysch di Gorgolione (Appennino Meridionale), Rivista Italiana di Paleontologia e stratigrafia, v. 87, no. 3, pp.511-560 with permission.

J. *Paleodictyon.* Sample FG 5. Gorgoglione Formation, Castelmezzano, Italy (Middle - Upper Miocene). Figured in D'Alessandro, 1982 Tavola 41 Fig. 3. Scale = 2 cm. (Originally identified as *Paleodictyon minimum*). Reprinted from D'Alessandro, A, 1982, Processi tafonomici e distribuzione delle tracce fossili nel flysch di Gorgolione (Appennino Meridionale), Rivista Italiana di Paleontologia e stratigrafia, v. 87, no. 3, pp.511-560 with permission.

K. *Paleodictyon.* Sample UUIC 722. Gorgoglione Formation, Gorgoglione River Gorge, Italy (Middle - Upper Miocene). Photographed by J.R. Lehane. Scale = 5 cm.

L. *Protopaleodictyon.* Sample FG 13. Gorgoglione Formation, Castelmezzano, Italy (Middle - Upper Miocene). Figured in D'Alessandro, 1982 Tavola 43 Fig. 3. Scale = 5 cm. (Originally identified as *Protopaleodictyon incompositum*). Reprinted from D'Alessandro, A, 1982, Processi tafonomici e distribuzione delle tracce fossili nel flysch di Gorgolione (Appennino Meridionale), Rivista Italiana di Paleontologia e stratigrafia, v. 87, no. 3, pp.511-560 with permission.

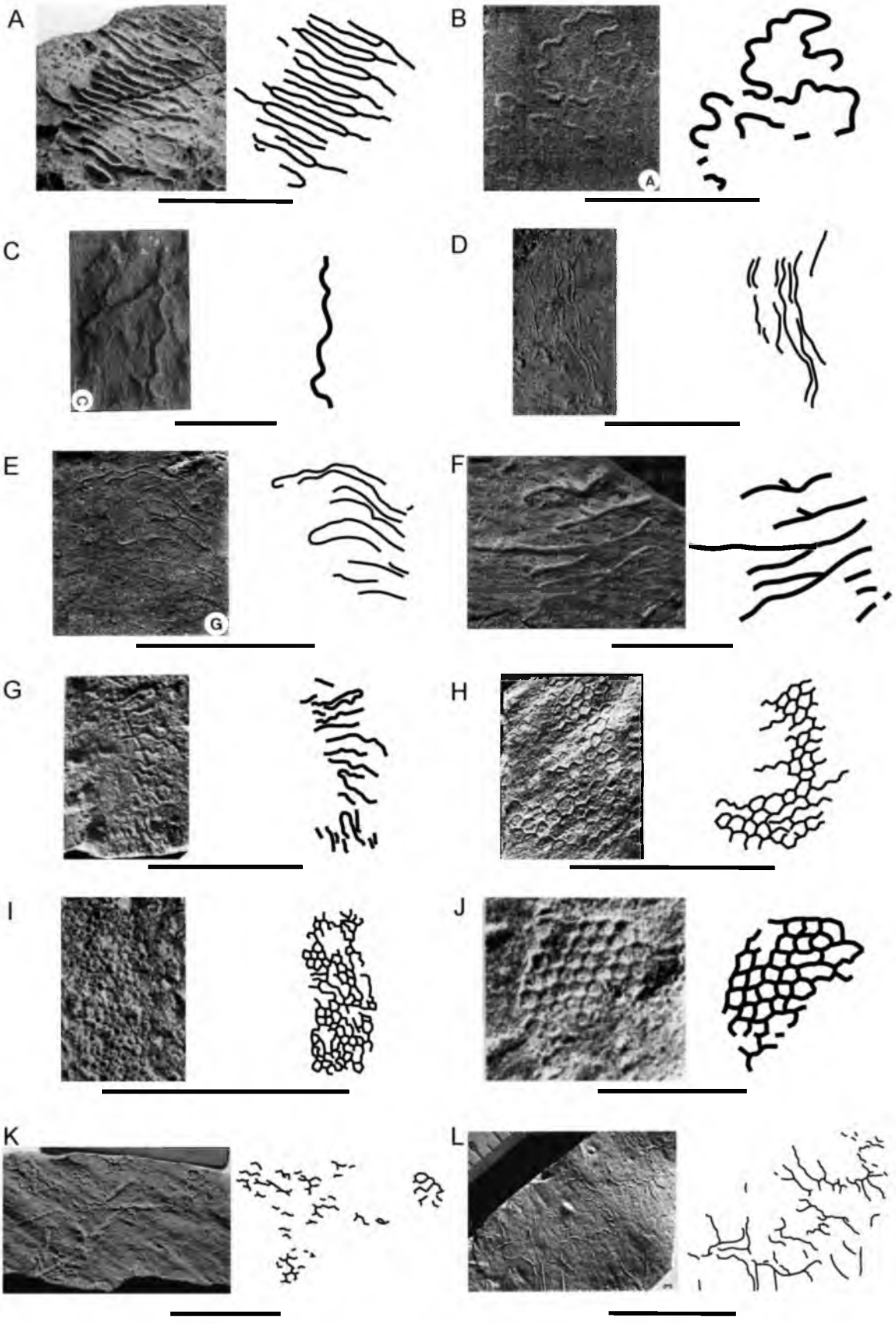
A
B
C
D
E
F
G
H
I
J
K
L

Figure E.4. Miocene trace fossils.
Miocene trace fossils.

A. *Urohelminthoida.* Sample CM 29-1. Gorgoglione Formation, Castelmezzano, Italy (Middle - Upper Miocene). Figured in D'Alessandro, 1980 Tavola 42 Fig. 1. Scale = 5 cm. (Originally identified as *Urohelminthoida dertonensis*). Reprinted from D'Alessandro, A, 1980, Prime osservazioni sulla ichnofaua Miocenica della 'formazione di Gorgoglione' (Castelmezzano, Potenza), Rivista Italiana di Paleontologia e stratigrafia, v. 86, no. 2, pp.357-398, with permission.
B. *Urohelminthoida.* Sample CM 29-2. Gorgoglione Formation, Castelmezzano, Italy (Middle - Upper Miocene). Figured in D'Alessandro, 1980 Tavola 43 Fig. 3. Scale = 5 cm. (Originally identified as *Urohelminthoida dertonensis*). Reprinted from D'Alessandro, A, 1980, Prime osservazioni sulla ichnofaua Miocenica della 'formazione di Gorgoglione' (Castelmezzano, Potenza), Rivista Italiana di Paleontologia e stratigrafia, v. 86, no. 2, pp.357-398, with permission.
C. *Urohelminthoida.* Sample UUIC 1549. Gorgoglione Formation, Gorgoglione River Gorge, Italy (Middle - Upper Miocene). Photograph taken by J.R. Lehane. Scale = 5 cm.
D. *Helminthopsis*. Sample PIW1993X 103. Marnoso-arenacea Formation, Montone Valley, Italy (Langhian – Tortonian). Figured in Uchman, 1995 Plate 12.2. Scale = 5 cm. (Originally identified as *Helminthopsis* isp.). Reprinted from Uchman, A, 1995, Taxonomy and palaeoecology of flysch trace fossils: The Marnoso-arenacea Formation and associated facies (Miocene, Northern Apenines, Italy), Beringeria, v. 15, pp. 1-115, with permission.
E. *Helminthopsis*. Sample PIW1993X 104. Marnoso-arenacea Formation, Coniale, Santerno Valley, Italy (Langhian – Tortonian). Figured in Uchman, 1995 Plate 12.4. Scale = 5 cm. (Originally identified as *Helminthopsis* isp.). Reprinted from Uchman, A, 1995, Taxonomy and palaeoecology of flysch trace fossils: The Marnoso-arenacea Formation and associated facies (Miocene, Northern Apenines, Italy), Beringeria, v. 15, pp. 1-115, with permission.
F. *Helminthorhaphe*. Sample PIW1993X 93. Marnoso-arenacea Formation, Rabbi Valley, Italy (Langhian – Tortonian). Figured in Uchman, 1995 Plate 11.6. Scale = 5 cm. (Originally identified as *Helminthorhaphe flexuosa*). Reprinted from Uchman, A, 1995, Taxonomy and palaeoecology of flysch trace fossils: The Marnoso-arenacea Formation and associated facies (Miocene, Northern Apenines, Italy), Beringeria, v. 15, pp. 1-115, with permission.
G. *Helminthorhaphe*. Sample PIW1993X 96. Marnoso-arenacea Formation, Bidente Valley, Italy (Langhian – Tortonian). Figured in Uchman, 1995 Plate 11.5. Scale = 5 cm. (Originally identified as *Helminthorhaphe flexuosa*). Reprinted from Uchman, A, 1995, Taxonomy and palaeoecology of flysch trace fossils: The Marnoso-arenacea Formation and associated facies (Miocene, Northern Apenines, Italy), Beringeria, v. 15, pp. 1-115, with permission.

Figure E.4 continued.
Miocene trace fossils.

H. *Paleodictyon*. Sample PIW1993X 50. Marnoso-arenacea Formation, Quarto, Savio Valley, Italy (Langhian – Tortonian). Figured in Uchman, 1995 Plate 14.9. Scale = 5 cm. (Originally identified as *Paleodictyon maximum*). Reprinted from Uchman, A, 1995, Taxonomy and palaeoecology of flysch trace fossils: The Marnoso-arenacea Formation and associated facies (Miocene, Northern Apenines, Italy), Beringeria, v. 15, pp. 1-115, with permission.

I. *Paleodictyon*. Sample PIW1993X 56. Marnoso-arenacea Formation, Tramazzo Valley, Italy (Langhian – Tortonian). Figured in Uchman, 1995 Plate 14.8. Scale = 5 cm. (Originally identified as *Paleodictyon maximum*). Reprinted from Uchman, A, 1995, Taxonomy and palaeoecology of flysch trace fossils: The Marnoso-arenacea Formation and associated facies (Miocene, Northern Apenines, Italy), Beringeria, v. 15, pp. 1-115, with permission.

J. *Paleodictyon*. Sample PIW1993X 59. Marnoso-arenacea Formation, Castel del Rio, Santerno Valley, Italy (Langhian – Tortonian). Figured in Uchman, 1995 Plate 14.6. Scale = 5 cm. (Originally identified as *Paleodictyon strozzii*). Reprinted from Uchman, A, 1995, Taxonomy and palaeoecology of flysch trace fossils: The Marnoso-arenacea Formation and associated facies (Miocene, Northern Apenines, Italy), Beringeria, v. 15, pp. 1-115, with permission.

K. *Paleodictyon*. Sample PIW1993X 61. Marnoso-arenacea Formation, Savio Valley, road to Mandrioli Pass, Italy (Langhian – Tortonian). Figured in Uchman, 1995 Plate 14.10. Scale = 5 cm. (Originally identified as *Paleodictyon hexagonum*). Reprinted from Uchman, A, 1995, Taxonomy and palaeoecology of flysch trace fossils: The Marnoso-arenacea Formation and associated facies (Miocene, Northern Apenines, Italy), Beringeria, v. 15, pp. 1-115, with permission.

L. *Paleodictyon*. Sample PIW1993X 68. Marnoso-arenacea Formation, Tramazzo Valley, Italy (Langhian – Tortonian). Figured in Uchman, 1995 Plate 14.7. Scale = 5 cm. (Originally identified as *Paleodictyon majus*). Reprinted from Uchman, A, 1995, Taxonomy and palaeoecology of flysch trace fossils: The Marnoso-arenacea Formation and associated facies (Miocene, Northern Apenines, Italy), Beringeria, v. 15, pp. 1-115, with permission.

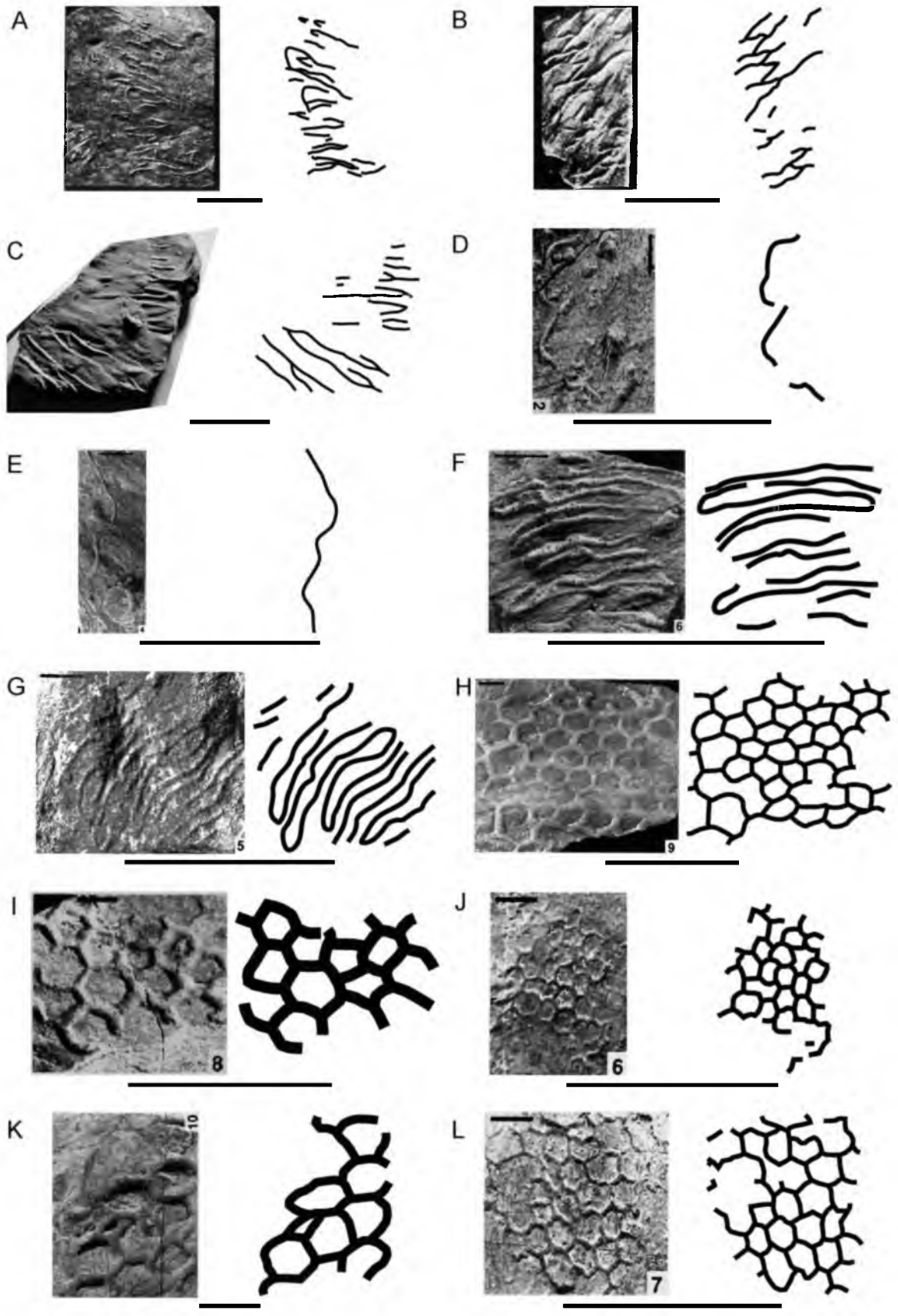
A
B
C
D
E
F
G
H
I
J
K
L

Figure E.5. Miocene and Oligocene trace fossils.
Miocene trace fossils.

A. *Urohelminthoida*. Sample PIW1993X 84. Marnoso-arenacea Formation, Quarto, Savio Valley, Italy (Langhian – Tortonian). Figured in Uchman, 1995 Plate 13.7. Scale = 5 cm. (Originally identified as *Urohelminthoida dertonensis*). Reprinted from Uchman, A, 1995, Taxonomy and palaeoecology of flysch trace fossils: The Marnoso-arenacea Formation and associated facies (Miocene, Northern Apenines, Italy), Beringeria, v. 15, pp. 1-115, with permission.
B. *Urohelminthoida*. Sample Uchman 1995 Plate 14.2. Marnoso-arenacea Formation, Rabbi Valley, Italy (Langhian – Tortonian). Figured in Uchman, 1995 Plate 14.2. Scale = 5 cm. (Originally identified as *Urohelminthoida dertonensis*). Reprinted from Uchman, A, 1995, Taxonomy and palaeoecology of flysch trace fossils: The Marnoso-arenacea Formation and associated facies (Miocene, Northern Apenines, Italy), Beringeria, v. 15, pp. 1-115, with permission.
C. *Urohelminthoida*. Sample PIW199X 81. Verghereto Marls, Verghereto, Italy (Serravallian - Lower Messinian). Figured in Uchman, 1995 Plate 13.6. Scale = 5 cm. (Originally identified as *Urohelminthoida dertonensis*). Reprinted from Uchman, A, 1995, Taxonomy and palaeoecology of flysch trace fossils: The Marnoso-arenacea Formation and associated facies (Miocene, Northern Apenines, Italy), Beringeria, v. 15, pp. 1-115, with permission.

Oligocene trace fossils.

D. *Gordia*. Sample UJTF 245. Krosno Beds, Skrzydlna, Poland (Upper Oligocene). Photographed by J.R. Lehane. Scale = 5 cm. (Originally figured in Książkiewicz, 1977 Plate 20.6 as *Gordia molassica*).
E. *Gordia*. Sample UJTF 1219. Krosno Beds, Wetlina, Poland (Upper Oligocene). Photographed by J.R. Lehane. Scale = 5 cm. (Originally figured in Książkiewicz, 1977 Plate 20.8 as *Gordia arcuata*).
F. *Helminthopsis*. Sample UJTF 1320. Krosno Beds, Radoszyce, Poland (Upper Oligocene). Photographed by J.R. Lehane. Scale = 5 cm. (Originally figured in Książkiewicz, 1977 Plate 12.4 as *Helminthopsis hieroglyphica*).
G. *Helminthopsis*. Sample UJTF 1587. Krosno Beds, Kąty k.Żmigrodu, Poland (Upper Oligocene). Photographed by J.R. Lehane. Scale = 5 cm.
H. *Helminthorhaphe*. Sample UJTF 39. Krosno Beds, Słonne Góry K.Załuża, Poland (Upper Oligocene). Photographed by J.R. Lehane. Scale = 5 cm.
I. *Helminthorhaphe*. Sample UJTF 1361. Krosno Beds, Dźwiniacz Dolny, Poland (Upper Oligocene). Photographed by J.R. Lehane. Scale = 5 cm. (Originally figured in Książkiewicz, 1977 Plate 21.7 as *Helminthoida crassa*).
J. *Helminthorhaphe*. Sample UJTF 1362. Krosno Beds, Dźwiniacz Dolny, Poland (Upper Oligocene). Photographed by J.R. Lehane. Scale = 5 cm. (Originally figured in Książkiewicz, 1977 Plate 21.5 as *Helminthoida crassa*).
K. *Paleodictyon*. Sample UJTF 835-1. Krosno Beds, Mymoń, Poland (Upper Oligocene). Photographed by J.R. Lehane. Scale = 5 cm. (Originally figured in Książkiewicz, 1977 Plate 27.13 as *Paleodictyon miocenicum*).
L. *Paleodictyon*. Sample UJTF 835-2. Krosno Beds, Mymoń, Poland (Upper Oligocene). Photographed by J.R. Lehane. Scale = 5 cm. (Originally figured in Książkiewicz, 1977 Plate 27.14 as *Paleodictyon miocenicum*).

G
H
I
J
K
L

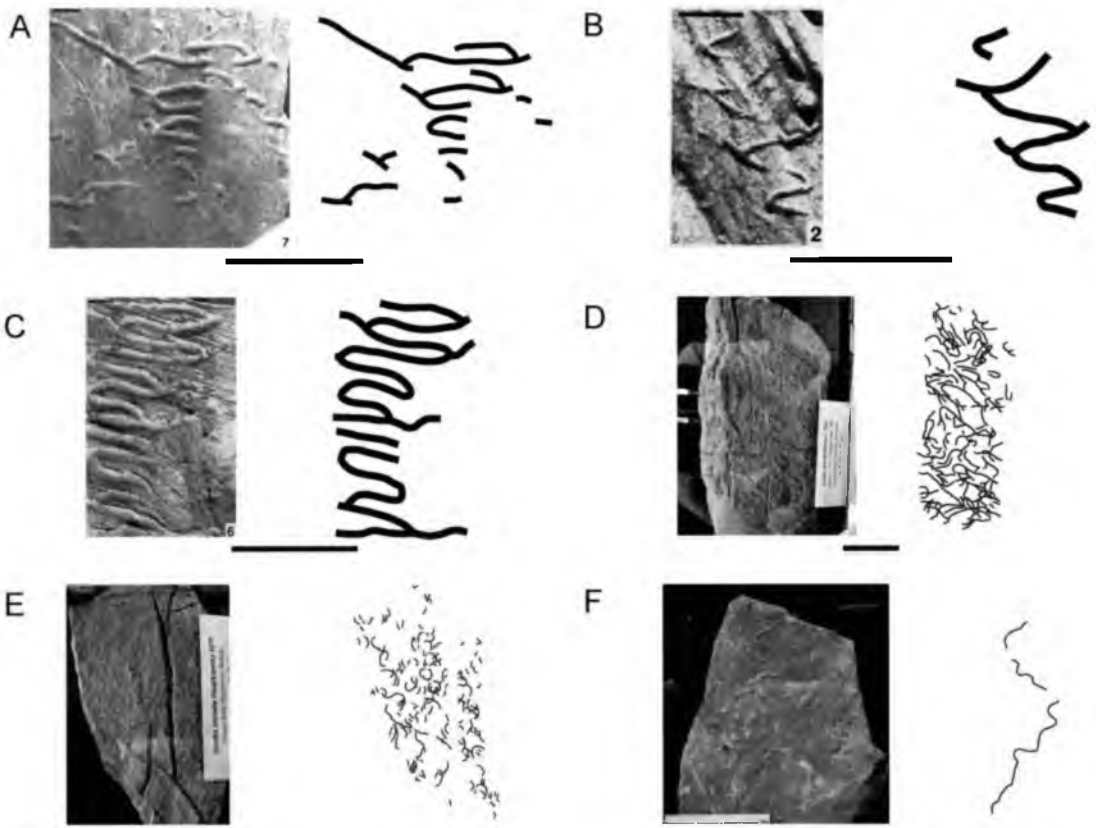
A
B
C
D
E
F

Figure E.6. Oligocene and Eocene trace fossils.
Oligocene trace fossils.

A. *Paleodictyon.* Sample UJTF unk. Krosno Beds, Mymoń, Poland (Upper Oligocene). Photographed by J.R. Lehane. Scale = 5 cm.
B. *Gordia.* Sample IGP t.f. 71b. Podhale Flysch, Gliczarow stream, Poland (Oligocene). Figured in Roniewicz and Pienkowski, 1977 Plate 2c. Scale = 5 cm. (Originally identified as *Gordia* sp.). Reprinted from Roniewicz, P., and G. Pienkowski, 1977, Trace fossils of the Podhale Flysch Basin, pp.273-288 in T. P. Crimes, and J. C. Harper, eds., Trace Fossils 2, published by John Wiley & Sons Ltd with permission.
C. *Gordia.* Sample IGP t.f. 184a. Podhale Flysch, Kaniowski stream, Poland (Oligocene). Figured in Roniewicz and Pienkowski, 1977 Plate 2d. Scale = 5 cm. (Originally identified as *Gordia* sp.). Reprinted from Roniewicz, P., and G. Pienkowski, 1977, Trace fossils of the Podhale Flysch Basin, pp.273-288 in T. P. Crimes, and J. C. Harper, eds., Trace Fossils 2, published by John Wiley & Sons Ltd with permission.
D. *Helminthopsis.* Sample IGP t.f. 102. Podhale Flysch, Bystry stream, Poland (Oligocene). Figured in Roniewicz and Pienkowski, 1977 Plate 2b. Scale = 5 cm. (Originally identified as *Helminthopsis tenuis*). Reprinted from Roniewicz, P., and G. Pienkowski, 1977, Trace fossils of the Podhale Flysch Basin, pp.273-288 in T. P. Crimes, and J. C. Harper, eds., Trace Fossils 2, published by John Wiley & Sons Ltd with permission.
E. *Helminthopsis.* Sample IGP t.f. 306c. Podhale Flysch, Czarny Dunajec River (Oligocene). Figured in Roniewicz and Pienkowski, 1977 Plate 2a. Scale = 5 cm. (Originally identified as *Helminthopsis tenuis*). Reprinted from Roniewicz, P., and G. Pienkowski, 1977, Trace fossils of the Podhale Flysch Basin, pp.273-288 in T. P. Crimes, and J. C. Harper, eds., Trace Fossils 2, published by John Wiley & Sons Ltd with permission.

Eocene trace fossils.

F. *Belocosmorhaphe*. Sample UJTF 716. Beloveža Beds, Szczawa, Poland (Lower - Middle Eocene). Photographed by J.R. Lehane. Scale = 5 cm. (Originally figured in Uchman, 1998 Fig. 92 as *Belocosmorhaphe aculeata*).
G. *Belocosmorhaphe*. Sample UJTF 1360. Beloveža Beds, Szczawa, Poland (Lower - Middle Eocene). Photographed by J.R. Lehane. Scale = 5 cm. (Originally figured in Książkiewicz, 1977 Plate 19.8 as *Helminthoida aculeata*).
H. *Belorhaphe*. Sample UJTF 1443. Beloveža Beds, Sidzina, Poland (Lower - Middle Eocene). Photographed by J.R. Lehane. Scale = 5 cm.
I. *Cosmorhaphe.* Sample UJTF 1. Beloveža Beds, Sidzina, Poland (Lower - Middle Eocene). Photographed by J.R. Lehane. Scale = 5 cm.
J. *Cosmorhaphe.* Sample UJTF 5. Beloveža Beds, Lipnica Mała, Poland (Lower - Middle Eocene). Photographed by J.R. Lehane. Scale = 5 cm.
K. *Cosmorhaphe.* Sample UJTF 8. Beloveža Beds, Sidzina, Poland (Lower - Middle Eocene). Photographed by J.R. Lehane. Scale = 5 cm.
L. *Cosmorhaphe.* Sample UJTF 9. Beloveža Beds, Zubrzyca Górna, Pasieka, Poland (Lower - Middle Eocene). Photographed by J.R. Lehane. Scale = 5 cm.

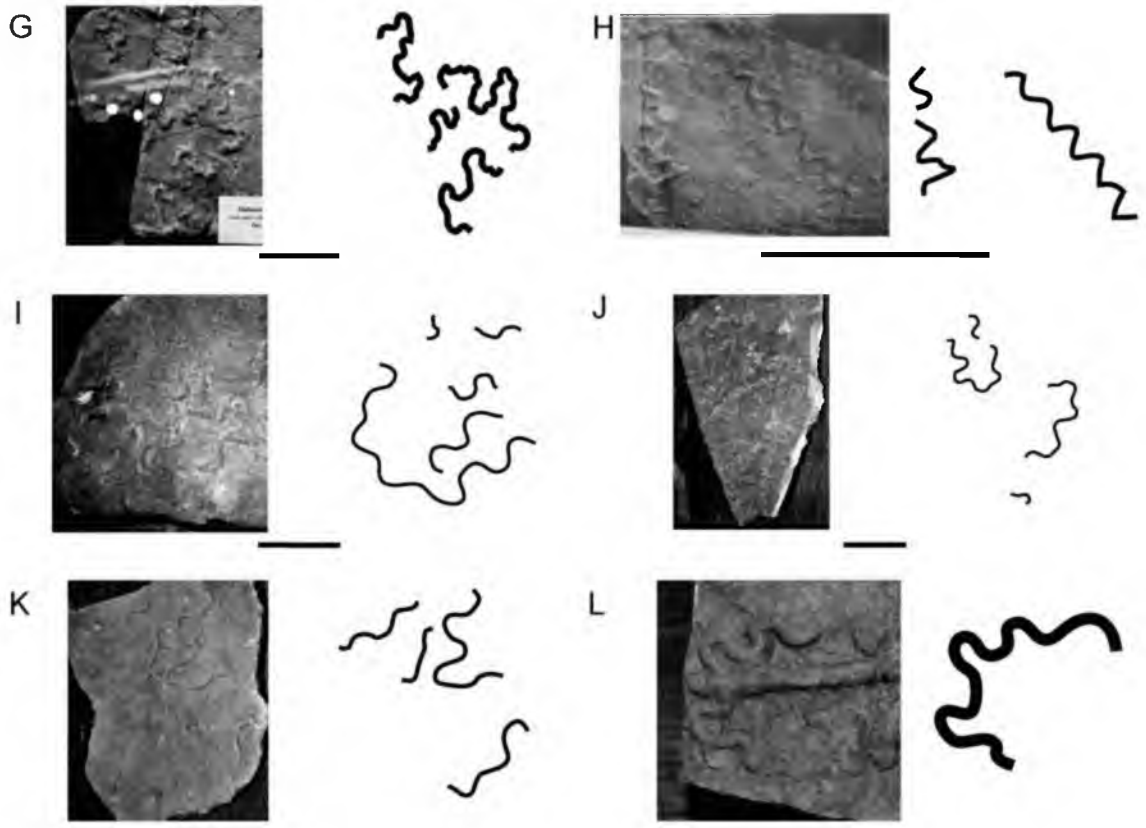
G
H
I
J
K
L

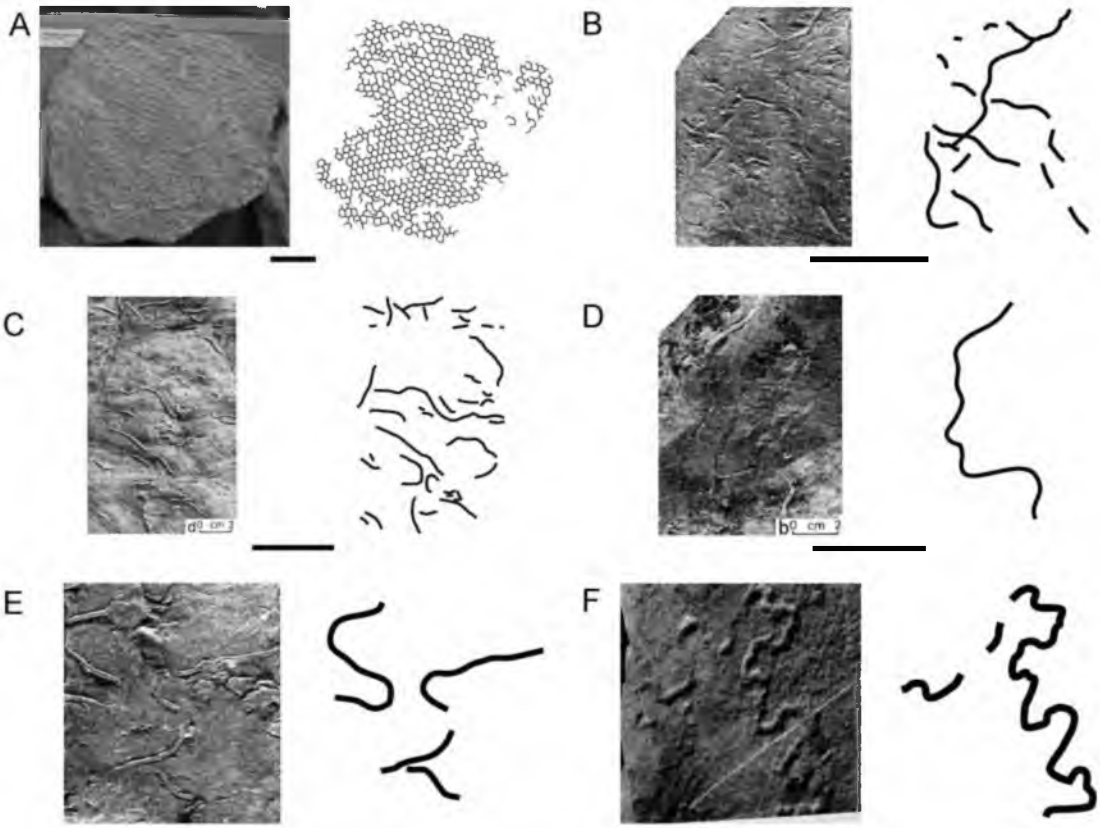
A
B
C
D
E
F

Figure E.7. Eocene trace fossils.
Eocene trace fossils.

A. *Cosmorhaphe.* Sample UJTF 11. Beloveža Beds, Lipnica Wielka, Poland (Lower - Middle Eocene). Photographed by J.R. Lehane. Scale = 5 cm.
B. *Cosmorhaphe.* Sample UJTF 12. Beloveža Beds, Lipnica Mała, Poland (Lower - Middle Eocene). Photographed by J.R. Lehane. Scale = 5 cm.
C. *Cosmorhaphe.* Sample UJTF 13. Beloveža Beds, Lipnica Mała, Poland (Lower - Middle Eocene). Photographed by J.R. Lehane. Scale = 5 cm.
D. *Cosmorhaphe.* Sample UJTF 18. Beloveža Beds, Lubomierz, Poland (Lower - Middle Eocene). Photographed by J.R. Lehane. Scale = 5 cm.
E. *Cosmorhaphe*. Sample UJTF 77. Beloveža Beds, Lętownia Górna, Poland (Lower - Middle Eocene). Photographed by J.R. Lehane. Scale = 5 cm. (Originally figured in Książkiewicz, 1977 Plate 19.6 as *Cosmorhaphe helminthopsoidea*).
F. *Cosmorhaphe.* Sample UJTF 242. Beloveža Beds, Sidzina, Poland (Lower - Middle Eocene). Photographed by J.R. Lehane. Scale = 5 cm.
G. *Helminthopsis.* Sample UJTF 252. Beloveža Beds, Lipnica Mała, Poland (Lower - Middle Eocene). Photographed by J.R. Lehane. Scale = 5 cm.
H. *Helminthopsis*. Sample UJTF 1082. Beloveža Beds, Sidzina, Poland (Lower - Middle Eocene). Photographed by J.R. Lehane. Scale = 5 cm. (Originally figured in Książkiewicz, 1977 Plate 12.3 as *Helminthopsis hieroglyphica*).
I. *Helminthopsis*. Sample UJTF 1661. Beloveža Beds, Sidzina, Mała Głaza, Poland (Lower - Middle Eocene). Photographed by J.R. Lehane. Scale = 5 cm. (Originally figured in Uchman, 1998 Fig. 83 as *Helminthopsis tunuis*).
J. *Helminthorhaphe*. Sample UJTF 102. Beloveža Beds, Sidzina, Poland (Lower - Middle Eocene). Photographed by J.R. Lehane. Scale = 5 cm. (Originally figured in Książkiewicz, 1977 Plate 21.9 as *Helminthoida helminthopsoidea*).
K. *Helminthorhaphe.* Sample UJTF 708. Beloveža Beds, Szczawa, Poland (Lower - Middle Eocene). Photographed by J.R. Lehane. Scale = 5 cm.
L. *Helminthorhaphe.* Sample UJTF 1100. Beloveža Beds, Zubrzyca Górna, Poland (Lower - Middle Eocene). Photographed by J.R. Lehane. Scale = 5 cm.

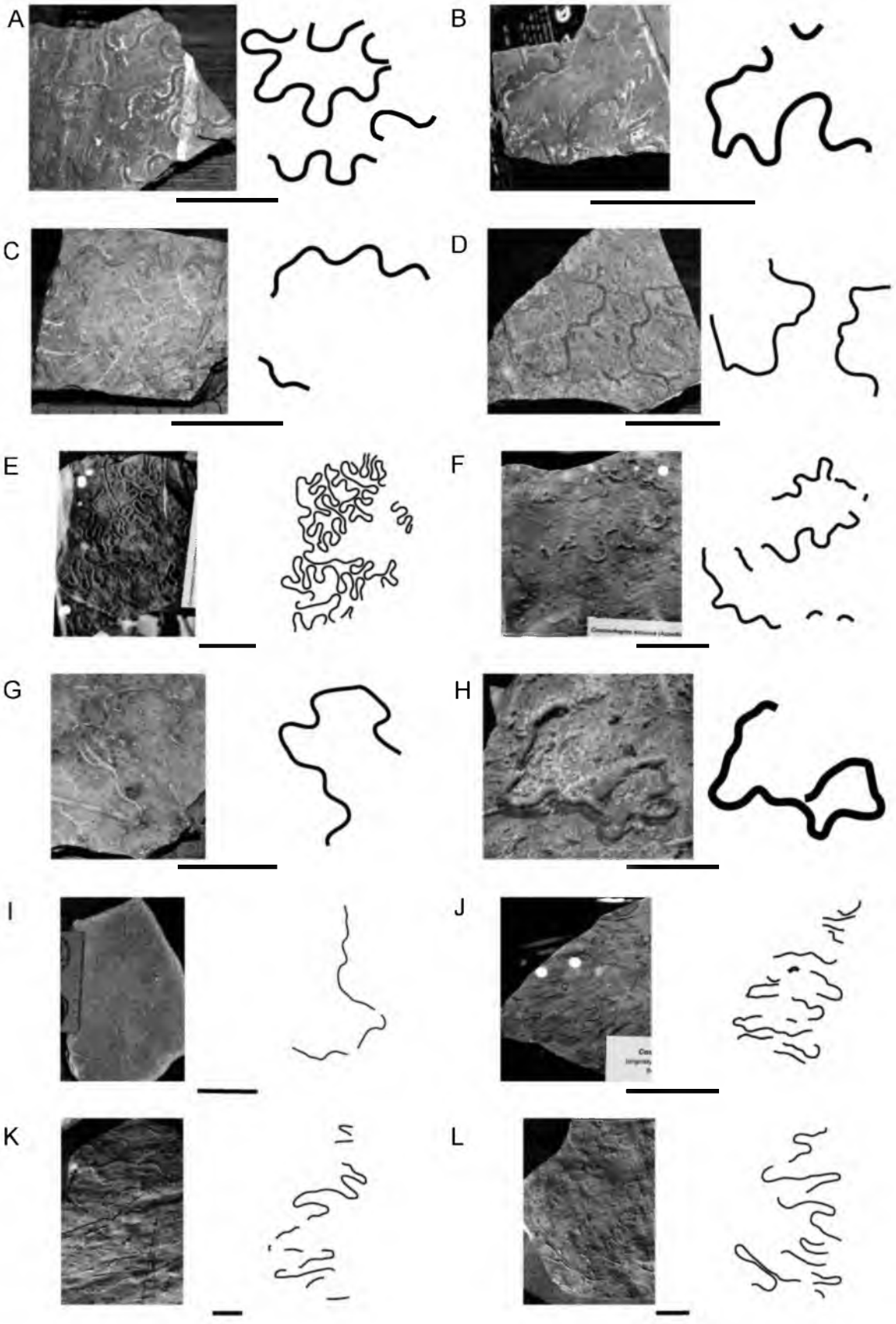
A
B
C
D
E
F
G
H
I
J
K
L

Figure E.8. Eocene trace fossils.

Eocene trace fossils.

A. *Helminthorhaphe.* Sample UJTF unk. Beloveža Beds, Lipnica Mała, Poland (Lower - Middle Eocene). Photographed by J.R. Lehane. Scale = 5 cm.
B. *Megagrapton.* Sample UJTF 80a. Beloveža Beds, Lipnica Mała, Poland (Lower - Middle Eocene). Photographed by J.R. Lehane. Scale = 5 cm. (Originally figured in Książkiewicz, 1977 Plate 25.3 as *Protopaleodictyon submontanum*).
C. *Megagrapton.* Sample UJTF 387. Beloveža Beds, Zubrzyca Górna, Poland (Lower - Middle Eocene). Photographed by J.R. Lehane. Scale = 5 cm. (Originally figured in Książkiewicz, 1977 Plate 25.7 as *Megagrapton irregulare*).
D. *Megagrapton.* Sample UJTF 388. Beloveža Beds, Lipnica Mała, Poland (Lower - Middle Eocene). Photographed by J.R. Lehane. Scale = 5 cm. (Originally figured in Książkiewicz, 1977 Plate 25.2 as *Protopaleodictyon submontanum*).
E. *Megagrapton.* Sample UJTF 390. Beloveža Beds, Lipnica Mała, Poland (Lower - Middle Eocene). Photographed by J.R. Lehane. Scale = 5 cm.
F. *Megagrapton.* Sample UJTF 455. Beloveža Beds, Zubrzyca Górna, Poland (Lower - Middle Eocene). Photographed by J.R. Lehane. Scale = 5 cm.
G. *Megagrapton.* Sample UJTF 809. Beloveža Beds, Berest, Poland (Lower - Middle Eocene). Photographed by J.R. Lehane. Scale = 5 cm. (Originally figured in Książkiewicz, 1977 Plate 25.6 as *Megagrapton irregulare*).
H. *Paleodictyon.* Sample UJTF 64. Beloveža Beds, Lipnica Mała, Poland (Lower - Middle Eocene). Photographed by J.R. Lehane. Scale = 2 cm. (Originally figured in Książkiewicz, 1977 Plate 27.11 as *Paleodictyon miocenicum*).
I. *Paleodictyon.* Sample UJTF 158. Beloveža Beds, Lubomierz, Poland (Lower - Middle Eocene). Photographed by J.R. Lehane. Scale = 5 cm. (Originally figured in Książkiewicz, 1977 Plate 28.4 as *Paleodictyon carpathicum*).
J. *Paleodictyon.* Sample UJTF 161. Beloveža Beds, Sidzina, Poland (Lower - Middle Eocene). Photographed by J.R. Lehane. Scale = 5 cm.
K. *Paleodictyon.* Sample UJTF 163. Beloveža Beds, Sidzina, p.Kamieński, Poland (Lower - Middle Eocene). Photographed by J.R. Lehane. Scale = 5 cm.
L. *Paleodictyon.* Sample UJTF 164. Beloveža Beds, Sidzina, p.Kamieński, Poland (Lower - Middle Eocene). Photographed by J.R. Lehane. Scale = 5 cm.

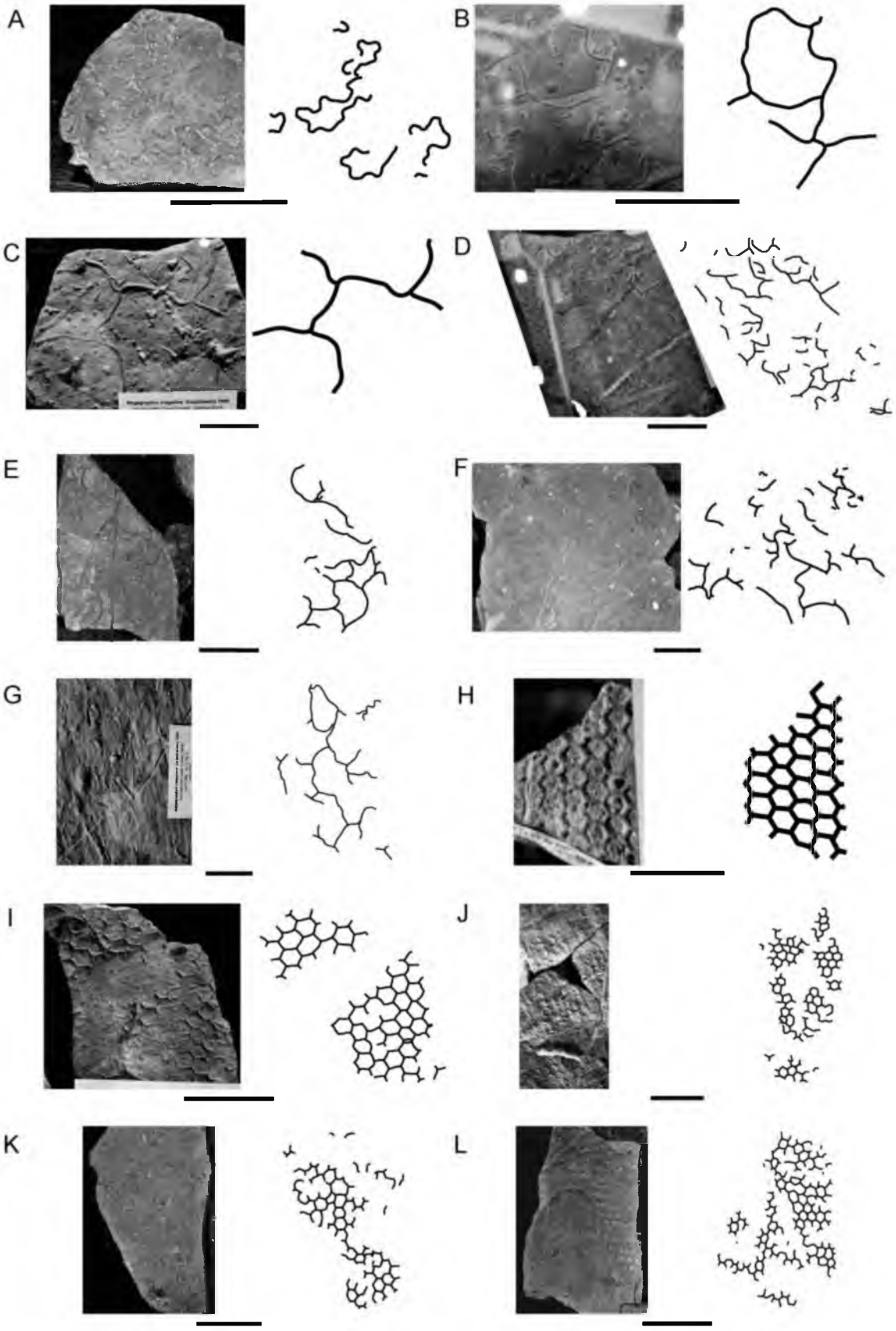
A
B
C
D
E
F
G
H
I
J
K
L

Figure E.9. Eocene trace fossils.
Eocene trace fossils.

A. *Paleodictyon*. Sample UJTF 167. Beloveža Beds, Zubrzyca Górna, Poland (Lower - Middle Eocene). Photographed by J.R. Lehane. Scale = 5 cm. (Originally figured in Książkiewicz, 1977 Plate 28.6 as *Paleodictyon regulare*)
B. *Paleodictyon*. Sample UJTF 168. Beloveža Beds, Lipnica Wielka, Poland (Lower - Middle Eocene). Photographed by J.R. Lehane. Scale = 2 cm. (Originally figured in Książkiewicz, 1977 Plate 27.4 as *Paleodictyon minimum*).
C. *Paleodictyon*. Sample UJTF 171. Beloveža Beds, Lipnica Wielka, Poland (Lower - Middle Eocene). Photographed by J.R. Lehane. Scale = 5 cm.
D. *Paleodictyon*. Sample UJTF 172-1. Beloveža Beds, Zubrzyca Górna, Poland (Lower - Middle Eocene). Photographed by J.R. Lehane. Scale = 2 cm. (Originally figured in Książkiewicz, 1977 Plate 27.5 as *Paleodictyon latum*).
E. *Paleodictyon*. Sample UJTF 172-2. Beloveža Beds, Zubrzyca Górna, Poland (Lower - Middle Eocene). Photographed by J.R. Lehane. Scale = 2 cm.
F. *Paleodictyon*. Sample UJTF 186. Beloveža Beds, Lipnica Mała, Poland (Lower - Middle Eocene). Photographed by J.R. Lehane. Scale = 5 cm. (Originally figured in Książkiewicz, 1977 Plate 28.8 as *Paleodictyon majus*).
G. *Paleodictyon*. Sample UJTF 294. Beloveža Beds, Lubomierz, Poland (Lower - Middle Eocene). Photographed by J.R. Lehane. Scale = 5 cm.
H. *Paleodictyon*. Sample UJTF 305. Beloveža Beds, Lipnica Mała, Poland (Lower - Middle Eocene). Photographed by J.R. Lehane. Scale = 5 cm.
I. *Paleodictyon*. Sample UJTF 894. Beloveža Beds, Berest, Poland (Lower - Middle Eocene). Photographed by J.R. Lehane. Scale = 2 cm. (Originally figured in Książkiewicz, 1977 Plate 27.7 as *Paleodictyon minimum*).
J. *Paleodictyon*. Sample UJTF unk. Beloveža Beds, Zbludza, Poland (Lower - Middle Eocene). Photographed by J.R. Lehane. Scale = 5 cm.
K. *Paleomeandron*. Sample UJTF 231. Beloveža Beds, Lipnica Mała, Poland (Lower - Middle Eocene). Photographed by J.R. Lehane. Scale = 5 cm. (Originally figured in Książkiewicz, 1977 Plate 23.3 as *Paleomeandron robustum*).
L. *Protopaleodictyon*. Sample UJTF 228. Beloveža Beds, Lipnica Mała, Poland (Lower - Middle Eocene). Photographed by J.R. Lehane. Scale = 5 cm.

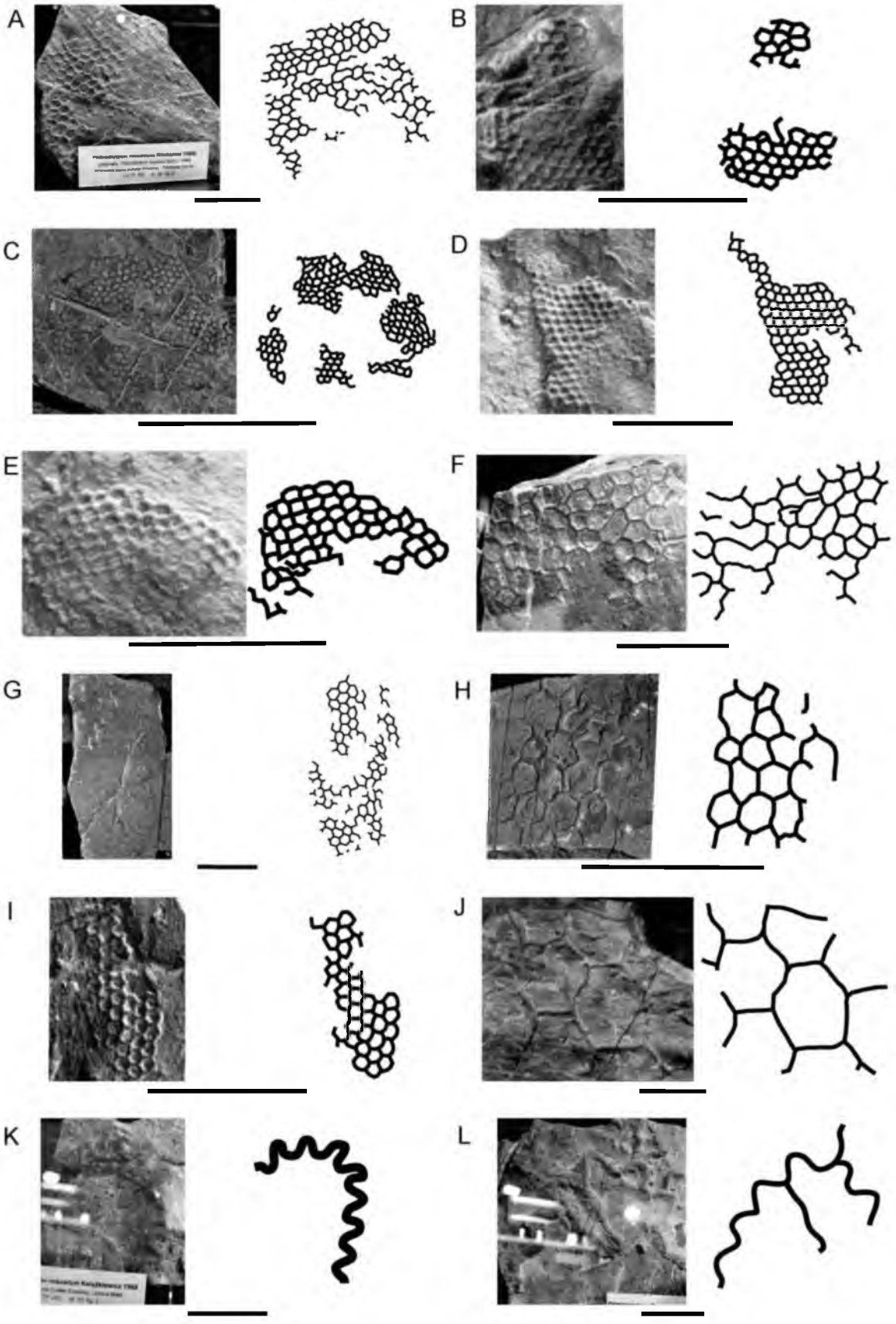
A
B
C
D
E
F
G
H
J
I
J
K
L

Figure E.10. Eocene trace fossils.
Eocene trace fossils.

A. *Protopaleodictyon*. Sample UJTF 454. Beloveža Beds, Zubrzyca Górna, Poland (Lower - Middle Eocene). Photographed by J.R. Lehane. Scale = 5 cm.
B. *Protopaleodictyon*. Sample UJTF 2005. Beloveža Beds, Sidzina, Poland (Lower - Middle Eocene). Photographed by J.R. Lehane. Scale = 5 cm. (Originally figured in Książkiewicz, 1977 Plate 29.4 as *Paleodictyon* aff. *gomezi*).
C. *Urohelminthoida*. Sample UJTF 141. Beloveža Beds, Osielec, Poland (Lower - Middle Eocene). Photographed by J.R. Lehane. Scale = 5 cm. (Originally figured in Książkiewicz, 1977 Plate 26.5 as *Urohelminthoida dertonensis*).
D. *Urohelminthoida*. Sample UJTF 344. Beloveža Beds, Lipnica Wielka, Poland (Lower - Middle Eocene). Photographed by J.R. Lehane. Scale = 5 cm.
E. *Urohelminthoida*. Sample UJTF 352. Beloveža Beds, Sidzina, Poland (Lower - Middle Eocene). Photographed by J.R. Lehane. Scale = 5 cm.
F. *Urohelminthoida*. Sample UJTF 354. Beloveža Beds, Lętownia Górna, Poland (Lower - Middle Eocene). Photographed by J.R. Lehane. Scale = 5 cm.
G. *Urohelminthoida*. Sample UJTF 356. Beloveža Beds, Zubrzyca Górna, Moniaków, Poland (Lower - Middle Eocene). Photographed by J.R. Lehane. Scale = 5 cm.
H. *Urohelminthoida*. Sample UJTF 359. Beloveža Beds, Zubrzyca Górna, Ochlipów, Poland (Lower - Middle Eocene). Photographed by J.R. Lehane. Scale = 5 cm.
I. *Urohelminthoida*. Sample UJTF 360. Beloveža Beds, Zubrzyca Górna, Poland (Lower - Middle Eocene). Photographed by J.R. Lehane. Scale = 5 cm.
J. *Urohelminthoida*. Sample UJTF 722. Beloveža Beds, Szczawa, Poland (Lower - Middle Eocene). Photographed by J.R. Lehane. Scale = 5 cm.
K. *Urohelminthoida*. Sample UJTF 1593. Beloveža Beds, Lipnica Mała, Poland (Lower - Middle Eocene). Photographed by J.R. Lehane. Scale = 5 cm.
L. *Helminthopsis*. Sample UJTF 100. Ciezkowice Sandstone, Znamirowice, Poland (Lower - Middle Eocene). Photographed by J.R. Lehane. Scale = 5 cm.

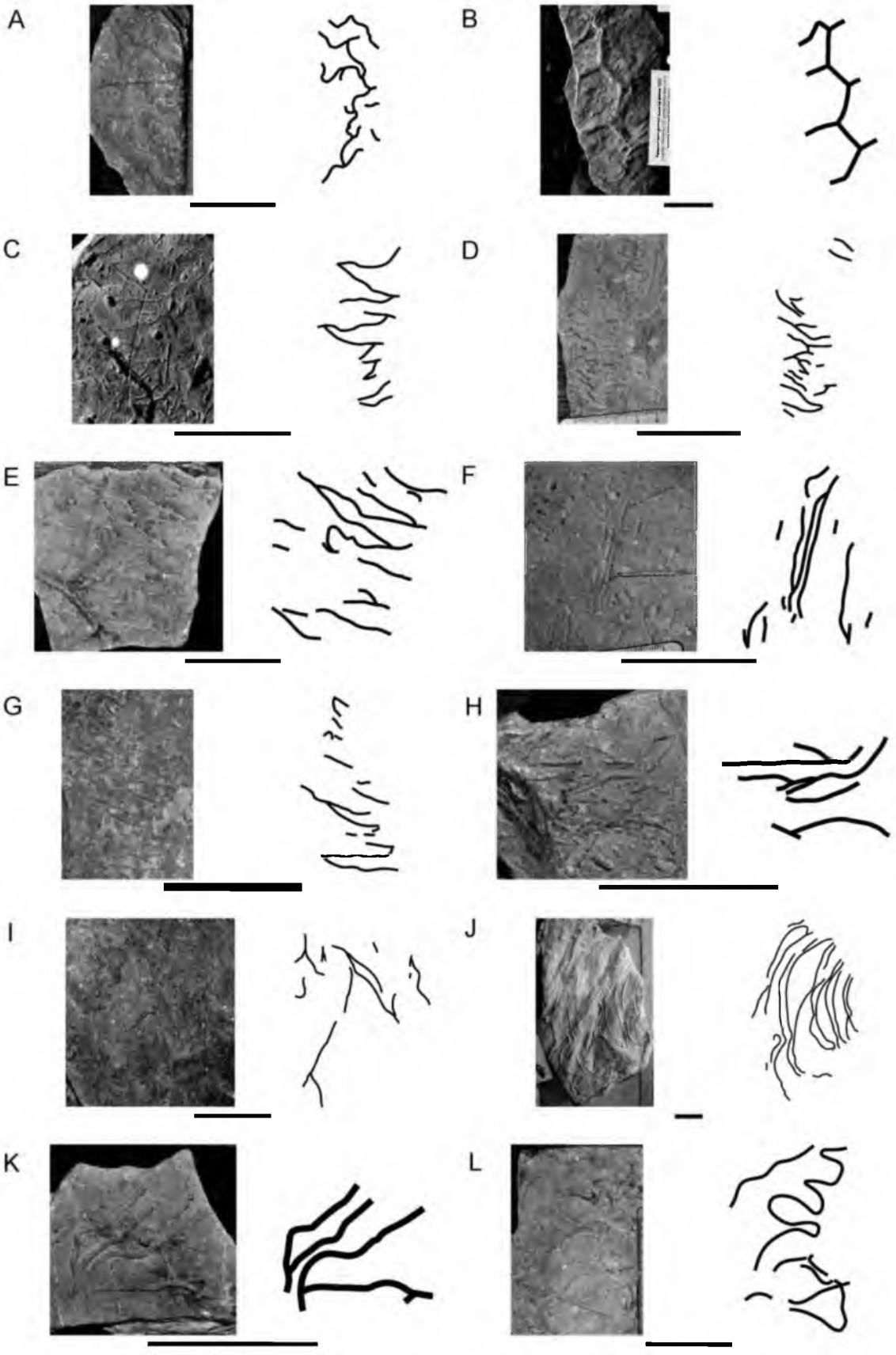
A
B
C
D
E
F
G
H
I
J
K
L

Figure E.11. Eocene trace fossils.
Eocene trace fossils.

A. *Helminthorhaphe.* Sample UJTF 42a. Ciezkowice Sandstone, Grodek, Poland (Lower - Middle Eocene). Photographed by J.R. Lehane. Scale = 5 cm.
B. *Helminthorhaphe*. Sample UJTF 104. Ciezkowice Sandstone, Znamirowice, Poland (Lower - Middle Eocene). Photographed by J.R. Lehane. Scale = 5 cm. (Originally figured in Książkiewicz, 1977 Plate 21.8 as *Helminthoida crassa*).
C. *Helminthorhaphe.* Sample UJTF 426. Ciezkowice Sandstone, Grodek, Poland (Lower - Middle Eocene). Photographed by J.R. Lehane. Scale = 5 cm.
D. *Oscillorhaphe*. Sample UJTF 144. Ciezkowice Sandstone, Znamirowice, Poland (Lower - Middle Eocene). Photographed by J.R. Lehane. Scale = 5 cm. (Originally figured in Książkiewicz, 1977 Plate 26.6 as *Urohelminthoida* aft. *dertonensis*).
E. *Paleodictyon.* Sample UJTF 78. Ciezkowice Sandstone, Znamirowice, Poland (Lower - Middle Eocene). Photographed by J.R. Lehane. Scale = 5 cm. (Originally figured in Książkiewicz, 1977 Plate 27.17 as *Paleodictyon intermedium*).
F. *Paleodictyon.* Sample UJTF 89. Ciezkowice Sandstone, Znamirowice, Poland (Lower - Middle Eocene). Photographed by J.R. Lehane. Scale = 2 cm.
G. *Paleodictyon.* Sample UJTF 101. Ciezkowice Sandstone, Znamirowice, Poland (Lower - Middle Eocene). Photographed by J.R. Lehane. Scale = 2 cm. (Originally figured in Książkiewicz, 1977 Plate 27.15 as *Paleodictyon intermedium*).
H. *Paleodictyon.* Sample UJTF 113. Ciezkowice Sandstone, Znamirowice, Poland (Lower - Middle Eocene). Photographed by J.R. Lehane. Scale = 5 cm. (Originally figured in Książkiewicz, 1977 Plate 29.3 as *Paleodictyon regulare*).
I. *Protopaleodictyon.* Sample UJTF 343. Ciezkowice Sandstone, Jaworki, p.Skalny, Poland (Lower - Middle Eocene). Photographed by J.R. Lehane. Scale = 5 cm.
J. *Spirorhaphe.* Sample UJTF 211. Ciezkowice Sandstone, Grodek, Poland (Lower - Middle Eocene). Photographed by J.R. Lehane. Scale = 5 cm.
K. *Spirorhaphe.* Sample UJTF 552. Ciezkowice Sandstone, Grodek, Poland (Lower - Middle Eocene). Photographed by J.R. Lehane. Scale = 5 cm. (Originally figured in Książkiewicz, 1977 Plate 18.2 as *Spirorhaphe involuta*).
L. *Spirorhaphe.* Sample UJTF 1519. Ciezkowice Sandstone, Grodek, Poland (Lower - Middle Eocene). Photographed by J.R. Lehane. Scale = 5 cm. (Originally figured in Książkiewicz, 1977 Plate 18.1 as *Spirorhaphe involuta*).

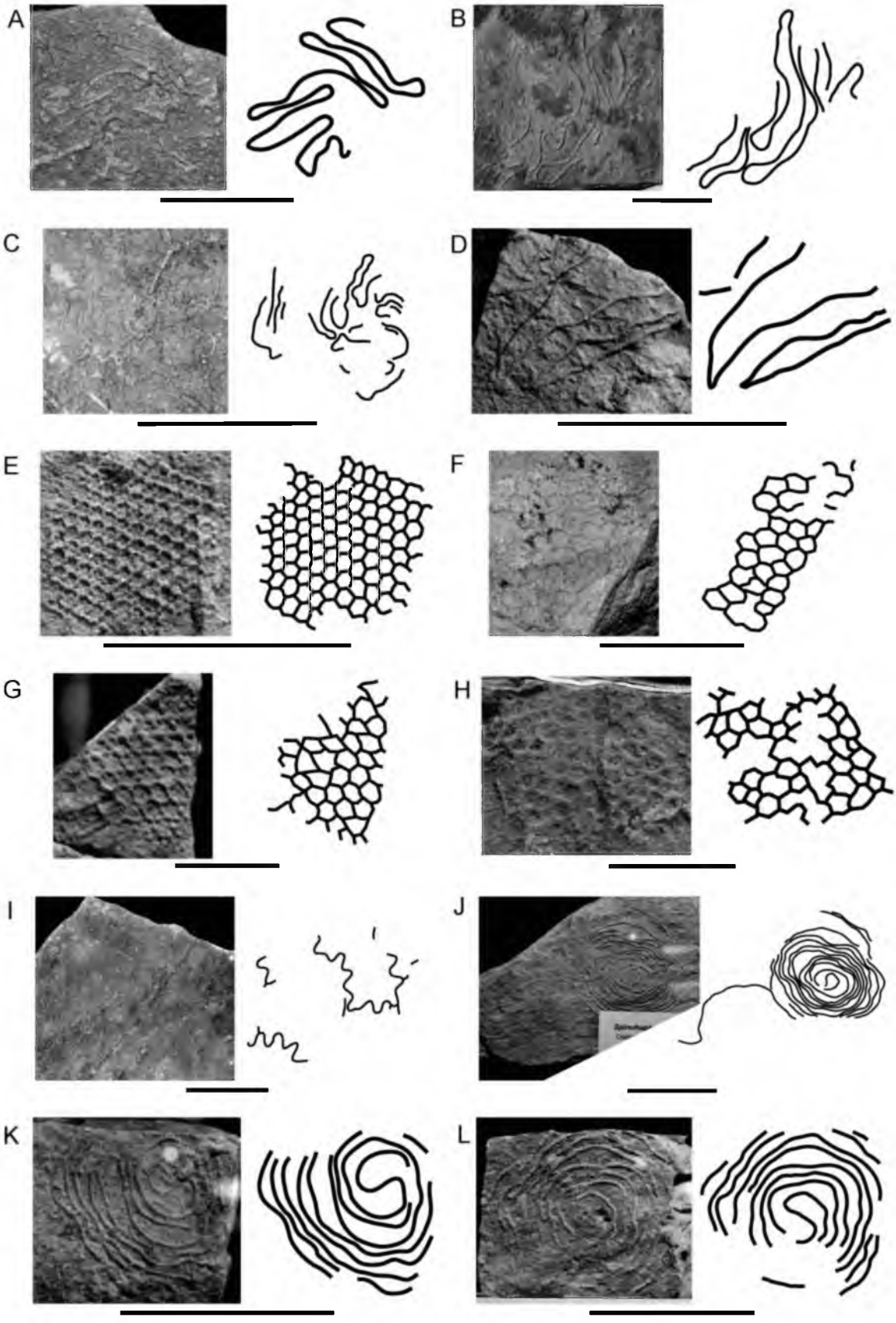
A
B
C
D
E
F
G
H
I
J
K
L

Figure E.12. Eocene trace fossils.

Eocene trace fossils.

A. *Spirocosmorhaphe.* Sample UJTF 149P3. Flysch del Grivo, Vernasso Quarry, NE Italy (Upper Paleocene - Lower Eocene). Photographed by J.R. Lehane. Scale = 2 cm. (Originally figured in Tunis and Uchman, 1992 Fig. 7F as *Spirocosmorhaphe helicoidea*).
B. *Cosmorhaphe.* Sample UJTF 1607. Ganei Slate, Near Seewis, Switzerland (Eocene). Photographed by J.R. Lehane. Scale = 2 cm.
C. *Protopaleodictyon.* Sample UJTF 1597. Ganei Slate, Near Seewis, Switzerland (Eocene). Photographed by J.R. Lehane. Scale = 5 cm.
D. *Cosmorhaphe.* Sample UJTF 10. Hieroglyphic Beds, Lesna k.Żywca, Poland (Middle Eocene). Photographed by J.R. Lehane. Scale = 2 cm.
E. *Gordia.* Sample UJTF 1249. Hieroglyphic Beds, Juszczyn, Poland (Middle Eocene). Photographed by J.R. Lehane. Scale = 5 cm. (Originally figured in Książkiewicz, 1977 Plate 20.7 as *Gordia molassica*).
F. *Helminthorhaphe.* Sample UJTF 44. Hieroglyphic Beds, Grzechynia, Poland (Middle Eocene). Photographed by J.R. Lehane. Scale = 5 cm.
G. *Helminthorhaphe.* Sample UJTF 45. Hieroglyphic Beds, Dąbrówka k.Skawiec, Poland (Middle Eocene). Photographed by J.R. Lehane. Scale = 5 cm.
H. *Helminthorhaphe.* Sample UJTF 788. Hieroglyphic Beds, Tokarnia, Poland (Middle Eocene). Figured in Uchman, 1998 Fig. 107. Scale = 5 cm. (Originally identified as *Helminthoida crassa*). Reprinted from Uchman, A., 1998, Taxonomy and ethology of flysch trace fossils: Revision of the Marian Książkiewicz collection and studies of complementary material, Annales Societatis Geologorum Poloniae, v. 68, pp.105-218, with permission from the Polish Geological Society.
I. *Megagrapton.* Sample UJTF 793. Hieroglyphic Beds, Tokarnia, Poland (Middle Eocene). Photographed by J.R. Lehane. Scale = 5 cm. (Originally figured in Książkiewicz, 1977 Plate 25.1 as *Protopaleodictyon submontanum*).
J. *Paleodictyon.* Sample UJTF 63. Hieroglyphic Beds, Istebna, dol.Olzy, Poland (Middle Eocene). Photographed by J.R. Lehane. Scale = 5 cm.
K. *Paleodictyon.* Sample UJTF 157. Hieroglyphic Beds, Osielec, Poland (Middle Eocene). Photographed by J.R. Lehane. Scale = 5 cm. (Originally figured in Książkiewicz, 1977 Plate 28.2 as *Paleodictyon strozzi*).
L. *Paleodictyon.* Sample UJTF 159. Hieroglyphic Beds, Tylmanowa, Poland (Middle Eocene). Photographed by J.R. Lehane. Scale = 5 cm.

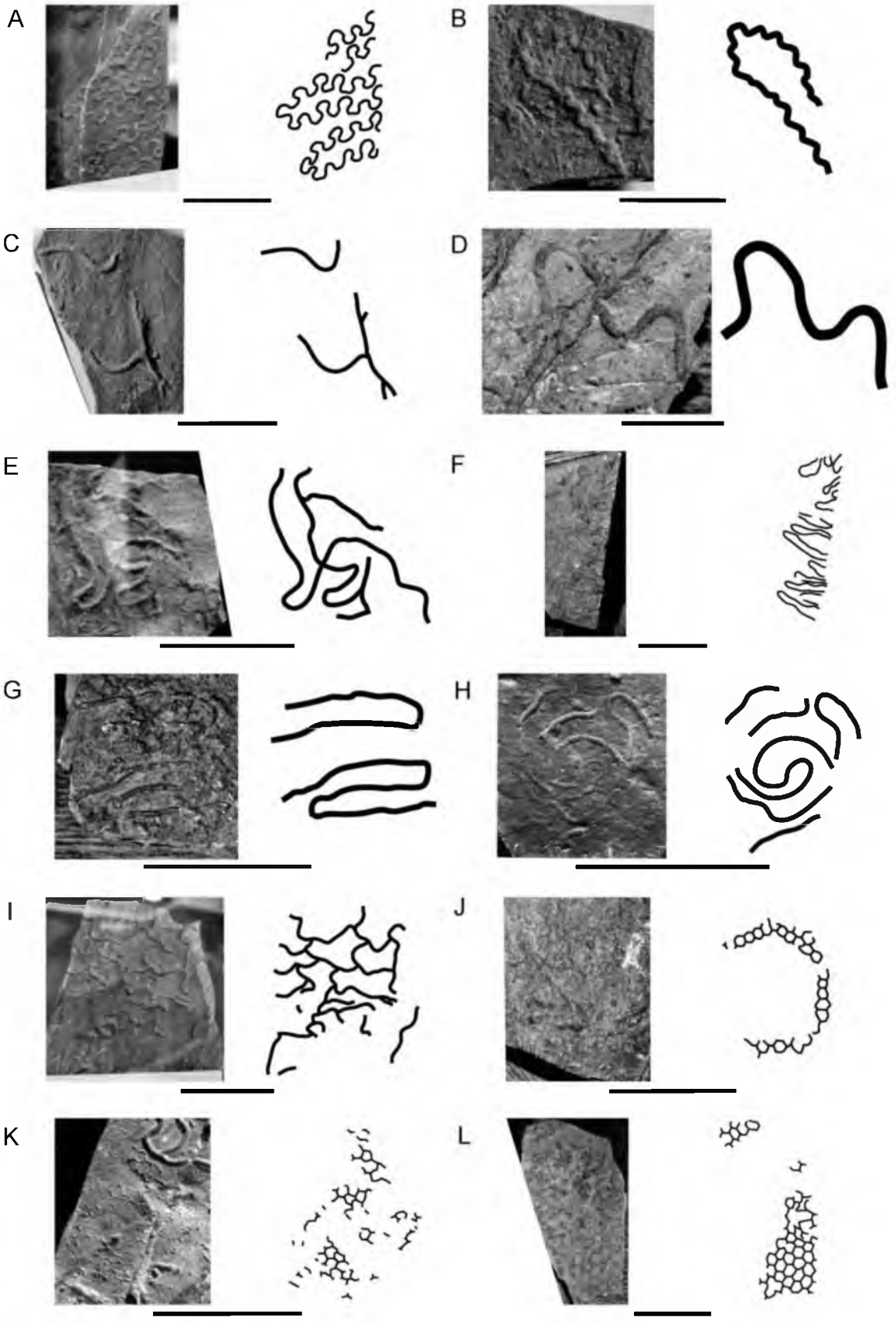
A
B
C
D
E
F
G
H
I
J
K
L

Figure E.13. Eocene trace fossils.

Eocene trace fossils.

A. *Paleodictyon.* Sample UJTF 304. Hieroglyphic Beds, Koninka k.Mszany Dolnej, Poland (Middle Eocene). Photographed by J.R. Lehane. Scale = 5 cm.
B. *Paleodictyon.* Sample UJTF 323. Hieroglyphic Beds, Lesna k.Żywca, Poland (Middle Eocene). Photographed by J.R. Lehane. Scale = 5 cm.
C. *Paleomeandron.* Sample UJTF 138. Hieroglyphic Beds, Grzechynia, Poland (Middle Eocene). Photograph courtesy of Waldemar Obcowski. Scale = 5 cm. (Originally figured in Książkiewicz, 1977 Plate 23.2 as *Paleomeandron rude*)
D. *Protopaleodictyon.* Sample UJTF 130. Hieroglyphic Beds, Osielec, Poland (Middle Eocene). Photographed by J.R. Lehane. Scale = 5 cm. (Originally figured in Książkiewicz, 1977 Plate 24.4 as *Protopaleodictyon incompositum*).
E. *Protopaleodictyon.* Sample UJTF 338. Hieroglyphic Beds, Jordanow, Poland (Middle Eocene). Photographed by J.R. Lehane. Scale = 5 cm.
F. *Protopaleodictyon.* Sample UJTF 342. Hieroglyphic Beds, Jordanow, g.Przykrzec, Poland (Middle Eocene). Photographed by J.R. Lehane. Scale = 5 cm. (Originally figured in Uchman, 1998 Fig. 100B as *Protopaleodictyon incompositum*).
G. *Protopaleodictyon.* Sample UJTF 763. Hieroglyphic Beds, Munkacz k.Jordanowa, Poland (Middle Eocene). Photographed by J.R. Lehane. Scale = 5 cm.
H. *Protopaleodictyon.* Sample UJTF 900. Hieroglyphic Beds, Osielec, Poland (Middle Eocene). Photographed by J.R. Lehane. Scale = 5 cm.
I. *Protopaleodictyon.* Sample UJTF 1121. Hieroglyphic Beds, Kamionka Wielka, Poland (Middle Eocene). Photographed by J.R. Lehane. Scale = 5 cm.
J. *Protopaleodictyon.* Sample UJTF 1483. Hieroglyphic Beds, Letowaia Gorna, Poland (Middle Eocene). Photographed by J.R. Lehane. Scale = 5 cm.
K. *Protopaleodictyon.* Sample UJTF 1484. Hieroglyphic Beds, Osielec, Poland (Middle Eocene). Photographed by J.R. Lehane. Scale = 5 cm. (Originally figured in Książkiewicz, 1977 Plate 24.3 as *Protopaleodictyon incompositum*).
L. *Belorhaphe*. Sample UJTF 1442. Lącko Beds, Zubrzyca Górna, Poland (Middle Eocene). Photographed by J.R. Lehane. Scale = 5 cm. (Originally figured in Książkiewicz, 1977 Plate 24.2 as *Belorhaphe zickzack*).

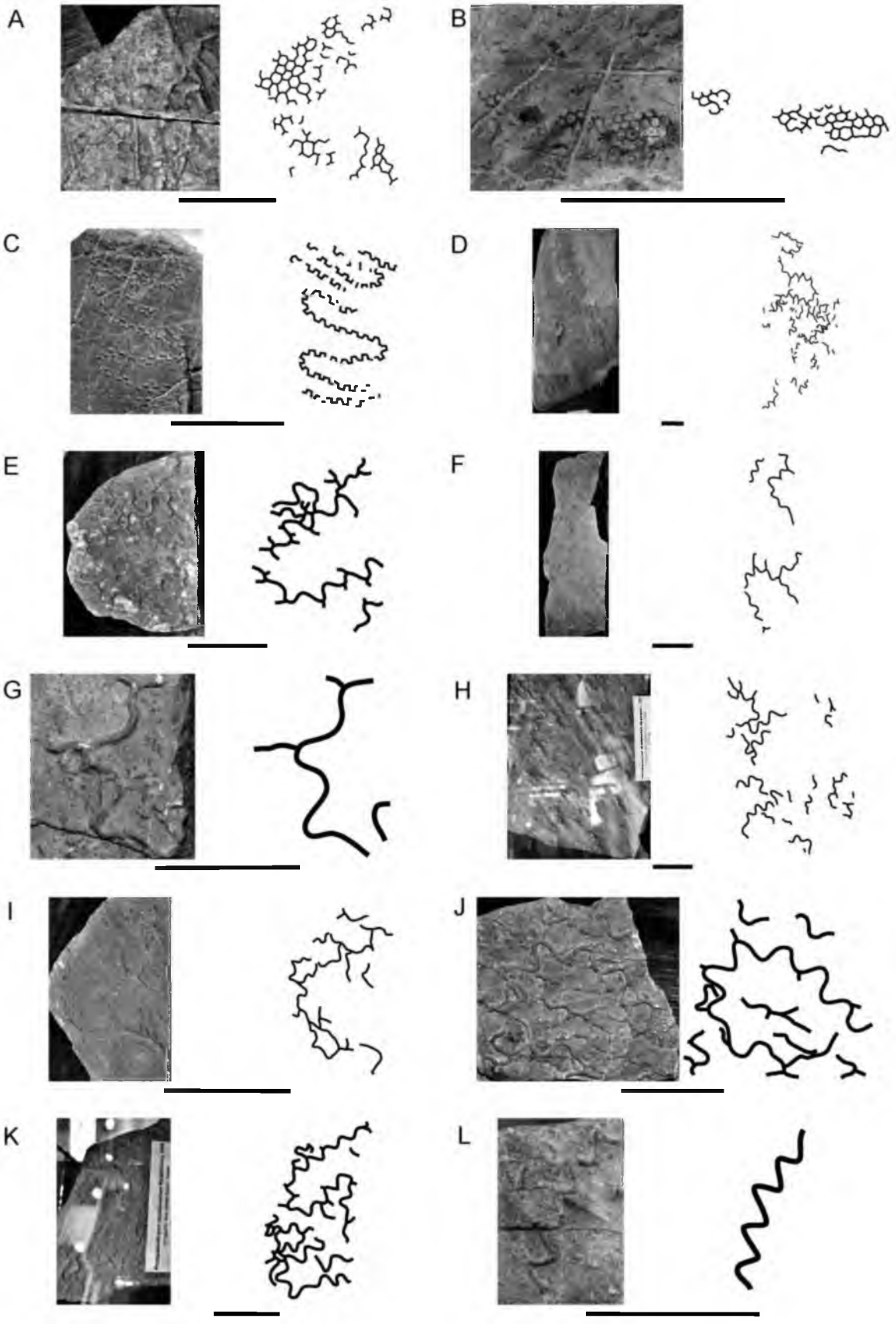
A
B
C
D
E
F
G
H
I
J
K
L

Figure E.14. Eocene trace fossils.
Eocene trace fossils.

A. *Cosmorhaphe*. Sample UJTF 243. Lącko Beds, Zubrzyca Górna, Poland (Middle Eocene). Photographed by J.R. Lehane. Scale = 5 cm. (Originally figured in Książkiewicz, 1977 Plate 19.7 as *Cosmorhaphe fuchsi*).
B. *Megagrapton.* Sample UJTF 985. Lącko Beds, Myślec, Poland (Middle Eocene). Photographed by J.R. Lehane. Scale = 5 cm. (Originally figured in Książkiewicz, 1977 Plate 25.8 as *Megagrapton irregulare*).
C. *Paleomeandron.* Sample UJTF 229. Lącko Beds, Podwilk, Poland (Middle Eocene). Photographed by J.R. Lehane. Scale = 5 cm.
D. *Belocosmorhaphe.* Sample UJTF 121. Magura Sandstone, Marcówka, Poland (Lower - Middle Eocene). Photographed by J.R. Lehane. Scale = 5 cm. (Originally figured in Książkiewicz, 1977 Plate 24.5 as *Protopaleodictyon minutum*).
E. *Belocosmorhaphe.* Sample UJTF 334a. Magura Sandstone, Marcówka, Poland (Lower - Middle Eocene). Photographed by J.R. Lehane. Scale = 5 cm.
F. *Protopaleodictyon.* Sample UJTF 171P4. Magura Sandstone, Mniszek Member, Konina, Poland (Lower - Middle Eocene). Photographed by J.R. Lehane. Scale = 5 cm.
G. *Protopaleodictyon.* Sample UJTF 334b. Magura Sandstone, Marcówka k.Suchej, Poland (Lower - Middle Eocene). Photographed by J.R. Lehane. Scale = 5 cm.
H. *Paleodictyon*. Sample UUIC 109. Punta Carnero Formation, Isla de Margarita, Venezuela (Lower – Middle Eocene). Photographed by J.R. Lehane. Scale = 5 cm.
I. *Helminthorhaphe.* Sample UJTF 750. Szczawnica Formation, Krościenko, Poland (Upper Paleocene -Lower Eocene). Photographed by J.R. Lehane. Scale = 5 cm. (Originally figured in Książkiewicz, 1977 Plate 21.6 as *Helminthoida crassa*).
J. *Paleodictyon.* Sample UJTF 749. Szczawnica Formation, Krościenko, Poland (Upper Paleocene -Lower Eocene). Photographed by J.R. Lehane. Scale = 5 cm.
K. *Urohelminthoida.* Sample UJTF 1599. Szczawnica Formation, Krościenko, Poland (Upper Paleocene -Lower Eocene). Photographed by J.R. Lehane. Scale = 5 cm. (Originally figured in Książkiewicz, 1977 Plate 26.4 as *Urohelminthoida dertonensis*).
L. *Helminthorhaphe*. Sample UJTF unk. Zumaia Flysch, Zumaia, Spain (Ypresian). Photographed by J.R. Lehane. Scale = 5 cm.

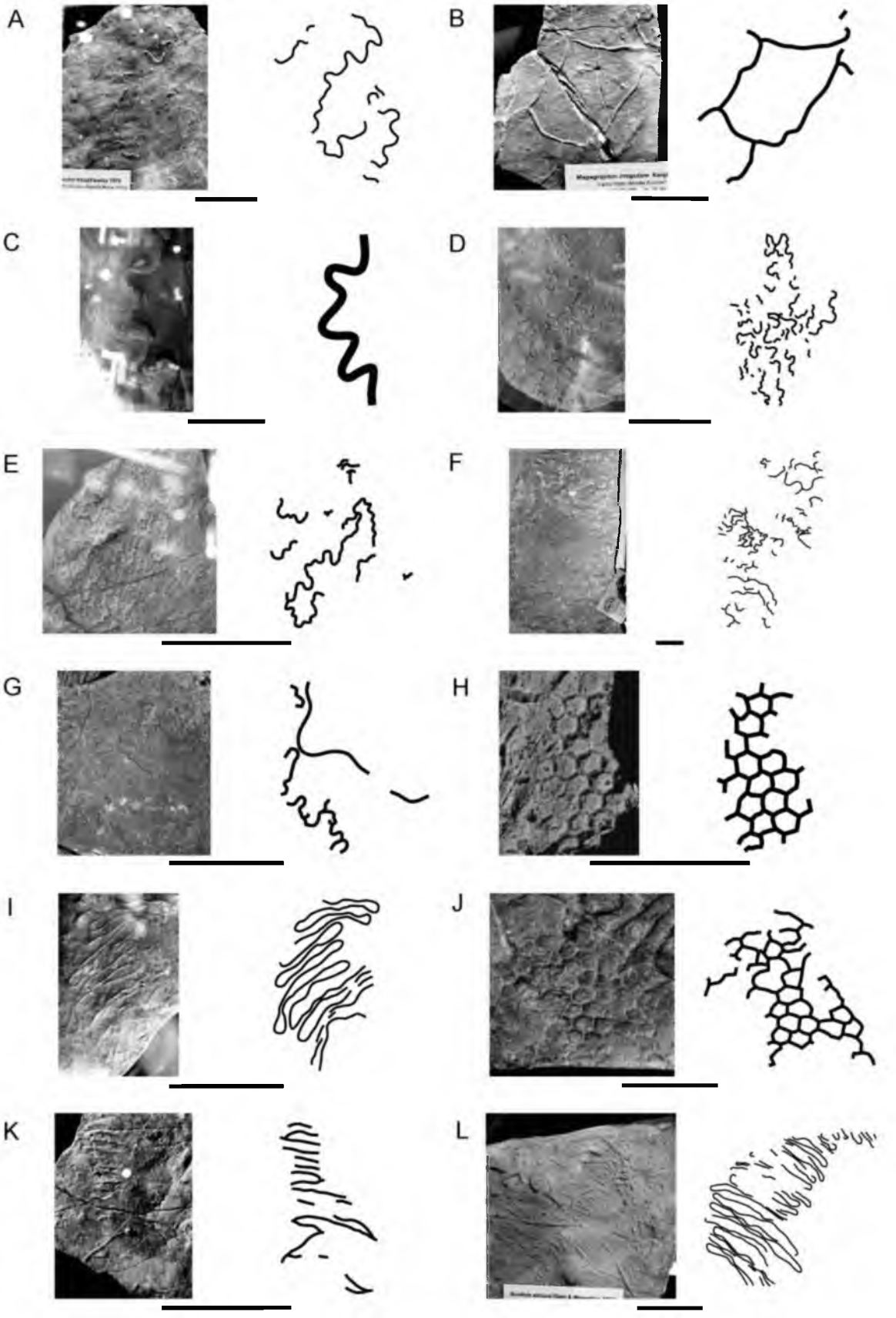
A
B
C
D
E
F
G
H
I
J
K
L

Figure E.15. Eocene trace fossils.
Eocene trace fossils.

A. *Helminthorhaphe*. Sample UUIC 429. Zumaia Flysch, Roadcut west of Zumaia, Spain (Ypresian). Photographed by J.R. Lehane. Scale = 5 cm.
B. *Paleodictyon.* Sample UUIC 428. Zumaia Flysch, Roadcut west of Zumaia, Spain (Ypresian). Photographed by J.R. Lehane. Scale = 5 cm.
C. *Cosmorhaphe.* Sample Z_Cos1. Zumaia Flysch, Road Cut 2, west of Zumaia, Spain (Ypresian). Photographed by J.R. Lehane. Scale = 5 cm.
D. *Cosmorhaphe.* Sample Z_Cos2. Zumaia Flysch, Road Cut 2, west of Zumaia, Spain (Ypresian). Photographed by J.R. Lehane. Scale = 5 cm.
E. *Cosmorhaphe.* Sample Z_Cos3. Zumaia Flysch, Road Cut 2, west of Zumaia, Spain (Ypresian). Photographed by J.R. Lehane. Scale = 5 cm.
F. *Cosmorhaphe.* Sample Z_Cos4. Zumaia Flysch, Road Cut 2, west of Zumaia, Spain (Ypresian). Photographed by J.R. Lehane. Scale = 5 cm.
G. *Cosmorhaphe.* Sample Z_Cos5. Zumaia Flysch, Road Cut 2, west of Zumaia, Spain (Ypresian). Photographed by J.R. Lehane. Scale = 5 cm.
H. *Helminthorhaphe.* Sample Z_Helmin1. Zumaia Flysch, Road Cut 2, west of Zumaia, Spain (Ypresian). Photographed by J.R. Lehane. Scale = 5 cm.
I. *Helminthorhaphe.* Sample Z_Helmin2. Zumaia Flysch, Road Cut 2, west of Zumaia, Spain (Ypresian). Photographed by J.R. Lehane. Scale = 5 cm.
J. *Helminthorhaphe.* Sample Z_Helmin3. Zumaia Flysch, Road Cut 2, west of Zumaia, Spain (Ypresian). Photographed by J.R. Lehane. Scale = 5 cm.
K. *Helminthorhaphe.* Sample Z_Helmin4. Zumaia Flysch, Road Cut 2, west of Zumaia, Spain (Ypresian). Photographed by J.R. Lehane. Scale = 2 cm.
L. *Helminthorhaphe.* Sample Z_Helmin5. Zumaia Flysch, Road Cut 2, west of Zumaia, Spain (Ypresian). Photographed by J.R. Lehane. Scale = 5 cm.

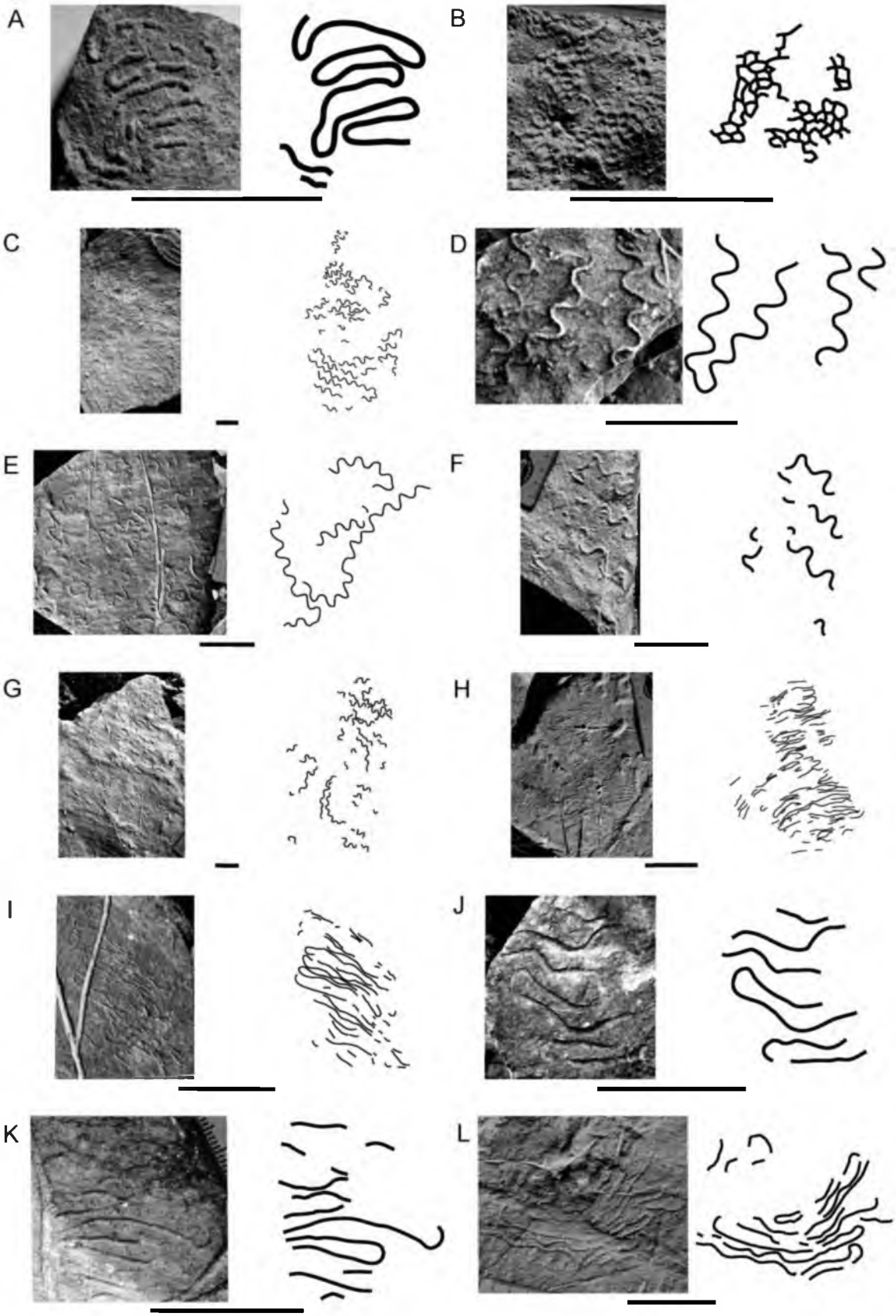
A
B
C
D
E
F
G
H
I
J
K
L

Figure E.16. Eocene trace fossils.
Eocene trace fossils.

A. *Megagrapton.* Sample Z_Mega1. Zumaia Flysch, Road Cut 2, west of Zumaia, Spain (Ypresian). Photographed by J.R. Lehane. Scale = 5 cm.
B. *Megagrapton.* Sample Z_Mega2. Zumaia Flysch, Road Cut 2, west of Zumaia, Spain (Ypresian). Photographed by J.R. Lehane. Scale = 5 cm.
C. *Megagrapton.* Sample Z_Mega3. Zumaia Flysch, Road Cut 2, west of Zumaia, Spain (Ypresian). Photographed by J.R. Lehane. Scale = 5 cm.
D. *Megagrapton.* Sample Z_Mega4. Zumaia Flysch, Road Cut 2, west of Zumaia, Spain (Ypresian). Photographed by J.R. Lehane. Scale = 5 cm.
E. *Megagrapton.* Sample Z_Mega5. Zumaia Flysch, Road Cut 2, west of Zumaia, Spain (Ypresian). Photographed by J.R. Lehane. Scale = 5 cm.
F. *Megagrapton.* Sample Z_Mega6. Zumaia Flysch, Road Cut 2, west of Zumaia, Spain (Ypresian). Photographed by J.R. Lehane. Scale = 5 cm.
G. *Megagrapton.* Sample Z_Mega7. Zumaia Flysch, Road Cut 2, west of Zumaia, Spain (Ypresian). Photographed by J.R. Lehane. Scale = 5 cm.
H. *Paleodictyon.* Sample Z_Paleo1. Zumaia Flysch, Road Cut 2, west of Zumaia, Spain (Ypresian). Photographed by J.R. Lehane. Scale = 5 cm.
I. *Paleodictyon.* Sample Z_Paleo2. Zumaia Flysch, Road Cut 2, west of Zumaia, Spain (Ypresian). Photographed by J.R. Lehane. Scale = 2 cm.
J. *Paleodictyon.* Sample Z_Paleo3. Zumaia Flysch, Road Cut 2, west of Zumaia, Spain (Ypresian). Photographed by J.R. Lehane. Scale = 2 cm.
K. *Paleodictyon.* Sample Z_Paleo4. Zumaia Flysch, Road Cut 2, west of Zumaia, Spain (Ypresian). Photographed by J.R. Lehane. Scale = 5 cm.
L. *Paleodictyon.* Sample Z_Paleo5. Zumaia Flysch, Road Cut 2, west of Zumaia, Spain (Ypresian). Photographed by J.R. Lehane. Scale = 5 cm.

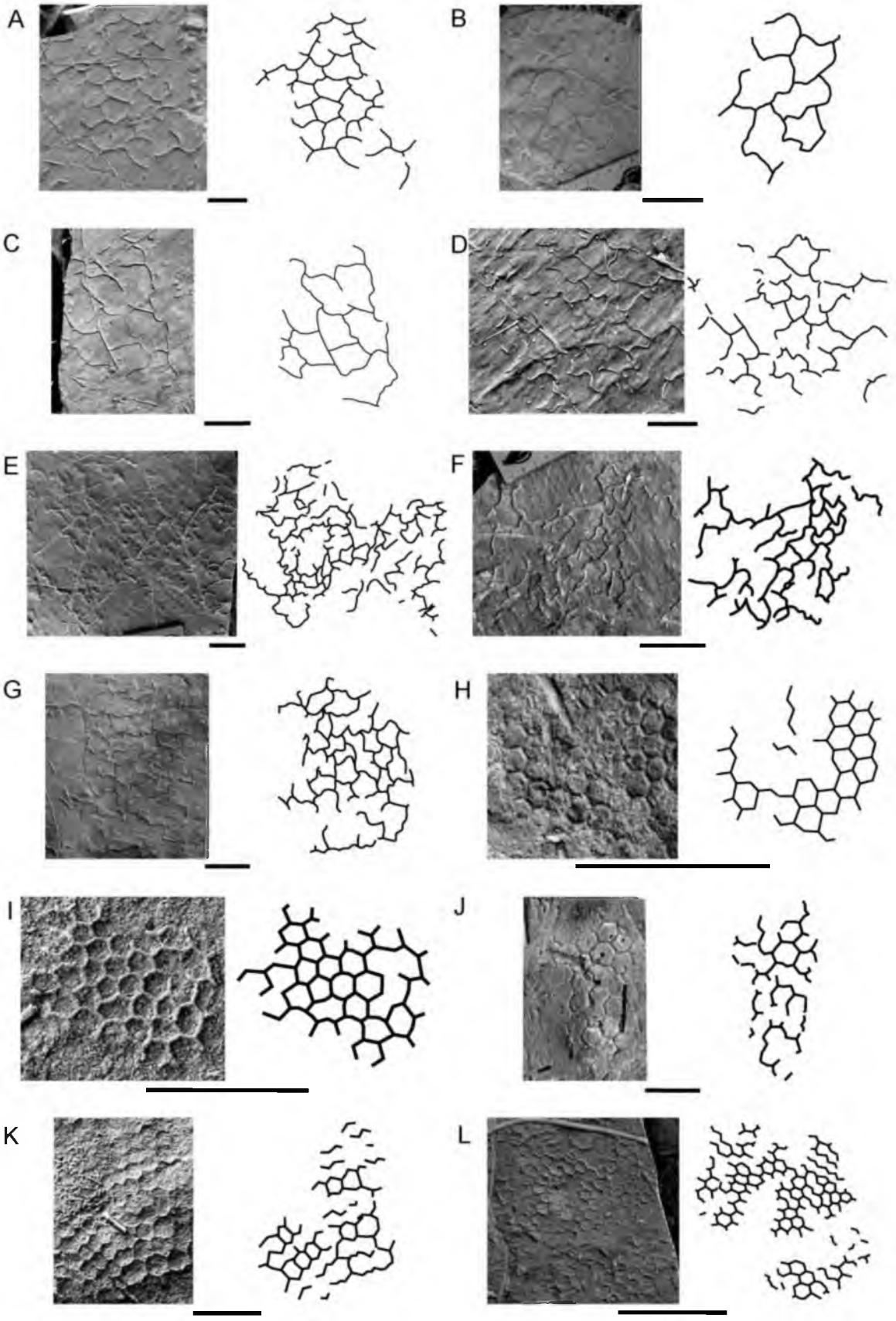
A
B
C
D
E
F
G
H
I
J
K
L

Figure E.17. Eocene and Paleocene trace fossils.
Eocene trace fossils.

A. *Paleomeandron.* Sample Z_Paleomeandron1. Zumaia Flysch, Road Cut 2, west of Zumaia, Spain (Ypresian). Photographed by J.R. Lehane. Scale = 5 cm.
B. *Spirorhaphe.* Sample Z_Spiror1. Zumaia Flysch, Road Cut 2, west of Zumaia, Spain (Ypresian). Photographed by J.R. Lehane. Scale = 5 cm.
C. *Spirorhaphe.* Sample Z_Spiror2. Zumaia Flysch, Road Cut 2, west of Zumaia, Spain (Ypresian). Photographed by J.R. Lehane. Scale = 5 cm.
D. *Spirorhaphe.* Sample Z_Spiror3. Zumaia Flysch, Road Cut 2, west of Zumaia, Spain (Ypresian). Photographed by J.R. Lehane. Scale = 5 cm.
E. *Spirorhaphe.* Sample Z_Spiror4. Zumaia Flysch, Road Cut 2, west of Zumaia, Spain (Ypresian). Photographed by J.R. Lehane. Scale = 5 cm.
F. *Spirorhaphe.* Sample Z_Spiror5. Zumaia Flysch, Road Cut 2, west of Zumaia, Spain (Ypresian). Photographed by J.R. Lehane. Scale = 5 cm.
G. *Urohelminthoida.* Sample Z_Urohelm1. Zumaia Flysch, Road Cut 2, west of Zumaia, Spain (Ypresian). Photographed by J.R. Lehane. Scale = 5 cm.
H. *Urohelminthoida.* Sample Z_Urohelm2. Zumaia Flysch, Road Cut 2, west of Zumaia, Spain (Ypresian). Photographed by J.R. Lehane. Scale = 5 cm.

Paleocene trace fossils.

I. *Helminthorhaphe*. Sample UJTF 1403. Gorzen Beds, Gorzen Gorny, Poland (Upper Paleocene). Photographed by J.R. Lehane. Scale = 5 cm. (Originally figured in Książkiewicz, 1977 Plate 21.10 as *Helminthoida miocenica*).
J. *Cosmorhaphe*. Sample 154P40. Greifensteiner Schichten, Greifenstein Quarry, Austria (Thanetian – Ypresian). Figured in Uchman, 1999 Plate 19 Fig. 4. Scale = 5 cm. (Originally identified as *Cosmorhaphe gracilis*). Reprinted from Uchman, A., 1999, Ichnology of the Rhenodanubian Flysch (Lower Cretaceous-Eocene) in Austria and Germany, Beringeria, v. 25, pp.67-173, with permission.
K. *Spirorhaphe*. Sample 154P39. Greifensteiner Schichten, Greifenstein Quarry, Austria (Thanetian – Ypresian). Figured in Uchman, 1999 Plate 17 Fig. 7. Scale = 5 cm. (Originally identified as *Spirohaphe involuta*). Reprinted from Uchman, A., 1999, Ichnology of the Rhenodanubian Flysch (Lower Cretaceous-Eocene) in Austria and Germany, Beringeria, v. 25, pp.67-173, with permission.
L. *Cosmorhaphe*. Sample UUIC 1723. Guarico Formation, Roadcut west of Baco de Uchire, Venezuela (Paleocene). Photographed by J.R. Lehane. Scale = 5 cm.

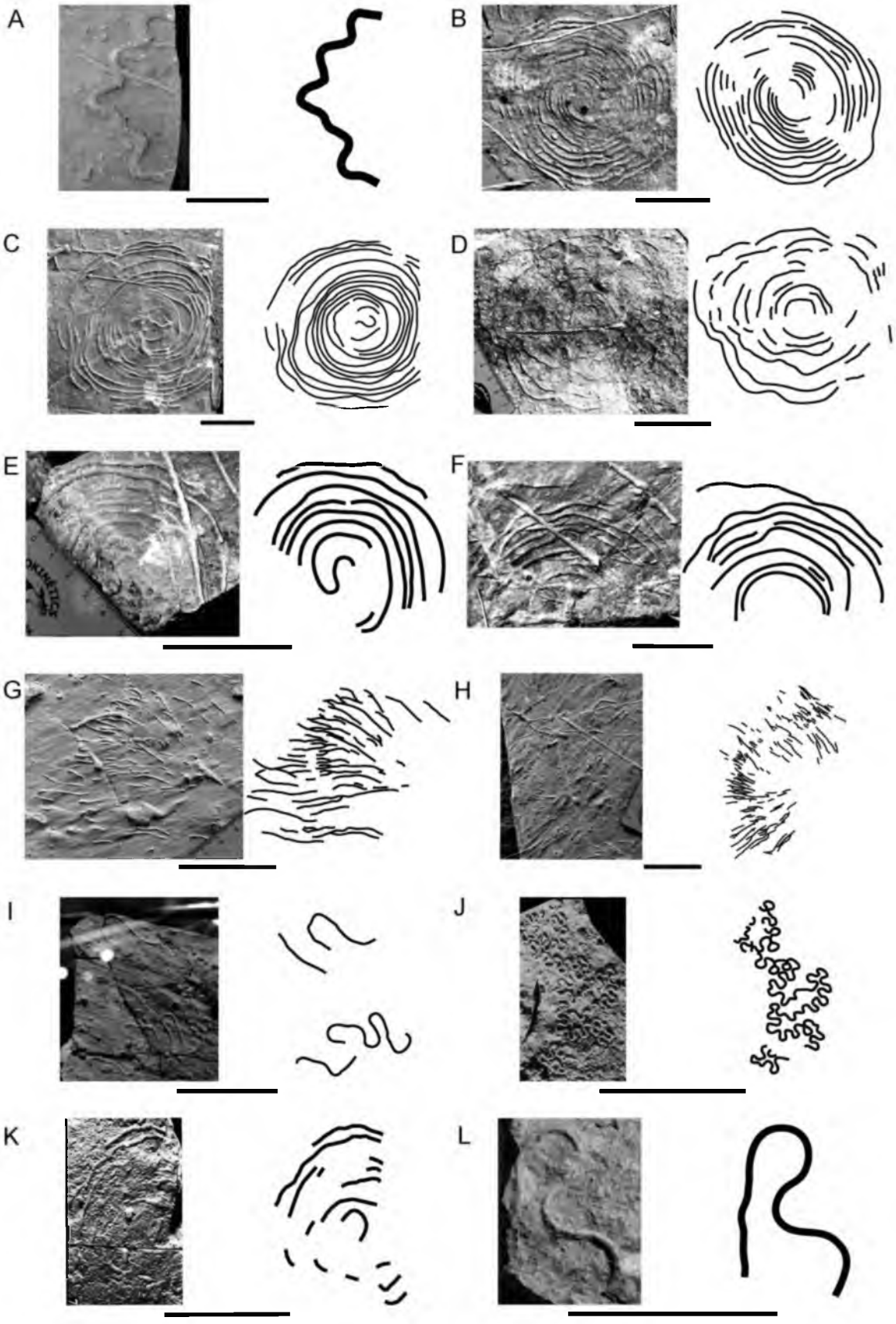
A
B
C
D
E
F
G
H
I
J
K
L

Figure E.18. Paleocene trace fossils.
Paleocene trace fossils.

A. *Spirorhaphe*. Sample Muñoz and Buatois, 2001 Fig. 2. Guárico Formation, Roadcut west of Baco de Uchire, Venezuela (Paleocene). Photographed by L. Buatois. Scale = 5 cm. (Originally figured in Muñoz and Buatois, 2001 Fig. 2 as *Spirorhaphe*).
B. *Spirorhaphe*. Sample UUIC 1721. Guárico Formation, Roadcut west of Baco de Uchire, Venezuela (Paleocene). Photographed by J.R. Lehane. Scale = 5 cm.
C. *Spirorhaphe*. Sample UUIC 1722. Guárico Formation, Roadcut west of Baco de Uchire, Venezuela (Paleocene). Photographed by J.R. Lehane. Scale = 5 cm.
D. *Helminthorhaphe*. Sample UJTF 46. Istebna Beds, Tabaszowa n/Dunajcem, Poland (Early Paleocene). Photographed by J.R. Lehane. Scale = 5 cm.
E. *Urohelminthoida*. Sample UJTF 348. Istebna Beds, Tabaszowa n/Dunajcem, Poland (Early Paleocene). Photographed by J.R. Lehane. Scale = 5 cm.
F. *Cosmorhaphe*. Sample UJTF 19. Variegated Shale, Osielec, Poland (Upper Paleocene - Lower Eocene). Photographed by J.R. Lehane. Scale = 5 cm.
G. *Cosmorhaphe*. Sample UJTF 74. Variegated Shale, Lipnica Wielka, Poland (Upper Paleocene - Lower Eocene). Photographed by J.R. Lehane. Scale = 5 cm. (Originally figured in Książkiewicz, 1977 Plate 19.5 as *Cosmorhaphe sinuosa*)
H. *Cosmorhaphe*. Sample UJTF 1451. Variegated Shale, Zubrzyca Górna, Poland (Upper Paleocene - Lower Eocene). Photographed by J.R. Lehane. Scale = 5 cm.
I. *Cosmorhaphe*. Sample UJTF 2684. Variegated Shale, Lipnica Wielka, Poland (Upper Paleocene - Lower Eocene). Photographed by J.R. Lehane. Scale = 5 cm. (Originally figured in Książkiewicz, 1977 Plate 19.3 as *Cosmorhaphe sinuosa.* Listed as UJ TF 244.).
J. *Cosmorhaphe*. Sample UJTF unk. Variegated Shale, Lipnica Wielka, Kiczora, Poland (Upper Paleocene - Lower Eocene). Photographed by J.R. Lehane. Scale = 5 cm.
K. *Helminthorhaphe*. Sample UJTF 34. Variegated Shale, Lipnica Mała, pol.Gubernas, Poland (Upper Paleocene - Lower Eocene). Photographed by J.R. Lehane. Scale = 2 cm.
L. *Megagrapton*. Sample UJTF 640. Variegated Shale, Lipowe, Poland (Upper Paleocene - Lower Eocene). Photographed by J.R. Lehane. Scale = 5 cm. (Originally figured in Książkiewicz, 1977 Plate 25.4 as *Protopaleodictyon submontanum*).

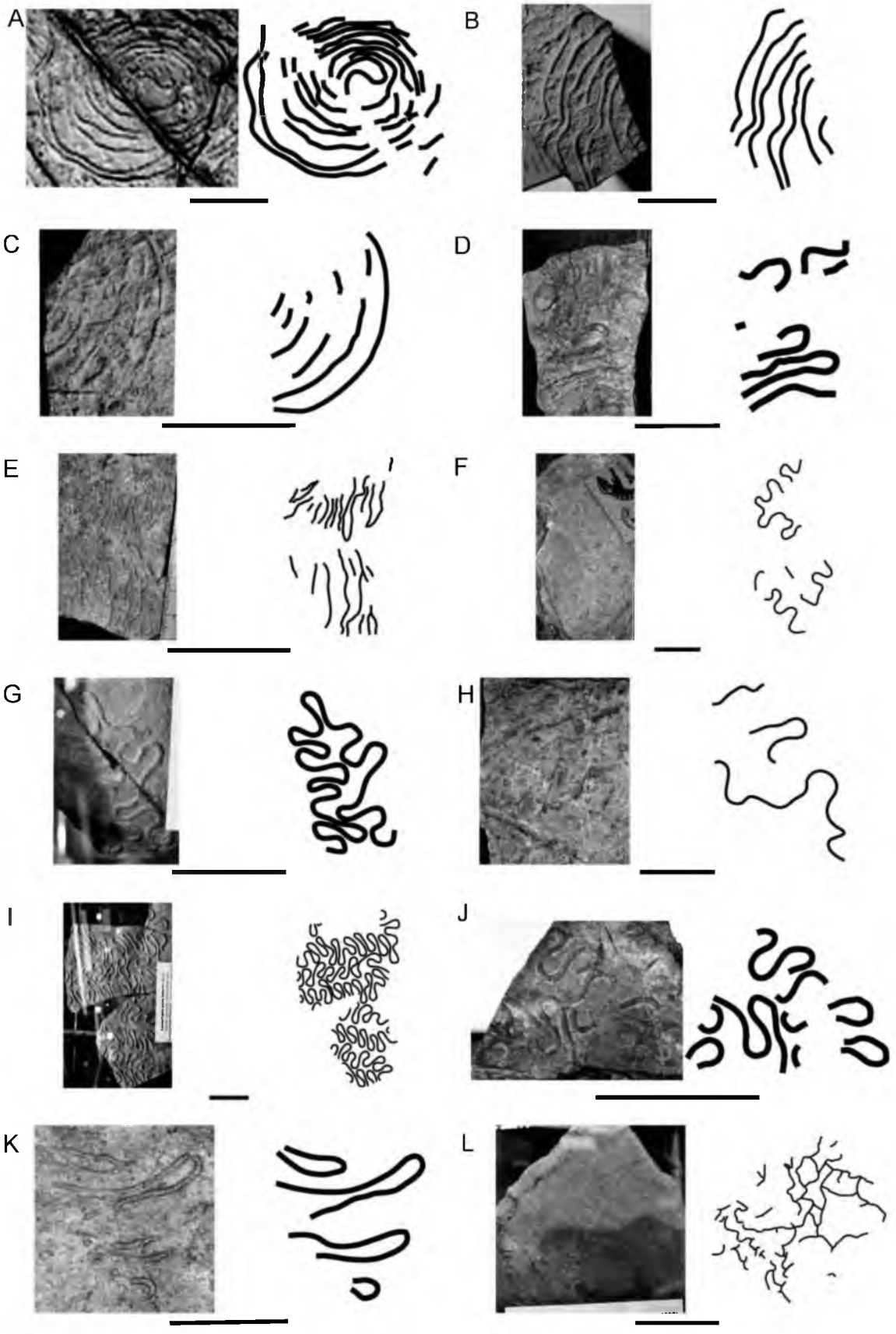
A
B
C
D
E
F
G
H
I
J
K
L

Figure E.19. Paleocene and Late Cretaceous trace fossils.
Paleocene trace fossils.

A. *Megagrapton*. Sample UJTF 657. Variegated Shale, Lipowe, Poland (Upper Paleocene - Lower Eocene). Photographed by J.R. Lehane. Scale = 2 cm. (Originally figured in Książkiewicz, 1977 Plate 25.5 as *Protopaleodictyon submontanum*).
B. *Megagrapton*. Sample UJTF 1873. Variegated Shale, Biczyce, Poland (Upper Paleocene - Lower Eocene). Photographed by J.R. Lehane. Scale = 5 cm. (Originally figured in Książkiewicz, 1977 Plate 25.5 as *Megagrapton* aff. *irregulare*).
C. *Paleodictyon*. Sample UJTF 272. Variegated Shale, Lipnica Mała, Gubernasówka, Poland (Upper Paleocene - Lower Eocene). Photographed by J.R. Lehane. Scale = 2 cm.
D. *Paleodictyon*. Sample UJTF 846. Variegated Shale, Berest k.Grybowa, Poland (Upper Paleocene -Lower Eocene). Photographed by J.R. Lehane. Scale = 2 cm.
E. *Protopaleodictyon*. Sample UJTF 341. Variegated Shale, Lubomierz, Poland (Upper Paleocene - Lower Eocene). Photographed by J.R. Lehane. Scale = 5 cm.
F. *Protopaleodictyon*. Sample UJTF 709. Variegated Shale, Stara Wieś k.Limanowej, Poland (Upper Paleocene - Lower Eocene). Photographed by J.R. Lehane. Scale = 5 cm. (Originally figured in Uchman, 1998 Fig. 100A as *Protopaleodictyon incompositum*).
G. *Urohelminthoida*. Sample UJTF 35. Variegated Shale, Zubrzyca Górna, Sylec, Poland (Upper Paleocene - Lower Eocene). Photographed by J.R. Lehane. Scale = 5 cm.

Late Cretaceous trace fossils.

H. *Ubinia*. Sample UJTF 2726. Godula Beds, Wisła, Poland (Coniacian – Santonian). Photographed by J.R. Lehane. Scale = 5 cm.
I. *Cosmorhaphe*. Sample UJTF 17. Ropianka (Inoceramian) Beds, Sidzina, Jarominy, Poland (Maastrichtian - Paleocene). Photographed by J.R. Lehane. Scale = 5 cm.
J. *Cosmorhaphe*. Sample UJTF 75. Ropianka (Inoceramian) Beds, Szczepanowice, Poland (Maastrichtian - Paleocene). Photographed by J.R. Lehane. Scale = 5 cm. (Originally figured in Książkiewicz, 1977 Plate 19.4 as *Cosmorhaphe sinuosa*)
K. *Cosmorhaphe*. Sample UJTF 250. Ropianka (Inoceramian) Beds, Grybów, Poland (Maastrichtian - Paleocene). Photographed by J.R. Lehane. Scale = 5 cm.
L. *Cosmorhaphe*. Sample UJTF 1872. Ropianka (Inoceramian) Beds, Grybów, Poland (Maastrichtian - Paleocene). Photographed by J.R. Lehane. Scale = 5 cm.

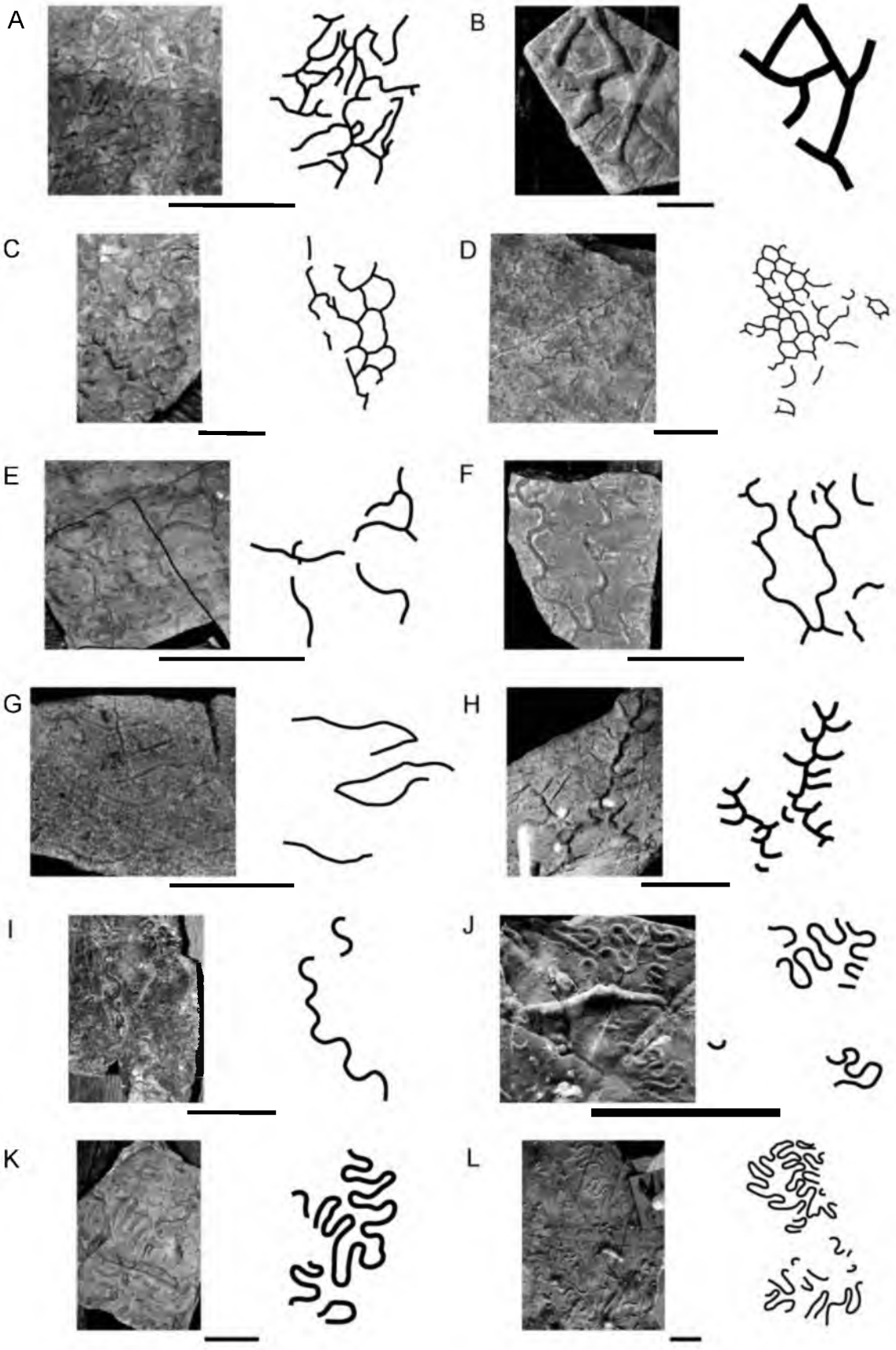
A
B
C
D
E
F
G
H
I
J
K
L

Figure E.20. Late Cretaceous trace fossils.
Late Cretaceous trace fossils.

A. *Helminthopsis*. Sample UJTF 225. Ropianka (Inoceramian) Beds, Lodzina k. Rybotycz, Poland (Maastrichtian - Paleocene). Photographed by J.R. Lehane. Scale = 5 cm.
B. *Helminthopsis*. Sample UJTF 333. Ropianka (Inoceramian) Beds, Maszna Dolna, Poland (Maastrichtian - Paleocene). Photographed by J.R. Lehane. Scale = 5 cm.
C. *Helminthorhaphe*. Sample UJTF 40. Ropianka (Inoceramian) Beds, Lipnica Mała, Poland (Maastrichtian - Paleocene). Photographed by J.R. Lehane. Scale = 5 cm.
D. *Helminthorhaphe*. Sample UJTF 49. Ropianka (Inoceramian) Beds, Poręba Wielka, Poland (Maastrichtian - Paleocene). Photographed by J.R. Lehane. Scale = 5 cm.
E. *Helminthorhaphe*. Sample UJTF 99. Ropianka (Inoceramian) Beds, Biała Wyżna, Poland (Maastrichtian - Paleocene). Photographed by J.R. Lehane. Scale = 5 cm. (Originally figured in Książkiewicz, 1977 Plate 21.9 as *Helminthoida crassa*)
F. *Helminthorhaphe*. Sample UJTF 1014. Ropianka (Inoceramian) Beds, Wola Brzezińska, Poland (Maastrichtian - Paleocene). Photographed by J.R. Lehane. Scale = 5 cm.
G. *Paleodictyon*. Sample UJTF 89A. Ropianka (Inoceramian) Beds, Grybów, Poland (Maastrichtian - Paleocene). Photographed by J.R. Lehane. Scale = 5 cm.
H. *Paleodictyon*. Sample UJTF 188. Ropianka (Inoceramian) Beds, Koninka (Konin), Poland (Maastrichtian - Paleocene). Photographed by J.R. Lehane. Scale = 5 cm. (Originally figured in Książkiewicz, 1977 Plate 28.3 as *Paleodictyon tellinii*).
I. *Paleodictyon*. Sample UJTF 1102. Ropianka (Inoceramian) Beds, Lipnica Wielka, Poland (Maastrichtian - Paleocene). Photographed by J.R. Lehane. Scale = 5 cm. (Originally figured in Książkiewicz, 1977 Plate 28.1 as *Paleodictyon strozzii*).
J. *Paleodictyon*. Sample UJTF 1259. Ropianka (Inoceramian) Beds, Maszna Dolna, Poland (Maastrichtian - Paleocene). Photographed by J.R. Lehane. Scale = 5 cm. (Originally figured in Książkiewicz, 1977 Plate 27.12 as *Paleodictyon miocenicum*).
K. *Protopaleodictyon*. Sample UJTF 923. Ropianka (Inoceramian) Beds, Huwniki, Poland (Maastrichtian - Paleocene). Photographed by J.R. Lehane. Scale = 5 cm.
L. *Protopaleodictyon*. Sample UJTF 955. Ropianka (Inoceramian) Beds, Kąkolowka, Poland (Maastrichtian - Paleocene). Photographed by J.R. Lehane. Scale = 5 cm.

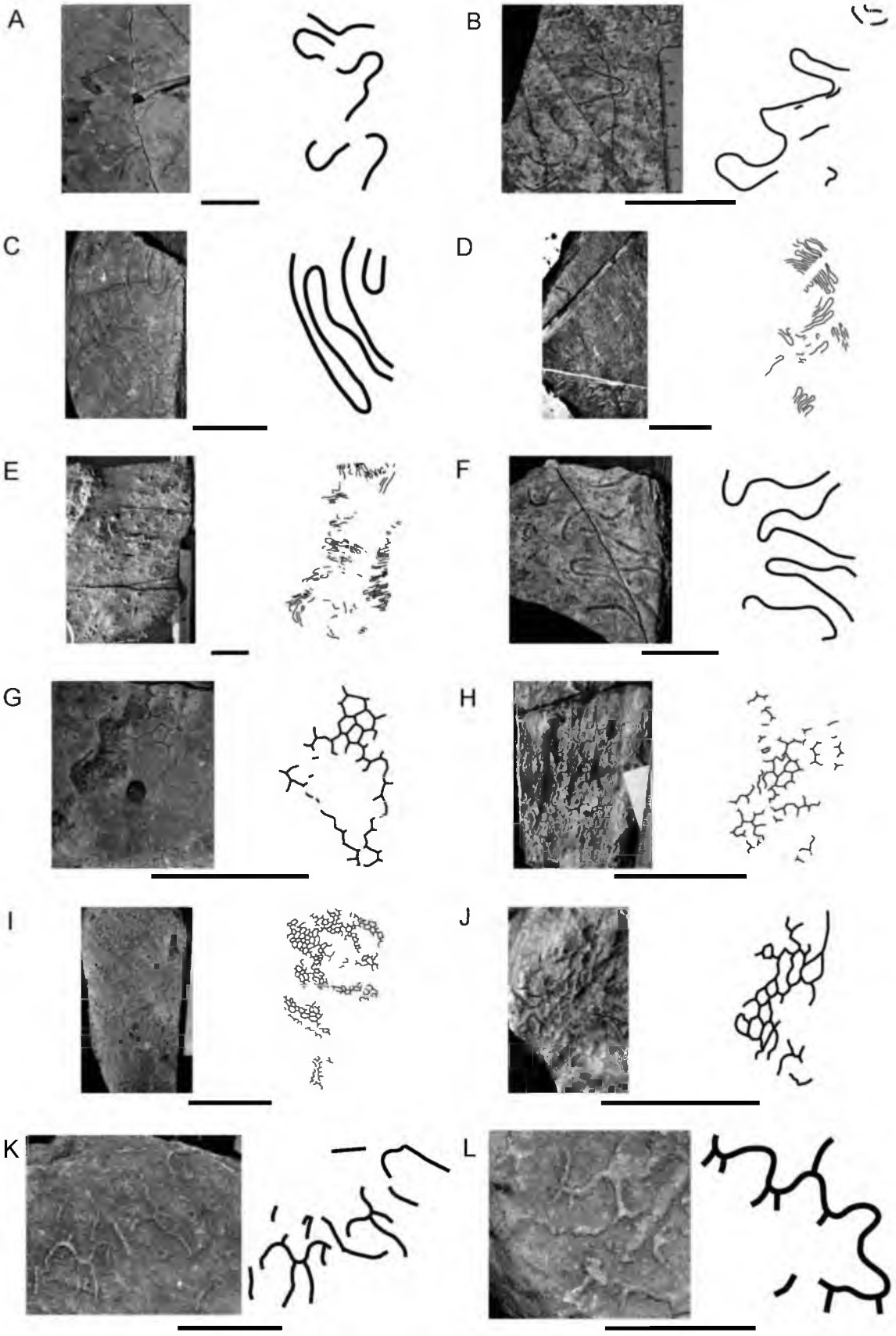
A
B
C
D
E
F
G
H
I
J
K
L

Figure E.21. Late Cretaceous trace fossils.
Late Cretaceous trace fossils.

A. *Spirorhaphe*. Sample UJTF 603a. Ropianka (Inoceramian) Beds, Lipnica Mała, Poland (Maastrichtian - Paleocene). Photographed by J.R. Lehane. Scale = 5 cm.
B. *Urohelminthoida*. Sample UJTF 120. Ropianka (Inoceramian) Beds, Grybów, Poland (Maastrichtian - Paleocene). Photographed by J.R. Lehane. Scale = 5 cm. (Originally figured in Książkiewicz, 1977 Plate 26.1 as *Urohelminthoida appendiculata*).
C. *Urohelminthoida*. Sample UJTF 351. Ropianka (Inoceramian) Beds, Zawoja, Zalas, Poland (Maastrichtian - Paleocene). Photographed by J.R. Lehane. Scale = 5 cm.
D. *Urohelminthoida*. Sample UJTF 1591. Ropianka (Inoceramian) Beds, Lipnica Wielka, Poland (Maastrichtian - Paleocene). Photographed by J.R. Lehane. Scale = 5 cm. (Originally figured in Książkiewicz, 1977 Plate 26.3 as *Urohelminthoida appendiculata*).
E. *Urohelminthoida*. Sample UJTF 1592. Ropianka (Inoceramian) Beds, Lipnica Wielka, Poland (Maastrichtian - Paleocene). Photographed by J.R. Lehane. Scale = 5 cm. (Originally figured in Książkiewicz, 1977 Plate 26.3 as *Urohelminthoida appendiculata*).
F. *Urohelminthoida*. Sample UJTF 2677. Ropianka (Inoceramian) Beds, Limanowa, Poland (Maastrichtian - Paleocene). Photographed by J.R. Lehane. Scale = 5 cm.
G. *Cosmorhaphe*. Sample McCann and Pickerill 1988 Fig 3-5. Kodiak Formation, Gibson Cove, Alaska, USA (Upper Cretaceous). Figured in McCann and Pickerill, 1988 Fig 3-5. Scale = 5 cm. (Originally identified as *Cosmorhaphe sinuosa*). Used with permission from the Paleontological Society.
H. *Gordia*. Sample GSC 81259. Kodiak Formation, Gibson Cove, Alaska, USA (Upper Cretaceous). Figured in McCann and Pickerill, 1988 Fig 3-10. Scale = 5 cm. (Originally identified as *Gordia marina*). Used with permission from the Paleontological Society.
I. *Helminthorhaphe*. Sample McCann and Pickerill 1988 Fig 3-12. Kodiak Formation, Gibson Cove, Alaska, USA (Upper Cretaceous). Figured in McCann and Pickerill, 1988 Fig 3-12. Scale = 5 cm. (Originally identified as *Helminthoida crassa*). Used with permission from the Paleontological Society.
J. *Paleodictyon*. Sample McCann and Pickerill 1988 Fig 5-2. Kodiak Formation, Southern tip of Near Island, Alaska, USA (Upper Cretaceous). Figured in McCann and Pickerill, 1988 Fig 5-2. Scale = 5 cm. (Originally identified as *Paleodictyon miocenium*). Used with permission from the Paleontological Society.
K. *Spirorcosmorhaphe*. Sample GSC 81257. Kodiak Formation, Southern tip of Near Island, Alaska, USA (Upper Cretaceous). Figured in McCann and Pickerill, 1988 Fig 3-6. Scale = 2 cm. (Originally identified as *Cosmorhaphe helicoidea*). Used with permission from the Paleontological Society.
L. *Spirorhaphe*. McCann and Pickerill 1988 Fig 5-7-1. Kodiak Formation, Southern tip of Near Island, Alaska, USA (Upper Cretaceous). Figured in McCann and Pickerill, 1988 Fig 5-7-1. Scale = 2 cm. (Originally identified as *Spirorhaphe involuta*). Used with permission from the Paleontological Society.

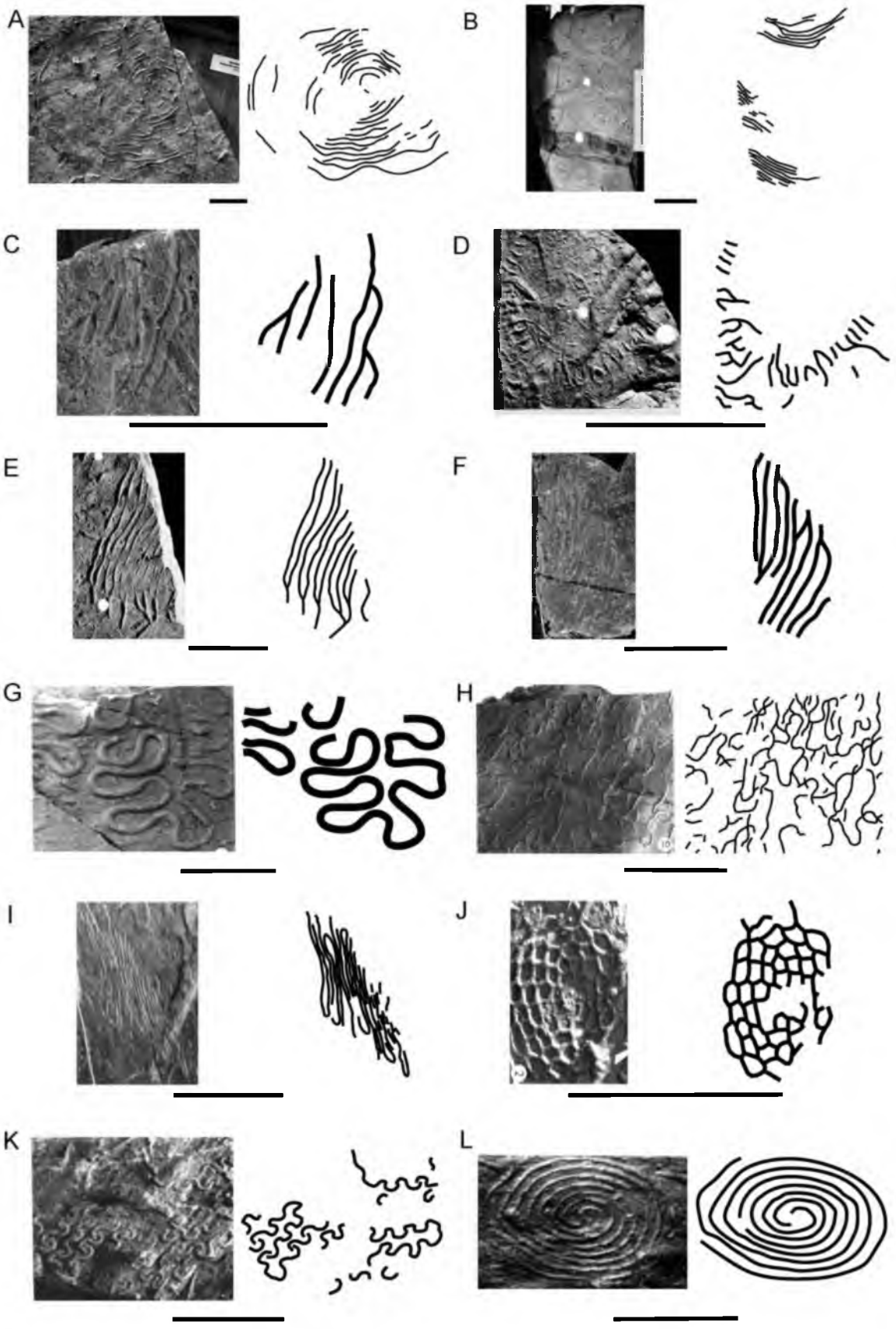
A
B
C
D
E
F
G
H
I
J
K
L

Figure E.22. Late Cretaceous trace fossils.

Late Cretaceous trace fossils.

A. *Spirorhaphe*. Sample McCann and Pickerill, 1988 Fig 5-7-2. Kodiak Formation, Southern tip of Near Island, Alaska, USA (Upper Cretaceous). Figured in McCann and Pickerill, 1988 Fig 5-7-2. Scale = 2 cm. (Originally identified as *Spirorhaphe involuta*). Used with permission from the Paleontological Society.
B. *Cosmorhaphe*. Sample UJTF unk. Skrzydlna Beds, Przenosza, Poland (Coniacian - Santonian). Photographed by J.R. Lehane. Scale = 2 cm.
C. *Paleodictyon*. Sample UJTF 1668. Skrzydlna Beds, Przenosza, Poland (Coniacian - Santonian). Photographed by J.R. Lehane. Scale = 2 cm. (Originally figured in Książkiewicz, 1977 Plate 27.16 as *Paleodictyon miocenium* forma *pluerodictyonoides*).
D. *Helminthorhaphe*. Sample UJTF 103. Sromowce Beds, Sromowce Wyżne, Poland (Coniacian – Late Campanian). Photographed by J.R. Lehane. Scale = 5 cm. (Originally figured in Książkiewicz, 1977 Plate 21.4 as *Helminthoida crassa*).
E. *Paleodictyon*. Sample UJTF 67. Sromowce Beds, Sromowce Wyżne, Poland (Coniacian – Late Campanian). Photographed by J.R. Lehane. Scale = 2 cm. (Originally figured in Książkiewicz, 1977 Plate 27.9 as *Paleodictyon intermedium*).
F. *Paleodictyon*. Sample UJTF 92. Sromowce Beds, Jaworki, Skalski stream, Poland (Coniacian – Late Campanian). Photographed by J.R. Lehane. Scale = 5 cm. (Originally figured in Książkiewicz, 1977 Plate 29.1 as *Paleodictyon regulare* forma *pluerodictyonoides*).
G. *Paleodictyon*. Sample UJTF 111. Sromowce Beds, Sromowce Wyżne, Poland (Coniacian – Late Campanian). Photographed by J.R. Lehane. Scale = 2 cm. (Originally figured in Książkiewicz, 1977 Plate 27.6 as *Paleodictyon minimum*).
H. *Paleodictyon*. Sample UJTF 320. Sromowce Beds, Sromowce Wyżne, Poland (Coniacian – Late Campanian). Photographed by J.R. Lehane. Scale = 1 cm.
I. *Paleodictyon*. Sample UJTF 324. Sromowce Beds, Sromowce Wyżne, Poland (Coniacian – Late Campanian). Photographed by J.R. Lehane. Scale = 1 cm.
J. *Paleodictyon*. Sample UJTF 330. Sromowce Beds, Jaworki, Poland (Coniacian – Late Campanian). Photographed by J.R. Lehane. Scale = 2 cm. (Originally figured in Książkiewicz, 1977 Plate 27.10 as *Paleodictyon strozzii*).
K. *Paleodictyon*. Sample UJTF 333. Sromowce Beds Jaworki, Skalski stream, Poland (Coniacian – Late Campanian). Photographed by J.R. Lehane. Scale = 1 cm.
L. *Cosmorhaphe*. Sample UJTF 1162. Szydlowiec Beds, Kobielnik, Poland (Upper Senonian (Campanian - Maastrichtian)). Photographed by J.R. Lehane. Scale = 2 cm. (Originally figured in Książkiewicz, 1977 Plate 19.1 as *Cosmorhaphe gracilis*).

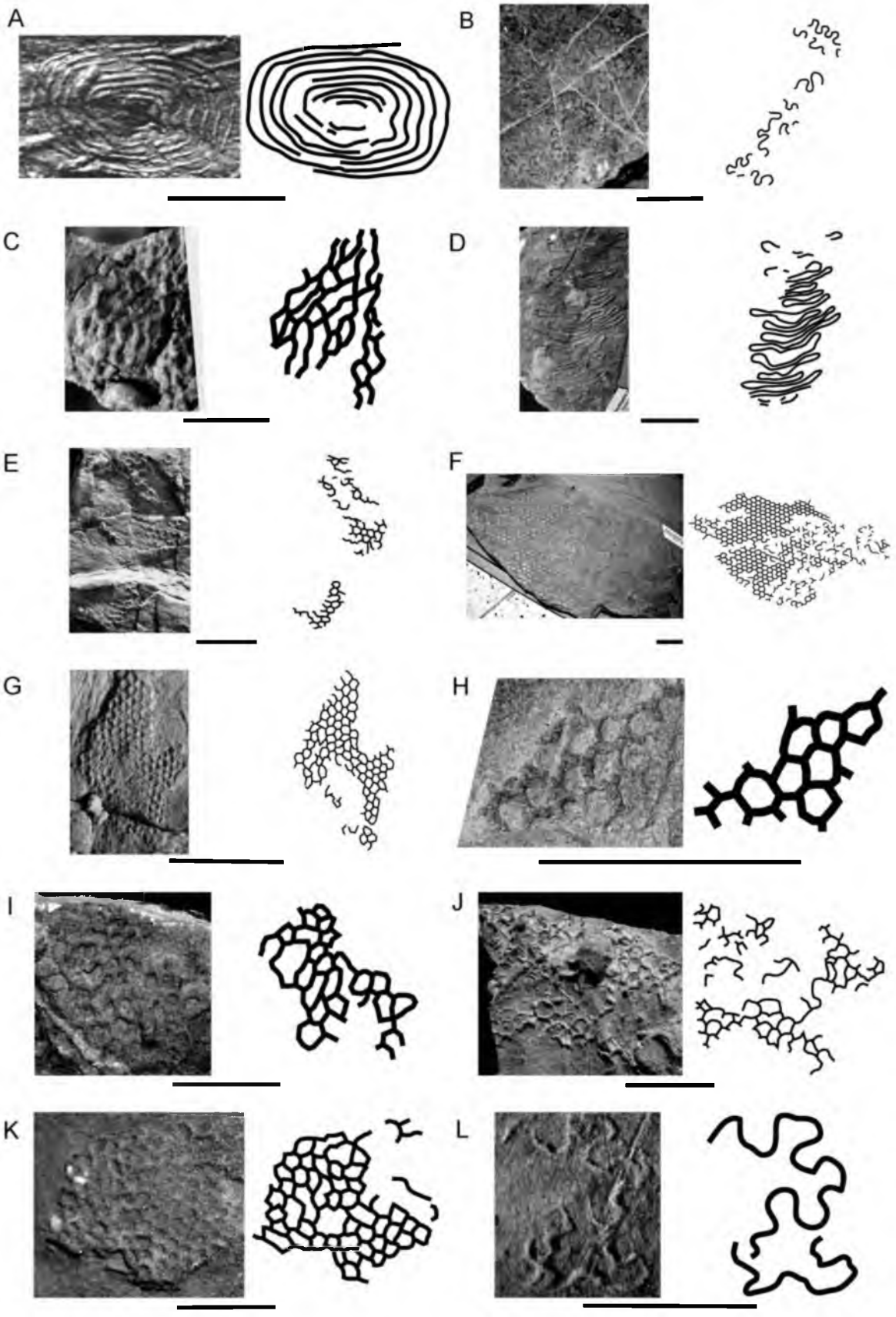
A
B
C
D
E
F
G
H
I
J
K
L

Figure E.23. Late Cretaceous trace fossils.

Late Cretaceous trace fossils.

A. *Belorhaphe*. Sample UUIC 1949. Unnamed Formation, west of Kilwa, Tanzania, Section 3A (Uppermost Lower Campanian). Photographed by J.R. Lehane. Scale = 1 cm.
B. *Helminthorhaphe*. Sample UUIC 1911. Unnamed Formation, west of Kilwa, Tanzania, Section 3 (Uppermost Lower Campanian). Photographed by J.R. Lehane. Scale = 1 cm. (Originally figured in Ernst and Zander, 1993 Plate 2.6 as *Cosmorhaphe* ichnosp.).
C. *Helminthorhaphe*. Sample UUIC 1912. Unnamed Formation, west of Kilwa, Tanzania, Section 4A (Lowermost Upper Campanian). Photographed by J.R. Lehane. Scale = 5 cm.
D. *Helminthorhaphe*. Sample UUIC 1913. Unnamed Formation, west of Kilwa, Tanzania, Section 1A (Santonian). Photographed by J.R. Lehane. Scale = 5 cm.
E. *Paleodictyon*. Sample UUIC 1916. Unnamed Formation, west of Kilwa, Tanzania, Section 2A (Uppermost Lower Campanian). Photographed by J.R. Lehane. Scale = 2 cm.
F. *Paleodictyon*. Sample UUIC 1917. Unnamed Formation, west of Kilwa, Tanzania, Section 3A (Uppermost Lower Campanian). Photographed by J.R. Lehane. Scale = 2 cm.
G. *Paleodictyon*. Sample UUIC 1918. Unnamed Formation, west of Kilwa, Tanzania, Section 3E (Uppermost Lower Campanian). Photographed by J.R. Lehane. Scale = 1 cm.
H. *Paleodictyon*. Sample UUIC 1919. Unnamed Formation, west of Kilwa, Tanzania, Section 3 (Uppermost Lower Campanian). Photographed by J.R. Lehane. Scale = 1 cm.
I. *Spirorhaphe*. Sample UUIC 1902. Unnamed Formation, west of Kilwa, Tanzania, Section 4A (Lowermost Upper Campanian). Photographed by J.R. Lehane. Scale = 2 cm.
J. *Spirorhaphe*. Sample UUIC 1903. Unnamed Formation, west of Kilwa, Tanzania (Campanian). Photographed by J.R. Lehane. Scale = 2 cm.
K. *Spirorhaphe*. Sample UUIC 1904. Unnamed Formation, west of Kilwa, Tanzania, Section 3A (Uppermost Lower Campanian). Photographed by J.R. Lehane. Scale = 2 cm.
L. *Spirorhaphe*. Sample UUIC 1905. Unnamed Formation, west of Kilwa, Tanzania (Campanian). Photographed by J.R. Lehane. Scale = 5 cm.

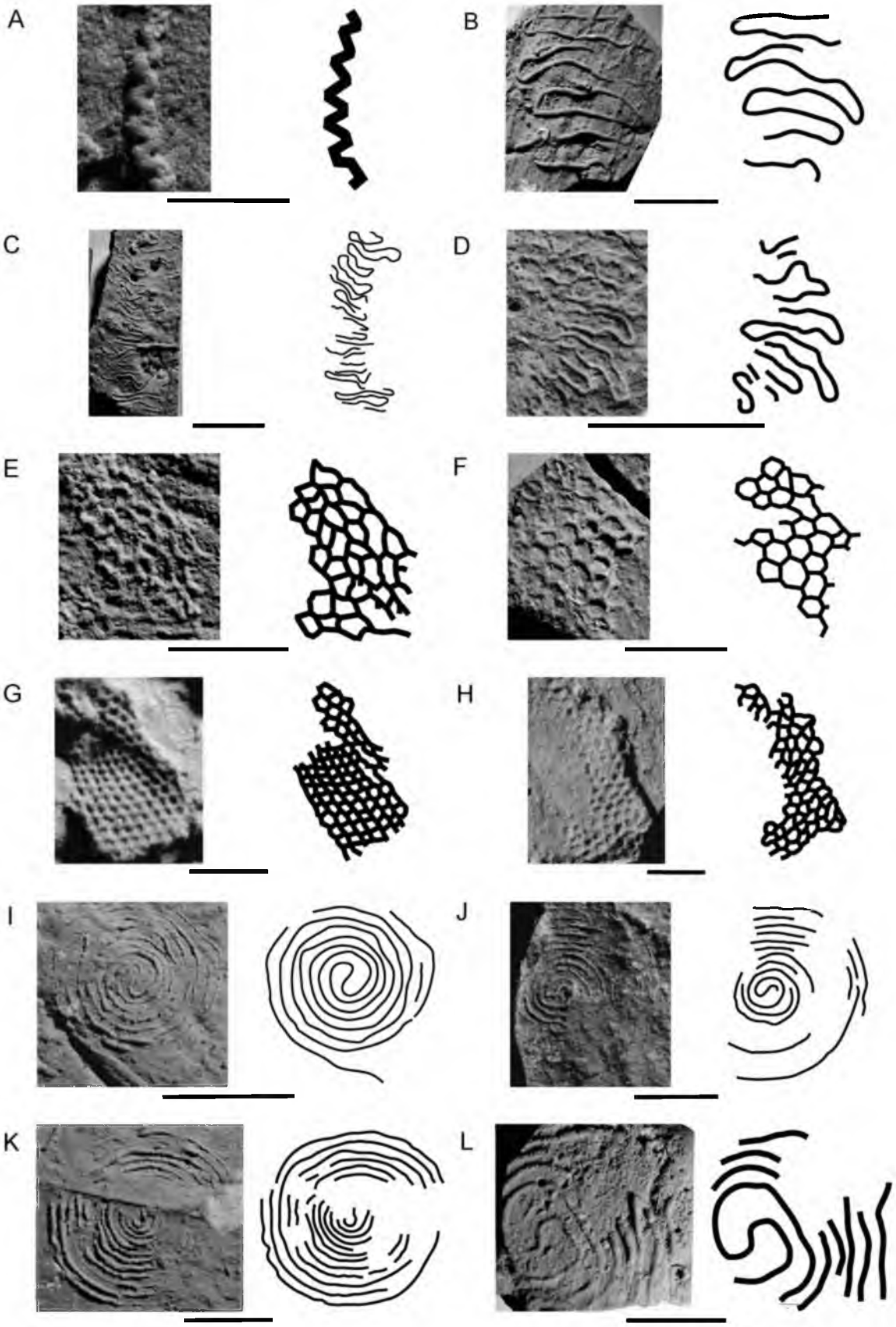
A
B
C
D
E
F
G
H
I
J
K
L

Figure E.24. Late Cretaceous and Early Cretaceous trace fossils.
Late Cretaceous trace fossils.

A. *Spirorhaphe*. Sample UUIC 1906. Unnamed Formation, west of Kilwa, Tanzania, Section 4 (Lowermost Upper Campanian). Photographed by J.R. Lehane. Scale = 5 cm.
B. *Spirorhaphe*. Sample UUIC 1907. Unnamed Formation, west of Kilwa, Tanzania (Campanian). Photographed by J.R. Lehane. Scale = 5 cm.
C. *Spirorhaphe*. Sample UUIC 1908. Unnamed Formation, west of Kilwa, Tanzania, Section 4B (Lowermost Upper Campanian). Photographed by J.R. Lehane. Scale = 5 cm. (Originally figured in Ernst and Zander, 1993 Plate 2.4 as *Spirorhaphe* ichnosp.).
D. *Spirorhaphe*. Sample UUIC 1909. Unnamed Formation, west of Kilwa, Tanzania (Campanian). Photographed by J.R. Lehane. Scale = 5 cm.
E. *Spirorhaphe*. Sample UUIC 1910. Unnamed Formation, west of Kilwa, Tanzania, Section 3D (Uppermost Lower Campanian). Photographed by J.R. Lehane. Scale = 2 cm.
F. *Urohelminthoida*. Sample UUIC 1914. Unnamed Formation, west of Kilwa, Tanzania, Section 3A (Uppermost Lower Campanian). Photographed by J.R. Lehane. Scale = 2 cm.
G. *Helminthopsis*. Sample Yeh 1987 Fig 2C. Unnamed Formation, Wheeler Gorge, California, USA (Campanian – Maastrichtian). Figured in Yeh, 1987 Fig 2C. Scale = 2 cm. (Originally identified as *Helminthopsis*). Reproduced with permission from Pacific Section SEPM (Society for Sedimentary Geology).
H. *Helminthorhaphe*. Sample Yeh 1987 Fig 2A. Unnamed Formation, Wheeler Gorge, California, USA (Campanian – Maastrichtian). Figured in Yeh, 1987 Fig 2A. Scale = 2 cm. (Originally identified as *Cosmorhaphe*). Reproduced with permission from Pacific Section SEPM (Society for Sedimentary Geology).
I. *Helminthorhaphe*. Sample Yeh 1987 Fig 2B. Unnamed Formation, Wheeler Gorge, California, USA (Campanian – Maastrichtian). Figured in Yeh, 1987 Fig 2B. Scale = 5 cm. (Originally identified as *Helminthoida*). Reproduced with permission from Pacific Section SEPM (Society for Sedimentary Geology).
J. *Cosmorhaphe*. Sample PIW1998IV 140. Zementmergelserie, Jenbach Valley, Germany (Santonian – Campanian). Figured in Uchman, 1999 Plate 19 Fig. 7. Scale = 5 cm. (Originally identified as *Cosmorhaphe carpathica*). Reprinted from Uchman, A., 1999, Ichnology of the Rhenodanubian Flysch (Lower Cretaceous-Eocene) in Austria and Germany, Beringeria, v. 25, pp.67-173, with permission.

Early Cretaceous trace fossils.

K. *Belorhaphe*. Sample UJTF 119. Cieszyn Beds, Jaroszowice, Poland (Upper Tithonian – Berriasian). Photographed by J.R. Lehane. Scale = 5 cm. (Originally figured in Książkiewicz, 1977 Plate 24.1 as *Belorhaphe zickzack*).
L. *Helminthopsis*. Sample UJTF 1465. Cieszyn Beds, Goleszów, Poland (Upper Tithonian – Berriasian). Photographed by J.R. Lehane. Scale = 5 cm. (Originally figured in Książkiewicz, 1977 Plate 12.1 as *Helminthopsis tenuis*).

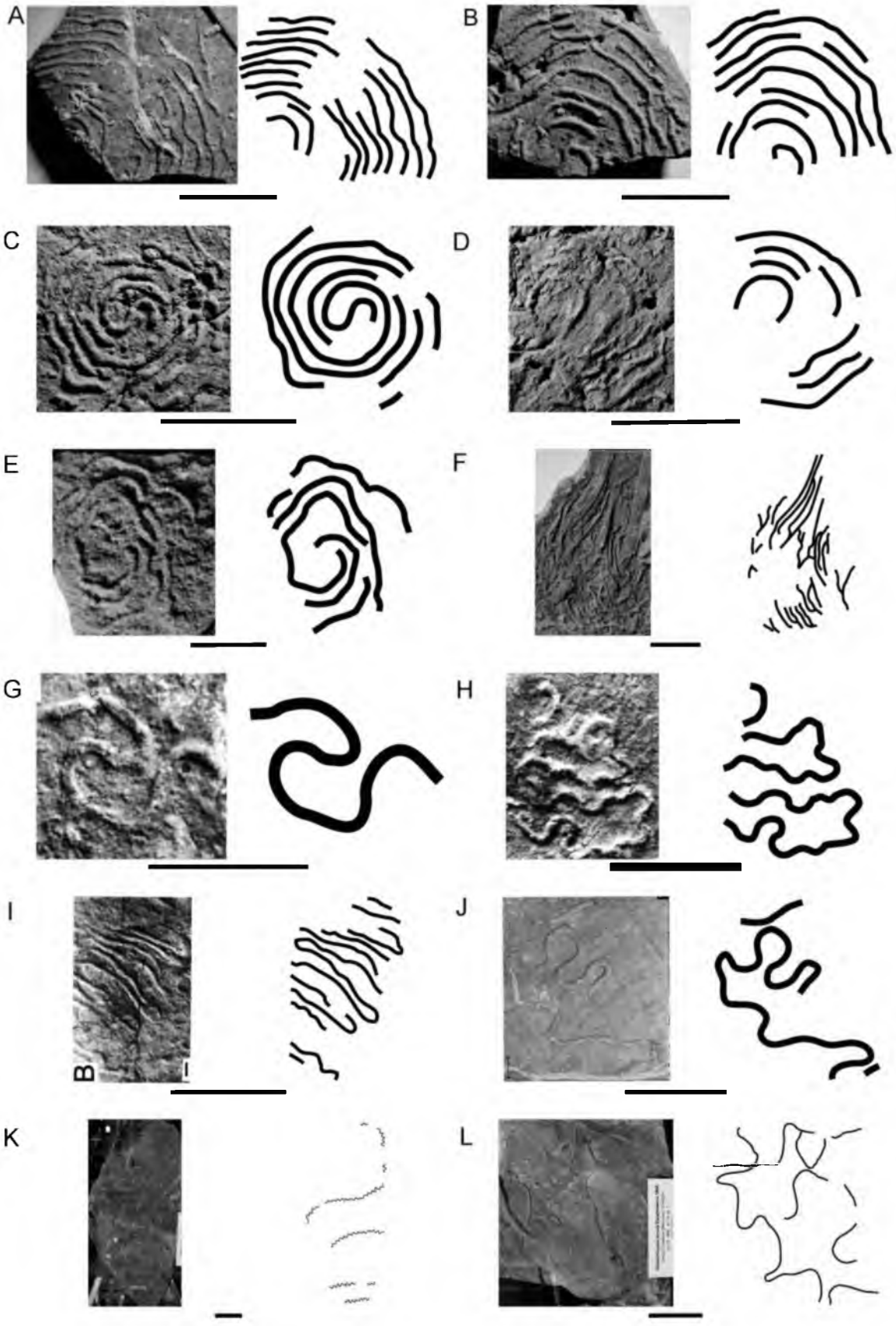
A
B
C
D
E
F
G
H
I
J
K
L

Figure E.25. Early Cretaceous trace fossils.

Early Cretaceous trace fossils.

A. *Megagrapton*. Sample UJTF 391. Cieszyn Beds, Goleszów, Poland (Upper Tithonian – Berriasian). Photographed by J.R. Lehane. Scale = 5 cm. (Originally figured in Książkiewicz, 1977 Plate 25.10 as *Megagrapton tenue*).
B. *Paleodictyon*. Sample UJTF 316. Cieszyn Beds, Goleszów, Poland (Upper Tithonian – Berriasian). Photographed by J.R. Lehane. Scale = 2 cm.
C. *Belorhaphe*. Sample UCMP 398563. Yolla Bolly Terrane, Del Norte, California (Tithonian – Hauterivian). Photographed by J.R. Lehane. Scale = 2 cm.
D. *Cosmorhaphe*. Sample UCMP 38606. Franciscan Flysch, Trinidad Harbor, California (Tithonian – Hauterivian). Photographed by J.R. Lehane. Scale = 2 cm. (Originally figured in Miller, 1991a Fig 4A as *Cosmorhaphe tremens*).
E. *Cosmorhaphe*. Sample UCMP 398570. Yolla Bolly Terrane, Del Norte, California (Tithonian – Hauterivian). Photographed by J.R. Lehane. Scale = 2 cm. (Originally figured in Miller, 1993 Fig 5G as *?Cosmorhaphe* ichnosp.).
F. *Gordia*. Sample UCMP 398574. Yolla Bolly Terrane, Del Norte, California (Tithonian – Hauterivian). Photographed by J.R. Lehane. Scale = 5 cm. (Originally figured in Miller, 1993 Fig 4E as *Gordia molassica*).
G. *Helminthopsis*. Sample UCMP 398575. Yolla Bolly Terrane, Del Norte, California (Tithonian – Hauterivian). Photographed by J.R. Lehane. Scale = 5 cm. (Originally figured in Miller, 1993 Fig 5H as *Helminthopsis abeli*).
H. *Helminthorhaphe*. Sample UCMP 38608. Franciscan Flysch, Trinidad Harbor, California (Tithonian – Hauterivian). Photographed by J.R. Lehane. Scale = 5 cm. (Originally figured in Miller, 1991a Fig 4C as *Helminthoida crassa*).
I. *Helminthorhaphe*. Sample UCMP 38609. Franciscan Flysch, Trinidad Harbor, California (Tithonian – Hauterivian). Photographed by J.R. Lehane. Scale = 5 cm.
J. *Helminthorhaphe*. Sample UCMP 398578. Yolla Bolly Terrane, Del Norte, California (Tithonian – Hauterivian). Photographed by J.R. Lehane. Scale = 5 cm. (Originally figured in Miller, 1993 Fig 5E as *?Helminthoida* ichnosp.).
K. *Megagrapton*. Sample UCMP 398582. Yolla Bolly Terrane, Del Norte, California (Tithonian – Hauterivian). Photographed by J.R. Lehane. Scale = 5 cm. (Originally figured in Miller, 1993 Fig 5P as *Megagrapton irregulare*).
L. *Squamodictyon*. Sample UCMP 398595. Yolla Bolly Terrane, Del Norte, California (Tithonian – Hauterivian). Photographed by J.R. Lehane. Scale = 2 cm. (Originally figured in Miller, 1993 Fig 5L as *Squamodictyon squamosum*).

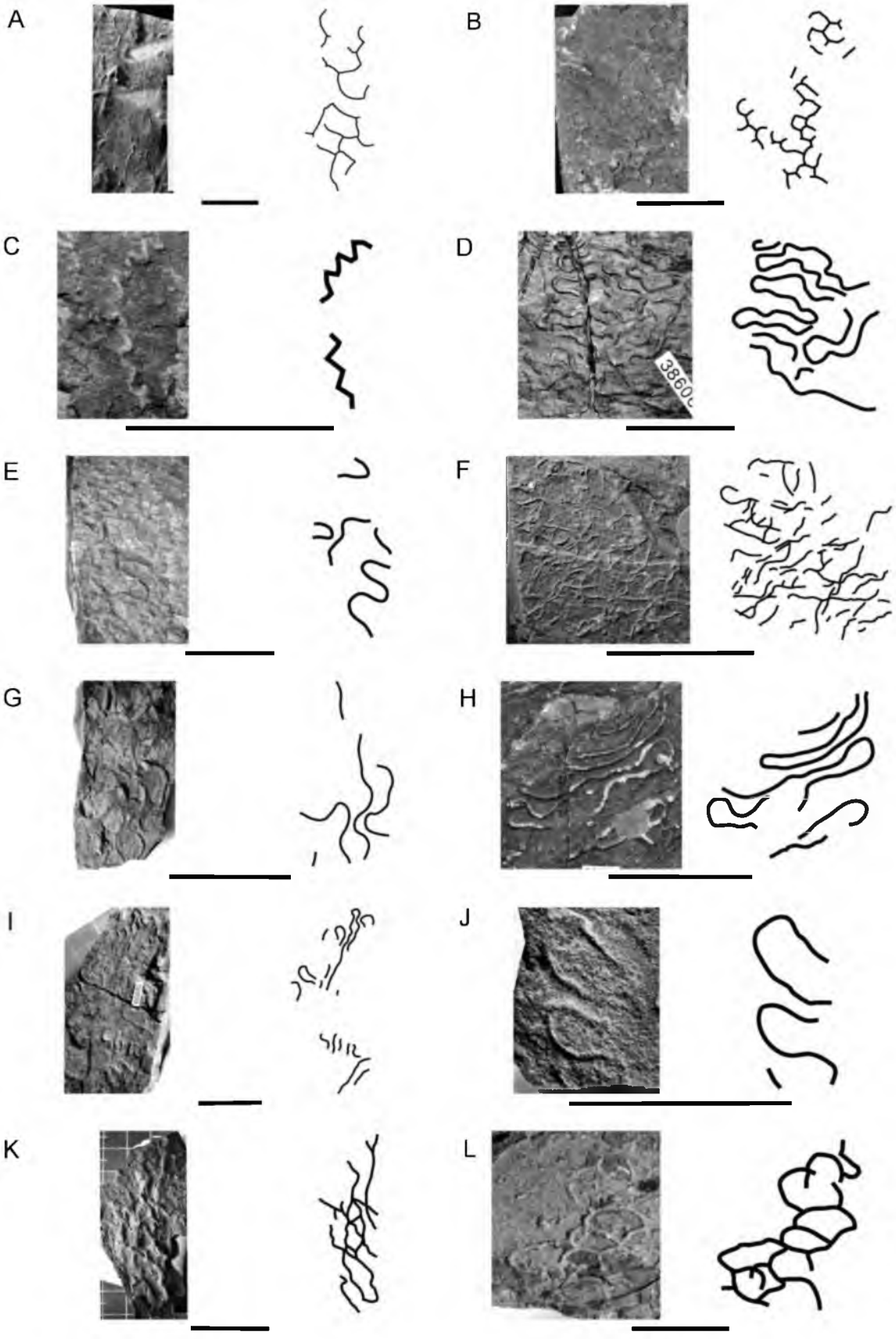
A
B
C
D
E
F
G
H
I
J
K
L

Figure E.26. Early Cretaceous and Jurassic trace fossils.
Early Cretaceous trace fossils.

A. *Helminthopsis*. Sample UJTF 331. Grodziszcze Beds, Woźniki, Poland (Upper Hauterivian – Barremian). Photographed by J.R. Lehane. Scale = 5 cm.
B. *Helminthopsis*. Sample UJTF 1321. Grodziszcze Beds, Poznachowice, Poland (Upper Hauterivian – Barremian). Photographed by J.R. Lehane. Scale = 5 cm. (Originally figured in Książkiewicz, 1977 Plate 12.5 as *Helminthopsis abeli*).
C. *Paleodictyon*. Sample UJTF 1172-1. Grodziszcze Beds, Wiśniowa, Poland (Upper Hauterivian – Barremian). Photographed by J.R. Lehane. Scale = 5 cm.
D. *Paleodictyon*. Sample UJTF 1172-2. Grodziszcze Beds, Wiśniowa, Poland (Upper Hauterivian – Barremian). Photographed by J.R. Lehane. Scale = 5 cm. (Originally figured in Książkiewicz, 1977 Plate 27.8 as *Paleodictyon intermedium*).

Jurassic trace fossils.

E. *Squamodictyon*. Sample MP-US J1150. Balaban Formation, Kodzader River north of Tarnak, Bulgaria (Toarcian). Figured in Tchoumatchenco and Uchman, 1999 Fig. 11E. Scale = 5 cm. (Originally identified as *Paleodictyon (Squamodictyon) petaloideum*). Reprinted from Tchoumatchenco, P., and A. Uchman, 1999, Lower and Middle Jurassic flysch trace fossils from the Eastern Stara Planina Mountains, Bulgaria: A contribution to the evolution of Mesozoic ichnodiversity, Neues Jahrbuch für Geologie und Paläontologie - Abhandlungen (www.schweizerbart.de), v. 213, no. 2, pp.169-199 with permission.
F. *Paleodictyon*. Sample UUIC 1312. Unnamed, Central and Eastern High Atlas Mountains, Tunnel of the Légionnaire, Gorge of Ziz Morocco (Sinemurian – Torarcian). Photographed by J.R. Lehane. Scale = 5 cm.
G. *Belorhaphe*. Sample BAN-Jich-0017. Kostel Formation, Locality 5. Stanyovtsi, Bulgaria (Tithonian). Figured in Tchoumatchenco and Uchman, 2001 Fig. 8D. Scale = 2 cm. (Originally identified as *Belorhaphe zickzack*). Reprinted from Palaeogeography, Palaeoclimatology, Palaeoecology, v. 169, 2001 with permission from Elsevier.
H. *Paleodictyon*. Sample BAN-Jich-0033b. Kostel Formation, Locality 2. Berende, Berenderska Reka River, Bulgaria (Berriasian). Figured in Tchoumatchenco and Uchman, 2001 Fig. 8H. Scale = 2 cm. (Originally identified as *Paleodictyon strozzii*). Reprinted from Palaeogeography, Palaeoclimatology, Palaeoecology, v. 169, 2001 with permission from Elsevier.
I. *Protopaleodictyon*. Sample BAN-Jich-0012. Kostel Formation, Locality 6. Chepino, valley Bokyovets, Bulgaria (uppermost Kimmeridgian – Lower Tithonian). Figured in Tchoumatchenco and Uchman, 2001 Fig. 6C. Scale = 5 cm. (Originally identified as *Protopaleodictyon incompositum*). Reprinted from Palaeogeography, Palaeoclimatology, Palaeoecology, v. 169, 2001 with permission from Elsevier.
J. *Protopaleodictyon*. Sample BAN-Jich-0014b. Kostel Formation, Locality 2. Berende, Berenderska Reka River, Bulgaria (Berriasian). Figured in Tchoumatchenco and Uchman, 2001 Fig. 6F. Scale = 5 cm. (Originally identified as *Protopaleodictyon incompositum*). Reprinted from Palaeogeography, Palaeoclimatology, Palaeoecology, v. 169, 2001 with permission from Elsevier.

Figure E. 26 continued.
Jurassic trace fossils.

K. *Paleodictyon*. Sample UUIC 721. Longobucco Sequence, Longobucco, Italy (Middle to Late Jurassic). Photographed by J.R. Lehane. Scale = 5 cm.

L. *Paleodictyon*. Sample UUIC 1164. Longobucco Sequence, Longobucco, Italy (Middle to Late Jurassic). Photographed by J.R. Lehane. Scale = 5 cm.

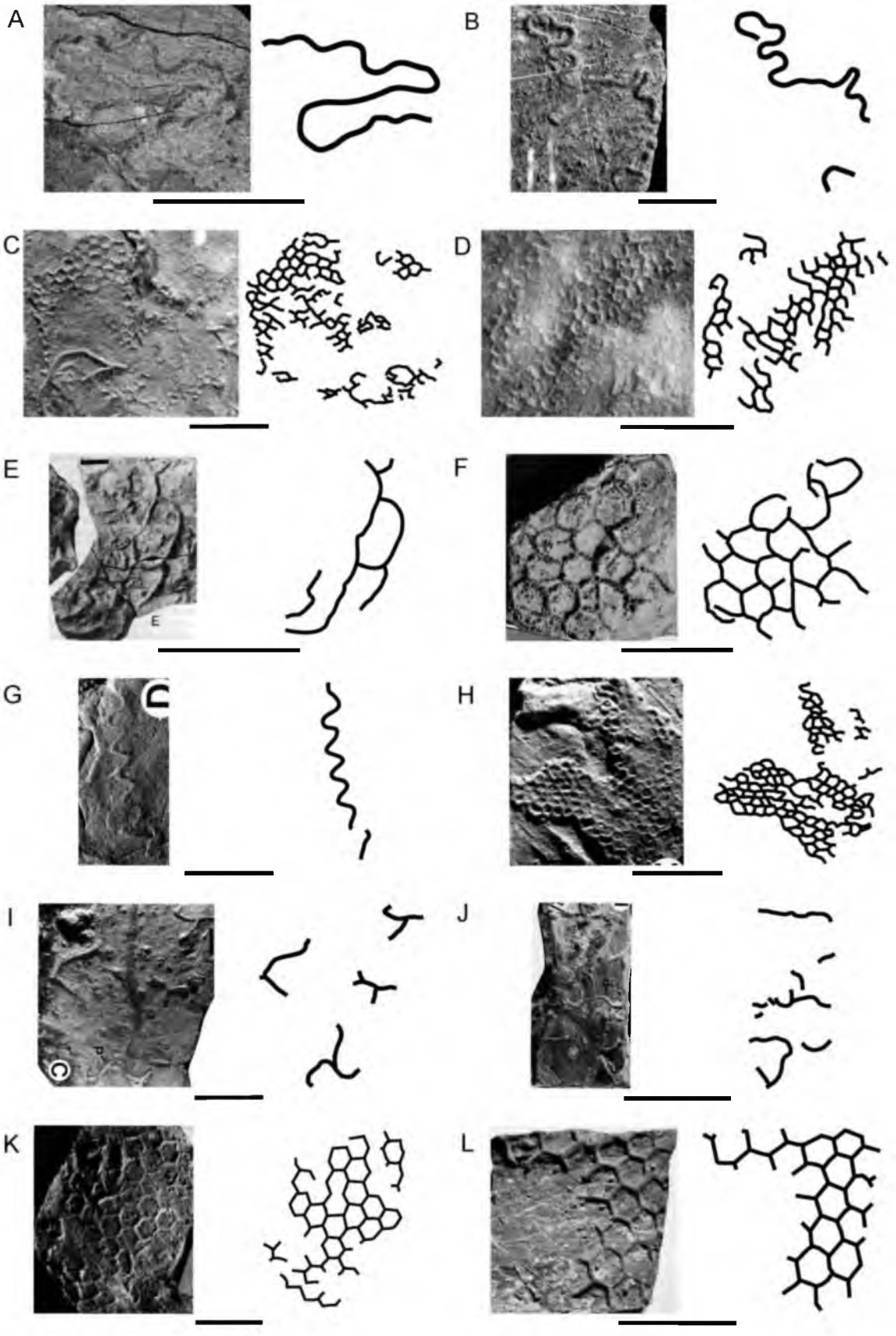
A
B
C
D
E
F
G
H
I
J
K
L

Figure E.27. Jurassic and Permian trace fossils.
Jurassic trace fossils.

A. *Gordia*. Sample MP-US J1131. Sini Vir Formation, Emirovo, Bulgaria (Pliensbachian – Toarcian). Figured in Tchoumatchenco and Uchman, 1999 Fig. 4D. Scale = 5 cm. (Originally identified as *Gordia marina*). Reprinted from Tchoumatchenco, P., and A. Uchman, 1999, Lower and Middle Jurassic flysch trace fossils from the Eastern Stara Planina Mountains, Bulgaria: A contribution to the evolution of Mesozoic ichnodiversity, Neues Jahrbuch für Geologie und Paläontologie - Abhandlungen (www.schweizerbart.de), v. 213, no. 2, pp.169-199 with permission.
B. *Gordia*. Sample MP-US J1133. Sini Vir Formation, Emirovo, Bulgaria (Pliensbachian – Toarcian). Figured in Tchoumatchenco and Uchman, 1999 Fig. 4C. Scale = 5 cm. (Originally identified as *Gordia marina*). Reprinted from Tchoumatchenco, P., and A. Uchman, 1999, Lower and Middle Jurassic flysch trace fossils from the Eastern Stara Planina Mountains, Bulgaria: A contribution to the evolution of Mesozoic ichnodiversity, Neues Jahrbuch für Geologie und Paläontologie - Abhandlungen (www.schweizerbart.de), v. 213, no. 2, pp.169-199 with permission.
C. *Paleodictyon*. Sample MP-US J1142. Sini Vir Formation, Valley of the Elesnica River, Bulgaria (Pliensbachian – Toarcian). Figured in Tchoumatchenco and Uchman, 1999 Fig. 11D. Scale = 5 cm. (Originally identified as *Paleodictyon hexagonum*). Reprinted from Tchoumatchenco, P., and A. Uchman, 1999, Lower and Middle Jurassic flysch trace fossils from the Eastern Stara Planina Mountains, Bulgaria: A contribution to the evolution of Mesozoic ichnodiversity, Neues Jahrbuch für Geologie und Paläontologie - Abhandlungen (www.schweizerbart.de), v. 213, no. 2, pp.169-199 with permission.
D. *Paleodictyon*. Sample MP-US J1143. Sini Vir Formation, East of Kotel, Bulgaria (Pliensbachian – Toarcian). Figured in Tchoumatchenco and Uchman, 1999 Fig. 11C. Scale = 5 cm. (Originally identified as *Paleodictyon majus*). Reprinted from Tchoumatchenco, P., and A. Uchman, 1999, Lower and Middle Jurassic flysch trace fossils from the Eastern Stara Planina Mountains, Bulgaria: A contribution to the evolution of Mesozoic ichnodiversity, Neues Jahrbuch für Geologie und Paläontologie - Abhandlungen (www.schweizerbart.de), v. 213, no. 2, pp.169-199 with permission.
E. *Paleodictyon*. Sample MP-US J1144. Sini Vir Formation, Emirovo, Bulgaria (Pliensbachian – Toarcian). Figured in Tchoumatchenco and Uchman, 1999 Fig. 11B. Scale = 5 cm. (Originally identified as *Paleodictyon miocenicum*). Reprinted from Tchoumatchenco, P., and A. Uchman, 1999, Lower and Middle Jurassic flysch trace fossils from the Eastern Stara Planina Mountains, Bulgaria: A contribution to the evolution of Mesozoic ichnodiversity, Neues Jahrbuch für Geologie und Paläontologie - Abhandlungen (www.schweizerbart.de), v. 213, no. 2, pp.169-199 with permission.

Figure E.27 continued.
Jurassic trace fossils.

F. *Paleodictyon*. Sample MP-US J1145. Sini Vir Formation, Emirovo, Bulgaria (Pliensbachian – Toarcian). Figured in Tchoumatchenco and Uchman, 1999 Fig. 11A. Scale = 5 cm. (Originally identified as *Paleodictyon miocenicum*). Reprinted from Tchoumatchenco, P., and A. Uchman, 1999, Lower and Middle Jurassic flysch trace fossils from the Eastern Stara Planina Mountains, Bulgaria: A contribution to the evolution of Mesozoic ichnodiversity, Neues Jahrbuch für Geologie und Paläontologie - Abhandlungen (www.schweizerbart.de), v. 213, no. 2, pp.169-199 with permission.
G. *Protopaleodictyon*. Sample MP-US J1138. Sini Vir Formation, Emirovo, Bulgaria (Pliensbachian – Toarcian). Figured in Tchoumatchenco and Uchman, 1999 Fig. 11G. Scale = 5 cm. (Originally identified as *Megagrapton submontanum*). Reprinted from Tchoumatchenco, P., and A. Uchman, 1999, Lower and Middle Jurassic flysch trace fossils from the Eastern Stara Planina Mountains, Bulgaria: A contribution to the evolution of Mesozoic ichnodiversity, Neues Jahrbuch für Geologie und Paläontologie - Abhandlungen (www.schweizerbart.de), v. 213, no. 2, pp.169-199 with permission.
H. *Protopaleodictyon*. Sample MP-US J1149. Sini Vir Formation, Valley of the Elesnica River, Bulgaria (Pliensbachian – Toarcian). Figured in Tchoumatchenco and Uchman, 1999 Fig. 11F. Scale = 5 cm. (Originally identified as *Megagrapton submontanum*). Reprinted from Tchoumatchenco, P., and A. Uchman, 1999, Lower and Middle Jurassic flysch trace fossils from the Eastern Stara Planina Mountains, Bulgaria: A contribution to the evolution of Mesozoic ichnodiversity, Neues Jahrbuch für Geologie und Paläontologie - Abhandlungen (www.schweizerbart.de), v. 213, no. 2, pp.169-199 with permission.

Permian trace fossils.

I. *Megagrapton*. Sample BKKM I-3. Lercara Formation, Locality 3, Sicily, Italy (Cathedralian). Figured in Kozur et al, 1996 Plate 39 Fig. 2. Scale = 5 cm. (Originally identified as *Megagrapton permicum*). Reprinted from Spring and Facies, v. 34, 1996, pp. 123-150, Ichnology and sedimentology of the early Permian deep-water deposits from the Lercara-Roccapalumba area (Western Sicily, Italy), Kozur, H., K. Krainer, and H. Mostler, with kind permission from Springer Science and Business Media.
J. *Megagrapton*. Sample BKKM I-10. Lercara Formation, Locality 3, Sicily, Italy (Cathedralian). Figured in Kozur et al, 1996 Plate 39 Fig. 1. Scale = 5 cm. (Originally identified as *Megagrapton transitum*). Reprinted from Spring and Facies, v. 34, 1996, pp. 123-150, Ichnology and sedimentology of the early Permian deep-water deposits from the Lercara-Roccapalumba area (Western Sicily, Italy), Kozur, H., K. Krainer, and H. Mostler, with kind permission from Springer Science and Business Media.

Figure E.27 continued.
Permian trace fossils.

K. *Megagrapton*. Sample BKKM I-24. Lercara Formation, Locality 3, Sicily, Italy (Cathedralian). Figured in Kozur et al, 1996 Plate 41 Fig. 2. Scale = 5 cm. (Originally identified as *Megagrapton transitum*). Reprinted from Spring and Facies, v. 34, 1996, pp. 123-150, Ichnology and sedimentology of the early Permian deep-water deposits from the Lercara-Roccapalumba area (Western Sicily, Italy), Kozur, H., K. Krainer, and H. Mostler, with kind permission from Springer Science and Business Media.

L. *Megagrapton*. Sample IKKM I-4. Lercara Formation, Locality 3, Sicily, Italy (Cathedralian). Figured in Kozur et al, 1996 Plate 40 Fig. 5. Scale = 5 cm. (Originally identified as *Megagrapton permicum*). Reprinted from Spring and Facies, v. 34, 1996, pp. 123-150, Ichnology and sedimentology of the early Permian deep-water deposits from the Lercara-Roccapalumba area (Western Sicily, Italy), Kozur, H., K. Krainer, and H. Mostler, with kind permission from Springer Science and Business Media.

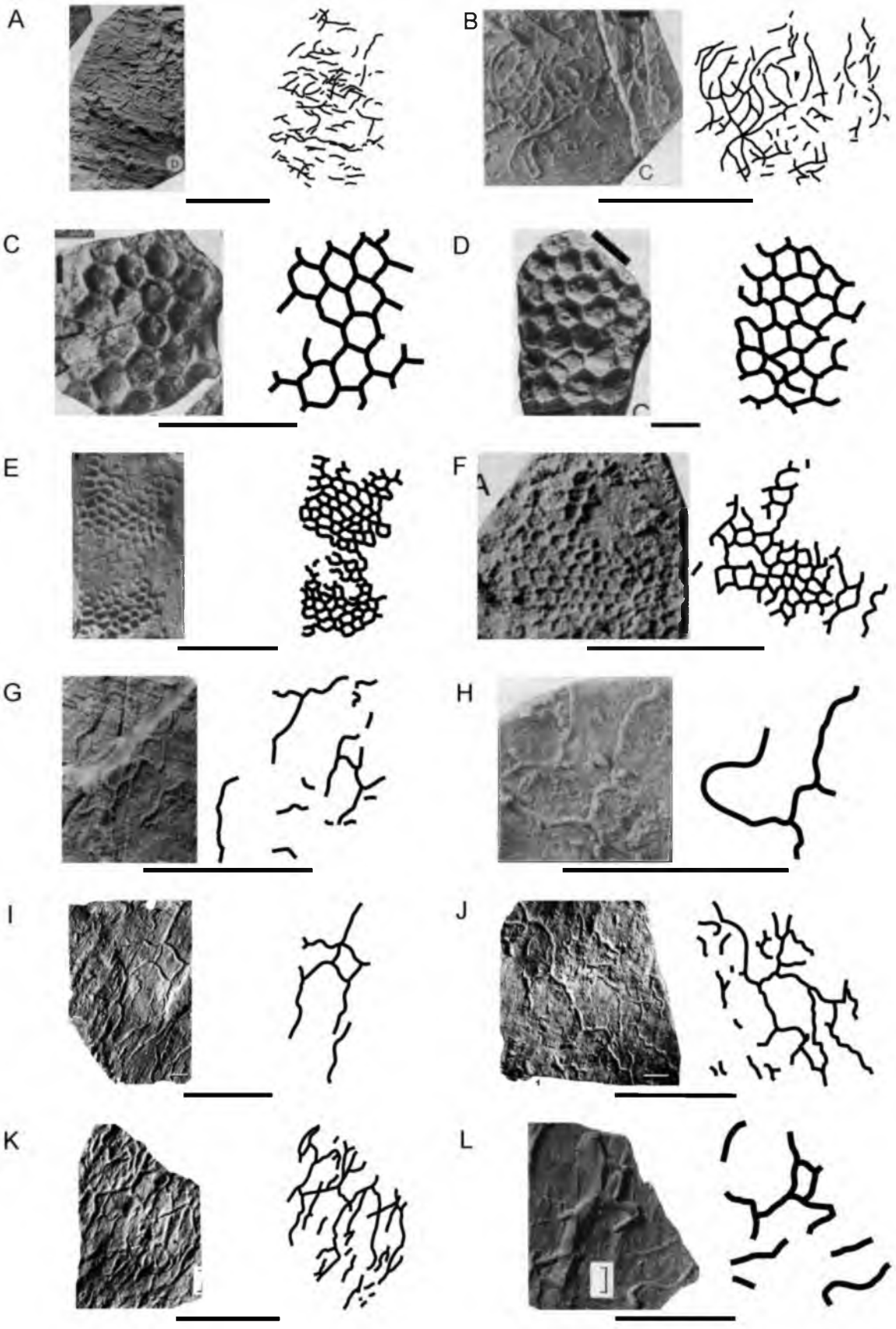
A
B
C
D
E
F
G
H
I
J
K
L

Figure E.28. Permian and Carboniferous trace fossils.
Permian trace fossils.

A. *Megagrapton*. Sample IKKM I-5. Lercara Formation, Locality 3, Sicily, Italy (Cathedralian). Figured in Kozur et al, 1996 Plate 40 Fig. 7. Scale = 5 cm. (Originally identified as *Paleodictyon (Squamodictyon) siciliense*). Reprinted from Spring and Facies, v. 34, 1996, pp. 123-150, Ichnology and sedimentology of the early Permian deep-water deposits from the Lercara-Roccapalumba area (Western Sicily, Italy), Kozur, H., K. Krainer, and H. Mostler, with kind permission from Springer Science and Business Media.
B. *Megagrapton*. Sample IKKM I-6. Lercara Formation, Locality 3, Sicily, Italy (Cathedralian). Figured in Kozur et al, 1996 Plate 40 Fig. 1. Scale = 5 cm. (Originally identified as *Paleodictyon (Squamodictyon) siciliense*). Reprinted from Spring and Facies, v. 34, 1996, pp. 123-150, Ichnology and sedimentology of the early Permian deep-water deposits from the Lercara-Roccapalumba area (Western Sicily, Italy), Kozur, H., K. Krainer, and H. Mostler, with kind permission from Springer Science and Business Media.
C. *Megagrapton*. Sample IKKM I-12. Lercara Formation, Locality 3, Sicily, Italy (Cathedralian). Figured in Kozur et al, 1996 Plate 39 Fig. 5. Scale = 5 cm. (Originally identified as *Megagrapton transitum*). Reprinted from Spring and Facies, v. 34, 1996, pp. 123-150, Ichnology and sedimentology of the early Permian deep-water deposits from the Lercara-Roccapalumba area (Western Sicily, Italy), Kozur, H., K. Krainer, and H. Mostler, with kind permission from Springer Science and Business Media.
D. *Megagrapton*. Sample IKKM I-15. Lercara Formation, Locality 3, Sicily, Italy (Cathedralian). Figured in Kozur et al, 1996 Plate 40 Fig. 2. Scale = 5 cm. (Originally identified as *Megagrapton permicum*). Reprinted from Spring and Facies, v. 34, 1996, pp. 123-150, Ichnology and sedimentology of the early Permian deep-water deposits from the Lercara-Roccapalumba area (Western Sicily, Italy), Kozur, H., K. Krainer, and H. Mostler, with kind permission from Springer Science and Business Media.
E. *Paleodictyon*. Sample IKKM I-2. Lercara Formation, Locality 3, Sicily, Italy (Cathedralian). Figured in Kozur et al, 1996 Plate 39 Fig. 7. Scale = 5 cm. (Originally identified as *Paleodictyon muelleri*). Reprinted from Spring and Facies, v. 34, 1996, pp. 123-150, Ichnology and sedimentology of the early Permian deep-water deposits from the Lercara-Roccapalumba area (Western Sicily, Italy), Kozur, H., K. Krainer, and H. Mostler, with kind permission from Springer Science and Business Media.
F. *Paleodictyon*. Sample IKKM I-7. Lercara Formation, Locality 3, Sicily, Italy (Cathedralian). Figured in Kozur et al, 1996 Plate 40 Fig. 4. Scale = 5 cm. (Originally identified as *Paleodictyon (Squamodictyon) siciliense*). Reprinted from Spring and Facies, v. 34, 1996, pp. 123-150, Ichnology and sedimentology of the early Permian deep-water deposits from the Lercara-Roccapalumba area (Western Sicily, Italy), Kozur, H., K. Krainer, and H. Mostler, with kind permission from Springer Science and Business Media.

Figure E.28 continued.
Permian trace fossils.

G. *Paleodictyon*. Sample IKKM I-8. Lercara Formation, Locality 3, Sicily, Italy (Cathedralian). Figured in Kozur et al, 1996 Plate 39 Fig. 6. Scale = 5 cm. (Originally identified as *Paleodictyon (Squamodictyon) siciliense*). Reprinted from Spring and Facies, v. 34, 1996, pp. 123-150, Ichnology and sedimentology of the early Permian deep-water deposits from the Lercara-Roccapalumba area (Western Sicily, Italy), Kozur, H., K. Krainer, and H. Mostler, with kind permission from Springer Science and Business Media.

H. *Protopaleodictyon*. Sample IKKM I-9. Lercara Formation, Locality 3, Sicily, Italy (Cathedralian). Figured in Kozur et al, 1996 Plate 40 Fig. 3. Scale = 5 cm. (Originally identified as *Megagrapton irregulare*). Reprinted from Spring and Facies, v. 34, 1996, pp. 123-150, Ichnology and sedimentology of the early Permian deep-water deposits from the Lercara-Roccapalumba area (Western Sicily, Italy), Kozur, H., K. Krainer, and H. Mostler, with kind permission from Springer Science and Business Media.

I. *Protopaleodictyon*. Sample IKKM I-14. Lercara Formation, Locality 3, Sicily, Italy (Cathedralian). Figured in Kozur et al, 1996 Plate 40 Fig. 6. Scale = 5 cm. (Originally identified as *Megagrapton permicum*). Reprinted from Spring and Facies, v. 34, 1996, pp. 123-150, Ichnology and sedimentology of the early Permian deep-water deposits from the Lercara-Roccapalumba area (Western Sicily, Italy), Kozur, H., K. Krainer, and H. Mostler, with kind permission from Springer Science and Business Media.

Carboniferous trace fossils.

J. *Megagrapton*. Sample UW 1495. Atoka Formation, Atoka, Oklahoma, USA (Lower - Middle Pennsylvanian). Figured in Chamberlain, 1971 Plate 31 Fig. 3. Scale = 5 cm. (Originally identified as *Squamodictyon* aff. *S. squamosum*). Reprinted from Chamberlain, C. K., 1971, Morphology and ethology of trace fossils from the Ouachita Mountains, Southeast Oklahoma, Journal of Paleontology, v. 45, no. 2, pp. 212-246 with permission.

K. *Protopaleodictyon*. Sample UW 1497. Atoka Formation, Atoka, Oklahoma, USA (Lower - Middle Pennsylvanian). Figured in Chamberlain, 1971 Plate 31 Fig. 5. Scale = 2 cm. (Originally identified as *Paleodictyon majus*). Reprinted from Chamberlain, C. K., 1971, Morphology and ethology of trace fossils from the Ouachita Mountains, Southeast Oklahoma, Journal of Paleontology, v. 45, no. 2, pp. 212-246 with permission.

L. *Squamodictyon*. Sample Llompart and Wieczorek 1997 Plate II.1. Culm Siliciclastic Sequence, Cala Presili, Minorca (Uppermost Visean - Namurian). Figured in Llompart and Wieczorek, 1997 Plate II.1. Scale = 5 cm. (Originally identified as *Paleodictyon*). Reprinted from Llompart, C., and J. Wieczorek, 1997, Trace fossils from Culm Facies of Miorca Island, Prace Panstwowego Instytutu Geologiczego, v. 157, pp. 99-103 under the Creative Commons License 4.0 (http://creativecommons.org/licenses/by-sa/4.0/).

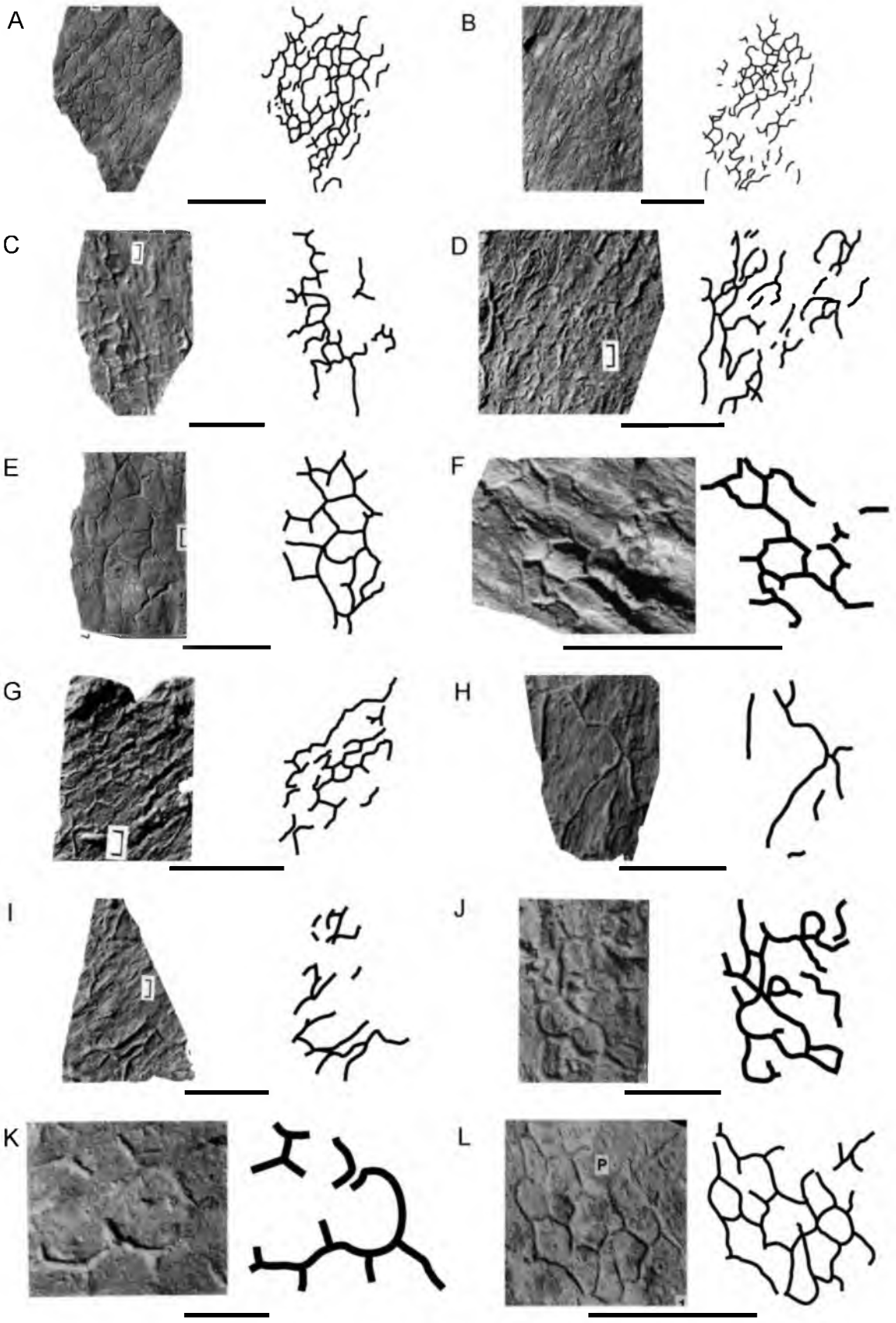
A
B
C
D
E
F
G
H
I
J
K
L
P

Figure E.29. Carboniferous and Devonian trace fossils.
Carboniferous trace fossils.

A. *Squamodictyon*. Sample PIW 89I130. Dürrenwaider Slate, Nordhalben, Germany (Lower Visean). Figured in Stepanek and Geyer, 1989 Tafel 3 Fig. 25. Scale = 5 cm. (Originally identified as *Squamodictyon* sp. incert.). Reprinted from Stepanek, J., and G. Geyer, 1989, Spurenfossilien aus dem Kulm (Unterkarbon) des Frankenwaldes, Beringeria, v. 1, pp.1-55, with permission.
B. *Megagrapton*. Sample PIW 89I6. Mittlere Wechsellagerung Grauwacke, Nordhalben, Germany (Lower Visean). Figured in Stepanek and Geyer, 1989 Tafel 3 Fig. 22. Scale = 2 cm. (Originally identified as *Megagrapton angulare*). Reprinted from Stepanek, J., and G. Geyer, 1989, Spurenfossilien aus dem Kulm (Unterkarbon) des Frankenwaldes, Beringeria, v. 1, pp.1-55, with permission.
C. *Megagrapton*. Sample PIW 89I9. Mittlere Wechsellagerung Grauwacke, Nordhalben, Germany (Lower Visean). Figured in Stepanek and Geyer, 1989 Tafel 3 Fig. 23. Scale = 2 cm. (Originally identified as *Megagrapton angulare*). Reprinted from Stepanek, J., and G. Geyer, 1989, Spurenfossilien aus dem Kulm (Unterkarbon) des Frankenwaldes, Beringeria, v. 1, pp.1-55, with permission.
D. *Megagrapton*. Sample PIW 89I10. Mittlere Wechsellagerung Grauwacke, Nordhalben, Germany (Lower Visean). Figured in Stepanek and Geyer, 1989 Tafel 3 Fig. 20. Scale = 5 cm. (Originally identified as *Megagrapton angulare*). Reprinted from Stepanek, J., and G. Geyer, 1989, Spurenfossilien aus dem Kulm (Unterkarbon) des Frankenwaldes, Beringeria, v. 1, pp.1-55, with permission.
E. *Megagrapton*. Sample PIW 89I98b. Mittlere Wechsellagerung Grauwacke, Nordhalben, Germany (Lower Visean). Figured in Stepanek and Geyer, 1989 Tafel 3 Fig. 21. Scale = 5 cm. (Originally identified as *Megagrapton angulare*). Reprinted from Stepanek, J., and G. Geyer, 1989, Spurenfossilien aus dem Kulm (Unterkarbon) des Frankenwaldes, Beringeria, v. 1, pp.1-55, with permission.
F. *Megagrapton*. Sample PIW 89I241. Mittlere Wechsellagerung Grauwacke, Nordhalben, Germany (Lower Visean). Figured in Stepanek and Geyer, 1989 Tafel 3 Fig. 24. Scale = 5 cm. (Originally identified as *Megagrapton angulare*). Reprinted from Stepanek, J., and G. Geyer, 1989, Spurenfossilien aus dem Kulm (Unterkarbon) des Frankenwaldes, Beringeria, v. 1, pp.1-55, with permission.
G. *Megagrapton*. Sample PIW 89I244. Mittlere Wechsellagerung Grauwacke, Nordhalben, Germany (Lower Visean). Figured in Stepanek and Geyer, 1989 Tafel 3 Fig. 19. Scale = 5 cm. (Originally identified as *Megagrapton angulare*). Reprinted from Stepanek, J., and G. Geyer, 1989, Spurenfossilien aus dem Kulm (Unterkarbon) des Frankenwaldes, Beringeria, v. 1, pp.1-55, with permission.
H. *Helminthopsis*. Sample Mikuláš et al 2004 Plate III-3. Moravice Formation, Maly Rabstyn Locality, Czech Republic (Late Visean). Figured in Mikuláš et al., 2004 Plate III-3. Scale = 5 cm. (Originally identified as *?Cosmorhaphe* isp.). Reprinted from Mikuláš, R., T. Lehotský, and O. Bábek, 2004, Trace fossils of the Moravice Formation from the southern Nízký Jeseník Mts. (Lower Carboniferous, Culm facies; Moravia, Czech Republic), Bulletin of Geosciences, v. 79, no. 2, pp.81-98, with permission.

Figure E.29 continued.
Carboniferous trace fossils.

I. *Megagrapton*. Sample Mikuláš et al 2004 Plate V-2. Moravice Formation, Maly Rabstyn Locality, Czech Republic (Late Visean). Figured in Mikuláš et al., 2004 Plate V-2. Scale = 5 cm. (Originally identified as *Protopaleodictyon* isp.). Reprinted from Mikuláš, R., T. Lehotský, and O. Bábek, 2004, Trace fossils of the Moravice Formation from the southern Nízký Jeseník Mts. (Lower Carboniferous, Culm facies; Moravia, Czech Republic), Bulletin of Geosciences, v. 79, no. 2, pp.81-98, with permission.
J. *Protopaleodictyon*. Sample Mikuláš et al 2004 Plate V-3. Moravice Formation, Maly Rabstyn Locality, Czech Republic (Late Visean). Figured in Mikuláš et al., 2004 Plate V-3. Scale = 5 cm. (Originally identified as *Protopaleodictyon* isp.). Reprinted from Mikuláš, R., T. Lehotský, and O. Bábek, 2004, Trace fossils of the Moravice Formation from the southern Nízký Jeseník Mts. (Lower Carboniferous, Culm facies; Moravia, Czech Republic), Bulletin of Geosciences, v. 79, no. 2, pp.81-98, with permission.

Devonian trace fossils.

K. *Cosmorhaphe*. Sample NBMG 9675. Wapske Formation, Riley Brook, Nictau, New Brunswick, Canada (Lochkovian – Pragian). Figured in Han and Pickerill, 1994 Fig. 5C. Scale = 5 cm. (Originally identified as *Helminthpsis abeli*). Reprinted from Han, Y., and R. K. Pickerill, 1994, Palichnology of the Lower Devonian Wapske Formation, Perth-Andover-Mount Carleton region, northwestern New Brunswick, eastern Canada, Atlantic Geology, v. 30, pp.217-245, with permission.
L. *Cosmorhaphe*. Sample TF.F142. Wapske Formation, Riley Brook, Nictau, New Brunswick, Canada (Lochkovian – Pragian). Figured in Han and Pickerill, 1994 Fig. 4G. Scale = 5 cm. (Originally identified as *Cosmorhaphe sinuosa*). Reprinted from Han, Y., and R. K. Pickerill, 1994, Palichnology of the Lower Devonian Wapske Formation, Perth-Andover-Mount Carleton region, northwestern New Brunswick, eastern Canada, Atlantic Geology, v. 30, pp.217-245, with permission.

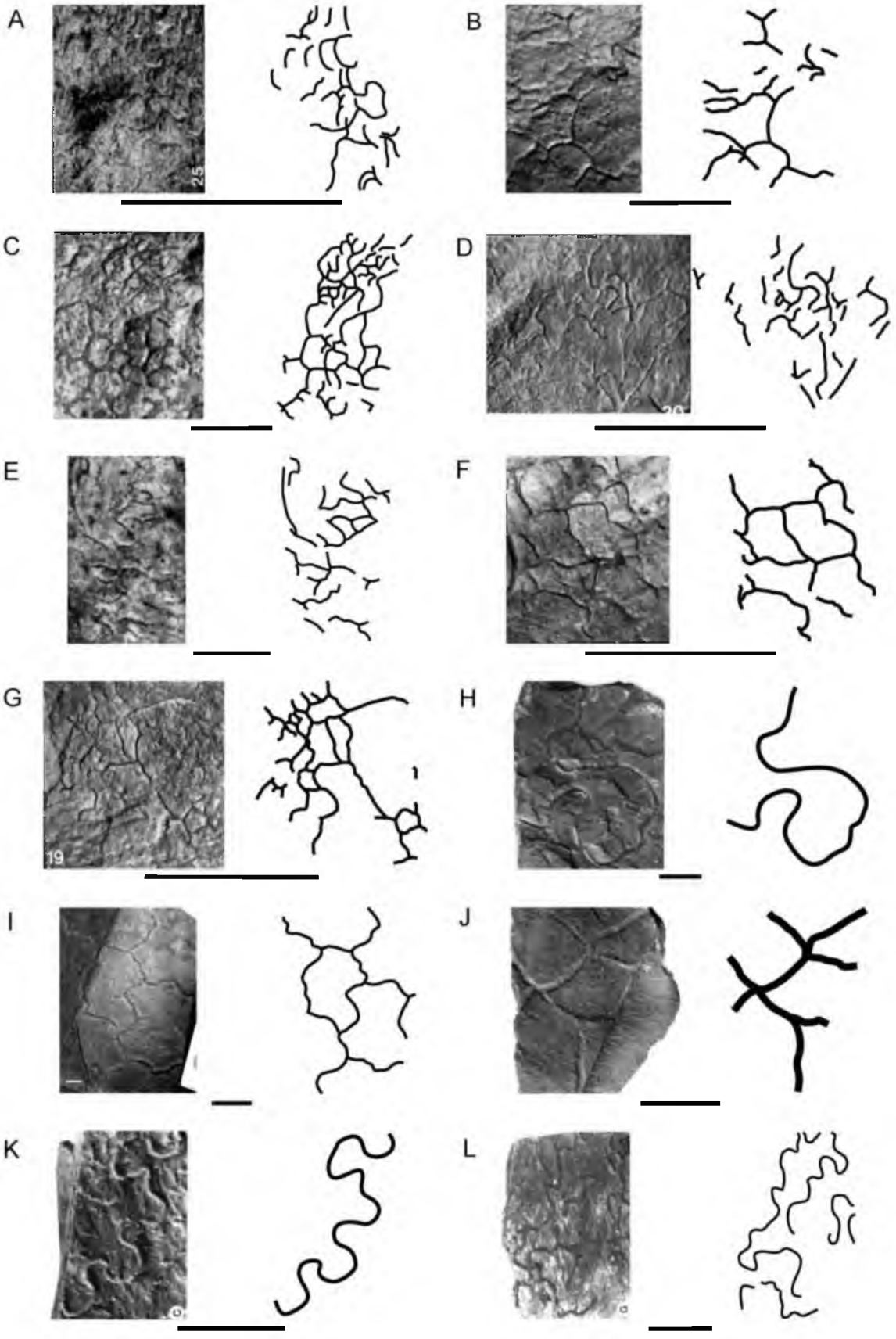
A
B
C
D
E
F
G
H
I
J
K
L

Figure E.30. Devonian and Silurian trace fossils.
Devonian trace fossils.

A. *Cosmorhaphe*. Sample TF9208-1-30. Wapske Formation, Riley Brook, Nictau, New Brunswick, Canada (Lochkovian – Pragian). Figured in Han and Pickerill, 1994 Fig. 4C. Scale = 5 cm. (Originally identified as *Cosmorhaphe fuchsi*). Reprinted from Han, Y., and R. K. Pickerill, 1994, Palichnology of the Lower Devonian Wapske Formation, Perth-Andover-Mount Carleton region, northwestern New Brunswick, eastern Canada, Atlantic Geology, v. 30, pp.217-245, with permission.
B. *Gordia*. Sample NBMG 9683. Wapske Formation, Riley Brook, Nictau, New Brunswick, Canada (Lochkovian – Pragian). Figured in Han and Pickerill, 1994 Fig. 5E. Scale = 5 cm. (Originally identified as *Helminthopsis* isp.). Reprinted from Han, Y., and R. K. Pickerill, 1994, Palichnology of the Lower Devonian Wapske Formation, Perth-Andover-Mount Carleton region, northwestern New Brunswick, eastern Canada, Atlantic Geology, v. 30, pp.217-245, with permission.
C. *Helminthopsis*. Sample NBMG 9680. Wapske Formation, Riley Brook, Nictau, New Brunswick, Canada (Lochkovian – Pragian). Figured in Han and Pickerill, 1994 Fig. 5F. Scale = 5 cm. (Originally identified as *Helminthopsis hieroglyphica*). Reprinted from Han, Y., and R. K. Pickerill, 1994, Palichnology of the Lower Devonian Wapske Formation, Perth-Andover-Mount Carleton region, northwestern New Brunswick, eastern Canada, Atlantic Geology, v. 30, pp.217-245, with permission.
D. *Helminthorhaphe*. Sample TF.F111. Wapske Formation, Riley Brook, Nictau, New Brunswick, Canada (Lochkovian – Pragian). Figured in Han and Pickerill, 1994 Fig. 5A. Scale = 2 cm. (Originally identified as *Helminthoida miocenica*). Reprinted from Han, Y., and R. K. Pickerill, 1994, Palichnology of the Lower Devonian Wapske Formation, Perth-Andover-Mount Carleton region, northwestern New Brunswick, eastern Canada, Atlantic Geology, v. 30, pp.217-245, with permission.
E. *Protopaleodictyon*. Sample TF9208-1-15. Wapske Formation, Riley Brook, Nictau, New Brunswick, Canada (Lochkovian – Pragian). Figured in Han and Pickerill, 1994 Fig. 7F. Scale = 5 cm. (Originally identified as *Protopaleodictyon incompositum*). Reprinted from Han, Y., and R. K. Pickerill, 1994, Palichnology of the Lower Devonian Wapske Formation, Perth-Andover-Mount Carleton region, northwestern New Brunswick, eastern Canada, Atlantic Geology, v. 30, pp.217-245, with permission.
F. *Protopaleodictyon*. Sample TF9208-1-17. Wapske Formation, Riley Brook, Nictau, New Brunswick, Canada (Lochkovian – Pragian). Figured in Han and Pickerill, 1994 Fig. 7A. Scale = 5 cm. (Originally identified as *Paleodictyon* isp.). Reprinted from Han, Y., and R. K. Pickerill, 1994, Palichnology of the Lower Devonian Wapske Formation, Perth-Andover-Mount Carleton region, northwestern New Brunswick, eastern Canada, Atlantic Geology, v. 30, pp.217-245, with permission.

Figure E.30 continued.
Silurian trace fossils.

G. *Gordia*. Sample Crimes and Crossley 1991 Fig 9a. Aberystwyth Grits Formation, Locality 1, Wales (Late Llandovery). Figured in Crimes and Crossley, 1991 Fig. 9a. Scale = 5 cm. (Originally identified as *Gordia marina*). Reproduced with permission from Crimes and Crossley (1991), A diverse ichnofauna from Silurian flysch of the Aberystwyth Grits Formation, Wales, Geological Journal, copyright 1991 by John Wiley & Sons, Ltd.

H. *Gordia*. Sample NMW 90.44G.14. Aberystwyth Grits Formation, Locality 3, Wales (Late Llandovery). Figured in Crimes and Crossley, 1991 Fig. 4f. Scale = 5 cm. (Originally identified as *Gordia marina*). Reproduced with permission from Crimes and Crossley (1991), A diverse ichnofauna from Silurian flysch of the Aberystwyth Grits Formation, Wales, Geological Journal, copyright 1991 by John Wiley & Sons, Ltd.

I. *Helminthopsis*. Sample Crimes and Crossley 1991 Fig 4c. Aberystwyth Grits Formation, Locality 1, Wales (Late Llandovery). Figured in Crimes and Crossley, 1991 Fig. 4c. Scale = 5 cm. (Originally identified as *Helminthopsis regularis*). Reproduced with permission from Crimes and Crossley (1991), A diverse ichnofauna from Silurian flysch of the Aberystwyth Grits Formation, Wales, Geological Journal, copyright 1991 by John Wiley & Sons, Ltd.

J. *Helminthopsis*. Sample Crimes and Crossley 1991 Fig 4d. Aberystwyth Grits Formation, Locality 1, Wales (Late Llandovery). Figured in Crimes and Crossley, 1991 Fig. 4d. Scale = 5 cm. (Originally identified as *Helminthopsis regularis*). Reproduced with permission from Crimes and Crossley (1991), A diverse ichnofauna from Silurian flysch of the Aberystwyth Grits Formation, Wales, Geological Journal, copyright 1991 by John Wiley & Sons, Ltd.

K. *Helminthopsis*. Sample Crimes and Crossley 1991 Fig 4e. Aberystwyth Grits Formation, Locality 1, Wales (Late Llandovery). Figured in Crimes and Crossley, 1991 Fig. 4e. Scale = 5 cm. (Originally identified as *Helminthopsis regularis*). Reproduced with permission from Crimes and Crossley (1991), A diverse ichnofauna from Silurian flysch of the Aberystwyth Grits Formation, Wales, Geological Journal, copyright 1991 by John Wiley & Sons, Ltd.

L. *Paleodictyon*. Sample Crimes and Crossley 1991 Fig 9c. Aberystwyth Grits Formation, Locality 1, Wales (Late Llandovery). Figured in Crimes and Crossley, 1991 Fig. 9c. Scale = 5 cm. (Originally identified as *Paleodictyon* ichnosp.). Reproduced with permission from Crimes and Crossley (1991), A diverse ichnofauna from Silurian flysch of the Aberystwyth Grits Formation, Wales, Geological Journal, copyright 1991 by John Wiley & Sons, Ltd.

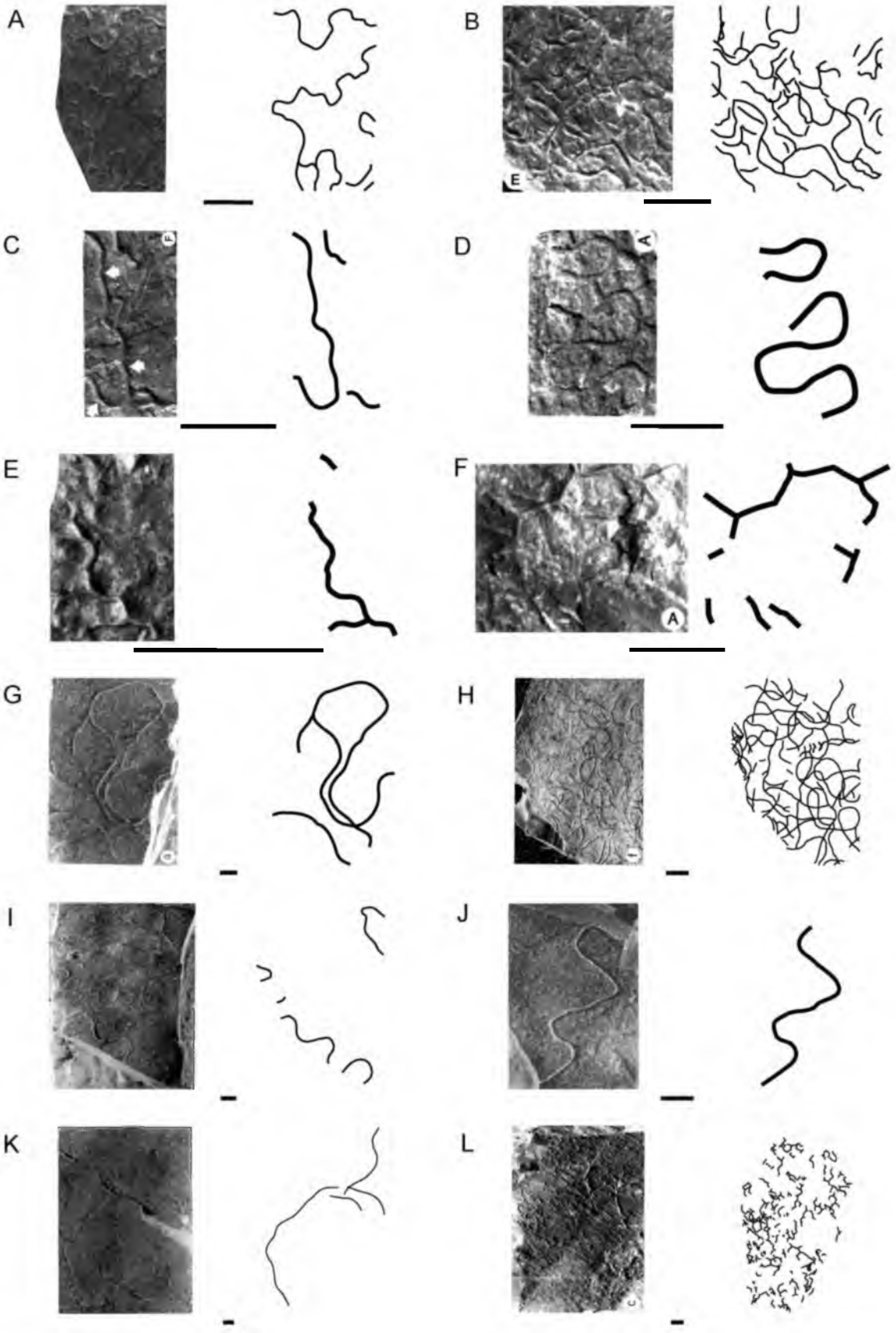
A
B
C
D
E
F
G
H
I
J
K
L

Figure E.31. Silurian trace fossils.
Silurian trace fossils.

A. *Paleodictyon*. Sample Crimes and Crossley 1991 Fig 9d. Aberystwyth Grits Formation, Locality 1, Wales (Late Llandovery). Figured in Crimes and Crossley, 1991 Fig. 9d. Scale = 5 cm. (Originally identified as *Paleodictyon* ichnosp.). Reproduced with permission from Crimes and Crossley (1991), A diverse ichnofauna from Silurian flysch of the Aberystwyth Grits Formation, Wales, Geological Journal, copyright 1991 by John Wiley & Sons, Ltd.
B. *Paleodictyon*. Sample Crimes and Crossley 1991 Fig 9e. Aberystwyth Grits Formation, Locality 1, Wales (Late Llandovery). Figured in Crimes and Crossley, 1991 Fig. 9e. Scale = 5 cm. (Originally identified as *Paleodictyon* ichnosp.). Reproduced with permission from Crimes and Crossley (1991), A diverse ichnofauna from Silurian flysch of the Aberystwyth Grits Formation, Wales, Geological Journal, copyright 1991 by John Wiley & Sons, Ltd.
C. *Paleodictyon*. Sample Crimes and Crossley 1991 Fig 9f. Aberystwyth Grits Formation, Locality 1, Wales (Late Llandovery). Figured in Crimes and Crossley, 1991 Fig. 9f. Scale = 5 cm. (Originally identified as *Paleodictyon* ichnosp.). Reproduced with permission from Crimes and Crossley (1991), A diverse ichnofauna from Silurian flysch of the Aberystwyth Grits Formation, Wales, Geological Journal, copyright 1991 by John Wiley & Sons, Ltd.
D. *Paleodictyon*. Sample Crimes and Crossley 1991 Fig 13a. Aberystwyth Grits Formation, Locality 1, Wales (Late Llandovery). Figured in Crimes and Crossley, 1991 Fig. 13a. Scale = 5 cm. (Originally identified as *Paleodictyon* ichnosp.). Reproduced with permission from Crimes and Crossley (1991), A diverse ichnofauna from Silurian flysch of the Aberystwyth Grits Formation, Wales, Geological Journal, copyright 1991 by John Wiley & Sons, Ltd.
E. *Paleodictyon*. Sample Crimes and Crossley 1991 Fig 13b. Aberystwyth Grits Formation, Locality 1, Wales (Late Llandovery). Figured in Crimes and Crossley, 1991 Fig. 13b. Scale = 5 cm. (Originally identified as *Paleodictyon* ichnosp.). Reproduced with permission from Crimes and Crossley (1991), A diverse ichnofauna from Silurian flysch of the Aberystwyth Grits Formation, Wales, Geological Journal, copyright 1991 by John Wiley & Sons, Ltd.
F. *Paleodictyon*. Sample Crimes and Crossley 1991 Fig 13c. Aberystwyth Grits Formation, Locality 1, Wales (Late Llandovery). Figured in Crimes and Crossley, 1991 Fig. 13c. Scale = 5 cm. (Originally identified as *Paleodictyon* ichnosp.). Reproduced with permission from Crimes and Crossley (1991), A diverse ichnofauna from Silurian flysch of the Aberystwyth Grits Formation, Wales, Geological Journal, copyright 1991 by John Wiley & Sons, Ltd.
G. *Squamodictyon*. Sample Crimes and Crossley 1991 Fig 13e. Aberystwyth Grits Formation, Locality 1, Wales (Late Llandovery). Figured in Crimes and Crossley, 1991 Fig. 13e. Scale = 5 cm. (Originally identified as *Squamodictyon squamosum*). Reproduced with permission from Crimes and Crossley (1991), A diverse ichnofauna from Silurian flysch of the Aberystwyth Grits Formation, Wales, Geological Journal, copyright 1991 by John Wiley & Sons, Ltd.

Figure E.31 continued.
Silurian trace fossils.

H. *Squamodictyon*. Sample Crimes and Crossley 1991 Fig 17c. Aberystwyth Grits Formation, Locality 1, Wales (Late Llandovery). Figured in Crimes and Crossley, 1991 Fig. 17c. Scale = 5 cm. (Originally identified as *Squamodictyon squamosum*). Reproduced with permission from Crimes and Crossley (1991), A diverse ichnofauna from Silurian flysch of the Aberystwyth Grits Formation, Wales, Geological Journal, copyright 1991 by John Wiley & Sons, Ltd.

I. *Squamodictyon*. Sample GPIT 1503/2. Aberystwyth Grits Formation, Wales (Late Llandovery). Figured in Seilacher, 1977 Plate 1b. Scale = 5 cm. (Originally identified as *Paleodictyon (Squamodictyon) petaloideum*). Reprinted from Seilacher, A., 1977, Pattern analysis of *Paleodictyon* and related trace fossils, pp.289-334, in T. P. Crimes, and J. C. Harper, eds., Trace Fossils 2, published by John Wiley & Sons Ltd with permission.

J. *Squamodictyon*. Sample NMW 90.44G.6. Aberystwyth Grits Formation, Locality 6, Wales (Late Llandovery). Figured in Crimes and Crossley, 1991 Fig. 13f. Scale = 5 cm. (Originally identified as *Squamodictyon squamosum*). Reproduced with permission from Crimes and Crossley (1991), A diverse ichnofauna from Silurian flysch of the Aberystwyth Grits Formation, Wales, Geological Journal, copyright 1991 by John Wiley & Sons, Ltd.

K. *Squamodictyon*. Sample NMW 90.44G.7. Aberystwyth Grits Formation, Locality 6, Wales (Late Llandovery). Figured in Crimes and Crossley, 1991 Fig. 16a. Scale = 5 cm. (Originally identified as *Squamodictyon squamosum*). Reproduced with permission from Crimes and Crossley (1991), A diverse ichnofauna from Silurian flysch of the Aberystwyth Grits Formation, Wales, Geological Journal, copyright 1991 by John Wiley & Sons, Ltd.

L. *Squamodictyon*. Sample NMW 90.44G.8. Aberystwyth Grits Formation, Locality 6, Wales (Late Llandovery). Figured in Crimes and Crossley, 1991 Fig. 16b. Scale = 5 cm. (Originally identified as *Squamodictyon squamosum*). Reproduced with permission from Crimes and Crossley (1991), A diverse ichnofauna from Silurian flysch of the Aberystwyth Grits Formation, Wales, Geological Journal, copyright 1991 by John Wiley & Sons, Ltd.

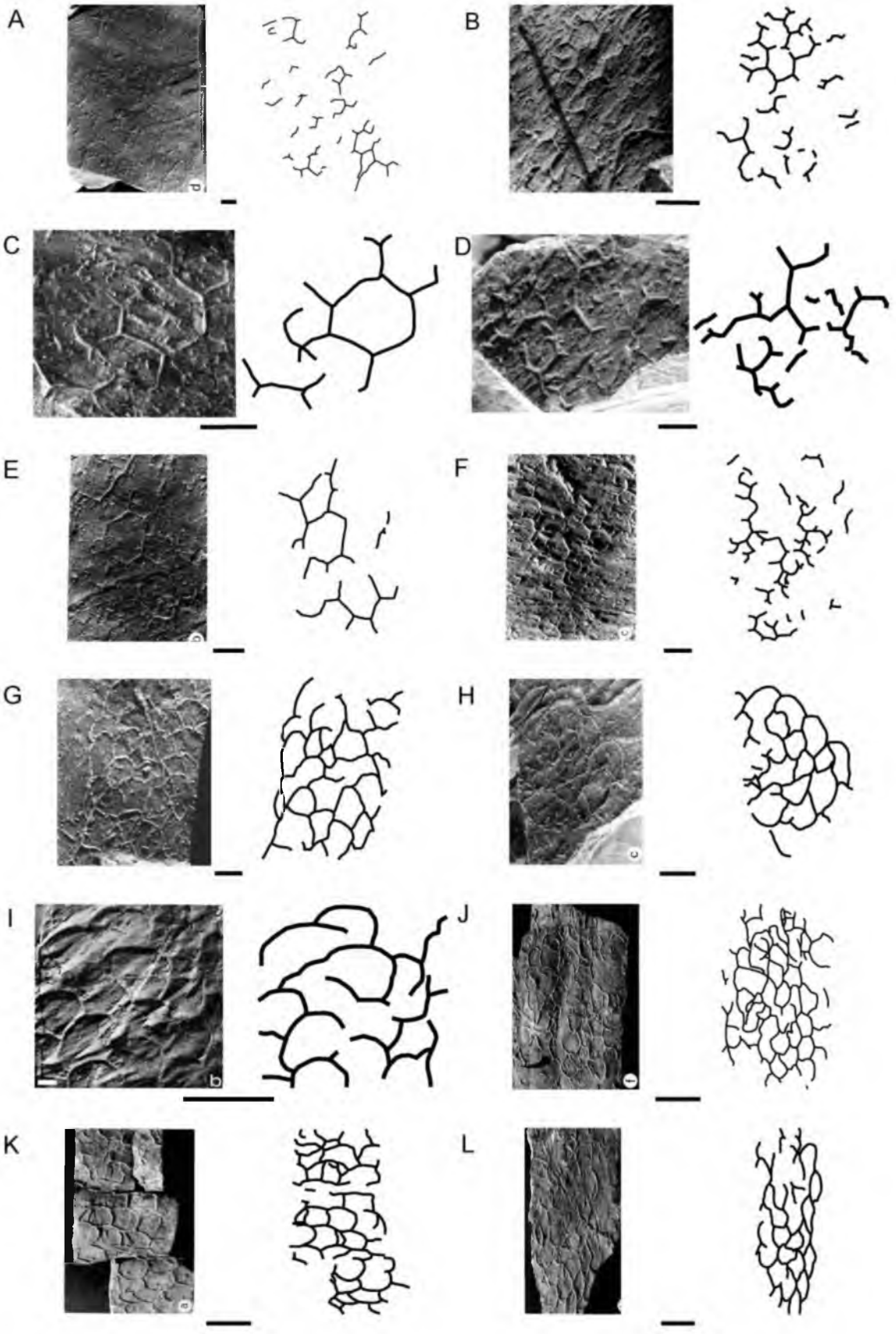
A
B
C
D
E
F
G
H
I
J
K
L

Figure E.32. Silurian trace fossils.
Silurian trace fossils.

A. *Squamodictyon*. Sample NMW 90.44G.10. Aberystwyth Grits Formation, Locality 9, Wales (Late Llandovery). Figured in Crimes and Crossley, 1991 Fig. 17b. Scale = 5 cm. (Originally identified as *Squamodictyon squamosum*). Reproduced with permission from Crimes and Crossley (1991), A diverse ichnofauna from Silurian flysch of the Aberystwyth Grits Formation, Wales, Geological Journal, copyright 1991 by John Wiley & Sons, Ltd.
B. *Squamodictyon*. Sample NMW 90.44G.16. Aberystwyth Grits Formation, Locality 6, Wales (Late Llandovery). Figured in Crimes and Crossley, 1991 Fig. 16c. Scale = 5 cm. (Originally identified as *Squamodictyon squamosum*). Reproduced with permission from Crimes and Crossley (1991), A diverse ichnofauna from Silurian flysch of the Aberystwyth Grits Formation, Wales, Geological Journal, copyright 1991 by John Wiley & Sons, Ltd.
C. *Squamodictyon*. Sample NMW 90.44G.17. Aberystwyth Grits Formation, Locality 6, Wales (Late Llandovery). Figured in Crimes and Crossley, 1991 Fig. 16d. Scale = 5 cm. (Originally identified as *Squamodictyon squamosum*). Reproduced with permission from Crimes and Crossley (1991), A diverse ichnofauna from Silurian flysch of the Aberystwyth Grits Formation, Wales, Geological Journal, copyright 1991 by John Wiley & Sons, Ltd.
D. *Squamodictyon*. Sample NMW 90.44G.18. Aberystwyth Grits Formation, Locality 6, Wales (Late Llandovery). Figured in Crimes and Crossley, 1991 Fig. 16e. Scale = 5 cm. (Originally identified as *Squamodictyon squamosum*). Reproduced with permission from Crimes and Crossley (1991), A diverse ichnofauna from Silurian flysch of the Aberystwyth Grits Formation, Wales, Geological Journal, copyright 1991 by John Wiley & Sons, Ltd.
E. *Squamodictyon*. Sample NMW 90.44G.19. Aberystwyth Grits Formation, Locality 6, Wales (Late Llandovery). Figured in Crimes and Crossley, 1991 Fig. 16f. Scale = 5 cm. (Originally identified as *Squamodictyon squamosum*). Reproduced with permission from Crimes and Crossley (1991), A diverse ichnofauna from Silurian flysch of the Aberystwyth Grits Formation, Wales, Geological Journal, copyright 1991 by John Wiley & Sons, Ltd.
F. *Squamodictyon*. Sample NMW 90.44G.20. Aberystwyth Grits Formation, Locality 6, Wales (Late Llandovery). Figured in Crimes and Crossley, 1991 Fig. 17d. Scale = 5 cm. (Originally identified as *Squamodictyon squamosum*). Reproduced with permission from Crimes and Crossley (1991), A diverse ichnofauna from Silurian flysch of the Aberystwyth Grits Formation, Wales, Geological Journal, copyright 1991 by John Wiley & Sons, Ltd.
G. *Megagrapton*. Sample RSM 1981.30.68. Gala Group, Hunter Hill, Scotland (Late Llandovery). Figured in Benton, 1982 Fig. 8C. Scale = 5 cm. (Originally identified as *Megagrapton* isp.). Reproduced by permission of The Royal Society of Edinburgh and Michael Benton from *Transactions of the Royal Society of Edinburgh: Earth Sciences* volume 73 (1982), pp. 67–87.

Figure E.32 continued.
Silurian trace fossils.

H. *Gordia*. Sample RSM 1981.30.100. Hawick Rocks, Stirches, Scotland (Late Llandovery). Figured in Benton, 1982 Fig. 8A. Scale = 5 cm. (Originally identified as *Gordia marina*). Reproduced by permission of The Royal Society of Edinburgh and Michael Benton from *Transactions of the Royal Society of Edinburgh: Earth Sciences* volume 73 (1982), pp. 67–87.

I. *Paleodictyon*. Sample UEGIG 46275. Hawick Rocks, Mull Point, Scotland (Late Llandovery). Figured in Benton, 1982 Fig. 9A. Scale = 5 cm. (Originally identified as *Paleodictyon imperfectum*). Reproduced by permission of The Royal Society of Edinburgh and Michael Benton from *Transactions of the Royal Society of Edinburgh: Earth Sciences* volume 73 (1982), pp. 67–87.

J. *Gordia*. Sample Aceñolaza 1978 Lám III-3. Los Espejos Formation, Argentina (Ludlow). Figured in Aceñolaza, 1978 Lám. III-3. Scale = 5 cm. (Originally identified as *Gordia* sp.). Reprinted from Aceñolaza, F. G., 1978, El Paleozoica inferior de Argentina segun sus trazas fosiles, Ameghiniana, v. 15, no. 1-2, pp. 15-64, with permission.

K. *Helminthorhaphe*. Sample Aceñolaza 1978 Lám IV-6. Los Espejos Formation, Argentina (Ludlow). Figured in Aceñolaza, 1978 Lám. IV-6. Scale = 5 cm. (Originally identified as *Cosmorhaphe* sp.). Reprinted from Aceñolaza, F. G., 1978, El Paleozoica inferior de Argentina segun sus trazas fosiles, Ameghiniana, v. 15, no. 1-2, pp. 15-64, with permission.

L. *Paleodictyon*. Sample Aceñolaza 1978 Lám III-1. Los Espejos Formation, Argentina (Ludlow). Figured in Aceñolaza, 1978 Lám. III-1. Scale = 5 cm. (Originally identified as *Paleodictyon* sp.). Reprinted from Aceñolaza, F. G., 1978, El Paleozoica inferior de Argentina segun sus trazas fosiles, Ameghiniana, v. 15, no. 1-2, pp. 15-64, with permission.

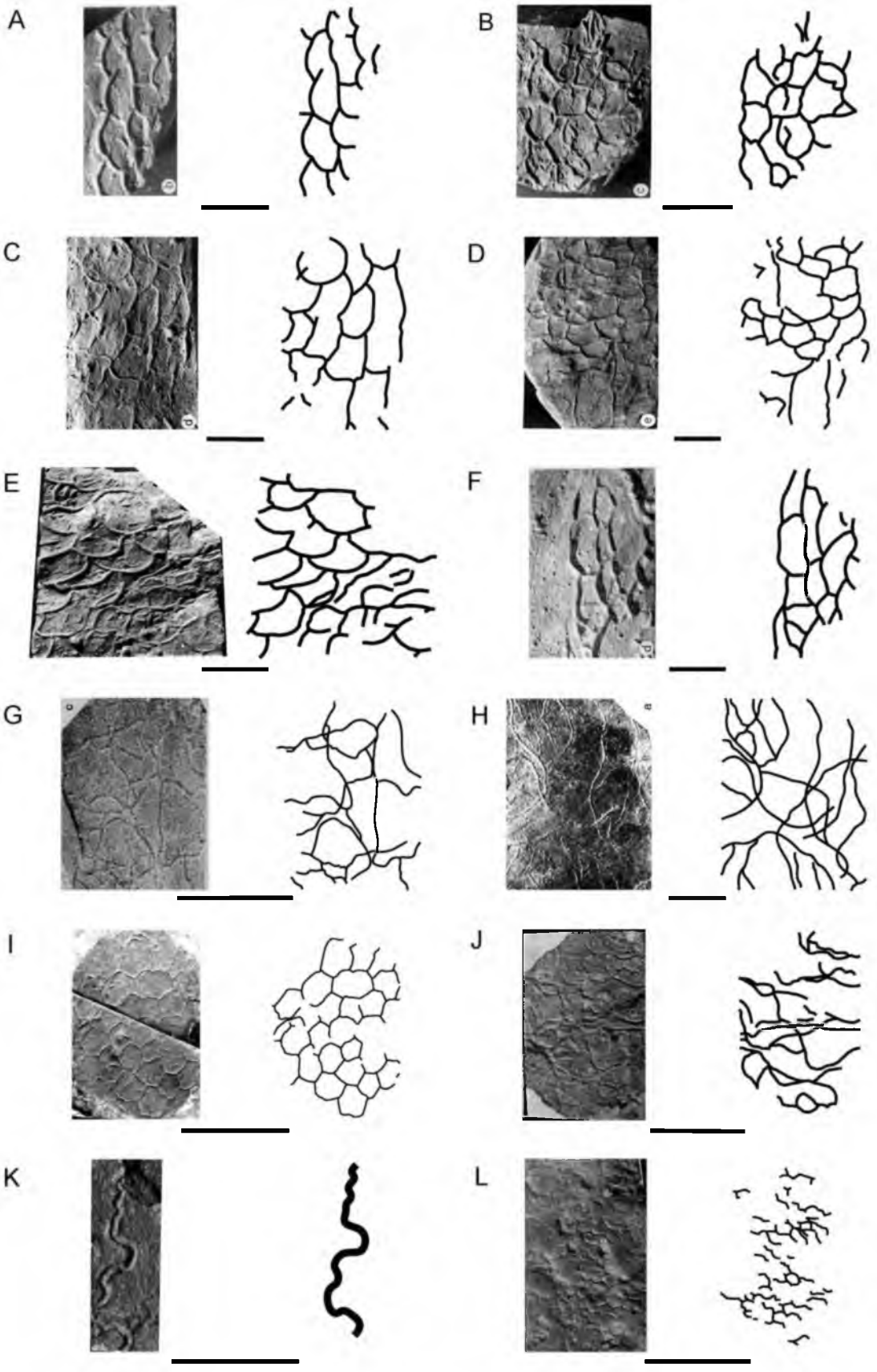
A
B
C
D
E
F
G
H
I
J
K
L

Figure E.33. Silurian and Ordovician trace fossils.
Silurian trace fossils.

A. *Protopaleodictyon*. Sample Aceñolaza 1978 Lám III-2. Los Espejos Formation, Argentina (Ludlow). Figured in Aceñolaza, 1978 Lám. III-2. Scale = 5 cm. (Originally identified as *Paleodictyon* sp.). Reprinted from Aceñolaza, F. G., 1978, El Paleozoica inferior de Argentina segun sus trazas fosiles, Ameghiniana, v. 15, no. 1-2, pp. 15-64, with permission.
B. *Gordia*. Sample Pickerill 1981 Fig 2d. Siegas Formation, Siegas, New Brunswick, Canada (Early Llandovery). Figured in Pickerill, 1981 Fig 2d. Scale = 5 cm. (Originally identified as *Gordia* sp.). Reprinted from Pickerill, R. K, 1981, Trace fossils in a Lower Palaeozoic submarine canyon sequence - the Siegas Formation of northwestern New Brunswick, Canada, Maritime Sediments and Atlantic Geology, v. 17, pp.36-58, with permission.
C. *Gordia*. Sample Pickerill 1981 Fig 3a. Siegas Formation, Siegas, New Brunswick, Canada (Early Llandovery). Figured in Pickerill, 1981 Fig 3a. Scale = 5 cm. (Originally identified as *Gordia arcuata*). Reprinted from Pickerill, R. K, 1981, Trace fossils in a Lower Palaeozoic submarine canyon sequence - the Siegas Formation of northwestern New Brunswick, Canada, Maritime Sediments and Atlantic Geology, v. 17, pp.36-58, with permission.
D. *Helminthopsis*. Sample Pickerill 1981 Fig 2b. Siegas Formation, Siegas, New Brunswick, Canada (Early Llandovery). Figured in Pickerill, 1981 Fig 2b. Scale = 5 cm. (Originally identified as *Helminthopsis* cf. *abeli*). Reprinted from Pickerill, R. K, 1981, Trace fossils in a Lower Palaeozoic submarine canyon sequence - the Siegas Formation of northwestern New Brunswick, Canada, Maritime Sediments and Atlantic Geology, v. 17, pp.36-58, with permission.
E. *Protopaleodictyon* Sample Pickerill 1981 Fig 5a. Siegas Formation, Siegas, New Brunswick, Canada (Early Llandovery). Figured in Pickerill, 1981 Fig 5a. Scale = 5 cm. (Originally identified as *Protopaleodictyon* sp.). Reprinted from Pickerill, R. K, 1981, Trace fossils in a Lower Palaeozoic submarine canyon sequence - the Siegas Formation of northwestern New Brunswick, Canada, Maritime Sediments and Atlantic Geology, v. 17, pp.36-58, with permission.

Ordovician trace fossils.

F. *Helminthopsis*. Sample GSC 78129. Beach Formation, The Beach (E), Newfoundland, Canada (Tremadocian). Figured in Fillion and Pickerill, 1990 Plate 8 Fig. 15. Scale = 2 cm. (Originally identified as *Helminthopsis tenuis*). Reprinted from Fillion, D., and R. K. Pickerill, 1990, Ichnology of the Upper Cambrian? to Lower Ordovician Bell Island and Wabana groups of eastern Newfoundland, Canada, Palaeontographica Canadiana, v. 7, pp.1-119, with permission.
G. *Helminthopsis*. Sample GSC 78146. Beach Formation, Between Dominion and Scotia piers (D), Newfoundland, Canada (Tremadocian). Figured in Fillion and Pickerill, 1990 Plate 8 Fig. 11. Scale = 5 cm. (Originally identified as *Helminthopsis abeli*). Reprinted from Fillion, D., and R. K. Pickerill, 1990, Ichnology of the Upper Cambrian? to Lower Ordovician Bell Island and Wabana groups of eastern Newfoundland, Canada, Palaeontographica Canadiana, v. 7, pp.1-119, with permission.

Figure E.33 continued.
Ordovician trace fossils.

H. *Gordia*. Sample Crimes et al 1992 Fig 2E. Breanoge Formation, Breanoge Head, Ireland (Arenig). Figured in Crimes et al., 1992 Fig 2E. Scale = 5 cm. (Originally identified as *Gordia* aff. *arcuata*). Reprinted with permission from Taylor & Francis.

I. *Gordia*. Sample Crimes et al 1992 Fig 2F. Breanoge Formation, Breanoge Head, Ireland (Arenig). Figured in Crimes et al., 1992 Fig 2F. Scale = 5 cm. (Originally identified as *Gordia* aff. *arcuata*). Reprinted with permission from Taylor & Francis.

J. *Helminthopsis*. Sample Pickerill 1980 Fig 5d. Grog Brook Group, Matapedia District, New Brunswick, Canada (Lower - Middle Ordovician). Figured in Pickerill, 1980 Fig 5d. Scale = 5 cm. (Originally identified as *Helminthopsis* sp.).

K. *Helminthorhaphe*. Sample Pickerill 1980 Fig 4d. Grog Brook Group, Matapedia District, New Brunswick, Canada (Lower - Middle Ordovician). Figured in Pickerill, 1980 Fig 4d. Scale = 5 cm. (Originally identified as *Cosmorhaphe* sp.).

L. *Paleodictyon*. Sample Pickerill 1980 Fig 2f. Grog Brook Group, Matapedia District, New Brunswick, Canada (Lower - Middle Ordovician). Figured in Pickerill, 1980 Fig 2f. Scale = 5 cm. (Originally identified as *Paleodictyon* sp.).

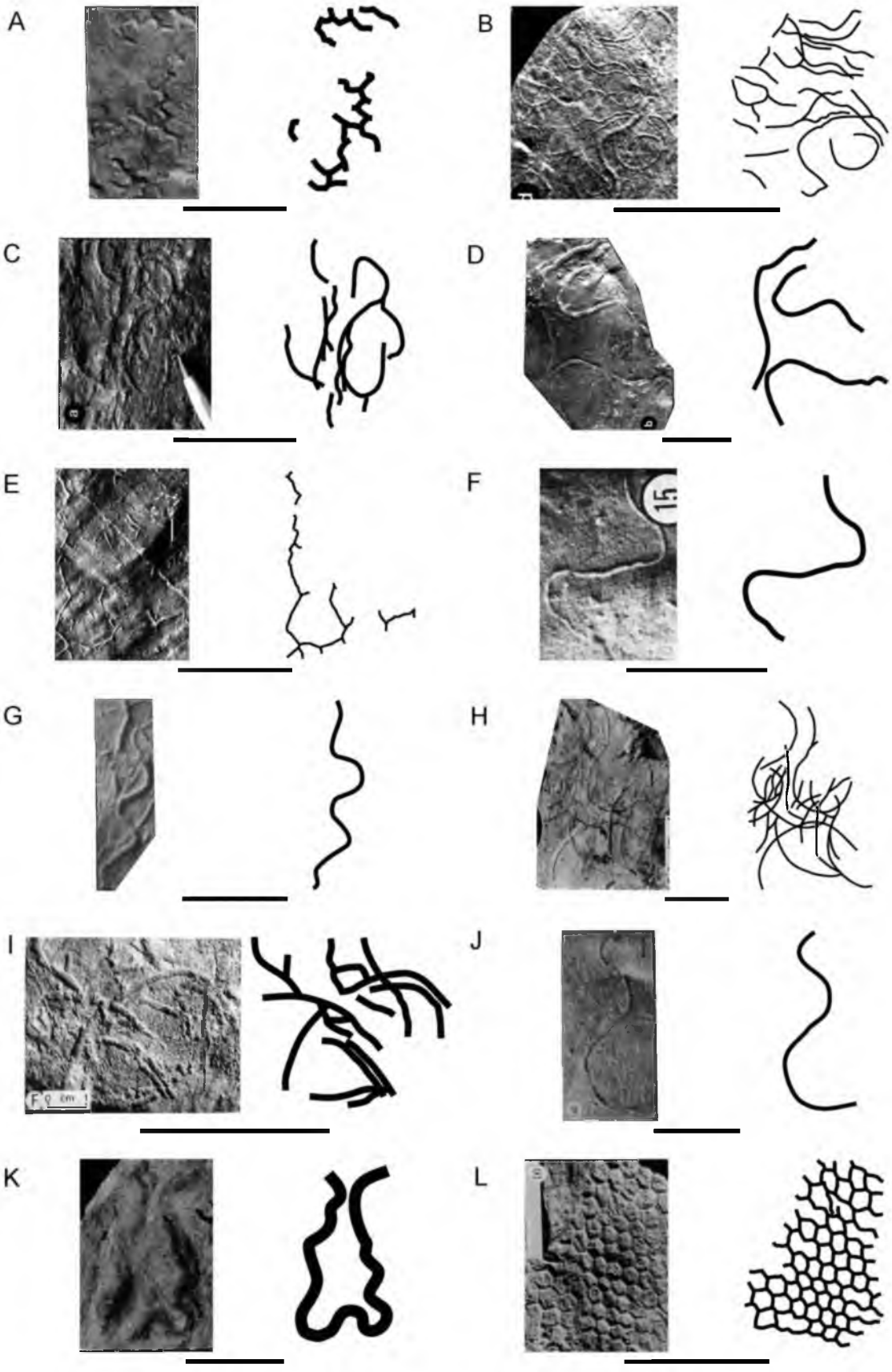
A
B
C
D
E
F
G
H
I
J
K
L

Figure E.34. Ordovician and Cambrian trace fossils.
Ordovician trace fossils.

A. *Protopaleodictyon*. Sample Pickerill 1980 Fig 4b. Grog Brook Group, Matapedia District, New Brunswick, Canada (Lower - Middle Ordovician). Figured in Pickerill, 1980 Fig 4b. Scale = 5 cm. (Originally identified as *Protopaleodictyon* sp.). © 2008 Canadian Science Publishing or its licensors. Reproduced with permission from Pickerill, R. K., 1980, Phanerozoic flysch trace fossil diversity—observations based on an Ordovician flysch ichnofauna from the Aroostook–Matapedia Carbonate Belt of northern New Brunswick, Canadian Journal of Earth Sciences, v. 17, no. 9, pp.1259-1270.
B. *Spirorhaphe*. Sample Pickerill 1980 Fig 2b. Grog Brook Group, Matapedia District, New Brunswick, Canada (Lower - Middle Ordovician). Figured in Pickerill, 1980 Fig 2b. Scale = 2 cm. (Originally identified as *Spirorhaphe* sp.). © 2008 Canadian Science Publishing or its licensors. Reproduced with permission from Pickerill, R. K., 1980, Phanerozoic flysch trace fossil diversity—observations based on an Ordovician flysch ichnofauna from the Aroostook–Matapedia Carbonate Belt of northern New Brunswick, Canadian Journal of Earth Sciences, v. 17, no. 9, pp.1259-1270.
C. *Megagrapton*. Sample Pickerill et al 1988 Fig 2e. Matapedia Group, Tobique River, western New Brunswick, Canda (Late Ordovician - Lower Llandovery). Figured in Pickerill et al., 1988 Fig 2e. Scale = 5 cm. (Originally identified as *Megagrapton irregulare*). Reprinted from Pickerill, R. K., L. R. Fyffe, and W. H. Forbes, 1988, Late Ordovician-Early Silurian trace fossils from the Matapedia Group, Tobique River, western New Brunswick, Canada. II. Additional discoveries with descriptions and comments, Maritime Sediments and Atlantic Geology, v. 24, pp.139-148, with permission.
D. *Helminthopsis*. Sample Crimes et al 1992 Fig 5A. Seamount Formation, South of Breanoge Head, Ireland (Arenig). Figured in Crimes et al., 1992 Fig 5A. Scale = 5 cm. (Originally identified as *Helminthopsis hieroglypica*). Reprinted with permission from Taylor & Francis.
E. *Gordia*. Sample A40389-1. Skiddaw Group, Locality 14, Scotland (Early Ordovician). Figured in Orr, 1996 Fig. 9b. Scale = 5 cm. (Originally identified as *?Gordia* aff. *marina*). Reproduced with permission from Orr, P. J. 1996. The ichnofauna of the Skiddaw Group (early Ordovician) of the Lake District, England, Geological Magazine, v. 133, no. 2, pp. 193-216.
F. *Gordia*. Sample A40389-2. Skiddaw Group, Locality 14, Scotland (Early Ordovician). Figured in Orr, 1996 Fig. 9c. Scale = 5 cm. (Originally identified as *?Gordia* aff. *marina*). Reproduced with permission from Orr, P. J. 1996. The ichnofauna of the Skiddaw Group (early Ordovician) of the Lake District, England, Geological Magazine, v. 133, no. 2, pp. 193-216.

Figure E.34 continued.
Cambrian trace fossils.

G. *Helminthopsis*. Sample Crimes and Anderson 1985 Fig 7.6. Chapel Island Formation, Grand Bank Head, Newfoundland, Canada (Tommotian). Figured in Crimes and Anderson, 1985 Fig. 7.6. Scale = 5 cm. (Originally identified as *Helminthopsis abeli*). Reprinted from Crimes, T. P., and M. M. Anderson, 1985, Trace fossils from late Precambrian-Early Cambrian strata of southeastern Newfoundland (Canada); temporal and environmental implications, Journal of Paleontology, v. 59, no. 2, pp. 310-343, with permission.

H. *Helminthorhaphe*. Sample Crimes and Anderson 1985 Fig 7.3. Chapel Island Formation, Grand Bank Head, Newfoundland, Canada (Tommotian). Figured in Crimes and Anderson, 1985 Fig. 7.3. Scale = 5 cm. (Originally identified as *Helminthoida miocenica*). Reprinted from Crimes, T. P., and M. M. Anderson, 1985, Trace fossils from late Precambrian-Early Cambrian strata of southeastern Newfoundland (Canada); temporal and environmental implications, Journal of Paleontology, v. 59, no. 2, pp. 310-343, with permission.

I. *Helminthorhaphe*. Sample Crimes and Anderson 1985 Fig 7.5. Chapel Island Formation, Grand Bank Head, Newfoundland, Canada (Tommotian). Figured in Crimes and Anderson, 1985 Fig. 7.5. Scale = 5 cm. (Originally identified as *Helminthoida miocenica*). Reprinted from Crimes, T. P., and M. M. Anderson, 1985, Trace fossils from late Precambrian-Early Cambrian strata of southeastern Newfoundland (Canada); temporal and environmental implications, Journal of Paleontology, v. 59, no. 2, pp. 310-343, with permission.

J. *Helminthorhaphe*. Sample GSC 73327. Chapel Island Formation, Grand Bank Head, Newfoundland, Canada (Tommotian). Figured in Crimes and Anderson, 1985 Fig. 7.1. Scale = 5 cm. (Originally identified as *Helminthoida crassa*). Reprinted from Crimes, T. P., and M. M. Anderson, 1985, Trace fossils from late Precambrian-Early Cambrian strata of southeastern Newfoundland (Canada); temporal and environmental implications, Journal of Paleontology, v. 59, no. 2, pp. 310-343, with permission.

K. *Helminthorhaphe*. Sample GSC 73330. Chapel Island Formation, Grand Bank Head, Newfoundland, Canada (Tommotian). Figured in Crimes and Anderson, 1985 Fig. 7.2. Scale = 5 cm. (Originally identified as *Helminthoida crassa*). Reprinted from Crimes, T. P., and M. M. Anderson, 1985, Trace fossils from late Precambrian-Early Cambrian strata of southeastern Newfoundland (Canada); temporal and environmental implications, Journal of Paleontology, v. 59, no. 2, pp. 310-343, with permission.

L. *Gordia*. Sample Aceñolaza 1978 Fig 10. Puncoviscana Formation, Cachi, Argentina (Early Cambrian). Figured in Aceñolaza, 1978 Fig 10. Scale = 5 cm. (Originally identified as *Gordia* sp.). Reprinted from Aceñolaza, F. G., 1978, El Paleozoica inferior de Argentina segun sus trazas fosiles, Ameghiniana, v. 15, no. 1-2, pp. 15-64, with permission.

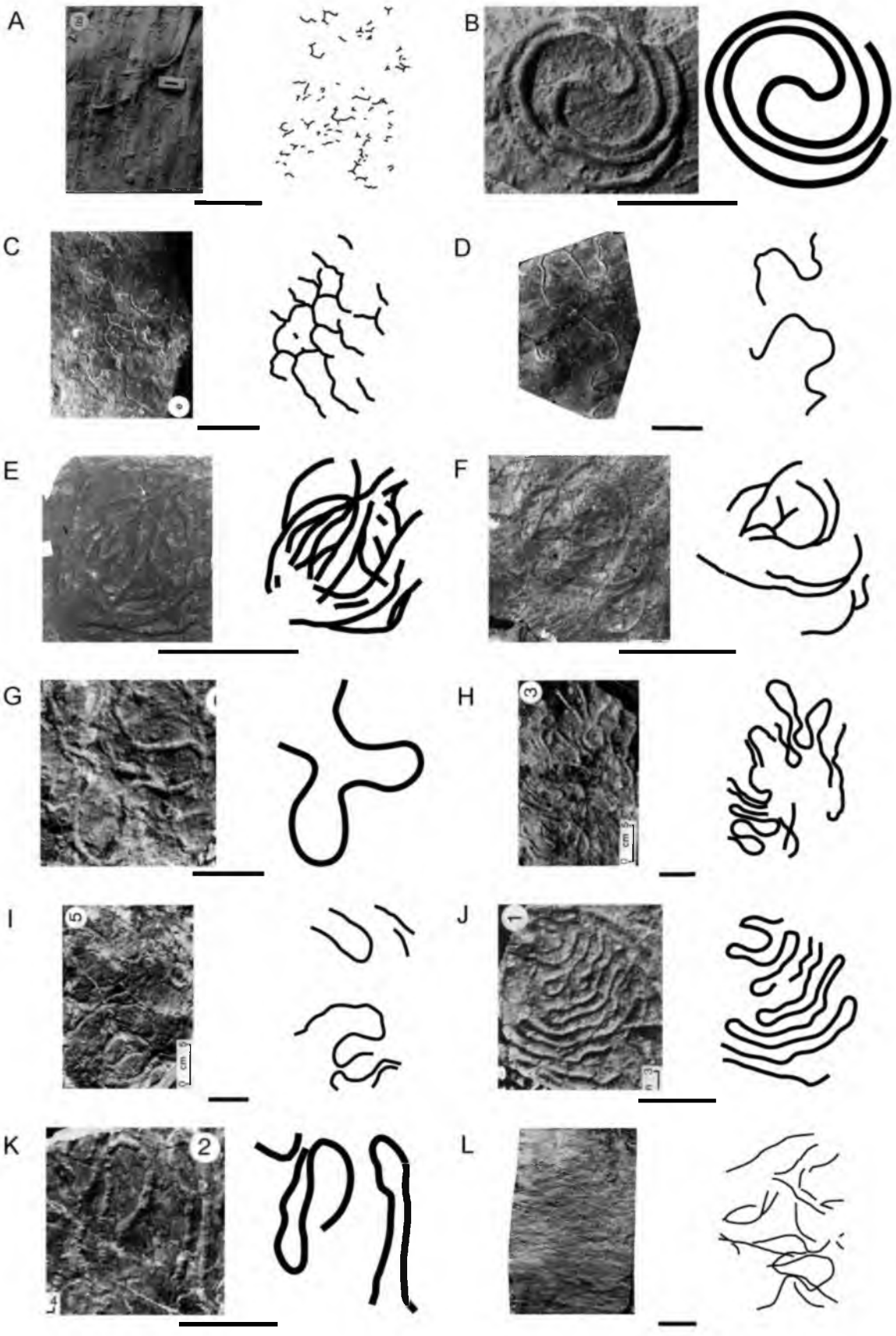
A
B
C
D
E
F
G
H
I
J
K
L

Figure E.35. Cambrian trace fossils.
Cambrian trace fossils.

A. *Gordia*. Sample Aceñolaza and Torelli 1981 pg 57-1. Puncoviscana Formation, Cachi, Argentina (Early Cambrian). Figured in Aceñolaza and Torelli, 1981 pg 57-1. Scale = 5 cm. (Originally identified as *Gordia* sp.). Reprinted from Aceñolaza, F. G., and A. J. Toselli, 1981, Geologia del noroeste Argentino, Universidad Nacional de Tucuman: Facultad de Ciencias Naturales, with permission.
B. *Helminthopsis*. Sample Aceñolaza 1978 Fig 11. Puncoviscana Formation, Muñano, Argentina (Early Cambrian). Figured in Aceñolaza, 1978 Fig 11. Scale = 5 cm. (Originally identified as *Helminthopsis* sp.). Reprinted from Aceñolaza, F. G., 1978, El Paleozoica inferior de Argentina segun sus trazas fosiles, Ameghiniana, v. 15, no. 1-2, pp. 15-64, with permission.
C. *Helminthorhaphe*. Sample Aceñolaza and Torelli 1981 pg 55-1. Puncoviscana Formation, Muñano, Argentina (Early Cambrian). Figured in Aceñolaza and Torelli 1981 pg 55-1. Scale = 5 cm. (Originally identified as *Helminthopsis* sp.). Reprinted from Aceñolaza, F. G., and A. J. Toselli, 1981, Geologia del noroeste Argentino, Universidad Nacional de Tucuman: Facultad de Ciencias Naturales, with permission.
D. *Helminthorhaphe*. Sample Aceñolaza and Torelli 1981 pg 55-2. Puncoviscana Formation, Muñano, Argentina (Early Cambrian). Figured in Aceñolaza and Torelli 1981 pg 55-2. Scale = 5 cm. (Originally identified as *Helminthopsis* sp.). Reprinted from Aceñolaza, F. G., and A. J. Toselli, 1981, Geologia del noroeste Argentino, Universidad Nacional de Tucuman: Facultad de Ciencias Naturales, with permission.
E. *Gordia*. Sample Crimes and Anderson 1985 Fig 5.7. Random Formation, Long Cove, Newfoundland, Canada (Tommotian). Figured in Crimes and Anderson, 1985 Fig. 5.7. Scale = 5 cm. (Originally identified as *Gordia molassica*). Reprinted from Crimes, T. P., and M. M. Anderson, 1985, Trace fossils from late Precambrian-Early Cambrian strata of southeastern Newfoundland (Canada); temporal and environmental implications, Journal of Paleontology, v. 59, no. 2, pp. 310-343, with permission.
F. *Squamodictyon*. Sample Crimes and Anderson 1985 Fig 10.4. Random Formation, Long Cove, Newfoundland, Canada (Tommotian). Figured in Crimes and Anderson, 1985 Fig. 10.4. Scale = 5 cm. (Originally identified as *Paleodictyon* sp. and *Squamodictyon* sp.). Reprinted from Crimes, T. P., and M. M. Anderson, 1985, Trace fossils from late Precambrian-Early Cambrian strata of southeastern Newfoundland (Canada); temporal and environmental implications, Journal of Paleontology, v. 59, no. 2, pp. 310-343, with permission.

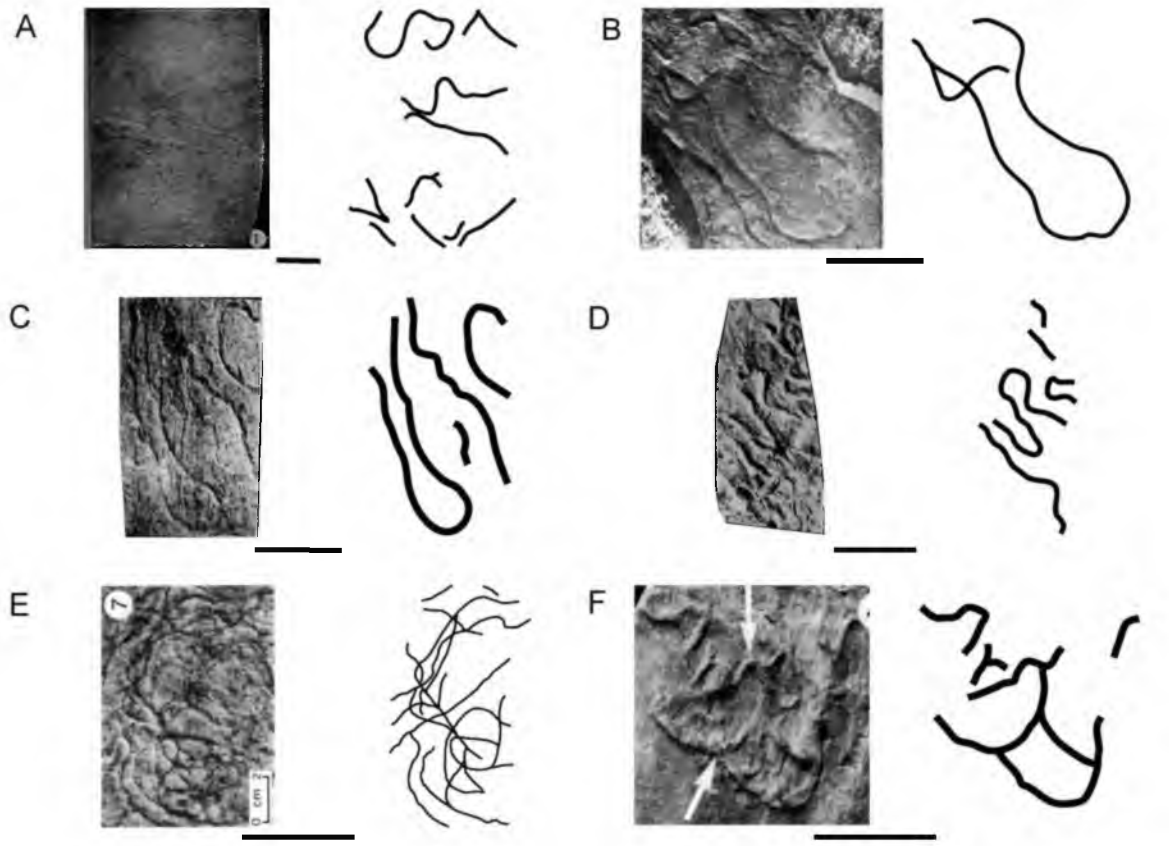
A
B
C
D
E
F

APPENDIX F

LIST OF TURBIDITE LOCALITIES

Table F.1. List of turbidite localities. Localities and ages of flysch deposits as presented in Figure 5.2. The Time Period indicates the starting time period of the rock units. The Age is the age listed in the text. The Source is where the entry for these deposits are mentioned. A = Uchman, 2004; B = Nilsen et al., 2007; C = Crimes and Anderson, 1985; D = Fillion and Pickerill, 1980; E = Acenolaza, 1978; F = Tchoumatchenco and Uchman, 1991; G = Zuffa et al., 1980; H = Gielowski-Kordesch and Ernst, 1987; I = Książkiewicz, 1977; J = Macsotay and Feraza, 2005; K = Uchman, 1995.

Time Period	Formation	Location	Age	Source
Neoproterozoic	Upper Kaza Group, Windermere Supergroup	British Columbia, Canada	Neoproterozoic	B
	Isaac Formation, Windmere Supergroup	British Columbia, Canada	Neoproterozoic	B
	Brak River Formation	Western central region, Namibia	Neoproterozoic	B
	Kongsfjord Formation	Varanger Peninsula, Norway	Late Riphean, Neoproterozoic	B
Cambrian	Bunkers Sandstone	Northern Flinders Range, South Australia	E. Cambrian	B
	Chapel Island Formation	Newfoundland, Canada	Tommotia	C
	Random Formation	Newfoundland, Canada	Tommotia	C
	St. Roch Formation	Quebec, Canada	L.-M. Cambrian	B
	Cahore Group	South Ireland	L.-M. Cambrian	A
	Hells Mouth Grits	North Wales	L. Cambrian	A
	Cilan Grits	North Wales	u.L. – l.M. Cambrian	A
	Puncoviscana Formation	Argentina	L.-M. Cambrian	A
	Suncho Formation	Northwest Argentina	L.-M. Cambrian	A
	Meguma Group	Nova Scotia, Canada	Middle Cambrian	A
Ordovician	Tourelle Formation	Quebec, Canada	E. Ordovician	B
	Beach Formation, Bell Group	Newfoundland, Canada	Tremadocian	D
	Cloridorme Formation	Quebec, Canada	M.-L. Ordovician	B
	Skiddaw Group	Northern England	L. Ordovician	A
	Seamount Formation	Wexford County, Ireland	Arenig	A
	Breanoge Formation	Wexford County, Ireland	Arenig	A
	Manx Group	Isle of Man	L. Ordovician	A
	Upper Hovin Group	Central Norway	L.-M. Ordovician	A
	Grog Brook Group	New Brunswick, Canada	M.-U. Ordovician	A
	Agüeira Formation	W Asturias	Upper Ordovician	A
	Rügen Depression	Rügen, Germany	Ordovician	A
	Barrancos Region	Portugal	Ordovician	A
	Matapedia Group	New Brunswick, Canada	M. Ordovician – L. Silurian	A
Silurian	Siegas Formation	New Brunswick, Canada	Llandovery	A
	Waterville Formation	Maine, USA	L. Silurian	A
	Aberystwyth Grits	Central Wales	L. Llandovery	A
	Devil's Bridge Formation	Welsh Basin, Wales	Llandovery	A
	Neuadd Fawr Locality	Welsh Basin, Wales	Llandovery	A
	Gala Group	Scotland	L. Llanovery	A
	Penkill Group	Scotland	L. Llanovery	A
	Hawick Rocks	Scotland	L. Llanovery	A
	Hauptquarzit	Thüringia, East Germany	?Llandeilo-Caradoc	A
	Heceta Formation,	SE Alaska, USA	Llandovery-Ludlow	A

Table F.1 continued.

Time Period	Formation	Location	Age	Source
Silurian	Los Espejos Formation	Argentina	Ludlow	E
	Riccarton Group	Southern Uplands, Scotland	Wenlock	A
Devonian	Nereitenquarzit	Thüringia, East Germany	L. Devonian	A
	Wapske Formation	New Brunswick, Canada	Lower Devonian	A
	Barrancos Region	Portugal	Devonian	A
Carboniferous	Dürrenwaider Slate, Kulm-facies	Frankenwalds, Germany	Visean	A
	Mittlere Wechsellagerung Grauwacke/ Bordenschiefer	Frankenwalds, Germany	Visean	A
	Culm Siliciclastic sequence	Minorca Island, Spain	Visean-Namurian	A
	Culm facies	Thüringia, East Germany	Lower Carboniferous	A
	Moravice Formation, Culm facies	Moravia-Silesia region, Czech Republic	Lower Caboniferous	A
	Argosy Creek Formation	Idaho, USA	Meramecian-Chesterian	B
	Jackfork Formation	Arkansa, USA	E. Pennsylvanian	B
	Wildhorse Mountain Formation, Jackfork Group	Oklahoma, USA	Morrowan	B
	Jejenes Formation	San Juan, Argentina	Pennsylvanian	B
	Quebrada de las Lajas Paleofjord	Quebrada de las Lajas, Argentina	Pennsylvanian	B
	Paleocene Flysch of Minorca	Minorca, Spain	L. Carboniferous	A
	Ross Formation	County Clare, Ireland	Namurian	B
	Gull Island Formation	Counties Clare and Kerry, Ireland	Namurian	B
	Atoka Formation	Oklahoma, USA	U. Carboniferous	A
	Wood River Formation	Idaho, USA	Pennsylvanian-Permian	A
Permian	Lercara Formation	W Sicily, Italy	Cathedralian	A
	Skoorsteenberg Formation	Cape Province, South Africa	Permian	B
	Bell Canyon Formation	Texas, USA	Guadalupian	B
	Brushy Canyon Formation	Texas, USA	Guadalupian	B
	Cherry Canyon Formation	Texas, USA	Guadalupian	B
	Vischkuil Formation	Western Cape, South Africa	Middle Permian	B
	Laingsburg Formation	Western Cape, South Africa	Middle Permian	B
	Gudongjing	Inner Mongolia	L. Permian	A

Table F.1 continued.

Time Period	Formation	Location	Age	Source
Permian	Maquen and Mandoi, Yushu, Guoluo	Qinghai Province, China	Permian-Triassic	A
Triassic	Heweitan Group	E Karokorum, China	L.-M. Triassic	A
	Songpan-Ganzi Complex	Sichuan Province, China	Ladinian-Norian	B
	Baiyu area	W Sichuan, China	Late Triassic	A
	Zanda	SW Tibet	U. Triassic	A
	Tavrida Group	Crimea, Ukraine	U.Triassic-L. Jurassic	A
Jurassic	Sini Vir Formation	Stara Planina Mountains, Bulgaria	Pliensbachian-Toarcian	A
	High Atlas	Morocco	L.-M.Jurassic	A
	Balaban Formation	Stara Planina Mountains, Bulgaria	Toarcian	F
	Szlachtowa Formation	Carpathians, Poland	Toarcian-Aalenian	A
	Lower Cieszyn Shale	Carpathians, Poland	Tithonian	A
	Longobucco Sequence	Longobucco, Italy	M.-L. Jurassic	G
	Himalia Ridge Formation	Fossil Bluff Group, Alexander Island, Antarctica	L. Jurassic - Cretaceous	B
	Cieszyn Limestone	Carpathians, Poland	Tithonian-Berriasian	A
	Kostel Formation	Stara Planina Mountains, Bulgaria	u. U. Kimm-Beriassian	A
Early Cretaceous	Risong Formation	NW Tibet	L. Cretaceous	A
	Franciscan Flysch	California, USA	Tithonian - Hauterivian	A
	Upper Cieszyn Shale	Carpathians, Poland	Valanginian-Hauterivian	A
	Kamchia Formation	Bulgaria	M.-L. Valanginian	A
	Grodziszcze Beds	Carpathians, Poland	Hauterivian-Aptian	A
	Verovice Beds	Carpathians, Poland	Barremian-Aptian	A
	Triestelschichten, Rhenodanubian Flysch	Austria & Germany	U. Barremian-L. Aptian	A
	Çağlayan Formation	Sinop Basin, Turkey	Barremian-Aptian	A
	Gault Flysch	Austria & Germany	M. Aptian-U. Albian	A
	Middle Yezo Group	Japan	Albian	A
	Torok Formation	Alaska, USA	Albian	B
	Lgota Beds	Carpathians, Poland	Albian-Cenomanian	A
	Ofterschwanger Schichten	Austria & Germany	U. Albian-U. Cenomanian	A

Table F.1 continued.

Time Period	Formation	Location	Age	Source
Early Cretaceous	Whisky Bay Formation	Antarctica	U. Albian-Turonian	A
Late Cretaceous	Reiselberger Sandstone	Austria & Germany	U. Cenomanian-U. Turonian	A
	Malinowa Formation	Carpathians, Poland	Cenomanian-Campanian	A
	Zementmergelserie	Austria & Germany	Turonian-Maastrichtian	A
	Helminthoid Flysch	Liguria, Italy	Turonian-Campanian	A
	Piesenkopfschichten	Austria & Germany	U. Turonian-U. Campanian	A
	Cârnu Formation, Romania	Carpathians, Romania	Turonian-Coniacian	A
	Trawne Beds	Carpathians, Poland	Turonian-?Coniacian	A
	Siliceous Marls, Silesian unit	Carpathians, Poland	Turonian	A
	Yemişliçay Formation	Sinop Basin, Turkey	Coniacian - Campanian	A
	Sromowce Formation	Carpathians, Poland	Conician – L. Campanian	A
	Kaumberger Schichten	Austria & Germany	Coniacian-L. Maastrichtian	A
	Godula Beds	Carpathians, Poland	Coniacian-Santonian	A
	Lower Istebna Beds, Skole Unit	Carpathians, Poland	Campanian-Maastrichtian	A
	Skrzydlna Beds	Carpathians, Poland	Coniacian-Santonian	A
	Siliceous Marls, Skole Unit	Carpathians, Poland	Coniacian-Santonian	A
	Matanuska Formation	Talkeetna Mts., Alaska, USA	Upper Cretaceous	A
	Kodiak Formation	Alaska, USA	Upper Cretaceous	A
	Zumaia Flysch	Basque Country, Spain	Upper Cretaceous	A
	Hallritzer Serie	Austria & Germany	U. Campanian - ?L. Maastrichtian	A
	Hangu Beds, Romania	Carpathians, Romania	Senonian	A
	Kahlenberger Schichten	Austria & Germany	Santonian-Maestrichtian	A
	Unnamed Formation, District of Kilwa	Kilwa, Tanzania	Campanian	H
	Point Loma	California, USA	Campanian	A

Table F.1 continued.

Time Period	Formation	Location	Age	Source
Late Cretaceous	Szydlowiec Beds	Carpathians, Poland	Upper Senonian (Campanian - Maastrichtian)	I
	Unnamed Formation, Wheeler Gorge	California, USA	Campanian-Maestrichtian	A
	Rosario Formation	Baja California del Norte, Mexico	Campanian-Maastrichtian	B
	Punta Barrosa Formation	Ultima Esperanza District, Chile	L. Cretaceous	B
	Cerro Toro Formation	Ultima Esperanza District, Chile	Cenomanian-Campanian	B
	Tres Pasos Formation	Ultima Esperanza District, Chile	L. Cretaceous	B
	Lewis Shale	Wyoming, USA	Maastrichtian	B
	Pab Formation	Baluchistan, Pakistan	Maastrichtian	B
	Bleicherhornserie	Austria & Germany	Maastrichtian	A
	Pre-flysch of the Julian Prealps	Julian Prealps, Italy	Maastrichtian	A
	Inocermanian Beds, Skole Unit	Carpathians, Poland	Coniacian - Paleocene	A
	Emine Flysch	Bulgaria	Campanian-M. Paleocene	A
	Altlengbacher Schichten	Austria & Germany	Maastrichtian-Danian	A
	Sieveringer Schichten	Austria & Germany	Maastrichtian-Paleocene	A
	Ropianka Beds, Magura Nappe	Carpathians, Poland	Maastrichtian-Paleocene	A
	Akvaren Formation, Sinop Basin	Sinop Basin, Turkey	Maastrichtian-L. Paleocene	A
	Solán Formation, Magura Nappe	Carpathians, Czech Republic and Slovakia	Maastrichtian-Paleocene	A
	Cisna Beds	Carpathians, Poland	Maastrichtian-L. Paleocene	A
	Fimberenheit Flysch	Switzerland	Coniacian-?L. Eocene	A
Paleocene	Zumaia Flysch	Basque Country, Spain	Paleocene	A; B
	Gurnigel Flysch	Switzerland	Paleocene	A
	Tuz Gölü Basin	Turkey	Paleocene	A
	Guárico Formation	Venezuela	Paleocene	A
	Upper Istebna Beds, Silesian Unit	Carpathians, Poland	Paleocene	A
	Calla Unit	Julian Prealps, Italy	Danian; Paleocene	A
	Atbaşi Formation	Sinop Basin, Turkey	Paleocene	A
	Chicontepec Formation	Hidalgo State, Mexico	Paleocene	A; B
	Carmelo Formation	California, USA	L. Paleocene	B
	Gorzen Beds	Carpathians, Poland	U. Paleocene	I

Table F.1 continued.

Time Period	Formation	Location	Age	Source
Paleocene	Szczawnica Beds, Magura Unit	Carpathians, Poland	U. Paleocene-L. Eocene	A
	Variegated Shale, Magure Unit	Carpathians, Poland	U. Paleocene-L. Eocene	A
	Masarolis Unit	Julian Prealps, Italy	L. Thanetian; L. Eocene	A
	Tarcau Sandstone	Carpathians, Romania	Paleocene-M.Eocene	A
	Laaber Schichten	Austria & Germany	U. Paleocene-M. Eocene	A
	Greifensteiner Schichten	Austria & Germany	Thanetian - Ypresian	A
Eocene	Carnian Prealps	Southern Alps, NE Italy	u. L. Eocene	A
	Battfjellet Formation	Spitsbergen, Norway	E. Eocene	B
	Gilsonryggen Formation	Spitsbergen, Norway	E. Eocene	B
	Kirkgecit Formation	Elazig Province, Turkey	Eocene	B
	Høgsnyta Outcrop	Norway	Eocene	B
	Arro Turbidites	Sobrarbe region, Spain	Eocene	B
	Isla de Margarita	Venezuela	Eocene	A
	Zumaia Flysch	Basque Country, Spain	Eocene	A; B
	Gurnigel Flysch	Switzerland	Eocene	A
	Schlieren Flysch	Switzerland	Eocene	A
	Kusuri Formation	Sinop Basin, Turkey	Eocene	A
	Ganei Slate	Switzerland	Eocene	A
	Şortile	Carpathians, Romania	Eocene	A
	La Jolla Group	California, USA	Eocene	B
	Punta Carnero Formation	Isla de Margarita, Venuzuela	Eocene	J
	Flysch del Grivò	Julian Prealps, Italy	L.-M. Eocene	A
	Belluno Flysch	Italy	L.-M. Eocene	A
	San Vincente Formation; Hecho Group	Pyrenees, Spain	L.-M. Eocene	A; B
	Hieroglyphic Beds, Dukla Unit	Carpathians, Poland	L.-M. Eocene	A
	Ciężkowice Sandstone, Silesian Unit	Carpathians, Poland	L.-M. Eocene	A
	Beloveža Beds	Carpathians, Poland	L.-M. Eocene	A
	Tyee Formation	Oregon, USA	M. Eocene	B
	Brito Fm, Rivas	Nicaragua	M. to L. Eocene	B
	Lącko Beds	Carpathians, Poland	M.-U. Eocene	A
	Hieroglyphic Beds, Magura unit	Carpathians, Poland	M.-U. Eocene	A
	Hieroglyphic Beds, Silesian unit	Carpathians, Poland	M.-U. Eocene	A
	Brkini Flysch, Slovenia	Slovenia	M.-U. Eocene	A
	Saraceno Formation	Italy	M.-U. Eocene	A
	Cormons unit	Julian Prealps, Italy	M.-U. Eocene	A
	Talara Formation	Talara basin, Peru	L. Eocene	B

Table F.1 continued.

Time Period	Formation	Location	Age	Source
Eocene	Plopu Beds	Carpathians, Romania	U. Eocene	A
	Podu Secu Beds	Carpathians, Romania	U. Eocene	A
	Punta Mosquito Formation	Venezuela	U. Eocene	A
	Niedanowa Marls, Skole Unit	Carpathians, Poland	L/M. Eocene	A
	Globigerina Marls, Silesian Unit	Carpathians, Poland	Upper Eocene	A
	Magura Sandstone, Magura Unit	Carpathians, Poland	U. Eocene-L. Oligocene	A
	Grès d'Annot Formation	Provence-Alpes-Cote d'Azur, France	Priabonian-Rupelian	B
	Internidi Units	Cilento, Italy	Eocene - L. Miocene	B
Oligocene	Malcov Beds, Magura Unit	Carpathians, Poland	L. Oligocene	A
	Grès du Champsaur	Haute Alpes, France	E. Oligocene	B
	Podhale Flysch	Carpathians, Poland	Oligocene	A
	Vathia Beds	Peloponese, Greece	Oligocene	A
	Algeciras unit	Gibraltar	Oligocene	A
	Izvoarele Beds, Tarcău Unit	Romania	Oligocene	A
	Karpathos Flysch	Greece	Oligocene	A
	Kattavia Flysch	Rhodes, Greece	L. Oligocene	A
	Krosno Beds, Silesian Unit	Carpathians, Poland	U. Oligocene	A
	Messanagros Sandstone	Rhodes, Greece	M. Oligocene-Aquitanian	A
	West Crocker Formation	Northwest Borneo region, Malaysia	Oligocene - E. Miocene	B
	Podu Mori Formation	Carpathians, Romania	Oligocene-Lower Miocene	A
Miocene	Marnoso-Arenacea Formation	Emilia-Romagna, Italy	?Langhian-Tortonian	A; B
	Cingöz Formation	Adana Basin, Turkey	Burdigalian-Serravallian	A; B
	Sartenella Formation	Tabernas-Sorbas Basin, Spain	Tortonian	B
	Loma de los Baños Formation	Tabernas-Sorbas Basin, Spain	Tortonian	B
	Verdelecho Formation	Tabernas-Sorbas Basin, Spain	Tortonian	B
	Capistrano Formation	California, USA	Miocene	B
	Laga Formation	Italy	Miocene	B
	Pollica Sandstones	Campania, Italy	Langhian	B
	Verghereto Marls	Verghereto, Italy	Langhian - Tortonian	K

Table F.1 continued.

Time Period	Formation	Location	Age	Source
Miocene	Mount Messanger Formation	Taranaki Provence, New Zealand	Tortonian	B
	Urenui Formation	Taranaki Provence, New Zealand	Tortonian	B
	Alikayasi Member, Tekir Formation	Kahramanmaras, Turkey	M. - U. Miocene	B
	Monte Sacro Conglomerates	Campania, Italy	Tortonian	B
	Chozas Formation	Almeria, Spain	Tortonian	B
	Gorgoglione Flysch	Italy	M.-U. Miocene	A
	Azgador Limestone, Vera Basin	Betic Cordillera, Spain	Messinian, Miocene	A
	Laga Formation	Apennines, Italy	Messinian	A
Pliocene - Pleistocene	Schiramazu Formation	Boso Peninsula, Japan	Pliocene-Pleistocene	A
	Otadai Formation	Boso Peninsula, Japan	Pliocene-Pleistocene	A

APPENDIX G

PALEOGEOGRAPHIC SAMPLE LOCALITY MAPS

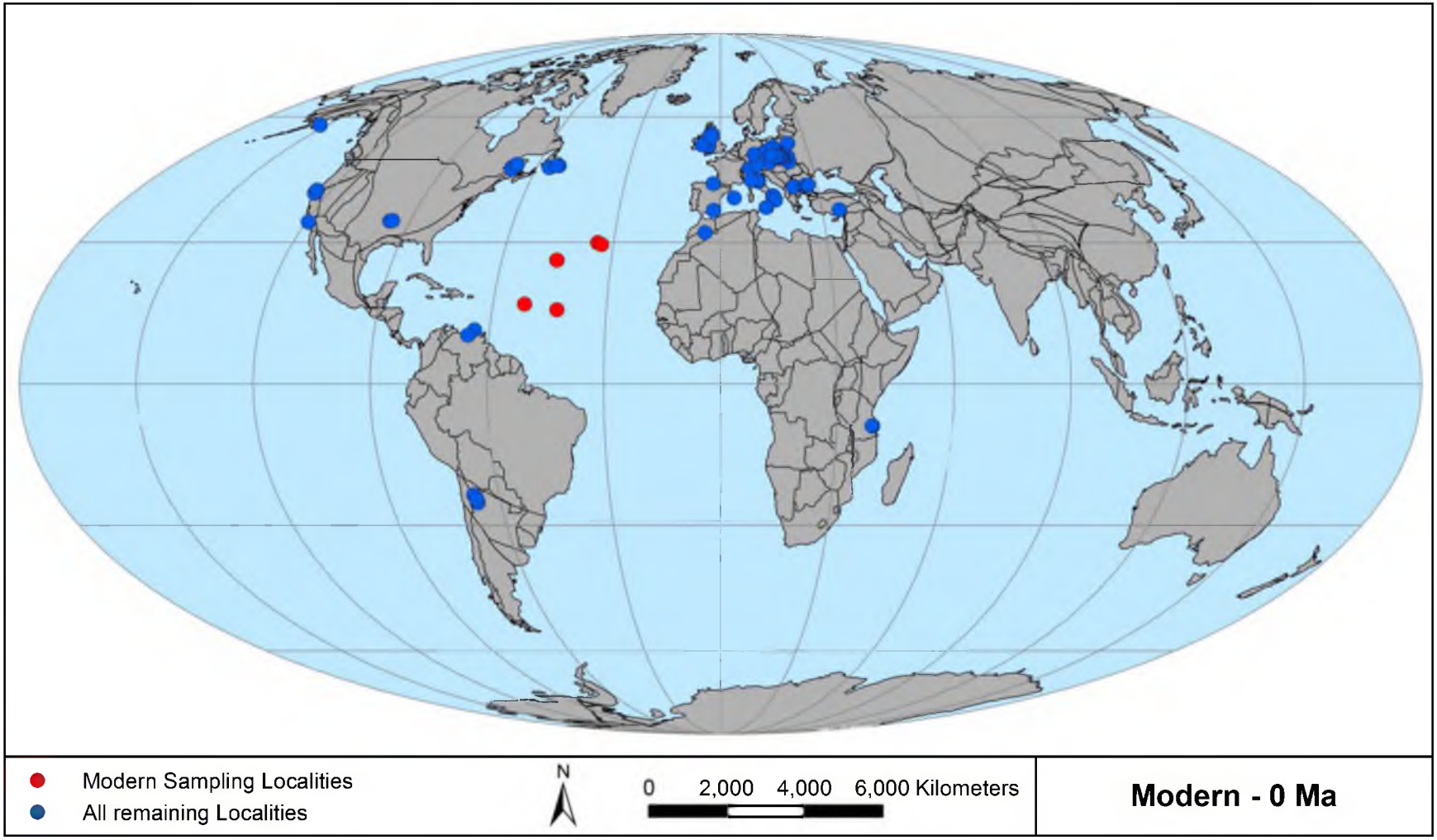

Figure G.1. Locality map of the samples analyzed. Red points indicate deep sea, modern samples. Blue points indicate all fossil localities. Localities are further illustrated with time period specific maps in the following figures. Plate tectonic map produced by C. Scotese (2011a). Use of PointTracker and PALEOMAP courtesy of Christopher Scotese.

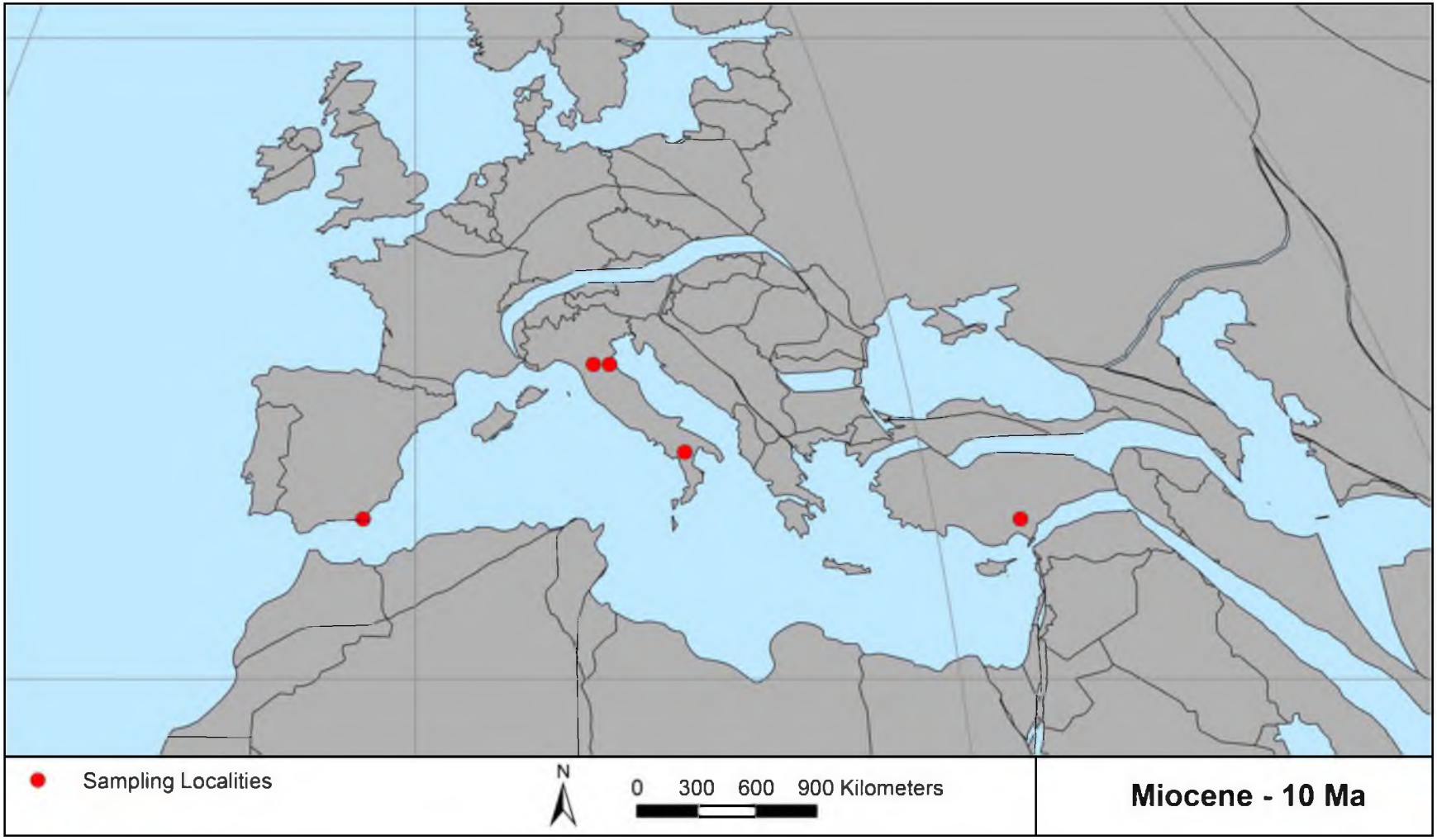

Figure G.2. Locality map of the samples analyzed that were Miocene in age. GPS locations were converted using the PointTracker program (Scotese, 2010) and all points were converted using an age of 10 Ma. Plate tectonic map produced by C. Scotese (2011a). Use of PointTracker and PALEOMAP courtesy of Christopher Scotese.

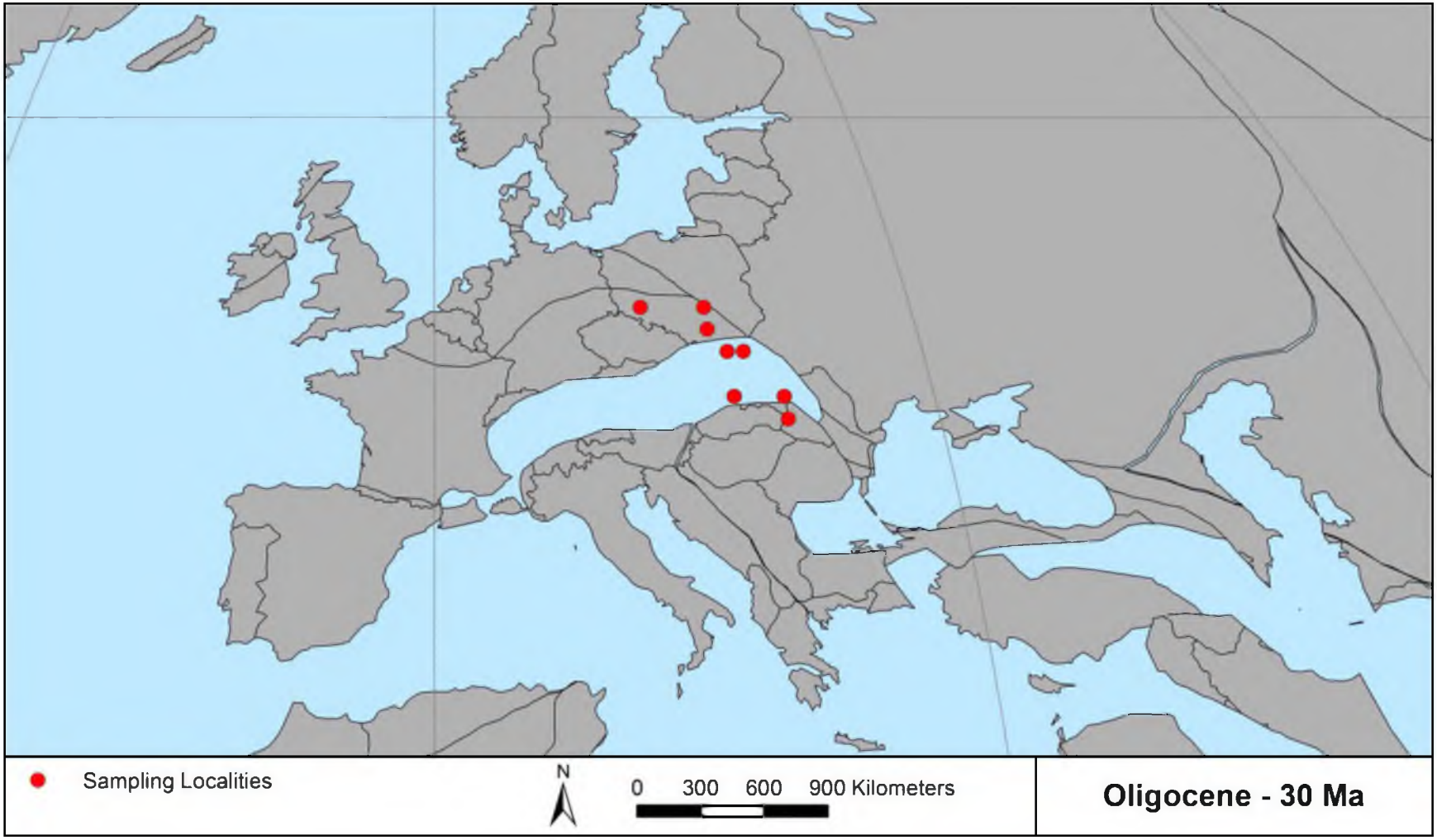

Figure G.3. Locality map of the samples analyzed that were Oligocene in age. GPS locations were converted using the PointTracker program (Scotese, 2010) and all points were converted using an age of 30 Ma. Plate tectonic map produced by C. Scotese (2011a). Use of PointTracker and PALEOMAP courtesy of Christopher Scotese.

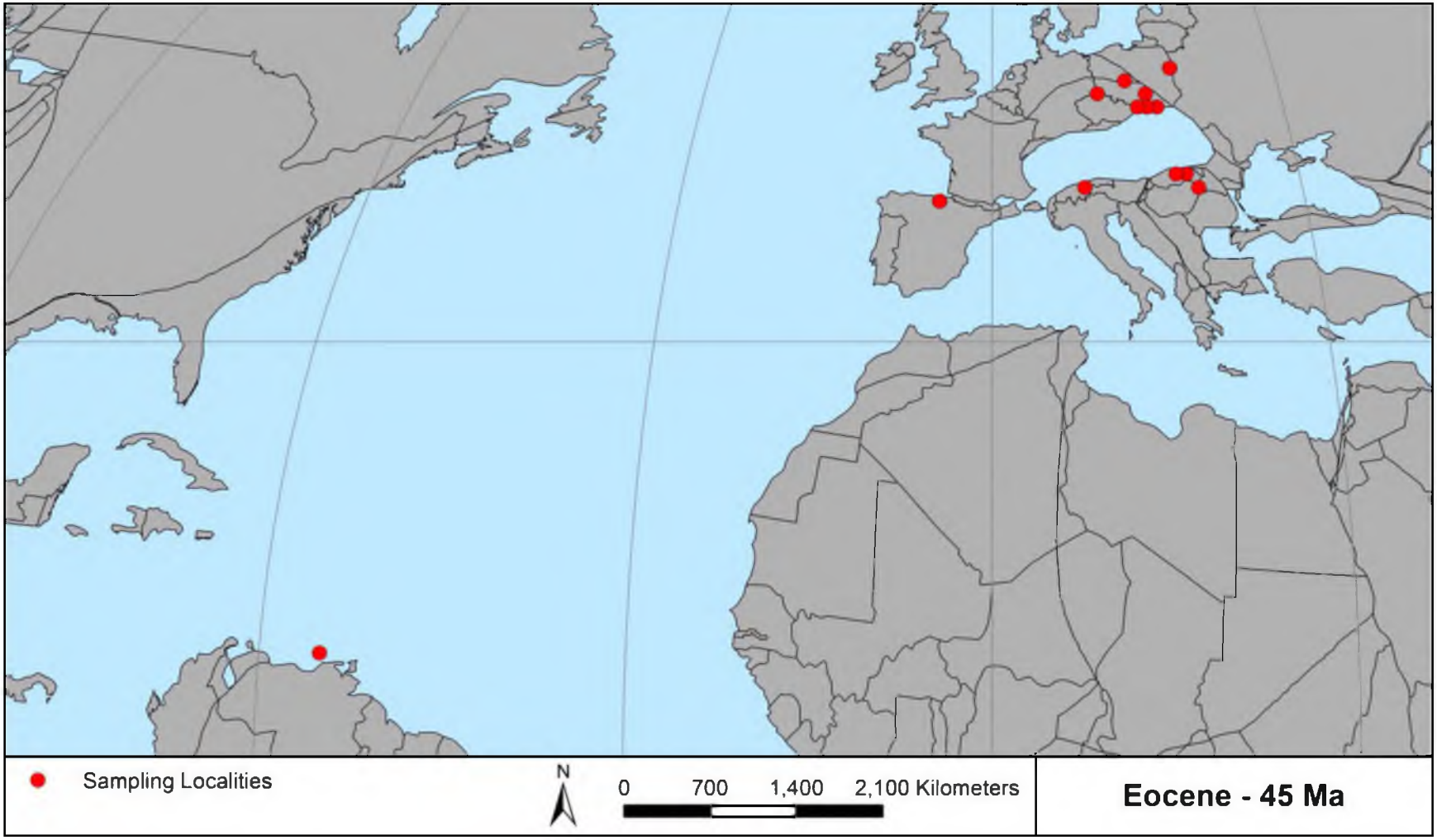

Figure G.4. Locality map of the samples analyzed that were Eocene in age. GPS locations were converted using the PointTracker program (Scotese, 2010) and all points were converted using an age of 45 Ma. Plate tectonic map produced by C. Scotese (2011a). Use of PointTracker and PALEOMAP courtesy of Christopher Scotese.

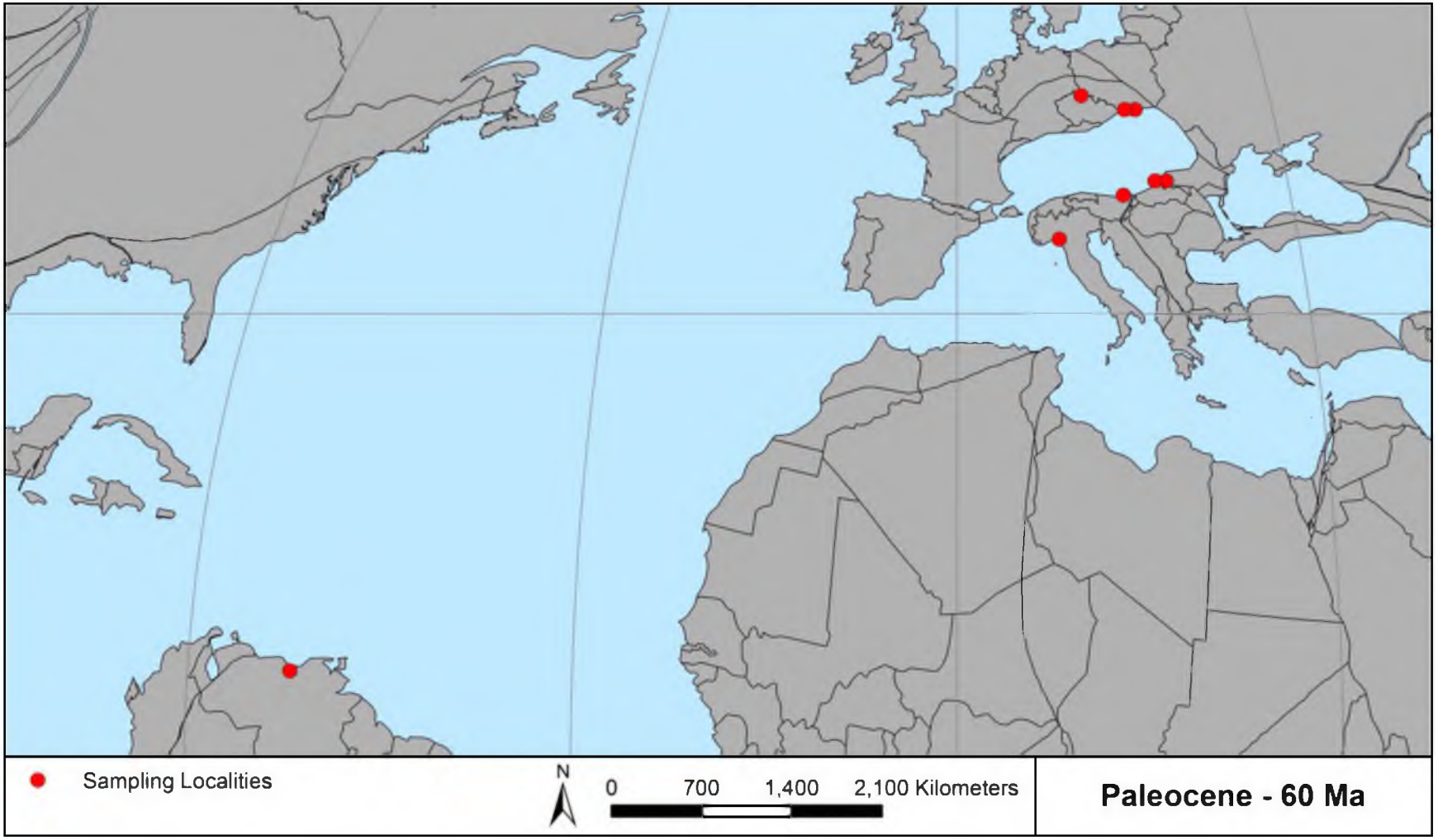

Figure G.5. Locality map of the samples analyzed that were Paleocene in age. GPS locations were converted using the PointTracker program (Scotese, 2010) and all points were converted using an age of 60 Ma. Plate tectonic map produced by C. Scotese (2011a). Use of PointTracker and PALEOMAP courtesy of Christopher Scotese.

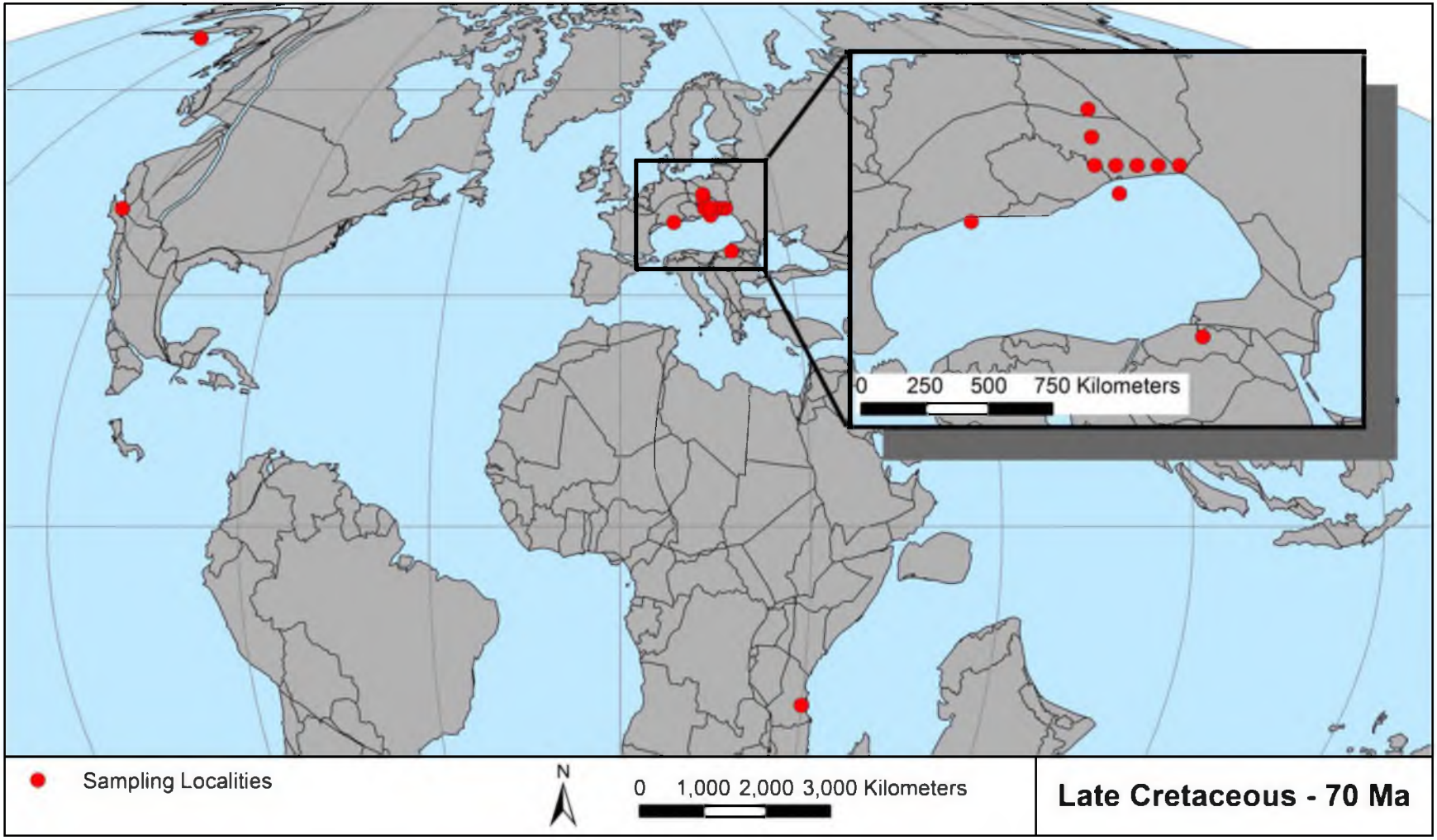

Figure G.6. Locality map of the samples analyzed that were Late Cretaceous in age. GPS locations were converted using the PointTracker program (Scotese, 2010) and all points were converted using an age of 70 Ma. Plate tectonic map produced by C. Scotese (2011b). Use of PointTracker and PALEOMAP courtesy of Christopher Scotese.

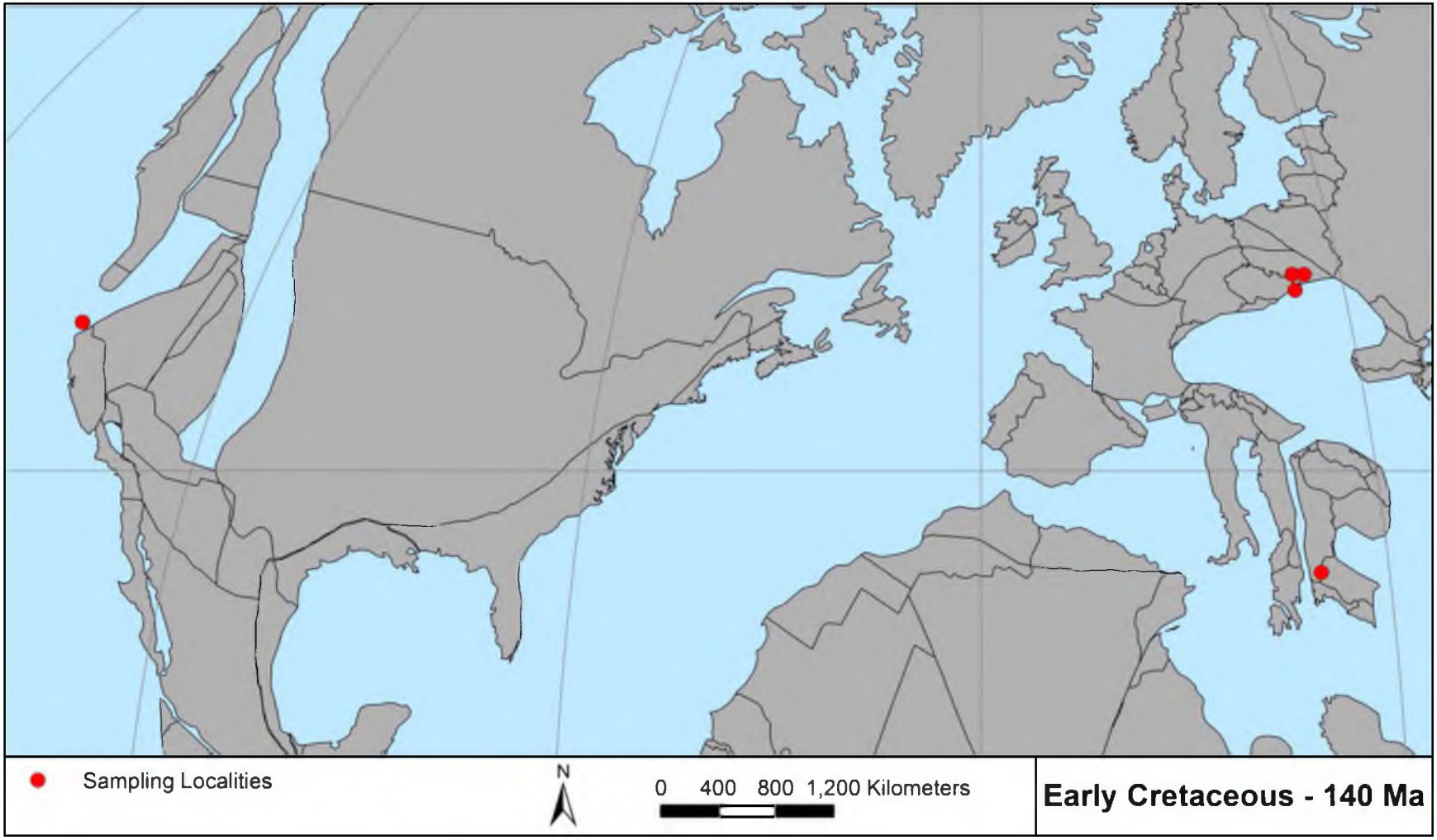

Figure G.7. Locality map of the samples analyzed that were Early Cretaceous in age. GPS locations were converted using the PointTracker program (Scotese, 2010) and all points were converted using an age of 140 Ma. Plate tectonic map produced by C. Scotese (2011b). Use of PointTracker and PALEOMAP courtesy of Christopher Scotese.

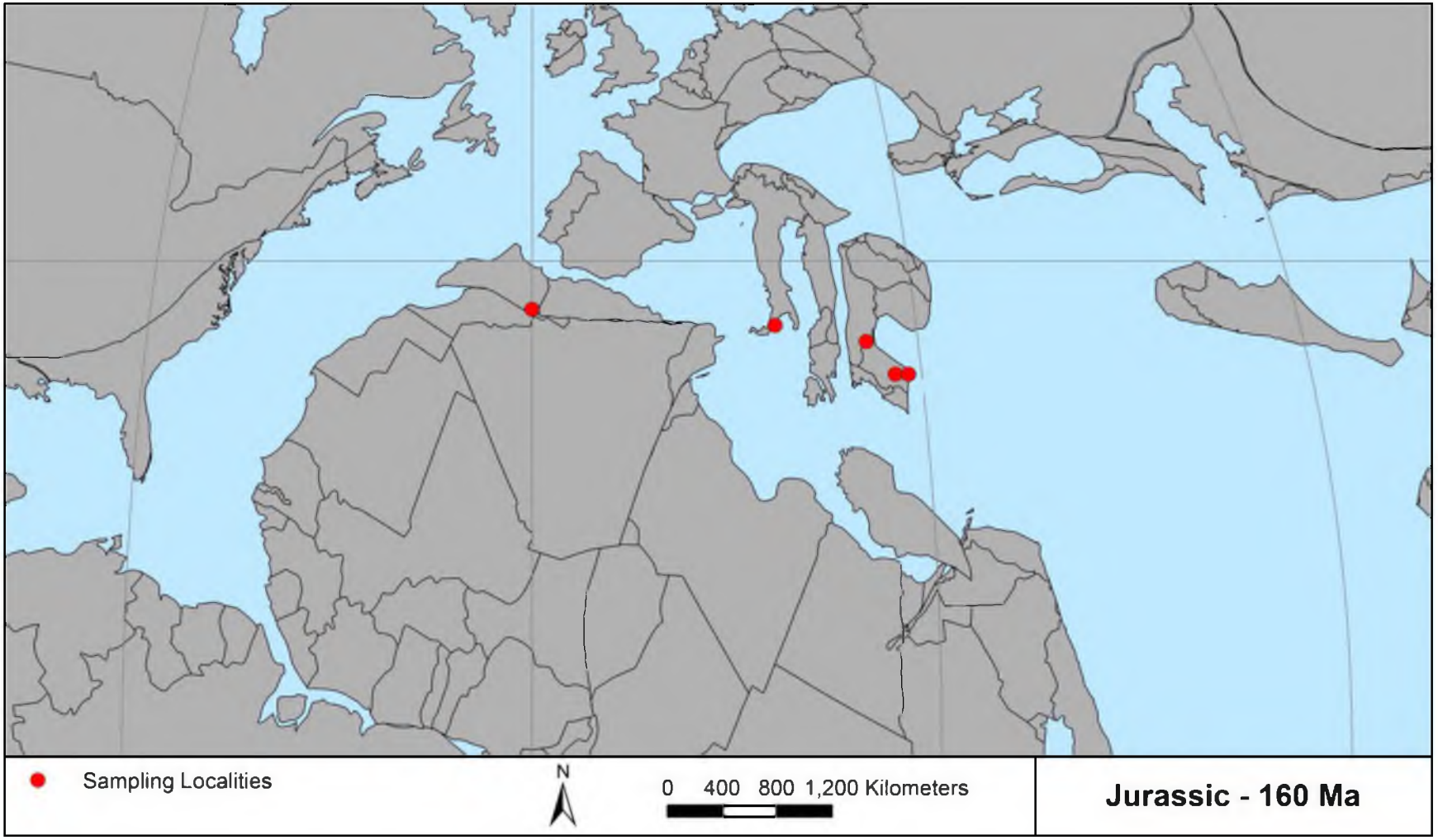

Figure G.8. Locality map of the samples analyzed that were Jurassic in age. GPS locations were converted using the PointTracker program (Scotese, 2010) and all points were converted using an age of 160 Ma. Plate tectonic map produced by C. Scotese (2011c). Use of PointTracker and PALEOMAP courtesy of Christopher Scotese.

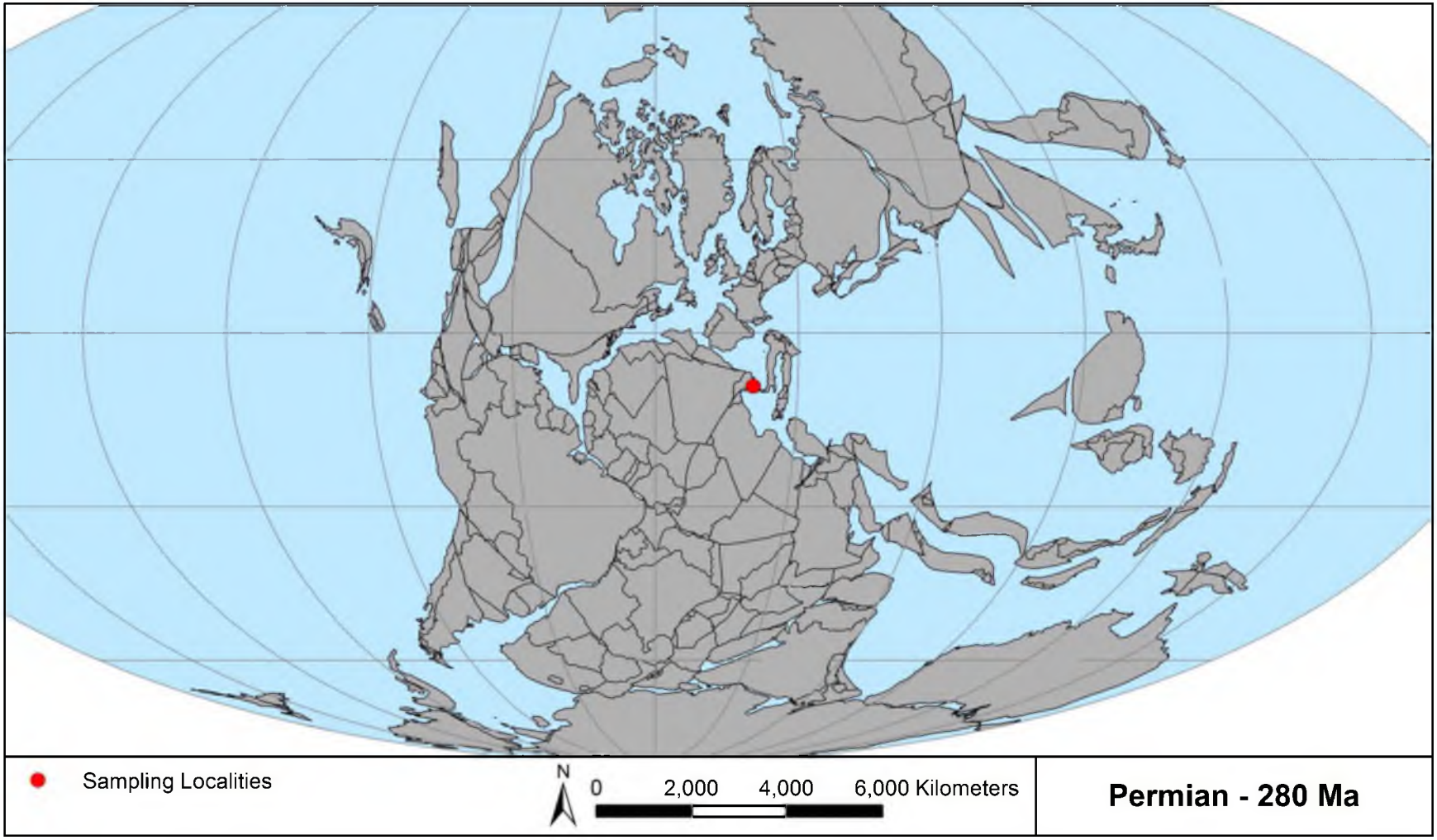

Figure G.9. Locality map of the samples analyzed that were Permian in age. GPS locations were converted using the PointTracker program (Scotese, 2010) and all points were converted using an age of 280 Ma. Plate tectonic map produced by C. Scotese (2011d). Use of PointTracker and PALEOMAP courtesy of Christopher Scotese.

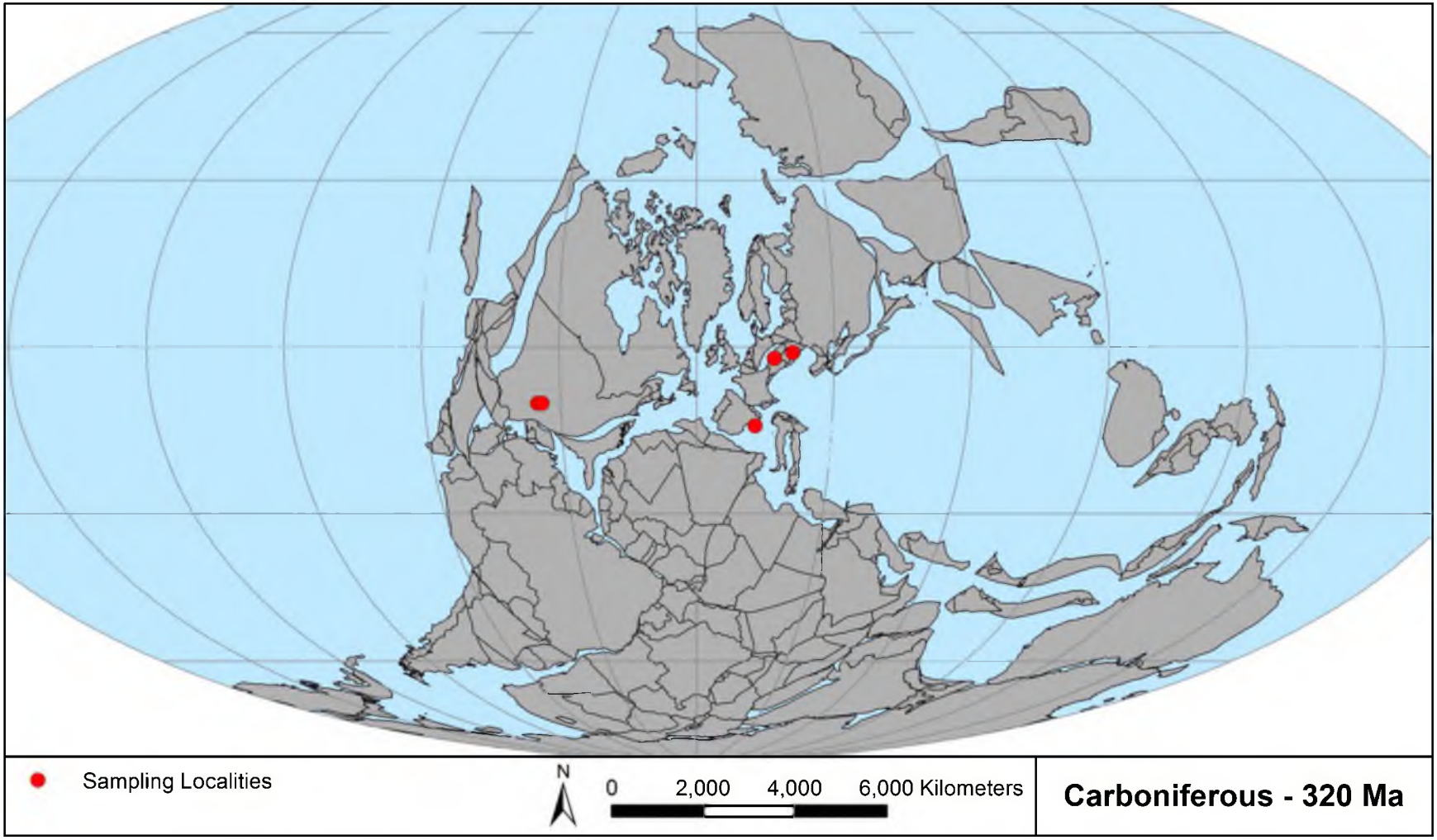

Figure G.10. Locality map of the samples analyzed that were Carboniferous in age. GPS locations were converted using the PointTracker program (Scotese, 2010) and all points were converted using an age of 320 Ma. Plate tectonic map produced by C. Scotese (2011d). Use of PointTracker and PALEOMAP courtesy of Christopher Scotese.

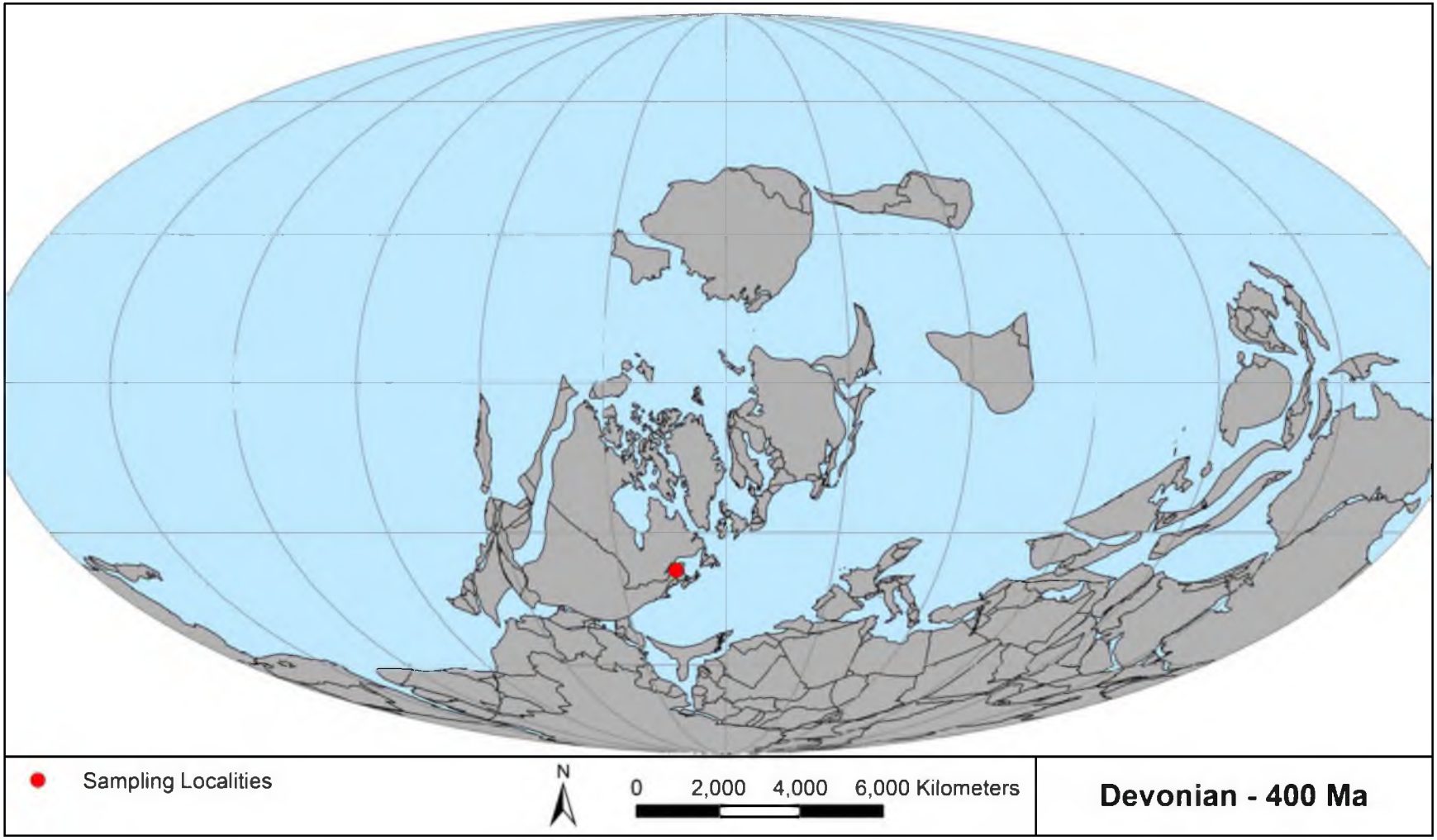

Figure G.11. Locality map of the samples analyzed that were Devonian in age. GPS locations were converted using the PointTracker program (Scotese, 2010) and all points were converted using an age of 400 Ma. Plate tectonic map produced by C. Scotese (2011d). Use of PointTracker and PALEOMAP courtesy of Christopher Scotese.

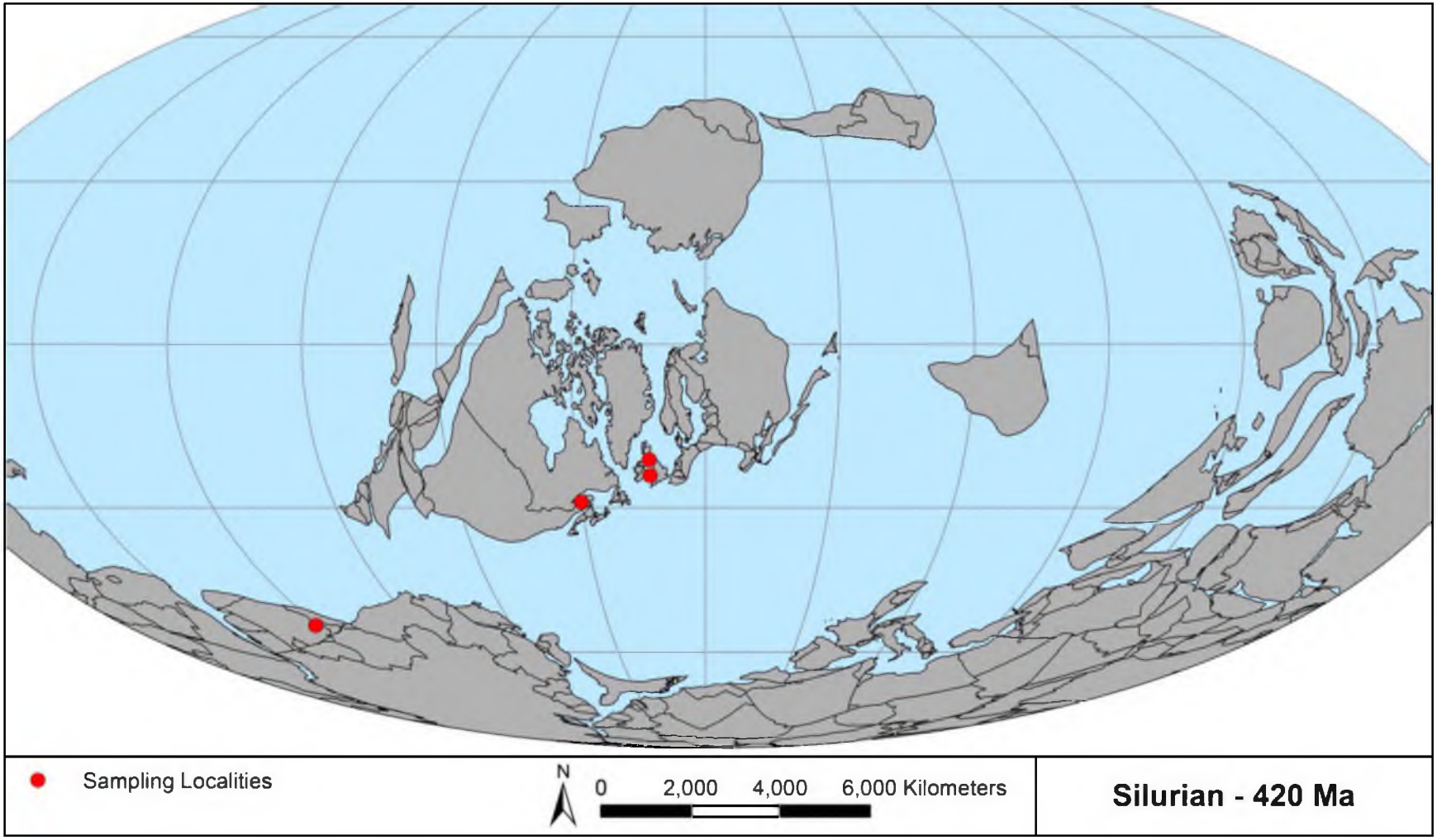

Figure G.12. Locality map of the samples analyzed that were Silurian in age. GPS locations were converted using the PointTracker program (Scotese, 2010) and all points were converted using an age of 420 Ma. Plate tectonic map produced by C. Scotese (2011e). Use of PointTracker and PALEOMAP courtesy of Christopher Scotese.

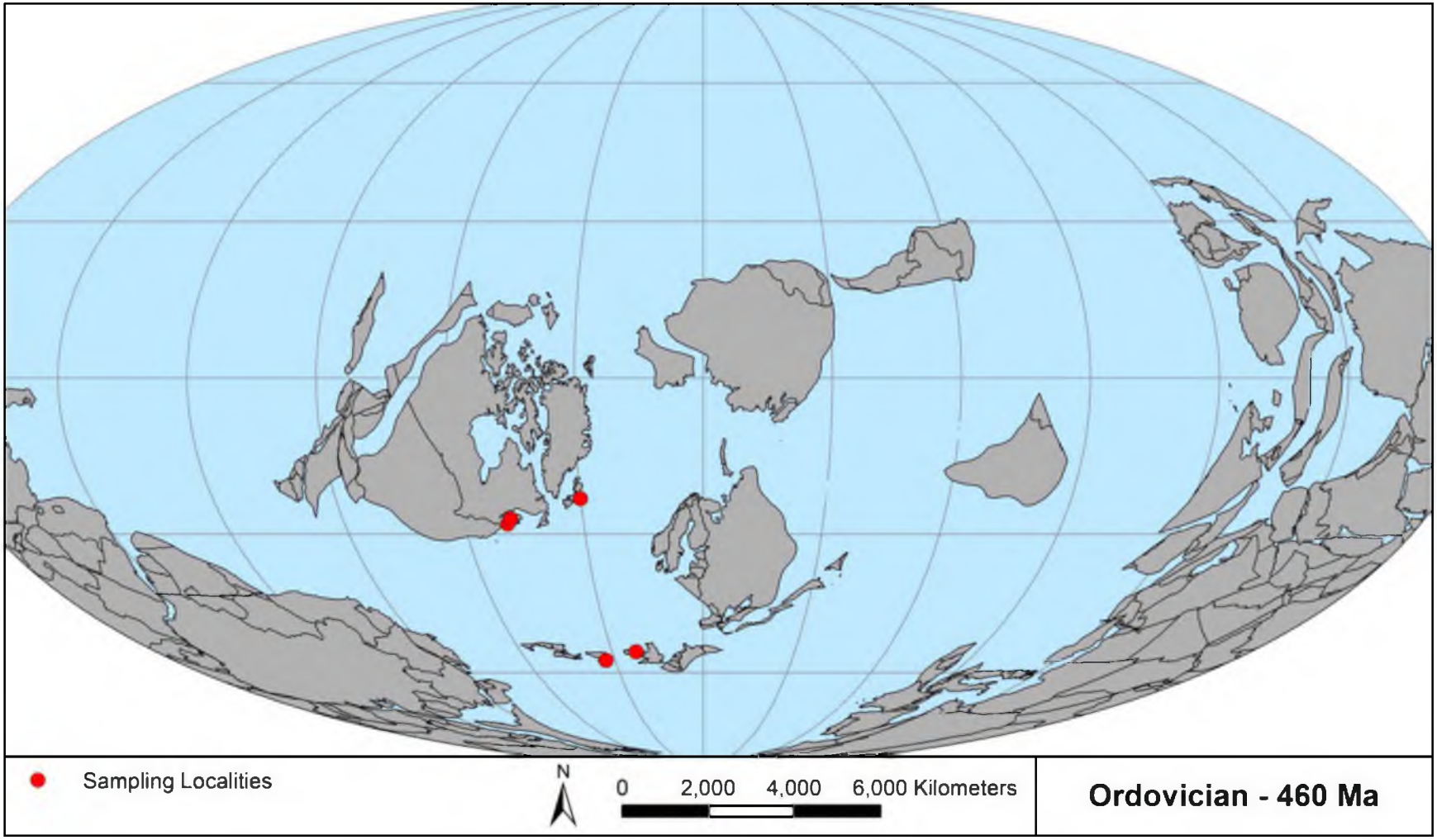

Figure G.13. Locality map of the samples analyzed that were Ordovician in age. GPS locations were converted using the PointTracker program (Scotese, 2010) and all points were converted using an age of 460 Ma. Plate tectonic map produced by C. Scotese (2011e). Use of PointTracker and PALEOMAP courtesy of Christopher Scotese.

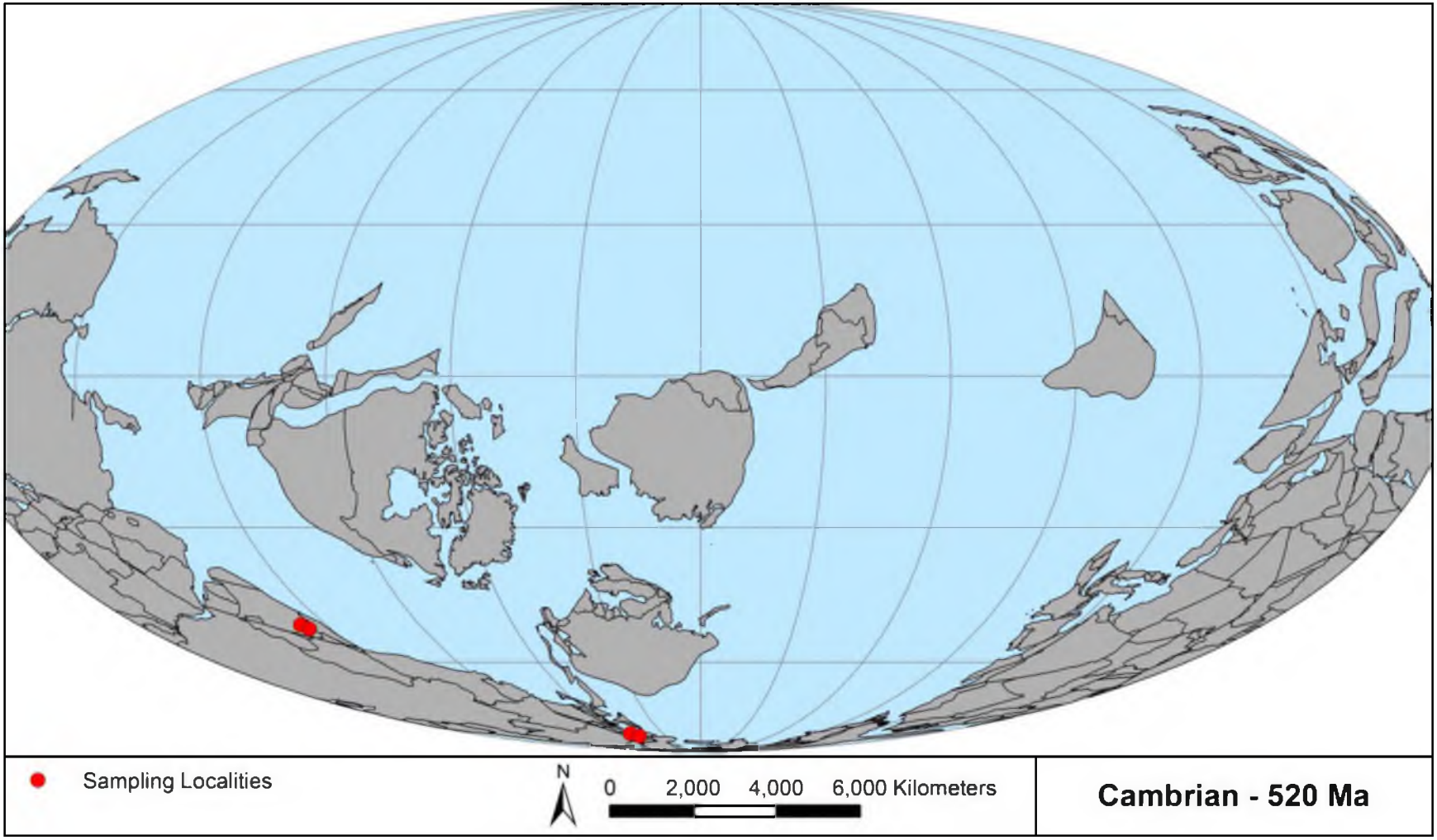

Figure G.14. Locality map of the samples analyzed that were Cambrian in age. GPS locations were converted using the PointTracker program (Scotese, 2010) and all points were converted using an age of 520 Ma. Plate tectonic map produced by C. Scotese (2011e). Use of PointTracker and PALEOMAP courtesy of Christopher Scotese.

APPENDIX H

DATA TABLES OF ANALYSIS RESULTS

Table H.1. Results of analyses on meandering trace fossils. Complete sample locality and date information can be found in Appendix E. The table contains the estimated latitude and longitude of the sample localities. The age is the median age of the formation in which the sample was found. The age error encompasses the length of time the formation has been estimated to have been deposited. Abbreviations: a = amplitude; BAS = burrow area shape; D_{Box} = fractal dimension using the Box Counting Method; Ind = indeterminate analyses; λ = wavelength; MS = mesh size; OSP = occupied space percentage; τ = tortuosity; W = burrow width. The τ and D_{Box} variance is represented by the standard error.

Ichnogenera	Sample ID	Latitude
Cosmorhaphe	INMD 98BX	15° 31' N
Helminthorhaphe	VBHelmin1	37° 8' 46" N
Cosmorhaphe	Uchman and Demircan 1999 Fig 5A	37° 18' 58" N
Cosmorhaphe	Uchman and Demircan 1999 Fig 5C	37° 18' 58" N
Helminthorhaphe	Uchman and Demircan 1999 Fig 7F	37° 18' 58" N
Helminthorhaphe	Uchman and Demircan 1999 Fig 7G	37° 18' 58" N
Helminthorhaphe	CS 12	40° 31' 26" N
Helminthopsis	PIW1993X 103	43° 59' N
Helminthopsis	PIW1993X 104	44° 9' 16" N
Helminthorhaphe	PIW1993X 93	44° 4' N
Helminthorhaphe	PIW1993X 96	44° 0' N
Helminthopsis	UJTF 1320	51° 4' 25" N
Helminthopsis	UJTF 1587	51° 35' 10" N
Helminthorhaphe	UJTF 39	49° 32' 30" N
Helminthorhaphe	UJTF 1361	49° 28' 12" N
Helminthorhaphe	UJTF 1362	49° 28' 12" N
Helminthopsis	IGP t.f. 102	49° 23' N
Helminthopsis	IGP t.f. 306c	49° 23' N
Helminthopsis	UJTF 100	49° 43' 43" N
Helminthorhaphe	UJTF 42a	53° 5' 45" N
Helminthorhaphe	UJTF 104	49° 43' 43" N
Helminthorhaphe	UJTF 426	53° 5' 45" N
Oscillorhaphe	UJTF 144	49° 43' 43" N
Spirocosmorhaphe	UJTF 149P3	44° 8' 6" N
Cosmorhaphe	UUIC 1607	46° 59' 26" N
Belorhaphe	UJTF 1442	49° 33' 46" N
Cosmorhaphe	UJTF 243	49° 33' 46" N

Longitude	Period/Epoch	Age (Ma)	W (mm)
42° 57' W	Modern	0.0 ± 0.00	0.7
1° 56' 11" W	Miocene	6.3 ± 0.96	2.2
35° 13' 22" E	Miocene	13.8 ± 2.18	1.6
35° 13' 22" E	Miocene	13.8 ± 2.18	2.5
35° 13' 22" E	Miocene	13.8 ± 2.18	1.0
35° 13' 22" E	Miocene	13.8 ± 2.18	0.7
16° 2' 57" E	Miocene	10.7 ± 5.32	1.1
11° 56' E	Miocene	13.8 ± 2.18	1.1
11° 27' 29" E	Miocene	13.8 ± 2.18	0.8
11° 56' E	Miocene	13.8 ± 2.18	0.9
11° 57' E	Miocene	13.8 ± 2.18	1.1
20° 15' 30" E	Oligocene	25.7 ± 2.69	1.3
16° 51' 36" E	Oligocene	25.7 ± 2.69	3.2
22° 22' 01" E	Oligocene	25.7 ± 2.69	1.1
22° 33' 41" E	Oligocene	25.7 ± 2.69	1.2
22° 33' 41" E	Oligocene	25.7 ± 2.69	1.5
20° 1' E	Oligocene	28.5 ± 5.44	1.8
20° 1' E	Oligocene	28.5 ± 5.44	2.0
20° 40' 21" E	Eocene	46.5 ± 9.30	1.8
23° 41' 48" E	Eocene	46.5 ± 9.30	1.5
20° 40' 21" E	Eocene	46.5 ± 9.30	1.6
23° 41' 48" E	Eocene	46.5 ± 9.30	0.6
20° 40' 21" E	Eocene	46.5 ± 9.30	0.9
9° 41' 7" E	Eocene	53.7 ± 5.05	0.6
9° 38' 18" E	Eocene	44.9 ± 10.95	1.2
19° 38' 58" E	Eocene	42.9 ± 5.70	1.5
19° 38' 58" E	Eocene	42.9 ± 5.70	1.7

Table H.1 continued.

Ichnogenera	Sample ID	Latitude	Longitude
Paleomeandron	UJTF 229	49° 32' 50" N	19° 44' 19" E
Belocosmorhaphe	UJTF 121	49° 47' 32" N	19° 37' 2" E
Belocosmorhaphe	UJTF 334a	49° 47' 32" N	19° 37' 2" E
Helminthorhaphe	UJTF 750	49° 26' 28" N	20° 25' 39" E
Belocosmorhaphe	UJTF 716	49° 36' 36" N	20° 17' 41" E
Belocosmorhaphe	UJTF 1360	49° 36' 36" N	20° 17' 41" E
Belorhaphe	UJTF 1443	49° 59' 14" N	19° 52' 33" E
Cosmorhaphe	UJTF 1	49° 59' 14" N	19° 52' 33" E
Cosmorhaphe	UJTF 5	49° 30' 50" N	19° 38' 00" E
Cosmorhaphe	UJTF 8	49° 59' 14" N	19° 52' 33" E
Cosmorhaphe	UJTF 9	49° 33' 46" N	19° 38' 58" E
Cosmorhaphe	UJTF 11	49° 28' 27" N	19° 38' 24" E
Cosmorhaphe	UJTF 12	49° 30' 50" N	19° 38' 00" E
Cosmorhaphe	UJTF 13	49° 30' 50" N	19° 38' 00" E
Cosmorhaphe	UJTF 18	51° 00' 46" N	15° 30' 38" E
Cosmorhaphe	UJTF 77	49° 41' 6" N	19° 50' 3" E
Cosmorhaphe	UJTF 242	49° 59' 14" N	19° 52' 33" E
Helminthopsis	UJTF 252	49° 30' 50" N	19° 38' 00" E
Helminthopsis	UJTF 1082	49° 59' 14" N	19° 52' 33" E
Helminthopsis	UJTF 1661	49° 59' 14" N	19° 52' 33" E
Helminthorhaphe	UJTF 102	49° 59' 14" N	19° 52' 33" E
Helminthorhaphe	UJTF 708	49° 36' 36" N	20° 17' 41" E
Helminthorhaphe	UJTF 1100	49° 33' 46" N	19° 38' 58" E
Helminthorhaphe	UJTF unk	49° 30' 50" N	19° 38' 00" E
Paleomeandron	UJTF 231	49° 30' 50" N	19° 38' 00" E
Cosmorhaphe	UJTF 10	49° 40' 12" N	19° 7' 39" E
Helminthorhaphe	UJTF 44	49° 42' 48" N	19° 38' 41" E
Helminthorhaphe	UJTF 45	49° 35' 25" N	20° 41' 2" E
Helminthorhaphe	UJTF 788	50° 45' 56" N	20° 26' 40" E
Paleomeandron	UJTF 138	49° 42' 48" N	19° 38' 41" E
Helmithorhaphe	UJTF unk	43° 18.540' N	2° 13.882' W

Period/Epoch	Age (Ma)	W (mm)
Eocene	42.9 ± 5.70	5.3
Eocene	46.5 ± 9.30	1.2
Eocene	46.5 ± 9.30	1.1
Eocene	53.7 ± 5.05	1.0
Eocene	46.5 ± 9.30	2.0
Eocene	46.5 ± 9.30	4.0
Eocene	46.5 ± 9.30	1.1
Eocene	46.5 ± 9.30	1.9
Eocene	46.5 ± 9.30	2.2
Eocene	46.5 ± 9.30	2.3
Eocene	46.5 ± 9.30	2.2
Eocene	46.5 ± 9.30	2.3
Eocene	46.5 ± 9.30	1.8
Eocene	46.5 ± 9.30	1.9
Eocene	46.5 ± 9.30	1.8
Eocene	46.5 ± 9.30	1.6
Eocene	46.5 ± 9.30	2.2
Eocene	46.5 ± 9.30	1.9
Eocene	46.5 ± 9.30	4.3
Eocene	46.5 ± 9.30	1.1
Eocene	46.5 ± 9.30	1.0
Eocene	46.5 ± 9.30	2.7
Eocene	46.5 ± 9.30	2.4
Eocene	46.5 ± 9.30	1.2
Eocene	46.5 ± 9.30	5.4
Eocene	42.9 ± 5.70	1.8
Eocene	42.9 ± 5.70	1.1
Eocene	42.9 ± 5.70	1.7
Eocene	42.9 ± 5.70	1.2
Eocene	42.9 ± 5.70	0.8
Eocene	52.2 ± 3.60	0.9

Table H.1 continued.

Ichnogenera	Sample ID	Latitude	Longitude
Helmithorhaphe	UUIC 429	43° 18.540' N	2° 13.882' W
Cosmorhaphe	Z_Cos1	43° 18.540' N	2° 13.882' W
Cosmorhaphe	Z_Cos2	43° 18.540' N	2° 13.882' W
Cosmorhaphe	Z_Cos3	43° 18.540' N	2° 13.882' W
Cosmorhaphe	Z_Cos4	43° 18.540' N	2° 13.882' W
Cosmorhaphe	Z_Cos5	43° 18.540' N	2° 13.882' W
Helminthorhaphe	Z_Helmin1	43° 18.540' N	2° 13.882' W
Helminthorhaphe	Z_Helmin2	43° 18.540' N	2° 13.882' W
Helminthorhaphe	Z_Helmin3	43° 18.540' N	2° 13.882' W
Helminthorhaphe	Z_Helmin4	43° 18.540' N	2° 13.882' W
Helminthorhaphe	Z_Helmin5	43° 18.540' N	2° 13.882' W
Paleomeandron	Z_Paleomendron1	43° 18.540' N	2° 13.882' W
Helminthorhaphe	UJTF 1403	49° 51' 20" N	19° 29' 52" E
Cosmorhaphe	154P40	48° 20' 57" N	16° 15' 25" E
Cosmorhaphe	UUIC 1723	10° 8' 20" N	65° 28' 00" W
Helminthorhaphe	UJTF 46	49° 44' 39" N	20° 41' 14" E
Cosmorhaphe	UJTF 19	49° 40' 50" N	19° 46' 56" E
Cosmorhaphe	UJTF 74	49° 28' 27" N	19° 38' 24" E
Cosmorhaphe	UJTF 1451	49° 33' 46" N	19° 38' 58" E
Cosmorhaphe	UJTF 2684	49° 28' 27" N	19° 38' 24" E
Cosmorhaphe	UJTF unk	49° 28' 27" N	19° 38' 24" E
Helminthorhape	UJTF 34	49° 30' 50" N	19° 38' 00" E
Cosmorhaphe	UJTF 17	49° 59' 14" N	19° 52' 33" E
Cosmorhaphe	UJTF 75	50° 39' 30" N	17° 53' 40" E
Cosmorhaphe	UJTF 250	49° 37' 26" N	20° 56' 52" E
Cosmorhaphe	UJTF 1872	49° 37' 26" N	20° 56' 52" E
Helminthopsis	UJTF 225	49° 38' 47" N	22° 16' 14" E
Helminthopsis	UJTF 333	49° 40' 27" N	20° 04' 47" E
Helminthorhaphe	UJTF 40	49° 30' 50" N	19° 38' 00" E
Helminthorhaphe	UJTF 49	49° 36' 27" N	20° 03' 41" E
Helminthorhaphe	UJTF 99	49° 36' 27" N	20° 57' 9" E

Period/Epoch	Age (Ma)	W (mm)
Eocene	52.2 ± 3.60	1.5
Eocene	52.2 ± 3.60	2.5
Eocene	52.2 ± 3.60	1.1
Eocene	52.2 ± 3.60	1.2
Eocene	52.2 ± 3.60	1.9
Eocene	52.2 ± 3.60	2.3
Eocene	52.2 ± 3.60	0.9
Eocene	52.2 ± 3.60	0.7
Eocene	52.2 ± 3.60	1.2
Eocene	52.2 ± 3.60	0.6
Eocene	52.2 ± 3.60	1.3
Eocene	52.2 ± 3.60	5.1
Paleocene	57.3 ± 1.45	1.2
Paleocene	53.7 ± 5.05	0.9
Paleocene	60.7 ± 4.85	1.7
Paleocene	63.3 ± 2.20	3.9
Paleocene	53.7 ± 5.05	2.0
Paleocene	53.7 ± 5.05	2.2
Paleocene	53.7 ± 5.05	1.8
Paleocene	53.7 ± 5.05	2.2
Paleocene	53.7 ± 5.05	1.8
Paleocene	53.7 ± 5.05	0.9
Late Cretaceous	63.2 ± 7.40	2.1
Late Cretaceous	63.2 ± 7.40	0.9
Late Cretaceous	63.2 ± 7.40	4.4
Late Cretaceous	63.2 ± 7.40	3.5
Late Cretaceous	63.2 ± 7.40	3.0
Late Cretaceous	63.2 ± 7.40	1.0
Late Cretaceous	63.2 ± 7.40	2.7
Late Cretaceous	63.2 ± 7.40	0.6
Late Cretaceous	63.2 ± 7.40	1.1

Table H.1 continued.

Ichnogenera	Sample ID	Latitude	Longitude
Helminthorhaphe	UJTF 1014	51° 32' 3" N	18° 33' 46" E
Cosmorhaphe	McCann and Pickerill 1988 Fig 3-5	57° 46' 44" N	152° 26' 55" W
Helminthorhaphe	McCann and Pickerill 1988 Fig 3-12	57° 46' 44" N	152° 26' 55" W
Spirocosmorhaphe	GSC 81257	57° 46' 19" N	152° 24' 59" W
Cosmorhaphe	UJTF unk	49° 45' 6" N	20° 9' 8" E
Helminthorhaphe	UJTF 103	49° 24' 29" N	20° 20' 21" E
Cosmorhaphe	UJTF 1162	49° 46' 8" N	20° 5' 4" E
Belorhaphe	UUIC 1949	8° 46' 24" S	39° 19' 25" E
Helminthorhaphe	UUIC 1911	8° 46' 24" S	39° 19' 25" E
Helminthorhaphe	UUIC 1912	8° 48' 13" S	39° 20' 16" E
Helminthorhaphe	UUIC 1913	8° 45' 24" S	39° 18' 34" E
Helminthopsis	Yeh 1987 Fig 2C	34° 31' 44" N	119° 14' 46" W
Helminthorhaphe	Yeh 1987 Fig 2A	34° 31' 44" N	119° 14' 46" W
Helminthorhaphe	Yeh 1987 Fig 2B	34° 31' 44" N	119° 14' 46" W
Cosmorhaphe	PIW1998IV 140	47° 44' 45" N	12° 3' 33" E
Belorhaphe	UJTF 119	49° 51' 44" N	19° 31' 9" E
Helminthopsis	UJTF 1465	49° 44' 6" N	18° 45' 55" E
Belorhaphe	UCMP 398563	41° 46' 41" N	124° 15' 7" W
Cosmorhaphe	UCMP 38606	41° 3' 6" N	124° 7' 46" W
Cosmorhaphe	UCMP 398570	41° 46' 41" N	124° 15' 7" W
Helminthopsis	UCMP 398575	41° 46' 41" N	124° 15' 7" W
Helminthorhaphe	UCMP 38608	41° 3' 6" N	124° 7' 46" W
Helminthorhaphe	UCMP 38609	41° 3' 6" N	124° 7' 46" W
Helminthorhaphe	UCMP 398578	41° 46' 41" N	124° 15' 7" W
Helminthopsis	UJTF 331	50° 35' 18" N	19° 3' 37" E
Helminthopsis	UJTF 1321	49° 49' 01" N	20° 7' 00" E
Belorhaphe	BAN-Jich-0017	42° 41' 36" N	22° 40' 58" E
Helminthopsis	Mikuláš et al 2004 Plate III-3	50° 5' 8" N	17° 17' 41" E

Period/Epoch	Age (Ma)	W (mm)
Late Cretaceous	63.2 ± 7.40	1.8
Late Cretaceous	82.6 ± 17.05	3.9
Late Cretaceous	82.6 ± 17.05	1.1
Late Cretaceous	82.6 ± 17.05	0.5
Late Cretaceous	86.1 ± 2.55	0.4
Late Cretaceous	79.6 ± 9.00	1.8
Late Cretaceous	74.5 ± 9.00	0.6
Late Cretaceous	81.5 ± 2.00	0.9
Late Cretaceous	81.5 ± 2.00	2.4
Late Cretaceous	78.0 ± 1.50	1.2
Late Cretaceous	84.9 ± 1.40	1.5
Late Cretaceous	74.5 ± 9.00	1.4
Late Cretaceous	74.5 ± 9.00	1.1
Late Cretaceous	74.5 ± 9.00	1.4
Late Cretaceous	78.2 ± 7.60	3.1
Early Cretaceous	145.5 ± 5.30	0.9
Early Cretaceous	145.5 ± 5.30	1.4
Early Cretaceous	140.4 ± 10.40	0.4
Early Cretaceous	140.4 ± 10.40	0.6
Early Cretaceous	140.4 ± 10.40	0.7
Early Cretaceous	140.4 ± 10.40	0.9
Early Cretaceous	140.4 ± 10.40	1.3
Early Cretaceous	140.4 ± 10.40	1.4
Early Cretaceous	140.4 ± 10.40	0.4
Early Cretaceous	129.5 ± 4.45	1.8
Early Cretaceous	129.5 ± 4.45	3.2
Jurassic	148.3 ± 2.75	0.8
Carboniferous	338.8 ± 7.90	5.2

Table H.1 continued.

Ichnogenera	Sample ID	Latitude	Longitude
Cosmorhaphe	NBMG 9675	47° 12' 12" N	67° 11' 25" W
Cosmorhaphe	TF.F142	47° 12' 12" N	67° 11' 25" W
Cosmorhaphe	TF9208-1-30	47° 12' 12" N	67° 11' 25" W
Helminthopsis	NBMG 9680	47° 12' 12" N	67° 11' 25" W
Helminthorhaphe	TF.F111	47° 12' 12" N	67° 11' 25" W
Helminthopsis	Crimes and Crossley 1991 Fig 4c	52° 29' 17" N	4° 3' 14" W
Helminthopsis	Crimes and Crossley 1991 Fig 4d	52° 29' 17" N	4° 3' 14" W
Helminthopsis	Crimes and Crossley 1991 Fig 4e	52° 29' 17" N	4° 3' 14" W
Helminthorhaphe	Acenolaza 1978 Lam IV-6	23° 22' S	66° 40' W
Helminthopsis	Pickerill 1981 Fig 2b	47° 13' 00" N	67° 59' 19" W
Helminthopsis	GSC 78129	47° 38' 00" N	52° 55' 16" W
Helminthopsis	GSC 78146	47° 37' 20" N	52° 56' 24" W
Helminthopsis	Pickerill 1980 Fig 5d	47° 53' N	66° 50' W
Helminthorhaphe	Pickerill 1980 Fig 4d	47° 53' N	66° 50' W
Helminthopsis	Crimes et al 1992 Fig 5A	52° 38' 17" N	6° 13' 34" W
Helminthopsis	Crimes and Anderson 1985 Fig 7.6	47° 6' 30" N	55° 46' 18" W
Helminthorhaphe	Crimes and Anderson 1985 Fig 7.3	47° 6' 30" N	55° 46' 18" W
Helminthorhaphe	Crimes and Anderson 1985 Fig 7.5	47° 6' 30" N	55° 46' 18" W
Helminthorhaphe	GSC 73327	47° 6' 30" N	55° 46' 18" W
Helminthorhaphe	GSC 73330	47° 6' 30" N	55° 46' 18" W
Helminthopsis	Acenolaza 1978 Fig 11	24° 15' 5" S	66° 13' 16" W
Helminthorhaphe	Acenolaza and Torelli 1981 pg 55-1	24° 15' 5" S	66° 13' 16" W
Helminthorhaphe	Acenolaza and Torelli 1981 pg 55-2	24° 15' 5" S	66° 13' 16" W

Period/Epoch	Age (Ma)	W (mm)
Devonian	411.5 ± 4.50	1.7
Devonian	411.5 ± 4.50	1.8
Devonian	411.5 ± 4.50	2.1
Devonian	411.5 ± 4.50	2.0
Devonian	411.5 ± 4.50	1.2
Silurian	432.1 ± 3.90	5.7
Silurian	432.1 ± 3.90	5.7
Silurian	432.1 ± 3.90	4.7
Silurian	420.8 ± 2.10	2.6
Silurian	439.9 ± 3.85	3.3
Ordovician	483.5 ± 4.85	0.7
Ordovician	483.5 ± 4.85	2.0
Ordovician	474.6 ± 13.70	2.3
Ordovician	474.6 ± 13.70	6.1
Ordovician	472.5 ± 6.50	3.1
Cambrian	524.5 ± 3.50	4.3
Cambrian	524.5 ± 3.50	4.9
Cambrian	524.5 ± 3.50	4.0
Cambrian	524.5 ± 3.50	2.5
Cambrian	524.5 ± 3.50	3.5
Cambrian	537.5 ± 2.50	2.0
Cambrian	537.5 ± 2.50	4.1
Cambrian	537.5 ± 2.50	3.1

Table H.1 continued.

Ichnogenera	Sample ID	τ for 5 cm	τ for 10 cm	τ for 15 cm	τ for 20 cm	τ for 25 cm	τ for 30 cm
Cosmorhaphe	INMD 98BX	2.353 ± 0.207	2.934 ± 0.374	10.887 ± 5.836	Ind	Ind	Ind
Helminthorhaphe	VBHelmin1	2.231 ± 0.385	3.795 ± 0.690	7.402 ± 0.839	5.141 ± 1.385	8.466 ± 0.517	Ind
Cosmorhaphe	Uchman and Demircan 1999 Fig 5A	1.807 ± 0.170	2.132 ± 0.151	Ind	Ind	Ind	Ind
Cosmorhaphe	Uchman and Demircan 1999 Fig 5C	1.150 ± 0.080	Ind	Ind	Ind	Ind	Ind
Helminthorhaphe	Uchman and Demircan 1999 Fig 7F	1.058 ± 0.010	Ind	Ind	Ind	Ind	Ind
Helminthorhaphe	Uchman and Demircan 1999 Fig 7G	1.258 ± 0.165	Ind	Ind	Ind	Ind	Ind
Helminthorhaphe	CS 12	4.088 ± 1.494	Ind	Ind	Ind	Ind	Ind
Helminthopsis	PIW1993X 103	Ind	Ind	Ind	Ind	Ind	Ind
Helminthopsis	PIW1993X 104	1.114 ± 0.038	Ind	Ind	Ind	Ind	Ind
Helminthorhaphe	PIW1993X 93	1.525 ± 0.225	Ind	Ind	Ind	Ind	Ind
Helminthorhaphe	PIW1993X 96	2.367 ± 0.659	7.429 ± 1.465	Ind	Ind	Ind	Ind
Helminthopsis	UJTF 1320	1.207 ± 0.047	1.226 ± 0.054	Ind	Ind	Ind	Ind
Helminthopsis	UJTF 1587	1.125 ± 0.066	1.299 ± 0.102	1.378 ± 0.131	Ind	Ind	Ind
Helminthorhaphe	UJTF 39	4.815 ± 2.393	2.460 ± 0.305	Ind	Ind	Ind	Ind
Helminthorhaphe	UJTF 1361	3.990 ± 1.534	7.777 ± 3.053	Ind	Ind	Ind	Ind
Helminthorhaphe	UJTF 1362	3.541 ± 0.554	4.431 ± 1.104	3.703 ± 0.437	3.755 ± 0.308	3.655 ± 0.165	3.526 ± 0.155
Helminthopsis	IGP t.f. 102	1.209 ± 0.080	1.257 ± 0.129	1.342 ± 0.093	Ind	Ind	Ind
Helminthopsis	IGP t.f. 306c	1.732 ± 0.378	1.798 ± 0.319	Ind	Ind	Ind	Ind
Helminthopsis	UJTF 100	1.381 ± 0.134	2.063 ± 0.302	2.271 ± 0.078	2.465 ± 0.103	Ind	Ind
Helminthorhaphe	UJTF 42a	3.042 ± 0.624	4.985 ± 1.586	7.127 ± 0.552	6.399 ± 0.285	8.055 ± 1.079	6.46 ± 1.403
Helminthorhaphe	UJTF 104	1.413 ± 0.222	15.792 ± 9.459	2.661 ± 1.027	10.839 ± 2.411	11.37 ± 6.418	7.914 ± 3.14
Helminthorhaphe	UJTF 426	2.999 ± 0.747	Ind	Ind	Ind	Ind	Ind
Oscillorhaphe	UJTF 144	1.077 ± 0.039	18.307 ± 13.754	Ind	Ind	Ind	Ind
Spirocosmorhaphe	UJTF 149P3	3.169 ± 0.686	8.779 ± 6.459	Ind	Ind	Ind	Ind
Cosmorhaphe	UUIC 1607	1.415 ± 0.256	Ind	Ind	Ind	Ind	Ind
Belorhaphe	UJTF 1442	1.464 ± 0.002	Ind	Ind	Ind	Ind	Ind
Cosmorhaphe	UJTF 243	1.495 ± 0.076	1.931 ± 0.268	1.814 ± 0.360	Ind	Ind	Ind

Table H.1 continued.

Ichnogenera	Sample ID	τ for 5 cm	τ for 10 cm	τ for 15 cm	τ for 20 cm	τ for 25 cm	τ for 30 cm
Paleomeandron	UJTF 229	1.45 ± 0.094	1.493 ± 0.130	1.618 ± 0.006	Ind	Ind	Ind
Belocosmorhaphe	UJTF 121	1.703 ± 0.225	Ind	Ind	Ind	Ind	Ind
Belocosmorhaphe	UJTF 334a	2.092 ± 0.314	2.787 ± 1.008	Ind	Ind	Ind	Ind
Helminthorhaphe	UJTF 750	1.546 ± 0.231	10.550 ± 3.592	6.760 ± 1.580	6.547 ± 1.533	10.640 ± 0.843	7.753 ± 2.035
Belocosmorhaphe	UJTF 716	2.121 ± 0.167	2.349 ± 0.400	Ind	Ind	Ind	Ind
Belocosmorhaphe	UJTF 1360	2.127 ± 0.248	2.374 ± 0.164	2.748 ± 0.073	Ind	Ind	Ind
Belorhaphe	UJTF 1443	1.578 ± 0.145	Ind	Ind	Ind	Ind	Ind
Cosmorhaphe	UJTF 1	1.399 ± 0.071	1.455 ± 0.053	1.530 ± 0.044	1.645 ± 0.052	Ind	Ind
Cosmorhaphe	UJTF 5	1.443 ± 0.049	1.784 ± 0.151	2.816 ± 0.818	Ind	Ind	Ind
Cosmorhaphe	UJTF 8	1.283 ± 0.069	1.637 ± 0.273	Ind	Ind	Ind	Ind
Cosmorhaphe	UJTF 9	1.505 ± 0.097	Ind	Ind	Ind	Ind	Ind
Cosmorhaphe	UJTF 11	1.896 ± 0.146	2.251 ± 0.494	2.420 ± 0.303	Ind	Ind	Ind
Cosmorhaphe	UJTF 12	1.478 ± 0.075	1.966 ± 0.023	Ind	Ind	Ind	Ind
Cosmorhaphe	UJTF 13	1.263 ± 0.069	Ind	Ind	Ind	Ind	Ind
Cosmorhaphe	UJTF 18	1.298 ± 0.044	1.747 ± 0.116	Ind	Ind	Ind	Ind
Cosmorhaphe	UJTF 77	2.978 ± 0.366	3.073 ± 0.328	4.447 ± 0.566	5.770 ± 1.065	6.196 ± 1.660	8.738 ± 2.657
Cosmorhaphe	UJTF 242	1.630 ± 0.170	1.746 ± 0.155	Ind	Ind	Ind	Ind
Helminthopsis	UJTF 252	1.433 ± 0.132	1.721 ± 0.176	1.989 ± 0.379	Ind	Ind	Ind
Helminthopsis	UJTF 1082	1.483 ± 0.170	1.979 ± 0.543	12.05 ± 9.822	3.612 ± 1.221	Ind	Ind
Helminthopsis	UJTF 1661	1.091 ± 0.038	1.121 ± 0.035	Ind	Ind	Ind	Ind
Helminthorhaphe	UJTF 102	2.883 ± 0.782	Ind	Ind	Ind	Ind	Ind
Helminthorhaphe	UJTF 708	1.496 ± 0.199	2.559 ± 0.433	2.218 ± 0.397	3.298 ± 0.518	2.776 ± 0.036	Ind
Helminthorhaphe	UJTF 1100	1.280 ± 0.088	2.838 ± 0.52	1.761 ± 0.321	2.517 ± 0.73	Ind	Ind
Helminthorhaphe	UJTF unk	2.277 ± 0.525	7.73 ± 3.347	Ind	Ind	Ind	Ind
Paleomeandron	UJTF 231	1.662 ± 0.083	1.721 ± 0.164	1.668 ± 0.135	2.021 ± 0.168	Ind	Ind
Cosmorhaphe	UJTF 10	1.943 ± 0.404	Ind	Ind	Ind	Ind	Ind
Helminthorhaphe	UJTF 44	3.240 ± 1.193	19.183 ± 6.336	Ind	Ind	Ind	Ind
Helminthorhaphe	UJTF 45	1.135 ± 0.051	4.873 ± 1.908	Ind	Ind	Ind	Ind
Helminthorhaphe	UJTF 788	2.907 ± 0.649	Ind	Ind	Ind	Ind	Ind
Paleomeandron	UJTF 138	2.374 ± 0.538	Ind	Ind	Ind	Ind	Ind
Helmithorhaphe	UJTF unk	1.947 ± 0.382	5.944 ± 2.420	7.821 ± 4.410	9.963 ± 3.869	Ind	Ind

Table H.1 continued.

Ichnogenera	Sample ID	τ for 5 cm	τ for 10 cm	τ for 15 cm	τ for 20 cm	τ for 25 cm	τ for 30 cm
Helmithorhaphe	UUIC 429	4.140 ± 1.622	3.640 ± 0.719	4.966 ± 0.966	4.747 ± 0.523	Ind	Ind
Cosmorhaphe	Z_Cos1	1.603 ± 0.043	1.843 ± 0.139	2.961 ± 0.912	Ind	Ind	Ind
Cosmorhaphe	Z_Cos2	1.482 ± 0.019	1.651 ± 0.168	3.396 ± 0.247	Ind	Ind	Ind
Cosmorhaphe	Z_Cos3	1.602 ± 0.105	2.005 ± 0.239	2.217 ± 0.292	1.994 ± 0.282	Ind	Ind
Cosmorhaphe	Z_Cos4	1.583 ± 0.034	1.632 ± 0.050	Ind	Ind	Ind	Ind
Cosmorhaphe	Z_Cos5	1.523 ± 0.059	1.699 ± 0.207	Ind	Ind	Ind	Ind
Helminthorhaphe	Z_Helmin1	2.790 ± 0.908	2.030 ± 0.627	Ind	Ind	Ind	Ind
Helminthorhaphe	Z_Helmin2	1.192 ± 0.092	13.807 ± 12.461	Ind	Ind	Ind	Ind
Helminthorhaphe	Z_Helmin3	1.197 ± 0.081	Ind	Ind	Ind	Ind	Ind
Helminthorhaphe	Z_Helmin4	3.759 ± 2.705	Ind	Ind	Ind	Ind	Ind
Helminthorhaphe	Z_Helmin5	2.847 ± 1.171	Ind	Ind	Ind	Ind	Ind
Paleomeandron	Z_Paleomendron1	1.241 ± 0.056	1.252 ± 0.034	1.478 ± 0.078	Ind	Ind	Ind
Helminthorhaphe	UJTF 1403	1.979 ± 0.447	2.933 ± 0.390	Ind	Ind	Ind	Ind
Cosmorhaphe	154P40	3.952 ± 0.621	12.597 ± 7.826	5.361 ± 0.803	9.361 ± 1.168	8.128 ± 0.601	Ind
Cosmorhaphe	UUIC 1723	1.422 ± 0.030	Ind	Ind	Ind	Ind	Ind
Helminthorhaphe	UJTF 46	1.782 ± 0.485	1.612 ± 0.540	Ind	Ind	Ind	Ind
Cosmorhaphe	UJTF 19	2.097 ± 0.269	2.178 ± 0.079	3.997 ± 1.687	Ind	Ind	Ind
Cosmorhaphe	UJTF 74	2.637 ± 0.324	3.09 ± 0.219	4.372 ± 1.021	3.457 ± 0.279	6.649 ± 1.81	7.916 ± 1.553
Cosmorhaphe	UJTF 1451	1.396 ± 0.119	2.153 ± 0.534	1.841 ± 0.279	Ind	Ind	Ind
Cosmorhaphe	UJTF 2684	4.094 ± 0.412	4.045 ± 0.389	4.073 ± 0.313	4.573 ± 0.532	5.202 ± 0.875	3.678 ± 0.309
Cosmorhaphe	UJTF unk	5.114 ± 1.293	2.927 ± 0.563	Ind	Ind	Ind	Ind
Helminthorhape	UJTF 34	6.306 ± 0.322	Ind	Ind	Ind	Ind	Ind
Cosmorhaphe	UJTF 17	1.474 ± 0.053	1.402 ± 0.025	Ind	Ind	Ind	Ind
Cosmorhaphe	UJTF 75	3.407 ± 0.810	Ind	Ind	Ind	Ind	Ind
Cosmorhaphe	UJTF 250	2.304 ± 0.223	3.364 ± 0.626	3.513 ± 0.502	3.251 ± 0.226	4.651 ± 0.904	3.851 ± 0.742
Cosmorhaphe	UJTF 1872	2.259 ± 0.235	3.519 ± 0.390	3.234 ± 0.231	2.902 ± 0.273	3.314 ± 0.205	3.705 ± 0.298
Helminthopsis	UJTF 225	1.184 ± 0.058	2.074 ± 0.612	Ind	Ind	Ind	Ind
Helminthopsis	UJTF 333	2.349 ± 0.360	2.861 ± 0.737	2.669 ± 0.441	Ind	Ind	Ind
Helminthorhaphe	UJTF 40	1.224 ± 0.163	2.976 ± 1.146	1.212 ± 0.090	3.286 ± 1.113	8.835 ± 1.633	7.162 ± 1.402
Helminthorhaphe	UJTF 49	12.345 ± 3.468	Ind	Ind	Ind	Ind	Ind
Helminthorhaphe	UJTF 99	2.894 ± 0.514	4.726 ± 2.081	Ind	Ind	Ind	Ind

Table H.1 continued.

Ichnogenera	Sample ID	τ for 5 cm	τ for 10 cm	τ for 15 cm	τ for 20 cm	τ for 25 cm	τ for 30 cm
Helminthorhaphe	UJTF 1014	1.754 ± 0.311	1.283 ± 0.092	3.782 ± 0.796	Ind	Ind	Ind
Cosmorhaphe	McCann and Pickerill 1988 Fig 3-5	2.634 ± 0.431	4.599 ± 1.175	4.748 ± 0.765	3.790 ± 0.414	4.034 ± 0.53	6.645 ± 0.654
Helminthorhaphe	McCann and Pickerill 1988 Fig 3-12	1.480 ± 0.230	21.135 ± 14.674	Ind	Ind	Ind	Ind
Spirocosmorhaphe	GSC 81257	9.170 ± 2.135	Ind	Ind	Ind	Ind	Ind
Cosmorhaphe	UJTF unk	2.274 ± 0.082	Ind	Ind	Ind	Ind	Ind
Helminthorhaphe	UJTF 103	2.673 ± 0.434	11.069 ± 3.668	10.485 ± 1.789	6.662 ± 1.458	10.581 ± 2.035	12.263 ± 3.888
Cosmorhaphe	UJTF 1162	2.648 ± 0.302	Ind	Ind	Ind	Ind	Ind
Belorhaphe	UUIC 1949	Ind	Ind	Ind	Ind	Ind	Ind
Helminthorhaphe	UUIC 1911	1.626 ± 0.267	2.640 ± 0.672	5.233 ± 1.122	4.389 ± 0.637	4.994 ± 0.151	Ind
Helminthorhaphe	UUIC 1912	2.264 ± 0.480	5.586 ± 1.377	6.587 ± 1.437	5.226 ± 1.172	Ind	Ind
Helminthorhaphe	UUIC 1913	4.712 ± 1.012	20.847 ± 14.351	7.315 ± 2.931	Ind	Ind	Ind
Helminthopsis	Yeh 1987 Fig 2C	2.439 ± 0.951	Ind	Ind	Ind	Ind	Ind
Helminthorhaphe	Yeh 1987 Fig 2A	3.618 ± 2.117	Ind	Ind	Ind	Ind	Ind
Helminthorhaphe	Yeh 1987 Fig 2B	1.406 ± 0.237	3.623 ± 0.58	Ind	Ind	Ind	Ind
Cosmorhaphe	PIW1998IV 140	1.798 ± 0.289	2.208 ± 0.195	2.507 ± 0.771	4.608 ± 2.36	5.787 ± 2.79	Ind
Belorhaphe	UJTF 119	1.475 ± 0.030	1.479 ± 0.029	1.441 ± 0.035	1.470 ± 0.004	Ind	Ind
Helminthopsis	UJTF 1465	1.235 ± 0.046	1.797 ± 0.183	1.519 ± 0.164	1.675 ± 0.043	1.933 ± 0.305	1.974 ± 0.026
Belorhaphe	UCMP 398563	Ind	Ind	Ind	Ind	Ind	Ind
Cosmorhaphe	UCMP 38606	6.050 ± 2.835	10.484 ± 0.179	Ind	Ind	Ind	Ind
Cosmorhaphe	UCMP 398570	Ind	Ind	Ind	Ind	Ind	Ind
Helminthopsis	UCMP 398575	1.370 ± 0.145	Ind	Ind	Ind	Ind	Ind
Helminthorhaphe	UCMP 38608	1.929 ± 0.497	16.513 ± 12.911	Ind	Ind	Ind	Ind
Helminthorhaphe	UCMP 38609	3.388 ± 1.51	1.924 ± 0.889	Ind	Ind	Ind	Ind
Helminthorhaphe	UCMP 398578	Ind	Ind	Ind	Ind	Ind	Ind
Helminthopsis	UJTF 331	1.605 ± 0.423	3.777 ± 1.875	5.217 ± 0.671	Ind	Ind	Ind
Helminthopsis	UJTF 1321	2.137 ± 0.452	6.31 ± 4.540	3.243 ± 1.622	2.493 ± 0.715	Ind	Ind
Belorhaphe	BAN-Jich-0017	Ind	Ind	Ind	Ind	Ind	Ind
Helminthopsis	Mikuláš et al 2004 Plate III-3	1.141 ± 0.041	1.236 ± 0.044	1.696 ± 0.137	1.928 ± 0.114	2.123 ± 0.357	1.788 ± 0.158

Table H.1 continued.

Ichnogenera	Sample ID	τ for 5 cm	τ for 10 cm	τ for 15 cm	τ for 20 cm	τ for 25 cm	τ for 30 cm
Cosmorhaphe	NBMG 9675	1.827 ± 0.163	2.218 ± 0.527	2.238 ± 0.198	2.077 ± 0.096	Ind	Ind
Cosmorhaphe	TF.F142	1.490 ± 0.099	1.796 ± 0.182	1.712 ± 0.233	1.908 ± 0.362	Ind	Ind
Cosmorhaphe	TF9208-1-30	1.362 ± 0.125	2.291 ± 0.883	1.615 ± 0.127	1.726 ± 0.132	1.873 ± 0.028	Ind
Helminthopsis	NBMG 9680	1.345 ± 0.272	1.703 ± 0.617	Ind	Ind	Ind	Ind
Helminthorhaphe	TF.F111	4.037 ± 0.931	Ind	Ind	Ind	Ind	Ind
Helminthopsis	Crimes and Crossley 1991 Fig 4c	1.080 ± 0.028	1.236 ± 0.096	1.512 ± 0.222	1.672 ± 0.247	1.611 ± 0.250	Ind
Helminthopsis	Crimes and Crossley 1991 Fig 4d	1.129 ± 0.046	1.416 ± 0.095	1.257 ± 0.11	1.468 ± 0.028	1.439 ± 0.093	1.515 ± 0.079
Helminthopsis	Crimes and Crossley 1991 Fig 4e	1.007 ± 0.001	1.021 ± 0.004	1.039 ± 0.008	1.054 ± 0.012	1.064 ± 0.016	1.061 ± 0.027
Helminthorhaphe	Acenolaza 1978 Lam IV-6	1.386 ± 0.049	Ind	Ind	Ind	Ind	Ind
Helminthopsis	Pickerill 1981 Fig 2b	1.076 ± 0.012	1.259 ± 0.102	1.557 ± 0.206	Ind	Ind	Ind
Helminthopsis	GSC 78129	Ind	Ind	Ind	Ind	Ind	Ind
Helminthopsis	GSC 78146	1.241 ± 0.028	1.277 ± 0.019	Ind	Ind	Ind	Ind
Helminthopsis	Pickerill 1980 Fig 5d	1.157 ± 0.054	1.401 ± 0.131	Ind	Ind	Ind	Ind
Helminthorhaphe	Pickerill 1980 Fig 4d	1.220 ± 0.038	1.537 ± 0.358	1.688 ± 0.042	2.160 ± 0.223	Ind	Ind
Helminthopsis	Crimes et al 1992 Fig 5A	1.305 ± 0.073	1.644 ± 0.174	1.795 ± 0.215	1.877 ± 0.185	Ind	Ind
Helminthopsis	Crimes and Anderson 1985 Fig 7.6	1.146 ± 0.046	1.491 ± 0.123	1.325 ± 0.026	2.654 ± 0.465	2.061 ± 0.280	2.556 ± 0.351
Helminthorhaphe	Crimes and Anderson 1985 Fig 7.3	1.327 ± 0.086	2.361 ± 0.405	6.325 ± 1.558	3.455 ± 0.617	5.026 ± 1.501	5.651 ± 3.179
Helminthorhaphe	Crimes and Anderson 1985 Fig 7.5	1.153 ± 0.062	1.597 ± 0.260	2.178 ± 0.617	3.813 ± 0.827	3.573 ± 0.515	Ind
Helminthorhaphe	GSC 73327	2.104 ± 0.368	1.936 ± 0.247	3.127 ± 0.639	6.292 ± 1.859	5.856 ± 1.676	4.155 ± 0.777
Helminthorhaphe	GSC 73330	1.312 ± 0.166	3.316 ± 1.664	10.116 ± 7.138	6.518 ± 1.797	Ind	Ind
Helminthopsis	Acenolaza 1978 Fig 11	1.130 ± 0.036	1.223 ± 0.069	1.671 ± 0.572	1.170 ± 0.04	2.077 ± 0.134	Ind
Helminthorhaphe	Acenolaza and Torelli 1981 pg 55-1	1.138 ± 0.068	1.581 ± 0.375	1.141 ± 0.071	2.183 ± 0.635	3.484 ± 1.333	Ind
Helminthorhaphe	Acenolaza and Torelli 1981 pg 55-2	1.702 ± 0.38	2.589 ± 1.109	3.884 ± 0.83	Ind	Ind	Ind

Table H.1 continued.

Ichnogenera	Sample ID	a (cm)	λ (cm)
Cosmorhaphe	INMD 98BX	0.167	0.668
Helminthorhaphe	VBHelmin1	2.125	1.017
Cosmorhaphe	Uchman and Demircan 1999 Fig 5A	0.224	0.745
Cosmorhaphe	Uchman and Demircan 1999 Fig 5C	0.218	1.878
Helminthorhaphe	Uchman and Demircan 1999 Fig 7F	Ind	0.586
Helminthorhaphe	Uchman and Demircan 1999 Fig 7G	Ind	0.646
Helminthorhaphe	CS 12	Ind	0.586
Helminthopsis	PIW1993X 103	0.039	0.777
Helminthopsis	PIW1993X 104	0.154	1.506
Helminthorhaphe	PIW1993X 93	1.583	0.539
Helminthorhaphe	PIW1993X 96	1.574	0.581
Helminthopsis	UJTF 1320	0.408	2.239
Helminthopsis	UJTF 1587	0.893	4.638
Helminthorhaphe	UJTF 39	0.962	1.072
Helminthorhaphe	UJTF 1361	Ind	0.831
Helminthorhaphe	UJTF 1362	1.337	2.868
Helminthopsis	IGP t.f. 102	0.375	1.940
Helminthopsis	IGP t.f. 306c	0.515	2.593
Helminthopsis	UJTF 100	0.549	1.801
Helminthorhaphe	UJTF 42a	1.610	1.853
Helminthorhaphe	UJTF 104	4.759	1.463
Helminthorhaphe	UJTF 426	0.793	0.718
Oscillorhaphe	UJTF 144	Ind	0.684
Spirocosmorhaphe	UJTF 149P3	0.168	0.470
Cosmorhaphe	UUIC 1607	0.045	0.365
Belorhaphe	UJTF 1442	0.276	1.019
Cosmorhaphe	UJTF 243	0.347	1.893

MI	D_{Box}	OSP	BAS
0.2507	1.407 ± 0.005	7.3%	0.546
2.0899	1.736 ± 0.006	24.1%	0.930
0.3001	1.6 ± 0.023	12.6%	0.845
0.1161	1.605 ± 0.029	5.4%	0.762
Ind	1.56 ± 0.009	13.1%	0.638
Ind	1.528 ± 0.012	9.5%	0.872
Ind	1.604 ± 0.009	14.7%	0.755
0.0505	1.539 ± 0.04	5.9%	0.676
0.1021	1.465 ± 0.043	2.2%	0.797
2.9381	1.673 ± 0.008	17.8%	0.940
2.7074	1.657 ± 0.007	18.3%	0.952
0.1822	1.289 ± 0.029	2.7%	0.516
0.1925	1.498 ± 0.036	3.3%	0.735
0.8975	1.532 ± 0.011	8.9%	0.852
Ind	1.61 ± 0.013	12.6%	0.937
0.4661	1.527 ± 0.006	6.7%	0.739
0.1933	1.485 ± 0.038	4.5%	0.720
0.1986	1.554 ± 0.036	4.1%	0.929
0.3050	1.521 ± 0.019	7.6%	0.877
0.8691	1.643 ± 0.009	9.5%	0.966
3.2533	1.559 ± 0.007	11.3%	0.763
1.1042	1.526 ± 0.012	8.0%	0.882
Ind	1.563 ± 0.022	9.9%	0.919
0.3579	1.596 ± 0.005	13.7%	0.887
0.1225	1.655 ± 0.022	16.1%	0.764
0.2712	1.607 ± 0.029	7.3%	0.771
0.1831	1.435 ± 0.025	5.1%	0.867

Table H.1 continued.

Ichnogenera	Sample ID	a (cm)	λ (cm)
Paleomeandron	UJTF 229	0.841	2.498
Belocosmorhaphe	UJTF 121	0.099	0.543
Belocosmorhaphe	UJTF 334a	0.082	0.367
Helminthorhaphe	UJTF 750	2.067	1.565
Belocosmorhaphe	UJTF 716	0.363	1.205
Belocosmorhaphe	UJTF 1360	0.804	2.720
Belorhaphe	UJTF 1443	0.211	0.799
Cosmorhaphe	UJTF 1	0.465	2.795
Cosmorhaphe	UJTF 5	0.368	2.295
Cosmorhaphe	UJTF 8	0.508	2.795
Cosmorhaphe	UJTF 9	0.215	1.030
Cosmorhaphe	UJTF 11	0.688	2.526
Cosmorhaphe	UJTF 12	0.324	1.389
Cosmorhaphe	UJTF 13	0.381	2.312
Cosmorhaphe	UJTF 18	0.269	2.155
Cosmorhaphe	UJTF 77	0.725	1.272
Cosmorhaphe	UJTF 242	0.451	2.261
Helminthopsis	UJTF 252	0.415	2.150
Helminthopsis	UJTF 1082	0.387	2.491
Helminthopsis	UJTF 1661	0.231	2.050
Helminthorhaphe	UJTF 102	2.342	0.995
Helminthorhaphe	UJTF 708	3.220	2.714
Helminthorhaphe	UJTF 1100	2.756	3.923
Helminthorhaphe	UJTF unk	0.109	0.800
Paleomeandron	UJTF 231	0.471	1.831
Cosmorhaphe	UJTF 10	0.307	1.831
Helminthorhaphe	UJTF 44	Ind	0.916
Helminthorhaphe	UJTF 45	1.836	1.890
Helminthorhaphe	UJTF 788	0.699	1.055
Paleomeandron	UJTF 138	0.085	0.437
Helmithorhaphe	UJTF unk	3.063	0.943

MI	D_{Box}	OSP	BAS
0.3367	1.652 ± 0.025	10.5%	0.826
0.1823	1.507 ± 0.006	12.8%	0.637
0.2225	1.513 ± 0.023	14.3%	0.281
1.3207	1.615 ± 0.003	11.0%	0.925
0.3014	1.616 ± 0.025	9.4%	0.814
0.2954	1.631 ± 0.015	11.5%	0.887
0.2634	1.536 ± 0.03	6.6%	0.396
0.1665	1.471 ± 0.036	4.2%	0.985
0.1605	1.451 ± 0.033	4.7%	0.626
0.1819	1.515 ± 0.032	4.7%	0.867
0.2085	1.724 ± 0.018	11.0%	0.873
0.2723	1.559 ± 0.025	6.8%	0.970
0.2331	1.622 ± 0.028	6.9%	0.941
0.1649	1.55 ± 0.036	3.5%	0.790
0.1248	1.497 ± 0.035	4.2%	0.923
0.5697	1.599 ± 0.002	15.7%	0.662
0.1993	1.463 ± 0.033	5.0%	0.869
0.1929	1.552 ± 0.032	4.5%	0.940
0.1554	1.677 ± 0.024	9.8%	0.916
0.1128	1.337 ± 0.03	2.6%	0.607
2.3537	1.442 ± 0.015	6.8%	0.767
1.1861	1.386 ± 0.018	5.8%	0.568
0.7024	1.433 ± 0.013	4.8%	0.839
0.1368	1.491 ± 0.023	8.5%	0.540
0.2570	1.734 ± 0.017	16.9%	0.748
0.1678	1.688 ± 0.023	4.3%	0.948
ind	1.547 ± 0.005	12.0%	0.590
0.9717	1.633 ± 0.024	7.4%	0.986
0.6623	1.609 ± 0.018	10.0%	0.971
0.1947	1.49 ± 0.01	11.3%	0.453
3.2471	1.544 ± 0.002	12.4%	0.694

Table H.1 continued.

Ichnogenera	Sample ID	a (cm)	λ (cm)
Helmithorhaphe	UUIC 429	1.273	1.242
Cosmorhaphe	Z_Cos1	0.348	1.360
Cosmorhaphe	Z_Cos2	0.373	1.423
Cosmorhaphe	Z_Cos3	0.392	1.580
Cosmorhaphe	Z_Cos4	0.467	1.716
Cosmorhaphe	Z_Cos5	0.336	1.629
Helminthorhaphe	Z_Helmin1	3.133	0.425
Helminthorhaphe	Z_Helmin2	2.502	0.589
Helminthorhaphe	Z_Helmin3	Ind	1.709
Helminthorhaphe	Z_Helmin4	Ind	0.521
Helminthorhaphe	Z_Helmin5	2.946	0.926
Paleomeandron	Z_Paleomendron1	0.406	2.632
Helminthorhaphe	UJTF 1403	0.972	2.091
Cosmorhaphe	154P40	0.176	0.460
Cosmorhaphe	UUIC 1723	0.624	2.777
Helminthorhaphe	UJTF 46	Ind	1.548
Cosmorhaphe	UJTF 19	0.881	2.399
Cosmorhaphe	UJTF 74	0.790	1.542
Cosmorhaphe	UJTF 1451	0.542	2.925
Cosmorhaphe	UJTF 2684	1.144	1.637
Cosmorhaphe	UJTF unk	0.759	0.813
Helminthorhape	UJTF 34	Ind	0.709
Cosmorhaphe	UJTF 17	0.427	2.243
Cosmorhaphe	UJTF 75	0.376	0.670
Cosmorhaphe	UJTF 250	1.641	2.512
Cosmorhaphe	UJTF 1872	1.529	2.260
Helminthopsis	UJTF 225	3.071	3.044
Helminthopsis	UJTF 333	1.117	2.924
Helminthorhaphe	UJTF 40	5.073	2.847
Helminthorhaphe	UJTF 49	Ind	0.472
Helminthorhaphe	UJTF 99	1.533	0.460

MI	D_{Box}	OSP	BAS
1.0249	1.672 ± 0.012	12.2%	0.968
0.2555	1.405 ± 0.003	8.3%	0.334
0.2623	1.482 ± 0.026	5.7%	0.864
0.2479	1.373 ± 0.011	5.1%	0.514
0.2725	1.456 ± 0.028	5.5%	0.802
0.2064	1.382 ± 0.009	9.2%	0.355
7.3651	1.497 ± 0.002	14.1%	0.269
4.2489	1.498 ± 0.005	10.3%	0.782
Ind	1.528 ± 0.022	5.9%	0.966
Ind	1.468 ± 0.018	9.6%	0.813
3.1811	1.566 ± 0.005	15.8%	0.731
0.1542	1.671 ± 0.029	8.8%	0.814
0.4650	1.461 ± 0.029	3.5%	0.919
0.3829	1.645 ± 0.003	20.4%	0.674
0.2246	1.645 ± 0.027	2.8%	0.971
Ind	1.666 ± 0.017	15.1%	0.820
0.3674	1.425 ± 0.019	5.3%	0.751
0.5122	1.704 ± 0.007	16.4%	0.937
0.1853	1.455 ± 0.035	3.6%	0.908
0.6989	1.667 ± 0.001	20.4%	0.741
0.9343	1.644 ± 0.012	16.1%	0.877
Ind	1.645 ± 0.017	10.2%	0.961
0.1904	1.507 ± 0.033	4.5%	0.782
0.5614	1.563 ± 0.015	10.9%	0.967
0.6530	1.66 ± 0.009	15.6%	0.918
0.6763	1.573 ± 0.004	13.9%	0.723
1.0089	1.504 ± 0.032	5.8%	0.867
0.3821	1.395 ± 0.023	2.3%	0.902
1.7818	1.515 ± 0.017	8.7%	0.922
Ind	1.462 ± 0.001	11.2%	0.465
3.3314	1.452 ± 0.002	16.6%	0.105

Table H.1 continued.

Ichnogenera	Sample ID	a (cm)	λ (cm)
Helminthorhaphe	UJTF 1014	Ind	3.168
Cosmorhaphe	McCann and Pickerill 1988 Fig 3-5	1.342	2.331
Helminthorhaphe	McCann and Pickerill 1988 Fig 3-12	2.115	0.310
Spirocosmorhaphe	GSC 81257	0.089	0.352
Cosmorhaphe	UJTF unk	0.143	0.338
Helminthorhaphe	UJTF 103	2.817	2.808
Cosmorhaphe	UJTF 1162	0.205	0.614
Belorhaphe	UUIC 1949	0.053	0.265
Helminthorhaphe	UUIC 1911	3.488	2.453
Helminthorhaphe	UUIC 1912	1.064	0.753
Helminthorhaphe	UUIC 1913	0.991	1.156
Helminthopsis	Yeh 1987 Fig 2C	0.682	1.050
Helminthorhaphe	Yeh 1987 Fig 2A	0.107	0.571
Helminthorhaphe	Yeh 1987 Fig 2B	2.072	1.138
Cosmorhaphe	PIW1998IV 140	0.488	2.583
Belorhaphe	UJTF 119	0.202	0.839
Helminthopsis	UJTF 1465	0.908	4.790
Belorhaphe	UCMP 398563	0.063	0.227
Cosmorhaphe	UCMP 38606	0.696	0.628
Cosmorhaphe	UCMP 398570	0.359	0.835
Helminthopsis	UCMP 398575	0.302	2.653
Helminthorhaphe	UCMP 38608	2.327	1.313
Helminthorhaphe	UCMP 38609	Ind	0.946
Helminthorhaphe	UCMP 398578	Ind	0.669
Helminthopsis	UJTF 331	0.656	1.546
Helminthopsis	UJTF 1321	0.501	1.766
Belorhaphe	BAN-Jich-0017	0.139	0.624
Helminthopsis	Mikuláš et al 2004 Plate III-3	1.467	8.274

MI	D_{Box}	OSP	BAS
Ind	1.484 ± 0.023	4.5%	0.942
0.5758	1.709 ± 0.008	16.8%	0.953
6.8243	1.74 ± 0.004	38.9%	0.580
0.2536	1.557 ± 0.01	12.3%	0.647
0.4231	1.436 ± 0.009	8.6%	0.462
1.0032	1.68 ± 0.001	13.1%	0.911
0.3333	1.607 ± 0.021	8.6%	0.947
0.199	1.721 ± 0.024	15.4%	0.754
1.422	1.59 ± 0.019	9.3%	0.982
1.413	1.57 ± 0.002	12.4%	0.662
0.857	1.621 ± 0.01	10.6%	0.928
0.6501	1.706 ± 0.022	7.3%	0.970
0.1875	1.649 ± 0.019	14.0%	0.961
1.8203	1.605 ± 0.009	12.0%	0.909
0.1889	1.636 ± 0.019	8.5%	0.920
0.2407	1.19 ± 0.018	5.8%	0.081
0.1896	1.36 ± 0.021	2.4%	0.953
0.2759	1.571 ± 0.031	8.5%	0.626
1.1096	1.593 ± 0.009	10.8%	0.939
0.4303	1.414 ± 0.016	4.4%	0.880
0.1138	1.433 ± 0.023	2.0%	0.898
1.7728	1.582 ± 0.014	9.3%	0.920
Ind	1.435 ± 0.014	9.1%	0.358
Ind	1.53 ± 0.032	3.1%	0.951
0.4243	1.603 ± 0.025	7.6%	0.945
0.2836	1.618 ± 0.023	9.8%	0.619
0.2227	1.535 ± 0.032	6.7%	0.701
0.1774	1.564 ± 0.033	3.8%	0.962

Table H.1 continued.

Ichnogenera	Sample ID	a (cm)	λ (cm)	MI	D_{Box}	OSP	BAS
Cosmorhaphe	NBMG 9675	0.654	2.511	0.2603	1.513 ± 0.026	4.5%	0.836
Cosmorhaphe	TF.F142	0.361	2.032	0.1774	1.443 ± 0.017	6.3%	0.871
Cosmorhaphe	TF9208-1-30	0.494	3.377	0.1464	1.418 ± 0.022	4.1%	0.907
Helminthopsis	NBMG 9680	0.121	2.009	0.0603	1.499 ± 0.036	4.8%	0.770
Helminthorhaphe	TF.F111	1.032	1.464	0.7051	1.603 ± 0.029	5.6%	0.951
Helminthopsis	Crimes and Crossley 1991 Fig 4c	1.543	10.209	0.1511	1.366 ± 0.038	2.4%	0.734
Helminthopsis	Crimes and Crossley 1991 Fig 4d	3.297	11.212	0.2941	1.515 ± 0.046	2.1%	0.926
Helminthopsis	Crimes and Crossley 1991 Fig 4e	0.773	16.602	0.0465	1.284 ± 0.017	1.6%	0.712
Helminthorhaphe	Acenolaza 1978 Lam IV-6	0.171	1.132	0.1507	1.615 ± 0.032	10.3%	0.766
Helminthopsis	Pickerill 1981 Fig 2b	0.279	3.103	0.0900	1.58 ± 0.028	6.5%	0.934
Helminthopsis	GSC 78129	0.577	2.038	0.2832	1.603 ± 0.031	1.2%	0.978
Helminthopsis	GSC 78146	0.452	2.790	0.1620	1.523 ± 0.038	3.0%	0.837
Helminthopsis	Pickerill 1980 Fig 5d	1.190	6.673	0.1784	1.512 ± 0.042	1.2%	0.953
Helminthorhaphe	Pickerill 1980 Fig 4d	0.335	2.397	0.1396	1.748 ± 0.016	14.6%	0.905
Helminthopsis	Crimes et al 1992 Fig 5A	0.624	3.417	0.1827	1.474 ± 0.034	4.9%	0.886
Helminthopsis	Crimes and Anderson 1985 Fig 7.6	1.463	8.207	0.1783	1.615 ± 0.036	2.8%	0.981
Helminthorhaphe	Crimes and Anderson 1985 Fig 7.3	4.838	3.795	1.2749	1.628 ± 0.009	13.2%	0.951
Helminthorhaphe	Crimes and Anderson 1985 Fig 7.5	3.921	5.875	0.6674	1.496 ± 0.027	4.9%	0.942
Helminthorhaphe	GSC 73327	2.491	2.627	0.9481	1.641 ± 0.008	12.1%	0.977
Helminthorhaphe	GSC 73330	3.243	2.109	1.5374	1.655 ± 0.021	12.2%	0.953
Helminthopsis	Acenolaza 1978 Fig 11	0.338	4.688	0.0722	1.479 ± 0.025	2.9%	0.921
Helminthorhaphe	Acenolaza and Torelli 1981 pg 55-1	4.282	3.429	1.2488	1.601 ± 0.023	9.0%	0.946
Helminthorhaphe	Acenolaza and Torelli 1981 pg 55-2	2.337	2.745	0.8514	1.56 ± 0.019	7.5%	0.848

Table H.2. Results of analyses on spiraling trace fossils. Complete sample locality and date information can be found in Appendix E. The table contains the estimated latitude and longitude of the sample localities. The age is the median age of the formation in which the sample was found. The age error encompasses the length of time the formation has been estimated to have been deposited. Abbreviations: BAS = burrow area shape; $BAS_{Trimmed}$ = BAS of a trimmed drown trace; D_{Box} = fractal dimension using the Box Counting Method; Ind = indeterminate analyses; NA = not applicable analyses; OSP = occupied space percentage; SS = spiral spacing; τ = tortuosity; W = burrow width. The τ and D_{Box} variance is represented by the standard error.

Ichnogenera	Sample ID	Latitude	Longitude
Spirohaphe	INMD 94BX	16° 43' N	51° 35' W
Spirohaphe	INMD 123BX	29° 31' N	33° 14' W
Spirorhaphe	UJTF 211	53° 5' 45" N	23° 41' 48" E
Spirorhaphe	UJTF 552	53° 5' 45" N	23° 41' 48" E
Spirorhaphe	UJTF 1519	53° 5' 45" N	23° 41' 48" E
Spirorhape	Z_Spiror1	43° 18.540' N	2° 13.882' W
Spirorhape	Z_Spiror2	43° 18.540' N	2° 13.882' W
Spirorhape	Z_Spiror3	43° 18.540' N	2° 13.882' W
Spirorhape	Z_Spiror4	43° 18.540' N	2° 13.882' W
Spirorhape	Z_Spiror5	43° 18.540' N	2° 13.882' W
Spirorhaphe	154P39	48° 20' 57" N	16° 15' 25" E
Spirohaphe	Munoz and Buatois, 2001 Fig. 2	10° 8' 20" N	65° 28' 00" W
Spirohaphe	UUIC 1721	10° 8' 20" N	65° 28' 00" W
Spirohaphe	UUIC 1722	10° 8' 20" N	65° 28' 00" W
Spirorhaphe	UJTF 603a	49° 30' 50" N	19° 38' 00" E
Spirorhaphe	McCann and Pickerill 1988 Fig 5-7-1	57° 46' 30" N	152° 24' 40" W
Spirorhaphe	McCann and Pickerill 1988 Fig 5-7-2	57° 46' 30" N	152° 24' 40" W
Spirorhaphe	UUIC 1902	8° 48' 13" S	39° 20' 16" E
Spirorhaphe	UUIC 1903	8° 46' 51" S	39° 20' 11" E
Spirorhaphe	UUIC 1904	8° 46' 24" S	39° 19' 25" E
Spirorhaphe	UUIC 1905	8° 46' 51" S	39° 20' 11" E
Spirorhaphe	UUIC 1906	8° 47' 42" E	39° 20' 39" E
Spirorhaphe	UUIC 1907	8° 46' 51" S	39° 20' 11" E
Spirorhaphe	UUIC 1908	8° 47' 13" S	39° 21' 00" E
Spirorhaphe	UUIC 1909	8° 46' 51" S	39° 20' 11" E
Spirorhaphe	UUIC 1910	8° 46' 24" S	39° 19' 25" E
Spirorhaphe	Pickerill 1980 Fig 2b	47° 53' N	66° 50' W

Period/Epoch	Age (Ma)	W (mm)
Modern	0.0 ± 0.00	0.5
Modern	0.0 ± 0.00	0.5
Eocene	46.5 ± 9.30	0.9
Eocene	46.5 ± 9.30	0.9
Eocene	46.5 ± 9.30	1.0
Eocene	52.2 ± 3.60	1.3
Eocene	52.2 ± 3.60	1.5
Eocene	52.2 ± 3.60	1.3
Eocene	52.2 ± 3.60	1.4
Eocene	52.2 ± 3.60	1.8
Paleocene	53.7 ± 5.05	1.4
Paleocene	60.7 ± 4.85	0.4
Paleocene	60.7 ± 4.85	2.4
Paleocene	60.7 ± 4.85	1.7
Late Cretaceous	63.2 ± 7.40	2.1
Late Cretaceous	82.6 ± 17.05	0.5
Late Cretaceous	82.6 ± 17.05	0.7
Late Cretaceous	78.0 ± 1.50	0.5
Late Cretaceous	77.8 ± 5.70	0.5
Late Cretaceous	81.5 ± 2.00	0.5
Late Cretaceous	77.8 ± 5.70	2.0
Late Cretaceous	78.0 ± 1.50	2.2
Late Cretaceous	77.8 ± 5.70	2.3
Late Cretaceous	78.0 ± 1.50	2.3
Late Cretaceous	77.8 ± 5.70	1.9
Late Cretaceous	81.5 ± 2.00	1.5
Ordovician	474.6 ± 13.70	1.4

Table H.2 continued.

Ichnogenera	Sample ID	τ for 5 cm	τ for 10 cm	τ for 15 cm	τ for 20 cm	τ for 25 cm	τ for 30 cm
Spirohaphe	INMD 94BX	1.640 ± 0.311	Ind	Ind	Ind	Ind	Ind
Spirohaphe	INMD 123BX	1.316 ± 0.125	Ind	Ind	Ind	Ind	Ind
Spirorhaphe	UJTF 211	2.266 ± 0.639	4.131 ± 0.928	8.566 ± 0.776	7.537 ± 0.717	8.057 ± 2.747	26.423 ± 5.773
Spirorhaphe	UJTF 552	1.658 ± 0.245	3.727 ± 1.367	Ind	Ind	Ind	Ind
Spirorhaphe	UJTF 1519	1.909 ± 0.512	2.453 ± 0.361	Ind	Ind	Ind	Ind
Spirorhape	Z_Spiror1	1.052 ± 0.008	1.157 ± 0.085	Ind	Ind	Ind	Ind
Spirorhape	Z_Spiror2	1.071 ± 0.017	1.194 ± 0.032	1.568 ± 0.166	3.368 ± 0.982	5.492 ± 1.595	9.223 ± 3.558
Spirorhape	Z_Spiror3	1.100 ± 0.024	1.167 ± 0.064	1.200 ± 0.047	Ind	Ind	Ind
Spirorhape	Z_Spiror4	1.298 ± 0.103	1.981 ± 0.638	1.186 ± 0.026	Ind	Ind	Ind
Spirorhape	Z_Spiror5	1.045 ± 0.007	1.983 ± 0.113	1.326 ± 0.107	Ind	Ind	Ind
Spirorhaphe	154P39	1.082 ± 0.022	Ind	Ind	Ind	Ind	Ind
Spirohaphe	Muñoz and Buatois, 2001 Fig. 2	Ind	Ind	Ind	Ind	Ind	Ind
Spirohaphe	UUIC 1721	1.057 ± 0.009	1.076 ± 0.005	Ind	Ind	Ind	Ind
Spirohaphe	UUIC 1722	1.073 ± 0.009	Ind	Ind	Ind	Ind	Ind
Spirorhaphe	UJTF 603a	1.031 ± 0.007	1.059 ± 0.011	1.173 ± 0.092	1.093 ± 0.001	Ind	Ind
Spirorhaphe	McCann and Pickerill 1988 Fig 5-7-1	3.522 ± 0.686	7.923 ± 1.056	10.366 ± 3.831	Ind	Ind	Ind
Spirorhaphe	McCann and Pickerill 1988 Fig 5-7-2	1.820 ± 0.253	5.787 ± 2.627	15.131 ± 5.737	5.684 ± 0.906	Ind	Ind
Spirorhaphe	UUIC 1902	2.58 ± 0.483	7.670 ± 1.867	6.436 ± 1.059	11.806 ± 2.213	25.117 ± 11.406	11.899 ± 1.557
Spirorhaphe	UUIC 1903	2.559 ± 0.889	Ind	Ind	Ind	Ind	Ind
Spirorhaphe	UUIC 1904	1.199 ± 0.025	3.264 ± 1.648	Ind	Ind	Ind	Ind
Spirorhaphe	UUIC 1905	1.069 ± 0.023	1.257 ± 0.099	2.406 ± 0.651	2.747 ± 0.673	3.666 ± 0.760	Ind
Spirorhaphe	UUIC 1906	1.065 ± 0.015	1.064 ± 0.012	Ind	Ind	Ind	Ind
Spirorhaphe	UUIC 1907	1.107 ± 0.053	1.174 ± 0.049	1.146 ± 0.015	Ind	Ind	Ind
Spirorhaphe	UUIC 1908	1.317 ± 0.113	2.654 ± 0.886	4.035 ± 0.675	Ind	Ind	Ind
Spirorhaphe	UUIC 1909	1.279 ± 0.220	Ind	Ind	Ind	Ind	Ind
Spirorhaphe	UUIC 1910	1.683 ± 0.239	5.144 ± 3.402	Ind	Ind	Ind	Ind
Spirorhaphe	Pickerill 1980 Fig 2b	2.713 ± 0.908	10.631 ± 5.513	5.308 ± 0.451	12.375 ± 6.058	Ind	Ind

Table H.2 continued.

Ichnogenera	Sample ID	SS	D_{Box}	OSP	BAS	$BAS_{Trimmed}$
Spirohaphe	INMD 94BX	3.517	1.54 ± 0.009	15.3%	0.492	NA
Spirohaphe	INMD 123BX	4.581	1.554 ± 0.008	15.8%	0.722	NA
Spirorhaphe	UJTF 211	2.959	1.607 ± 0.001	29.0%	0.297	0.939
Spirorhaphe	UJTF 552	2.912	1.678 ± 0.004	26.0%	0.882	NA
Spirorhaphe	UJTF 1519	3.054	1.644 ± 0.004	25.0%	0.769	NA
Spirorhape	Z_Spiror1	3.235	1.573 ± 0.004	19.2%	0.966	NA
Spirorhape	Z_Spiror2	3.880	1.633 ± 0.003	21.8%	0.614	NA
Spirorhape	Z_Spiror3	5.353	1.481 ± 0.008	11.3%	0.764	NA
Spirorhape	Z_Spiror4	3.576	1.627 ± 0.006	21.1%	0.670	NA
Spirorhape	Z_Spiror5	3.581	1.604 ± 0.005	19.8%	0.420	NA
Spirorhaphe	154P39	2.992	1.505 ± 0.025	13.1%	0.339	NA
Spirohaphe	Muñoz and Buatois, 2001 Fig. 2	2.078	1.701 ± 0.003	31.2%	0.600	NA
Spirohaphe	UUIC 1721	4.011	1.605 ± 0.009	17.8%	0.824	NA
Spirohaphe	UUIC 1722	4.417	1.56 ± 0.024	12.2%	0.870	NA
Spirorhaphe	UJTF 603a	3.619	1.501 ± 0.003	17.3%	0.233	NA
Spirorhaphe	McCann and Pickerill 1988 Fig 5-7-1	3.112	1.683 ± 0.003	27.8%	0.938	NA
Spirorhaphe	McCann and Pickerill 1988 Fig 5-7-2	2.752	1.702 ± 0.002	30.3%	0.927	NA
Spirorhaphe	UUIC 1902	4.428	1.575 ± 0.007	17.1%	0.820	NA
Spirorhaphe	UUIC 1903	3.791	1.539 ± 0.008	17.9%	0.171	NA
Spirorhaphe	UUIC 1904	3.891	1.611 ± 0.004	22.2%	0.397	NA
Spirorhaphe	UUIC 1905	5.767	1.646 ± 0.013	21.1%	0.648	NA
Spirorhaphe	UUIC 1906	2.807	1.638 ± 0.006	22.8%	0.464	NA
Spirorhaphe	UUIC 1907	3.225	1.642 ± 0.01	21.4%	0.868	NA
Spirorhaphe	UUIC 1908	2.583	1.705 ± 0.006	27.9%	0.913	NA
Spirorhaphe	UUIC 1909	3.488	1.591 ± 0.019	15.4%	0.486	NA
Spirorhaphe	UUIC 1910	2.557	1.677 ± 0.011	23.5%	0.881	NA
Spirorhaphe	Pickerill 1980 Fig 2b	2.184	1.719 ± 0.01	26.8%	0.986	NA

Table H.3. Results of analyses on branching trace fossils. Complete sample locality and date information can be found in Appendix E. The table contains the estimated latitude and longitude of the sample localities. The age is the median age of the formation in which the sample was found. The age error encompasses the length of time the formation has been estimated to have been deposited. Abbreviations: a = amplitude; BA = branching angle; BAS = burrow area shape; BAV = branching angle variance; D_{Box} = fractal dimension using the Box Counting Method; Ind = indeterminate analyses; λ = wavelength; MI = motility index; OSP = occupied space percentage; τ = tortuosity; W = burrow width. The BA, τ, and D_{Box} variance is represented by the standard error.

Ichnogenera	Sample ID	Latitude	Longitude
Urohelminthoida	VBUrohelm1	37° 8' 46" N	1° 56' 11" W
Urohelminthoida	VBUrohelm2	37° 8' 46" N	1° 56' 11" W
Urohelminthoida	VBUrohelm2b	37° 8' 46" N	1° 56' 11" W
Urohelminthoida	VBUrohelm3	37° 8' 46" N	1° 56' 11" W
Urohelminthoida	Uchman and Demircan 1999 Fig 5B	37° 18' 58" N	35° 13' 22" E
Protopaleodictyon	FG 13	40° 31' 26" N	16° 2' 57" E
Urohelminthoida	CM 29-1	40° 31' 26" N	16° 2' 57" E
Urohelminthoida	CM 29-2	40° 31' 26" N	16° 2' 57" E
Urohelminthoida	UUIC 1549	40° 23' 37" N	16° 9' 29" E
Urohelminthoida	PIW1993X 84	43° 53' 38" N	12° 5' 24" E
Urohelminthoida	Uchman 1995 Plate 14.2	44° 4' N	11° 56' E
Urohelminthoida	PIW199X 81	43° 47' 39" N	12° 0' 17" E
Protopaleodictyon	UJTF 343	49° 24' 37" N	20° 33' 8" E
Protopaleodictyon	UUIC 1597	46° 59' 26" N	9° 38' 18" E
Protopaleodictyon	UJTF 171P4	49° 35' 59" N	20° 8' 3" E
Protopaleodictyon	UJTF 334b	49° 47' 32" N	19° 37' 2" E
Urohelminthoida	UJTF 1599	49° 26' 28" N	20° 25' 39" E
Protopaleodictyon	UJTF 228	49° 30' 50" N	19° 38' 00" E
Protopaleodictyon	UJTF 454	49° 33' 46" N	19° 38' 58" E
Protopaleodictyon	UJTF 2005	49° 59' 14" N	19° 52' 33" E
Urohelminthoida	UJTF 141	49° 40' 50" N	19° 46' 56" E
Urohelminthoida	UJTF 344	49° 28' 27" N	19° 38' 24" E
Urohelminthoida	UJTF 352	49° 59' 14" N	19° 52' 33" E
Urohelminthoida	UJTF 354	49° 41' 6" N	19° 50' 3" E
Urohelminthoida	UJTF 356	49° 33' 46" N	19° 38' 58" E
Urohelminthoida	UJTF 359	49° 33' 46" N	19° 38' 58" E

Period/Epoch	Age (Ma)	W (mm)
Miocene	6.3 ± 0.96	1.3
Miocene	6.3 ± 0.96	2.0
Miocene	6.3 ± 0.96	2.2
Miocene	6.3 ± 0.96	1.2
Miocene	13.8 ± 2.18	2.1
Miocene	10.7 ± 5.32	0.6
Miocene	10.7 ± 5.32	2.0
Miocene	10.7 ± 5.32	1.6
Miocene	10.7 ± 5.32	1.6
Miocene	13.8 ± 2.18	2.0
Miocene	13.8 ± 2.18	2.4
Miocene	9.6 ± 4.25	2.8
Eocene	46.5 ± 9.30	1.2
Eocene	44.9 ± 10.95	2.0
Eocene	46.5 ± 9.30	2.0
Eocene	46.5 ± 9.30	1.4
Eocene	53.7 ± 5.05	1.0
Eocene	46.5 ± 9.30	4.2
Eocene	46.5 ± 9.30	1.5
Eocene	46.5 ± 9.30	4.5
Eocene	46.5 ± 9.30	1.0
Eocene	46.5 ± 9.30	1.1
Eocene	46.5 ± 9.30	1.6
Eocene	46.5 ± 9.30	1.2
Eocene	46.5 ± 9.30	0.9
Eocene	46.5 ± 9.30	1.2

Table H.3 continued.

Ichnogenera	Sample ID	Latitude	Longitude
Urohelminthoida	UJTF 360	49° 33' 46" N	19° 38' 58" E
Urohelminthoida	UJTF 722	49° 36' 36" N	20° 17' 41" E
Urohelminthoida	UJTF 1593	49° 30' 50" N	19° 38' 00" E
Protopaleodictyon	UJTF 130	49° 40' 50" N	19° 46' 56" E
Protopaleodictyon	UJTF 338	49° 38' 57" N	19° 49' 48" E
Protopaleodictyon	UJTF 342	49° 38' 57" N	19° 49' 48" E
Protopaleodictyon	UJTF 763	48° 25' 45" N	22° 42' 21" E
Protopaleodictyon	UJTF 900	49° 40' 50" N	19° 46' 56" E
Protopaleodictyon	UJTF 1121	49° 34' 4" N	20° 49' 26" E
Protopaleodictyon	UJTF 1483	49° 41' 6" N	19° 50' 3" E
Protopaleodictyon	UJTF 1484	49° 40' 50" N	19° 46' 56" E
Urohelminthoida	Z_Urohelm1	43° 18.540' N	2° 13.882' W
Urohelminthoida	Z_Urohelm2	43° 18.540' N	2° 13.882' W
Urohelminthoida	UJTF 348	49° 44' 39" N	20° 41' 14" E
Protopaleodictyon	UJTF 341	51° 00' 46" N	15° 30' 38" E
Protopaleodictyon	UJTF 709	49° 40' 34" N	20° 23' 53" E
Urohelminthoida	UJTF 35	49° 33' 46" N	19° 38' 58" E
Ubinia	UJTF 2726	49° 38' 50" N	18° 52' 4" E
Protopaleodictyon	UJTF 923	49° 39' 16" N	22° 42' 14" E
Protopaleodictyon	UJTF 955	49° 51' 2" N	22° 02' 51" E
Urohelminthoida	UJTF 120	49° 37' 26" N	20° 56' 52" E
Urohelminthoida	UJTF 351	50° 04' 35" N	19° 36' 36" E
Urohelminthoida	UJTF 1591	49° 28' 27" N	19° 38' 24" E
Urohelminthoida	UJTF 1592	49° 28' 27" N	19° 38' 24" E
Urohelminthoida	UJTF 2677	49° 42' 21" N	20° 25' 20" E
Urohelminthoida	UUIC 1914	8° 46' 24" S	39° 19' 25" E
Protopaleodictyon	Ban-Jich-0012	42° 37' 38" N	22° 45' 5" E
Protopaleodictyon	BAN-Jich-0014b	42° 37' 6" N	22° 49' 33" E

Period/Epoch	Age (Ma)	W (mm)
Eocene	46.5 ± 9.30	1.2
Eocene	46.5 ± 9.30	2.4
Eocene	46.5 ± 9.30	1.9
Eocene	42.9 ± 5.70	2.0
Eocene	42.9 ± 5.70	2.0
Eocene	42.9 ± 5.70	1.9
Eocene	42.9 ± 5.70	1.6
Eocene	42.9 ± 5.70	2.1
Eocene	42.9 ± 5.70	0.8
Eocene	42.9 ± 5.70	1.8
Eocene	42.9 ± 5.70	2.2
Eocene	52.2 ± 3.60	0.9
Eocene	52.2 ± 3.60	1.0
Paleocene	63.3 ± 2.20	0.9
Paleocene	53.7 ± 5.05	1.2
Paleocene	53.7 ± 5.05	1.5
Paleocene	53.7 ± 5.05	1.2
Late Cretaceous	86.1 ± 2.55	2.5
Late Cretaceous	63.2 ± 7.40	1.7
Late Cretaceous	63.2 ± 7.40	1.9
Late Cretaceous	63.2 ± 7.40	1.9
Late Cretaceous	63.2 ± 7.40	1.1
Late Cretaceous	63.2 ± 7.40	0.8
Late Cretaceous	63.2 ± 7.40	1.4
Late Cretaceous	63.2 ± 7.40	2.0
Late Cretaceous	81.5 ± 2.00	0.9
Jurassic	150.8 ± 5.25	3.1
Jurassic	142.8 ± 2.75	1.7

Table H.3 continued.

Ichnogenera	Sample ID	Latitude	Longitude
Protopaleodictyon	MP-US J1138	42° 57' 26" N	27° 16' 23" E
Protopaleodictyon	MP-US J1149	43° 1' 53" N	27° 22' 18" E
Protopaleodictyon	IKKM 1-9	37° 47' 7" N	13° 40' 2" E
Protopaleodictyon	IKKM 1-14	37° 47' 7" N	13° 40' 2" E
Protopaleodictyon	UW 1497	34° 53' 42" N	95° 6' 51" W
Protopaleodictyon	Mikuláš et al 2004 Plate V-3	50° 5' 8" N	17° 17' 41" E
Protopaleodictyon	TF9208-1-15	47° 12' 12" N	67° 11' 25" W
Protopaleodictyon	TF9208-1-17	47° 12' 12" N	67° 11' 25" W
Protopaleodictyon	Acenolaza 1978 Lám III-2	23° 22' S	66° 40' W
Protopaleodictyon	Pickerill 1981 Fig 5a	47° 13' 00" N	67° 59' 19" W
Protopaleodictyon	Pickerill 1980 Fig 4b	47° 53' N	66° 50' W

Period/Epoch	Age (Ma)	W (mm)
Jurassic	182.6 ± 7.00	1.0
Jurassic	182.6 ± 7.00	1.2
Permian	274.5 ± 1.50	1.7
Permian	274.5 ± 1.50	2.0
Carboniferous	312.7 ± 5.45	1.7
Carboniferous	338.8 ± 7.90	4.7
Devonian	411.5 ± 4.50	1.3
Devonian	411.5 ± 4.50	2.8
Silurian	420.8 ± 2.10	2.8
Silurian	439.9 ± 3.85	1.0
Ordovician	474.6 ± 13.70	2.1

Table H.3 continued.

Ichnogenera	Sample ID	τ for 5 cm	τ for 10 cm	τ for 15 cm	τ for 20 cm	τ for 25 cm	τ for 30 cm
Urohelminthoida	VBUrohelm1	3.248 ± 0.812	9.869 ± 0.968	5.777 ± 2.588	Ind	Ind	Ind
Urohelminthoida	VBUrohelm2	4.960 ± 1.093	4.119 ± 0.327	6.477 ± 1.184	7.657 ± 0.213	7.358 ± 0.475	Ind
Urohelminthoida	VBUrohelm2b	6.827 ± 1.203	4.529 ± 0.789	8.770 ± 0.433	5.682 ± 0.320	Ind	Ind
Urohelminthoida	VBUrohelm3	3.533 ± 0.821	8.470 ± 1.164	8.033 ± 2.383	Ind	Ind	Ind
Urohelminthoida	Uchman and Demircan 1999 Fig 5B	1.021 ± 0.005	1.043 ± 0.186	Ind	Ind	Ind	Ind
Protopaleodictyon	FG 13	1.370 ± 0.091	Ind	Ind	Ind	Ind	Ind
Urohelminthoida	CM 29-1	1.210 ± 0.085	4.566 ± 2.130	Ind	Ind	Ind	Ind
Urohelminthoida	CM 29-2	1.887 ± 0.315	2.261 ± 0.132	Ind	Ind	Ind	Ind
Urohelminthoida	UUIC 1549	2.198 ± 0.518	2.268 ± 0.604	Ind	Ind	Ind	Ind
Urohelminthoida	PIW1993X 84	1.920 ± 0.496	5.313 ± 2.369	Ind	Ind	Ind	Ind
Urohelminthoida	Uchman 1995 Plate 14.2	2.350 ± 0.236	2.536 ± 0.066	Ind	Ind	Ind	Ind
Urohelminthoida	PIW199X 81	3.768 ± 0.629	4.503 ± 0.707	4.716 ± 0.891	5.351 ± 0.937	Ind	Ind
Protopaleodictyon	UJTF 343	1.626 ± 0.075	1.890 ± 0.150	2.812 ± 0.924	Ind	Ind	Ind
Protopaleodictyon	UUIC 1597	1.221 ± 0.100	1.805 ± 0.429	Ind	Ind	Ind	Ind
Protopaleodictyon	UJTF 171P4	1.782 ± 0.162	1.834 ± 0.242	2.655 ± 1.172	Ind	Ind	Ind
Protopaleodictyon	UJTF 334b	1.564 ± 0.213	1.691 ± 0.324	Ind	Ind	Ind	Ind
Urohelminthoida	UJTF 1599	5.386 ± 0.978	Ind	Ind	Ind	Ind	Ind
Protopaleodictyon	UJTF 228	1.329 ± 0.088	1.374 ± 0.123	1.618 ± 0.292	1.732 ± 0.257	Ind	Ind
Protopaleodictyon	UJTF 454	1.343 ± 0.072	1.379 ± 0.144	Ind	Ind	Ind	Ind
Protopaleodictyon	UJTF 2005	1.119 ± 0.051	1.590 ± 0.332	1.468 ± 0.220	1.466 ± 0.188	Ind	Ind
Urohelminthoida	UJTF 141	1.617 ± 0.223	2.49 ± 0.329	3.044 ± 0.638	Ind	Ind	Ind
Urohelminthoida	UJTF 344	2.696 ± 1.205	Ind	Ind	Ind	Ind	Ind
Urohelminthoida	UJTF 352	1.414 ± 0.174	5.319 ± 0.905	5.341 ± 0.137	Ind	Ind	Ind
Urohelminthoida	UJTF 354	1.631 ± 0.180	6.892 ± 5.342	Ind	Ind	Ind	Ind
Urohelminthoida	UJTF 356	3.695 ± 1.650	Ind	Ind	Ind	Ind	Ind
Urohelminthoida	UJTF 359	1.427 ± 0.347	Ind	Ind	Ind	Ind	Ind

Table H.3 continued.

Ichnogenera	Sample ID	τ for 5 cm	τ for 10 cm	τ for 15 cm	τ for 20 cm	τ for 25 cm	τ for 30 cm
Urohelminthoida	UJTF 360	1.232 ± 0.142	2.623 ± 1.534	Ind	Ind	Ind	Ind
Urohelminthoida	UJTF 722	1.067 ± 0.037	1.122 ± 0.057	1.109 ± 0.055	1.196 ± 0.082	2.069 ± 0.911	1.090 ± 0.006
Urohelminthoida	UJTF 1593	1.106 ± 0.019	7.461 ± 4.057	Ind	Ind	Ind	Ind
Protopaleodictyon	UJTF 130	1.456 ± 0.044	1.541 ± 0.049	1.844 ± 0.208	1.563 ± 0.105	2.168 ± 0.039	2.689 ± 0.132
Protopaleodictyon	UJTF 338	1.444 ± 0.052	1.703 ± 0.140	1.622 ± 0.112	Ind	Ind	Ind
Protopaleodictyon	UJTF 342	1.336 ± 0.058	1.406 ± 0.113	1.669 ± 0.155	Ind	Ind	Ind
Protopaleodictyon	UJTF 763	1.387 ± 0.036	Ind	Ind	Ind	Ind	Ind
Protopaleodictyon	UJTF 900	1.595 ± 0.089	1.893 ± 0.103	2.298 ± 0.351	Ind	Ind	Ind
Protopaleodictyon	UJTF 1121	1.581 ± 0.094	Ind	Ind	Ind	Ind	Ind
Protopaleodictyon	UJTF 1483	1.531 ± 0.201	1.677 ± 0.180	1.674 ± 0.108	2.374 ± 0.207	Ind	Ind
Protopaleodictyon	UJTF 1484	1.849 ± 0.201	1.957 ± 0.227	2.366 ± 0.330	2.734 ± 0.144	Ind	Ind
Urohelminthoida	Z_Urohelm1	2.929 ± 0.650	Ind	Ind	Ind	Ind	Ind
Urohelminthoida	Z_Urohelm2	2.554 ± 0.403	3.627 ± 0.763	4.961 ± 1.206	Ind	Ind	Ind
Urohelminthoida	UJTF 348	2.461 ± 1.286	Ind	Ind	Ind	Ind	Ind
Protopaleodictyon	UJTF 341	1.265 ± 0.123	Ind	Ind	Ind	Ind	Ind
Protopaleodictyon	UJTF 709	1.348 ± 0.068	1.405 ± 0.037	2.22 ± 0.132	Ind	Ind	Ind
Urohelminthoida	UJTF 35	1.456 ± 0.340	5.482 ± 3.358	Ind	Ind	Ind	Ind
Ubinia	UJTF 2726	1.385 ± 0.097	1.404 ± 0.142	Ind	Ind	Ind	Ind
Protopaleodictyon	UJTF 923	1.385 ± 0.114	Ind	Ind	Ind	Ind	Ind
Protopaleodictyon	UJTF 955	1.741 ± 0.171	2.389 ± 0.861	Ind	Ind	Ind	Ind
Urohelminthoida	UJTF 120	1.309 ± 0.217	1.110 ± 0.049	9.694 ± 8.652	Ind	Ind	Ind
Urohelminthoida	UJTF 351	1.058 ± 0.021	Ind	Ind	Ind	Ind	Ind
Urohelminthoida	UJTF 1591	Ind	Ind	Ind	Ind	Ind	Ind
Urohelminthoida	UJTF 1592	1.357 ± 0.241	1.118 ± 0.048	5.542 ± 2.335	26.831 ± 9.819	Ind	Ind
Urohelminthoida	UJTF 2677	1.544 ± 0.315	5.933 ± 3.842	15.809 ± 1.708	Ind	Ind	Ind
Urohelminthoida	UUIC 1914	2.378 ± 0.533	7.935 ± 4.715	Ind	Ind	Ind	Ind
Protopaleodictyon	Ban-Jich-0012	1.280 ± 0.107	1.561 ± 0.009	Ind	Ind	Ind	Ind
Protopaleodictyon	BAN-Jich-0014b	2.149 ± 1.032	Ind	Ind	Ind	Ind	Ind

Table H.3 continued.

Ichnogenera	Sample ID	τ for 5 cm	τ for 10 cm	τ for 15 cm	τ for 20 cm	τ for 25 cm	τ for 30 cm
Protopaleodictyon	MP-US J1138	1.397 ± 0.265	Ind	Ind	Ind	Ind	Ind
Protopaleodictyon	MP-US J1149	1.599 ± 0.425	Ind	Ind	Ind	Ind	Ind
Protopaleodictyon	IKKM I-9	1.062 ± 0.042	Ind	Ind	Ind	Ind	Ind
Protopaleodictyon	IKKM I-14	1.599 ± 0.264	1.733 ± 0.522	Ind	Ind	Ind	Ind
Protopaleodictyon	UW 1497	1.606 ± 0.422	Ind	Ind	Ind	Ind	Ind
Protopaleodictyon	Mikuláš et al 2004 Plate V-3	1.065 ± 0.034	1.122 ± 0.086	1.334 ± 0.017	Ind	Ind	Ind
Protopaleodictyon	TF9208-1-15	Ind	Ind	Ind	Ind	Ind	Ind
Protopaleodictyon	TF9208-1-17	1.195 ± 0.046	1.296 ± 0.138	Ind	Ind	Ind	Ind
Protopaleodictyon	Acenolaza 1978 Lam III-2	1.851 ± 0.287	Ind	Ind	Ind	Ind	Ind
Protopaleodictyon	Pickerill 1981 Fig 5a	1.342 ± 0.094	1.531 ± 0.421	Ind	Ind	Ind	Ind
Protopaleodictyon	Pickerill 1980 Fig 4b	1.224 ± 0.039	2.031 ± 0.118	Ind	Ind	Ind	Ind

Table H.3 continued.

Ichnogenera	Sample ID	a (cm)	λ (cm)	MI	BA	BAV	D_{Box}	OSP	BAS
Urohelminthoida	VBUrohelm1	1.486	0.863	1.7218	94.5 ± 4.77	227.61	1.61 ± 0.006	15.8%	0.936
Urohelminthoida	VBUrohelm2	1.616	1.091	1.4814	80.9 ± 7.7	534.11	1.687 ± 0.008	18.7%	0.895
Urohelminthoida	VBUrohelm2b	1.449	0.857	1.6916	103.7 ± 2.09	26.27	1.752 ± 0.005	26.3%	0.909
Urohelminthoida	VBUrohelm3	1.633	0.800	2.0406	93.3 ± 4.37	191.34	1.63 ± 0.006	16.3%	0.942
Urohelminthoida	Uchman and Demircan 1999 Fig 5B	Ind	1.805	Ind	42 ± 2.27	20.67	1.568 ± 0.023	8.4%	0.956
Protopaleodictyon	FG 13	0.064	0.587	0.1083	77.4 ± 3.51	307.58	1.386 ± 0.007	6.3%	0.678
Urohelminthoida	CM 29-1	Ind	1.018	Ind	42 ± 3.12	77.71	1.593 ± 0.007	15.3%	0.660
Urohelminthoida	CM 29-2	0.486	0.784	0.6208	56.5 ± 2.29	62.82	1.532 ± 0.021	12.1%	0.654
Urohelminthoida	UUIC 1549	3.204	0.973	3.2947	50.4 ± 4.26	127.29	1.512 ± 0.014	11.0%	0.656
Urohelminthoida	PIW1993X 84	1.840	1.009	1.8234	73.2 ± 4	95.77	1.564 ± 0.023	11.2%	0.570
Urohelminthoida	Uchman 1995 Plate 14.2	0.889	1.955	0.4549	63.3 ± 18.02	974.33	1.649 ± 0.023	7.8%	0.946
Urohelminthoida	PIW199X 81	1.490	1.479	1.0069	64.9 ± 5.6	219.48	1.673 ± 0.01	16.7%	0.814
Protopaleodictyon	UJTF 343	0.307	1.121	0.2739	80.6 ± 7.1	252.30	1.415 ± 0.023	5.7%	0.898
Protopaleodictyon	UUIC 1597	Ind	Ind	Ind	49.7 ± 4.67	65.33	1.526 ± 0.039	Ind	Ind
Protopaleodictyon	UJTF 171P4	0.292	1.558	0.1872	82.1 ± 3.8	289.31	1.408 ± 0.005	8.2%	0.338
Protopaleodictyon	UJTF 334b	0.178	0.998	0.1787	86 ± 12.58	632.67	1.523 ± 0.029	7.9%	0.561
Urohelminthoida	UJTF 1599	0.971	0.826	1.1759	52.9 ± 6.73	317.14	1.544 ± 0.012	9.4%	0.751
Protopaleodictyon	UJTF 228	0.676	3.304	0.2047	Ind	Ind	1.58 ± 0.032	7.1%	0.880
Protopaleodictyon	UJTF 454	0.201	1.417	0.1419	75 ± 7.62	406.67	1.518 ± 0.018	7.5%	0.785
Protopaleodictyon	UJTF 2005	0.750	6.318	0.1186	109.2 ± 1.56	12.20	1.571 ± 0.034	3.5%	0.936
Urohelminthoida	UJTF 141	0.923	1.408	0.6559	49.2 ± 3.77	85.37	1.499 ± 0.02	5.8%	0.883
Urohelminthoida	UJTF 344	0.630	0.798	0.7890	68.2 ± 7.86	370.97	1.491 ± 0.013	10.0%	0.806
Urohelminthoida	UJTF 352	2.075	1.950	1.0644	46.2 ± 3.69	68.20	1.464 ± 0.016	6.4%	0.959
Urohelminthoida	UJTF 354	1.900	0.486	3.9100	37.5 ± 2.1	17.67	1.547 ± 0.02	13.8%	0.362
Urohelminthoida	UJTF 356	1.249	0.648	1.9275	65.8 ± 14.52	842.92	1.474 ± 0.018	7.9%	0.682
Urohelminthoida	UJTF 359	Ind	0.885	Ind	38.3 ± 8.1	262.25	1.599 ± 0.019	9.9%	0.864

Table H.3 continued.

Ichnogenera	Sample ID	a (cm)	λ (cm)	MI	BA	BAV	D_{Box}	OSP	BAS
Urohelminthoida	UJTF 360	2.612	0.537	4.8634	42.7 ± 5.99	215.47	1.402 ± 0.027	10.7%	0.216
Urohelminthoida	UJTF 722	Ind	3.200	Ind	Ind	Ind	1.494 ± 0.003	9.1%	0.902
Urohelminthoida	UJTF 1593	1.685	1.770	0.9519	64.7 ± 6.01	108.33	1.673 ± 0.02	7.7%	0.977
Protopaleodictyon	UJTF 130	0.302	1.663	0.1816	83.2 ± 2.66	276.66	1.394 ± 0.003	8.2%	0.361
Protopaleodictyon	UJTF 338	0.276	1.417	0.1950	87.5 ± 2.71	176.35	1.565 ± 0.016	10.1%	0.889
Protopaleodictyon	UJTF 342	0.459	1.585	0.2896	92.2 ± 4.13	102.57	1.379 ± 0.02	6.2%	0.344
Protopaleodictyon	UJTF 763	0.375	2.503	0.1498	Ind	Ind	1.571 ± 0.032	3.1%	0.968
Protopaleodictyon	UJTF 900	0.334	1.653	0.2023	91.4 ± 4.61	212.27	1.406 ± 0.014	7.8%	0.447
Protopaleodictyon	UJTF 1121	0.073	0.628	0.1170	76 ± 5.98	429.09	1.476 ± 0.015	8.2%	0.566
Protopaleodictyon	UJTF 1483	0.396	1.779	0.2227	78 ± 5.18	348.67	1.543 ± 0.021	8.4%	0.954
Protopaleodictyon	UJTF 1484	0.298	1.411	0.2114	85.2 ± 3.36	271.13	1.584 ± 0.008	13.6%	0.844
Urohelminthoida	Z_Urohelm1	0.565	0.617	0.9169	44.8 ± 2.12	103.81	1.574 ± 0.003	16.2%	0.694
Urohelminthoida	Z_Urohelm2	0.613	0.415	1.4776	43.1 ± 2.15	202.48	1.526 ± 0.002	17.7%	0.193
Urohelminthoida	UJTF 348	Ind	0.304	Ind	55.8 ± 7.51	225.58	1.539 ± 0.007	18.0%	0.393
Protopaleodictyon	UJTF 341	0.204	1.592	0.1282	79.5 ± 8.86	313.67	1.494 ± 0.034	4.0%	0.935
Protopaleodictyon	UJTF 709	0.359	2.146	0.1671	69.3 ± 8.6	444.27	1.523 ± 0.028	4.9%	0.954
Urohelminthoida	UJTF 35	1.730	2.537	0.6819	Ind	Ind	1.476 ± 0.033	2.9%	0.963
Ubinia	UJTF 2726	0.095	1.555	0.0612	78.5 ± 3.45	201.76	1.597 ± 0.019	11.0%	0.879
Protopaleodictyon	UJTF 923	0.419	1.930	0.2169	89 ± 5.94	212.00	1.468 ± 0.022	5.9%	0.917
Protopaleodictyon	UJTF 955	0.448	2.181	0.2054	85.8 ± 4.96	196.50	1.553 ± 0.029	5.4%	0.952
Urohelminthoida	UJTF 120	2.430	0.802	3.0312	44.7 ± 4.06	49.33	1.578 ± 0.008	21.0%	0.241
Urohelminthoida	UJTF 351	Ind	0.971	Ind	47 ± 8.02	193.00	1.592 ± 0.019	9.3%	0.946
Urohelminthoida	UJTF 1591	Ind	0.564	Ind	66.2 ± 10.11	613.37	1.517 ± 0.013	9.7%	0.587
Urohelminthoida	UJTF 1592	Ind	0.954	Ind	43.5 ± 5.41	175.50	1.608 ± 0.004	16.5%	0.802
Urohelminthoida	UJTF 2677	1.584	0.830	1.9077	41.4 ± 4.93	121.30	1.689 ± 0.005	23.4%	0.816
Urohelminthoida	UUIC 1914	0.941	0.467	2.0137	57.6 ± 5.24	412.26	1.594 ± 0.005	17.3%	0.538
Protopaleodictyon	Ban-Jich-0012	0.471	3.666	0.1284	73.2 ± 13.08	855.20	1.494 ± 0.041	3.5%	0.924
Protopaleodictyon	BAN-Jich-0014b	0.081	1.182	0.0684	Ind	Ind	1.496 ± 0.036	6.5%	0.762

Table H.3 continued.

Ichnogenera	Sample ID	a (cm)	λ (cm)	MI	BA	BAV	D_{Box}	OSP	BAS
Protopaleodictyon	MP-US J1138	0.111	0.851	0.1308	90.9 ± 6.53	298.81	1.518 ± 0.023	7.3%	0.916
Protopaleodictyon	MP-US J1149	0.100	0.972	0.1025	Ind	Ind	1.581 ± 0.031	6.3%	0.898
Protopaleodictyon	IKKM I-9	0.172	2.344	0.0736	91.3 ± 6.17	114.33	1.513 ± 0.034	4.1%	0.953
Protopaleodictyon	IKKM I-14	0.708	1.629	0.4347	61.8 ± 6.64	528.70	1.535 ± 0.02	8.5%	0.858
Protopaleodictyon	UW 1497	0.154	1.777	0.0867	96.6 ± 4.1	117.62	1.64 ± 0.027	5.5%	0.949
Protopaleodictyon	Mikuláš et al 2004 Plate V-3	0.167	3.100	0.0538	56.3 ± 7.36	216.92	1.64 ± 0.029	7.9%	0.927
Protopaleodictyon	TF9208-1-15	0.115	1.102	0.1046	Ind	Ind	1.547 ± 0.037	4.9%	0.778
Protopaleodictyon	TF9208-1-17	0.215	2.928	0.0736	93.5 ± 5.95	141.67	1.499 ± 0.042	4.2%	0.969
Protopaleodictyon	Acenolaza 1978 Lam III-2	0.142	0.857	0.1657	88.8 ± 5.26	331.42	1.615 ± 0.024	15.1%	0.519
Protopaleodictyon	Pickerill 1981 Fig 5a	0.204	1.932	0.1054	83.5 ± 5.29	279.39	1.427 ± 0.029	2.9%	0.810
Protopaleodictyon	Pickerill 1980 Fig 4b	Ind	Ind	Ind	86.1 ± 2.9	201.16	1.289 ±	Ind	Ind

Table H.4. Results of analyses on network trace fossils. Complete sample locality and date information can be found in Appendix E. The table contains the estimated latitude and longitude of the sample localities. The age is the median age of the formation in which the sample was found. The age error encompasses the length of time the formation has been estimated to have been deposited. Abbreviations: BA = branching angle; BAS = burrow area shape; $BAS_{Trimmed}$ = BAS of a trimmed drown trace; BAV = branching angle variance; C_{Size} = average size of the network cells; D_{Box} = fractal dimension using the Box Counting Method; MS = mesh size; NA = not applicable analyses; NT = network tortuosity; OSP = occupied space percentage; $S_{Average}$ = weighted average of cell sides; S_{Mode} = mode of the cell sides; $S_{Variance}$ = variance of the number of cell sides; W = burrow width. The BA, NT, and D_{Box} variance is represented by the standard error.

Ichnogenera	Sample ID	Latitude	Longitude
Paleodictyon	INMD 128BX-1	29° 55' N	34° 21' W
Paleodictyon	INMD 128BX-2	29° 55' N	34° 21' W
Paleodictyon	VOTD-3957	26° 09' N	44° 48' W
Paleodictyon	VOTD-4001	26° 09' N	44° 48' W
Paleodictyon	VOTD-4003	26° 09' N	44° 48' W
Paleodictyon	VOTD-4006	26° 09' N	44° 48' W
Paleodictyon	VOTD-4009	26° 09' N	44° 48' W
Paleodictyon	VOTD-4012	26° 09' N	44° 48' W
Paleodictyon	VBPaleo1	37° 8' 46" N	1° 56' 11" W
Paleodictyon	VBPaleo2	37° 8' 46" N	1° 56' 11" W
Paleodictyon	VBPaleo3	37° 8' 46" N	1° 56' 11" W
Paleodictyon	VBPaleo4	37° 8' 46" N	1° 56' 11" W
Paleodictyon	VBPale4b	37° 8' 46" N	1° 56' 11" W
Paleodictyon	VBPaleo5	37° 8' 46" N	1° 56' 11" W
Paleodictyon	VBPaleo6	37° 8' 46" N	1° 56' 11" W
Paleodictyon	VBPaleo6b	37° 8' 46" N	1° 56' 11" W
Paleodictyon	VBPaleo7	37° 8' 46" N	1° 56' 11" W
Paleodictyon	CM 22	40° 31' 26" N	16° 2' 57" E
Paleodictyon	FG 1	40° 31' 26" N	16° 2' 57" E
Paleodictyon	FG 5	40° 31' 26" N	16° 2' 57" E
Paleodictyon	UUIC 722	40° 23' 37" N	16° 9' 29" E
Paleodictyon	PIW1993X 50	43° 53' 38" N	12° 5' 24" E
Paleodictyon	PIW1993X 56	44° 10' N	11° 48' E
Paleodictyon	PIW1993X 59	44° 12' 48" N	11° 30' 12" E
Paleodictyon	PIW1993X 61	43° 50' N	11° 58' E
Paleodictyon	PIW1993X 68	44° 10' N	11° 48' E
Gordia	UJTF 245	49° 45' 9" N	20° 11' 13" E
Gordia	UJTF 1219	49° 8' 36" N	22° 29' 5" E
Paleodictyon	UJTF 835-1	49° 34' 24" N	21° 56' 40" E
Paleodictyon	UJTF 835-2	49° 34' 24" N	21° 56' 40" E
Paleodictyon	UJTF unk	49° 34' 24" N	21° 56' 40" E

Period/Epoch	Age (Ma)	W (mm)
Modern	0.0 ± 0.00	0.6
Modern	0.0 ± 0.00	0.4
Modern	0.0 ± 0.00	0.8
Modern	0.0 ± 0.00	0.8
Modern	0.0 ± 0.00	0.8
Modern	0.0 ± 0.00	0.6
Modern	0.0 ± 0.00	0.7
Modern	0.0 ± 0.00	0.6
Miocene	6.3 ± 0.96	2.2
Miocene	6.3 ± 0.96	2.0
Miocene	6.3 ± 0.96	2.2
Miocene	6.3 ± 0.96	1.1
Miocene	6.3 ± 0.96	0.6
Miocene	6.3 ± 0.96	0.8
Miocene	6.3 ± 0.96	2.7
Miocene	6.3 ± 0.96	1.2
Miocene	6.3 ± 0.96	2.5
Miocene	10.7 ± 5.32	0.6
Miocene	10.7 ± 5.32	0.5
Miocene	10.7 ± 5.32	0.6
Miocene	10.7 ± 5.32	0.8
Miocene	13.8 ± 2.18	1.7
Miocene	13.8 ± 2.18	2.9
Miocene	13.8 ± 2.18	1.2
Miocene	13.8 ± 2.18	7.2
Miocene	13.8 ± 2.18	1.1
Oligocene	25.7 ± 2.69	1.2
Oligocene	25.7 ± 2.69	0.6
Oligocene	25.7 ± 2.69	0.5
Oligocene	25.7 ± 2.69	0.6
Oligocene	25.7 ± 2.69	0.7

Table H.4 continued.

Ichnogenera	Sample ID	Latitude	Longitude
Gordia	IGP t.f. 71b	49° 23' N	20° 1' E
Gordia	IGP t.f. 184a	49° 23' N	20° 1' E
Paleodictyon	UJTF 78	49° 43' 43" N	20° 40' 21" E
Paleodictyon	UJTF 89	49° 43' 43" N	20° 40' 21" E
Paleodictyon	UJTF 101	49° 43' 43" N	20° 40' 21" E
Paleodictyon	UJTF 113	49° 43' 43" N	20° 40' 21" E
Megagrapton	UJTF 985	49° 33' 22" N	20° 40' 26" E
Paleodictyon	UUIC 109	11° 15' 52" N	63° 50' 55" W
Paleodictyon	UJTF 749	49° 26' 28" N	20° 25' 39" E
Megagrapton	UJTF 80a	49° 30' 50" N	19° 38' 00" E
Megagrapton	UJTF 387	49° 33' 46" N	19° 38' 58" E
Megagrapton	UJTF 388	49° 30' 50" N	19° 38' 00" E
Megagrapton	UJTF 390	49° 30' 50" N	19° 38' 00" E
Megagrapton	UJTF 455	49° 33' 46" N	19° 38' 58" E
Megagrapton	UJTF 809	49° 30' 11" N	20° 58' 16" E
Paleodictyon	UJTF 64	49° 30' 50" N	19° 38' 00" E
Paleodictyon	UJTF 158	51° 00' 46" N	15° 30' 38" E
Paleodictyon	UJTF 161	49° 59' 14" N	19° 52' 33" E
Paleodictyon	UJTF 163	49° 59' 14" N	19° 52' 33" E
Paleodictyon	UJTF 164	49° 59' 14" N	19° 52' 33" E
Paleodictyon	UJTF 167	49° 33' 46" N	19° 38' 58" E
Paleodictyon	UJTF 168	49° 28' 27" N	19° 38' 24" E
Paleodictyon	UJTF 171	49° 28' 27" N	19° 38' 24" E
Paleodictyon	UJTF 172-1	49° 33' 46" N	19° 38' 58" E
Paleodictyon	UJTF 172-2	49° 33' 46" N	19° 38' 58" E
Paleodictyon	UJTF 186	49° 30' 50" N	19° 38' 00" E
Paleodictyon	UJTF 294	51° 00' 46" N	15° 30' 38" E
Paleodictyon	UJTF 305	49° 30' 50" N	19° 38' 00" E
Paleodictyon	UJTF 894	49° 30' 11" N	20° 58' 16" E
Paleodictyon	UJTF unk	49° 36' 00" N	20° 21' 6" E
Gordia	UJTF 1249	49° 37' 46" N	19° 13' 13" E

Period/Epoch	Age (Ma)	W (mm)
Oligocene	28.5 ± 5.44	1.6
Oligocene	28.5 ± 5.44	1.5
Eocene	46.5 ± 9.30	0.6
Eocene	46.5 ± 9.30	0.4
Eocene	46.5 ± 9.30	0.6
Eocene	46.5 ± 9.30	1.5
Eocene	42.9 ± 5.70	2.5
Eocene	44.9 ± 10.95	1.7
Eocene	53.7 ± 5.05	0.7
Eocene	46.5 ± 9.30	1.3
Eocene	46.5 ± 9.30	3.4
Eocene	46.5 ± 9.30	1.3
Eocene	46.5 ± 9.30	1.5
Eocene	46.5 ± 9.30	2.1
Eocene	46.5 ± 9.30	1.3
Eocene	46.5 ± 9.30	0.9
Eocene	46.5 ± 9.30	0.9
Eocene	46.5 ± 9.30	1.3
Eocene	46.5 ± 9.30	1.2
Eocene	46.5 ± 9.30	1.0
Eocene	46.5 ± 9.30	1.4
Eocene	46.5 ± 9.30	0.6
Eocene	46.5 ± 9.30	0.8
Eocene	46.5 ± 9.30	0.4
Eocene	46.5 ± 9.30	0.5
Eocene	46.5 ± 9.30	1.3
Eocene	46.5 ± 9.30	1.2
Eocene	46.5 ± 9.30	1.1
Eocene	46.5 ± 9.30	0.5
Eocene	46.5 ± 9.30	3.0
Eocene	42.9 ± 5.70	1.7

Table H.4 continued.

Ichnogenera	Sample ID	Latitude	Longitude
Megagrapton	UJTF 793	50° 45' 56" N	20° 26' 40" E
Paleodictyon	UJTF 63	49° 33' 48" N	18° 54' 41" E
Paleodictyon	UJTF 157	49° 40' 50" N	19° 46' 56" E
Paleodictyon	UJTF 159	49° 28' 47" N	20° 24' 52" E
Paleodictyon	UJTF 304	52° 13' 23" N	18° 15' 4" E
Paleodictyon	UJTF 323	49° 40' 12" N	19° 7' 39" E
Paleodictyon	UUIC 428	43° 18.540' N	2° 13.882' W
Megagrapton	Z_Mega1	43° 18.540' N	2° 13.882' W
Megagrapton	Z_Mega2	43° 18.540' N	2° 13.882' W
Megagrapton	Z_Mega3	43° 18.540' N	2° 13.882' W
Megagrapton	Z_Mega4	43° 18.540' N	2° 13.882' W
Megagrapton	Z_Mega5	43° 18.540' N	2° 13.882' W
Megagrapton	Z_Mega6	43° 18.540' N	2° 13.882' W
Megagrapton	Z_Mega7	43° 18.540' N	2° 13.882' W
Paleodictyon	Z_Paleo1	43° 18.540' N	2° 13.882' W
Paleodictyon	Z_Paleo2	43° 18.540' N	2° 13.882' W
Paleodictyon	Z_Paleo3	43° 18.540' N	2° 13.882' W
Paleodictyon	Z_Paleo4	43° 18.540' N	2° 13.882' W
Paleodictyon	Z_Paleo5	43° 18.540' N	2° 13.882' W
Megagrapton	UJTF 640	49° 42' 34" N	20° 23' 6" E
Megagrapton	UJTF 657	49° 42' 34" N	20° 23' 6" E
Megagrapton	UJTF 1873	49° 37' 52" N	20° 38' 40" E
Paleodictyon	UJTF 272	49° 30' 50" N	19° 38' 00" E
Paleodictyon	UJTF 846	49° 30' 11" N	20° 58' 16" E
Paleodictyon	UJTF 89A	49° 37' 26" N	20° 56' 52" E
Paleodictyon	UJTF 188	52° 13' 23" N	18° 15' 4" E
Paleodictyon	UJTF 1102	49° 28' 27" N	19° 38' 24" E
Paleodictyon	UJTF1259	49° 40' 27" N	20° 04' 47" E
Gordia	GSC 81259	57° 46' 44" N	152° 26' 55" W
Paleodictyon	McCann and Pickerill 1988 Fig 5-2	57° 46' 19" N	152° 24' 59" W

Period/Epoch	Age (Ma)	W (mm)
Eocene	42.9 ± 5.70	1.8
Eocene	42.9 ± 5.70	0.7
Eocene	42.9 ± 5.70	0.5
Eocene	42.9 ± 5.70	0.9
Eocene	42.9 ± 5.70	0.7
Eocene	42.9 ± 5.70	0.3
Eocene	52.2 ± 3.60	0.8
Eocene	52.2 ± 3.60	1.7
Eocene	52.2 ± 3.60	1.5
Eocene	52.2 ± 3.60	1.0
Eocene	52.2 ± 3.60	1.2
Eocene	52.2 ± 3.60	2.0
Eocene	52.2 ± 3.60	2.0
Eocene	52.2 ± 3.60	2.0
Eocene	52.2 ± 3.60	0.5
Eocene	52.2 ± 3.60	0.4
Eocene	52.2 ± 3.60	0.8
Eocene	52.2 ± 3.60	0.6
Eocene	52.2 ± 3.60	0.8
Paleocene	53.7 ± 5.05	1.0
Paleocene	53.7 ± 5.05	0.5
Paleocene	53.7 ± 5.05	8.1
Paleocene	53.7 ± 5.05	0.6
Paleocene	53.7 ± 5.05	0.4
Late Cretaceous	63.2 ± 7.40	0.6
Late Cretaceous	63.2 ± 7.40	0.4
Late Cretaceous	63.2 ± 7.40	0.5
Late Cretaceous	63.2 ± 7.40	0.7
Late Cretaceous	82.6 ± 17.05	0.9
Late Cretaceous	82.6 ± 17.05	0.9

Table H.4 continued.

Ichnogenera	Sample ID	Latitude	Longitude
Paleodictyon	UJTF 1668	49° 45' 6" N	20° 9' 8" E
Paleodictyon	UJTF 67	49° 24' 29" N	20° 20' 21" E
Paleodictyon	UJTF 92	49° 24' 37" N	20° 33' 8" E
Paleodictyon	UJTF 111	49° 24' 29" N	20° 20' 21" E
Paleodictyon	UJTF 320	49° 24' 29" N	20° 20' 21" E
Paleodictyon	UJTF 324	49° 24' 29" N	20° 20' 21" E
Paleodictyon	UJTF 330	49° 24' 37" N	20° 33' 8" E
Paleodictyon	UJTF 333	49° 24' 37" N	20° 33' 8" E
Paleodictyon	UUIC 1916	8° 45' 54" S	39° 18' 56" E
Paleodictyon	UUIC 1917	8° 46' 24" S	39° 19' 25" E
Paleodictyon	UUIC 1918	8° 46' 24" S	39° 19' 25" E
Paleodictyon	UUIC 1919	8° 46' 24" S	39° 19' 25" E
Megagrapton	UJTF 391	49° 44' 6" N	18° 45' 55" E
Paleodictyon	UJTF 316	49° 44' 6" N	18° 45' 55" E
Gordia	UCMP 398574	41° 46' 41" N	124° 15' 7" W
Megagrapton	UCMP 398582	41° 46' 41" N	124° 15' 7" W
Squamodictyon	UCMP 398595	41° 46' 41" N	124° 15' 7" W
Paleodictyon	UJTF 1172-1	49° 47' 15" N	20° 6' 52" E
Paleodictyon	UJTF 1172-2	49° 47' 15" N	20° 6' 52" E
Squamodictyon	MP-US J1150	42° 57' 13" N	27° 12' 42" E
Paleodictyon	UUIC 1312	32° 10' 20" N	4° 22' 4" W
Paleodictyon	BAN-Jich-0033b	42° 37' 6" N	22° 49' 33" E
Paleodictyon	UUIC 721	39° 26' 58" N	16° 36' 37" E
Paleodictyon	UUIC 1164	39° 26' 58" N	16° 36' 37" E
Gordia	MP-US J1131	42° 57' 26" N	27° 16' 23" E
Gordia	MP-US J1133	42° 57' 26" N	27° 16' 23" E
Paleodictyon	MP-US J1142	43° 1' 53" N	27° 22' 18" E
Paleodictyon	MP-US J1143	42° 53' 16" N	26° 26' 2" E
Paleodictyon	MP-US J1144	42° 57' 26" N	27° 16' 23" E
Paleodictyon	MP-US J1145	42° 57' 26" N	27° 16' 23" E
Megagrapton	BKKM 1-3	37° 47' 7" N	13° 40' 2" E

Period/Epoch	Age (Ma)	W (mm)
Late Cretaceous	86.1 ± 2.55	1.3
Late Cretaceous	79.6 ± 9.00	0.5
Late Cretaceous	79.6 ± 9.00	1.5
Late Cretaceous	79.6 ± 9.00	0.2
Late Cretaceous	79.6 ± 9.00	0.3
Late Cretaceous	79.6 ± 9.00	0.5
Late Cretaceous	79.6 ± 9.00	0.5
Late Cretaceous	79.6 ± 9.00	0.4
Late Cretaceous	81.5 ± 2.00	0.9
Late Cretaceous	81.5 ± 2.00	1.0
Late Cretaceous	81.5 ± 2.00	0.6
Late Cretaceous	81.5 ± 2.00	0.8
Early Cretaceous	145.5 ± 5.30	1.1
Early Cretaceous	145.5 ± 5.30	0.5
Early Cretaceous	140.4 ± 10.40	0.6
Early Cretaceous	140.4 ± 10.40	1.5
Early Cretaceous	140.4 ± 10.40	0.8
Early Cretaceous	129.5 ± 4.45	0.7
Early Cretaceous	129.5 ± 4.45	0.6
Jurassic	179.3 ± 3.70	1.3
Jurassic	186.1 ± 10.45	1.6
Jurassic	142.8 ± 2.75	0.6
Jurassic	160.6 ± 15.05	1.8
Jurassic	160.6 ± 15.05	1.6
Jurassic	182.6 ± 7.00	1.1
Jurassic	182.6 ± 7.00	0.7
Jurassic	182.6 ± 7.00	1.9
Jurassic	182.6 ± 7.00	1.0
Jurassic	182.6 ± 7.00	1.9
Jurassic	182.6 ± 7.00	1.0
Permian	274.5 ± 1.50	1.9

Table H.4 continued.

Ichnogenera	Sample ID	Latitude	Longitude
Megagrapton	BKKM 1-10	37° 47' 7" N	13° 40' 2" E
Megagrapton	BKKM 1-24	37° 47' 7" N	13° 40' 2" E
Megagrapton	IKKM 1-4	37° 47' 7" N	13° 40' 2" E
Megagrapton	IKKM 1-5	37° 47' 7" N	13° 40' 2" E
Megagrapton	IKKM 1-6	37° 47' 7" N	13° 40' 2" E
Megagrapton	IKKM 1-12	37° 47' 7" N	13° 40' 2" E
Megagrapton	IKKM 1-15	37° 47' 7" N	13° 40' 2" E
Paleodictyon	IKKM 1-2	37° 47' 7" N	13° 40' 2" E
Paleodictyon	IKKM 1-7	37° 47' 7" N	13° 40' 2" E
Paleodictyon	IKKM 1-8	37° 47' 7" N	13° 40' 2" E
Megagrapton	UW 1495	34° 42' 53" N	95° 49' 6" W
Squamodictyon	Llompart and Wieczorek 1997 Plate II.1	39° 59' 33" N	4° 15' 19" E
Squamodictyon	PIW 891130	50° 20' 54" N	11° 33' 17" E
Megagrapton	PIW 8916	50° 20' 54" N	11° 33' 17" E
Megagrapton	PIW 8919	50° 20' 54" N	11° 33' 17" E
Megagrapton	PIW 89110	50° 20' 54" N	11° 33' 17" E
Megagrapton	PIW 89198b	50° 20' 54" N	11° 33' 17" E
Megagrapton	PIW 891241	50° 20' 54" N	11° 33' 17" E
Megagrapton	PIW 891244	50° 20' 54" N	11° 33' 17" E
Megagrapton	Mikuláš et al 2004 Plate V-2	50° 5' 8" N	17° 17' 41" E
Gordia	NBMG 9683	47° 12' 12" N	67° 11' 25" W
Gordia	Crimes and Crossley 1991 Fig 9a	52° 29' 17" N	4° 3' 14" W
Gordia	NMW 90.44G.14	52° 25' 54" N	4° 3' 40" W
Paleodictyon	Crimes and Crossley 1991 Fig 9c	52° 29' 17" N	4° 3' 14" W

Period/Epoch	Age (Ma)	W (mm)
Permian	274.5 ± 1.50	1.5
Permian	274.5 ± 1.50	1.4
Permian	274.5 ± 1.50	2.4
Permian	274.5 ± 1.50	1.3
Permian	274.5 ± 1.50	1.0
Permian	274.5 ± 1.50	1.8
Permian	274.5 ± 1.50	1.4
Permian	274.5 ± 1.50	1.8
Permian	274.5 ± 1.50	0.9
Permian	274.5 ± 1.50	1.3
Carboniferous	312.7 ± 5.45	1.4
Carboniferous	329.2 ± 16.15	1.0
Carboniferous	340.9 ± 4.40	0.5
Carboniferous	340.9 ± 4.40	0.6
Carboniferous	340.9 ± 4.40	0.6
Carboniferous	340.9 ± 4.40	0.8
Carboniferous	340.9 ± 4.40	1.5
Carboniferous	340.9 ± 4.40	0.9
Carboniferous	340.9 ± 4.40	0.9
Carboniferous	338.8 ± 7.90	3.3
Devonian	411.5 ± 4.50	1.4
Silurian	432.1 ± 3.90	8.2
Silurian	432.1 ± 3.90	2.7
Silurian	432.1 ± 3.90	4.1

Table H.4 continued.

Ichnogenera	Sample ID	Latitude	Longitude
Paleodictyon	Crimes and Crossley 1991 Fig 9d	52° 29' 17" N	4° 3' 14" W
Paleodictyon	Crimes and Crossley 1991 Fig 9e	52° 29' 17" N	4° 3' 14" W
Paleodictyon	Crimes and Crossley 1991 Fig 9f	52° 29' 17" N	4° 3' 14" W
Paleodictyon	Crimes and Crossley 1991 Fig 13a	52° 29' 17" N	4° 3' 14" W
Paleodictyon	Crimes and Crossley 1991 Fig 13b	52° 29' 17" N	4° 3' 14" W
Paleodictyon	Crimes and Crossley 1991 Fig 13c	52° 29' 17" N	4° 3' 14" W
Squamodictyon	Crimes and Crossley 1991 Fig 13e	52° 29' 17" N	4° 3' 14" W
Squamodictyon	Crimes and Crossley 1991 Fig 17c	52° 29' 17" N	4° 3' 14" W
Squamodictyon	GPIT 1503/2	52° 21' 31" N	4° 6' 39" W
Squamodictyon	NMW 90.44G.6	52° 21' 31" N	4° 6' 39" W
Squamodictyon	NMW 90.44G.7	52° 21' 31" N	4° 6' 39" W
Squamodictyon	NMW 90.44G.8	52° 21' 31" N	4° 6' 39" W
Squamodictyon	NMW 90.44G.10	52° 13' 23" N	4° 17' 45" W
Squamodictyon	NMW 90.44G.16	52° 21' 31" N	4° 6' 39" W
Squamodictyon	NMW 90.44G.17	52° 21' 31" N	4° 6' 39" W
Squamodictyon	NMW 90.44G.18	52° 21' 31" N	4° 6' 39" W

Period/Epoch	Age (Ma)	W (mm)
Silurian	432.1 ± 3.90	3.4
Silurian	432.1 ± 3.90	2.8
Silurian	432.1 ± 3.90	2.6
Silurian	432.1 ± 3.90	5.4
Silurian	432.1 ± 3.90	3.2
Silurian	432.1 ± 3.90	3.8
Silurian	432.1 ± 3.90	4.1
Silurian	432.1 ± 3.90	3.2
Silurian	432.1 ± 3.90	2.2
Silurian	432.1 ± 3.90	1.7
Silurian	432.1 ± 3.90	2.7
Silurian	432.1 ± 3.90	3.2
Silurian	432.1 ± 3.90	2.3
Silurian	432.1 ± 3.90	2.2
Silurian	432.1 ± 3.90	2.5
Silurian	432.1 ± 3.90	2.7

Table H.4 continued.

Ichnogenera	Sample ID	Latitude	Longitude
Squamodictyon	NMW 90.44G.19	52° 21' 31" N	4° 6' 39" W
Squamodictyon	NMW 90.44G.20	52° 29' 17" N	4° 3' 14" W
Megagrapton	RSM 1981.30.68	55° 30' 27" N	3° 14' 26" W
Gordia	RSM 1981.30.100	55° 25' 55" N	2° 51' 41" W
Paleodictyon	UEGIG 46275	54° 46' 44" N	4° 6' 51" W
Gordia	Acenolaza 1978 Lam III-3	23° 22' S	66° 40' W
Paleodictyon	Acenolaza 1978 Lam III-1	23° 22' S	66° 40' W
Gordia	Pickerill 1981 Fig 2d	47° 13' 00" N	67° 59' 19" W
Gordia	Pickerill 1981 Fig 3a	47° 13' 00" N	67° 59' 19" W
Gordia	Crimes et al 1992 Fig 2E	52° 38' 26" N	6° 13' 27" W
Gordia	Crimes et al 1992 Fig 2F	52° 38' 26" N	6° 13' 27" W
Paleodictyon	Pickerill 1980 Fig 2f	47° 53' N	66° 50' W
Megagrapton	Pickerill et al 1988 Fig 2e	46° 46' 33" N	67° 41' 37" W
Gordia	A40389-1	54° 39' 20" N	3° 10' 18" W
Gordia	A40389-2	54° 39' 20" N	3° 10' 18" W
Gordia	Acenolaza 1978 Fig 10	25° 6' 4" S	66° 11' 4" W
Gordia	Acenolaza and Torelli 1981 pg 57-1	25° 6' 4" S	66° 11' 4" W
Gordia	Crimes and Anderson 1985 Fig 5.7	47° 33' 54" N	53° 40' 13" W
Squamodictyon	Crimes and Anderson 1985 Fig 10.4	47° 33' 54" N	53° 40' 13" W

Period/Epoch	Age (Ma)	W (mm)
Silurian	432.1 ± 3.90	2.6
Silurian	432.1 ± 3.90	2.8
Silurian	432.1 ± 3.90	0.8
Silurian	432.1 ± 3.90	1.9
Silurian	432.1 ± 3.90	0.6
Silurian	420.8 ± 2.10	1.4
Silurian	420.8 ± 2.10	1.0
Silurian	439.9 ± 3.85	0.6
Silurian	439.9 ± 3.85	1.5
Ordovician	472.5 ± 6.50	1.5
Ordovician	472.5 ± 6.50	1.7
Ordovician	474.6 ± 13.70	1.2
Ordovician	448.5 ± 12.45	2.5
Ordovician	480.1 ± 8.25	0.2
Ordovician	480.1 ± 8.25	0.2
Cambrian	537.5 ± 2.50	2.2
Cambrian	537.5 ± 2.50	3.9
Cambrian	524.5 ± 3.50	0.8
Cambrian	524.5 ± 3.50	2.8

Table H.4 continued.

Ichnogenera	Sample ID	C_{Size}	MS
Paleodictyon	INMD 128BX-1	0.329	5.484
Paleodictyon	INMD 128BX-2	0.174	4.358
Paleodictyon	VOTD-3957	0.823	10.289
Paleodictyon	VOTD-4001	0.964	12.049
Paleodictyon	VOTD-4003	0.913	11.413
Paleodictyon	VOTD-4006	0.911	15.176
Paleodictyon	VOTD-4009	0.887	12.675
Paleodictyon	VOTD-4012	0.849	14.152
Paleodictyon	VBPaleo1	1.163	5.286
Paleodictyon	VBPaleo2	0.774	3.872
Paleodictyon	VBPaleo3	0.959	4.359
Paleodictyon	VBPaleo4	0.593	5.387
Paleodictyon	VBPale4b	0.293	4.886
Paleodictyon	VBPaleo5	0.303	3.785
Paleodictyon	VBPaleo6	0.851	3.150
Paleodictyon	VBPaleo6b	0.577	4.809
Paleodictyon	VBPaleo7	1.135	4.538
Paleodictyon	CM 22	0.309	5.143
Paleodictyon	FG 1	0.157	3.145
Paleodictyon	FG 5	0.222	3.701
Paleodictyon	UUIC 722	0.384	4.799
Paleodictyon	PIW1993X 50	0.929	5.464
Paleodictyon	PIW1993X 56	0.982	3.387
Paleodictyon	PIW1993X 59	0.456	3.802
Paleodictyon	PIW1993X 61	3.250	4.513
Paleodictyon	PIW1993X 68	0.630	5.727
Gordia	UJTF 245	0.532	4.433
Gordia	UJTF 1219	0.366	6.098
Paleodictyon	UJTF 835-1	0.283	5.660
Paleodictyon	UJTF 835-2	0.253	4.218
Paleodictyon	UJTF unk	0.760	10.851

NT	BA	BAV
1.312 ± 0.003	89.9 ± 3.3	348.24
1.5 ± 0.002	81.3 ± 2.98	311.76
1.231 ± 0.004	99.5 ± 2.23	234.34
1.231 ± 0.003	100.7 ± 2.24	150.63
1.266 ± 0.003	100 ± 2.74	225.14
1.28 ± 0.011	109.9 ± 1.7	54.94
1.259 ± 0.004	99.3 ± 2.93	377.85
1.245 ± 0.005	99.5 ± 3.39	297.94
1.199 ± 0.003	105.6 ± 1.4	113.94
1.36 ± 0.007	96.3 ± 1.41	188.34
1.393 ± 0.006	105.5 ± 2.24	164.88
1.373 ± 0.006	94.6 ± 2.49	370.65
Ind	99.9 ± 2.88	166.13
1.462 ± 0.006	101.1 ± 3.53	236.54
1.338 ± 0.021	98.2 ± 1.6	140.73
1.352 ± 0.006	88.5 ± 4.76	520.08
1.239 ± 0.002	104 ± 1.45	119.98
1.356 ± 0.015	92.2 ± 2.04	270.27
1.292 ± 0.02	90.7 ± 1.43	262.28
1.299 ± 0.002	82.5 ± 2.57	363.66
Ind	88.2 ± 4.1	452.85
1.263 ± 0	93.7 ± 1.92	262.02
1.363 ± 0.004	98.4 ± 2.91	186.44
1.262 ± 0.003	95.7 ± 2.4	208.10
1.41 ± 0.007	80.4 ± 4.92	387.72
1.337 ± 0.003	95.8 ± 2.49	278.83
1.427 ± 0.018	60.5 ± 2.11	350.61
1.361 ± 0.012	69.3 ± 2.54	252.46
1.376 ± 0.018	87.7 ± 2.88	374.54
1.41 ± 0.029	77.6 ± 3.95	437.05
1.118 ± 0.003	102.3 ± 0.43	162.24

Table H.4 continued.

Ichnogenera	Sample ID	C_{Size}	MS
Gordia	IGP t.f. 71b	1.461	9.130
Gordia	IGP t.f. 184a	0.958	6.386
Paleodictyon	UJTF 78	0.321	5.356
Paleodictyon	UJTF 89	0.207	5.180
Paleodictyon	UJTF 101	0.340	5.664
Paleodictyon	UJTF 113	0.716	4.775
Megagrapton	UJTF 985	4.771	19.083
Paleodictyon	UUIC 109	0.914	5.374
Paleodictyon	UJTF 749	0.351	5.009
Megagrapton	UJTF 80a	1.779	13.682
Megagrapton	UJTF 387	7.988	23.495
Megagrapton	UJTF 388	1.343	10.330
Megagrapton	UJTF 390	1.809	12.058
Megagrapton	UJTF 455	1.937	9.225
Megagrapton	UJTF 809	2.797	21.516
Paleodictyon	UJTF 64	0.423	4.695
Paleodictyon	UJTF 158	0.927	10.297
Paleodictyon	UJTF 161	0.767	5.902
Paleodictyon	UJTF 163	0.819	6.826
Paleodictyon	UJTF 164	0.636	6.365
Paleodictyon	UJTF 167	0.765	5.466
Paleodictyon	UJTF 168	0.170	2.839
Paleodictyon	UJTF 171	0.190	2.378
Paleodictyon	UJTF 172-1	0.158	3.943
Paleodictyon	UJTF 172-2	0.145	2.907
Paleodictyon	UJTF 186	0.984	7.570
Paleodictyon	UJTF 294	0.760	6.334
Paleodictyon	UJTF 305	0.796	7.235
Paleodictyon	UJTF 894	0.174	3.482
Paleodictyon	UJTF unk	4.896	16.321
Gordia	UJTF 1249	1.061	6.242

NT	BA	BAV
1.503 ± 0.002	66.7 ± 9.53	272.33
1.315 ± 0.004	Ind	Ind
1.191 ± 0.003	104.1 ± 0.95	153.83
1.254 ± 0.009	94.8 ± 2.68	329.65
1.235 ± 0.001	86.3 ± 2.52	400.77
1.345 ± 0.002	96.4 ± 2.08	299.92
Ind	87.5 ± 2.02	16.33
1.267 ± 0.001	105.5 ± 1.94	121.03
1.276 ± 0.006	94.1 ± 1.91	170.75
Ind	84.6 ± 5.31	140.80
Ind	95.3 ± 2.67	21.33
Ind	86.1 ± 3.33	243.32
1.425 ± 0.013	83.1 ± 4.93	340.13
1.41 ± 0.012	85 ± 4.48	421.35
1.378 ± 0.02	75 ± 4.78	388.50
1.249 ± 0.01	110.4 ± 1.07	57.26
1.346 ± 0.006	100.8 ± 1.35	156.75
1.239 ± 0.004	98.9 ± 1.46	221.36
1.271 ± 0.009	99.3 ± 1.66	223.44
Ind	96.3 ± 1.19	182.88
1.281 ± 0.006	98.9 ± 1.01	172.67
1.222 ± 0.009	97.6 ± 1.68	209.20
1.174 ± 0.004	96.9 ± 0.91	215.53
1.248 ± 0.004	96.5 ± 1.1	218.18
1.435 ± 0.014	95.7 ± 1.86	292.87
1.256 ± 0.004	97.6 ± 1.89	186.36
1.416 ± 0.01	106.7 ± 1	119.26
1.382 ± 0.005	97.7 ± 1.92	133.18
1.272 ± 0.008	99.4 ± 1.69	180.66
1.371 ± 0.012	81.5 ± 7.63	639.67
Ind	58.3 ± 13.38	537.33

Table H.4 continued.

Ichnogenera	Sample ID	C_{Size}	MS
Megagrapton	UJTF 793	1.169	6.494
Paleodictyon	UJTF 63	0.398	5.681
Paleodictyon	UJTF 157	0.350	6.999
Paleodictyon	UJTF 159	0.788	8.753
Paleodictyon	UJTF 304	0.537	7.677
Paleodictyon	UJTF 323	0.209	6.962
Paleodictyon	UUIC 428	0.265	3.318
Megagrapton	Z_Mega1	2.722	16.010
Megagrapton	Z_Mega2	2.988	19.918
Megagrapton	Z_Mega3	3.191	31.911
Megagrapton	Z_Mega4	2.405	20.039
Megagrapton	Z_Mega5	1.828	9.141
Megagrapton	Z_Mega6	1.327	6.634
Megagrapton	Z_Mega7	2.218	11.092
Paleodictyon	Z_Paleo1	0.635	12.706
Paleodictyon	Z_Paleo2	0.315	7.885
Paleodictyon	Z_Paleo3	0.677	8.464
Paleodictyon	Z_Paleo4	0.511	8.513
Paleodictyon	Z_Paleo5	0.541	6.763
Megagrapton	UJTF 640	0.826	8.261
Megagrapton	UJTF 657	0.302	6.039
Megagrapton	UJTF 1873	4.152	5.125
Paleodictyon	UJTF 272	0.652	10.863
Paleodictyon	UJTF 846	0.363	9.083
Paleodictyon	UJTF 89A	0.569	9.489
Paleodictyon	UJTF 188	0.406	10.153
Paleodictyon	UJTF 1102	0.263	5.256
Paleodictyon	UJTF1259	0.395	5.642
Gordia	GSC 81259	0.574	6.378
Paleodictyon	McCann and Pickerill 1988 Fig 5-2	0.342	3.800

NT	BA	BAV
1.461 ± 0.015	76.6 ± 4.16	311.08
Ind	98.2 ± 2.49	222.77
Ind	101.8 ± 1.95	170.36
1.271 ± 0.007	97.3 ± 1.92	260.56
1.231 ± 0.009	102.6 ± 1.16	113.79
1.212 ± 0.003	98.4 ± 2.84	339.36
1.379 ± 0.007	87.5 ± 2	283.31
1.314 ± 0.004	85.2 ± 3.04	304.19
1.334 ± 0.009	85.7 ± 5.11	287.02
1.355 ± 0.002	77.9 ± 3.19	183.52
1.877 ± 0.028	79.9 ± 2.1	154.70
1.818 ± 0.016	80.6 ± 2.07	326.65
1.434 ± 0.014	78 ± 2.88	373.77
1.418 ± 0.017	80.4 ± 2.42	335.02
1.412 ± 0.009	110.6 ± 0.97	30.18
1.205 ± 0.003	105.4 ± 1.42	93.27
1.434 ± 0.023	105.3 ± 2.53	134.03
1.284 ± 0.005	99.8 ± 2.54	200.07
1.291 ± 0.015	104.5 ± 1.04	113.75
1.389 ± 0.005	80.7 ± 2.61	231.86
1.493 ± 0.011	73 ± 3.8	374.64
1.274 ± 0.003	81.6 ± 1.33	8.80
1.352 ± 0.001	85 ± 6.64	616.92
1.346 ± 0.009	93.8 ± 2.69	333.16
Ind	103 ± 1.72	100.70
1.388 ± 0.001	99.6 ± 2.16	219.94
Ind	97.2 ± 0.95	217.90
1.277 ± 0.026	75.2 ± 4.47	579.05
1.688 ± 0.021	73.3 ± 3.71	398.65
1.289 ± 0.013	85.3 ± 1.88	236.65

Table H.4 continued.

Ichnogenera	Sample ID	C_{Size}	MS
Paleodictyon	UJTF 1668	0.351	2.703
Paleodictyon	UJTF 67	0.223	4.467
Paleodictyon	UJTF 92	0.839	5.596
Paleodictyon	UJTF 111	0.134	6.699
Paleodictyon	UJTF 320	0.127	4.237
Paleodictyon	UJTF 324	0.156	3.119
Paleodictyon	UJTF 330	0.247	4.934
Paleodictyon	UJTF 333	0.162	4.038
Paleodictyon	UUIC 1916	0.286	3.226
Paleodictyon	UUIC 1917	0.288	2.881
Paleodictyon	UUIC 1918	0.134	2.229
Paleodictyon	UUIC 1919	0.182	2.272
Megagrapton	UJTF 391	1.895	17.225
Paleodictyon	UJTF 316	0.359	7.188
Gordia	UCMP 398574	0.370	6.160
Megagrapton	UCMP 398582	0.807	5.380
Squamodictyon	UCMP 398595	0.528	6.599
Paleodictyon	UJTF 1172-1	0.239	3.412
Paleodictyon	UJTF 1172-2	0.232	3.868
Squamodictyon	MP-US J1150	1.128	8.675
Paleodictyon	UUIC 1312	1.381	8.631
Paleodictyon	BAN-Jich-0033b	0.184	3.075
Paleodictyon	UUIC 721	1.510	8.390
Paleodictyon	UUIC 1164	1.335	8.342
Gordia	MP-US J1131	0.455	4.134
Gordia	MP-US J1133	0.423	6.049
Paleodictyon	MP-US J1142	1.247	6.562
Paleodictyon	MP-US J1143	0.566	5.656
Paleodictyon	MP-US J1144	0.506	2.663
Paleodictyon	MP-US J1145	0.438	4.378
Megagrapton	BKKM 1-3	1.875	9.870

NT	BA	BAV
1.364 ± 0.013	76.4 ± 3.59	374.24
Ind	93 ± 2.51	359.14
1.494 ± 0.03	104 ± 0.57	142.46
1.3 ± 0.007	94.6 ± 1.32	249.45
1.283 ± 0.015	97.6 ± 4.24	377.25
1.425 ± 0.017	97.1 ± 2.38	226.68
Ind	86.5 ± 2.11	307.90
1.26 ± 0.007	89.4 ± 1.86	326.83
1.228 ± 0.003	80 ± 2.8	469.68
1.223 ± 0.003	101.5 ± 2.3	233.28
1.279 ± 0.001	87.3 ± 1.38	235.67
1.584 ± 0.001	86.7 ± 2.12	396.11
Ind	93.6 ± 4.32	205.45
Ind	90.5 ± 3.46	311.70
1.4 ± 0.009	60.6 ± 3.74	308.24
1.479 ± 0.023	57.2 ± 3.8	188.14
1.461 ± 0.012	75.2 ± 3.71	206.89
1.35 ± 0.004	93.7 ± 1.6	238.54
Ind	91.5 ± 2.06	251.22
Ind	89 ± 5.58	124.67
1.473 ± 0.009	92.6 ± 3.87	358.94
1.332 ± 0.011	82 ± 1.55	344.84
1.278 ± 0.002	107.2 ± 1.35	76.14
1.266 ± 0.007	105.6 ± 2.39	177.38
1.468 ± 0.008	68.3 ± 4.11	422.21
1.533 ± 0.024	65.7 ± 3.51	492.28
1.3 ± 0.01	90.2 ± 2.33	157.33
1.313 ± 0.01	90.2 ± 3.1	383.77
1.208 ± 0.004	94.2 ± 1.3	221.69
1.396 ± 0.01	88.6 ± 1.91	263.40
Ind	91.3 ± 8.2	403.87

Table H.4 continued.

Ichnogenera	Sample ID	C_{Size}	MS
Megagrapton	BKKM 1-10	0.954	6.532
Megagrapton	BKKM 1-24	0.623	4.365
Megagrapton	IKKM 1-4	1.730	7.226
Megagrapton	IKKM 1-5	0.783	5.993
Megagrapton	IKKM 1-6	0.814	7.953
Megagrapton	IKKM 1-12	1.242	6.829
Megagrapton	IKKM 1-15	0.734	5.259
Paleodictyon	IKKM 1-2	1.552	8.813
Paleodictyon	IKKM 1-7	0.587	6.518
Paleodictyon	IKKM 1-8	0.769	5.883
Megagrapton	UW 1495	0.683	4.880
Squamodictyon	Llompart and Wieczorek 1997 Plate II.1	0.938	9.382
Squamodictyon	PIW 891130	0.386	7.715
Megagrapton	PIW 8916	0.639	10.658
Megagrapton	PIW 8919	0.353	5.889
Megagrapton	PIW 89110	0.439	5.485
Megagrapton	PIW 89198b	1.157	7.715
Megagrapton	PIW 891241	1.075	11.944
Megagrapton	PIW 891244	0.579	6.431
Megagrapton	Mikuláš et al 2004 Plate V-2	6.949	21.058
Gordia	NBMG 9683	1.152	8.230
Gordia	Crimes and Crossley 1991 Fig 9a	13.865	16.909
Gordia	NMW 90.44G.14	1.863	6.902
Paleodictyon	Crimes and Crossley 1991 Fig 9c	1.918	4.678

NT	BA	BAV
1.389 ± 0.009	79.9 ± 5.32	453.45
1.54 ± 0.029	67.2 ± 3.68	378.69
Ind	84 ± 8.91	397.00
1.261 ± 0.003	77.7 ± 2.49	427.11
1.5 ± 0.004	71.1 ± 2.45	359.84
Ind	82.3 ± 4	287.41
1.543 ± 0.005	70.2 ± 3.8	347.04
1.313 ± 0.005	83.5 ± 4.43	470.26
1.583 ± 0.013	88.5 ± 5.46	357.36
1.727 ± 0.027	90.3 ± 4.78	343.21
1.413 ± 0.007	81.4 ± 4.81	393.01
1.288 ± 0.004	77.9 ± 3.79	359.69
1.518 ± 0.021	63.7 ± 5.67	513.56
1.295 ± 0.008	87.7 ± 5.81	405.33
1.472 ± 0.041	81.4 ± 3.25	443.47
1.724 ± 0.002	69.3 ± 6.96	581.84
1.533 ± 0.059	70.7 ± 4.66	326.38
1.292 ± 0.017	73.3 ± 4.95	342.99
1.43 ± 0.021	79.2 ± 3.23	333.81
1.447 ± 0.032	84.2 ± 4.27	109.37
1.435 ± 0.011	70.2 ± 4.12	424.72
Ind	Ind	Ind
1.273 ± 0.011	66.7 ± 1.83	332.38
Ind	87.4 ± 2.3	424.89

Table H.4 continued.

Ichnogenera	Sample ID	C_{Size}	MS
Paleodictyon	Crimes and Crossley 1991 Fig 9d	5.867	17.256
Paleodictyon	Crimes and Crossley 1991 Fig 9e	2.633	9.405
Paleodictyon	Crimes and Crossley 1991 Fig 9f	6.021	23.157
Paleodictyon	Crimes and Crossley 1991 Fig 13a	4.536	8.399
Paleodictyon	Crimes and Crossley 1991 Fig 13b	5.580	17.438
Paleodictyon	Crimes and Crossley 1991 Fig 13c	2.674	7.036
Squamodictyon	Crimes and Crossley 1991 Fig 13e	4.199	10.241
Squamodictyon	Crimes and Crossley 1991 Fig 17c	3.013	9.415
Squamodictyon	GPIT 1503/2	2.230	10.138
Squamodictyon	NMW 90.44G.6	1.511	8.891
Squamodictyon	NMW 90.44G.7	1.777	6.581
Squamodictyon	NMW 90.44G.8	2.199	6.871
Squamodictyon	NMW 90.44G.10	2.055	8.933
Squamodictyon	NMW 90.44G.16	1.614	7.338
Squamodictyon	NMW 90.44G.17	2.858	11.431
Squamodictyon	NMW 90.44G.18	2.345	8.684

NT	BA	BAV
Ind	93.6 ± 5.72	686.55
1.26 ± 0.004	95 ± 3.99	365.95
1.336 ± 0.01	92.6 ± 6.96	435.78
1.383 ± 0.012	88.5 ± 4.19	227.77
1.331 ± 0.008	97.8 ± 4.11	219.69
Ind	90.4 ± 2.98	328.69
1.335 ± 0.008	78.4 ± 3.2	378.31
1.304 ± 0.003	71.7 ± 4.3	590.87
1.415 ± 0.009	80.1 ± 4.23	286.33
1.405 ± 0.012	75.1 ± 2.29	384.21
1.329 ± 0.021	76.2 ± 2.28	312.15
1.545 ± 0.024	69.2 ± 3.39	460.34
1.448 ± 0.007	74.4 ± 5.08	335.59
1.283 ± 0.002	76.6 ± 3.57	357.29
1.343 ± 0.006	81.6 ± 3.92	306.68
1.385 ± 0.004	80 ± 2.94	258.90

Table H.4 continued.

Ichnogenera	Sample ID	C_{Size}	MS
Squamodictyon	NMW 90.44G.19	1.749	6.727
Squamodictyon	NMW 90.44G.20	1.848	6.601
Megagrapton	RSM 1981.30.68	0.918	11.480
Gordia	RSM 1981.30.100	1.825	9.608
Paleodictyon	UEGIG 46275	1.104	18.405
Gordia	Acenolaza 1978 Lam III-3	0.838	5.986
Paleodictyon	Acenolaza 1978 Lam III-1	0.492	4.916
Gordia	Pickerill 1981 Fig 2d	2.781	46.342
Gordia	Pickerill 1981 Fig 3a	0.805	5.369
Gordia	Crimes et al 1992 Fig 2E	0.897	5.979
Gordia	Crimes et al 1992 Fig 2F	0.681	4.004
Paleodictyon	Pickerill 1980 Fig 2f	0.583	4.857
Megagrapton	Pickerill et al 1988 Fig 2e	2.143	8.571
Gordia	A40389-1	0.064	3.225
Gordia	A40389-2	0.112	5.575
Gordia	Acenolaza 1978 Fig 10	2.209	10.040
Gordia	Acenolaza and Torelli 1981 pg 57-1	5.339	13.691
Gordia	Crimes and Anderson 1985 Fig 5.7	0.794	9.922
Squamodictyon	Crimes and Anderson 1985 Fig 10.4	1.893	6.762

NT	BA	BAV
1.455 ± 0.014	74.2 ± 3.46	383.43
1.321 ± 0.011	74.1 ± 3.48	278.99
1.292 ± 0.01	65.2 ± 3.98	380.26
1.265 ± 0.014	63.4 ± 3.57	369.39
1.312 ± 0.002	89.9 ± 2.42	229.05
1.37 ± 0.006	53.1 ± 4.97	542.66
Ind	84.5 ± 3.59	386.46
1.519 ± 0.015	56.6 ± 6.9	428.03
1.573 ± 0.021	47.3 ± 8.46	644.75
1.345 ± 0.005	55.2 ± 3.56	418.61
1.329 ± 0.005	61.9 ± 6.02	398.49
1.215 ± 0.006	94.3 ± 1.48	196.98
1.326 ± 0.004	74.1 ± 3.1	134.69
1.966 ± 0.049	44.9 ± 4.46	337.68
1.57 ± 0.011	50.6 ± 7.42	385.62
1.448 ± 0.015	48.4 ± 6.43	331.13
1.323 ± 0.01	58 ± 16.5	817.00
1.262 ± 0.005	55.9 ± 3.98	349.32
1.41 ± 0.011	66.8 ± 6.55	214.70

Table H.4 continued.

Ichnogenera	Sample ID	$S_{Average}$	$S_{Variance}$	S_{Mode}
Paleodictyon	INMD 128BX-1	5.70	0.46	6
Paleodictyon	INMD 128BX-2	5.00	0.40	5
Paleodictyon	VOTD-3957	6.00	0.00	6
Paleodictyon	VOTD-4001	6.00	0.00	6
Paleodictyon	VOTD-4003	6.00	0.00	6
Paleodictyon	VOTD-4006	6.00	0.00	6
Paleodictyon	VOTD-4009	6.00	0.00	6
Paleodictyon	VOTD-4012	6.00	0.00	6
Paleodictyon	VBPaleo1	6.00	0.00	6
Paleodictyon	VBPaleo2	5.86	0.33	6
Paleodictyon	VBPaleo3	6.00	0.00	6
Paleodictyon	VBPaleo4	5.64	0.55	6
Paleodictyon	VBPale4b	Ind	Ind	Ind
Paleodictyon	VBPaleo5	5.83	0.17	6
Paleodictyon	VBPaleo6	6.00	0.12	6
Paleodictyon	VBPaleo6b	5.80	0.18	6
Paleodictyon	VBPaleo7	6.00	0.00	6
Paleodictyon	CM 22	6.06	0.06	6
Paleodictyon	FG 1	5.28	0.46	5
Paleodictyon	FG 5	5.33	0.35	5
Paleodictyon	UUIC 722	Ind	Ind	Ind
Paleodictyon	PIW1993X 50	6.00	0.00	6
Paleodictyon	PIW1993X 56	5.57	0.29	6
Paleodictyon	PIW1993X 59	5.92	0.08	6
Paleodictyon	PIW1993X 61	5.83	0.97	6
Paleodictyon	PIW1993X 68	6.00	0.29	6
Gordia	UJTF 245	3.35	0.96	3
Gordia	UJTF 1219	2.75	0.25	3
Paleodictyon	UJTF 835-1	5.00	0.50	5
Paleodictyon	UJTF 835-2	4.17	1.37	3
Paleodictyon	UJTF unk	6.00	0.09	6

D_{Box}	OSP	BAS	$BAS_{Trimmed}$
1.67 ± 0.01	18.2%	0.942	NA
1.699 ± 0.008	22.2%	0.834	NA
1.563 ± 0.012	11.1%	0.965	NA
1.509 ± 0.012	8.2%	0.912	NA
1.541 ± 0.019	8.2%	0.970	NA
1.488 ± 0.019	5.6%	0.948	NA
1.49 ± 0.012	7.7%	0.947	NA
1.466 ± 0.018	6.2%	0.934	NA
1.658 ± 0.006	18.9%	0.825	NA
1.668 ± 0.005	23.1%	0.610	NA
1.677 ± 0.012	18.7%	0.918	NA
1.608 ± 0.006	17.7%	0.775	NA
1.648 ± 0.013	16.4%	0.880	NA
1.689 ± 0.016	17.4%	0.914	NA
1.711 ± 0.007	25.5%	0.599	NA
1.67 ± 0.012	17.6%	0.921	NA
1.596 ± 0.009	21.6%	0.821	NA
1.608 ± 0.005	18.2%	0.698	NA
1.686 ± 0.002	28.9%	0.735	NA
1.712 ± 0.005	26.3%	0.874	NA
1.42 ± 0.01	10.5%	0.261	NA
1.654 ± 0.008	18.6%	0.887	NA
1.758 ± 0.011	22.6%	0.937	NA
1.688 ± 0.009	21.8%	0.889	NA
1.719 ± 0.015	17.3%	0.926	NA
1.64 ± 0.012	16.3%	0.962	NA
1.588 ± 0.003	18.1%	0.535	NA
1.415 ± 0.004	9.5%	0.168	0.583
1.467 ± 0.006	12.6%	0.387	0.736
1.501 ± 0.007	14.1%	0.577	NA
1.572 ± 0.018	12.3%	0.466	NA

Table H.4 continued.

Ichnogenera	Sample ID	$S_{Average}$	$S_{Variance}$	S_{Mode}
Gordia	IGP t.f. 71b	Ind	Ind	Ind
Gordia	IGP t.f. 184a	Ind	Ind	Ind
Paleodictyon	UJTF 78	6.00	0.00	6
Paleodictyon	UJTF 89	6.00	0.20	6
Paleodictyon	UJTF 101	5.95	0.05	6
Paleodictyon	UJTF 113	5.79	0.40	6
Megagrapton	UJTF 985	Ind	Ind	Ind
Paleodictyon	UUIC 109	6.00	0.00	6
Paleodictyon	UJTF 749	6.00	0.20	6
Megagrapton	UJTF 80a	Ind	Ind	Ind
Megagrapton	UJTF 387	Ind	Ind	Ind
Megagrapton	UJTF 388	Ind	Ind	Ind
Megagrapton	UJTF 390	Ind	Ind	Ind
Megagrapton	UJTF 455	Ind	Ind	Ind
Megagrapton	UJTF 809	Ind	Ind	Ind
Paleodictyon	UJTF 64	6.00	0.00	6
Paleodictyon	UJTF 158	5.96	0.19	6
Paleodictyon	UJTF 161	6.00	0.08	6
Paleodictyon	UJTF 163	6.08	0.24	6
Paleodictyon	UJTF 164	6.00	0.17	6
Paleodictyon	UJTF 167	5.82	0.28	6
Paleodictyon	UJTF 168	5.77	0.42	6
Paleodictyon	UJTF 171	5.73	0.33	6
Paleodictyon	UJTF 172-1	6.00	0.00	6
Paleodictyon	UJTF 172-2	5.70	0.33	6
Paleodictyon	UJTF 186	6.08	0.08	6
Paleodictyon	UJTF 294	5.92	0.08	6
Paleodictyon	UJTF 305	6.00	0.00	6
Paleodictyon	UJTF 894	6.00	0.00	6
Paleodictyon	UJTF unk	Ind	Ind	Ind
Gordia	UJTF 1249	Ind	Ind	Ind

D_{Box}	OSP	BAS	$BAS_{Trimmed}$
1.408 ± 0.014	6.2%	0.750	NA
1.477 ± 0.027	7.8%	0.354	0.796
1.689 ± 0.003	24.6%	0.951	NA
1.602 ± 0.006	16.9%	0.774	NA
1.635 ± 0.006	17.8%	0.885	NA
1.635 ± 0.005	19.5%	0.892	NA
1.509 ± 0.033	3.1%	0.943	NA
1.643 ± 0.012	16.5%	0.879	NA
1.598 ± 0.009	16.1%	0.736	NA
1.504 ± 0.028	4.7%	0.952	NA
1.521 ± 0.034	1.9%	0.965	NA
Ind	Ind	0.647	NA
1.438 ± 0.018	5.9%	0.783	NA
1.399 ± 0.02	6.2%	0.741	NA
1.352 ± 0.014	3.9%	0.859	NA
1.686 ± 0.008	20.6%	0.894	NA
1.486 ± 0.005	9.6%	0.460	0.904
1.513 ± 0.004	13.2%	0.518	NA
1.483 ± 0.006	11.1%	0.555	NA
1.512 ± 0.004	12.6%	0.504	NA
1.601 ± 0.003	18.5%	0.530	NA
1.723 ± 0.006	30.9%	0.480	0.901
1.703 ± 0.006	36.5%	0.218	0.717
1.69 ± 0.002	29.1%	0.604	NA
1.728 ± 0.004	31.1%	0.699	NA
1.562 ± 0.009	12.6%	0.801	NA
1.522 ± 0.004	13.2%	0.506	NA
1.615 ± 0.016	13.0%	0.944	NA
1.689 ± 0.005	25.4%	0.724	NA
1.546 ± 0.028	4.4%	0.977	NA
1.609 ± 0.018	11.8%	0.875	NA

Table H.4 continued.

Ichnogenera	Sample ID	$S_{Average}$	$S_{Variance}$	S_{Mode}
Megagrapton	UJTF 793	Ind	Ind	Ind
Paleodictyon	UJTF 63	6.00	0.00	6
Paleodictyon	UJTF 157	5.80	0.20	6
Paleodictyon	UJTF 159	6.00	0.00	6
Paleodictyon	UJTF 304	6.00	0.00	6
Paleodictyon	UJTF 323	6.00	0.00	6
Paleodictyon	UUIC 428	5.47	0.51	6
Megagrapton	Z_Mega1	6.00	0.51	6
Megagrapton	Z_Mega2	5.25	0.00	5
Megagrapton	Z_Mega3	5.50	0.25	5
Megagrapton	Z_Mega4	5.00	0.70	4
Megagrapton	Z_Mega5	5.13	1.00	5
Megagrapton	Z_Mega6	5.13	0.55	5
Megagrapton	Z_Mega7	5.19	0.38	5
Paleodictyon	Z_Paleo1	6.00	0.43	6
Paleodictyon	Z_Paleo2	6.00	0.00	6
Paleodictyon	Z_Paleo3	6.00	0.00	6
Paleodictyon	Z_Paleo4	6.00	0.00	6
Paleodictyon	Z_Paleo5	6.00	0.00	6
Megagrapton	UJTF 640	5.00	4.67	Ind
Megagrapton	UJTF 657	4.00	4.67	Ind
Megagrapton	UJTF 1873	Ind	Ind	Ind
Paleodictyon	UJTF 272	5.33	0.33	5
Paleodictyon	UJTF 846	5.83	0.17	6
Paleodictyon	UJTF 89A	6.00	0.50	6
Paleodictyon	UJTF 188	Ind	Ind	Ind
Paleodictyon	UJTF 1102	5.81	0.33	6
Paleodictyon	UJTF1259	4.80	0.20	5
Gordia	GSC 81259	3.67	2.25	4
Paleodictyon	McCann and Pickerill 1988 Fig 5-2	5.59	0.26	6

D_{Box}	OSP	BAS	$BAS_{Trimmed}$
1.569 ± 0.015	12.0%	0.832	NA
1.518 ± 0.015	12.4%	0.331	NA
1.416 ± 0.013	8.5%	0.332	NA
1.514 ± 0.005	13.5%	0.404	0.802
1.44 ± 0.005	9.7%	0.326	0.778
1.482 ± 0.009	13.1%	0.430	0.725
1.667 ± 0.008	24.1%	0.526	NA
1.423 ± 0.01	5.9%	0.842	NA
1.457 ± 0.02	4.9%	0.955	NA
1.344 ± 0.011	3.1%	0.953	NA
1.399 ± 0.011	5.0%	0.965	NA
1.491 ± 0.005	10.8%	0.628	NA
1.562 ± 0.008	13.3%	0.788	NA
1.511 ± 0.008	9.6%	0.920	NA
1.468 ± 0.017	6.3%	0.943	NA
1.588 ± 0.011	12.7%	0.937	NA
1.507 ± 0.013	9.7%	0.833	NA
1.507 ± 0.011	10.5%	0.828	NA
1.478 ± 0.008	13.4%	0.674	NA
1.459 ± 0.009	8.7%	0.736	NA
1.585 ± 0.01	14.0%	0.911	NA
1.698 ± 0.022	12.0%	0.936	NA
1.501 ± 0.016	7.3%	0.873	NA
1.488 ± 0.009	9.2%	0.676	NA
Ind	Ind	0.843	NA
1.398 ± 0.009	6.9%	0.402	0.753
1.512 ± 0.001	15.2%	0.174	0.402
1.552 ± 0.009	14.5%	0.592	NA
1.523 ± 0.005	12.8%	0.796	NA
1.692 ± 0.005	25.7%	0.912	NA

Table H.4 continued.

Ichnogenera	Sample ID	$S_{Average}$	$S_{Variance}$	S_{Mode}
Paleodictyon	UJTF 1668	5.00	1.00	4
Paleodictyon	UJTF 67	6.00	0.00	6
Paleodictyon	UJTF 92	6.00	0.00	6
Paleodictyon	UJTF 111	5.89	0.10	6
Paleodictyon	UJTF 320	6.00	0.00	6
Paleodictyon	UJTF 324	5.55	0.47	5
Paleodictyon	UJTF 330	5.55	1.07	6
Paleodictyon	UJTF 333	5.68	0.69	6
Paleodictyon	UUIC 1916	5.60	0.25	6
Paleodictyon	UUIC 1917	5.86	0.13	6
Paleodictyon	UUIC 1918	5.43	0.52	6
Paleodictyon	UUIC 1919	5.48	0.26	5
Megagrapton	UJTF 391	Ind	Ind	Ind
Paleodictyon	UJTF 316	Ind	Ind	Ind
Gordia	UCMP 398574	3.22	1.44	3
Megagrapton	UCMP 398582	3.75	0.25	4
Squamodictyon	UCMP 398595	Ind	Ind	Ind
Paleodictyon	UJTF 1172-1	5.50	0.28	6
Paleodictyon	UJTF 1172-2	5.67	0.75	6
Squamodictyon	MP-US J1150	Ind	Ind	Ind
Paleodictyon	UUIC 1312	5.86	0.14	6
Paleodictyon	BAN-Jich-0033b	5.62	0.46	6
Paleodictyon	UUIC 721	6.00	0.00	6
Paleodictyon	UUIC 1164	6.00	0.00	6
Gordia	MP-US J1131	3.33	0.27	3
Gordia	MP-US J1133	4.11	0.61	4
Paleodictyon	MP-US J1142	6.00	0.00	6
Paleodictyon	MP-US J1143	5.80	0.18	6
Paleodictyon	MP-US J1144	5.84	0.33	6
Paleodictyon	MP-US J1145	5.85	0.14	6
Megagrapton	BKKM 1-3	Ind	Ind	Ind

D_{Box}	OSP	BAS	$BAS_{Trimmed}$
1.743 ± 0.004	31.3%	0.804	NA
1.523 ± 0.005	16.4%	0.311	NA
1.596 ± 0.007	17.1%	0.486	NA
1.58 ± 0.002	17.8%	0.420	0.537
1.705 ± 0.014	19.3%	0.872	NA
1.718 ± 0.006	26.4%	0.741	NA
1.527 ± 0.007	13.7%	0.497	NA
1.688 ± 0.004	25.8%	0.736	NA
1.75 ± 0.004	31.0%	0.852	NA
1.669 ± 0.008	19.7%	0.850	NA
1.822 ± 0.003	47.3%	0.794	NA
1.761 ± 0.005	38.5%	0.616	NA
1.351 ± 0.016	Ind	0.756	NA
Ind	Ind	0.540	NA
1.499 ± 0.008	11.9%	0.571	NA
1.551 ± 0.01	13.8%	0.623	NA
1.611 ± 0.013	13.0%	0.868	NA
1.608 ± 0.006	22.1%	0.239	0.604
1.613 ± 0.005	19.0%	0.715	NA
1.519 ± 0.026	7.3%	0.778	NA
1.574 ± 0.016	10.4%	0.924	NA
1.696 ± 0.003	31.7%	0.408	0.752
1.537 ± 0.011	11.1%	0.910	NA
1.576 ± 0.018	10.1%	0.811	NA
1.536 ± 0.005	15.0%	0.647	NA
1.542 ± 0.005	13.9%	0.695	NA
1.638 ± 0.017	13.1%	0.958	NA
1.673 ± 0.01	18.4%	0.959	NA
1.756 ± 0.002	36.7%	0.684	NA
1.649 ± 0.006	20.7%	0.703	NA
1.518 ± 0.026	6.3%	0.866	NA

Table H.4 continued.

Ichnogenera	Sample ID	$S_{Average}$	$S_{Variance}$	S_{Mode}
Megagrapton	BKKM 1-10	Ind	Ind	Ind
Megagrapton	BKKM 1-24	3.33	0.33	3
Megagrapton	IKKM 1-4	Ind	Ind	Ind
Megagrapton	IKKM 1-5	5.36	0.86	6
Megagrapton	IKKM 1-6	5.18	0.76	6
Megagrapton	IKKM 1-12	3.75	0.25	4
Megagrapton	IKKM 1-15	3.60	0.80	3
Paleodictyon	IKKM 1-2	5.67	0.67	5
Paleodictyon	IKKM 1-7	Ind	Ind	Ind
Paleodictyon	IKKM 1-8	Ind	Ind	Ind
Megagrapton	UW 1495	3.75	5.58	2
Squamodictyon	Llompart and Wieczorek 1997 Plate II.1	4.86	2.81	4
Squamodictyon	PIW 891130	Ind	Ind	Ind
Megagrapton	PIW 8916	Ind	Ind	Ind
Megagrapton	PIW 8919	4.56	0.53	4
Megagrapton	PIW 89110	Ind	Ind	Ind
Megagrapton	PIW 89198b	4.00	0.00	4
Megagrapton	PIW 891241	5.67	0.33	6
Megagrapton	PIW 891244	5.17	2.57	4
Megagrapton	Mikuláš et al 2004 Plate V-2	Ind	Ind	Ind
Gordia	NBMG 9683	3.58	1.72	2
Gordia	Crimes and Crossley 1991 Fig 9a	Ind	Ind	Ind
Gordia	NMW 90.44G.14	3.75	1.35	3
Paleodictyon	Crimes and Crossley 1991 Fig 9c	Ind	Ind	Ind

D_{Box}	OSP	BAS	$BAS_{Trimmed}$
1.557 ± 0.016	11.0%	0.855	NA
1.606 ± 0.008	17.7%	0.872	NA
1.566 ± 0.031	7.6%	0.941	NA
1.589 ± 0.004	16.5%	0.827	NA
1.481 ± 0.005	10.4%	0.685	NA
1.51 ± 0.018	9.7%	0.832	NA
1.536 ± 0.008	13.6%	0.767	NA
1.561 ± 0.014	10.2%	0.927	NA
1.61 ± 0.021	10.7%	0.913	NA
1.55 ± 0.011	12.5%	0.785	NA
1.642 ± 0.013	16.1%	0.878	NA
1.547 ± 0.014	9.6%	0.909	NA
1.499 ± 0.013	10.1%	0.805	NA
1.515 ± 0.024	6.9%	0.869	NA
1.574 ± 0.004	15.4%	0.709	NA
1.494 ± 0.014	10.6%	0.664	NA
1.487 ± 0.013	8.9%	0.749	NA
1.538 ± 0.022	6.7%	0.970	NA
1.542 ± 0.016	11.0%	0.593	NA
1.474 ± 0.03	3.2%	0.949	NA
1.505 ± 0.007	10.6%	0.759	NA
1.488 ± 0.025	4.6%	0.943	NA
1.566 ± 0.004	15.0%	0.779	NA
1.488 ± 0.004	13.0%	0.205	0.563

Table H.4 continued.

Ichnogenera	Sample ID	$S_{Average}$	$S_{Variance}$	S_{Mode}
Paleodictyon	Crimes and Crossley 1991 Fig 9d	Ind	Ind	Ind
Paleodictyon	Crimes and Crossley 1991 Fig 9e	Ind	Ind	Ind
Paleodictyon	Crimes and Crossley 1991 Fig 9f	Ind	Ind	Ind
Paleodictyon	Crimes and Crossley 1991 Fig 13a	Ind	Ind	Ind
Paleodictyon	Crimes and Crossley 1991 Fig 13b	Ind	Ind	Ind
Paleodictyon	Crimes and Crossley 1991 Fig 13c	Ind	Ind	Ind
Squamodictyon	Crimes and Crossley 1991 Fig 13e	5.20	2.62	5
Squamodictyon	Crimes and Crossley 1991 Fig 17c	5.36	1.45	5
Squamodictyon	GPIT 1503/2	5.33	0.33	5
Squamodictyon	NMW 90.44G.6	5.10	2.39	6
Squamodictyon	NMW 90.44G.7	5.25	1.40	6
Squamodictyon	NMW 90.44G.8	4.70	0.90	5
Squamodictyon	NMW 90.44G.10	Ind	Ind	Ind
Squamodictyon	NMW 90.44G.16	5.50	3.14	4
Squamodictyon	NMW 90.44G.17	6.00	4.00	Ind
Squamodictyon	NMW 90.44G.18	5.11	0.86	5

D_{Box}	OSP	BAS	$BAS_{Trimmed}$
Ind	Ind	0.626	NA
1.459 ± 0.019	6.7%	0.933	NA
1.46 ± 0.026	3.1%	0.949	NA
1.564 ± 0.023	8.3%	0.951	NA
1.417 ± 0.027	3.9%	0.943	NA
1.469 ± 0.019	8.4%	0.527	NA
1.527 ± 0.009	9.9%	0.894	NA
1.549 ± 0.01	10.9%	0.927	NA
1.562 ± 0.022	8.5%	0.968	NA
1.537 ± 0.004	12.2%	0.885	NA
1.578 ± 0.006	14.7%	0.833	NA
1.582 ± 0.006	14.5%	0.769	NA
1.54 ± 0.017	9.5%	0.850	NA
1.593 ± 0.011	13.3%	0.934	NA
1.504 ± 0.02	7.6%	0.947	NA
1.527 ± 0.011	10.3%	0.919	NA

Table H.4 continued.

Ichnogenera	Sample ID	$S_{Average}$	$S_{Variance}$	S_{Mode}	D_{Box}	OSP	BAS	$BAS_{Trimmed}$
Squamodictyon	NMW 90.44G.19	4.67	3.07	4	1.595 ± 0.01	13.9%	0.893	NA
Squamodictyon	NMW 90.44G.20	5.43	1.62	6	1.583 ± 0.011	13.3%	0.840	NA
Megagrapton	RSM 1981.30.68	4.63	1.98	5	1.486 ± 0.011	8.2%	0.777	NA
Gordia	RSM 1981.30.100	3.91	1.89	3	1.528 ± 0.009	10.3%	0.914	NA
Paleodictyon	UEGIG 46275	5.89	0.86	6	1.44 ± 0.009	6.3%	0.956	NA
Gordia	Acenolaza 1978 Lam III-3	2.78	0.94	2	1.581 ± 0.008	14.7%	0.876	NA
Paleodictyon	Acenolaza 1978 Lam III-1	Ind	Ind	Ind	1.502 ± 0.009	12.5%	0.582	NA
Gordia	Pickerill 1981 Fig 2d	3.25	0.25	3	1.496 ± 0.009	9.4%	0.932	NA
Gordia	Pickerill 1981 Fig 3a	Ind	Ind	Ind	1.595 ± 0.017	13.0%	0.884	NA
Gordia	Crimes et al 1992 Fig 2E	3.94	0.56	4	1.557 ± 0.005	15.4%	0.533	NA
Gordia	Crimes et al 1992 Fig 2F	3.33	0.33	3	1.681 ± 0.014	19.1%	0.888	NA
Paleodictyon	Pickerill 1980 Fig 2f	5.97	0.03	6	1.673 ± 0.005	22.3%	0.891	NA
Megagrapton	Pickerill et al 1988 Fig 2e	Ind	Ind	Ind	1.522 ± 0.019	8.5%	0.942	NA
Gordia	A40389-1	3.40	1.30	3	1.708 ± 0.007	25.6%	0.959	NA
Gordia	A40389-2	Ind	Ind	Ind	1.565 ± 0.02	10.2%	0.937	NA
Gordia	Acenolaza 1978 Fig 10	2.75	0.25	3	1.445 ± 0.011	7.6%	0.722	NA
Gordia	Acenolaza and Torelli 1981 pg 57-1	Ind	Ind	Ind	1.449 ± 0.031	4.7%	0.925	NA
Gordia	Crimes and Anderson 1985 Fig 5.7	3.81	0.96	3	1.472 ± 0.006	9.2%	0.789	NA
Squamodictyon	Crimes and Anderson 1985 Fig 10.4	Ind	Ind	Ind	1.603 ± 0.028	8.7%	0.916	NA

APPENDIX I

SAMPLE IDENTIFICATION AND ANALYTICAL PROCEDURAL ADJUSTMENTS

Several of the analyses performed as described in Lehane and Ekdale (2014) have been adjusted based on repeated measurements to improve the quality of the data. These adjustments along with the procedure for naming the samples are described below.

I.1 Procedure for sample identifications

All samples were identified by the museum IDs where the samples are housed, if the samples were housed in a museum and the ID was known. Museum samples that did not have an identification number were just referred to their museum ID followed by "unk". For samples obtained from the literature, museum IDs were used if they were published; if not the samples were identified by the last names of the author(s), the year published, and the figure number of the specimen. If multiple specimens contained the same museum ID, then the samples were denoted with the museum ID, a dash (-), and a number starting with 1 and going up from there. Samples photographed in the field were identified with an abbreviation of the field locality (i.e., Z for Zumaia, VB for Vera Basin), a shortened species name, and a sequential numbering system.

I.2 Procedures for analyses

Generally, analyses were carried out as described in a previous publication (Lehane and Ekdale, 2014). However, there were some modifications to those procedures as described below. For a review of the consistency of the analytical results, please refer to Appendix K.

I.2.1 Meandering forms

For the meandering forms analyses it was determined that the burrow spacing for meandering forms should be equal to the average wavelength. To calculate out the average wavelength, the average half-wavelength was calculated by measuring the distance between the amplitudes along the midline of the burrow. The half-wavelength was then doubled to determine the full wavelength. If there is not enough information to calculate the amplitude, the half-wavelength was calculated by measuring the average distance between known adjacent burrows, and then doubled.

The method for calculating out the tortuosity produces segments of lines that are not exactly the length being measure (i.e., 5 cm, 10 cm, etc.). Therefore, each value in the spreadsheet (Appendix F) takes into effect a range of values. The smallest value being measured, the 5.0 cm range, includes line segments from 2.5 cm to 5.0 cm in length. The segment values continue as such: 5.1 to 10.0 cm (10 cm), 10.1 to 15.0 cm (15 cm), 15.1 to 20.0 cm (20 cm), 20.1 to 25.0 cm (25 cm), and 25.1 to 32.5 cm (30 cm) in length.

I.2.2 Spiraling forms

Calculations of tortuosity were adjusted according to the method in the meandering forms in the same manner.

I.2.3. Branching forms

For the branching forms, the motility index (MI) was calculated much the same as it was for the meandering forms. However, only the main trunk of the trace was used for the calculations. The main trunk was determined to be the series of branches that

produced the longest continuous trace. As for the meandering forms, the burrow spacing also was calculated using the average wavelength. To create a more reliable measurement of the branching angle, the results of the branching angles were only reported if there were at least three clearly measurable branches available. For samples with less than three branches, the analyses were denoted as indeterminate. Calculations of tortuosity were adjusted according to the method in the meandering forms in the same manner.

I.2.4 Network forms

For the network forms, the weighted average of cell sides ($S_{Average}$), the variance in cell sides ($S_{Variance}$), and the mode in cell sides (S_{Mode}) were only calculated for samples were three clearly defined cells could be measured. For samples with less than three, the analyses were denoted as indeterminate. Network tortuosity was calculated by using progressively smaller boxes, each of which was reduced in size by 150 pixels on each edge. If the network tortuosity values did not level out, then they were either thrown out or the image was cropped to ensure that the center of the image was where the main portion of the trace fossil was located. As mentioned for the branching forms, the branching angles were only calculated for samples where at least three clearly measurable branches were available. For samples with less than three branches, the analyses were denoted as indeterminate. During measuring of the branching angles it was noticed that reproducibility of an individual measurement was within ± 2.5° (a range of 5°).

APPENDIX J

NETWORK TORTUOSITY EXTENDED MATLAB SCRIPT

J.1 Network tortuosity script update

Previous employment of the network tortuosity (NT) script (Lehane and Ekdale, 2014) involved reiterating the script for each generation of the image, slowly shrinking the size of the analysis box. This process was continued until either the entire image was analyzed or 10 iterations were performed, where each iteration was a box size of 300 pixels smaller in each direction. The current version of the script does this process for the user, with inputs that include the location of the image being analyzed and the original dimensions of the image. The script then produces an image with the original image analyzed and a graphical interpretation of the tortuosity through the image. Next to the images are the resulting NT of the vertical and the horizontal directions across the image as well as an average of the two. These NT values are listed for each of the 10 runs (Fig. J.1).

The analyses are designed to run on an image of a white trace on a black background; however this can be switched as described in the code. The other image parameters are a grayscale, bitmap image (BMP). For these analyses all images were performed at 500 dpi with a long side of 19 cm (7.5") and a short side dependent on the individual image. The visualizing of the output is affected by the periodicity input of the script. This affects how close together the gray to black bands on the second image in the output is. Changing this number does not alter the resulting NT. The initial value is set at 18 but can be altered to the user's preference.

J.1.1 Matlab updated network tortuosity (NT) script

```
% This algorithm calculates the network tortuosity in images. It is
% based on the script used in 'The determination of relative path
% length as a measure for tortuosity in compacts using image analysis',
```

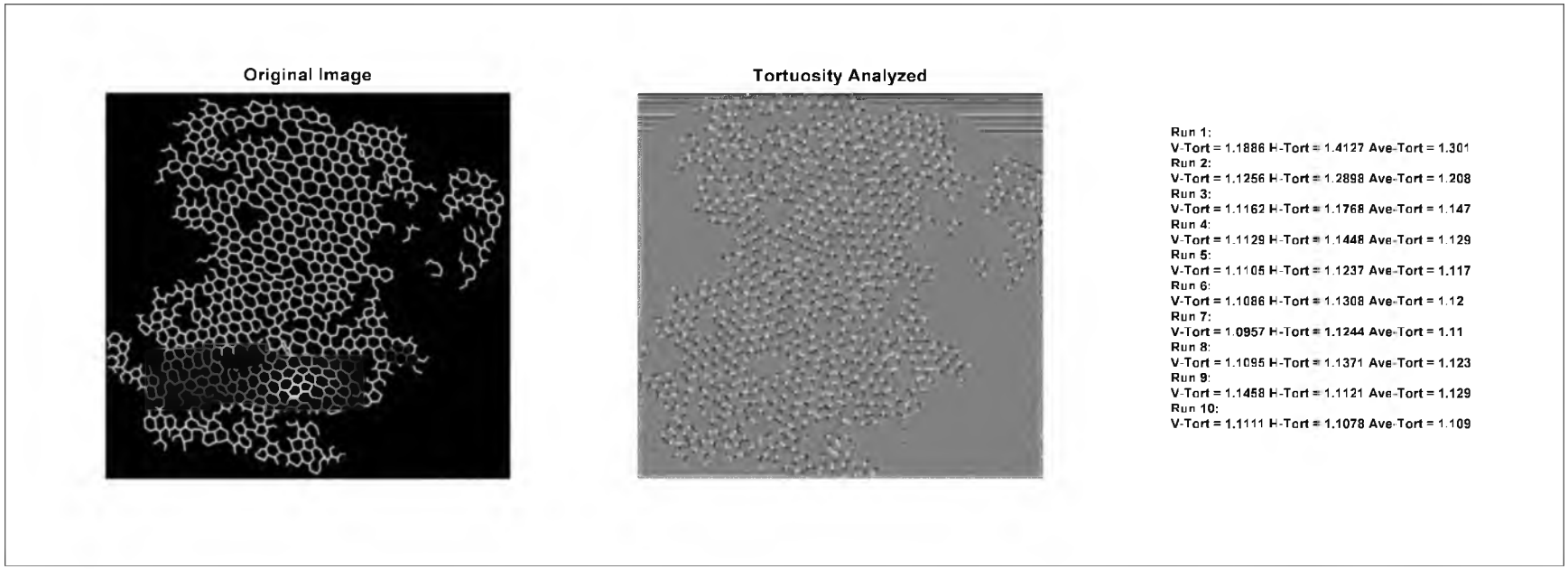

Figure J.1. Output of the Matlab script for the network tortuosity, highlighting the results for each of the 10 runs with decreasing analytical box size.

```
% Eur.J.Pharm.Sci. 2006, 28 (5): 433-440 and Lehane and Ekdale (in
% press). For more information on DIPimage see www.diplib.org

clc;                %Clears workspace
clear all;          %Delete all variables
close all;          %Close all windows except those created by imtool
imtool close all;   %Close all figure windows created by imtool
workspace;          %Make sure the workspace panel is showing
fontSize = 14;

% Pull in original image in MATLAB in 8-bit grayscale, reverse image
%(or see line 19), 500 DPI, file format = jpg, bmp, or tif
grayImage = imread('C:\document.bmp');
a = dip_image(grayImage);

% Insert original dimensions
ODx = 3751;
ODy = 3577;

OriginalSize_b1 = (ODx-150);
OriginalSize_d1 = (ODy-150);
OriginalSize_a1 = (150);
OriginalSize_c1 = (150);

% Select a square image set away from the edge to remove any edge-
% effect
a = a(OriginalSize_a1:OriginalSize_b1,OriginalSize_c1:OriginalSize_d1);

% Switch to "255-subsample(a,1)" for an image with white background and
% black traces.
a = subsample(a,1)-255;

% Make network slightly thicker for the wave to propagate through
a = dilation(a,3,'elliptic');
a = subsample(a,2);

% Fill in the scaling (Matrix vs. Trace speed), then thresholding.
% The best value for scaling is found to be 30.
scaling = 30;
b = (scaling-1) * threshold(a,'isodata',Inf)+ 1;

% Fill in the filter size for opening and closing
fsize = 4;
b = maxf(minf(b,fsize,'elliptic'),fsize,'elliptic');

% Search for the fastest vertical path through the traces
% Output image d = time, e = distance
% Seedimage = c
c = yy(b)-min(yy(b));
c = (c>1);
[d1,e1] = gdt(c,max(b)-b+1,3);
Vert_Trace = mean(e1(2:end-2,end-2))/size(e1,2);
Vert_Trace2 = round(Vert_Trace*10000)/10000;

% Search for the fastest horizontal path through the traces
```

```
% Output image d = time, e = distance
% Seedimage = c
c = xx(b)-min(xx(b));
c = (c>1);
[d2,e2] = gdt(c,max(b)-b+1,3);
Hor_Trace = mean(e2(end-2,2:end-2))/size(e2,1);
Hor_Trace2 = round(Hor_Trace*10000)/10000;

Avrg_Tortuosity = round(((Vert_Trace2+Hor_Trace2)/2)*1000)/1000;

%%%%%%%%%%%%%%%%%%%%%%%%%%%%%%%%%%%%%%%%%%%%%%%%%%%%%%%%%%%%%%%%

% Run 2nd wave

z2 = (OriginalSize_b1-OriginalSize_a1-300)*(OriginalSize_d1-
OriginalSize_c1-300);
        OriginalSize_a2 = (OriginalSize_a1 + 150);
        OriginalSize_b2 = (OriginalSize_b1 - 150);
        OriginalSize_c2 = (OriginalSize_c1 + 150);
        OriginalSize_d2 = (OriginalSize_d1 - 150);

if (z2 > 0)
        a2 = dip_image(grayImage);
        % Select a square image set away from the edge to remove any
        % edge-effect
        a2 =
a2(OriginalSize_a2:OriginalSize_b2,OriginalSize_c2:OriginalSize_d2);

        % Switch to "255-subsample(a,1)" for an image with white
        % background and black traces.
        a2 = subsample(a2,1)-255;

        % Make network slightly thicker for the wave to propagate
        % through
        a2 = dilation(a2,3,'elliptic');
        a2 = subsample(a2,2);

        % Fill in the scaling (Matrix vs. Trace speed), then
        % thresholding.
        % The best value for scaling is found to be 30.
        scaling = 30;
        b2 = (scaling-1) * threshold(a2,'isodata',Inf)+ 1;

        % Fill in the filter size for opening and closing
        fsize = 4;
        b2 = maxf(minf(b2,fsize,'elliptic'),fsize,'elliptic');

        % Search for the fastest vertical path through the traces
        % Output image d = time, e = distance
        % Seedimage = c
        c2 = yy(b2)-min(yy(b2));
        c2 = (c2>1);
        [d_2,e_2] = gdt(c2,max(b2)-b2+1,3);
        Vert_Trace_2 = mean(e_2(2:end-2,end-2))/size(e_2,2);
        Vert_Trace2_2 = round(Vert_Trace_2*10000)/10000;
```

```
        % Search for the fastest horizontal path through the traces
        % Output image d = time, e = distance
        % Seedimage = c
        c2 = xx(b2)-min(xx(b2));
        c2 = (c2>1);
        [d2_2,e2_2] = gdt(c2,max(b2)-b2+1,3);
        Hor_Trace_2 = mean(e2_2(end-2,2:end-2))/size(e2_2,1);
        Hor_Trace2_2 = round(Hor_Trace_2*10000)/10000;

        Avrg_Tortuosity2 =
round(((Vert_Trace2_2+Hor_Trace2_2)/2)*1000)/1000;

else
    Vert_Trace2_2 = 0;
    Hor_Trace2_2 = 0;
    Avrg_Tortuosity2 = 0;

end

%%%%%%%%%%%%%%%%%%%%%%%%%%%%%%%%%%%%%%%%%%%%%%%%%%%%%%%%%%%%%%%%%%%%%%%

% Run 3rd wave

z3 = (OriginalSize_b2-OriginalSize_a2-300)*(OriginalSize_d2-
OriginalSize_c2-300);
        OriginalSize_a3 = (OriginalSize_a2 + 150);
        OriginalSize_b3 = (OriginalSize_b2 - 150);
        OriginalSize_c3 = (OriginalSize_c2 + 150);
        OriginalSize_d3 = (OriginalSize_d2 - 150);

if (z3 > 0)
        a3 = dip_image(grayImage);
        % Select a square image set away from the edge to remove any
        % edge-effect
        a3 =
a3(OriginalSize_a3:OriginalSize_b3,OriginalSize_c3:OriginalSize_d3);

        % Switch to "255-subsample(a,1)" for an image with white
        % background and black traces.
        a3 = subsample(a3,1)-255;

        % Make network slightly thicker for the wave to propagate
        % through
        a3 = dilation(a3,3,'elliptic');
        a3 = subsample(a3,2);

        % Fill in the scaling (Matrix vs. Trace speed), then
        % thresholding.
        % The best value for scaling is found to be 30.
        scaling = 30;
        b3 = (scaling-1) * threshold(a3,'isodata',Inf)+ 1;

        % Fill in the filter size for opening and closing
        fsize = 4;
```

```
        b3 = maxf(minf(b3,fsize,'elliptic'),fsize,'elliptic');

        % Search for the fastest vertical path through the traces
        % Output image d = time, e = distance
        % Seedimage = c
        c3 = yy(b3)-min(yy(b3));
        c3 = (c3>1);
        [d_3,e_3] = gdt(c3,max(b3)-b3+1,3);
        Vert_Trace_3 = mean(e_3(2:end-2,end-2))/size(e_3,2);
        Vert_Trace2_3 = round(Vert_Trace_3*10000)/10000;

        % Search for the fastest horizontal path through the traces
        % Output image d = time, e = distance
        % Seedimage = c
        c3 = xx(b3)-min(xx(b3));
        c3 = (c3>1);
        [d2_3,e2_3] = gdt(c3,max(b3)-b3+1,3);
        Hor_Trace_3 = mean(e2_3(end-2,2:end-2))/size(e2_3,1);
        Hor_Trace2_3 = round(Hor_Trace_3*10000)/10000;

        Avrg_Tortuosity3 =
round(((Vert_Trace2_3+Hor_Trace2_3)/2)*1000)/1000;

else
    Vert_Trace2_3 = 0;
    Hor_Trace2_3 = 0;
    Avrg_Tortuosity3 = 0;

end

%%%%%%%%%%%%%%%%%%%%%%%%%%%%%%%%%%%%%%%%%%%%%%%%%%%%%%%%%%%%%%%%%%%%%%%

% Run 4th wave

z4 = (OriginalSize_b3-OriginalSize_a3-300)*(OriginalSize_d3-
OriginalSize_c3-300);
        OriginalSize_a4 = (OriginalSize_a3 + 150);
        OriginalSize_b4 = (OriginalSize_b3 - 150);
        OriginalSize_c4 = (OriginalSize_c3 + 150);
        OriginalSize_d4 = (OriginalSize_d3 - 150);

if (z4 > 0)
        a4 = dip_image(grayImage);
        % Select a square image set away from the edge to remove any
        % edge-effect
        a4 =
a4(OriginalSize_a4:OriginalSize_b4,OriginalSize_c4:OriginalSize_d4);

        % Switch to "255-subsample(a,1)" for an image with white
        % background and black traces.
        a4 = subsample(a4,1)-255;

        % Make network slightly thicker for the wave to propagate
        % through
        a4 = dilation(a4,3,'elliptic');
```

```
        a4 = subsample(a4,2);

        % Fill in the scaling (Matrix vs. Trace speed), then
        % thresholding.
        % The best value for scaling is found to be 30.
        scaling = 30;
        b4 = (scaling-1) * threshold(a4,'isodata',Inf)+ 1;

        % Fill in the filter size for opening and closing
        fsize = 4;
        b4 = maxf(minf(b4,fsize,'elliptic'),fsize,'elliptic');

        % Search for the fastest vertical path through the traces
        % Output image d = time, e = distance
        % Seedimage = c
        c4 = yy(b4)-min(yy(b4));
        c4 = (c4>1);
        [d_4,e_4] = gdt(c4,max(b4)-b4+1,3);
        Vert_Trace_4 = mean(e_4(2:end-2,end-2))/size(e_4,2);
        Vert_Trace2_4 = round(Vert_Trace_4*10000)/10000;

        % Search for the fastest horizontal path through the traces
        % Output image d = time, e = distance
        % Seedimage = c
        c4 = xx(b4)-min(xx(b4));
        c4 = (c4>1);
        [d2_4,e2_4] = gdt(c4,max(b4)-b4+1,3);
        Hor_Trace_4 = mean(e2_4(end-2,2:end-2))/size(e2_4,1);
        Hor_Trace2_4 = round(Hor_Trace_4*10000)/10000;

        Avrg_Tortuosity4 =
round(((Vert_Trace2_4+Hor_Trace2_4)/2)*1000)/1000;

else
    Vert_Trace2_4 = 0;
    Hor_Trace2_4 = 0;
    Avrg_Tortuosity4 = 0;

end

%%%%%%%%%%%%%%%%%%%%%%%%%%%%%%%%%%%%%%%%%%%%%%%%%%%%%%%%%%%%%%%%%%%%%%%

% Run 5th wave

z5 = (OriginalSize_b4-OriginalSize_a4-300)*(OriginalSize_d4-
OriginalSize_c4-300);
        OriginalSize_a5 = (OriginalSize_a4 + 150);
        OriginalSize_b5 = (OriginalSize_b4 - 150);
        OriginalSize_c5 = (OriginalSize_c4 + 150);
        OriginalSize_d5 = (OriginalSize_d4 - 150);

if (z5 > 0)
        a5 = dip_image(grayImage);
        % Select a square image set away from the edge to remove any
        % edge-effect
```

```
        a5 =
a5(OriginalSize_a5:OriginalSize_b5,OriginalSize_c5:OriginalSize_d5);

        % Switch to "255-subsample(a,1)" for an image with white
        % background and black traces.
        a5 = subsample(a5,1)-255;

        % Make network slightly thicker for the wave to propagate
        % through
        a5 = dilation(a5,3,'elliptic');
        a5 = subsample(a5,2);

        % Fill in the scaling (Matrix vs. Trace speed), then
        % thresholding.
        % The best value for scaling is found to be 30.
        scaling = 30;
        b5 = (scaling-1) * threshold(a5,'isodata',Inf)+ 1;

        % Fill in the filter size for opening and closing
        fsize = 4;
        b5 = maxf(minf(b5,fsize,'elliptic'),fsize,'elliptic');

        % Search for the fastest vertical path through the traces
        % Output image d = time, e = distance
        % Seedimage = c
        c5 = yy(b5)-min(yy(b5));
        c5 = (c5>1);
        [d_5,e_5] = gdt(c5,max(b5)-b5+1,3);
        Vert_Trace_5 = mean(e_5(2:end-2,end-2))/size(e_5,2);
        Vert_Trace2_5 = round(Vert_Trace_5*10000)/10000;

        % Search for the fastest horizontal path through the traces
        % Output image d = time, e = distance
        % Seedimage = c
        c5 = xx(b5)-min(xx(b5));
        c5 = (c5>1);
        [d2_5,e2_5] = gdt(c5,max(b5)-b5+1,3);
        Hor_Trace_5 = mean(e2_5(end-2,2:end-2))/size(e2_5,1);
        Hor_Trace2_5 = round(Hor_Trace_5*10000)/10000;

        Avrg_Tortuosity5 =
round(((Vert_Trace2_5+Hor_Trace2_5)/2)*1000)/1000;

else
    Vert_Trace2_5 = 0;
    Hor_Trace2_5 = 0;
    Avrg_Tortuosity5 = 0;

end

%%%%%%%%%%%%%%%%%%%%%%%%%%%%%%%%%%%%%%%%%%%%%%%%%%%%%%%%%%%%%%%%%%%%%%%%

% Run 6th wave
```

```
z6 = (OriginalSize_b5-OriginalSize_a5-300)*(OriginalSize_d5-
OriginalSize_c5-300);
        OriginalSize_a6 = (OriginalSize_a5 + 150);
        OriginalSize_b6 = (OriginalSize_b5 - 150);
        OriginalSize_c6 = (OriginalSize_c5 + 150);
        OriginalSize_d6 = (OriginalSize_d5 - 150);

if (z6 > 0)
        a6 = dip_image(grayImage);
        % Select a square image set away from the edge to remove any
        % edge-effect
        a6 =
a6(OriginalSize_a6:OriginalSize_b6,OriginalSize_c6:OriginalSize_d6);

        % Switch to "255-subsample(a,1)" for an image with white
        % background and black traces.
        a6 = subsample(a6,1)-255;

        % Make network slightly thicker for the wave to propagate
        % through
        a6 = dilation(a6,3,'elliptic');
        a6 = subsample(a6,2);

        % Fill in the scaling (Matrix vs. Trace speed), then
        % thresholding.
        % The best value for scaling is found to be 30.
        scaling = 30;
        b6 = (scaling-1) * threshold(a6,'isodata',Inf)+ 1;

        % Fill in the filter size for opening and closing
        fsize = 4;
        b6 = maxf(minf(b6,fsize,'elliptic'),fsize,'elliptic');

        % Search for the fastest vertical path through the traces
        % Output image d = time, e = distance
        % Seedimage = c
        c6 = yy(b6)-min(yy(b6));
        c6 = (c6>1);
        [d_6,e_6] = gdt(c6,max(b6)-b6+1,3);
        Vert_Trace_6 = mean(e_6(2:end-2,end-2))/size(e_6,2);
        Vert_Trace2_6 = round(Vert_Trace_6*10000)/10000;

        % Search for the fastest horizontal path through the traces
        % Output image d = time, e = distance
        % Seedimage = c
        c6 = xx(b6)-min(xx(b6));
        c6 = (c6>1);
        [d2_6,e2_6] = gdt(c6,max(b6)-b6+1,3);
        Hor_Trace_6 = mean(e2_6(end-2,2:end-2))/size(e2_6,1);
        Hor_Trace2_6 = round(Hor_Trace_6*10000)/10000;

        Avrg_Tortuosity6 =
round(((Vert_Trace2_6+Hor_Trace2_6)/2)*1000)/1000;

else
```

```
    Vert_Trace2_6 = 0;
    Hor_Trace2_6 = 0;
    Avrg_Tortuosity6 = 0;

end

%%%%%%%%%%%%%%%%%%%%%%%%%%%%%%%%%%%%%%%%%%%%%%%%%%%%%%%%%%%%%%%%%%%%%%%

% Run 7th wave

z7 = (OriginalSize_b6-OriginalSize_a6-300)*(OriginalSize_d6-
OriginalSize_c6-300);
        OriginalSize_a7 = (OriginalSize_a6 + 150);
        OriginalSize_b7 = (OriginalSize_b6 - 150);
        OriginalSize_c7 = (OriginalSize_c6 + 150);
        OriginalSize_d7 = (OriginalSize_d6 - 150);

if (z7 > 0)
        a7 = dip_image(grayImage);
        % Select a square image set away from the edge to remove any
        % edge-effect
        a7 =
a7(OriginalSize_a7:OriginalSize_b7,OriginalSize_c7:OriginalSize_d7);

        % Switch to "255-subsample(a,1)" for an image with white
        % background and black traces.
        a7 = subsample(a7,1)-255;

        % Make network slightly thicker for the wave to propagate
        % through
        a7 = dilation(a7,3,'elliptic');
        a7 = subsample(a7,2);

        % Fill in the scaling (Matrix vs. Trace speed), then
        % thresholding.
        % The best value for scaling is found to be 30.
        scaling = 30;
        b7 = (scaling-1) * threshold(a7,'isodata',Inf)+ 1;

        % Fill in the filter size for opening and closing
        fsize = 4;
        b7 = maxf(minf(b7,fsize,'elliptic'),fsize,'elliptic');

        % Search for the fastest vertical path through the traces
        % Output image d = time, e = distance
        % Seedimage = c
        c7 = yy(b7)-min(yy(b7));
        c7 = (c7>1);
        [d_7,e_7] = gdt(c7,max(b7)-b7+1,3);
        Vert_Trace_7 = mean(e_7(2:end-2,end-2))/size(e_7,2);
        Vert_Trace2_7 = round(Vert_Trace_7*10000)/10000;

        % Search for the fastest horizontal path through the traces
        % Output image d = time, e = distance
        % Seedimage = c
```

```
        c7 = xx(b7)-min(xx(b7));
        c7 = (c7>1);
        [d2_7,e2_7] = gdt(c7,max(b7)-b7+1,3);
        Hor_Trace_7 = mean(e2_7(end-2,2:end-2))/size(e2_7,1);
        Hor_Trace2_7 = round(Hor_Trace_7*10000)/10000;

        Avrg_Tortuosity7 =
round(((Vert_Trace2_7+Hor_Trace2_7)/2)*1000)/1000;

else
    Vert_Trace2_7 = 0;
    Hor_Trace2_7 = 0;
    Avrg_Tortuosity7 = 0;

end

%%%%%%%%%%%%%%%%%%%%%%%%%%%%%%%%%%%%%%%%%%%%%%%%%%%%%%%%%%%%%%%%%%%%%%%%

% Run 8th wave

z8 = (OriginalSize_b7-OriginalSize_a7-300)*(OriginalSize_d7-
OriginalSize_c7-300);
        OriginalSize_a8 = (OriginalSize_a7 + 150);
        OriginalSize_b8 = (OriginalSize_b7 - 150);
        OriginalSize_c8 = (OriginalSize_c7 + 150);
        OriginalSize_d8 = (OriginalSize_d7 - 150);

if (z8 > 0)
        a8 = dip_image(grayImage);
        % Select a square image set away from the edge to remove any
        % edge-effect
        a8 =
a8(OriginalSize_a8:OriginalSize_b8,OriginalSize_c8:OriginalSize_d8);

        % Switch to "255-subsample(a,1)" for an image with white
        % background and black traces.
        a8 = subsample(a8,1)-255;

        % Make network slightly thicker for the wave to propagate
        % through
        a8 = dilation(a8,3,'elliptic');
        a8 = subsample(a8,2);

        % Fill in the scaling (Matrix vs. Trace speed), then
        % thresholding.
        % The best value for scaling is found to be 30.
        scaling = 30;
        b8 = (scaling-1) * threshold(a8,'isodata',Inf)+ 1;

        % Fill in the filter size for opening and closing
        fsize = 4;
        b8 = maxf(minf(b8,fsize,'elliptic'),fsize,'elliptic');

        % Search for the fastest vertical path through the traces
        % Output image d = time, e = distance
```

```
        % Seedimage = c
        c8 = yy(b8)-min(yy(b8));
        c8 = (c8>1);
        [d_8,e_8] = gdt(c8,max(b8)-b8+1,3);
        Vert_Trace_8 = mean(e_8(2:end-2,end-2))/size(e_8,2);
        Vert_Trace2_8 = round(Vert_Trace_8*10000)/10000;

        % Search for the fastest horizontal path through the traces
        % Output image d = time, e = distance
        % Seedimage = c
        c8 = xx(b8)-min(xx(b8));
        c8 = (c8>1);
        [d2_8,e2_8] = gdt(c8,max(b8)-b8+1,3);
        Hor_Trace_8 = mean(e2_8(end-2,2:end-2))/size(e2_8,1);
        Hor_Trace2_8 = round(Hor_Trace_8*10000)/10000;

        Avrg_Tortuosity8 =
round(((Vert_Trace2_8+Hor_Trace2_8)/2)*1000)/1000;

else
    Vert_Trace2_8 = 0;
    Hor_Trace2_8 = 0;
    Avrg_Tortuosity8 = 0;

end

%%%%%%%%%%%%%%%%%%%%%%%%%%%%%%%%%%%%%%%%%%%%%%%%%%%%%%%%%%%%%%%%%%%%%%%

% Run 9th wave

z9 = (OriginalSize_b8-OriginalSize_a8-300)*(OriginalSize_d8-
OriginalSize_c8-300);
        OriginalSize_a9 = (OriginalSize_a8 + 150);
        OriginalSize_b9 = (OriginalSize_b8 - 150);
        OriginalSize_c9 = (OriginalSize_c8 + 150);
        OriginalSize_d9 = (OriginalSize_d8 - 150);

if (z9 > 0)
        a9 = dip_image(grayImage);
        % Select a square image set away from the edge to remove any
        % edge-effect
        a9 =
a9(OriginalSize_a9:OriginalSize_b9,OriginalSize_c9:OriginalSize_d9);

        % Switch to "255-subsample(a,1)" for an image with white
        % background and black traces.
        a9 = subsample(a9,1)-255;

        % Make network slightly thicker for the wave to propagate
        % through
        a9 = dilation(a9,3,'elliptic');
        a9 = subsample(a9,2);

        % Fill in the scaling (Matrix vs. Trace speed), then
        % thresholding.
```

```
        % The best value for scaling is found to be 30.
        scaling = 30;
        b9 = (scaling-1) * threshold(a9,'isodata',Inf)+ 1;

        % Fill in the filter size for opening and closing
        fsize = 4;
        b9 = maxf(minf(b9,fsize,'elliptic'),fsize,'elliptic');

        % Search for the fastest vertical path through the traces
        % Output image d = time, e = distance
        % Seedimage = c
        c9 = yy(b9)-min(yy(b9));
        c9 = (c9>1);
        [d_9,e_9] = gdt(c9,max(b9)-b9+1,3);
        Vert_Trace_9 = mean(e_9(2:end-2,end-2))/size(e_9,2);
        Vert_Trace2_9 = round(Vert_Trace_9*10000)/10000;

        % Search for the fastest horizontal path through the traces
        % Output image d = time, e = distance
        % Seedimage = c
        c9 = xx(b9)-min(xx(b9));
        c9 = (c9>1);
        [d2_9,e2_9] = gdt(c9,max(b9)-b9+1,3);
        Hor_Trace_9 = mean(e2_9(end-2,2:end-2))/size(e2_9,1);
        Hor_Trace2_9 = round(Hor_Trace_9*10000)/10000;

        Avrg_Tortuosity9 =
round(((Vert_Trace2_9+Hor_Trace2_9)/2)*1000)/1000;

else
    Vert_Trace2_9 = 0;
    Hor_Trace2_9 = 0;
    Avrg_Tortuosity9 = 0;

end

%%%%%%%%%%%%%%%%%%%%%%%%%%%%%%%%%%%%%%%%%%%%%%%%%%%%%%%%%%%%%%%%%%%%%%%

% Run 10th wave

z10 = (OriginalSize_b9-OriginalSize_a9-300)*(OriginalSize_d9-
OriginalSize_c9-300);
        OriginalSize_a10 = (OriginalSize_a9 + 150);
        OriginalSize_b10 = (OriginalSize_b9 - 150);
        OriginalSize_c10 = (OriginalSize_c9 + 150);
        OriginalSize_d10 = (OriginalSize_d9 - 150);

if (z10 > 0)
        a10 = dip_image(grayImage);
        % Select a square image set away from the edge to remove any
        % edge-effect
        a10 =
a10(OriginalSize_a10:OriginalSize_b10,OriginalSize_c10:OriginalSize_d10
);
        % Switch to "255-subsample(a,1)" for an image with white
```

```
        % background and black traces.
        a10 = subsample(a10,1)-255;

        % Make network slightly thicker for the wave to propagate
        % through
        a10 = dilation(a10,3,'elliptic');
        a10 = subsample(a10,2);

        % Fill in the scaling (Matrix vs. Trace speed), then
        % thresholding.
        % The best value for scaling is found to be 30.
        scaling = 30;
        b10 = (scaling-1) * threshold(a10,'isodata',Inf)+ 1;

        % Fill in the filter size for opening and closing
        fsize = 4;
        b10 = maxf(minf(b10,fsize,'elliptic'),fsize,'elliptic');

        % Search for the fastest vertical path through the traces
        % Output image d = time, e = distance
        % Seedimage = c
        c10 = yy(b10)-min(yy(b10));
        c10 = (c10>1);
        [d_10,e_10] = gdt(c10,max(b10)-b10+1,3);
        Vert_Trace_10 = mean(e_10(2:end-2,end-2))/size(e_10,2);
        Vert_Trace2_10 = round(Vert_Trace_10*10000)/10000;

        % Search for the fastest horizontal path through the traces
        % Output image d = time, e = distance
        % Seedimage = c
        c10 = xx(b10)-min(xx(b10));
        c10 = (c10>1);
        [d2_10,e2_10] = gdt(c10,max(b10)-b10+1,3);
        Hor_Trace_10 = mean(e2_10(end-2,2:end-2))/size(e2_10,1);
        Hor_Trace2_10 = round(Hor_Trace_10*10000)/10000;

        Avrg_Tortuosity10 =
round(((Vert_Trace2_10+Hor_Trace2_10)/2)*1000)/1000;

else
    Vert_Trace2_10 = 0;
    Hor_Trace2_10 = 0;
    Avrg_Tortuosity10 = 0;

end

%%%%%%%%%%%%%%%%%%%%%%%%%%%%%%%%%%%%%%%%%%%%%%%%%%%%%%%%%%%%%%%%%%%%%%%

%Create output

% Creates image with a periodicity of the wave fronts set to 18.
Vert = stretch(mod(d1,50));
Hor = stretch(mod(d2,50));
```

```
% Creates an output image with the tortuosity listed
subplot(1, 3, 1);
imshow (grayImage);
title('Original Image', 'FontSize', fontSize);
subplot(1, 3, 2);
imshow (dip_array(Vert,'uint8'));
title('Tortuosity Analyzed', 'FontSize', fontSize);
message = sprintf('Run 1:\nV-Tort = %g H-Tort = %g Ave-Tort = %g\nRun
2:\nV-Tort = %g H-Tort = %g Ave-Tort = %g\nRun 3:\nV-Tort = %g H-Tort =
%g Ave-Tort = %g\nRun 4:\nV-Tort = %g H-Tort = %g Ave-Tort = %g\nRun
5:\nV-Tort = %g H-Tort = %g Ave-Tort = %g\nRun 6:\nV-Tort = %g H-Tort =
%g Ave-Tort = %g\nRun 7:\nV-Tort = %g H-Tort = %g Ave-Tort = %g\nRun
8:\nV-Tort = %g H-Tort = %g Ave-Tort = %g\nRun 9:\nV-Tort = %g H-Tort =
%g Ave-Tort = %g\nRun 10:\nV-Tort = %g H-Tort = %g Ave-Tort = %g\n',
Vert_Trace2, Hor_Trace2, Avrg_Tortuosity, Vert_Trace2_2, Hor_Trace2_2,
Avrg_Tortuosity2, Vert_Trace2_3, Hor_Trace2_3, Avrg_Tortuosity3,
Vert_Trace2_4, Hor_Trace2_4, Avrg_Tortuosity4, Vert_Trace2_5,
Hor_Trace2_5, Avrg_Tortuosity5, Vert_Trace2_6, Hor_Trace2_6,
Avrg_Tortuosity6, Vert_Trace2_7, Hor_Trace2_7, Avrg_Tortuosity7,
Vert_Trace2_8, Hor_Trace2_8, Avrg_Tortuosity8, Vert_Trace2_9,
Hor_Trace2_9, Avrg_Tortuosity9, Vert_Trace2_10, Hor_Trace2_10,
Avrg_Tortuosity10);

subplot(1, 3, 3);
axis([0 20 0 20]);
text (0,10,message);
axis off;
```

APPENDIX K

ANALYSIS CONSISTENCY TEST

K.1 Overview

A large proportion of the samples used were images taken in the field, specifically Zumaia, Spain. The method of collecting these field photographs was to hold the camera vertically above the specimen and take a picture. There is a possibility that by using this method of photography that the resulting sample images could have some parallax issues. The parallax would result in some variance of analytical results, depending on the degree of parallax. The current study within this appendix was performed to determine what degree of variance is possible with photographs of one sample taken over a period of several days at various times of day with the same method of photography as the one used in the field.

K.2 Materials and methods

In order to test and see how consistent the image results were from this sample collection method, a large number of photographs of the same specimen were needed. In order to do this a specimen was chosen from the University of Utah Ichnology Collection (UUIC) based on the degree of completeness of the specimen and the degree of well-defined burrows. These characteristics would make photographing and tracing the specimen easier and more reliable. The sample chosen was *Paleodictyon* from the Longobucco Sequence, Longobucco, Italy (UUIC 1164; Fig. E.26L; Fig. K.1).

The *Paleodictyon* sample was placed in the same orientation for a series of 10 photographs that differed by time of day and date. The dates ranged over five days from one hour after sunrise to one hour before sunset in April and May of 2014. Photographs

Figure K.1. *Paleodictyon* trace fossil used for consistency analyses. Specimen UUIC 1164 in the University of Utah Ichnology Collection.

were taken in the same method used for the field photographs in Lehane and Ekdale (2013; 2014; and Appendix E). This involved holding the camera vertically over the sample and taking a picture directly downward, perpendicular to the sample. Several photographs were taken at each time period and the best among them was chosen for analyses. The samples were then traced and analyzed in the same methods used for all of the other specimens in this study (see Lehane and Ekdale, 2013; 2014; and Appendix I for details).

K.3 Results

The results of the analyses are presented in Figures K.2-K.3. Each graph presents the results of each of the ten analyses runs along with the range of values (black arrows) seen in the dataset of 182 network traces. The graphs in figure K.2 display two sets of data each in order to simplify the results.

The range of results from the occupied space percentage (OSP) analyses of the ten samples was 0.6%, while the range of the entire dataset was 45.4% (Fig. K.2A). The range in values of the test samples represents approximately 1% of the entire dataset.

The range of results from the network tortuosity (NT) analyses of the ten samples was 0.044, while the range of the entire dataset was 0.848 (Fig. K.2A). The range of the test samples represents approximately 5% of the entire dataset. This is a high variance in the analyses and could account for the lack of any strong trend in the whole dataset.

The range of results of the fractal analysis (D_{Box}) calculation of the ten samples was 0.011, while the range of the entire dataset is 0.533 (Fig. K.2B). The range of the test samples represents approximately 2% of the entire dataset. Lehane and Ekdale (2013) had determined that a range of approximately 0.1 was the calculated range of a given ichnospecies.

The range of results of the mesh size (MA) analyses of the ten samples was 0.352, while the range of the entire dataset was 44.113 (Fig. K.2B). The range of the test samples represents approximately 0.8% of the entire dataset. This is the most reliable measurement.

The range of results of the branching angle (BA) analyses of the ten samples was 5.4°, while the range of the entire dataset was 65.7°. The range of the test samples

Figure K.2. Results of the consistency test analyses from the sample shown in Figure K.1. A. The consistency results of the occupied space percentage (OSP) and the network tortuosity (NT). The OSP (triangles) axis is along the left hand side of the graph, with the left arrow representing the entire range of OSP values from the total dataset. The NT (circles) axis is along the right hand side of the graph, with the right arrow representing the entire range of NT values from the total dataset. The error bars represent the standard error. B. The consistency results of the fractal analyses (D_{Box}) and mesh size (MS). The D_{Box} (circles) axis is along the left hand side of the graph, with the left arrow representing the entire range of D_{Box} values from the total dataset. The error bars represent the standard error. The MS (triangles) axis is along the right hand side of the graph, with the right arrow representing the entire range of MS values from the total dataset.

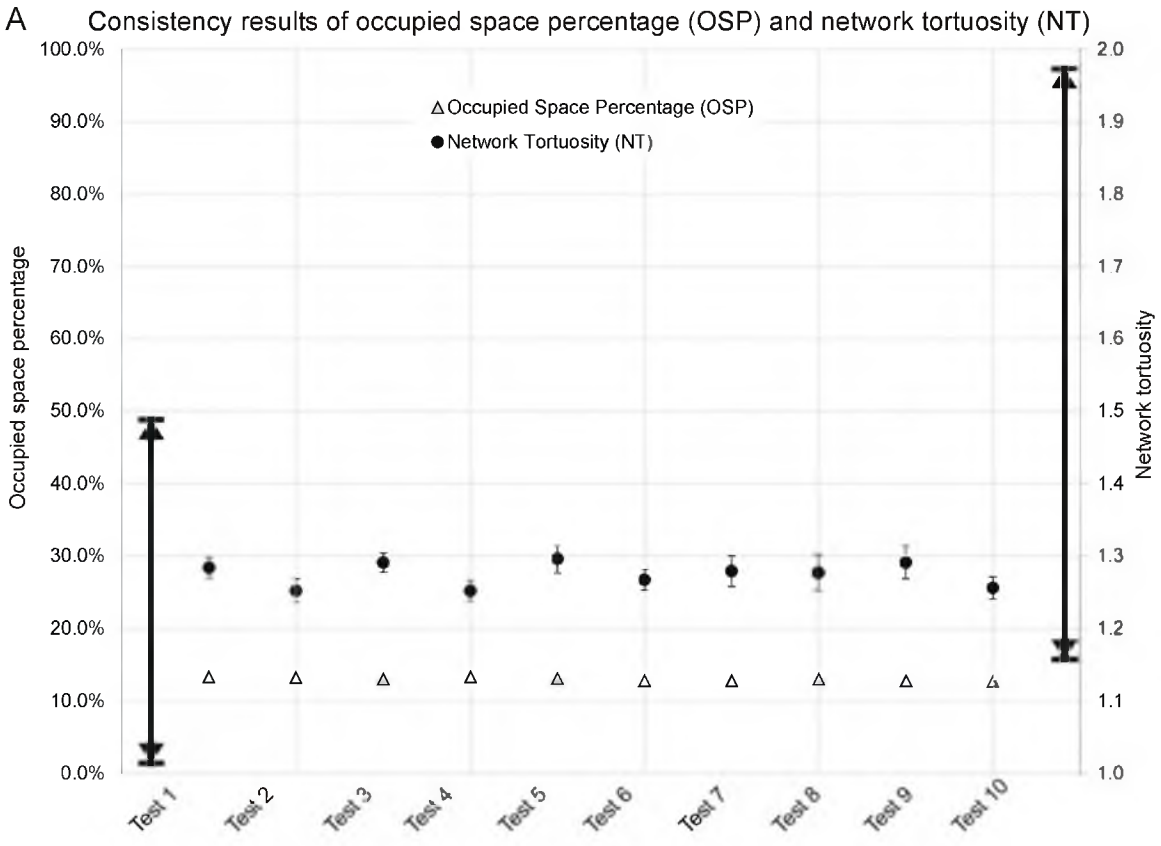
A
Consistency results of occupied space percentage (OSP) and network tortuosity (NT)
Occupied Space Percentage (OSP)
Network Tortuosity (NT)
Occupied space percentage
Network tortuosity
100.0%
90.0%
80.0%
70.0%
60.0%
50.0%
40.0%
30.0%
20.0%
10.0%
0.0%
2.0
1.9
1.8
1.7
1.6
1.5
1.4
1.3
1.2
1.1
1.0
Test 1
Test 2
Test 3
Test 4
Test 5
Test 6
Test 7
Test 8
Test 9
Test 10

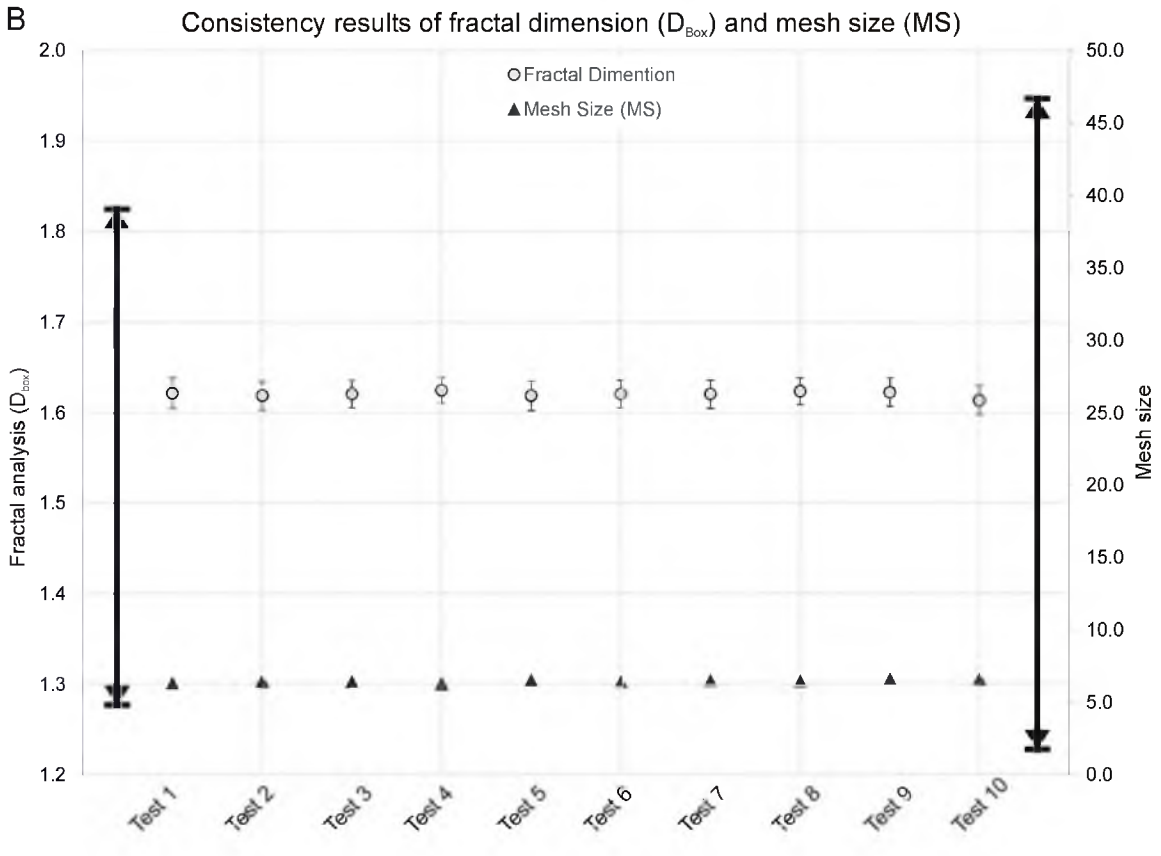
B
Consistency results of fractal dimension (D_{Box}) and mesh size (MS)
Fractal Dimention
Mesh Size (MS)
Fractal analysis (D_{box})
Mesh size
2.0
1.9
1.8
1.7
1.6
1.5
1.4
1.3
1.2
50.0
45.0
40.0
35.0
30.0
25.0
20.0
15.0
10.0
5.0
0.0
Test 1
Test 2
Test 3
Test 4
Test 5
Test 6
Test 7
Test 8
Test 9
Test 10

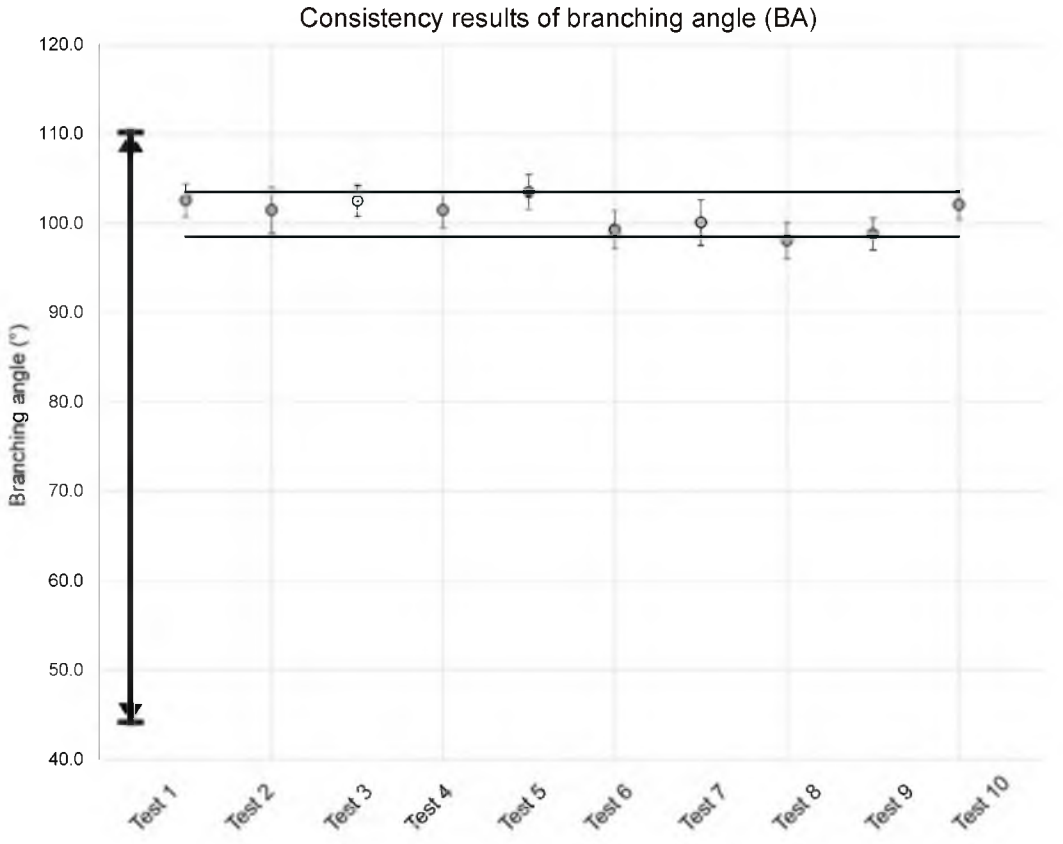

Figure K.3. Branching angle (BS) results of the consistency test analyses from the sample shown in Figure K.1. The arrow represents the entire range of BA values from the total dataset. The black bars represent the upper and lower limit of the 5° measurement error, centered on the average value for the analytical results presented. The error bars represent the standard error.

represents approximately 8% of the entire dataset. As noted previously (Appendix I), reproducibility of the branching angle measurements is about ± 2.5°. This 5° range is highlighted on the graph with the black bars representing ± 2.5° off of the average value of the test samples (101.0°). The 5° range encompasses almost the entire sample dataset.

K.4 Conclusion

In order to determine if the results of the analyses were able to be reproduced, a consistency test was done by taking pictures of the same specimen ten times during various times of day, over several days. These samples were treated exactly as the rest of the dataset in order to determine if the analyses were valid. After carefully analyzing the data, it has been determined that the results were indeed consistent for most of the analyses performed. The resulting range of variance from each set of analyses varied from 0.8 to 8% of the entire data range. Of the two analyses which showed the most variance, the branching angle variance is likely due to a $\pm 2.5°$ inherent error in the measurements to begin with. The other large variance value, the network tortuosity, could account for the lack of any visible trend seen in the larger dataset.

APPENDIX L

BUILDING AN EXAMPLE EQUATION

Several studies have attempted to apply mathematical formulas to various aspects of evolution (e.g., Calsina and Perelló, 1995; Lloyd, 1995; Baake and Gabriel, 1999; Huisman and Weissing, 2001; and López-Ruiz and Fournier-Prunaret, 2009). Most of them were written without all possible variables and the concept of morphospace into account. The problem is that some of the variables will be added later as the equation is being built, and some will be merged with others and thus be eliminated.

Here we state that species X' is a descendent species from species X. The evolution of species X to X' involves several crucial factors (see Table 6.1), but it is possible to reduce the number of these variables. Although sexual selection is an important variable in evolution, within a species sexual selection normally does not affect the number of individuals. Sexual selection more often affects subspecies or subgroups within a species (selecting for longer antlers, brighter colors, etc.), so this variable could be ignored for this equation. Food competition and population density are intricately linked. As you have more individuals, the competition for the same amount of food increases, so that Food Competition correlates directly with Population Density. There is also a carrying capacity to any biological system. As species X approaches that carrying capacity, the population density and the food competition would have the most impact. The extra-species interactions can be boiled down to individual species for these examples. Here Competition for Food and Space is represented by species X's interactions with Species Y, and Predation is represented by the predator Species Z.

As species evolve they adapt to a particular environment. This means that any changes in the environment would be harmful for the majority of a species; however there also is a small group where those changes would benefit. The environmental factors

themselves would be based as deviations from current values. It does not really matter what the previous temperature was, since the species already was acclimatized to the present temperature. Climate is closely linked to temperature, which in turn is closely linked to food availability. A change in a climate variable, c, is considered as a proxy for changes in food availability and changes in local temperature.

We start to build the equations with the interactions of species X, Y, and Z (López-Ruiz and Fournier-Prunaret, 2009). X and Y are in competition, so we have:

$$\dot{X} = \mu_x(Y)*X*(1-X) \qquad \text{(Eq. L.1)}$$

$$\dot{Y} = \mu_y(X)*Y*(1-Y)$$

where μ is the growth rate of the population.

They are in competition, so $\mu_x = \mu_y = \lambda_1(-3a + 4)$; where a = X or Y, respectively, and λ is the mutual competitive interaction constant (López-Ruiz and Fournier-Prunaret, 2009). So now we have:

$$\dot{X} = \lambda_1(-3Y + 4)*X*(1-X) \qquad \text{(Eq. L.2)}$$

$$\dot{Y} = \lambda_1(-3X + 4)*Y*(1-Y)$$

Now X and Z are in a predator-prey relationship, where X is the Prey and Z is the Predator. We have:

$$\dot{X} = \mu_x(Z)*X*(1-X) \qquad \text{(Eq. L.3)}$$

$$\dot{Z} = \mu_y(X)*Z*(1-Z)$$

They are predator prey so $\mu_x = \lambda_2(-3a + 4)$ and $\mu_z = \lambda_3(-3a + 1)$; where a = X or Z respectively (López-Ruiz and Fournier-Prunaret, 2009). So now we have:

$$\dot{X} = \lambda_2(-3Z + 4)*X*(1-X) \qquad \text{(Eq. L.4)}$$

$$\dot{Z} = \lambda_3(-3X + 1)*Z*(1-Z)$$

Combining equations 3 and 5 for an animal X that is in competition with Y and is the prey of Z, we have:

$$\dot{X} = [\lambda_1(-3Y + 4)\, X\, (1-X)] + [\lambda_2(-3Z + 4)\, X\, (1-X)]$$

$$\dot{Y} = \lambda_1(-3X + 4)\, Y\, (1-Y) \qquad \text{(Eq. L.5)}$$

$$\dot{Z} = \lambda_3(-3X + 1)\, Z\, (1-Z)$$

As populations of X increase and approach the carrying capacity, the number of animals lost to predation increase. Thus, in the natural evolution of the species, the number of animals in species X is kept below the carrying capacity due to predation as well as competition. This means that separate variables do not need to be added for population density and other related factors.

The mutation of species X now is added. To keep the equations simple, only species X mutates (Calsina and Perelló, 1995; Baake and Gabriel, 2000). Over time, mutations will reduce the numbers organisms in species X, but they will increase the number of individuals in species A, a daughter species of X. For these calculations, to keep things simple and to allow for the possibility that there are multiple species which may derive from any one species, we focus only on species X, Y, and Z and ignore any other derivative species (i.e., A_1, A_2, etc.).

It is possible to use the Baake and Gabriel (2000; Eq. 2) equation for simple population mutations ($x' = VWx$), where x is the initial population, x' is the number of individuals in the successive generation, V is the mutation matrix, and W is the reproduction matrix. If we assume for the simplest case that only the species that survive to reproduce are counted in the equation, eliminating the reproduction matrix (W), then only the mutation matrix (V) is left, which can be simplified to the species mutation

coefficient (m), representing the degree of mutation, where 1 is no mutation and 0 represents that the entire population has been mutated. The value of m for most species would be near 0.99.

$$\dot{X} = \{[\lambda_1(-3Y + 4)\, X\, (1-X)] + [\lambda_2(-3Z + 4)\, X\, (1-X)]\}(m)$$

$$\dot{Y} = \lambda_1(-3X + 4)\, Y\, (1-Y) \qquad \text{(Eq. L.6)}$$

$$\dot{Z} = \lambda_3(-3X + 1)\, Z\, (1-Z)$$

where m is the mutation coefficient.

The last variable to be introduced is the climate variable, c. Depending on the variable, changes in climate can be either a benefit to the species as a whole or a detriment. How each individual species is impacted by the climate change would be regarded by the climate influence factor, f. The overall evolutionary climate impact, I, would be calculated by the following equation:

$$I_n = c \cdot f_n \qquad \text{(Eq. L.7)}$$

where I is the climate impact factor for each individual species, c is the climate variable, which is independent of each species, f is the climate influence factor, which is dependent on each species, and n is the specific I and f factor for each species. The value of c would range from 1, no change, to 0, cataclysmic change. Typical climatic changes would fall in the 0.9 to 1 range.

$$\dot{X} = \{[\lambda_1(-3Y + 4)\, X\, (1-X)] + [\lambda_2(-3Z + 4)\, X\, (1-X)]\} \cdot (m \cdot I_X)$$

$$\dot{Y} = [\lambda_1(-3X + 4)\, Y\, (1-Y)] \cdot I_Y \qquad \text{(Eq. L.8)}$$

$$\dot{Z} = [\lambda_3(-3X + 1)\, Z\, (1-Z)] \cdot I_Z$$

With this set of equations, it is possible to determine the degree of impact that the various evolutionary factors played on the evolution of a set of species. The above set of

equations does not provide a totally comprehensive solution to all problems related to evolution, of course, but it is a step towards integrating many disparate ideas within one equation.

REFERENCES

Aalto, K. R. 1989. Franciscan Complex olistostrome at Crescent City, northern California. Sedimentology 36(3):471-495.

Aceñolaza, F. G. 1978. El Paleozoica inferior de Argentina segun sus trazas fosiles. Ameghiniana 15(1-2):15-64.

Aceñolaza, F. G., and A. J. Toselli. 1981. Geologia del noroeste Argentino. Universidad Nacional de Tucuman: Facultad de Ciencias Naturales.

Ackland, G. J., and I. D. Gallagher. 2004. Stabilization of Large Generalized Lotka-Volterra Foodwebs By Evolutionary Feedback. Physical Review Letters 93(15):158701.

Alberch, P. 1989. The logic of monsters: Evidence for internal constraint in development and evolution. Geobios 22(Supplement 2):21-57.

Aleem, A. A. 1950. The diatom community inhabiting the mud-flats at Whitstable. New Phytologist 49(2):174-188.

Alegret, L., S. Ortiz, and E. Molina. 2009. Extinction and recovery of benthic foraminifera across the Paleocene–Eocene Thermal Maximum at the Alamedilla section (Southern Spain). Palaeogeography, Palaeoclimatology, Palaeoecology 279(3–4):186-200.

Alexander, R. M. 1990. Size, speed and buoyancy adaptations in aquatic animals. American Zoologist 30(1):189-196.

Alpert, S. P. 1973. *Bergaueria Prantl* (Cambrian and Ordovician), a Probable Actinian Trace Fossil. Journal of Paleontology 47(5):919-924.

Alpert, S. P., and J. N. Moore. 1975. Lower Cambrian trace fossil evidence for predation on trilobites. Lethaia 8(3):223-230.

Baake, E., and W. Gabriel. 2000. Biological evolution through mutation, selection, and drift: An introductory review. Pp. 203-264. *In* D. Stauffer, ed. Annual Reviews of Computational Physics. World Scientific.

Bąk, K., J. Rubinkiewicz, M. Garecka, E. Machaniec, and B. Dziubińska. 2001. Exotics-bearing layer in the Oligocene Flysch of the Krosno Beds in the Fore-Dukla Zone (Silesian Nappe, Outer Carpathians), Poland. Geologica Carpathica -Bratislava- 52(3):159-171.

Bates, K. T., P. L. Manning, B. Vila, and D. Hodgetts. 2008. Three-dimensional modelling and analysis of dinosaur trackways. Palaeontology 51(4):999-1010.

Baucon, A. 2010. Da Vinci's *Paleodictyon*: The fractal beauty of traces. Acta Geologica Polonica 60(1):3-17.

Beatty, J. 2006. Replaying life's tape. The Journal of Philosophy 103(7):336-362.

Benhamou, S. 2004. How to reliably estimate the tortuosity of an animal's path: Straightness, sinuosity, or fractal dimension? Journal of Theoretical Biology 229(2):209-220.

Benton, M. J. 1982. Trace fossils from Lower Palaeozoic ocean-floor sediments of the Southern Uplands of Scotland. Transactions of the Royal Society of Edinburgh: Earth Sciences 73:67-87.

Berger, W. H., A. A. Ekdale, and P. P. Bryant. 1979. Selective preservation of burrows in deep-sea carbonates. Marine Geology 32:205-230.

Bernaola, G., M. Martín-Rubio, and J. I. Baceta. 2009. New high resolution calcareous nannofossil analysis across the Danian/Selandian transition at the Zumaia section: Comparison with South Tethys and Danish sections. Geologica Acta 7(1-2):79-92.

Blackledge, T. A., N. Scharff, J. A. Coddington, T. Szüts, J. W. Wenzel, C. Y. Hayashi, and I. Agnarsson. 2009. Reconstructing web evolution and spider diversification in the molecular era. Proceedings of the National Academy of Sciences 106(13):5229-5234.

Bostrom, N. 2009. The Future of Humanity. Pp. 551-557. A Companion to the Philosophy of Technology. Wiley-Blackwell.

Braga, J. C., J. M. Martin, and J. L. Wood. 2001. Submarine lobes and feeder channels of redeposited, temperate carbonate and mixed siliciclastic-carbonate platform deposits (Vera Basin, Almería, southern Spain). Sedimentology 48(1):99-116.

Bralower, T. J. 2002. Evidence of surface water oligotrophy during the Paleocene-Eocene thermal maximum: Nannofossil assemblage data from Ocean Drilling Program Site 690, Maud Rise, Weddell Sea. Paleoceanography 17(2):13-1-13-12.

Brasier, M., L. Cotton, and I. Yenney. 2009. First report of amber with spider webs and microbial inclusions from the earliest Cretaceous (*c.* 140 Ma) of Hastings, Sussex. Journal of the Geological Society 166(6):989-997.

Breder, C. M., Jr., and F. Halpern. 1946. Innate and acquired behavior affecting the aggregation of fishes. Physiological Zoology 19(2):154-190.

Brent, S. B. 1978. Prigogine's model for self-organization in nonequilibrium systems—its relevance for developmental psychology. Human Development 21(5-6):374-387.

Bromley, R. G. 1990. Trace Fossils: Biology and Taphonomy. Unwin and Hyman, London.

Bromley, R. G. 1996. Trace Fossils: Biology, Taphonomy and Applications (Second Edition). Chapman & Hall, New York.

Bromley, R. G., and R. W. Frey. 1974. Redescription of the trace fossil Gyrolithes and taxonomic evaluation of *Thalassinoides*, *Ophiomorpha* and *Spongeliomorpha*. Bulletin of the Geological Society of Denmark 23:311-335.

Brunel, P., L. Bossé, and G. Lamarche. 1998. Catalogue of the marine invertebrates of the Estuary and Gulf of Saint Lawrence. Canadian Special Publication of Fisheries and Aquatic Sciences 126:405.

Buatois, L. A., and M. G. Mángano. 2011. Ichnology: Organism-Substrate Interactions in Space and Time. Cambridge University Press, Cambridge, UK.

Buck, S. G., and R. Goldring. 2003. Conical sedimentary structures, trace fossils or not? Observations, experiments, and review. Journal of Sedimentary Research 73(3):338-353.

Calsina, A., and C. Perelló. 1995. Equations for biological evolution. Proceedings of the Royal Society of Edinburgh, Section: A Mathematics 125(05):939-958.

Cantor, G. 1883. Grundlagen einer allgemeinen Mannichfaltigkeitslehre. Mathematische Annalen 21:545-591.

Cantor, G. 1993. On the power of perfect sets of points. Pp. 11-23. *In* G. A. Edgar, ed. Classics on Fractals. Addison-Wesley Publishing Company, Reading, MA.

Carroll, S., and N. H. Trewin. 1995. *Cornulatichnus*: A new trace fossil from the Old Red Sandstone of Orkney. Scottish Journal of Geology 31(1):37-41.

Chamberlain, C. K. 1971. Morphology and ethology of trace fossils from the Ouachita Mountains, Southeast Oklahoma. Journal of Paleontology 45(2):212-246.

Charnov, E. L. 1976. Optimal foraging, the marginal value theorem. Theoretical Population Biology 9(2):129-36.

Chen, P. 1996. A random walk or color chaos on the stock market? Time-frequency analysis of S&P indexes. Studies in Nonlinear Dynamics and Econometrics 1(2):87-103.

Chertkov, V. Y., and I. Ravina. 1999. Tortuosity of crack networks in swelling clay soils. Soil Science Society of America Journal 63(6):1523-1530.

Crimes, T. P. 1977. Modular Construction of Deep-Water Trace Fossils from the Cretaceous of Spain. Journal of Paleontology 51(3):591-605.

Crimes, T. P., and M. M. Anderson. 1985. Trace fossils from late Precambrian-Early Cambrian strata of southeastern Newfoundland (Canada); temporal and environmental implications. Journal of Paleontology 59(2):310-343.

Crimes, T. P., and J. D. Crossley. 1991. A diverse ichnofauna from Silurian flysch of the Aberystwyth Grits Formation, Wales. Geological Journal 26(1):27-64.

Crimes, T. P., and M. A. Fedonkin. 1994. Evolution and dispersal of deepsea traces. Palaios 9(1):74-83.

Crimes, T. R., J. F. G. Hidalgo, and D. G. Poire. 1992. Trace fossils from Arenig flysch sediments of Eire and their bearing on the early colonisation of the deep seas. Ichnos 2(1):61-77.

Crist, T. O., D. S. Guertin, J. A. Wiens, and B. T. Milne. 1992. Animal movement in heterogeneous landscapes: An experiment with *Eleodes* beetles in shortgrass prairie. Functional Ecology 6(5):536-544.

Cummings, J. P., and D. M. Hodgson. 2011a. An agrichnial feeding strategy for deep-marine Paleogene *Ophiomorpha* group trace fossils. Palaios 26:212-224.

Cummings, J. P., and D. M. Hodgson. 2011b. Assessing controls on the distribution of ichnotaxa in submarine fan environments, the Basque Basin, Northern Spain. Sedimentary Geology 239(3-4):162-187.

D'Alessandro, A. 1980. Prime osservazioni sulla ichnofaua Miocenica della 'formazione di Gorgoglione' (Castelmezzano, Potenza). Rivista Italiana di Paleontologia e stratigrafia 86(2):357-398.

D'Alessandro, A. 1982. Processi tafonomici e distribuzione delle tracce fossili nel flysch di Gorgolione (Appennino Meridionale). Rivista Italiana di Paleontologia e stratigrafia 87(3):511-560.

Davis, R. B., N. J. Minter, and S. J. Braddy. 2007. The neoichnology of terrestrial arthropods. Palaeogeography, Palaeoclimatology, Palaeoecology 255(3–4):284-307.

de Gibert, J. M., and A. A. Ekdale. 2010. Paleobiology of the crustacean trace fossil *Spongeliomorpha iberica* in the Miocene of southeastern Spain. Acta Palaeontologica Polonica 55(4):733-740.

de Gibert, J. M., K. Jeong, and J. Martinell. 1999. Ethologic and ontogenic significance of the Pliocene trace fossil *Sinusichnus sinuosus* from the northwestern Mediterranean. Lethaia 32(1):31-40.

de Stefani, C. 1895. Aperçu géologique et description paléontologique de l'île de Karpathos. Pp. 1-28. *In* C. de Stefani, C. J. Forsyth Major, and W. Barbey, eds. Étude géologique, paléontologique et botanique. G. Bridel, Lausanne.

Droser, M. L., and D. J. Bottjer. 1986. A semiquantitative field classification of ichnofabric. Journal of Sedimentary Research 56(4):558-559.

Droser, M. L., and D. J. Bottjer. 1987. Development of ichnofabric indices for strata deposited in high energy nearshore terrigenous clastic enviroment. Pp. 29-34. *In* D. J. Bottjer, ed. New Concepts in the Use of Biogenic Sedimentary Structures for Paleoenvironmental Interpretation. Society of Economic Paleontologists and Mineralogists, Pacific Section.

Dudek, B. C., N. Adams, R. Boice, and M. E. Abbott. 1983. Genetic influences on digging behaviors in mice (*Mus musculus*) in laboratory and seminatural settings. Journal of Comparative Psychology 97(3):249-259.

Dzulynski, S., M. Książkiewicz, and P. H. Kuenen. 1959. Turbidites in flysch of the Polish Carpathian Mountains. Geological Society of America Bulletin 70(8):1089-1118.

Eberhard, W. G. 1990. Function and Phylogeny of Spider Webs. Annual Review of Ecology and Systematics 21(ArticleType: research-article / Full publication date: 1990 / Copyright © 1990 Annual Reviews):341-372.

Ekdale, A. A. 1980. Graphoglyptid burrows in modern deep-sea sediment. Science 207(4428):304-306.

Ekdale, A. A. 1985. Paleoecology of the marine endobenthos. Palaeogeography, Palaeoclimatology, Palaeoecology 50(1):63-81.

Ekdale, A. A., R. G. Bromley, and S. G. Pemberton. 1984a. Ichnology - the use of trace fossils in sedimentology and stratigraphy. SEPM Short Course 15:1-317.

Ekdale, A. A., and J. M. de Gibert. 2014. Late Miocene deep-sea trace fossil associations in the Vera Basin, Almería, Southeastern Spain. Spanish Journal of Paleontology 29(1):95-104.

Ekdale, A. A., and R. E. Lamond. 2003. Behavioral cladistics of trace fossils: Evolution of derived trace-making skills. Palaeogeography, Palaeoclimatology, Palaeoecology 192(1-4):335-343.

Ekdale, A. A., and D. W. Lewis. 1991. Trace fossils and paleoenvironmental control of ichnofacies in a late Quaternary gravel and loess fan delta complex, New Zealand. Palaeogeography, Palaeoclimatology, Palaeoecology 81(3–4):253-279.

Ekdale, A. A., L. N. Muller, and M. T. Novak. 1984b. Quantitative ichnology of modern pelagic deposits in the abyssal Atlantic. Palaeogeography, Palaeoclimatology, Palaeoecology 45(2):189-223.

Eldredge, N., and S. J. Gould. 1972. Punctuated equilibria: An alternative to phylogenetic gradualism. Pp. 82-115. *In* T. J. M. Schopf, ed. Models in Paleobiology. Freeman, Copper and Company, San Francisco.

Emmons, E. 1844. The Taconic System: Based on Observations in New-York, Massachusetts, Maine, Vermont, and Rhode-Island. Carroll and Cook, Albany, NY.

Ernst, G., and J. Zander. 1993. Stratigraphy, facies development, and trace fossils of the Upper Cretaceous of Southern Tanzania (Kilwa District). Pp. 259-278. *In* E. Abbate, M. Sagri, and F. P. Sassi, eds. Geology and Mineral Resources of Somalia and Surrounding Regions. Istituto Agronomico per l'Oltremare, Florence, Italy.

Etzenhouser, M. J., M. K. Owens, D. E. Spalinger, and S. B. Murden. 1998. Foraging behavior of browsing ruminants in a heterogeneous landscape. Landscape Ecology 13(1):55-64.

Feder, J. 1988. Fractals. Plenum Press, New York.

Fichter, L. S., E. J. Pyle, and S. J. Whitmeyer. 2010. Strategies and rubrics for teaching chaos and complex systems theories as elaborating, self-organizing, and fractionating evolutionary systems. Journal of Geoscience Education 58(2):65-85.

Fillion, D., and R. K. Pickerill. 1990. Ichnology of the Upper Cambrian? to Lower Ordovician Bell Island and Wabana groups of eastern Newfoundland, Canada. Palaeontographica Canadiana 7:1-119.

Fisher, W. K., and G. E. MacGinitie. 1928. A new echiuroid worm from California. Journal of Natural History Series 10 1(2):199-204.

Fuchs, T. 1895. Studien über Fucoiden und Hieroglyphen. Denkschriften der Mathematisch-Naturwissenschaftlichen Classe der Kaiserlichen Akademie der Wissenschaften 62:369-448.

Gaillard, C., and P. R. Racheboeuf. 2006. Trace fossils from nearshore to offshore environments: Lower Devonian of Bolivia. Journal of Paleontology 80(6):1205-1226.

Garlick, G. D., and W. Miller, III. 1993. Simulations of burrowing strategies and construction of *Paleodictyon*. Journal of Geological Education 41:159-163.

Gaston, G. R., J. A. McLelland, and R. W. Heard. 1992. Feeding biology, distribution, and ecology of two species of benthic polychaetes: *Paraonis fulgens* and *Paraonis pygoenigmatica* (Polychaeta: Paraonidae). Gulf Research Reports 8(4):395-399.

Gawenda, P., W. Winkler, B. Schmitz, and T. Adatte. 1999. Climate and bioproductivity control on carbonate turbidite sedimentation (Paleocene to earliest Eocene, Gulf of Biscay, Zumaia, Spain). Journal of Sedimentary Research 69(6):1253-1261.

Gingras, M. K., S. G. Pemberton, T. Saunders, and H. E. Clifton. 1999. The ichnology of modern and Pleistocene brackish-water deposits at Willapa Bay, Washington; variability in estuarine settings. Palaios 14(4):352-374.

Goldberger, A. L., D. R. Rigney, and B. J. West. 1990. Chaos and fractals in human physiology. Scientific American 262(2):42-49.

Gong, Y., and D. Huang. 1997. Topologic configuration of a graphoglyptid and its functional morphologic analysis. Chinese Science Bulletin 42(16):1394-1397.

Goodings, D. 1991. Nonlinear differential equations and attractors. Pp. 23-33. *In* G. V. Middleton, ed. Nonlinear Dynamics, Chaos and Fractals with Applications to Geological Systems. Geological Association of Canada, Toronto, Ontario.

Goodwin, P. W., and E. J. Anderson. 1974. Associated physical and biogenic structures in environmental subdivision of a Cambrian tidal sand body. The Journal of Geology 82(6):779-794.

Gould, S. J. 1989. A developmental constraint in *Cerion*, with comments on the definition and interpretation of constraint in evolution. Evolution 43:516-539.

Griffiths, D. 1980. The feeding biology of ant-lion larvae: Prey capture, handling and utilization. Journal of Animal Ecology 49(1):99-125.

Griffiths, D. 1986. Pit construction by ant-lion larvae: A cost-benefit analysis. Journal of Animal Ecology 55(1):39-57.

Grossgeim, V. A. 1961. Nekatoriye noviye gieroglifi iz nizhniemelovikh otl'ozheniy severo-zapaadnokho Kavkaza. Trudy Krasodarskoho Filial'a Vsesoyuznoho Neftegazovoho Nauchno-Issledovatielskoho Instituta 6:202-206.

Grossmann, S., and G. Mayer-Kress. 1989. Chaos in the international arms race. Nature 337(6209):701-704.

Hammer, Ø. 1998. Computer simulation of the evolution of foraging strategies: Application to the ichnological record. Palaeontologia Electronica 1(2):1-21.

Han, Y., and R. K. Pickerill. 1994. Palichnology of the Lower Devonian Wapske Formation, Perth-Andover-Mount Carleton region, northwestern New Brunswick, eastern Canada. Atlantic Geology 30:217-245.

Hansen, T. F. 1997. Stabilizing selection and the comparative analysis of adaptation. Evolution 51(5):1341-1351.

Häntzschel, W. 1975. Trace fossils and problematica (1st supplement). *In* R. C. Moore, ed. Treatise on Invertebrate Paleontology. W (2nd ed.), Miscellanea. The Geological Society of America and The University of Kansas

Harington, A. 1977. Burrowing biology of the scorpion *Cheloctonus jonesii* Pocock (Arachnida: Scorpionida: Scorpionidae). Journal of Arachnology 5(3):243-249.

Harvey, P. H., and S. Nee. 1997. The phylogenetic foundations of behavioural ecology. Pp. 334-3349. *In* J. R. Krebs, and N. B. Davies, eds. Behavioural Ecology; An Evolutionary Approach. Blackwell Publishing, Malden, MA.

Hay, S. I., T. C. Maitland, and D. M. Paterson. 1993. The speed of diatom migration through natural and artificial substrata. Diatom Research 8(2):371-384.

Heads, S. W., D. M. Martill, and R. F. Loveridge. 2005. An exceptionally preserved antlion (Insecta, Neuroptera) with colour pattern preservation from the Cretaceous of Brazil. Palaeontology 48(6):1409-1417.

Heer, O. 1877. Flora fossilis Helvetiae. Die Vorweltliche Flora der Schweiz. (1. und 2. Lieferung (1876), 1-90; 3. und 4. Lieferung (1877), 91-182). Wurster and Co., Zürich.

Heinrich, B., and M. J. E. Heinrich. 1984. The pit-trapping foraging strategy of the ant lion, *Myrmeleon immaculatus* DeGeer (Neuroptera: Myrmeleontidae). Behavioral Ecology and Sociobiology 14(2):151-160.

Hembree, D. I., L. M. Johnson, and R. W. Tenwalde. 2012. Neoichnology of the desert scorpion *Hadrurus arizonensis*: Burrows to biogenic cross lamination. Palaeontologia Electronica 15(1):1-34.

Higgins, J. A., and D. P. Schrag. 2006. Beyond methane: Towards a theory for the Paleocene–Eocene Thermal Maximum. Earth and Planetary Science Letters 245(3–4):523-537.

Hitchcock, E. 1858. Ichnology of New England: A report on the sandstone of the Connecticut Valley, especially its fossil footmarks, made to the government of the Commonwealth of Massachusetts. William White, Boston.

Huisman, J., and F. J. Weissing. 2001. Fundamental unpredictability in multispecies competition. The American Naturalist 157(5):488-494.

Jamer, M. C., J. A. MacEachern, and S. E. Dashtgard. 2011. Tidal-fluvial and wave-dominated estuarine valley fills: Ichnological-sedimentological-palynological comparison of central basin and lateral accretion deposits, Lower Cretaceous Glauconite and Viking Formations, Central Alberta. Recovery - 2011 CSPG CSEG CWLS Convention. Calgary, Alberta.

Janssen, P., M. Astin Nielsen, I. Hirsch, D. Svensson, P.-G. Gillberg, and L. Hultin. 2008. A novel method to assess gastric accommodation and peristaltic motility in conscious rats. Scandinavian Journal of Gastroenterology 43(1):34-43.

Jarzembowshi, E. A., D. Azar, and A. Nel. 2008. A new chironomid (Insecta: Diptera) from Wealden amber (Lower Cretaceous) of the Isle of Wight (UK). Geologica Acta 6(3):285-291.

Jensen, D. D. 1961. Operationism and the question "Is this behavior learned or innate?". Behaviour 17(1):1-8.

Jeong, K., and A. A. Ekdale. 1996. Fractal dimensions of invertebrate trace fossils: Applications in paleoethologic analysis of animal burrowing behavior. Geological Society of America Abstracts with Programs 28(7):A107.

Jeong, K., and A. A. Ekdale. 1997. Geometric modeling of branching patterns in the trace fossil *Chondrites*. Geological Society of America Abstracts with Programs 29(6):A107.

Kaston, B. J. 1964. The evolution of spider webs. American Zoologist 4(2):191-207.

Katrak, G., S. Dittmann, and L. Seuront. 2008. Spatial variation in burrow morphology of the mud shore crab *Helograpsus haswellianus* (Brachyura, Grapsidae) in South Australian saltmarshes. Marine and Freshwater Research 59(10):902-911.

Kauffman, S. A. 1991. Antichaos and adaption. Scientific American 265(2):78-84.

Kauffman, S. A. 1995. At Home in the Universe: The Search for the Laws of Self-Organization and Complexity. Oxford University Press, New York.

Kelsey, D. 1988. The economics of chaos or the chaos of economics. Oxford Economic Papers 40(1):1-31.

Kendler, K. S., and R. J. Greenspan. 2006. The nature of genetic influences on behavior: lessons from "simpler" organisms. The American Journal of Psychiatry 163(10):1683-1694.

Kjellesvig-Waering, E. N. 1986. A restudy of the fossil Scorpionida of the world. Palaeontographica Americana 55:1-287.

Klecker, R., P. Bentham, S. Palmer-Koleman, and J. Jaminski. 2001. A recent petroleum-geologic evaluation of the Central Carpathian Depression, Southeastern Poland. Marine and Petroleum Geology 18(1):65-85.

Knaust, D. 2012. Trace-fossil systematics. Pp. 79-101. *In* D. Knaust, and R. G. Bromley, eds. Trace Fossils as Indicators of Sedimentary Environments. Elsevier, New York.

Koy, K. A., and R. E. Plotnick. 2010. Ichnofossil morphology as a response to resource distribution: Insights from modern invertebrate foraging. Palaeogeography, Palaeoclimatology, Palaeoecology 292(1-2):272-281.

Kozur, H., K. Krainer, and H. Mostler. 1996. Ichnology and sedimentology of the early Permian deep-water deposits from the Lercara-Roccapalumba area (Western Sicily, Italy). Facies 34(1):123-150.

Kroodsma, D. E., and R. A. Canady. 1985. Differences in repertoire size, singing behavior, and associated neuroanatomy among marsh wren populations have a genetic basis. The Auk 102(3):439-446.

Książkiewicz, M. 1958. Stratigraphy of the Magura Series in the Średni Beskid (Carpathians). Instyut Geologiczny Biuletyn 153:43-96.

Książkiewicz, M. 1968. O niektórych problematykach z fliszu Karpat Polskich (Czesc III). Rocznik Polskiego Towarzystwa Geologiczego 38:3-17.

Książkiewicz, M. 1970. Observations on the ichnofauna of the Polish Carpathians. Pp. 283-322. *In* T. P. Crimes, and J. C. Harper, eds. Trace Fossils. Geol. J. Special Issues.

Książkiewicz, M. 1977. Trace fossils in the flysch of the Polish Carpathians. Palaeontologia Polonica 36:1-208.

Lauder, G. V. 1986. Homology, analogy, and the evolution of behavior. Pp. 9-40. *In* M. H. Nitecki, and J. A. Kitchell, eds. Evolution of Animal Behavior. Oxford University Press, New York.

Le Comber, S. C., A. C. Spinks, N. C. Bennett, J. U. M. Jarvis, and C. G. Faulkes. 2002. Fractal dimension of African mole-rat burrows. Canadian Journal of Zoology 80(3):436-441.

Lear, C. H., H. Elderfield, and P. A. Wilson. 2000. Cenozoic deep-sea temperatures and global ice volumes from Mg/Ca in benthic foraminiferal calcite. Science 287(5451):269-272.

Legendre, P., F.-J. Lapointe, and P. Casgrain. 1994. Modeling brain evolution from behavior: A permutational regression approach. Evolution 48(5):1487-1499.

Lehane, J. R., and A. A. Ekdale. 2013. Fractal analysis of graphoglyptid trace fossils. Palaios 28(1):23-32.

Lehane, J. R., and A. A. Ekdale. 2014. Analytical tools for quantifying the morphology of invertebrate trace fossils. Journal of Paleontology 88(4):747-759.

Leszczyński, S. 1991a. Oxygen-related controls on predepositional ichnofacies in turbidites, Guipúzcoan Flysch (Albian-Lower Eocene), Northern Spain. Palaios 6(3):271-280.

Leszczyński, S. 1991b. Trace-fossil tiering in flysch sediments: Examples from the Guipúzcoan flysch (Cretaceous-Paleogene), northern Spain. Palaeogeography, Palaeoclimatology, Palaeoecology 88(3-4):167-184.

Levin, L. A. 1994. Paleoecology and ecology of xenophyophores. Palaios 9:32-41.

Levinsen, G. 1882. Systematisk-geografisk Oversigt over de nordiske Annulata, Gephyrea, Chaetognathi og Balanoglossi. Videnskabelige Meddelelser fra Dansk naturhistorisk Forening i Köbenhavn:92-348.

Levinton, J., and B. Kelaher. 2004. Opposing organizing forces of deposit-feeding marine communities. Journal of Experimental Marine Biology and Ecology 300(1–2):65-82.

Levy, D. 1994. Chaos theory and strategy: Theory, application, and managerial implications. Strategic Management Journal 15(S2):167-178.

Llompart, C., and J. Wieczorek. 1997. Trace fossils from Culm Facies of Miorca Island. Prace Państwowego Instytutu Geologiczego 157:99-103.

Lloyd, A. L. 1995. The coupled logistic map: A simple model for the effects of spatial heterogeneity on population dynamics. Journal of Theoretical Biology 173(3):217-230.

Lopardo, L., M. J. Ramírez, C. Grismado, and L. A. Compagnucci. 2004. Web Building Behavior and the Phylogeny of Austrochiline Spiders. Journal of Arachnology 32(1):42-54.

López-Ruiz, R., and D. Fournier-Prunaret. 2009. Periodic and chaotic events in a discrete model of logistic type for the competitive interaction of two species. Chaos, Solitons & Fractals 41(1):334-347.

Lorenz, E. N. 1963. Deterministic nonperiodic flow. Journal of the Atmospheric Sciences 20(2):130-141.

Lorenz, K. 1965. Evolution and Modification of Behavior. The University of Chicago Press, Chicago.

Losos, J. B., T. R. Jackman, A. Larson, K. d. Queiroz, and L. Rodríguez-Schettino. 1998. Contingency and determinism in replicated adaptive radiations of island lizards. Science 279(5359):2115-2118.

Lotka, A. J. 1925. Elements of Physical Biology. Williams and Wilkins, Baltimore.

Low, S. 2003. Volcanoes of the Deep Sea. P. 45 mins.

MacEachern, J. A., and S. G. Pemberton. 1992. Ichnological aspects of Cretaceous shoreface successions and shoreface variability in the Western Interior Seaway of North America. Applications of Ichnology to Petroleum Exploration 17:57-84.

MacGinitie, G. E., and N. MacGinitie. 1968. Natural History of Marine Animals, 2nd Edition. McGraw-Hill, New York.

Magwood, J. P. A., and A. A. Ekdale. 1994. Computer-aided analysis of visually complex ichnofabrics in deep-sea sediments. Palaios 9(1):102-115.

Magyar, I., P. Müller, O. Sztanó, E. Babinszki, and M. Lantos. 2006. Oxygen-related facies in Lake Pannon deposits (Upper Miocene) at Budapest-Kőbánya. Facies 52(2):209-220.

Mandelbrot, B. B. 1983. The Fractal Geometry of Nature. W. H. Freeman and Company, New York.

Mårell, A., J. P. Ball, and A. Hofgaard. 2002. Foraging and movement paths of female reindeer: Insights from fractal analysis, correlated random walks, and Lévy flights. Canadian Journal of Zoology 80(5):854-865.

Mata, S. A., C. L. Corsetti, F. A. Corsetti, S. M. Awramik, and D. J. Bottjer. 2012. Lower Cambrian anemone burrows from the Upper Member of the Wood Canyon Formation, Death Valley Region, United States: Paleoecological and paleoenvironmental significance Palaios 27(9):594-606.

McCann, T., and R. K. Pickerill. 1988. Flysch trace fossils from the Cretaceous Kodiak Formation of Alaska. Journal of Paleontology 62(3):330-348.

McIlroy, D. 2004. Some ichnological concepts, methodologies, applications and frontiers. Geological Society, London, Special Publications 228(1):3-27.

McKeever, P. J., and H. Haubold. 1996. Reclassification of vertebrate trackways from the Permian of Scotland and related forms from Arizona and Germany. Journal of Paleontology 70(6):1011-1022.

McLennan, D. A., and M. Y. Mattern. 2001. The phylogeny of the Gasterosteidae: Combining behavioral and morphological data sets. Cladistics 17(1):11-27.

Menger, K. 1926. Allgemeine räume und cartesische räume. Proceedings of the Section of Sciences, Koniklijke Akademie van Wetenschappen te Amsterdam 29:476-482, 1125-1128.

Menger, K. 1993. General spaces and cartesian spaces. Pp. 103-116. *In* G. A. Edgar, ed. Classics on Fractals. Addison-Wesley Publishing Company, Reading, MA.

Middleton, G. V., ed. 1991. Nonlinear Dynamics, Chaos and Fractals with Applications to Geological Systems. Geological Association of Canada, Toronto, Ontario.

Mikuláš, R., T. Lehotský, and O. Bábek. 2004. Trace fossils of the Moravice Formation from the southern Nízký Jeseník Mts. (Lower Carboniferous, Culm facies; Moravia, Czech Republic). Bulletin of Geosciences 79(2):81-98.

Miller, M. F., and S. E. Smail. 1997. A semiquantitative field method for evaluating bioturbation on bedding planes. Palaios 12(4):391-396.

Miller, W. 1991a. Intrastratal trace fossil zonation, Cretaceous flysch of northern California. Ichnos 1(3):161-171.

Miller, W. 1993. Trace fossil zonation in Cretaceous turbidite facies, northern California. Ichnos 3(1):11-28.

Miller, W. 2003. Paleobiology of complex trace fossils. Palaeogeography, Palaeoclimatology, Palaeoecology 192(1-4):3-14.

Miller, W., III. 1986. Discovery of trace fossils in Franciscan turbidites. Geology 14(4):343-345.

Miller, W., III. 1991b. Paleoecology of graphoglyptids. Ichnos 1:305-312.

Minter, N. J., L. A. Buatois, S. G. Lucas, S. J. Braddy, and J. A. Smith. 2006. Spiral-shaped graphoglyptids from an Early Permian intertidal flat. Geology 34(12):1057-1060.

Mishel, M. H. 1990. Reconceptualization of the Uncertainty in Illness Theory. Journal of Nursing Scholarship 22(4):256-262.

Monaco, P. 2008. Taphonomic Features of *Paleodictyon* and Other Graphoglyptid Trace Fossils in Oligo-Miocene Thin-Bedded Turbidites, Northern Apennines, Italy. Palaios 23(10):667-682.

Morris, S. C. 2003. Life's Solution: Inevitable Humans in a Lonely Universe. Cambridge University Press, Cambridge.

Morrissey, L. B., S. Braddy, C. Dodd, K. T. Higgs, and B. P. J. Williams. 2012. Trace fossils and palaeoenvironments of the Middle Devonian Caherbla Group, Dingle Peninsula, southwest Ireland. Geological Journal 47(1):1-29.

Muñoz, N. G., and L. A. Buatois. 2001. Perto La Cruz, Stop. No. 3, Guarico Formation: Excellent Nereites ichnofacies hyporelief traces of *Spirorhaphe*, *Cosmorhaphe*, *Paleodictyon*, *Helminthoida*. P. 7 pp. VI International Ichnofabric Workshop. Venezuela.

Myannil, R. 1966. O vertikalnikh norkakh zaryvaniya v Ordovikskikh izvestiyakakh Pribaltiki [A small vertically excavated cavity in Baltic Ordovician limestone]. Akademiya Nauk SSSR, Paleontologicheskiy Institut:200–207.

Nathorst, A. G. 1873. On the distribution of Arctic plants during the postglacial epoch. Journal of Botany, London New Series 2:225-228.

Nilsen, T. H., R. Shew, D., G. S. Steffens, and J. R. J. Studlick, eds. 2007. Atlas of deep-water outcrops. AAPG and Shell Exploration & Production, Tulsa, OK.

Orr, P. J. 1996. The ichnofauna of the Skiddaw Group (early Ordovician) of the Lake District, England. Geological Magazine 133(02):193-216.

Orr, P. J. 1999. Quantitative approaches to the resolution of taxonomic problems in invertebrate ichnology. Pp. 395-431. *In* D. A. T. Harper, ed. Numerical Paleobiology. John Wiley and Sons Ltd., Chichester.

Papentin, F. 1973. A Darwinian evolutionary system: III. Experiments on the evolution of feeding patterns. Journal of Theoretical Biology 39(2):431-445.

Paterson, A. M., G. P. Wallis, and R. D. Gray. 1995. Penguins, petrels, and parsimony: Does cladistic analysis of behavior reflect seabird phylogeny? Evolution 49(5):974-989.

Pawlick, J. R. 1992. Chemical ecology of the settlement of benthic marine invertebrates. Pp. 273-335. *In* M. Barnes, A. D. Ansell, and R. N. Gibson, eds. Oceanography and Marine Biology - An Annual Review.

Pemberton, S. G., and R. W. Frey. 1984. Quantitative methods in ichnology: Spatial distribution among populations. Lethaia 17(1):33-49.

Pemberton, S. G., J. A. MacEachern, M. K. Gingras, and T. D. A. Saunders. 2008. Biogenic chaos: Cryptobioturbation and the work of sedimentologically friendly organisms. Palaeogeography, Palaeoclimatology, Palaeoecology 270(3–4):273-279.

Penney, D. 2008. Dominican Amber Spiders: A Comparative Palaeontological-Neontological Approach to Identification, Faunistics, Ecology and Biogeography. Siri Scientific Press, Manchester.

Peruzzi, D. G. 1880. Osservazioni sui generi *Paleodictyon* e *Paleomeandron* dei terreni cretacei ed eocenici dell'Appennino sett. e centrale. Attii della Societ`a Toscana di Scienze Naturali Residente in Pisa, Memorie 5:3-8.

Pfefferkorn, H. W. 1971. Note on *Conostichus broadheadi* Lesquereux (Trace Fossil: Pennsylvanian). Journal of Paleontology 45(5):888-892.

Phelps, W. T. 2002. Comparative ichnology of Pleistocene eolianites and modern coastal dunes, Puerto Peñasco, Sonora, Mexico. MS. University of Utah, Salt Lake City.

Pickerill, R. K. 1980. Phanerozoic flysch trace fossil diversity—observations based on an Ordovician flysch ichnofauna from the Aroostook–Matapedia Carbonate Belt of northern New Brunswick. Canadian Journal of Earth Sciences 17(9):1259-1270.

Pickerill, R. K. 1981. Trace fossils in a Lower Palaeozoic submarine canyon sequence - the Siegas Formation of northwestern New Brunswick, Canada. Maritime Sediments and Atlantic Geology 17:36-58.

Pickerill, R. K., L. R. Fyffe, and W. H. Forbes. 1988. Late Ordovician-Early Silurian trace fossils from the Matapedia Group, Tobique River, western New Brunswick, Canada. II. Additional discoveries with descriptions and comments. Maritime Sediments and Atlantic Geology 24:139-148.

Piper, J., and E. Granum. 1987. Computing distance transformations in convex and non-convex domains. Pattern Recognition 20(6):599-615.

Platt, B. F., S. T. Hasiotis, and D. R. Hirmas. 2010. Use of low-cost multistripe laser triangulation (MLT) scanning technology for three-dimensional, quantitative paleoichnological and neoichnological studies. Journal of Sedimentary Research 80(7):590-610.

Plomin, R., M. J. Owen, and P. McGuffin. 1994. The genetic basis of complex human behaviors. Science 264(5166):1733-1739.

Plotnick, R. E. 2003. Ecological and L-system based simulations of trace fossils. Palaeogeography, Palaeoclimatology, Palaeoecology 192(1-4):45-58.

Plotnick, R. E., and K. Koy. 2005. Let us prey: Simulations of grazing traces in the fossil record. Pp. 1-13. Proceedings GeoComputation 2005: 8th International Conference on GeoComputation. Ann Arbor, Michigan.

Plotnick, R. E., and K. L. Prestegaard. 1995. Fractals and multifractal models and methods in stratigraphy. Pp. 73-96. *In* C. C. Barton, and P. R. La Pointe, eds. Fractals in Petroleum Geology and Earth Processes. Plenum Press, New York.

Pocock, R. I. 1892. Description of two new genera of scorpions, with notes upon some species of *Palamnaeus*. Annals and Magazine of Natural History, series 6 9:38-49.

Poinar, G., and R. Buckley. 2012. Predatory behaviour of the social orb-weaver spider, Geratonephila burmanica n. gen., n. sp. (Araneae: Nephilidae) with its wasp prey, Cascoscelio incassus n. gen., n. sp. (Hymenoptera: Platygastridae) in Early Cretaceous Burmese amber. Historical Biology 24(5):519-525.

Poinar, G., and R. Poinar. 1999. The Amber Forest: A Reconstruction of a Vanished World. Princeton University Press, Princeton, NJ.

Polis, G. A., C. Myers, and M. Quinlan. 1986. Burrowing biology and spatial distribution of desert scorpions. Journal of Arid Environments 10:137-146.

Pool, R. 1989. Chaos theory: How big an advance? Science 245(4913):26-28.

Price, J. J., and S. M. Lanyon. 2002. Reconstructing the evolution of complex bird song in the oropendolas. Evolution 56(7):1514-1529.

Puche, H., and N.-Y. Su. 2001. Application of fractal analysis for tunnel systems of subterranean termites (Isoptera: Rhinotermitidae) under laboratory conditions. Environmental Entomology 30(3):545-549.

Pujalte, V., S. Robles, X. Orue-Etxebarria, J. I. Baceta, A. Payros, and I. F. Larruzea. 2000. Uppermost Cretaceous-Middle Eocene strata of the Basque-Cantabrian region and Western Pyrenees: A sequence stratigraphic perspective. Revista de la Sociedad Geológica de España 13(2):191-211.

Ransom, T. 2012. Behavioral responses of a native salamander to native and invasive earthworms. Biological Invasions 14(12):2601-2616.

Rasnitsyn, A. P., and D. L. J. Quicke. 2002. History of Insects. Kluwer Academic Publishing, Dordrecht.

Raup, D. M. 1966. Geometric analysis of shell coiling: General problems. Journal of Paleontology 40(5):1178-1190.

Raup, D. M., and A. Seilacher. 1969. Fossil foraging behavior: Computer simulation. Science 166(3908):994-995.

Reichenbach, T., M. Mobilia, and E. Frey. 2006. Coexistence versus extinction in the stochastic cyclic Lotka-Volterra model. Physical Review E 74(5):051907.

Ricketts, E. F., and J. Calvin. 1968. Between Pacific Tides, 4th Edition. Stanford University Press, Stanford, CA.

Riedl, R. 1977. A systems-analytical approach to macro-evolutionary phenomena. The Quarterly Review of Biology 52(4):351-370.

Risk, M. J., and V. J. Tunnicliffe. 1978. Intertidal spiral burrows; *Paraonis fulgens* and *Spiophanes wigleyi* in the Minas Basin, Bay of Fundy. Journal of Sedimentary Petrology 48(4):1287-1292.

Röder, H. 1971. Gangsysteme von *Paraonis fulgens* Levinsen 1883 (Polychaeta) in ökologischer, ethologischer und aktuopaläontologischer Sicht. Senkenbergiana Maritima 3:3-51.

Rogers, H., J. Hille Ris Lambers, R. Miller, and J. J. Tewksbury. 2012. 'Natural experiment' Demonstrates Top-Down Control of Spiders by Birds on a Landscape Level. PLoS ONE 7(9):e43446.

Romañach, S. S., and S. C. Le Comber. 2004. Measures of pocket gopher (*Thomomys bottae*) burrow geometry: Correlates of fractal dimension. Journal of Zoology 262(4):399-403.

Rona, P. A., A. Seilacher, C. de Vargas, A. J. Gooday, J. M. Bernhard, S. Bowser, C. Vetriani, C. O. Wirsen, L. Mullineaux, R. Sherrell, J. Frederick Grassle, S. Low, and R. A. Lutz. 2009. *Paleodictyon nodosum*: A living fossil on the deep-sea floor. Deep Sea Research Part II: Topical Studies in Oceanography 56(19–20):1700-1712.

Roniewicz, P., and G. Pienkowski. 1977. Trace fossils of the Podhale Flysch Basin. Pp. 273-288. *In* T. P. Crimes, and J. C. Harper, eds. Trace Fossils 2.

Rosell, J., E. Remacha, M. Zamorano, and V. Gabaldon. 1985. Estratigrafía de la cuenca turbidítica terciaria de Guipúzcoa. Comparación con la cuenca turbidítica prepirenaica central. Boletín Geológico y Minero 96:471-482.

Ruelle, D. 1979. Sensitive dependence on initial condition and turbulent behavior of dynamical systems. Annals of the New York Academy of Sciences 316(1):408-416.

Ruelle, D., and F. Takens. 1971. On the nature of turbulence. Communications in Mathematical Physics 20(3):167-192.

Russell, D. A., and R. Séguin. 1982. Reconstructions of the small Cretaceous theropod *Stenonychosaurus inequalis* and a hypothetical dinosaurid. Syllogeus 37:1-43.

Rutovitz, D. 1968. Data structures for operations on digital images. Pp. 105-133. *In* G. C. Cheng, R. S. Ledley, D. K. Pollock, and A. Rosenfeld, eds. Pictorial Pattern Recognition. Thompson, Washington DC.

Ryan, M. J. 2005. Evolution of behavior. Pp. 294-314. *In* J. J. Bolhuis, and L.-A. Giraldeau, eds. The behavior of animals: Mechanisms, function, and evolution. Blackwell Publishing, Malden, MA.

Sacco, F. 1888. Note di Paleoichnologia Italiana. Atti della Societa Italiana di Scienze Naturali 31:151-192.

Sanders, H. L. 1968. Marine Benthic Diversity: A Comparative Study. The American Naturalist 102(925):243-282.

Sanders, H. L. 1969. Benthic marine diversity and the stability-time hypothesis. Pp. 71-80. *In* G. M. Woodwell, and H. H. Smith, eds. Diversity and Stability in Ecological Systems. Brookhaven National Laboratory, Upton, NY.

Schneider, K. J. 1984. Dominance, predation, and optimal foraging in white-throated sparrow flocks. Ecology 65(6):1820-1827.

Scotese, C. R. 2010. PointTracker v7h, Version v7h. Arlington, TX.

Scotese, C. R. 2011a. The PALEOMAP Project PaleoAtlas, Volume 1, Cenozoic paleogeographic and plate tectonic reconstructions. http://www.scotese.com, Arlington, TX.

Scotese, C. R. 2011b. The PALEOMAP Project PaleoAtlas, Volume 2, Cretaceous paleogeographic and plate tectonic reconstructions. http://www.scotese.com, Arlington, TX.

Scotese, C. R. 2011c. The PALEOMAP Project PaleoAtlas, Volume 3, Triassic and Jurassic paleogeographic and plate tectonic reconstructions. http://www.scotese.com, Arlington, TX.

Scotese, C. R. 2011d. The PALEOMAP Project PaleoAtlas, Volume 4, Late Paleozoic paleogeographic and plate tectonic reconstructions. http://www.scotese.com, Arlington, TX.

Scotese, C. R. 2011e. The PALEOMAP Project PaleoAtlas, Volume 5, Early Paleozoic paleogeographic and plate tectonic reconstructions. http://www.scotese.com, Arlington, TX.

Seilacher, A. 1953. Studien zur palichnologie. I. Über die methoden der palichnologie. Neues Jahrbuch für Geologie und Paläontologie. Abhandlungen 96:421-452.

Seilacher, A. 1962. Paleontological studies on turbidite sedimentation and erosion. The Journal of Geology 70(2):227-234.

Seilacher, A. 1967. Fossil behavior. Scientific American 217:72-80.

Seilacher, A. 1974. Flysch trace fossils: Evolution of behavioural diversity in the deep-sea. Neues Jahrbuch für Geologie und Paläontologie. Monatshefte 4:233-245.

Seilacher, A. 1977. Pattern analysis of *Paleodictyon* and related trace fossils. Pp. 289-334. *In* T. P. Crimes, and J. C. Harper, eds. Trace Fossils 2: Geological Journal, Special Issue 9.

Seilacher, A. 1986. Evolution of behavior as expressed in marine trace fossils. Pp. 62-87. *In* M. H. Nitecki, and J. A. Kitchell, eds. Evolution of animal behaviour. Oxford University Press, New York.

Seilacher, A. 1989. *Spirocosmorhaphe*, a New Graphoglyptid Trace Fossil. Journal of Paleontology 63(1):116-117.

Seilacher, A. 2007. Trace Fossil Analysis. Springer-Verlag, New York.

Selden, P. A., W. A. Shear, and M. D. Sutton. 2008. Fossil evidence for the origin of spider spinnerets, and a proposed arachnid order. Proceedings of the National Academy of Sciences 105(52):20781-20785.

Shanmugam, G. 1996. High-density turbidity currents; are they sandy debris flows? Journal of Sedimentary Research 66(1):2-10.

Shorthouse, D. J., and T. G. Marples. 1980. Observations on the Burrow and Associated Behaviour of the Arid-Zone Scorpion *Urodacus Yaschenkoi* (Birula). Australian Journal of Zoology 28(4):581-590.

Slater, G. J. 2013. Phylogenetic evidence for a shift in the mode of mammalian body size evolution at the Cretaceous-Palaeogene boundary. Methods in Ecology and Evolution 4(8):734-744.

Slice, D. E. 1993. The fractal analysis of shape. Pp. 164-190. *In* L. F. Marcus, E. Bello, and A. García-Valdecasas, eds. Contributions to Morphometrics. Monografías, Museo Nacional de Ciencias Naturales, Madrid.

Southard, A. E., L. J. Edelmann, and B. D. Gelb. 2012. Role of copy number variants in structural birth defects. Pediatrics 129(4):755-763.

Stepanek, J., and G. Geyer. 1989. Spurenfossilien aus dem Kulm (Unterkarbon) des Frankenwaldes. Beringeria 1:1-55.

Stern, D. L., and V. Orgogozo. 2009. Is genetic evolution predictable? Science 323(5915):746-751.

Strogatz, S. H. 1994. Nonlinear Dynamics and Chaos: With Applications in Physics, Biology, Chemistry, and Engineering. Westview Press, Cambridge, MA.

Sujkowski, Z. L. 1957. Flysch sedimentation. Geological Society of America Bulletin 68(5):543-554.

Tchoumatchenco, P., and A. Uchman. 1999. Lower and Middle Jurassic flysch trace fossils from the Eastern Stara Planina Mountains, Bulgaria: A contribution to the evolution of Mesozoic ichnodiversity. Neues Jahrbuch für Geologie und Paläontologie - Abhandlungen 213(2):169-199.

Tchoumatchenco, P., and A. Uchman. 2001. The oldest deep-sea *Ophiomorpha* and *Scolicia* and associated trace fossils from the Upper Jurassic–Lower Cretaceous deep-water turbidite deposits of SW Bulgaria. Palaeogeography, Palaeoclimatology, Palaeoecology 169(1–2):85-99.

Thulborn, R. A. 1990. Dinosaur Tracks. Chapman and Hall, London.

Travisano, M., J. Mongold, A. Bennett, and R. Lenski. 1995. Experimental tests of the roles of adaptation, chance, and history in evolution. Science 267(5194):87-90.

Tunis, G., and A. Uchman. 1992. Trace fossils in the "Flysch del Grivo" (Ypresian) in the Julian Pre-Alps, NE Italy: Preliminary observations. Gortania 14:71-104.

Turchin, P. 1998. Quantitative Analysis of Movement: Measuring and Modeling Population Redistribution in Animals and Plants. Sinauer Associates, Inc., Sunderland, MA.

Turcotte, D. L. 1991. Nonlinear dynamics of crust and mantle. Pp. 151-184. *In* G. V. Middleton, ed. Nonlinear dynamics, chaos and fractals with applications to geological systems. Geological Association of Canada, Toronto, Ontario.

Turcotte, D. L. 1997. Fractals and Choas in Geoogy and Geophysics 2nd Edition. Cambridge University Press, New York.

Turner, C. H. 1915. Notes on the behavior of the ant-lion with emphasis on the feeding activities and letisimulation. Biological Bulletin 29(5):277-307.

Uchman, A. 1995. Taxonomy and palaeoecology of flysch trace fossils: The Marnoso-arenacea Formation and associated facies (Miocene, Northern Apenines, Italy). Beringeria 15:1-115.

Uchman, A. 1998. Taxonomy and ethology of flysch trace fossils: Revision of the Marian Książkiewicz collection and studies of complementary material. Annales Societatis Geologorum Poloniae 68:105-218.

Uchman, A. 1999. Ichnology of the Rhenodanubian Flysch (Lower Cretaceous-Eocene) in Austria and Germany. Beringeria 25:67-173.

Uchman, A. 2003. Trends in diversity, frequency and complexity of graphoglyptid trace fossils: evolutionary and palaeoenvironmental aspects. Palaeogeography, Palaeoclimatology, Palaeoecology 192(1-4):123-142.

Uchman, A. 2004. Phanerozoic history of deep-sea trace fossils. Geological Society, London, Special Publications 228(1):125-139.

Uchman, A., and H. Demircan. 1999. Trace fossils of Miocene deep-sea fan fringe deposits from the Cingöz Formation, Southern Turkey. Annales Societatis Geologorum Poloniae 69:125-135.

Uchman, A., and A. Wetzel. 2012. Deep-sea fans. Pp. 643-671. *In* D. Knaust, and R. G. Bromley, eds. Trace Fossils as Indicators of Sedimentary Environments. Elsevier, New York.

Valentine, J. W. 1973. Other interpopulation interactions may contribute the regulation of community structure. Community Ecology and Evolution:283-285.

Verbeek, P. W., and B. J. H. Verwer. 1990. Shading from shape, the eikonal equation solved by grey-weighted distance transform. Pattern Recognition Letters 11(10):681-690.

Vialov, O. S., and B. T. Golev. 1960. K sistematike *Paleodictyon* Akademie Nauk U.S.S.R. Doklady 134:175-178.

Vollrath, F., and D. P. Knight. 2001. Liquid crystalline spinning of spider silk. Nature 410(6828):541-548.

Volterra, V. 1926. Fluctuations in the abundance of a species considered mathematically. Nature 118(2972):558-560.

von Koch, H. 1904. Sur une courbe continue sans tangente, obtenue par une construction geometrique elementaire. Arkiv för Mathematik, Astronomi och Fysik 1:681-702.

von Koch, H. 1993. On a continuous curve without tangents constructible from elementary geometry. Pp. 25-45. *In* G. A. Edgar, ed. Classics on Fractals. Addison-Wesley Publishing Company, Reading, MA.

Wagle, N., N. N. Do, J. Yu, and J. L. Borke. 2005. Fractal analysis of the PDL-bone interface and implications for orthodontic tooth movement. American Journal of Orthodontics and Dentofacial Orthopedics 127(6):655-661.

Weissbrod, T., and W. K. Barthel. 1998. An Early Aptian ichnofossil assemblage zone in southern Israel, Sinae and southwestern Egypt. Journal of African Earth Sciences 26(2):225-239.

Wenzel, J. W. 1992. Behavioral Homology and Phylogeny. Annual Review of Ecology and Systematics 23(ArticleType: research-article / Full publication date: 1992 / Copyright © 1992 Annual Reviews):361-381.

Wetzel, A. 2000. Giant *Paleodictyon* in Eocene flysch. Palaeogeography, Palaeoclimatology, Palaeoecology 160(3-4):171-178.

Wetzel, A., and R. G. Bromley. 1996. Re-evaluation of the ichnogenus *Helminthopsis* - A new look at the type material. Palaeontology 39(1):1-19.

Wetzel, A., and A. Uchman. 1997. Ichnology of deep-sea fan overbank deposits of the Ganei slates (Eocene, Switzerland)— a classical flysch trace fossil locality studied first by Oswald Heer. Ichnos 5(2):139-162.

Wetzel, A., and A. Uchman. 2001. Sequential colonization of muddy turbidites in the Eocene Beloveža Formation, Carpathians, Poland. Palaeogeography, Palaeoclimatology, Palaeoecology 168(1-2):171-186.

Williams, S. C. 1966. Burrowing activities of the scorpion *Anuroctonus phaeodactylus* (Wood) (Scorpionida: Vejovidae). Proceedings of the California Academy of Sciences 34(8):419-428.

With, K. A. 1994a. Ontogenetic shifts in how grasshoppers interact with landscape structure: An analysis of movement patterns. Functional Ecology 8(4):477-485.

With, K. A. 1994b. Using fractal analysis to assess how species perceive landscape structure. Landscape Ecology 9(1):25-36.

With, K. A., S. J. Cadaret, and C. Davis. 1999. Movement responses to patch structure in experimental fractal landscapes. Ecology 80(4):1340-1353.

Wolff, T. 1977. Diversity and faunal composition of the deep-sea benthos. Nature 267(5614):780-785.

Wu, Y. S. 2008. Looking into tablets, characterization of pore structure in tablets using image analysis. PhD Dissertation. Rijksuniversiteit Groningen, Amsterdam.

Wu, Y. S., L. J. van Vliet, H. W. Frijlink, and K. van der Voort Maarschalk. 2006. The determination of relative path length as a measure for tortuosity in compacts using image analysis. European Journal of Pharmaceutical Sciences 28(5):433-440.

Yeh, C.-C. 1987. A deep water trace fossil assemblage from Wheeler Gorge, Ventura County, California. Pp. 49-55. *In* D. J. Bottjer, ed. New concepts in the use of biogenic sedimentary structures for paleoenvironmental interpretation: Volume and guidebook. The Pacific Section SEPM (Society of Economic Paleontologists and Mineralogists), Los Angeles, California.

Zschokke, S. 2003. Palaeontology: Spider-web silk from the Early Cretaceous. Nature 424(6949):636-637.

Zschokke, S. 2004. Glue droplets in fossil spider webs. European Arachnology Special Issue 1:367-374.